Transactions of the ASME®

Transactions of the ASME, Journal of Heat Transfer (ISSN 0022-1481) is published bi-monthly (Feb., Apr., June, Aug., Oct., Dec.) by The American Society of Mechanical Engineers, Three Park Avenue, New York, NY 10016. Periodicals postage paid at New York, NY and additional mailing offices. POSTMASTER: Send address changes to Transactions of the ASME, Journal of Heat Transfer, c/o THE AMERICAN SOCIETY OF MECHANICAL ENGINEERS, 22 Law Drive, Box 2300, Fairfield, NJ 07007-2300. **CHANGES OF ADDRESS** must be received at Society headquarters seven weeks before they are to be effective. Please send old label and new address. **STATEMENT from By-Laws.** The Society shall not be responsible for statements or opinions advanced in papers or ... printed in its publications (B7.1, Para. 3), **COPYRIGHT** © **2003** by The American Society of Mechanical Engineers. For authorization to photocopy material for internal or personal use under those circumstances not falling within the fair use provisions of the Copyright Act, contact the Copyright Clearance Center (CCC), 222 Rosewood Drive, Danvers, MA 01923, tel: 978-750-8400, *www.copyright.com.* Request for special permission or bulk copying should be addressed to Reprints/Permission Department. **INDEXED** by Applied Mechanics Reviews and Engineering Information, Inc. Canadian Goods & Services Tax Registration #126148048.

Journal of Heat Transfer

Published Bimonthly by The American Society of Mechanical Engineers

VOLUME 125 • NUMBER 5 • OCTOBER 2003

TECHNICAL PAPERS

(Contents continued on inside back cover)

This journal is printed on acid-free paper, which exceeds the ANSI Z39.48-1992 specification for permanence of paper and library materials. ♾™
♲ 85% recycled content, including 10% post-consumer fibers.

Journal of Heat Transfer Volume 125, Number 5 OCTOBER 2003

The ASME Journal of Heat Transfer is abstracted and indexed in the following:

Applied Science and Technology Index, AMR Abstracts Database, Chemical Abstracts, Chemical Engineering and Biotechnology Abstracts (Electronic equivalent of Process and Chemical Engineering), Civil Engineering Abstracts, Compendex (The electronic equivalent of Engineering Index), Corrosion Abstracts, Current Contents, E & P Health, Safety, and Environment, Ei EncompassLit, Engineered Materials Abstracts, Engineering Index, Enviroline (The electronic equivalent of Environment Abstracts), Environment Abstracts, Environmental Engineering Abstracts, Environmental Science and Pollution Management, Fluidex, Fuel and Energy Abstracts, Index to Scientific Reviews, INSPEC, International Building Services Abstracts, Mechanical & Transportation Engineering Abstracts, Mechanical Engineering Abstracts, METADEX (The electronic equivalent of Metals Abstracts and Alloys Index), Petroleum Abstracts, Process and Chemical Engineering, Referativnyi Zhurnal, Science Citation Index, SciSearch (The electronic equivalent of Science Citation Index), Theoretical Chemical Engineering

Variable Property and Temperature Ratio Effects on Nusselt Numbers in a Rectangular Channel With 45 Deg Angled Rib Turbulators

G. I. Mahmood

P. M. Ligrani

K. Chen

Convective Heat Transfer Laboratory,
Department of Mechanical Engineering,
University of Utah,
Salt Lake City, UT 84112

Measured local and spatially-averaged Nusselt numbers and friction factors (all time-averaged) are presented which show the effects of temperature ratio and variable properties in a rectangular channel with rib turbulators, and an aspect ratio of 4. The ratio of air inlet stagnation temperature to local surface temperature T_{oi}/T_w varies from 0.66 to 0.95, and Reynolds numbers based on channel height range from 10,000 to 83,700. The square cross-section ribs are placed on two opposite surfaces, and are oriented at angles of +45 deg and −45 deg, respectively, with respect to the bulk flow direction. The ratio of rib height to channel hydraulic diameter is 0.078, the rib pitch-to-height ratio is 10, and the ribs block 25 percent of the channel cross-sectional area. Ratios of globally-averaged rib Nusselt numbers to baseline, constant property Nusselt numbers, $\overline{\overline{Nu}}/Nu_{o,cp}$, increase from 2.69 to 3.10 as the temperature ratio T_{oi}/T_w decreases from 0.95 to 0.66 (provided Reynolds number Re_H is approximately constant). Friction factor ratios $f/f_{o,cp}$ then decrease as T_{oi}/T_w decreases over this same range of values. In each case, a correlation equation is given which matches the measured global variations. Such global changes are a result of local Nusselt number ratio increases with temperature ratio, which are especially pronounced on the flat surfaces just upstream and just downstream of individual ribs. Thermal performance parameters are also given, which are somewhat lower in the ribbed channel than in channels with dimples and/or protrusions mostly because of higher rib form drag and friction factors. [DOI: 10.1115/1.1589503]

Keywords: Augmentation, Heat Transfer, Internal, Roughness, Turbulent, Rrb Turbulators

Introduction

Variable property effects are important in internal passages whenever the ratio of surface temperature to local mixed mean temperature is significantly different from one. This occurs in a variety of applications, including electronics cooling, heat exchangers, internal parts of turbine airfoils, and bio-medical devices. Changes to local heat transfer behavior occur in these situations (relative to situations with near unity temperature ratios) because of fluid property variations with internal passage location. The properties having the greatest influence on local Nusselt number behavior are those which then affect the largest changes to diffusion and advection of thermal energy: molecular thermal conductivity, absolute viscosity, specific heat, and static density. Static density variations can also induce buoyancy driven Nusselt number variations, provided forced flow velocities are approximately the same magnitude as the buoyancy driven fluid velocities. In many situations, this can occur near surfaces (where streamwise flow speeds are quite low) even though spatially-averaged velocities are high enough to insure the presence of fully turbulent flow [1].

Only a handful of papers consider the effects of temperature ratio and/or variable properties on flow and heat transfer in internal passages. Of these, Dipprey and Sabersky [2] examine the effects of different values of the molecular Prandtl number on heat transfer coefficients and friction factors in tubes with water and closed-packed sand-grain roughness on the walls. Results presented for different wall-to-fluid temperature differences, and different water Prandtl numbers show that average heat transfer coefficients generally increase as Pr decreases, and that thermal performance parameter magnitudes decrease as the Prandtl number increases. Bo et al. [3] describe numerical predictions of buoyancy-influenced flows in a heated square smooth duct rotating in an orthogonal mode. Their results in the developing duct flow show that turbulent intensity and Nusselt numbers are different in the rotating buoyant flow than in constant density flow. Parsons et al. [4] present experimental results which show the influences of buoyancy due to rotation on surface Nusselt numbers in two-pass square channels with angled-ribs. The influences of changing the channel orientation with respect to the axis of rotation are considered. Heat transfer data are presented which show that the influences of Coriolis forces and cross-stream flows decrease as channel orientation changes from normal to angled. Taslim and Lengkong [5] measure Nusselt numbers in square stationary channel with 45 deg angled ribs at different ratios of air inlet temperature to wall temperature. Results measured on the ribs at the mid-half and upstream end of the channel, with wall temperatures higher than air temperatures, show that rib-averaged Nusselt number ratios are about constant (at approximately 5.0), and have negligible dependence on the temperature ratio. This is mostly because the range of temperature ratios employed are close to 1, which results in negligible changes due to variable property effects.

Another rib turbulator investigation, described by Ligrani and Mahmood [6], provides information on the effects of conduction

Contributed by the Heat Transfer Division for publication in the JOURNAL OF HEAT TRANSFER. Manuscript received by the Heat Transfer Division March 26, 2002; revision received March 20, 2003. Associate Editor: H. Lee.

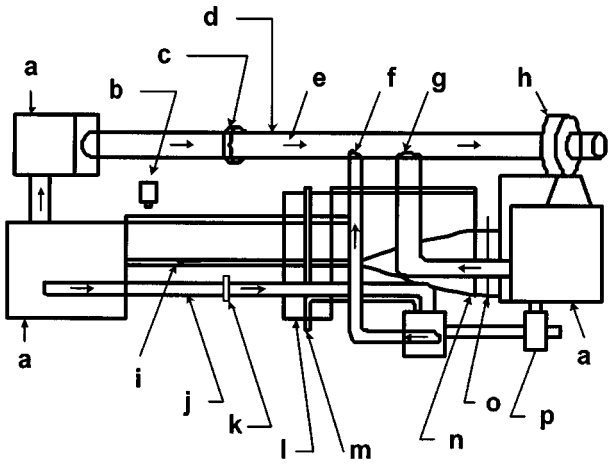

a. plenum
b. infrared camera
c. large orifice plate
d. large blower return duct
e. arrows show flow direction
f. large blower bleed air return
g. large blower by-pass
h. large blower
i. test section
j. small blower return duct
k. small orifice plate
l. boundary layer bleed-off plenum
m. bleed air return
n. inlet nozzle
o. flow straighteners
p. small blower

Fig. 1 Schematic diagram of experimental apparatus used for heat transfer measurements.

within the ribbed test surface on Nusselt number distributions. Some of the results presented show that local Nusselt numbers along the rib top are reduced substantially by three-dimensional rib conduction. Thurman and Poinsatte [7] employ liquid crystals to investigate heat transfer in a three-pass serpentine passage with 90 deg ribs and bleed holes. According to the authors, heat transfer enhancements are greater for ribs near bleed holes, compared to ribs between holes. Surface Nusselt number distributions for both configurations change as the flow rates are altered through bleed holes which are located upstream. Cho et al. [8] employ naphthalene sublimation techniques to measure surface Sherwood numbers in square passages with 10 different rib configurations. Significantly different vortex structures are produced by parallel rib arrays, crossed rib arrays, and rib arrays with gaps, which result in important changes to local and spatially-averaged Sherwood number ratios, and friction factor ratios.

The present experimental study is conducted using a large-scale test section, without rotation, so that detailed, spatially resolved surface heat transfer coefficients and friction factors can be measured. Of particular interest are the effects of variable properties, and the ratio of fluid inlet stagnation temperature to local surface temperature, on local Nusselt numbers, spatially averaged Nusselt numbers, globally-averaged friction factors, and thermal performance parameters. A single-pass channel with aspect ratio of 4 is employed, which models internal cooling passages employed near the mid-chord and trailing edge regions of turbine airfoils used in gas turbine engines for utility power generation. The ribs are placed so that they are perpendicular to each other on the two widest, opposite walls of the channel with 45 deg angles with respect to the streamwise flow direction. Data are measured with Reynolds number based on channel height Re_H varying from 10,300 to 83,700, and magnitudes of the temperature ratio T_{oi}/T_w varying from 0.66 to 0.93. Because no similar investigation of heat transfer and friction factors in a channel with rib turbulators is available in the literature, the results given in the present paper are new and unique. Although these results are directly applicable to internal cooling of turbine airfoils, they also have application to other devices, including components employed for cooling of electronic devices, bio-medical devices, combustion chamber liners, and heat exchanges.

Experimental Apparatus and Procedures

The overall experimental apparatus (but not the test section) is similar to the one described by Mahmood and Ligrani [9] and Ligrani et al. [10]. A brief description of this apparatus is also presented here.

Channel and Test Surface for Heat Transfer Measurements. A schematic of the facility used for heat transfer measurements is shown in Fig. 1. The air used within the facility is circulated in a closed-loop. One of three circuits is employed, depending upon the Reynolds number and flow rate requirements in the test section. In each case, the air mass flow rate from the test section is measured (upstream of whichever blower is employed) using an ASME standard orifice plate and Validyne M10 digital pressure manometer. The blower then exits into a series of two plenums (0.9 m square and 0.75 m square). A Bonneville cross-flow heat exchanger is located between two of these plenums, and is cooled with liquid nitrogen at flow rate appropriate to give the desired air temperature at the exit of the heat exchanger. As the air exits the heat exchanger, it enters the second plenum, from which the air passes into a rectangular bell mouth inlet, followed by a honeycomb, two screens, and a two-dimensional nozzle with a contraction ratio of 5.6. This nozzle leads to a rectangular cross-section, 411 mm by 103 mm inlet duct which is 1219 mm in length. This is equivalent to 7.4 hydraulic diameters (where hydraulic diameter is 164.7 mm). Two trips are employed on the top and bottom surfaces of the inlet duct, just upstream of the test section, which follows with the same cross-section dimensions. It exits to a 0.60 m square plenum, which is followed by two pipes, each containing an orifice plate, mentioned earlier.

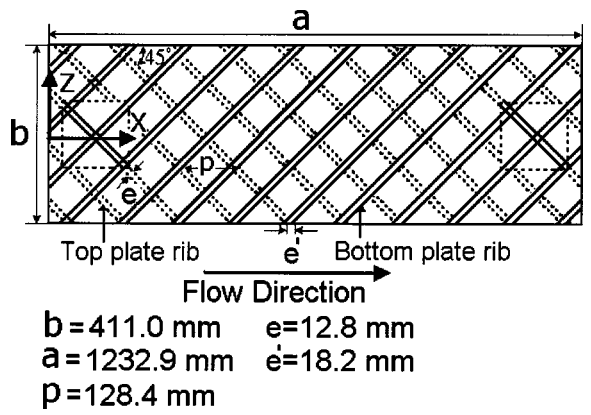

Fig. 2 Schematic diagram of the rib turbulator test surface, including the dimensions and coordinate system.

Figure 2 gives the geometric details of the test surface, including rib turbulator geometry and the coordinate system employed for the measurements. A total of 13 ribs or rib segments are used on the top wall and on the bottom wall of the test section. These are arranged with 45 deg angles with respect to the streamwise flow direction, such that the ribs on opposite walls of the channel are perpendicular to each other. Each rib has 12.8 mm height and square cross-section. The ratio of rib height to hydraulic diameter is 0.078, the rib pitch-to-height ratio is 10, and the blockage provided by the ribs is 25 percent of the channel cross-sectional area. The top wall of the test section also has two cut-out regions (one at the upstream end and one at the downstream end) where a zinc-selenide window can be installed to allow the infrared camera to view a portion of the test surface on the bottom wall. When this window is not in use, inserts with ribs (which exactly match the adjacent rib turbulators on the top wall) are used in its place.

All exterior surfaces of the facility (including the nozzle, inlet duct, and test section) are insulated with Styrofoam ($k=0.024$ W/mK), or 2 to 3 layers of 2.54 cm thick, Elastomer Products black neoprene foam insulation ($k=0.038$ W/mK) to minimize heat transfer to and from the air stream. Calibrated copper-constantan thermocouples are located between the three layers of insulation to determine conduction losses. Between the first layer and the 3.2 mm thick acrylic test surfaces are custom-made Electrofilm etched-foil heaters (each encapsulated between two thin layers of Kapton) to provide a constant heat flux boundary condition on the test surface. The acrylic surfaces, which are adjacent to the airstream, contain 35 copper-constantan thermocouples, which are placed within the ribs, within the flat portions of the test surface between the ribs, and in the smooth side walls. Each of these thermocouples is located 0.051 cm just below this surface to provide measurements of local surface temperatures, after correction for thermal contact resistance and temperature drop through the 0.051 cm thickness of acrylic. This correction is determined by measuring surface temperature distributions using calibrated liquid crystals. Acrylic is chosen because of its low thermal conductivity ($k=0.16$ W/mK at 20°C) to minimize streamwise and spanwise conduction along the test surface, and thus, minimize ''smearing'' of spatially varying temperature gradients along the test surface. The power to the foil heaters is controlled and regulated using variac power supply devices. Energy balances, performed on the heated test surface, then allow determination of local magnitudes of the convective heat flux.

Local Nusselt Number Measurement. The mixed-mean stagnation temperature of the air entering the test section is measured using five calibrated copper-constantan thermocouples spread across the inlet cross-section. To determine this temperature, thermocouple-measured temperatures are corrected for thermocouple wire conduction losses [11], channel velocity variations [12], as well as for the differences between stagnation and recovery temperature [11]. Magnitudes of the local mixed mean temperatures at different locations though the test section, T_{mx}, are then determined using energy balances, and the mixed mean temperature at the inlet of the test section. Because of the way in which it is measured, this inlet stagnation temperature T_{oi} is also a mixed mean value, and thus, determined over the cross-sectional area of the test section inlet. The thermal conductivity k used to determine local Nusselt numbers is based on this inlet stagnation temperature, T_{oi}. All measurements used to determine such Nusselt numbers are obtained when the test facility is at steady state.

To determine the surface heat flux (used to calculate heat transfer coefficients and local Nusselt numbers), the convective power levels provided by the etched foil heaters are divided by flat test surface areas. Spatially resolved temperature distributions along the rib turbulator test surface are determined using infrared imaging in conjunction with thermocouples, energy balances, and *in situ* calibration procedures. To accomplish this, the infrared radiation emitted by the heated interior surface of the channel is captured using a VideoTherm 340 Infrared Imaging Camera, which operates at infrared wave lengths from 8 μm to 14 μm. Temperatures, measured using the calibrated, copper-constantan thermocouples distributed along the test surface adjacent to the flow, are used to perform the *in situ* calibrations simultaneously as the radiation contours from surface temperature variations are recorded.

This is accomplished as the camera views the test surface through a custom-made, zinc-selenide window (which transmits infrared wave lengths between 6 and 17 μm) as mentioned. Frost build-up on the outside of the window is eliminated using a small heated air stream. Eleven to thirteen thermocouple junction locations are usually present in the infrared field viewed by the camera. The exact spatial locations and pixel locations of these thermocouple junctions and the coordinates of a 12.7 cm by 12.7 cm field of view are known from calibration maps obtained prior to measurements.

Images from the infrared camera are recorded as 8-bit gray scale images on commercial videotape using a Panasonic AG-1960 video recorder. Images are then digitized using NIH Image v1.60 software, operated on a Power Macintosh 7500 PC computer. Subsequent software is used to convert each of 256 possible gray scale values to local Nusselt number values at each pixel location using calibration data. Each individual image covers a 300 pixel by 300 pixel area. Voltages from the thermocouples (used for measurement of air temperatures and *in situ* calibration of infrared images) are acquired using Hewlett-Packard 44422T data acquisition cards installed in a Hewlett-Packard 3497A data acquisition control unit, which is controlled by a Hewlett-Packard A4190A Series computer. Mahmood and Ligrani [9] and Sargent et al. [13] provide additional details on the infrared imaging and measurement procedures.

Friction Factor Measurement. Wall static pressures are measured along the test section simultaneously as the heat transfer measurements are conducted, using 12 side wall pressure taps, located 25.4 mm apart near the downstream portion of the test section. These measurements are made in the test section with rib turbulators, as well as in a baseline test section with smooth surfaces on all four walls. Friction factors are then determined from streamwise pressure gradient magnitudes. Pressures from the wall pressure taps are measured using Celesco LCVR pressure transducers. Signals from these transducers are processed using Celesco CD10D Carrier-Demodulators. Voltages from the Carrier-Demodulators are acquired using a Hewlett-Packard 44422A data acquisition card installed in a Hewlett-Packard 3497A data acquisition control unit, which is controlled by a Hewlett-Packard A4190A Series computer.

Uncertainty Estimates. Uncertainty estimates are based on 95 percent confidence levels, and determined using procedures

described by Kline and McClintock [14] and Moffat [15]. Uncertainty of temperatures measured with thermocouples is 0.15°C. Spatial and temperature resolutions achieved with the infrared imaging are about 0.52 mm and 0.8°C, respectively. This magnitude of temperature resolution is mostly due to uncertainty in determining the exact locations of thermocouples with respect to pixel values used for the *in situ* calibrations. Local Nusselt number ratio uncertainty is then about ± 0.13 (for a ratio of 2.00), or about ± 6.5 percent. Reynolds number uncertainty is approximately ± 1.7 percent for Re_H of 10,000.

Experimental Results and Discussion

In the discussion which follows, constant-property refers to Nusselt numbers measured when T_{oi}/T_w is approximately 1.0, and density, specific heat, viscosity, and thermal conductivity are approximately constant throughout the flow in the channel. Variable-property then refers to Nusselt numbers measured when significant variations of these properties are present, which occurs as T_{oi}/T_w becomes less than about 0.9. The T_w value used for determining T_{oi}/T_w is measured just downstream of a rib located near the outlet of the test section.

Baseline Nusselt Numbers. Both variable-property and constant-property baseline Nusselt numbers are measured in a smooth rectangular test section with smooth walls replacing the two ribbed test surfaces. Except for the absence of the ribs, all geometric characteristics of the channel are the same as when the ribbed test surfaces are installed. These measurements are made in the downstream portion of the test section, where the channel flow is hydraulically and thermally fully developed. Average values are presented, which are determined from measurements made on the top and bottom walls. Baseline Nu_o values are also time-averaged, and obtained with a constant heat flux boundary condition around the entire test section (i.e. on all four channel walls), which is the same type of thermal boundary condition which is utilized when ribs are used in the channel.

The variations of the constant-property baseline Nusselt numbers $Nu_{o,cp}$ with Reynolds number Re_{Dh} are shown in Fig. 3 for $T_{oi}/T_w = 0.93-0.94$. The values in this figure are in agreement with the Dittus-Boelter smooth circular tube correlation [16] for the entire range of Reynolds numbers Re_{Dh} shown. These constant-property baseline Nusselt numbers $Nu_{o,cp}$, are employed in the next section to normalize ribbed channel Nusselt numbers.

Figure 4 gives variable property baseline Nu_o data (which are also spatially-averaged), as dependent upon the ratio of inlet stagnation temperature to local surface temperature, T_{oi}/T_w, where

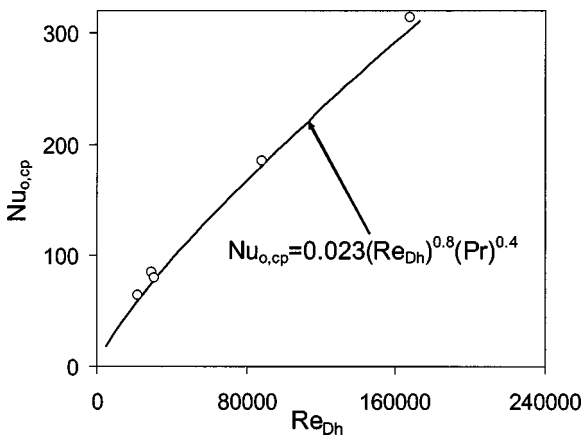

Fig. 3 Baseline, constant property Nusselt numbers, measured with smooth channel surfaces and constant heat flux boundary condition on all channel surfaces for $T_{oi}/T_w = 0.92-0.94$, as dependent upon Reynolds number Re_{Dh} based on hydraulic diameter.

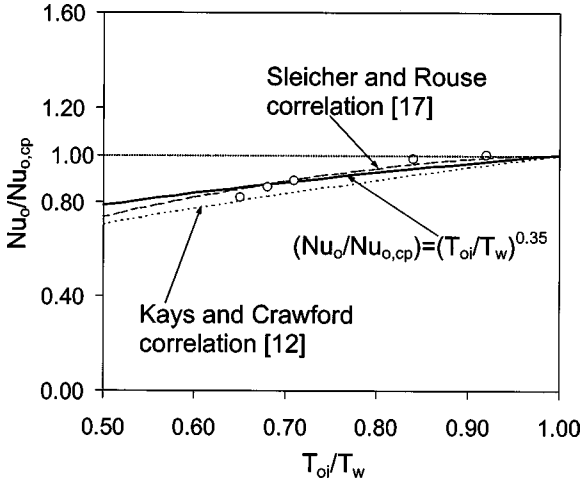

Fig. 4 Baseline, variable property Nusselt number ratios in a smooth channel, measured with a constant heat flux boundary condition on all channel surfaces, as dependent upon temperature ratio T_{oi}/T_w.

values of this parameter are as low as 0.66. Here, Re_{Dh} is approximately constant for these measurements, and ranges from 29,100 to 34,400. The data are normalized by the constant property baseline Nusselt number, $Nu_{o,cp}$, which is determined at $T_{oi}/T_w = 1.0$ and $Re_{Dh}=29{,}100$. The present data are well represented by an equation given by

$$Nu_o/Nu_{o,cp} = (T_{oi}/T_w)^n \tag{1}$$

where $n = 0.35$. Figure 4 also shows $Nu_o/Nu_{o,cp}$ variations based on two correlations given by Kays and Crawford [12] and Sleicher and Rouse [17] for variable property effects of turbulent gas flows in circular tubes with heating. Values of n for these correlations are 0.5, and approximately 0.4, respectively, which give Nu_o values which decrease relative to $Nu_{o,cp}$, as T_{oi}/T_w decreases. The present $Nu_o/Nu_{o,cp}$ results, correlated using Eq. (1), are then qualitatively consistent with the correlations from these two sources, since they also decrease as T_{oi}/T_w decreases. When uncertainty intervals are considered, the present data are then also in agreement with the correlations from Refs. [12] and [17].

Local Nusselt Numbers. Figures 5, 6, and 7 show spatially-resolved, local $Nu/Nu_{o,cp}$ variations along the test surface, measured at T_{oi}/T_w of 0.93, 0.82, and 0.74, respectively. Here, Nu is a variable property Nusselt number measured on the rib turbulator surface, and $Nu_{o,cp}$ is the constant property, baseline Nusselt number. Re_H is approximately constant for these measurements, and ranges between 18,300 and 27,400. The results are shown over about two periods of ribbed pattern on the bottom wall of the test section, and are measured when the zinc-selenide window on the top wall has no rib turbulators placed upon it. The bulk flow direction is from bottom to top in each figure, in direction of increasing X/D_h. Each distribution is time-averaged, determined from 25 instantaneous data sets measured over a time period of 25 seconds. The $Nu/Nu_{o,cp}$ contour level scale is the same in each of these three figures, and is included in each figure.

The darker diagonal contour regions in Fig. 5 represent $Nu/Nu_{o,cp}$ variations on the tops of the ribs. Here, $Nu/Nu_{o,cp}$ values are highest near the upstream and downstream edges of the rib top, mostly because of re-initialization of thermal boundary layers at these locations, a small re-circulation flow zone, and skewing of the shear layer which forms in the flow near these locations. These rib-top Nusselt number ratios are then much higher than ones measured on the flat surfaces between the ribs. Flat surface $Nu/Nu_{o,cp}$ values are lowest just downstream of the rib at slightly larger X/D_h values. A region of re-circulating flow, positioned just

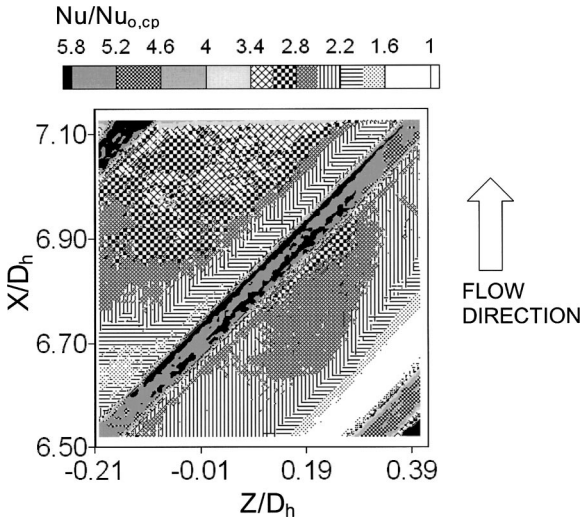

Fig. 5 Time-averaged local Nusselt number ratio Nu/Nu$_{o,cp}$ distribution along the rib turbulator test surface for Re$_H$ =18,300 and T_{oi}/T_w=0.93.

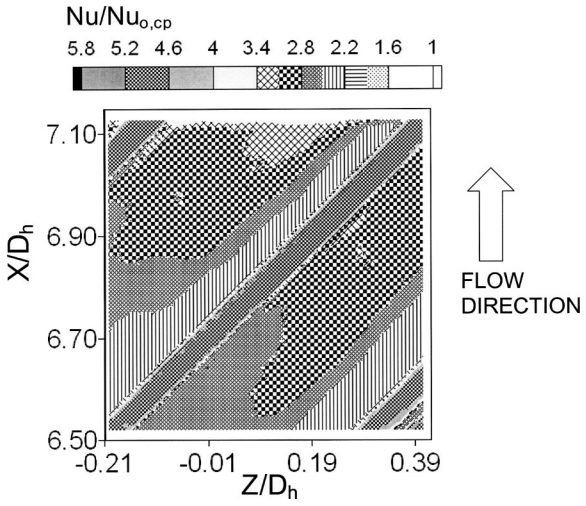

Fig. 7 Time-averaged local Nusselt number ratio Nu/Nu$_{o,cp}$ distribution along the rib turbulator test surface for Re$_H$ =27,400 and T_{oi}/T_w=0.74. Nu/Nu$_{o,cp}$ scale is same as one shown in Figure 5.

downstream of the rib, is responsible for this reduction, mostly because of reduced advection very near this part of the test surface. Nu/Nu$_{o,cp}$ values then increase continuously as X/D_h increases in this region, and the shear layer (which forms above the re-circulating flow region) reattaches to the flat test surface. This trend continues over much of the flat surface, until the flow reaches locations just upstream of the next rib. Here, local Nu/Nu$_{o,cp}$ values then decrease slightly as X/D_h increases because of weak re-circulating flows over a narrow region along the upstream side of the second rib. This pattern of surface Nu/Nu$_{o,cp}$ variations then repeats itself along the test surface, as additional ribs are encountered.

Surface distributions of Nu/Nu$_{o,cp}$, measured at lower values of T_{oi}/T_w, are presented in Figs. 6 and 7. Even though overall qualitative distributions are similar, quantitative magnitudes of Nu/Nu$_{o,cp}$ increase at many surface locations as T_{oi}/T_w decreases. Variations are especially apparent on the flat surfaces just downstream and just upstream of individual ribs. This is due to local temperature gradients in the re-circulating flows, and the shear layers that form just above them. Here, efficient mixing between the hot fluid originating at the wall, and cooler fluid from the central parts of the channel, gives increased transport levels as the temperature differences in the fluid become larger. Examination of the data in Figs. 5–7 reveals that local Nu/Nu$_{o,cp}$ magnitudes increase as the temperature ratio decreases from 0.93 to 0.74 at most all flat surface locations. Somewhat different Nusselt number ratio behavior is then apparent on the ribs themselves, since local Nu/Nu$_{o,cp}$ variations with T_{oi}/T_w at these surface locations are less significant.

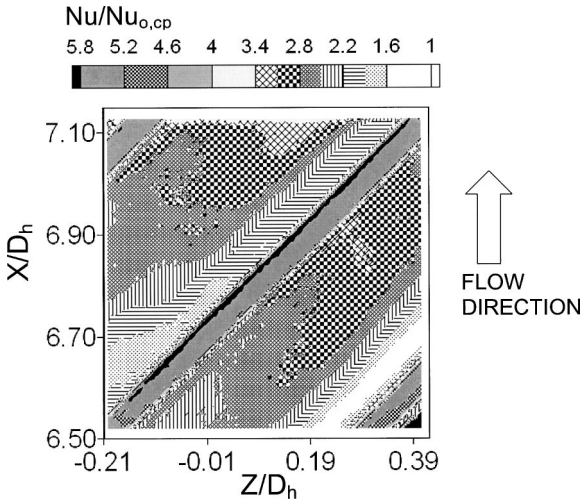

Fig. 6 Time-averaged local Nusselt number ratio Nu/Nu$_{o,cp}$ distribution along the rib turbulator test surface for Re$_H$ =22,100 and T_{oi}/T_w=0.82. Nu/Nu$_{o,cp}$ scale is same as one shown in Figure 5.

Note that the local Nusselt number data in Figs. 5, 6, and 7 are normalized using constant property baseline Nusselt numbers, Nu$_{o,cp}$, as mentioned. If variable property, baseline Nusselt numbers (such as the ones shown in Fig. 4 at each value of T_{oi}/T_w) are used instead, the differences between the data in these three figures would be even more substantial on a percentage basis.

The influences of temperature ratio on local Nu/Nu$_{o,cp}$ values are further illustrated by the results shown in Figs. 8 and 9. These data are obtained from the results presented in Figs. 5, 6, and 7, as well as from an additional data set measured at Re$_H$=27,400 and T_{oi}/T_w=0.66. The results shown in Fig. 8 show streamwise variations of Nu/Nu$_{o,cp}$ along a line of constant Z/D_h=0.0 (which is also the spanwise centerline of the test surface). Here, X/D_h =6.65 to X/D_h=6.77 correspond to surface locations upstream of the central rib, X/D_h=6.77 to X/D_h=6.83 correspond to locations on top of the central rib, and X/D_h=6.83 to X/D_h=7.13 correspond to locations which are downstream of this rib. In Fig. 9, Nu/Nu$_{o,cp}$ variations in the spanwise direction are presented along a line of constant X/D_h=6.90, also as T_{oi}/T_w decreases from 0.93 to 0.66. In this figure, Z/D_h=−0.20 to Z/D_h=0.15 and Z/D_h=0.24 to Z/D_h=0.41 correspond to spanwise locations on the flat surface between ribs. Z/D_h=0.15 to Z/D_h=0.24 are then located on top of the central rib. Like the data presented in Figs. 5–7, the results in Figs. 8 and 9 are obtained at Re$_H$ values between 18,300 and 27,400. Because Nusselt number effects over this range of Reynolds numbers are very small or completely negligible (as T_{oi}/T_w is held constant), the effects of variations of this parameter can be neglected compared to variations of the temperature ratio, T_{oi}/T_w.

Significant quantitative variations of Nu/Nu$_{o,cp}$ are apparent in Figs. 8 and 9 as the temperature ratio T_{oi}/T_w changes. Increases at all flat surface locations between the ribs are apparent as the temperature ratio decreases, especially at locations which are very close to the ribs. This further illustrates the connection between

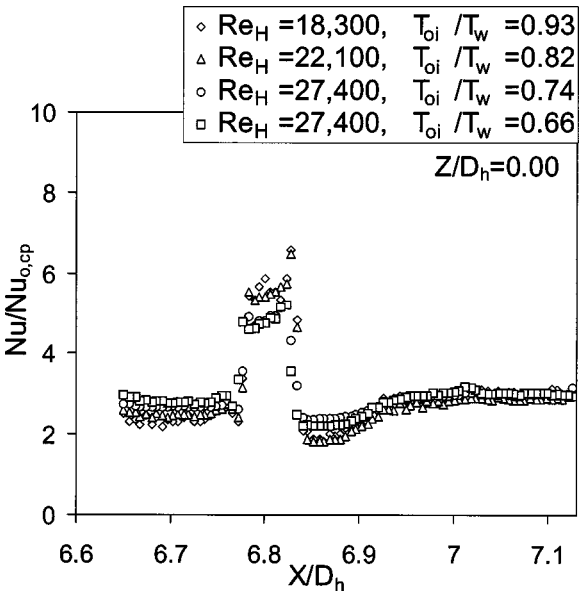

Fig. 8 Local Nusselt number ratios $Nu/Nu_{o,cp}$ as they vary in the normalized streamwise direction at $Z/D_h=0.00$ for different temperature ratios T_{oi}/T_w.

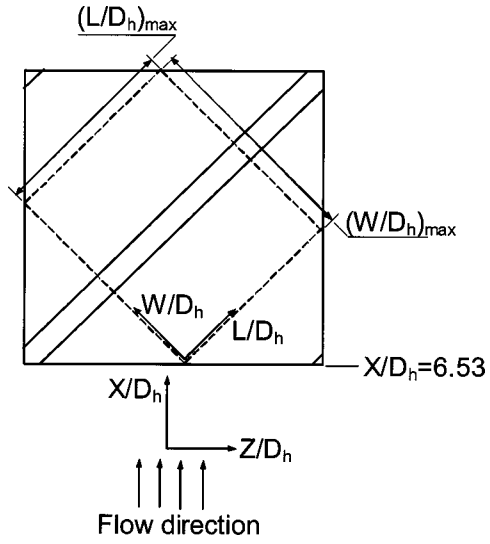

Fig. 10 Schematic diagram of a portion of the bottom rib turbulator test surface showing the layout of three ribs and the local coordinates W/D_h and L/D_h, which are oriented perpendicular and parallel to the ribs, respectively.

local flow structure and temperature ratio effects, especially on surfaces beneath flow re-circulation zones, where local advection velocities from the forced flow are relatively low, and increased buoyancy aids convection processes as T_{oi}/T_w decreases. Nusselt number ratios generally decrease with decreasing temperature ratio on tops of the ribs, where $Nu/Nu_{o,cp}$ values range from 4.5 to as high as 7. Here, the influences of the temperature ratio are connected to high velocities in the flow near to the rib tops, a small flow recirculation zone, and to thin, skewed, and newly initialized thermal boundary layers.

Spatially Averaged Nusselt Numbers. Spatially averaged Nusselt number ratios, $\overline{Nu}/Nu_{o,cp}$, are determined by averaging local, time-averaged data (such as that shown in Figs. 5, 6, and 7), in directions which are oriented perpendicular to and parallel to the rib direction, as shown in Fig. 10. In this particular case, this rib is located on the bottom test surface. The W/D_h coordinate is then directed perpendicular to such a rib, and the L/D_h coordinate is oriented in a direction which is parallel to this rib, as shown in Fig. 10. $(W/D_h)_{max}$ is then the normal pitch of the ribs, or the spacing between adjacent ribs in a direction normal to the ribs. The origin of the W/D_h and L/D_h coordinates is positioned at $X/D_h=6.53$. The area enclosed by $(L/D_h)_{max}$ and $(W/D_h)_{max}$ then represents one complete period of rib turbulator surface geometry.

Figures 11 and 12 show $\overline{Nu}/Nu_{o,cp}$ variations for T_{oi}/T_w from 0.66 to 0.93. As for the data in the previous figures, Re_H ranges from 18,300 to 27,400, and thus, has little or no effect on the variations shown. The $\overline{Nu}/Nu_{o,cp}$ variations in Fig. 11 are averaged in the W/D_h direction, and shown as they vary with L/D_h. These data are approximately constant with L/D_h at each temperature ratio, which is important because it indicates that the thermal field is nearly fully developed. When compared at each

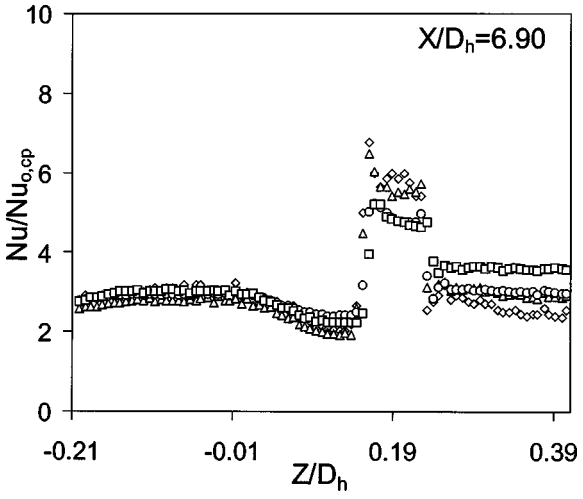

Fig. 9 Local Nusselt number ratios $Nu/Nu_{o,cp}$ as they vary in the normalized spanwise direction at $X/D_h=6.90$ for different temperature ratios T_{oi}/T_w. Symbols are defined in Figure 8.

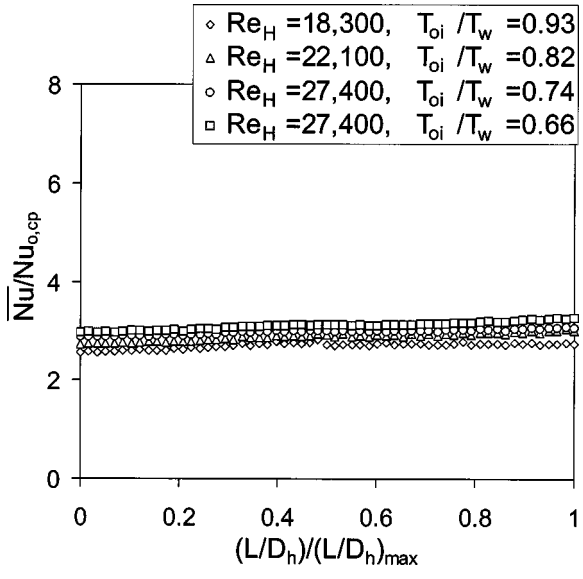

Fig. 11 Spatially-averaged Nusselt number ratios $\overline{Nu}/Nu_{o,cp}$ determined from averages in the W/D_h direction, as dependent upon the normalized L/D_h coordinate, for different values of T_{oi}/T_w.

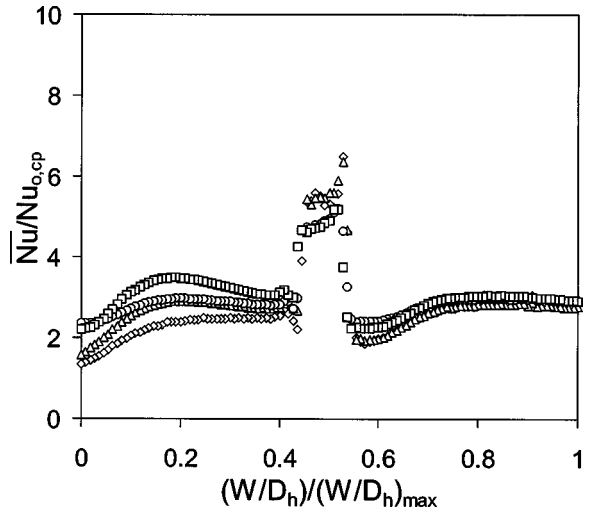

Fig. 12 Spatially-averaged Nusselt number ratios $\overline{Nu}/Nu_{o,cp}$ determined from averages in the L/D_h direction, as dependent upon the normalized W/D_h coordinate, for different values of T_{oi}/T_w. Symbols are defined in Figure 11.

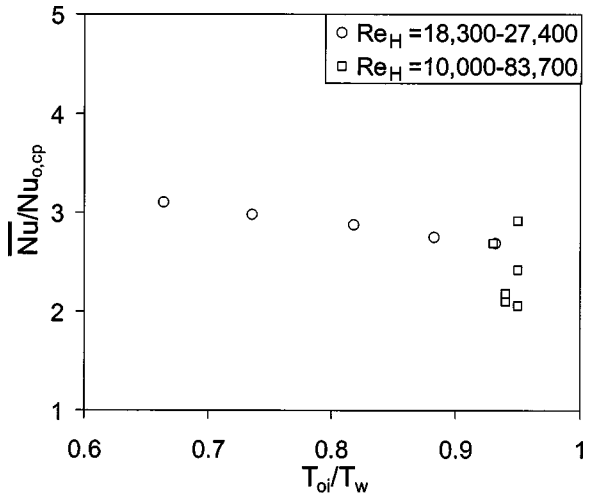

Fig. 13 Globally-averaged Nusselt number ratios $\overline{\overline{Nu}}/Nu_{o,cp}$ for fully developed flow conditions as dependent upon T_{oi}/T_w for different Re_H.

$(L/D_h)/(L/D_h)_{max}$ location, the Nusselt number ratio data in Fig. 11 also increase as T_{oi}/T_w decreases, which is consistent with the local data discussed in the previous section.

The $\overline{Nu}/Nu_{o,cp}$ distributions in Fig. 12 are shown as they vary with $(W/D_h)/(W/D_h)_{max}$, and are determined by averaging local data in the L/D_h direction. Here, the locations $0.44 \leqslant (W/D_h)/(W/D_h)_{max} \leqslant 0.54$ correspond to top of the central rib. The results in Fig. 12 thus show that $\overline{Nu}/Nu_{o,cp}$ values increase significantly on the flat surfaces, both upstream and downstream of the rib, as T_{oi}/T_w decreases. $\overline{Nu}/Nu_{o,cp}$ distributions on the rib top then generally decrease by small amounts as the temperature ratio T_{oi}/T_w decreases.

Interesting Nusselt number variations are also evident in Fig. 12 at each temperature ratio. For example, the $\overline{Nu}/Nu_{o,cp}$ data at $T_{oi}/T_w = 0.82$ initially increase with $(W/D_h)/(W/D_h)_{max}$ at values of this parameter less than 0.2, because of the augmented local mixing associated with shear layer reattachment. Nusselt number ratios then decrease slightly as $(W/D_h)/(W/D_h)_{max}$ increases further. The lowest local values in this region are then positioned just upstream of the rib (at abscissa values around 0.4), as a result of the small re-circulation zones at these locations. Dramatically higher $\overline{Nu}/Nu_{o,cp}$ values are then present on the rib itself (at $(W/D_h)/(W/D_h)_{max}$ from 0.44 to 0.54), with the highest local values positioned near the downstream edge. The lowest spatially averaged Nusselt number ratios are then present just downstream of the rib at $(W/D_h)/(W/D_h)_{max}$ from 0.54 to 0.80 because of the effects of flow recirculation at these locations. $\overline{Nu}/Nu_{o,cp}$ variations with $(W/D_h)/(W/D_h)_{max}$ at other values of T_{oi}/T_w are then qualitatively similar to the distribution for $T_{oi}/T_w = 0.82$.

According to Ligrani and Mahmood [6], three-dimensional conduction (and variable surface heat flux) along and within the test surface results in local Nusselt number ratios which are significantly lower than constant flux values along the rib top, except near the edges of rib tops, where variable flux values are slightly higher. In addition, variable flux Nusselt number ratio decreases (relative to constant flux values) on the flat regions between the ribs, near corners where the ribs join the flat surrounding surface. This last characteristic is important because it means such corners are potential hot spots, especially when located just downstream of a rib near the largest flow re-circulation zone.

Globally Averaged Nusselt Numbers and Friction Factors. Globally-averaged Nusselt numbers are determined from averages of local data over one complete period of rib turbulator geometry. As mentioned earlier, this is the rectangular region enclosed by the lengths $(L/D_h)_{max}$ and $(W/D_h)_{max}$ shown in Fig. 10. Globally-averaged friction factors are determined from wall static pressure drop measurements (at the same time as the Nusselt numbers are measured) along the portion of the test section where the flow is fully developed. In each case, the variable property Nusselt number and variable property faction factor values are normalized. In Figs. 13 and 14, constant property baseline values are employed for normalization to give $\overline{\overline{Nu}}/Nu_{o,cp}$, and $f/f_{o,cp}$, respectively. In Figs. 15 and 16, constant property rib turbulator measured values are employed for normalization to give $\overline{\overline{Nu}}/\overline{\overline{Nu}}_{cp}$, and f/f_{cp}, respectively. In all four cases, the ratios are presented as they are dependent upon the temperature ratio, T_{oi}/T_w, and are given for Re_H from 10,000 to 83,700, and for T_{oi}/T_w from 0.66 to 0.95.

The data in Figs. 13 and 14 are normalized using constant property, smooth channel values because this gives ratios which quantify magnitudes of augmentation relative to a smooth channel with no rib turbulators. The globally averaged Nusselt number ratios in Fig. 13 then increase from 2.69 to 3.10 as T_{oi}/T_w decreases from 0.95 to 0.66 (and Re_H Reynolds number is approximately constant

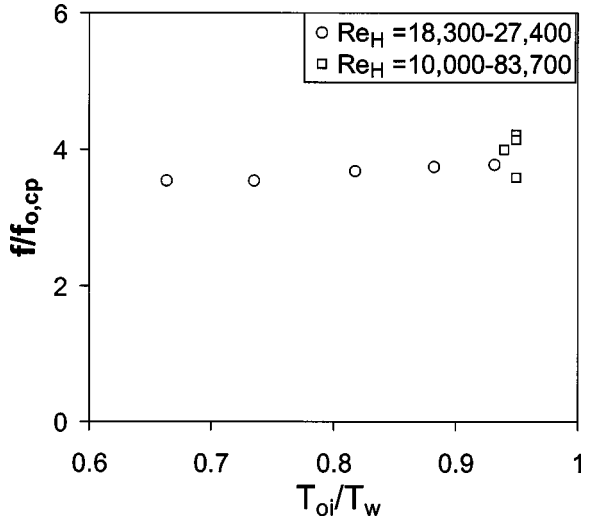

Fig. 14 Globally-averaged friction factor ratios $f/f_{o,cp}$ for fully developed flow conditions as dependent upon T_{oi}/T_w for different ranges of the Reynolds number, Re_H.

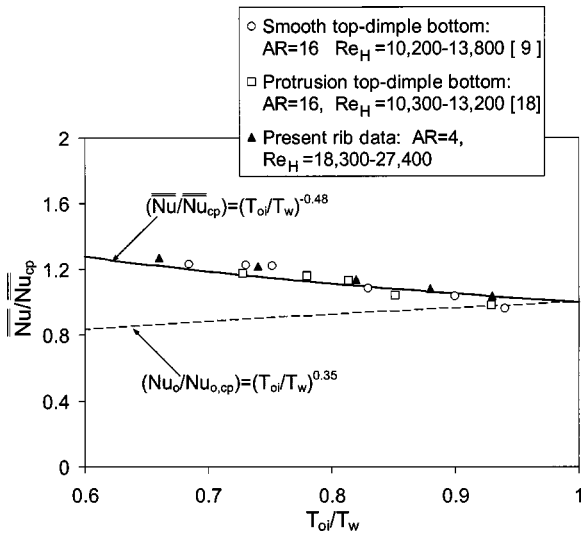

Fig. 15 Ratios of variable-property (globally-averaged) rib-turbulator Nusselt numbers to constant-property (globally-averaged) rib turbulator Nusselt numbers $\overline{\overline{Nu}}/\overline{\overline{Nu}}_{cp}$ as dependent upon the temperature ratio T_{oi}/T_w, for the present rib turbulator channel, and other heat transfer augmentation devices [9,18].

at 18,300 to 27,400). This figure also shows that the globally averaged ratio for $Re_H=10{,}000$ and $T_{oi}/T_w=0.93$ has roughly the same magnitude as data measured at about the same temperature ratio, but at different Reynolds numbers from 10,000 to 83,700. As for the data presented in other figures, this further illustrates the very weak dependence of Nusselt ratios on Reynolds number, and the strong dependence on temperature ratio. According to Ligrani and Mahmood [6], globally-averaged Nusselt number ratios decrease somewhat if three-dimensional conduction in the test surface is considered, especially for Reynolds numbers (based on channel height) greater than 60,000.

In contrast to the data in the previous figure, the variable property friction factor ratios in Fig. 14 decrease as T_{oi}/T_w decreases from 0.95 to 0.66 (and Re_H Reynolds number is approximately constant at 18,300 to 27,400). This means that the flow and thermal fields have different dependence on variable property/

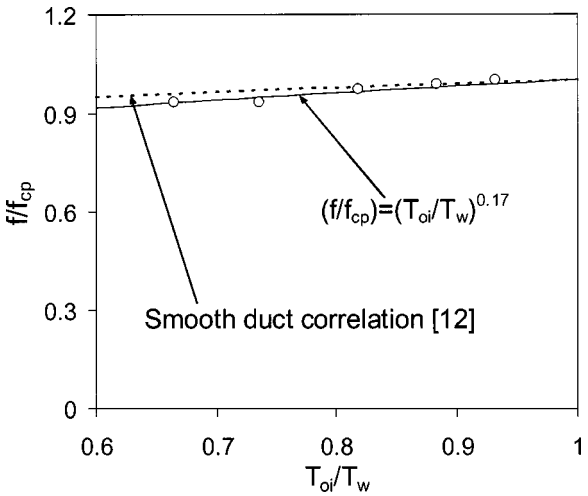

Fig. 16 Ratios of variable-property, rib turbulator friction factors to constant-property, rib turbulator friction factors f/f_{cp} as dependent upon temperature ratio T_{oi}/T_w, for the present rib turbulator channel.

temperature ratio effects, which is consistent with Kays and Crawford [12]. Figure 14 also shows that the globally-averaged friction factor ratio for $Re_H=10{,}000$ and $T_{oi}/T_w=0.95$ is just lower than values measured at similar temperature ratios, but at higher Reynolds numbers from 10,000 to 83,700. This indicates that normalized rib turbulator friction factor ratios show only slight Reynolds number dependence like normalized rib turbulator Nusselt number ratios.

The data in Figs. 15 and 16 are normalized using constant property rib turbulator values because this gives ratios which show the effects of different temperature ratios and variable properties. The present globally-averaged Nusselt number ratios in Fig. 15 are compared to values from a channel with a dimpled bottom wall and a smooth top wall [9], and to values from a channel with a dimpled bottom wall and a top wall with protrusions [18]. Note that the channel aspect ratio for these latter two cases is 16, compared to 4 for the present study. However, in spite of these differences, all three data sets presented in Fig. 15 show very similar dependence upon temperature ratio T_{oi}/T_w, and are well represented by an equation having the form

$$\overline{\overline{Nu}}/\overline{\overline{Nu}}_{cp}=(T_{oi}/T_w)^n \tag{2}$$

where $n=-0.48$. This is important because it means that heat transfer augmentations in channels with rib turbulators, dimples, or protrusions increase substantially as the ratio of inlet stagnation temperature to local surface temperature decreases.

The dependence of friction factor ratios f/f_{cp} on T_{oi}/T_w is shown in Fig. 16. These data are also given for Reynolds numbers Re_H from 10,000 to 83,700, and for T_{oi}/T_w from 0.66 to 0.95. These variable property rib turbulator data are well represented using an equation given by

$$f/f_{cp}=(T_{oi}/T_w)^n \tag{3}$$

where $n=0.17$. With this value, the present variable property friction factor ratios show slightly greater dependence on T_{oi}/T_w, than given by a correlation for smooth ducts from Ref. [12] (which is also included in Fig. 16).

Performance Parameters. The performance parameter, $(\overline{\overline{Nu}}/Nu_{o,cp})/(f/f_{o,cp})^{1/3}$, originally given by Gee and Webb [19], provides a measure of the amount of heat transfer augmentation relative to the pressure drop penalty, where each is given for the same ratio of mass flux in an internal passage with augmentation devices to mass flux in an internal passage with smooth surfaces. Figure 17 shows magnitudes of this performance parameter (as dependent upon the temperature ratio T_{oi}/T_w) for the present ribbed channel, along with values from a channel with a dimpled bottom wall and a smooth top wall [9], and values from a channel with a dimpled bottom wall and a top wall with protrusions [18]. The present data are obtained from the results presented in Figs. 13 and 14.

For each of these channel configurations, parameters increase as the temperature ratio T_{oi}/T_w decreases (and the Reynolds number is about constant) with a rate of increase which is roughly the same. This is a result of complex interactions between instantaneous secondary flows produced by the different devices, and the local temperature gradients in the fluid. According to the data in Figs. 13, 15, and 17, these interactions result in near-wall, thermal turbulent transport levels which become larger as the overall temperature gradients and overall temperature differences in the channel increase.

Also included in Fig. 17 are data from the present rib turbulator arrangement as the Reynolds number varies, and the temperature ratio is approximately constant. These results cover a range of values which are in approximate agreement with the $Re_H=10{,}000$ and $T_{oi}/T_w=0.93$ data point, which indicates low performance parameter dependence on Reynolds number Re_H.

The present rib turbulator performance parameters range from 1.73 to 2.03 as T_{oi}/T_w decreases from 0.95 to 0.66. Even though

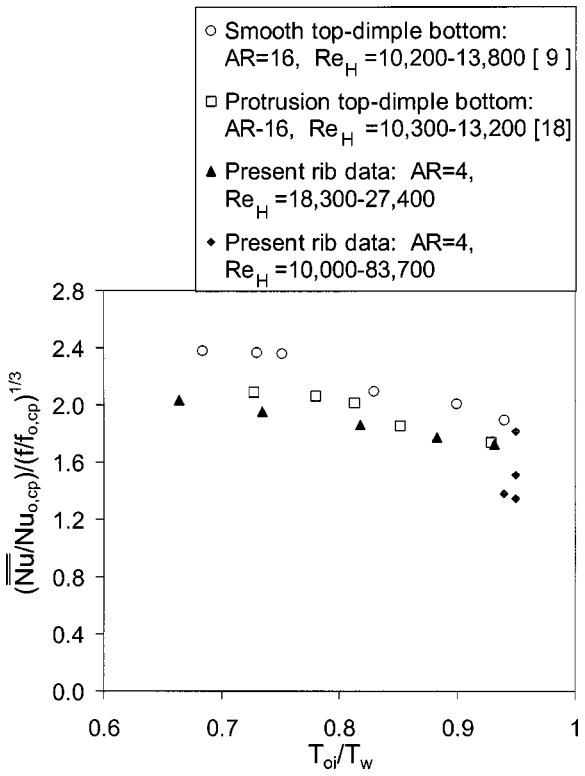

Fig. 17 Rib turbulator channel thermal performance parameters as dependent upon T_{oi}/T_w for Re_H from 10,000 to 83,700, including comparisons with thermal performance parameter magnitudes produced by other heat transfer augmentation devices [9,18].

these values are relatively high, Fig. 17 shows that they are somewhat lower than values measured at the same temperature ratios in channels with dimples and/or protrusions [9,10,18]. This is mostly due to the higher form drag and higher friction factors produced by the ribs, especially the contributions to these quantities by the flow separation and reattachment zones which are located just downstream of each rib.

Summary and Conclusions

The present results show the effects of temperature ratio and variable properties on spatially-resolved Nusselt numbers, spatially-averaged Nusselt numbers, and global friction factors in a channel with an aspect ratio of 4, and 45 deg inclined ribs (relative to the mainstream flow direction) oriented in perpendicular fashion to each other on two opposite walls. The ribs have square cross-section, $p/e=10$, $e/D_h=0.078$, and approximately 25 percent blockage of the channel cross-section. The data are given for values of the temperature ratio T_{oi}/T_w from 0.66 to 0.95, and Reynolds numbers Re_H from 10,000 to 83,700.

Globally averaged Nusselt numbers, measured in the rib turbulator channel, increase from 2.69 to 3.10 as the temperature ratio T_{oi}/T_w decreases from 0.95 to 0.66 (provided Reynolds number Re_H is approximately constant, and values are normalized by baseline, constant property Nusselt numbers to give $\overline{\overline{Nu}}/Nu_{o,cp}$). Friction factor ratios $f/f_{o,cp}$ then show different dependence on this temperature ratio, since they decrease as T_{oi}/T_w decreases from 0.95 to 0.66 (again with approximately constant Re_H). The dependence of these data on temperature ratio is given by Eqs. (2) and (3), respectively. For the former case, the rib turbulator Nusselt number ratios $\overline{\overline{Nu}}/\overline{\overline{Nu}}_{cp}$ show similar dependence on T_{oi}/T_w, as for data from other sources [9,18] for a channel with a dimpled bottom wall and a smooth top wall, and a channel with a dimpled bottom wall and a top wall with protrusions. This means that overall heat transfer augmentations in channels with rib turbulators, dimples, or protrusions increase, and that friction factor penalties in ribbed channels decrease, as channel temperature differences and overall temperature gradients become larger (provided the wall is hotter than the fluid).

These globally averaged variations in the ribbed channel are mostly a result of local Nusselt number ratio increases at all flat surface locations between the ribs as the temperature ratio T_{oi}/T_w decreases. These variations are especially apparent on the flat surfaces just upstream and just downstream of individual ribs. For the latter, this is due to the flow separation and reattachment zones located just downstream of each rib, and the local temperature gradients which develop in these flows. Local $Nu/Nu_{o,cp}$ distributions on the rib tops are then much higher than ones measured on the flat surfaces between the ribs, and generally decrease as the temperature ratio T_{oi}/T_w decreases.

Thermal performance parameters $(\overline{\overline{Nu}}/Nu_{o,cp})/(f/f_{o,cp})^{1/3}$ increase at about the same rate as the temperature ratio T_{oi}/T_w decreases for the present ribbed channel, as well as for the channels with dimples and/or protrusions (again provided that the Reynolds number is about constant). Of these arrangements, the rib turbulator values are slightly lower because of higher form drag and higher friction factors.

Acknowledgments

The work presented in this paper was sponsored by a AGTSR Advanced Gas Turbine Research Program research subcontract sponsored by the U.S. Department of Energy-National Energy Technology Laboratory through a cooperative agreement with the South Carolina Institute for Energy Studies at Clemson University.

Nomenclature

a = streamwise extent of test surface
AR = channel aspect ratio
b = spanwise extent of test surface
D_h = channel hydraulic diameter
e = rib turbulator width
e' = rib turbulator width in the streamwise direction
f = friction factor
f_o = baseline friction factor in a smooth channel with no rib turbulators
H = channel height
k = thermal conductivity
L = local coordinate in direction parallel to ribs
Nu = local Nusselt number, $\dot{q}''_o D_h/k(T_w-T_{mx})$
Nu_o = baseline Nusselt number in a smooth channel with no rib turbulators
p = streamwise pitch spacing of rib turbulators
Pr = molecular Prandtl number
$\dot{q}''_o$ = surface heat flux
Re_H = Reynolds number based on channel height
Re_{Dh} = Reynolds number based on hydraulic diameter
T = local static temperature
W = local coordinate in direction normal to ribs
X = streamwise coordinate measured from the test section inlet
Z = spanwise coordinate measured from the test surface centerline

Subscripts

cp = constant property value
max = maximum value
mx = local mixed-mean value
o = baseline value
oi = total or stagnation value at the test section inlet
w = local wall value

Superscripts

- $-$ = value spatially-averaged along a line either parallel or perpendicular to the rib direction
- $=$ = globally-averaged value

References

[1] Ligrani, P. M., and Choi, S., 1996, ''Mixed Convection in Straight and Curved Channels With Buoyancy Orthogonal to the Forced Flow,'' Int. J. Heat Mass Transfer, **39**(12), pp. 2473–2484.

[2] Dipprey, D. F., and Sabersky, R. H., 1963, ''Heat and Momentum Transfer in Smooth and Rough Tubes at Various Prandtl Numbers,'' Int. J. Heat Mass Transfer, **6**, pp. 329–353.

[3] Bo, T., Iacovides, H., and Launder, B. E., 1995, ''Developing Buoyancy-Modified Turbulent Flow in Ducts Rotating in Orthogonal Mode,'' ASME J. Turbomach., **117**, pp. 474–484.

[4] Parsons, J. A., Han, J. C., and Zhang, Y., 1995, ''Effects of Model Orientation and Wall Heating Condition on Local Heat Transfer in a Rotating Two-pass Square Channel With Rib Turbulators,'' Int. J. Heat Mass Transfer, **38**, pp. 1151–1159.

[5] Taslim, M. E., and Lengkong, A., 1998, ''45 deg Staggered Rib Heat Transfer Coefficient Measurements in a Square Channel,'' ASME J. Turbomach., **120**, pp. 571–580.

[6] Ligrani, P. M., and Mahmood, G. I., 2003, ''Spatially-Resolved Heat Transfer and Friction Factors in a Rectangular Channel with 45 Deg Angled Crossed-Rib Turbulators,'' ASME J. Turbomach., to appear.

[7] Thurman, D., and Poinsatte, P., 2001, ''Experimental Heat Transfer and Bulk Air Temperature Measurements for a Multipass Internal Cooling Model With Ribs and Bleed,'' ASME J. Turbomach., **123**(1), pp. 90–96.

[8] Cho, H. H., Lee, S. Y., and Wu, S. J., 2001, ''The Combined Effects of Rib Arrangement and Discrete Ribs on Local Heat/Mass Transfer in a Square Duct,'' Paper No. 2001-GT-175, International Gas Turbine and Aeroengine Congress and Exhibition, New Orleans, Louisiana, pp. 1–11.

[9] Mahmood, G. I., and Ligrani, P. M., 2002, ''Heat Transfer in a Dimpled Channel: Combined Influences of Aspect Ratio, Temperature Ratio, Reynolds Number, and Flow Structure,'' Int. J. Heat Mass Transfer, **45**(10), pp. 2011–2020.

[10] Ligrani, P. M., Mahmood, G. I., Harrison, J. L., Clayton, C. M., and Nelson, D. L., 2001, ''Flow Structure and Local Nusselt Number Variations in a Channel With Dimples and Protrusions on Opposite Walls,'' Int. J. Heat Mass Transfer, **44**(23), pp. 4413–4425.

[11] Moffat, R. J., 1962, ''Gas Temperature Measurement,'' *Temperature-Its Measurement and Control in Science and Industry*, Part 2, **3**, Reinhold Publishing Corp., New York, NY.

[12] Kays, W. M., and Crawford M. E., 1993, *Convective Heat and Mass Transfer*, Third Edition, McGraw Hill Book Co., New York.

[13] Sargent, S. R., Hedlund, C. R., and Ligrani, P. M., 1998, ''An Infrared Thermography Imaging System For Convective Heat Transfer Measurements in Complex Flows,'' Meas. Sci. Technol., **9**(12), pp. 1974–1981.

[14] Kline, S. J., and McClintock, F. A., 1953, ''Describing Uncertainties in Single Sample Experiments,'' Mech. Eng. (Am. Soc. Mech. Eng.), **75**, pp. 3–8.

[15] Moffat, R. J., 1988, ''Describing the Uncertainties in Experimental Results,'' Exp. Therm. Fluid Sci., **1**(1), pp. 3–17.

[16] Lienhard J. H., 1987, *A Heat Transfer Textbook*, Second Edition, Prentice-Hall Inc., Englewood Cliffs, New Jersey.

[17] Sleicher, C. A., and Rouse, M. W., 1975, ''A Convenient Correlation for Heat Transfer to Constant and Variable Property Fluids in Turbulent Pipe Flow,'' Int. J. Heat Mass Transfer, **18**, pp. 677–683.

[18] Mahmood, G. I., Sabbagh, M. Z., and Ligrani, P. M., 2001, ''Heat Transfer in a Channel With Dimples and Protrusions on Opposite Walls,'' J. Thermophys. Heat Transfer, **15**, pp. 275–283.

[19] Gee, D. L., and Webb, R. L., 1980, ''Forced Convection Heat Transfer in Helically Rib-Roughened Tubes,'' Int. J. Heat Mass Transfer, **23**, pp. 1127–1136.

Hideki Yanaoka
e-mail: yanaoka@cc.hirosaki-u.ac.jp
Assoc. Prof.
Department of Intelligent Machines and System Engineering,
Hirosaki University,
3 Bunkyo-cho, Hirosaki 036-8561,
Japan

Hiroyuki Yoshikawa
Research Associate

Terukazu Ota
Prof.

Department of Machine Intelligence and Systems Engineering,
Tohoku University,
01 Aramaki-Aoba, Aoba-ku,
Sendai 980-8579,
Japan

Direct Numerical Simulation of Turbulent Separated Flow and Heat Transfer Over a Blunt Flat Plate

Three-dimensional simulation of turbulent separated and reattached flow and heat transfer over a blunt flat plate is presented. The Reynolds number analyzed is 5000. The vortices shed from the reattachment flow region exhibit a hairpin-like structure. These large-scale vortex structures greatly influence the heat transfer in the reattachment region. Present results are compared with the previous three-dimensional calculations at low Reynolds number and it is found that there is no essential difference between two results with respect to the flow structure. The reattachment length is about five plate thicknesses, which is nearly equal to the previous experimental ones. The velocity distributions and turbulence intensities are in good agreement with the experimental data. Further, it is clarified that Nusselt number and temperature distributions greatly depend upon the Reynolds number, though their characteristic behaviors are qualitatively well simulated. [DOI: 10.1115/1.1597623]

Keywords: Computational, Heat Transfer, Reattachment, Separated, Turbulent

Introduction

There have been many studies on the turbulent flow and heat transfer in a separated and reattached flow over a blunt flat plate [1–10]. However, influences of the vortex structure on the detail of heat transfer mechanism are not fully clarified yet. This may be due to the facts that experiments with high reliability are very difficult since the flow is complicated as accompanying the reverse flow, shedding of the large-scale vortices, and strong unsteadiness, though a blunt flat plate is a simple geometrical configuration.

In the previous flow visualization studies at low Reynolds number [11–13], it is reported that the transition to turbulence by the instability of separated shear layer occurs downstream of the separation point and the reattachment length is almost constant when the Reynolds number based on the plate thickness and inlet uniform flow velocity becomes greater than about 700. From these points of view, the present authors performed a two-dimensional simulation of the turbulent flow and heat transfer at Reynolds number 1000, and they clarified the correlation between the large-scale vortex and heat transfer [14,15]. However, the three-dimensional flow structure is not treated by the two-dimensional calculation and the turbulence quantities are overestimated since the spanwise variations of vorticities are neglected. The three-dimensional simulation at the same Reynolds number was continuously conducted and it is found that the three-dimensional flow structure accompanying the hairpin-like vortex greatly influences the heat transfer mechanism [16]. However, the reattachment length predicted is larger than the previous experimental data at high Reynolds number, and accordingly, distributions of the velocity and turbulence intensity deviate from the experimental ones. Comparisons of the temperature profiles are not made since there is no experimental study at low Reynolds number, and subsequently influences of the Reynolds number on the temperature field are not fully investigated yet.

The purpose of the present study is to numerically predict the turbulent separated and reattached flow and heat transfer over a blunt flat plate with three-dimensional calculations at high Rey-

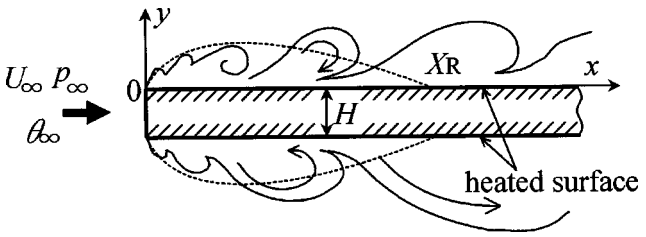

Fig. 1 Flow configuration and coordinate system

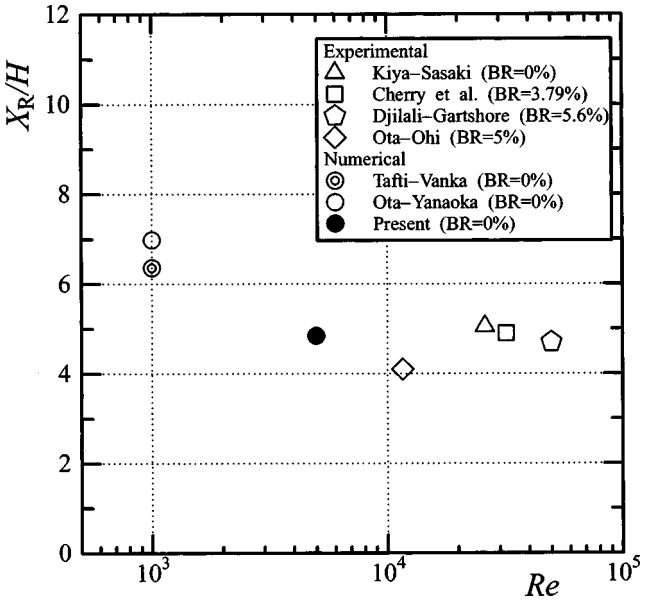

Fig. 2 Variation of reattachment length with Reynolds number

Contributed by the Heat Transfer Division for publication in the JOURNAL OF HEAT TRANSFER. Manuscript received by the Heat Transfer Division August 12, 2002; revision received April 30, 2003. Associate Editor: S. P. Vanka.

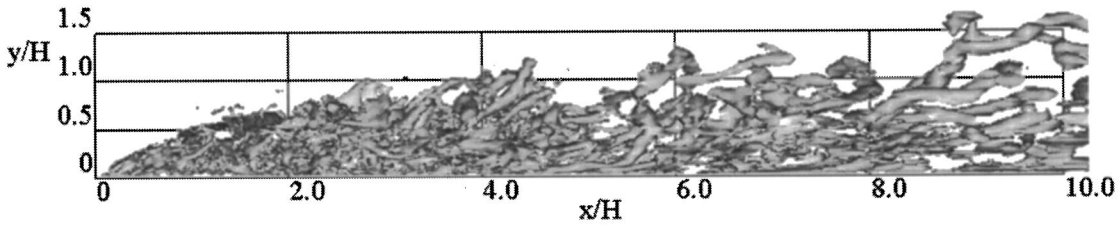

(*a*)

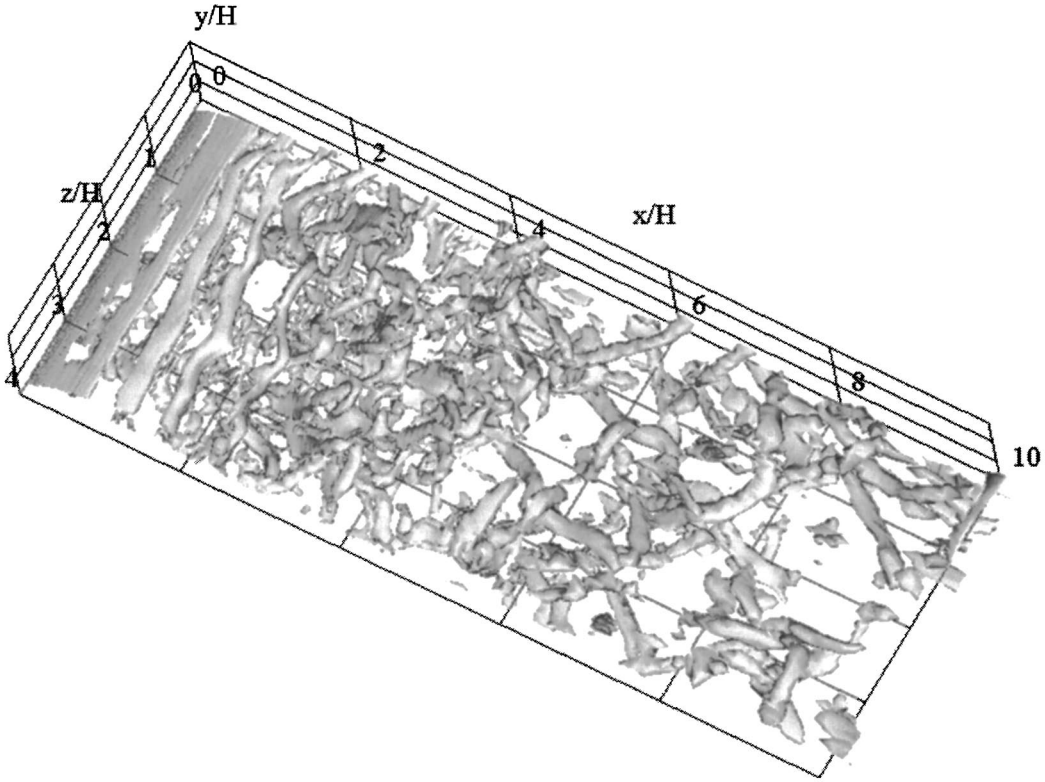

(*b*)

Fig. 3 Isosurface of curvature of equi-pressure surface at $T=120$ (a) side view; (b) top view

nolds number and to investigate influences of the Reynolds number upon the velocity and temperature fields as compared with experimental results.

Fundamental Equations and Numerical Procedures

Figure 1 represents the flow configuration, coordinate system and main physical parameters. A blunt flat plate of thickness H is located in a uniform flow. Fundamental equations analyzed in the following are the continuity, momentum and energy for a three-dimensional unsteady flow of incompressible viscous fluid with constant properties.

$$\nabla \cdot \mathbf{u}^* = 0 \tag{1}$$

$$\mathbf{u}_t^* + (\mathbf{u}^* \cdot \nabla)\mathbf{u}^* = -\nabla p^* + \frac{1}{\mathrm{Re}} \nabla^2 \mathbf{u}^* \tag{2}$$

$$\theta_t^* + (\mathbf{u}^* \cdot \nabla)\,\theta^* = \frac{1}{\mathrm{Re\,Pr}} \nabla^2 \theta^* \tag{3}$$

where the superscript $*$ denotes nondimensional quantities, and space coordinates $\mathbf{x}$, fluid velocity $\mathbf{u}$, pressure p and temperature θ are nondimensionalized by $\mathbf{x}^* = \mathbf{x}/H$, $\mathbf{u}^* = \mathbf{u}/U_\infty$, $p^* = p/\rho U_\infty^2$, and $\theta^* = \lambda(\theta - \theta_\infty)/(q_w H)$, respectively.

The numerical method employed in the present study is almost the same as our previous ones [14,17]. That is, the finite difference forms of these equations are obtained by the Crank-Nicholson method for the time differentials. The fifth-order upwind difference is applied for the convection terms in order to make clear the dynamics of vortices [18], the fourth-order central difference for the diffusion terms, and the second order central difference for other space differentials, respectively. Since high order upwind schemes are dissipative, the central difference schemes are preferred in DNS [18,19]. However, the oscillations occurred around the leading edge of blunt flat plate when the second order central difference method was used. Accordingly, the fifth-order upwind scheme is used in the present study. The Lagrange polynomial is used to obtain coefficients in the difference forms so that the

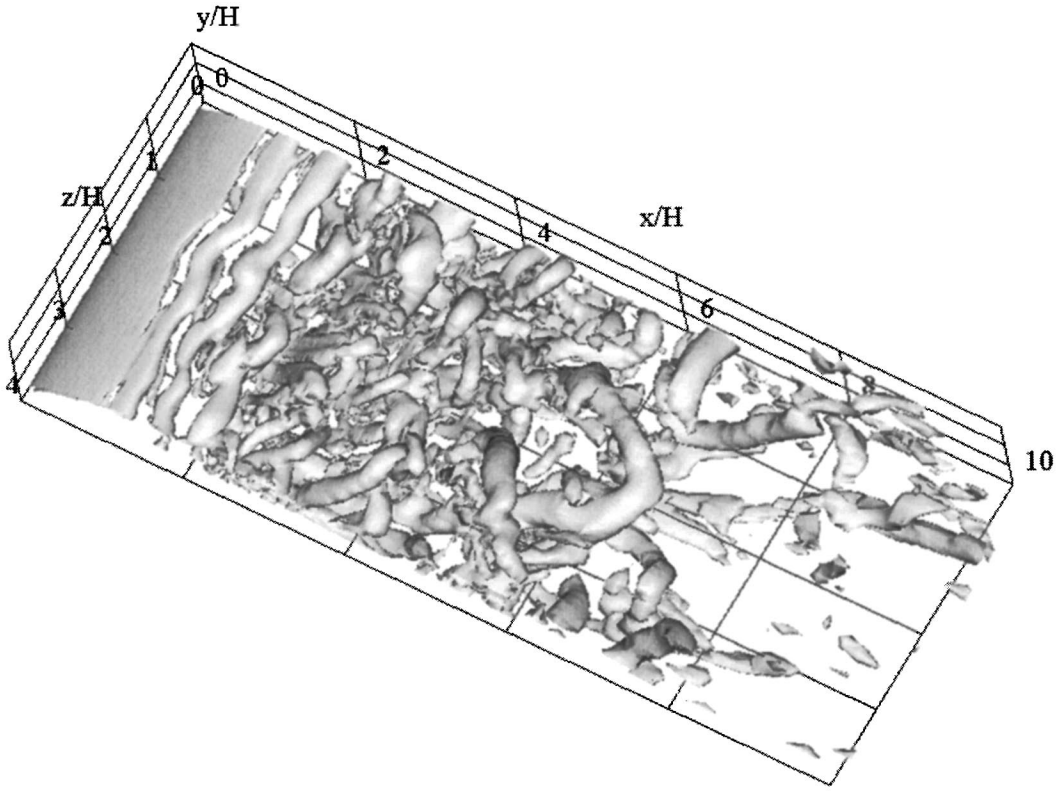

Fig. 4 Isosurface of second invariant of velocity gradient at $T=240$

present numerical method can be applied to nonuniform grid systems. Resulting finite difference equations are solved using the SMAC method [20].

The boundary conditions are as follows. As for the velocity, the uniform velocity profile at the inlet and the no-slip condition on the plate surface are assumed. At the outlet, the zero gradient is used. The influence of the separated shear layers on the upper and lower surfaces of plate propagates to the upstream and their weak interaction may be predicted. However, the symmetry on the *x*-axis upstream of the leading edge is assumed in the present study similarly to the previous numerical ones [8–10,16,17], since the time averaged flow filed is found to be symmetric as to the *x*-axis in the experimental study [7]. Some detailed discussions have been made on such symmetry condition by Tafti and Vanka [8]. On the upper boundary of the computational region, zero velocity in the *y*-direction and zero gradient for other velocity components are presumed because its boundary is very far from the plate. As for the temperature, it is assumed to be uniform at the inlet, and the plate surface is heated under a uniform heat flux, though the leading edge of the plate is adiabatic. The second derivative is assumed zero at the outlet and the symmetric condition on the *x*-axis upstream of the plate is used similarly to the velocity. On the upper boundary, zero gradient is presumed. The spanwise space between vortex structures formed is found to be about $3H\sim4H$ at low Reynolds number by the flow visualization study [13], and about $2.5H\sim3.5H$ at high Reynolds number [21]. Accordingly, the periodic boundary condition is employed in the spanwise direction.

The computational region extends from $-10H$ to $30H$ in the *x*-direction, $-0.5H$ to $9.5H$ in the *y*-direction and 0 to $4H$ in the *z*-direction, respectively.

The computational grids of 193×97, 246×123 and 269×146 for two-dimensional calculation at Reynolds number $\mathrm{Re}=1000$ was used in the previous study [15] and reasonable results were obtained by the grid number of 246×123. Three-dimensional calculation was performed at the same Reynolds number using the grid number of $246\times123\times41$ [16] and the results were in qualitatively good agreement with the previous experimental ones at high Reynolds number. As for the investigation at higher Reynolds number than the present study, Tamura et al. [22] performed flow calculations over a rectangular cylinder at $\mathrm{Re}=10^4$ using the grid number of 1,600,000 and their results agree well with the experimental ones. Considering these previous studies, the computational grid of $246\times123\times41$ generated by the orthogonal coordinates with non-uniform spacing is used in the present study.

The numerical calculations are performed on the flow at Reynolds number $\mathrm{Re}=5000$ and Prandtl number $\mathrm{Pr}=0.7$. The numerical calculation at higher Reynolds number was made preliminarily. However, the calculation did not succeed by the numerical instability. Therefore, we conducted the simulation at $\mathrm{Re}=5000$, which is lower than experimental ones [1,2,5,7]. However, it is

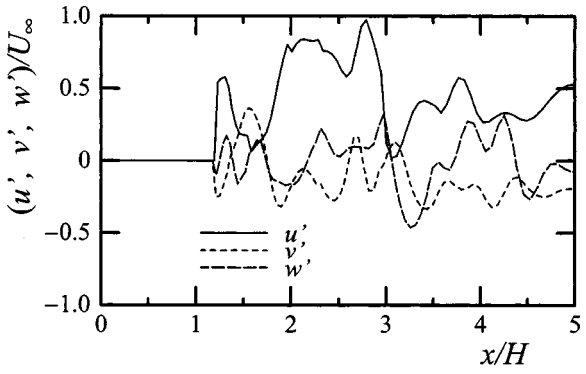

Fig. 5 Velocity fluctuations along separated shear layer at $z/H=2$ ($T=240$)

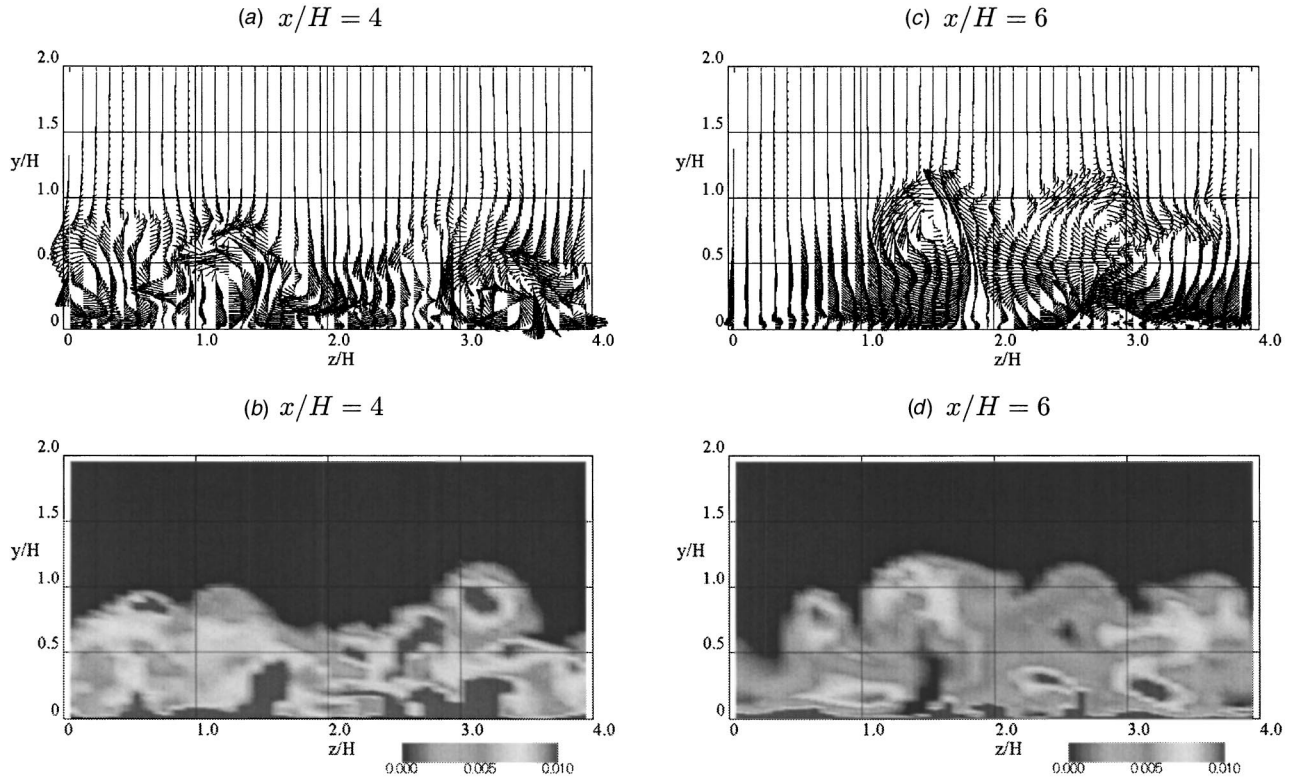

Fig. 6 Velocity vectors ((a) and (c)) and temperature contours ((b) and (d)) at $T=240$

considered that the essential characteristics of the turbulent separated and reattached flow are well simulated. The sampling of results is performed after the flow becomes statistically stationary. The sampling time and size are $360H/U_\infty$ and 2.88×10^6 for the mean quantities, respectively. The mean quantities are obtained by averaging both in time and in the spanwise direction. The sampling frequency of velocity, pressure, and temperature fluctuations is $100U_\infty/H$, which corresponds to nearly 820 times of vortex shedding frequency $0.12U_\infty/H$ in the present study. The sampling time is $360H/U_\infty$ and the sampling size is 36,000 for these instantaneous data. In the following, the starting time of sampling is presented as $T=0$.

Numerical Results and Discussion

Figure 2 shows a variation of the time averaged reattachment length with Reynolds number comparing with the previous experimental [4–7] and numerical results [9,16]. *BR* in the figure denotes the blockage ratio. In the present study, X_R is defined as a streamwise distance from the leading edge to a location of zero time averaged friction coefficient. The present result is about $4.9H$, which is in good agreement with experimental results at high Reynolds number. In the previous flow visualization studies [11–13], it is reported that the reattachment length is nearly constant, about $5H$, when the Reynolds number is greater than about 700. On the other hand, X_R is $7H$ in our previous numerical study at Re=1000 [16] and $6.36H$ in the numerical one by Tafti and Vanka [9], and they are different from the flow visualization data. This may be due to the fact that the free stream turbulence is not considered in the numerical calculations.

It is observed from the flow visualization results [11–13] that the present Reynolds number is included in the turbulent flow regime, thus the three-dimensional vortex structure exists in the flow. Figure 3 presents the isosurface of curvature of equipressure surface at $T=120$ in order to visualize the vortex structures. This method is well suitable for visualizing of the vortex tube as shown in the previous study [17]. The separated shear layer is two-dimensional immediately after the separation. It becomes unstable and wavy to the downstream, and rolls up into the spanwise vortex. This two-dimensional vortex breaks down upstream of the reattachment point and the flow in the recirculation region is three-dimensional at $x/H>2$. The streamwise vortices are generated upstream and downstream of the reattachment point. The isosurface of second invariant of velocity gradient at $T=240$ is shown in Fig. 4. It is very clear that the large-scale hairpin-like vortices exist downstream of the reattachment point. Such the hairpin-like vortex is observed by the flow visualization study [13] and also the previous numerical analyses [10,16]. The spanwise size of this large-scale vortex is found to be about $2H$, which is in good agreement with the LES result of Suksangpanomrung et al. [10]. There is no essential difference of flow structure except for the rolling up of the separated shear layer as compared with the previous numerical result at Re=1000 [16].

Figure 5 shows the velocity fluctuations along the separated shear layer for $z/H=2.0$ at $T=240$ in order to find the transition point of the separated shear layer. As shown in Fig. 4, it is found that the transition to turbulent flow occurs around $x/H=1$ in which the velocity fluctuations become very large. At the transition point, the spanwise velocity fluctuation rapidly varies and therefore the instability of separated shear layer may be attributed to the three-dimensional flow just downstream of the separation point inside the recirculation region. Three-dimensionality of flow is clearly presented as shown later in Fig. 8. The streamwise fluctuation reaches 100% of uniform velocity in the separated shear layer and the spanwise fluctuation of about 50% is observed. Therefore, it is found that three-dimensionality of the flow is very severe.

The velocity vectors and temperature distributions in the y-z plane at the same time $T=240$ are presented in Fig. 6. The streamwise points of $x/H=4$ and 6 locate inside the recirculation region and downstream of the reattachment point, respectively. From the results of velocity vectors at $x/H=4$, the relatively small streamwise vortices generated by the breakdown of spanwise vor-

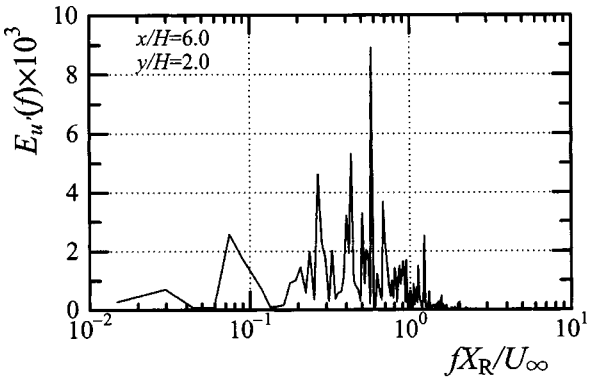

(*a*)

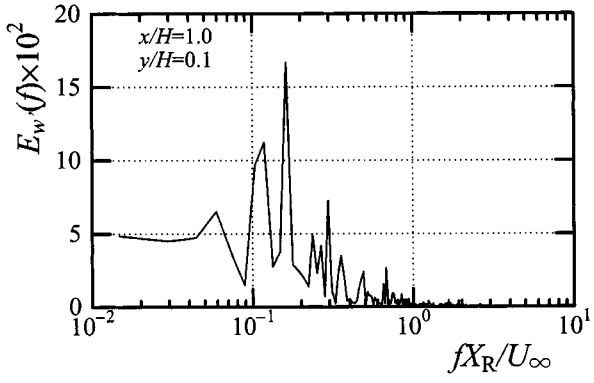

(*b*)

Fig. 7 Power spectrum (a) *x*-component velocity outside the separated shear layer and (b) *z*-component one near the leading edge

tex exist at several spanwise points. These streamwise vortices that exist upstream of the reattachment point increase the heat transfer near the wall and Nusselt number attains a maximum around $x/H=4$ as shown later in Fig. 9. At $x/H=6$ downstream of the reattachment point, the structure of the hairpin-like vortex becomes further clear and the vortex pair rotating in reverse direction exists around $z/H=2$. It is found from the temperature distribution that the fluid mass heated on the wall is entrained into the free stream by this vortex structure. Following the above descriptions and previous numerical results at Re=1000, it is confirmed that the correlation between the large-scale vortex and heat transfer is, in essence, independent of the Reynolds number and accordingly there is no essential variation of flow structure between Re=1000 and 5000.

The separated shear layer rolls up and grows into the spanwise vortex. This spanwise vortex becomes unstable and wavy, and subsequently breaks down in the reattachment region. These phenomena are periodically observed. This shedding of the large-scale vortex is investigated by examining the fluctuation of velocity. Figure 7(a) presents the power spectrum of *x*-component of velocity fluctuation just outside the separated shear layer downstream of the reattachment point. The fluctuating energy is dominant around $f=0.6U_\infty/X_R$, which exhibits the shedding frequency of the large-scale vortex from the reattachment flow region and this value is in good agreement with the previous experimental results of $f=(0.6\sim0.7)U_\infty/X_R$ [4–7]. The power spectrum of *z*-component of velocity fluctuation near the leading edge is shown in Fig. 7(b). The peak exists around $f=0.16U_\infty/X_R$ and its frequency is lower than the vortex shedding one. This exhibits the low frequency flapping which is observed in the previous experimental and numerical works [5–7,9,10,23]. Figure 8 shows the velocity vectors in the $x-y$ and $y-z$ planes at $T=240$. The fluid mass is entrained upstream by the rolling of

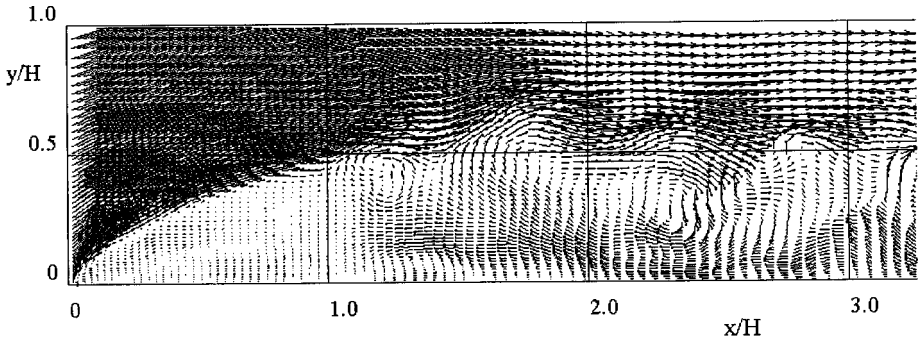

(*a*)

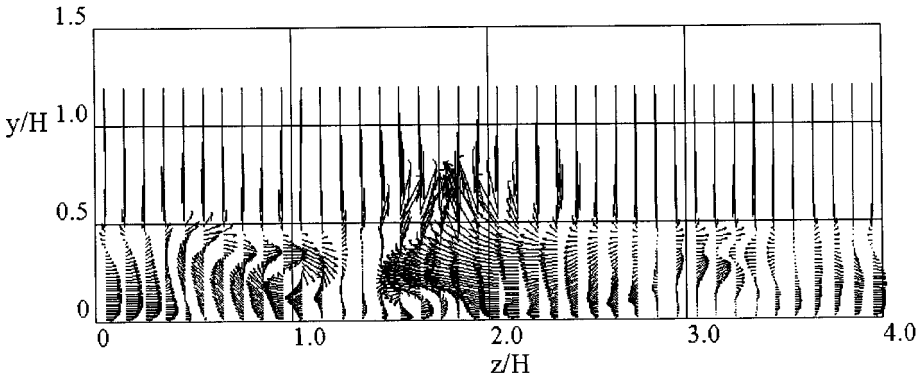

(*b*)

Fig. 8 Velocity vectors (a) $x-y$ plane at $z/H=2$ (b) $y-z$ plane at $x/H=1$ ($T=240$)

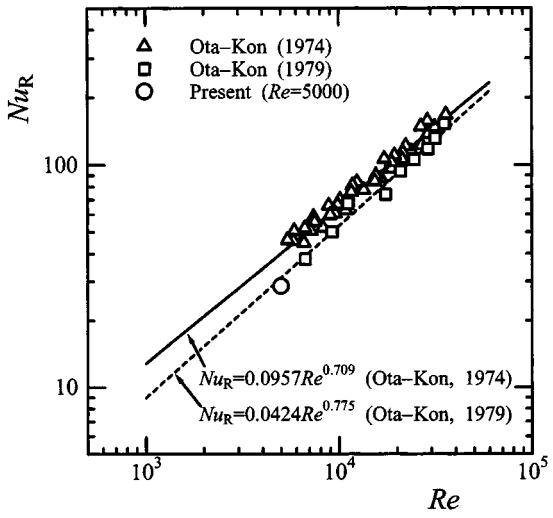

(a)

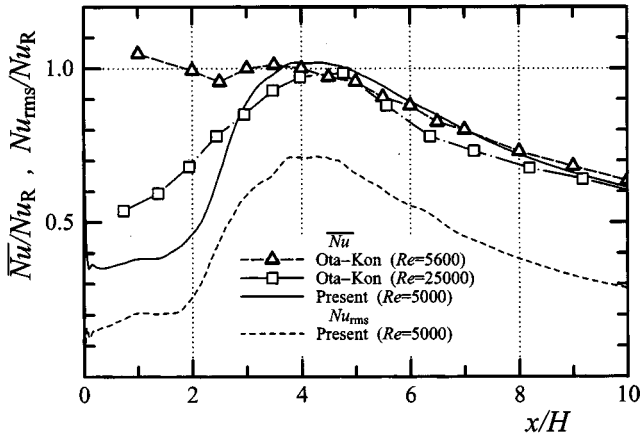

(b)

Fig. 9 (a) **Correlation of Nusselt number at reattachment point with Reynolds number; (b) Time averaged and rms values of Nusselt number.**

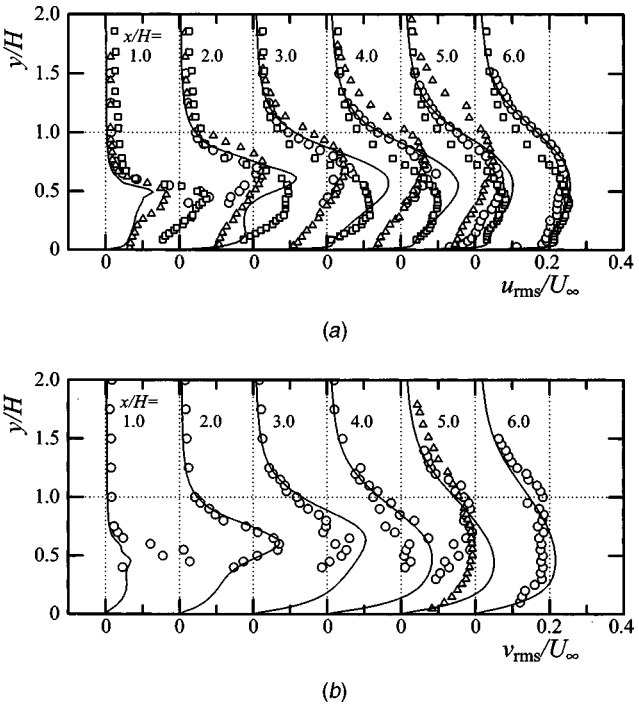

(a)

(b)

Fig. 11 Turbulence intensities of *x* and *y*-components of velocity fluctuation (○; Ota—Narita (Re=24000), △; Kiya—Sasaki (Re=26000), □; Djilali—Gartshore (Re=50,000), ——; Present (Re=5000))

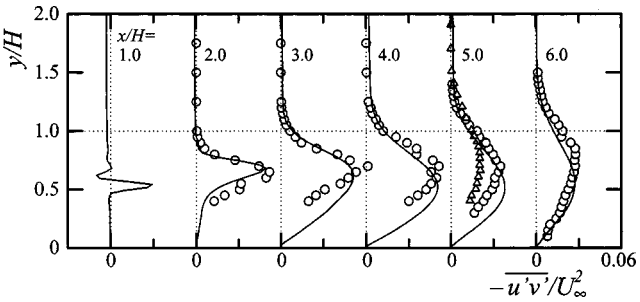

Fig. 12 Reynolds shear stress (○; Ota—Narita (Re=24000), △; Kiya—Sasaki (Re=26000), ——; Present (Re=5000))

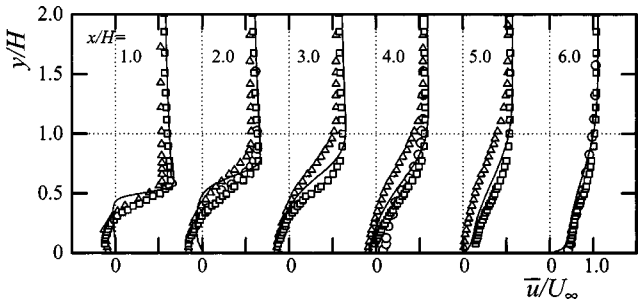

Fig. 10 *x*-component mean velocity (○; Ota—Kon (Re=23400), △; Kiya—Sasaki (Re=26000), □; Djilali—Gartshore (Re=50000), ——; Present (Re=5000))

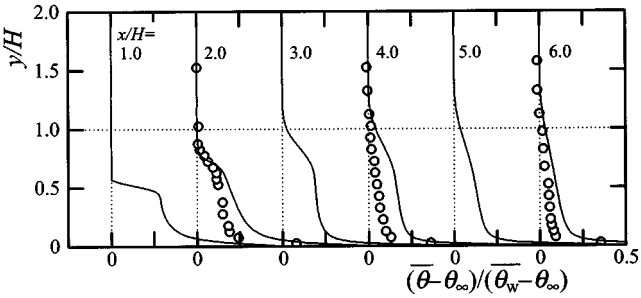

Fig. 13 Mean temperature (○; Ota—Kon (Re=23400), ——; Present (Re=5000))

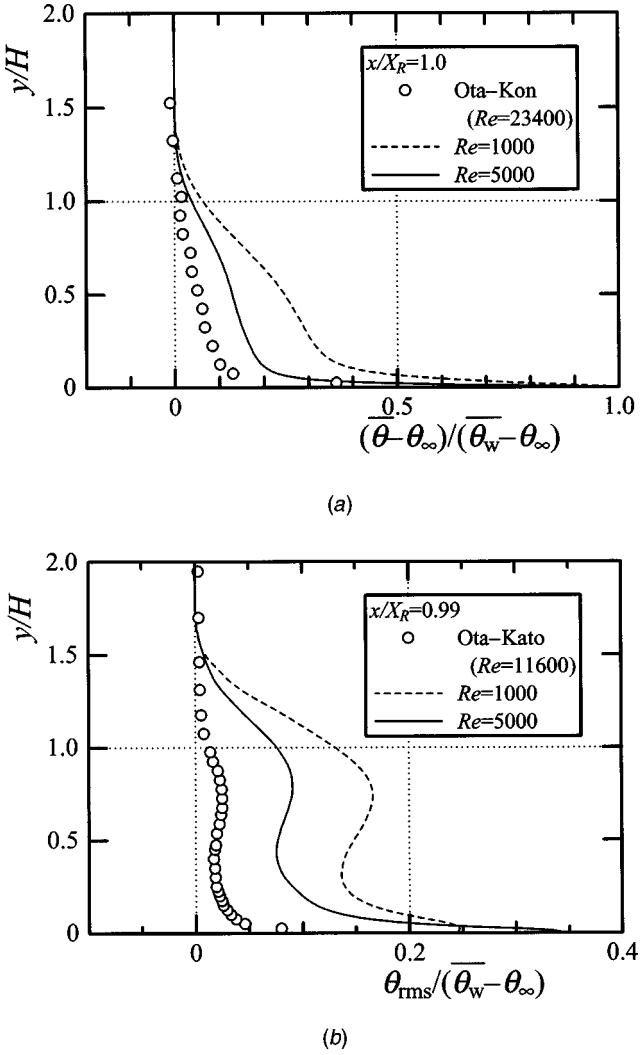

Fig. 14 Mean temperature and turbulence intensity of temperature fluctuation

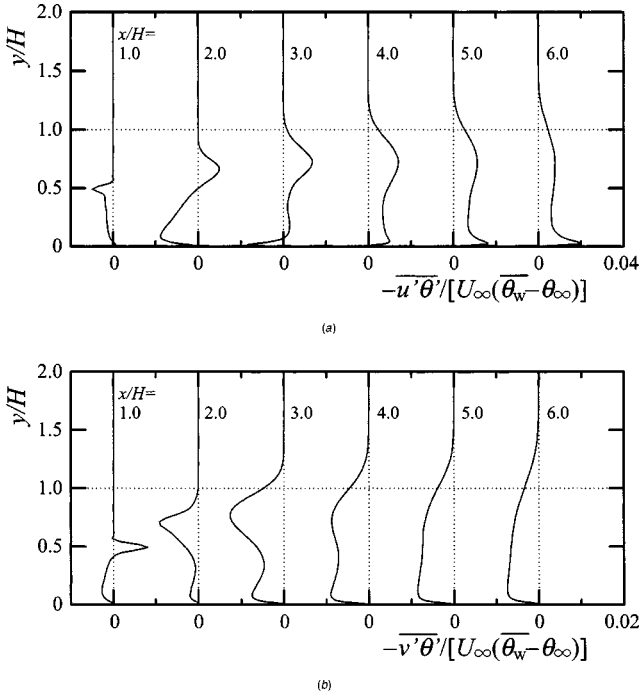

Fig. 15 *x* and *y*-components of turbulent heat flux

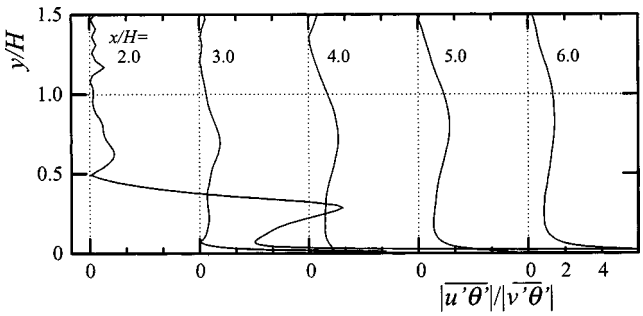

Fig. 16 Ratio of two components of turbulent heat flux

separated shear layer. The cross-stream and spanwise velocities are generated in the neighborhood of the separation because of the three-dimensional flow in the recirculation region near the wall and the separated shear layer is locally entrained into the free stream. The low frequency motion may partly be due to such the three-dimensional phenomena near the separation as mentioned by Tafti and Vanka [9]. It is observed in Fig. 5 that the spanwise velocity around the transition point is relatively large. However, the further investigation is necessary in order to make clear the mechanism of the low frequency motion.

It is reasonable to consider that the large-scale vortices have great effects upon the heat transfer in the reattachment region. The correlation of Nusselt number at the reattachment point, Nu_R, with Reynolds number is shown in Fig. 9(a). Ota and Kon [1,24] proposed a correlation formula of Nu_R based on their experimental data. It is found that the discrepancy between two experimental data of Nu_R increases at low Reynolds number though the experimental procedures are almost the same. The present result is in good agreement with the correlation proposed by Ota and Kon [24]. Figure 9(b) shows distributions of the time averaged Nusselt number Nu and the rms value Nu_{rms} as compared with the experimental data [1,24]. Nu and Nu_{rms} are normalized by Nu_R. The flow in the recirculation region is turbulent because of the transition of separated shear layer. Therefore, Nu rapidly increases in the downstream of the transition point and reaches a maximum around $x/H=4$ upstream the reattachment point. Its location is nearly consistent with the maximum point of Nu_{rms}. Such the tendency is similar to that at Re=1000. Difference of Nusselt number between two experimental studies is very large in the neighborhood of the leading edge. Ota and Kon [24] have reported that this may be due to the sizes of copper electrode, which are different from each other. Furthermore, there exists the free stream turbulence in the experiment, and the transition of separated shear layer occurs more upstream than that of the numerical simulation. When the rolling of separated shear layer is generated upstream, the heat transfer increases just after the separation. Accordingly, it may be reasonable that the discrepancy between the numerical and experimental data around the leading edge is due to the uncertainty of the experimental data and to the free stream turbulence.

Figure 10 compares the *x*-component of time averaged velocity with previous experimental results [1,5,7]. The data by Kiya and Sasaki [5] show values at 0.5% downstream of the streamwise location indicated in the figure. The present results are in good agreement with experimental ones. The strong reverse flow exists in the recirculation region and its velocity becomes $0.35U_\infty$ at $x/H=3.0$. Figures 11 and 12 show distributions of the turbulence intensities of *x* and *y*-components of velocity, and the Reynolds shear stress, respectively. There is much scatter in the experimen-

tal results [2,5,7]. It may partly be attributed to some difference of the experimental condition and measuring method. Ota and coworkers [1,2] used Pitot probes and hot-wires for the mean velocity and turbulence intensities, respectively. Kiya and Sasaki [5] measured data by split-film sensors. Djilali and Gartshore [7] used hot-wire and pulsed-wire probes, and they report that hot-wire data is reasonable when the local turbulence intensity is below 20%. Though there exists such scatter, it may be concluded that the present numerical results are in reasonably good agreement with the experimental ones. However, the fluctuating components at $x/H=1$ are underpredicted. The transition of the separated shear layer in all the experimental studies occurs more upstream than the present numerical simulation since the Reynolds number in the experimental studies is higher than the present one. Accordingly, this discrepancy is partly due to the difference of Reynolds number. In the previous numerical simulations [10], the results are found to be in good agreement with experimental data at Re $=50{,}000$.

Distributions of the time averaged temperature are compared with the measured ones [1] in Fig. 13. The present result is larger than the experimental ones especially near the plate surface. Such a discrepancy is mainly due to the difference of Reynolds number and also the uncertainty in the experiment as shown in Fig. 9. The temperature becomes maximum around just outside of the separated shear layer in the upstream location. The present results exhibit qualitatively a similar behavior to that of the experimental data.

As previously described in the above, the present numerical results agree well with experimental ones at higher Reynolds number for the velocity field. However, there are large differences for the temperature distribution. The numerical results at Re $=1000$ and 5000 and experimental ones are compared for the time averaged temperature and rms values at the reattachment point in Fig. 14. The numerical results clearly approach the experimental one [1,3] with an increase of Reynolds number. Accordingly, it is clearly indicated that the dependency of temperature field upon Reynolds number is large, which is different from the velocity field.

The x and y-components of turbulent heat flux are presented in Fig. 15. The peak of two components exists in the separated shear layer upstream of the reattachment point as showing the active heat transfer between the recirculation region and free stream. This peak value decreases to the downstream and a new peak appears near the plate surface. Figure 16 presents the ratio of two components of the turbulent heat flux. The streamwise turbulent heat flux is greater than the transversal one and its ratio is very high near the wall. Ota and Kon [25] reported the similar results in their experimental study. The streamwise turbulent heat flux exhibits great effects upon the turbulent heat transfer in the flow accompanying the separation and reattachment. The present results may be useful in establishing a turbulence model with high reliability for the turbulent heat transfer in the separated and reattached flow.

Concluding Remarks

Three-dimensional direct numerical calculations of the turbulent separated and reattached flow and heat transfer over a blunt flat plate are carried out at Re$=5000$ and Pr$=0.7$. It is found that the present numerical scheme simulates very well the complicated flow and heat transfer characteristics in the separated and reattached flow. The main results obtained are as follows.

1) It is clarified that the hairpin-like vortex exists similarly to the result at Reynolds number 1000 and there is no essential variation with the Reynolds number in the flow structure.
2) The shedding frequency of hairpin-like vortex from the reattachment flow region is about $0.6U_\infty/X_R$, which is in good agreement with the previous experimental results. The low frequency flapping, which is caused by the three-dimensional flow near the separation, is also observed.
3) The time averaged reattachment length is $4.9H$, which agrees well with the experimental data at high Reynolds number as compared with the result at Re$=1000$. Further, distributions of the velocity and turbulence intensity are in good agreement with the experimental results.
4) The dependency of temperature field upon Reynolds number is large as compared with the velocity field.

Acknowledgment

The authors acknowledge that the present calculations were conducted using a CRAY-C916 at the Institute of Fluid Science and a SX4/128H4 at the Information Synergy Center, Tohoku University.

Nomenclature

$E_q(f)$ = power spectrum of q
f = frequency of power spectrum
H = plate thickness
Nu = Nusselt number$=\alpha H/\lambda$
p = pressure
Pr = Prandtl number
q_w = heat flux per unit area and unit time
Re = Reynolds number$=U_\infty H/\nu$
t = time
T = non-dimensional sampling time
$\mathbf{u}$ = velocity vector (u,v,w)
U_∞ = velocity of upstream uniform flow
$\mathbf{x}$ = coordinates (x,y,z)
X_R = time averaged reattachment length
α = heat transfer coefficient$=q_w/(\theta_w-\theta_\infty)$
θ = temperature
λ = thermal conductivity
ν = kinematic viscosity
ρ = density
τ_w = wall friction stress

Subscript

rms = root mean square
w = wall
∞ = upstream uniform flow

Superscript

$\overline{\ }$ = time averaged
$'$ = fluctuation

References

[1] Ota, T., and Kon, N., 1974, "Heat Transfer in the Separated and Reattached Flow on a Blunt Flat Plate," ASME J. Heat Transfer, **96**, pp. 459–462.
[2] Ota, T., and Narita, M., 1978, "Turbulence Measurements in a Separated and Reattached Flow Over a Blunt Flat Plate," ASME J. Fluids Eng., **100**, pp. 224–228.
[3] Ota, T., and Kato, H., 1991, "Turbulent Heat Transfer in a Separated and Reattached Flow Over a Blunt Flat Plate," *Proceedings of The 3rd ASME/JSME Thermal Engineering Joint Conference*, J. R. Lloyd and Y. Kurosaki, eds., ASME, Reno, Nevada, **3**, pp. 191–196.
[4] Ota, T., and Ohi, N., 1995, "Turbulent Heat Transfer in a Separated and Reattached Flow Over a Blunt Flat Plate," *Proceedings of The 4th ASME/JSME Thermal Engineering Joint Conference*, L. S. Fletcher and T. Aihara, eds., ASME, Maui, Hawaii, **1**, pp. 363–370.
[5] Kiya, M., and Sasaki, K., 1983, "Structure of a Turbulent Separation Bubble," J. Fluid Mech., **137**, pp. 83–113.
[6] Cherry, N. J., Hillier, R., and Latour, M. E. M. P., 1984, "Unsteady Measurements in a Separated and Reattaching Flow," J. Fluid Mech., **144**, pp. 13–46.
[7] Djilali, N., and Gartshore, I. S., 1991, "Turbulent Flow Around a Bluff Rectangular Plate. Part I: Experimental Investigation," ASME J. Fluids Eng., **113**, pp. 51–59.
[8] Tafti, D. K., and Vanka, S. P., 1991, "A Numerical Study of Flow Separation and Reattachment on a Blunt Plate," Phys. Fluids A, **3**(7), pp. 1749–1759.
[9] Tafti, D. K., and Vanka, S. P., 1991, "A Three-Dimensional Numerical Study of Flow Separation and Reattachment on a Blunt Plate," Phys. Fluids A, **3**(12), pp. 2887–2909.
[10] Suksangpanomrung, A., Djilali, N., and Moinat, P., 2000, "Large-Eddy Simu-

lation of Separated Flow Over a Bluff Rectangular Plate,'' Int. J. Heat Fluid Flow, **21**, pp. 655–663.
[11] Lane, J. C., and Loehrke, R. I., 1980, ''Leading Edge Separation From a Blunt Plate at Low Reynolds Number,'' ASME J. Fluids Eng., **102**, pp. 494–496.
[12] Ota, T., Asano, Y., and Okawa, J., 1981, ''Reattachment Length and Transition of the Separated Flow Over Blunt Flat Plates,'' Bull. JSME, **24**(192), pp. 941–947.
[13] Sasaki, K., and Kiya, M., 1991, ''Three-Dimensional Vortex Structure in a Leading-Edge Separation Bubble at Moderate Reynolds Numbers,'' ASME J. Fluids Eng., **113**, pp. 405–410.
[14] Ota, T., and Yanaoka, H., 1993, ''Numerical Analysis of a Separated and Reattached Flow Over a Blunt Flat Plate,'' *Proceedings of the 5th International Symposium on Computational Fluid Dynamics*, H. Daiguji, ed., Jpn. Soc. Comp. Fluid Dynamics, Sendai, **2**, pp. 423–428.
[15] Yanaoka, H., and Ota, T., 1995, ''Numerical Analysis of Separated and Reattached Flow and Heat Transfer Over Blunt Flat Plate,'' Trans. Jpn. Soc. Mech. Eng., Ser. B, **61**(586), pp. 2213–2220.
[16] Yanaoka, H., and Ota, T., 1996, ''Three-Dimensional Numerical Simulation of Separated and Reattached Flow and Heat Transfer Over Blunt Flat Plate,'' Trans. Jpn. Soc. Mech. Eng., Ser. B, **62**(595), pp. 1111–1117.
[17] Yanaoka, H., Yoshikawa, H., and Ota, T., 2002, ''Numerical Simulation of Laminar Flow and Heat Transfer Over a Blunt Flat Plate in Square Channel,'' ASME J. Heat Transfer, **124**, pp. 8–16.
[18] Rai, M. M., and Moin, P., 1991, ''Direct Simulations of Turbulent Flow Using Finite-Difference Schemes,'' J. Comput. Phys., **96**, pp. 15–53.
[19] Najjar, F. M., and Tafti, D. K., 1996, ''Study of Discrete Test Filters and Finite Difference Approximations for the Dynamic Subgrid-Scale Stress Model,'' Phys. Fluids, **8**(4), pp. 1076–1088.
[20] Amsden, A. A., and Harlow, F. H., 1970, ''A Simplified MAC Technique for Incompressible Fluid Flow Calculations,'' J. Comput. Phys., **6**, pp. 322–325.
[21] Kiya, M., and Sasaki, K., 1985, ''Structure of Large-Scale Vortices and Unsteady Reverse Flow in the Reattaching Zone of a Turbulent Separation Bubble,'' J. Fluid Mech., **154**, pp. 463–491.
[22] Tamura, T., Itoh, Y., and Kuwahara, K., 1993, ''Computational Separated-Reattaching Flows Around a Rectangular Cylinder,'' J. Wind. Eng. Ind. Aerodyn., **50**, pp. 9–18.
[23] Eaton, J. K., and Johnston, J. P., 1982, ''Low Frequency Unsteadiness of a Reattaching Turbulent Shear Layer,'' in *Turbulent Shear Flow 3*, L. J. S. Bradbury et al., eds., Springer-Verlag, pp. 162–170.
[24] Ota, T., and Kon, N., 1979, ''Heat Transfer in the Separated and Reattached Flow Over Blunt Flat Plates—Effects of Nose Shape,'' Int. J. Heat Mass Transfer, **22**, pp. 197–206.
[25] Ota, T., and Kon, T., 2001, ''Turbulent Heat Transfer in a Separated and Reattached Flow on a Blunt Flat Plate,'' *Proceedings of the 5th World Conference on Experimental Heat Transfer, Fluid Mechanics, and Thermodynamics*, G. P. Celata, et al., eds., Edizioni ETS, Thessaloniki, pp. 1921–1926.

Flow and Heat Transfer Behavior for a Vortex-Enhanced Interrupted Fin

M. L. Smotrys
H. Ge
A. M. Jacobi
J. C. Dutton

Department of Mechanical and Industrial Engineering,
University of Illinois at Urbana-Champaign,
1206 West Green St.,
Urbana, IL 61801

The potential for enhanced air-side heat transfer in HVAC&R applications has been investigated using combined spanwise and streamwise vorticity. Spanwise vortices were created using an offset-strip fin array, and streamwise vortices were introduced into the flow using delta-wing vortex generators. Mass transfer measurements, obtained using the naphthalene sublimation technique, were used to quantify the heat transfer characteristics of a baseline and enhanced array, and these results were compared to flow visualization and particle image velocimetry measurements of the instantaneous velocity fields. Significant enhancement was observed over portions of the Reynolds number range tested ($400 \leqslant Re \leqslant 3700$), and a transitional Reynolds number range was identified within which the spanwise and streamwise vortices act to decrease the heat transfer performance of the array. [DOI: 10.1115/1.1597616]

Keywords: Convection, Enhancement, Heat Transfer, Heat Exchangers, Vortex

Introduction

Heat transfer enhancement is important in many end-use energy applications, especially in HVAC&R systems which typically use ''air-side limited'' heat exchangers. As such, several techniques for enhancing the heat transfer coefficient have been developed. Two techniques for enhancement are the use of highly interrupted fins, and flow manipulators known as vortex generators (VGs).

Interrupted fins cause boundary layer restarting and can cause periodic spanwise shedding, each of which has been shown to significantly increase the heat transfer coefficient [1–3]. The mechanisms for heat transfer enhancement and the onset of spanwise vortex shedding for flows through interrupted-surfaces and communicating channels have been studied in detail [4–6]. Vortex generators add streamwise vortices to the flow field, and local heat transfer enhancements of up to 150 percent, with average enhancements of 20 percent to 50 percent, have been measured downstream of vortex generators on a flat plate [7]. The potential for additional enhancements from the combination of these techniques is suggested by detailed experiments on vorticity in shear layers [8,9]. Within these shear layers, counter-rotating streamwise vortex pairs exist in the braid region between the dominant spanwise Brown–Roshko rollers. The locations where the streamwise vortices wrap around the spanwise vortices are regions of very high mixing of freestream fluid within the shear layer. To our knowledge, no studies of the heat transfer effect associated with combined spanwise and streamwise vortices have been reported in the literature. Moreover, no clear guidelines exist for the placement of vortex generators in interrupted-fin geometries with respect to heat transfer enhancement.

The purpose of this research is to contribute a fundamental understanding of the enhancement capability of combined spanwise and streamwise vortices in offset strip-fin arrays. In order to reduce the extensive parameter space of this problem, we consider the simple case of delta-wing VGs and a Reynolds number range typical to the motivating application in HVAC&R. The concept developed in this research is thus termed the vortex-enhanced interrupted fin (VEIF).

The offset-strip geometry was chosen because it is easy to implement and represents a commercial interrupted-fin heat exchanger. Vortex shedding characteristics within the offset-strip array vary depending on Reynolds number and geometry, allowing for great flexibility in designing an optimum VEIF. In addition, extensive research concerning offset-strip arrays has been performed, allowing for a comparison of the results to extant data [1,2,10–12].

Delta-wings have been selected as the VGs because they have been shown to be highly effective with respect to heat transfer enhancement per unit VG area [13]. Unfortunately, inducing streamwise vortices in this flow to enhance heat transfer will be accompanied by an increase in pressure drop [14]. However, since a substantial pressure loss is incurred by the use of offset-strip arrays [15], delta-wings can be chosen as the vortex generators in order to maximize the heat transfer enhancement without a large impact on the total pressure loss in the combined system. Furthermore, Gentry and Jacobi [7] have performed an extensive investigation characterizing the delta-wing VG on flat plates, with an emphasis on understanding the relationship between flow structure and heat transfer. The results of Gentry and Jacobi's work provide a basis for selecting delta-wing parameters (i.e., angle of attack, span, etc.) for desired heat transfer behavior.

Experimental Equipment and Methods

Flow visualization using dye-in-water experiments was performed to determine qualitative flow features. Full-field velocity data were also obtained, using particle image velocimetry (PIV). Heat transfer data are presented for comparison to the PIV and flow visualization results. The heat transfer data were obtained using the naphthalene sublimation technique [16]. Due to space limitations, only a brief description of the experimental methods and facilities is given; however, a complete description of apparatus and procedures has been provided by Smotrys et al. [17].

Flow Facilities and Arrays. Flow visualizations and PIV measurements were obtained using a recirculating water tunnel. The water tunnel test section has a free-surface flow, and dimensions of 15.24 cm wide by 15.24 cm high by 45.72 cm long; it was constructed from 1.27 cm thick Plexiglas. A Plexiglas end wall permits optical access from the downstream direction. The water tunnel has a nearly uniform mean velocity distribution (± 1–2 percent) and relatively low freestream turbulence (~ 1 percent) in the test section.

Contributed by the Heat Transfer Division for publication in the JOURNAL OF HEAT TRANSFER. Manuscript received by the Heat Transfer Division July 12, 2002; revision received April 9, 2003. Associate Editor: C. Amon.

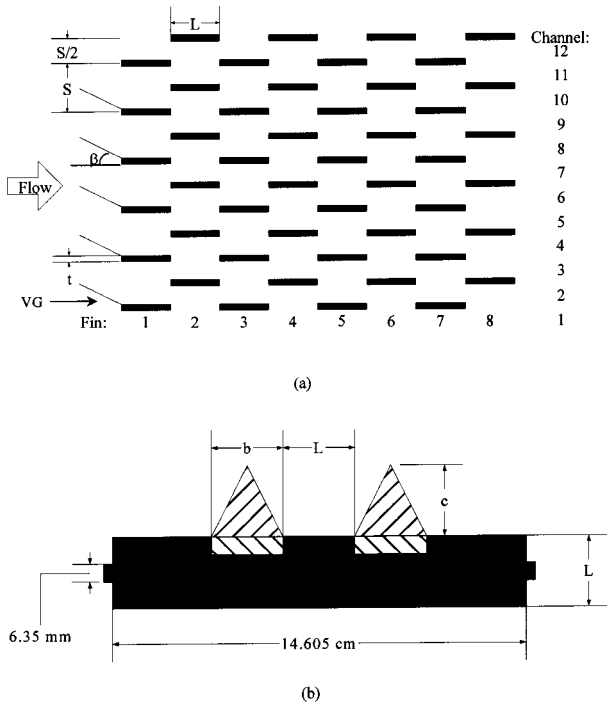

Fig. 1 Geometry and nomenclature for the (a) offset-strip fin array and (b) Two-VG enhanced fins. $S=L=b=c=2.54$ cm, $t=3.175$ mm, $\Lambda=2$, and $\beta=25$ deg.

Mass transfer measurements were obtained using an open-loop induction wind tunnel. The wind tunnel test section, also constructed from 1.27 cm thick Plexiglas, has a cross-sectional area of 15.24 cm by 15.24 cm, and a length of 30.48 cm. A variable-speed blower is used to control the freestream velocity, which has a range of 0.1 to 10 m/s. Calibrated platinum RTDs were placed in the inlet of the wind tunnel and 9 cm downstream of the test array to measure air temperature. The wind tunnel test section has a nearly uniform mean velocity distribution ($\pm 1-2$ percent) and low freestream turbulence (~ 1 percent).

The model offset-strip fin array has a 15.24 cm by 15.24 cm cross-section, and a length of 20.32 cm (Fig. 1). In order to simulate a wide range of approach velocities and array sizes, and to provide a fundamental understanding of the VEIF's potential to enhance air-side heat transfer in common HVAC&R applications, this model was tested over a broad Reynolds number range, $400 \leq \mathrm{Re} \leq 3700$. The Reynolds number was based on a length scale of $D_h = 39.5$ mm, where D_h is the hydraulic diameter, and the characteristic velocity was the core velocity through the array, U_c.

Two 3.18 mm thick Plexiglas base plates hold forty-eight 2.54 cm long (L) aluminum fins in the water tunnel array, while the fins are placed into a removable test section for wind tunnel measurements. The fins have a thickness of $t = 3.18$ mm and a spacing of $S = 2.54$ cm for geometric symmetry (i.e., $S = L$). For the PIV experiments, three Plexiglas fins were inserted into the array to allow laser light to pass unobstructed through the array. The remaining aluminum fins were anodized black to reduce reflection of laser light. For mass transfer measurements, carbon steel fins were fabricated with shallow cavities machined on one side, to be filled with naphthalene. The remaining fins were uncoated.

The conventional hydraulic diameter for both fin arrays is $D_h = 39.5$ mm. Although a simplified, symmetric array is adopted for this work, there are still numerous length scales relevant to the flow (e.g., S, t, and L, if the flow is two-dimensional). With geometric similarity and Reynolds number matching to provide dynamic similarity, the water and air flows are equivalent.

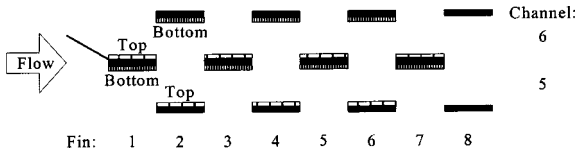

Fig. 2 Placement of cast fins for naphthalene sublimation experiments

The VGs are of the delta-wing type, with a span of $b = 2.54$ cm, a chord length of $c = 2.54$ cm, an aspect ratio of $\Lambda = 2b/c = 2$, a thickness of 0.25 mm, and an angle-of-attack of $\beta = 25$ deg; see Fig. 1. Two arrays are compared in this study: a baseline array (with no VGs) and a Two-VG enhanced array. The Two-VG enhanced array uses two metal delta-wing VGs attached to each of the leading fins of the baseline array (Fig. 1). The wings are attached to the fins using double-sided tape.

Naphthalene Sublimation. The naphthalene sublimation technique [16] was used to measure mass transfer within the test arrays at several fin locations. Using the well-known heat and mass transfer analogy, the mass transfer results provide a quantitative evaluation of the heat transfer characteristics of the baseline and Two-VG arrays. Thus, these experiments provide a measure of heat transfer performance. The naphthalene-coated fins were prepared by pouring molten scintillation-grade naphthalene into the machined cavity of a carbon steel fin. After solidification, excess naphthalene above the fin edges was removed and the surfaces were polished with fine-grit sandpaper. The naphthalene specimens were placed in the center columns of the test arrays with the naphthalene-coated sides directed towards the center channel, or directed outward if the fin lies on the middle column; see Fig. 2. The remaining fins in the arrays were made from aluminum.

The coated specimens were weighed before being placed into the arrays. The arrays were then inserted into the wind tunnel, and exposed continuously for 90 to 120 minutes for each Reynolds number. Flow was exhausted outside the laboratory to avoid freestream naphthalene contamination. Upstream and downstream RTDs recorded the temperature every five seconds during the run, and room atmospheric pressure and relative humidity were recorded at the beginning, middle, and end of the wind tunnel runs. The arrays were then removed, and the coated fins were once again weighed. The data reduction equations for the Reynolds number and Sherwood number are as given by DeJong and Jacobi [2]. The uncertainties in reduced data were determined by propagating all measurement uncertainties using standard methods as described by Kline and McClintock [18]. The resulting uncertainties at the 95 percent confidence level are 3.2 percent for Reynolds number and 5 percent for Sherwood number.

Flow Visualization. Flow visualization experiments were conducted by injecting neutrally buoyant dye through a stainless steel micro-tube (1.27 mm OD, 0.84 mm ID) and into the water tunnel. For a baseline experiment, dye was injected to impinge on the leading fin between channels 5 and 6 (see Fig. 1 for channel-numbering scheme). For the VG-enhanced case, dye impinged at the apex of the VG. The characteristic velocity for this study was the maximum core velocity through the array (U_c), corresponding to the volumetric flow rate divided by the minimum free-flow area. The minimum free-flow area is taken on a plane through a single row of fins. For the flow visualization experiments, the freestream (approach) velocity was measured by injecting a dye droplet into the water and measuring the time it took for the droplet to traverse a given distance. The core velocity was then determined using continuity.

Particle Image Velocimetry. A TSI PowerView Stereoscopic PIV system was used for acquisition and analysis of the instanta-

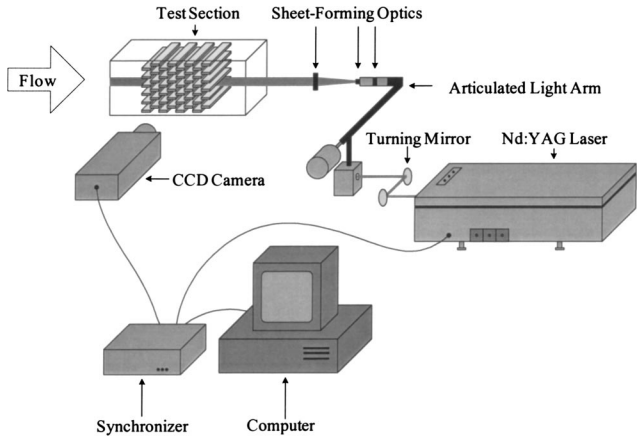

Fig. 3 Experimental setup for side-view PIV measurements

neous velocity fields. The PowerView system consists of a Laser Pulse Synchronizer, PIVCAM 13-8 cross-correlation camera (1280 (H) by 1024 (V) pixels), Insight Stereo PIV v3.3 software, and a Dell Precision 410 workstation with two Pentium III 600 MHz processors and 512 MB of RAM. Laser illumination was provided by a Continuum double-pulsed Surelite III PIV Nd:YAG laser.

The water flow was seeded using a neutrally buoyant solution of silver-coated hollow glass spheres and Kodak Photo-Flo 200 solution. The spheres had a true particle density of 1.6 g/cc, and a diameter range of 10–30 μm, with a mean diameter of 15 μm. The Photo-Flo solution reduced particle agglomeration. The particles were illuminated with a 30 mJ laser sheet. The laser beam was steered from the laser by a series of 45 deg, 532 nm mirrors into a Laser Mechanisms articulated laser light arm (Fig. 3), with a series of light sheet-forming optics at its end. A 700 mm plano-convex spherical lens, −25 mm plano-concave cylindrical lens, and a 300 mm plano-convex cylindrical lens were used to form a light sheet with a maximum thickness of 1 mm, and width of 4 cm. For measurements of streamwise-transverse velocity (spanwise vorticity, ω_Z), the light sheet was directed into the water tunnel through the Plexiglas endwall (Fig. 3), entering the array at fin 8 (see fin-numbering scheme in Fig. 1). For spanwise-transverse velocity measurements (streamwise vorticity, ω_X), the sheet was directed through the test section sidewall.

PIV images were acquired by capturing 100 image pairs (frames "*a*" and "*b*") for each Reynolds number and location. For the side view, the flow through the whole array was captured two fins at a time, including the flow immediately upstream and downstream of the fin array. In the end view, the dimensionless position, X^*, specifies the location of image capture; X^* is defined as the ratio of the distance from the entrance of the array (X) to fin length (L). The light sheet was placed at several X^* locations, as indicated in Fig. 4.

Interrogation consisted of a two-frame cross-correlation analysis performed using an FFT algorithm with a Gaussian peak-searching routine. For the current study, 32×32 pixel windows with an overlap of 50 percent were used for the majority of the end-view image processing, and for all of the side-view processing. For end-view images in which the tracer particle seeding was poor, or the light sheet did not adequately illuminate the full field of view, a window size of 64×64 pixels with an overlap of 75 percent was required. In all cases, the Nyquist sampling criterion was satisfied. For a detailed listing of PIV interrogation parameters (i.e., laser pulse timing, aspect ratio, etc.) for the various configurations and Reynolds numbers investigated, the reader is referred to Smotrys et al. [17]. The side-view images typically contained around 2400 vectors, and the end-view images contained about 1500. The number of interpolated vectors in a given image ranged between 0.07 percent to 3.9 percent.

The particle displacement error in PIV measurements has been found to be approximately 10 percent of the particle image diameter, d_τ [19]. The particle image diameter is defined as:

$$d_\tau = \sqrt{(M \cdot d_p)^2 + (2.44 \cdot f^\# \cdot (M+1) \cdot \lambda)^2} \quad (1)$$

where M is the magnification, d_p is the true particle diameter, $f^\#$ is the f-number, and λ is the wavelength of the laser light. For the present study, $d_\tau = 12.3\ \mu$m for the side-view images ($M = 0.16$, $f^\# = 8$), and $d_\tau = 11.5\ \mu$m for the end-view images ($M = 0.11$, $f^\# = 8$). The maximum velocity observed in the side-view images corresponds to a displacement of 180 μm. The uncertainty in this case is therefore 6.8 percent for the side-view experiments. Similarly, the end-view experiments have a maximum displacement of 600 μm, and an uncertainty of 1.9 percent.

Results and Discussion

Heat Transfer Enhancement. The heat transfer enhancement of the Two-VG array is summarized in Fig. 5. The enhancement was calculated by normalizing the average Sherwood number for the Two-VG array with the average Sherwood number for the baseline array. The averages were based on the measurements made at seven test fins, as seen in Fig. 2. At Re≤1000, Fig. 5 shows an increase in Sherwood-number enhancement with increasing Reynolds number for the Two-VG array. As the Reynolds number increases beyond Re=1000, however, the Sherwood number enhancement begins to diminish until Re≈1600, at which point a slight heat transfer degradation is manifest. A further increase in the Reynolds number results in a return to enhanced heat transfer, increasing with increasing Reynolds number, similar to the behavior below Re=1000.

Also shown in Fig. 5 are results for an ancillary experiment with a Four-VG array. The geometry of the Four-VG array is identical to the Two-VG array, except for the addition of two VGs per leading fin oriented with an angle of attack opposite to the existing VGs—that is, each fin has two sets of two VGs at both positive and negative attack angles at the same spanwise position

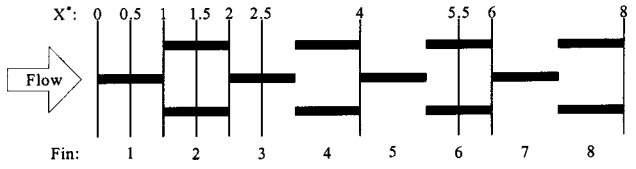

Fig. 4 X^* locations for end-view PIV images ($X^* = X/L$)

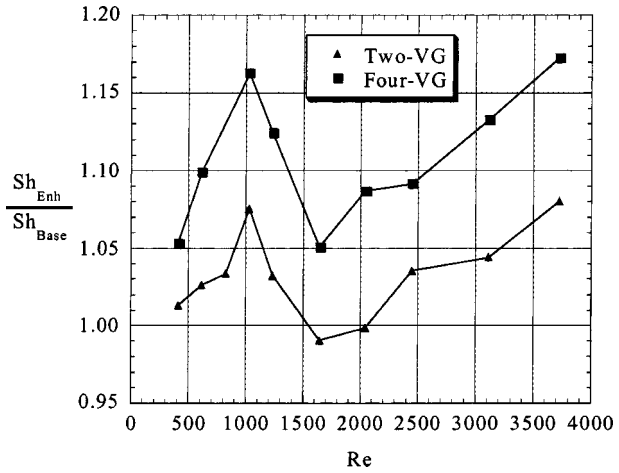

Fig. 5 Seven-fin average Sherwood number enhancement

on the fin. The Four-VG data are provided to confirm the heat transfer enhancement trends for the Two-VG array, which are larger than our conservative estimate of Sherwood number uncertainty. The Four-VG case exhibits the same trends but with a larger magnitude.

Flow Visualization. Flow visualization results for the baseline and Two-VG arrays are given in Figs. 6 and 7, respectively. At Reynolds numbers below 1280, the flow is laminar throughout the array. Figure 6(a) shows oscillatory flow developing immediately behind the trailing fins of the baseline array at Re=1280. Within a relatively narrow Reynolds number range, the flow oscillations prevalent at Re=1280 lead to clearly observable spanwise vortex shedding from fin 3, as demonstrated by Fig. 6(b) at Re=1330. By Re=1480, periodic spanwise shedding occurs at the first fin in the array, and the flow is well mixed by about fin 6 (see Fig. 6(c)).

The Two-VG array flow visualizations (Fig. 7) show results differing slightly from the baseline array. Similar to the baseline array, the flow is laminar up to Re=1280. However, by Re=1365, only weak oscillations are evident at fin 7, instead of spanwise shedding at fin 3 as observed for the baseline array at Re=1330. Further, Fig. 7(c) shows that spanwise vortices begin shedding at fin 1 for the Two-VG array by Re=1430. Despite the differences in the onset of spanwise oscillations, both arrays show a very narrow Reynolds number range between incipient wake unsteadiness and spanwise shedding at the leading fin.

Streamwise vortices were present at all Reynolds numbers in the Two-VG array. The presence of streamwise vortices in Fig. 7 is evidenced by the dye streak located approximately half a channel height above the middle-column fins. The dye streak is a side-view image of two sets of two spiraling, counter-rotating vortices generated at the VGs. From the flow visualizations for the baseline and Two-VG arrays, it is clear that no spanwise oscillations occur in either array below Re=1000. Therefore, the Sherwood number enhancement shown in Fig. 5 over this range is clearly the result of the streamwise vortices. The streamwise vortices effectively thin the thermal boundary layer on the fins, and complement the boundary layer restarting that naturally occurs within offset-strip arrays.

The flow visualizations indicate that spanwise oscillations, and eventually vortices, develop within the range $1280 \leqslant Re \leqslant 1480$ for the baseline array. The Two-VG array, however, showed only weak oscillations at Re=1365 but achieved spanwise vortex shedding at fin 1 by Re=1430. The development of spanwise oscillations in the baseline and Two-VG arrays corresponds to the region of decreasing enhancement seen in Fig. 5. Although dye-streak visualization does not conclusively elucidate the underlying fluid mechanics, it does suggest a destructive interaction between the spanwise and streamwise vortices in the range of $1280 \leqslant Re \leqslant 1430$. These interactions are apparent through the reduced spanwise oscillations observed in the Two-VG array as compared to the baseline array at these Reynolds numbers and also from the naphthalene sublimation data of Fig. 5.

The onset of spanwise vortex shedding throughout the Two-VG array at $Re \approx 1365$ takes place two-thirds of the way into the heat transfer decrement region shown in Fig. 5 ($1000 \leqslant Re \leqslant 1600$). Visualizations near Re=1430 (Fig. 7(c)) show spanwise vortices shed from the fins in the middle column, beginning at fin 1. At lower Reynolds numbers, spanwise vortices do not extend in the transverse direction to the location of the streamwise vortices, which are indicated by the streamwise dye-streak near the middle of the channel. However, as Reynolds number approaches Re =1430 in the Two-VG array, the dye-streak begins to thicken as the spanwise structures push away from the fin surfaces and into the streamwise vortices. This thickening indicates increased spanwise-streamwise interaction which leads to further heat transfer decrement. The heat transfer data of Fig. 5 support this hypothesis, since decreasing enhancement is shown below Re =1600. As the streamwise dye streak moves downstream in Fig. 7(c), it begins to lose coherence at fin 5, as indicated by the sharp, upward bulge of the dye-streak over this fin. The remainder of the dye-streak downstream of fin 5 begins to oscillate transversely in phase with the spanwise vortices. At higher Reynolds numbers, the destruction of the streamwise vortex moves upstream to fin 3.

Velocity Measurements. For further insight into the heat transfer data, PIV measurements were obtained. Instantaneous and averaged velocity magnitude contours were developed for both the baseline and Two-VG arrays. In the PIV images to be presented, black rectangular boxes indicate the areas where fins are located in the flow field.

In Fig. 8 an instantaneous vector field is shown for the baseline array at Re=1050 in which the mean *U*-component (streamwise) velocity has been subtracted from each vector to more clearly show shear layer instabilities. Several vortices can be seen rolling up from each side of the trailing fin (fin 7). The presence of shear layer instabilities at Re=1050 for the baseline array was not detected in the flow visualization results, due to the limited resolution of the dye-streak method. Flow visualization showed the first signs of spanwise oscillations at Re=1280, which did not explain why the heat transfer enhancement due to streamwise vorticity began decreasing after Re=1000. However, the flow visualizations did show that the onset of spanwise oscillations coincided with decreased heat transfer enhancement for the Two-VG array. Therefore, it is proposed that the heat transfer enhancement begins to decrease after Re=1000 because spanwise shear layer instabilities begin in the back of the array, and interfere destructively with the streamwise vortices generated by the VGs.

The characterization of the baseline and Two-VG arrays with PIV further demonstrates the nature of the spanwise-streamwise vortex interactions over the intermediate Reynolds number range, $1000 \leqslant Re \leqslant 1600$. Figure 9 shows instantaneous velocity-magnitude contours (*U* and *V* components) for the baseline and Two-VG arrays at Re=1330. The images were obtained for locations at fins 5 and 6. The baseline array clearly shows spanwise oscillations in the gap between fins 5 and 7. The oscillations wash against the leading edge of fin 7 and along its top and bottom surfaces, enhancing heat transfer. The Two-VG array lacks these oscillations, and instead experiences a velocity deficit in channel 6 as compared to channel 5, due to the presence of the streamwise vortices.

Flow visualization showed a very narrow range between the first appearance of spanwise oscillations at Re=1280 and spanwise vortex shedding from fin 1 at Re=1480 for the baseline array (Fig. 6). A narrower transitional range ($1365 \leqslant Re \leqslant 1430$) was shown for the Two-VG array (Fig. 7). The PIV measurements for the Two-VG array at these Reynolds numbers provide additional insight. For example, an interesting comparison can be made between Re=1330 and Re=1365. At Re=1330 in the baseline array, spanwise vortex shedding began at fin 3. Spanwise vortex shedding in the Two-VG array did not occur until Re=1365 (fin 7). A comparison of these two Reynolds numbers highlights flow field differences between the two arrays that affect vortex shedding characteristics.

Figure 10 shows spanwise-transverse velocity measurements for Re=1330 and Re=1365 at $X^*=8$ (exit of array) for the Two-VG array. The gold triangles located above part (a) indicate the spanwise location of the VGs in channel 6 of the Two-VG array, but do not reflect the transverse location, since the VGs are actually mounted on the middle fin in the end-views at the entrance to the array (i.e., fin 1). The size of the triangles reflects the relative size of the VGs with respect to channel 6.

While the spanwise-transverse flow at the exit of the array for both Re=1330 and 1365 is unsteady, a comparison of these flows shows a substantial change in the velocity magnitude between these two Reynolds numbers. Two large ''pockets'' of high-velocity (V-W component) flow exist at Re=1365 at locations that correspond to the VG placement. In fact, the width of the pockets is approximately equal to the base dimension of the VGs. The

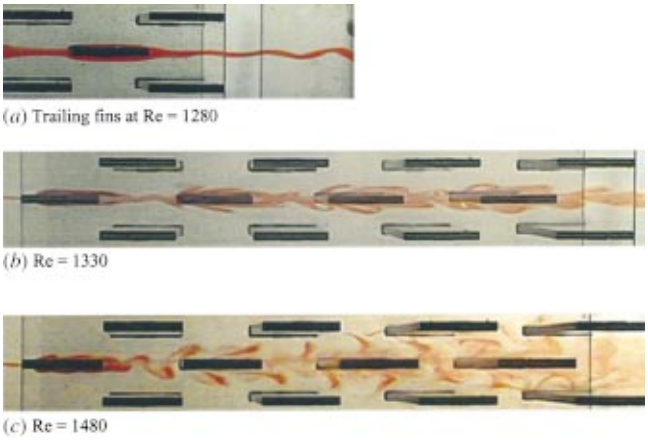

Fig. 6 Flow visualization of the baseline array for the various flow regimes: (a) Trailing fins at Re=1280; (b) Re=1330; and (c) Re=1480.

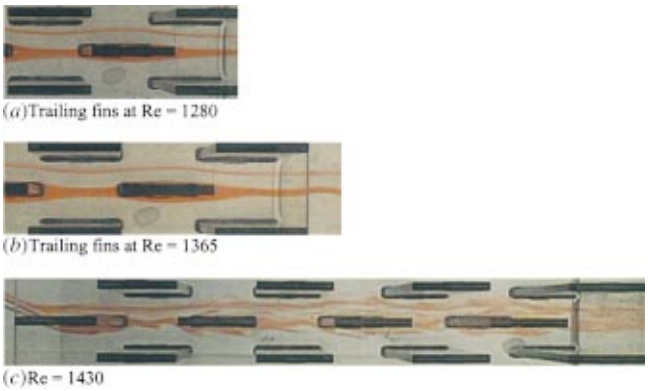

Fig. 7 Flow visualizations for the Two-VG array for the various flow regimes: (a) Trailing fins at Re=1280; (b) Trailing fins at Re=1365; and (c) Re=1430.

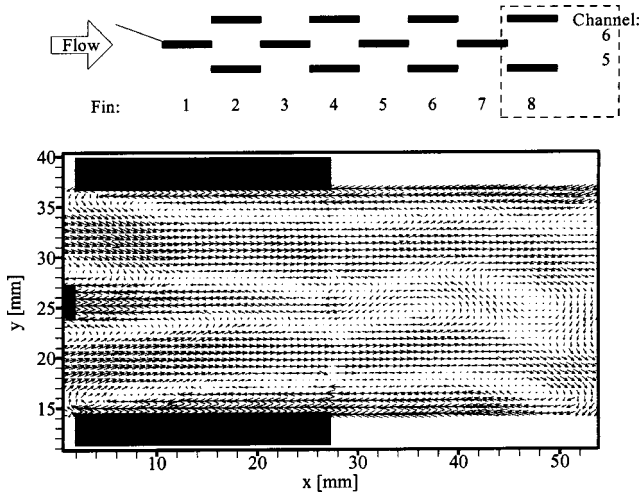

Fig. 8 Instantaneous vector field for baseline array at Re =1050, downstream. The vector-field mean *U*-component velocity has been subtracted from each vector to show shear layer instabilities.

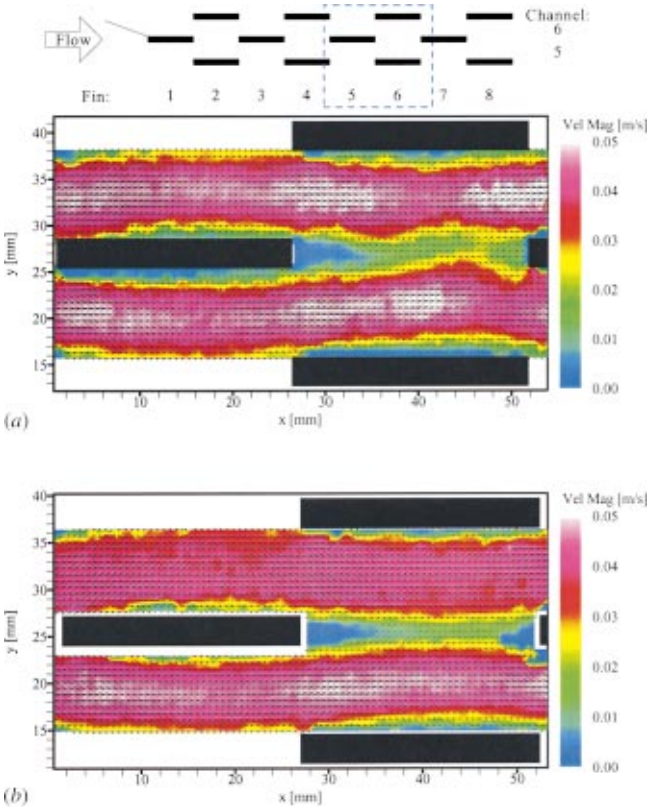

Fig. 9 Instantaneous velocity magnitude for (a) baseline array and (b) Two-VG array at Re=1330, fins 5 and 6

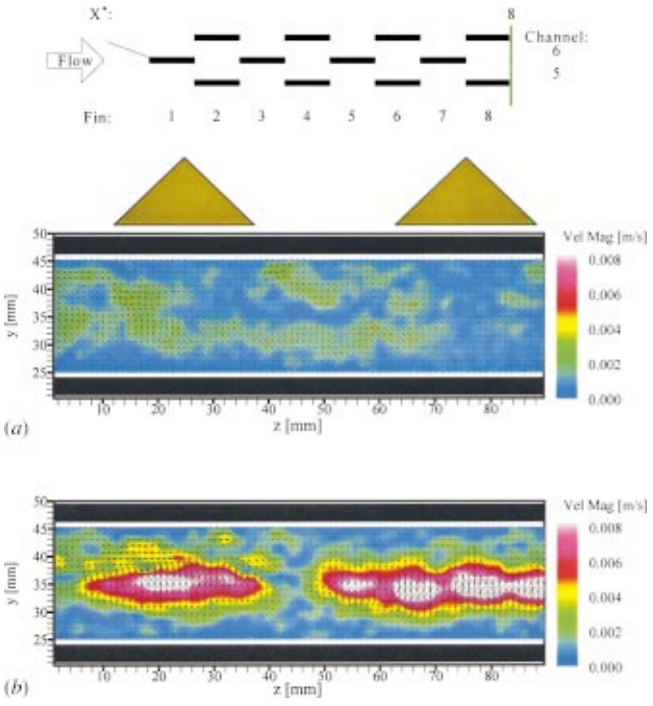

Fig. 10 Two-VG array instantaneous velocity magnitude for (a) Re=1330 and (b) Re=1365 at *X=8**

velocity magnitude is approximately four times greater within these pockets than at any point in the flow at Re=1330. The increase in V-W velocity over the fins coincides with the onset of spanwise oscillations near fin 7 in the Two-VG array. The V-W velocity decrement at Re=1330 must therefore contribute to the delay in spanwise vortex shedding seen in the flow visualizations for the Two-VG array (Figs. 6 and 7), and the decrease in heat transfer enhancement seen in Fig. 5.

Another fundamental difference in flow behavior between the two Reynolds numbers in Fig. 10 is the direction of flow behind the VGs. For instance, at Re=1330, the strength of the streamwise vortices at the array exit is such that the counter-rotating vortices are barely discernible. In addition, the flow field has some large areas of low velocity magnitude flow (blue contours). These areas indicate a dominance of the streamwise component of the velocity (U), or nearly stagnating V-W component flow. In contrast, the counter-rotating vortices at Re=1365 are distinguishable by the large vectors located within the high-velocity pockets. Interestingly, the counter-rotating vortices at Re=1365 from the two VGs are out-of-phase with each other. This effect is clearly unsteady, most likely due to interactions of the streamwise vortices with the spanwise vortices. It is important to note that the images in Fig. 10 are representative of the 100-image ensemble-average at each respective Reynolds number. The behavior of the streamwise flow shown in Fig. 10, when contrasted to the heat transfer and flow visualization data, clearly supports the assertion that streamwise vortices destructively interfere with the spanwise oscillations within the transitional Reynolds number range. These interactions delay the onset of spanwise vortex shedding in the Two-VG array as compared to the baseline array, as indicated by the flow visualizations of Figs. 6 and 7.

An analysis of the spanwise-transverse PIV measurements also shows that the flow at the exit of the Two-VG array tends to be unsteady in the transitional Reynolds number range at which spanwise oscillations first begin. Unsteadiness at the array exit begins as early as Re=880, and the location of the onset moves forward to $X^*=6$ at Re=1365. The only exception to the unsteady behavior occurs at Re=1525, for which a steady flow persists throughout the array.

The unsteadiness observed at the exit of the Two-VG array for the transitional Reynolds numbers might be due to the sudden area expansion in the wake region. At Re=1525, streamwise vortices appear to achieve dominance over the spanwise vortices. This Reynolds number corresponds to the region in Fig. 5 in which heat transfer enhancement returns. The steady flow behavior identified by the spanwise-transverse velocity measurements at Re =1525 suggests that as the strength of the streamwise vortices continues to increase with increasing Re and the spanwise vortices weaken, the heat transfer enhancement begins to return. Previous studies of offset-strip arrays without VGs have indicated the breakdown of spanwise vortices into a chaotic, unsteady flow at sufficiently high Reynolds numbers [1,2,10–12], thus limiting further heat transfer enhancement by regular vortex shedding. Flow visualizations (not presented here) confirm this behavior past Re =1525 for the baseline array under investigation. The unsteady flow that follows at higher Reynolds numbers for the VEIF array clearly shows an increasing heat transfer enhancement; see Fig. 5. Thus, the addition of streamwise vortices to a flow in the post-transitional Reynolds number range offers enhancement capability through higher streamwise circulation.

Conclusions

The implementation of the VEIF into an offset-strip fin array has demonstrated promising enhancements from combined spanwise and streamwise vortices for conditions typical to HVAC&R applications. The enhancement was evaluated by comparing heat transfer characteristics of a baseline and Two-VG enhanced array, and by obtaining flow visualizations and PIV measurements for the two arrays. The Two-VG array showed significant enhancement at Re<1000, and Re>1600. Although these flow regimes have different flow behavior, they exhibit similar heat transfer behavior. The addition of streamwise vortices to each flow regime offers increased mixing with the freestream flow, and thus increased heat transfer. This behavior was evidenced by an earlier transition to spanwise vortex shedding at fin 1 in the Two-VG array than in the baseline array.

The transitional Reynolds number regime, $1000 \leqslant Re \leqslant 1600$, is the least promising in terms of heat transfer enhancement for the Two-VG array, but shows interesting spanwise-streamwise vortex interactions. Small-scale spanwise shear layer instabilities detected at Re=1050 using PIV correlate to the sudden decrease in heat transfer enhancement in the Two-VG array. As the spanwise oscillations grow with Reynolds number in the transitional range, the heat transfer enhancement in the Two-VG array decreases. Flow visualizations and PIV measurements both showed a reduction of spanwise oscillations in the Two-VG array in the transitional Reynolds number regime as compared to the baseline array, thus indicating a destructive interaction of spanwise and streamwise structures.

Furthermore, a narrow Reynolds number range ($1280 \leqslant Re \leqslant 1480$) was identified for the baseline array in which spanwise vortices shedding at the exit of the array move forward to the entrance. A narrower range ($1365 \leqslant Re \leqslant 1430$) was found for the Two-VG array. Spanwise-transverse PIV measurements of the Two-VG array at the exit showed a fundamental difference in the flow behavior at Re=1330 (baseline array sees shedding at fin 3) and Re=1365 (Two-VG array sees shedding at fin 7). The flow at Re=1365 in the enhanced array showed the existence of strong, unsteady streamwise vortices as compared to Re=1330. The velocity magnitude difference between these Reynolds numbers for the V-W components was approximately 400 percent. Thus, the assertion that destructive interactions are the cause of lowered heat transfer in the transitional Reynolds number range for the Two-VG array is well supported.

While only relatively small heat transfer enhancements were realized in this initial attempt at configuring a VEIF, the work supports the idea that spanwise and streamwise vorticity can be coupled in HVAC&R applications to realize additional enhancements. Although these studies were geometrically limited, the focus on flow features and heat transfer response to mixed spanwise and streamwise vortices provides findings of general value. Future investigations can be guided by this effort to achieve a more promising VEIF. A variation of the number and placement of VGs implemented could lead to additional enhancements. Pressure measurements to determine total pressure loss resulting from inclusion of the VGs, as well as a frequency analysis of the spanwise-streamwise structures, would be beneficial to future efforts.

Nomenclature

English Symbols

A_C = minimum free-flow area of the test array
A_{total} = total surface area of the test array
b = vortex generator base dimension
c = vortex generator chord length
d_τ = particle image diameter
d_p = true particle diameter
D_{AB} = binary mass diffusion coefficient
D_h = hydraulic diameter, $D_h=(4\cdot A_C\cdot L_C)/A_{total}=2\cdot(S-t)\cdot L/(L+t)$
$f^\#$ = lens f-number
h_m = convection mass transfer coefficient
L = fin length
L_C = length of the test array
M = magnification
Re = Reynolds number, $Re=U_C\cdot D_h\cdot \nu^{-1}$
S = fin spacing

Sh = Sherwood number, $Sh = h_m \cdot L \cdot D_{AB}^{-1}$
t = fin thickness
U = streamwise velocity
U_C = core (maximum) velocity
V = transverse velocity normal to fin surface
W = spanwise velocity
X = streamwise coordinate or horizontal coordinate for image evaluation
X* = non-dimensional fin location, $X^* = X/L$
Y = transverse coordinate normal to fin surface or vertical coordinate for image evaluation
Z = spanwise coordinate

Greek Symbols

β = vortex generator angle of attack
λ = wavelength of light
Λ = vortex generator aspect ratio, $\Lambda = 2b/c$
ω = vorticity

Abbreviations

CCD = charge coupled device
Nd:YAG = neodymium-yttrium-aluminum-garnet
PIV = particle image velocimetry
RTD = resistance temperature detector
VEIF = vortex-enhanced interrupted fin
VG = vortex generator

References

[1] Mullisen, R. S., and Loehrke, R. I., 1986, "A Study of the Flow Mechanisms Responsible for Heat Transfer Enhancement in Interrupted-Plate Heat Exchangers," ASME J. Heat Transfer, **108**, pp. 377–385.

[2] DeJong, N. C., and Jacobi, A. M., 1997, "An Experimental Study of Flow and Heat Transfer in Parallel-Plate Arrays: Local, Row-by-Row and Surface Average Behavior," Int. J. Heat Mass Transfer, **40**(6), pp. 1365–1378.

[3] DeJong, N. C., and Jacobi, A. M., 1999, "Local Flow and Heat Transfer Behavior in Convex-Louver Fin Arrays," ASME J. Heat Transfer, **121**, pp. 136–141.

[4] Amon, C. H., Majumdar, D., Herman, C. V., Mayinger, F., Mikic, B. B., and Sekulic, D. P., 1992, "Numerical and Experimental Studies of Self-Sustained Oscillatory Flows in Communicating Channels," Int. J. Heat Mass Transfer, **35**(11), pp. 3115–3129.

[5] Majumdar, D., and Amon, C. H., 1992, "Heat and Momentum Transport in Self-Sustained Oscillatory Viscous Flows," ASME J. Heat Transfer, **114**(4), pp. 866–873.

[6] Majumdar, D., and Amon, C. H., 1997, "Oscillatory Momentum Transport Mechanisms in Transitional Complex Geometry Flows," ASME J. Fluids Eng., **119**(1), pp. 29–35.

[7] Gentry, M. C., and Jacobi, A. M., 1997, "Heat Transfer Enhancement by Delta-Wing Vortex Generators on a Flat Plate: Vortex Interactions With the Boundary Layer," Exp. Therm. Fluid Sci., **14**, pp. 231–242.

[8] Bernal, L. P., and Roshko, A., 1986, "Streamwise Vortex Structure in Plane Mixing Layers," J. Fluid Mech., **170**, pp. 499–525.

[9] Brown, G. L., and Roshko, A., 1974, "On Density Effects and Large Structure in Turbulent Mixing Layers," J. Fluid Mech., **64**(4), pp. 775–816.

[10] DeJong, N. C., Zhang, L. W., Jacobi, A. M., Balachandar, S., and Tafti, D. K., 1998, "A Complementary Experimental and Numerical Study of the Flow and Heat Transfer in Offset Strip-Fin Heat Exchangers," ASME J. Heat Transfer, **120**, pp. 690–698.

[11] Mochizuki, S., and Yagi, Y., 1982, "Characteristics of Vortex Shedding in Plate Arrays," *Flow Visualization II*, W. Merzkirch, ed., Hemisphere Publishing, Washington, D.C., pp. 99–103.

[12] Xi, G., Futagami, S., Hagiwara, Y., and Suzuki, K., 1991, "Flow and Heat Transfer Characteristics of Offset-Fin Array in the Middle Reynolds Number Range," *Proceedings, ASME/JSME Thermal Engineering*, ASME, New York.

[13] Fiebig, M., Kallweit, P., Mitra, N. K., and Tiggelbeck, S., 1991, "Heat Transfer Enhancement and Drag by Longitudinal Vortex Generators in Channel Flow," Exp. Therm. Fluid Sci., **4**, pp. 103–114.

[14] Biswas, G., Deb, P., and Biswas, S., 1994, "Generation of Longitudinal Streamwise Vortices—A Device for Improving Heat Exchanger Design," ASME J. Heat Transfer, **116**, pp. 588–597.

[15] Sparrow, E. M., and Liu, C. H., 1979, "Heat-Transfer, Pressure-Drop and Performance Relationships for In-Line, Staggered, and Continuous Plate Heat Exchangers," Int. J. Heat Mass Transfer, **22**, pp. 1613–1625.

[16] Goldstein, R. J., and Cho, H. H., 1995, "A Review of Mass Transfer Measurements Using Naphthalene Sublimation," Exp. Therm. Fluid Sci., **10**, pp. 416–434.

[17] Smotrys, M. L., Dutton, J. C., and Jacobi, A. M., 2001, "A Particle Image Velocimetry Study of Flow Structure in an Offset-Strip Array With Delta-Wing Vortex Generators," ACRC Technical Report TR-182, University of Illinois, Urbana, IL.

[18] Kline, S. J., and McClintock, F. A., 1953, "Describing Uncertainties in Single Sample Experiments," Mech. Eng. (Am. Soc. Mech. Eng.), **75**, pp. 3–8.

[19] Prasad, A. K., Adrian, R. J., Landreth, C. C., and Offutt, P. W., 1992, "Effect of Resolution on the Speed and Accuracy of Particle Image Velocimetry Interrogations," Exp. Fluids, **13**, pp. 105–116.

Transition in Homogeneously Heated Inclined Plane Parallel Shear Flows

S. Generalis
e-mail: s.c.generalis@aston.ac.uk
School of Engineering and Applied Sciences,
Division of Chemical Engineering and Applied Chemistry,
Aston University, United Kingdom

M. Nagata
Department of Aeronautics and Astronautics,
Graduate School of Engineering,
Kyoto University,
Japan

The transition of internally heated inclined plane parallel shear flows is examined numerically for the case of finite values of the Prandtl number Pr. We show that as the strength of the homogeneously distributed heat source is increased the basic flow loses stability to two-dimensional perturbations of the transverse roll type in a Hopf bifurcation for the vertical orientation of the fluid layer, whereas perturbations of the longitudinal roll type are most dangerous for a wide range of the value of the angle of inclination. In the case of the horizontal inclination transverse roll and longitudinal roll perturbations share the responsibility for the prime instability. Following the linear stability analysis for the general inclination of the fluid layer our attention is focused on a numerical study of the finite amplitude secondary travelling-wave solutions (TW) that develop from the perturbations of the transverse roll type for the vertical inclination of the fluid layer. The stability of the secondary TW against three-dimensional perturbations is also examined and our study shows that for Pr=0.71 the secondary instability sets in as a quasi-periodic mode, while for Pr=7 it is phase-locked to the secondary TW. The present study complements and extends the recent study by Nagata and Generalis (2002) in the case of vertical inclination for Pr=0. [DOI: 10.1115/1.1599370]

Keywords: Channel Flow, Heat Transfer, Secondary, Shear Flows, Stability

1 Introduction

Theoretical investigations aided by the advance of powerful hardware and parallel experimental studies of the stability of plane parallel shear flows have provided significant insights in identifying the mechanisms of instability and transition from laminar to turbulent fluid flow. Parallel shear flows include the well studied plane Couette flow, plane Poiseuille flow and natural convection. Another example of parallel shear flow which has recently attracted attention [1–5], because of its importance in industrial and environmental applications, is the homogeneously heated fluid flow. There are several ways in which such a heat source may be produced. Studies of convection in the earth's mantle or in the atmosphere and in nuclear safety engineering for predicting the behavior of the nuclear reactor core cooling are some of the applications of the present work[1]. Although the fluid used in these investigations has nonzero values of the Pr number, the case of the vanishing limit of the Prandtl number was studied by Nagata and Generalis (2002) [6] in order to extract only the fluid dynamic instability mechanisms.

In [6] the nonlinear stability analysis of shear flows in a vertical channel with or without the imposition of a constant pressure gradient was presented for Pr=0. There, it was shown that the secondary equilibrium states bifurcate supercritically or subcritically, depending on the value of the applied constant pressure gradient. The stability analysis on the secondary flow has indicated that the tertiary flow is made up of two frequencies (quasi-periodic) irrespective to the applied pressure gradient. The present work complements and extends the work of [6] to the more realistic case of nonzero Prandtl number. However, in the present study a vanishing pressure gradient is assumed.

In the following section we formulate the problem and in section 3 we investigate the linear stability of our basic steady state numerically by the Chebyshev collocation point method, for various values of the angle of inclination and the Prandtl number. The linear analysis shows that the basic state loses stability to perturbations of the transverse roll type at much lower values of the Grashof number than to perturbations of the longitudinal roll type for values of the angle of inclination close or equal to 90 deg (vertical orientation). We proceed in section 4 to calculate the two-dimensional nonlinear travelling-wave equilibrium states and investigate the stability of this secondary flow in section 5. Finally in section 6, we discuss the conclusions of this work.

2 Formulation of the Problem

We consider incompressible plane parallel convective flow induced by an internal heat source. The fluid layer is bounded between two parallel plates of infinite extent at an angle χ with respect to the horizontal plane. The origin of our cartesian coordinates x_*, y_*, and z_* with corresponding unit vectors $\mathbf{i}$, $\mathbf{j}$, and $\mathbf{k}$ is positioned in the midplane of the layer as shown in Fig. 1. Following [6] we apply the Boussinesq approximation and use h, h^2/ν and $qh^2/(2\kappa\mathrm{Gr})$, where $\mathrm{Gr}=(g\gamma q h^5)/(2\nu^2\kappa)$ is the Grashof number, as the units of length, time and temperature, respectively, to obtain the following nondimensional Navier-Stokes equations for the velocity $\mathbf{u}$ and the temperature T measured from the environment (h is the half width of the fluid layer, ν is the kinematic viscosity, q is the volume strength of the heat source that generates the basic flow, κ is the thermal diffusivity, g is the acceleration due to gravity, and γ is the coefficient of thermal expansion):

$$\frac{\partial}{\partial t}\mathbf{u}+\mathbf{u}\cdot\nabla\mathbf{u}=-\nabla\pi+(\hat{\mathbf{k}}\cos\chi+\hat{\mathbf{i}}\sin\chi)\mathrm{T}+\nabla^2\mathbf{u}, \qquad (2.1)$$

Contributed by the Heat Transfer Division for publication in the JOURNAL OF HEAT TRANSFER. Manuscript received by the Heat Transfer Division November 14, 2002; revision received May 16, 2003. Associate Editor: P. S. Ayyaswamy.

[1]For the experiments conducted in [5] a 20% in weight aqueous solution of $ZnCl_2$ was used. We note here that according to a recent study [7] for a 20% weight $ZnCl_2$ at 25°C, Pr=8.7, while at 40°C the corresponding value is Pr=6.08.

[2]The term Hopf bifurcation usually refers to the crossing of the imaginary axis by two complex conjugate eigenvalues. In the context of the present work, however, the term Hopf bifurcation is used when only one complex eigenvalue is active in the bifurcation process. This terminology has been used before and has been accepted in the literature [6,10,11].

[3]A similar behavior was found in [9] and [12].

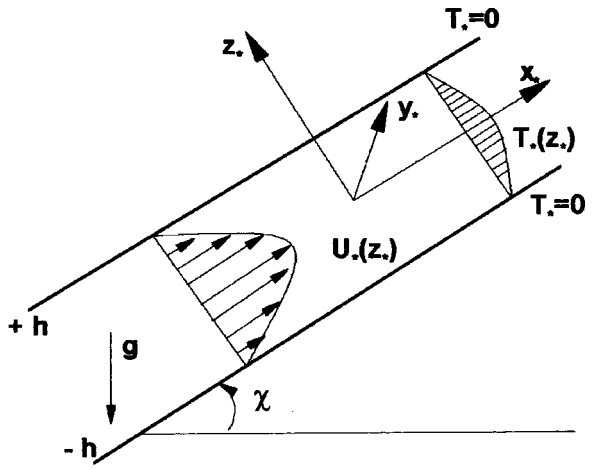

Fig. 1 The geometrical configuration exhibiting the basic symmetric velocity profile $U_*(z_*)$ of the plane-parallel shear flow in an inclined fluid layer heated internally. The temperature $T_*(z_*)$ is measured from the environment.

$$\frac{\partial}{\partial t}T+\mathbf{u}\cdot\nabla T=\mathrm{Pr}^{-1}(\nabla^2 T+2\mathrm{Gr}), \tag{2.2}$$

$$\nabla\cdot\mathbf{u}=0, \tag{2.3}$$

where $\mathrm{Pr}=\nu/\kappa$ is the Prandtl number. The two plates are kept at the same environment temperature so that T is equal to zero at the boundaries. The assumption of the Boussinesq approximation ensures that the density is regarded as constant except for the buoyancy term. Terms that can be written as gradients have been combined into the expression for $\nabla\pi$. The boundary conditions are

$$\mathbf{u}=0, \quad T=0, \quad \text{at } z=\pm 1. \tag{2.4}$$

The basic solution of Eqs. (2.1)–(2.3) consists of a basic velocity profile $\mathbf{u}_0=\mathrm{U}_0(z)\hat{\mathbf{i}}$ and a basic temperature distribution $T_0(z)$ of the form,

$$\mathrm{U}_0(z)=(\mathrm{Gr}\sin\chi/12)(z^4-6z^2+5), \tag{2.5}$$

$$T_0(z)=\mathrm{Gr}(1-z^2). \tag{2.6}$$

In order to obtain secondary solutions we separate the velocity deviations $\hat{\mathbf{u}}$ from $U_0(z)\hat{\mathbf{i}}$ and the temperature deviations θ from $T_0(z)$ into average parts $\breve{U}(z,t)\equiv\overline{\hat{\mathbf{u}}}$ and $\breve{T}(z,t)\equiv\overline{\theta}$ and residuals $\breve{\mathbf{u}}$ and $\breve{\theta}$, respectively:

$$\hat{\mathbf{u}}=\breve{U}(z,t)\hat{\mathbf{i}}+\breve{\mathbf{u}} \tag{2.7}$$

$$\theta=\breve{T}(z,t)+\breve{\theta} \tag{2.8}$$

where the average, indicated by an the overbar, is obtained by applying the operator $((\alpha\beta/4\pi^2)\int_0^{2\pi/\alpha}\int_0^{2\pi/\beta}dxdy\cdot)$. Further, we separate $\breve{\mathbf{u}}$ into the poloidal and toroidal parts:

$$\breve{\mathbf{u}}=\boldsymbol{\delta}\phi+\boldsymbol{\varepsilon}\psi=\nabla\times\nabla\times(\hat{\mathbf{k}}\phi)+\nabla\times(\hat{\mathbf{k}}\psi), \tag{2.9}$$

where φ and ψ refers to the poloidal and toroidal potentials of the velocity fluctuations, respectively, satisfying $\overline{\varphi}=\overline{\psi}=0$. It is worth pointing out that the incompressibility condition Eq. (2.3) is satisfied automatically for the decomposition of Eq. (2.9) and can therefore be eliminated from the rest of the analysis. The total mean flow and the total mean temperature are given by

$$\hat{U}(z,t)=\mathrm{U}_0(z)+\breve{U}(z,t), \tag{2.10}$$

$$\hat{T}(z,t)=T_0(z)+\breve{T}(z,t). \tag{2.11}$$

By applying the operators $\boldsymbol{\delta}\cdot$ and $\boldsymbol{\varepsilon}\cdot$ (and for simplicity of notation dropping the $\breve{}$ from the temperature fluctuations $\breve{\theta}$ hereafter) we obtain the following set of equations for the poloidal and toroidal parts:

$$\frac{\partial}{\partial t}\nabla^2\Delta_2\varphi-\nabla^4\Delta_2\varphi+\hat{U}\partial_x\nabla^2\Delta_2\varphi$$
$$=\partial_z^2\hat{U}\Delta_2\partial_x\varphi+\sin\chi\partial_x\partial_z\theta-\cos\chi\Delta_2\theta$$
$$-\boldsymbol{\delta}\cdot\{(\boldsymbol{\delta}\phi+\boldsymbol{\varepsilon}\psi)\cdot\nabla(\boldsymbol{\delta}\phi+\boldsymbol{\varepsilon}\psi)\}, \tag{2.12}$$

$$\frac{\partial}{\partial t}\Delta_2\psi-\sin\chi\partial_y\theta-\nabla^2\Delta_2\psi=\partial_z\hat{U}\Delta_2\partial_y\varphi-\hat{U}\partial_x\Delta_2\psi$$
$$-\boldsymbol{\varepsilon}\cdot\{(\boldsymbol{\delta}\phi+\boldsymbol{\varepsilon}\psi)\cdot\nabla(\boldsymbol{\delta}\phi+\boldsymbol{\varepsilon}\psi)\}, \tag{2.13}$$

where Δ_2 is the planform Laplacian. We can now rewrite the temperature equation as

$$\frac{\partial}{\partial t}\theta=-2\mathrm{Gr}(\mathbf{r}\cdot\hat{\mathbf{k}})\Delta_2\phi+\Delta_2\phi\partial_z\breve{T}-\hat{U}\partial_x\theta-(\boldsymbol{\delta}\phi+\boldsymbol{\varepsilon}\psi)\cdot\nabla\theta$$
$$+\mathrm{Pr}^{-1}\nabla^2\theta. \tag{2.14}$$

The mean flow and the mean temperature, $\breve{U}(z,t)$ and $\breve{T}(z,t)$, satisfy

$$\partial_z^2\breve{U}+\breve{T}\sin\chi+\partial_z\overline{\Delta_2\phi(\partial_x\partial_z\phi+\partial_y\psi)}=\partial_t\breve{U}, \tag{2.15}$$

$$\partial_z^2\breve{T}+\mathrm{Pr}\partial_z\overline{(\Delta_2\phi)\theta}=\mathrm{Pr}\partial_t\breve{T}. \tag{2.16}$$

For Eq. (2.15) we have considered the average of the $x-$ component of Eq. (2.1) and we additionally applied the fixed pressure condition $\overline{\partial_x\hat{\pi}}=0$. Eqs. (2.12–2.16) are subject to the homogeneous boundary conditions

$$\phi=\partial\phi/\partial z=\breve{U}=\psi=\breve{T}=\theta=0 \quad \text{at } z=\pm 1. \tag{2.17}$$

3 Linear Analysis

Analogs of Squire's transformations are available [8] for the present study, reducing the three-dimensional problem to a two-dimensional one. However, as is shown in [9] the most dangerous perturbations are not always of transverse roll type, but rather of the longitudinal roll type, depending on the value of Prandtl number and the orientation of the fluid layer. Our study in this section concentrates on examining the stability of our basic flow against infinitesimal perturbations of the transverse and the longitudinal roll types for various values of the Prandtl number over the range $0\ \mathrm{deg}\leqslant\chi\leqslant 90\ \mathrm{deg}$. For the linear analysis, Eqs. (2.15)–(2.16) are not involved. We begin our analysis by first considering transverse roll type perturbations ($\partial_y=0$), neglecting Eq. (2.13) and the nonlinear terms of Eqs. (2.12), and (2.14). We set

$$\phi=\exp\{i\alpha(x-ct)\}\sum_{n=0}^{N}a_n f_n(z),$$

$$\theta=\exp\{i\alpha(x-ct)\}\sum_{n=0}^{N}b_n g_n(z),$$

where $f_n(z)=(1-z^2)^2T_n(z)$ and $g_n(z)=(1-z^2)T_n(z)$ with T_n being the nth order Chebyshev polynomial and $a_0,\ldots,a_N$, $b_0,\ldots b_N$ are unknown complex coefficients. The factors $(1-z^2)^2$ and $(1-z^2)$ have been introduced in the expansions so that the boundary conditions for ϕ and θ are satisfied automatically. We employ the Chebyshev collocation point method to obtain an eigenvalue problem

$$A\mathbf{x}=\sigma B\mathbf{x}, \tag{3.1}$$

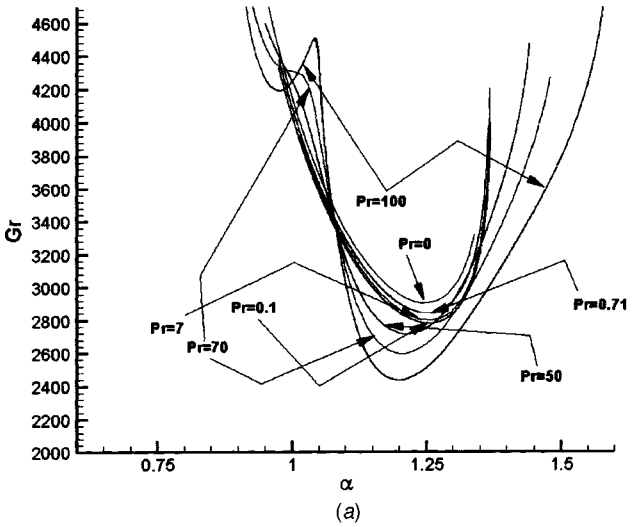

(a)

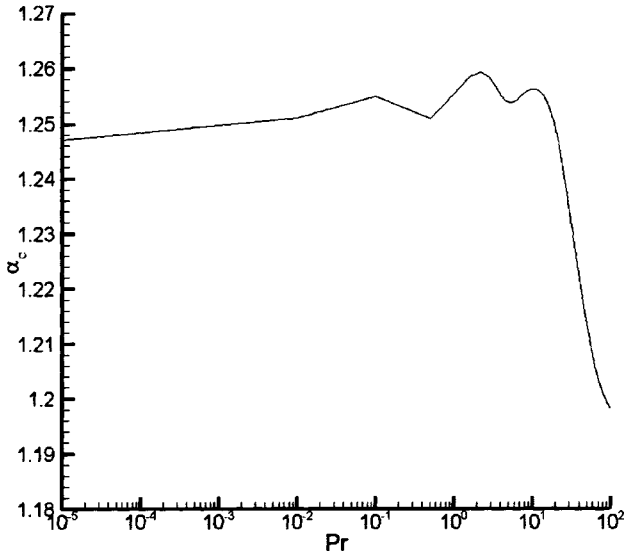

(b)

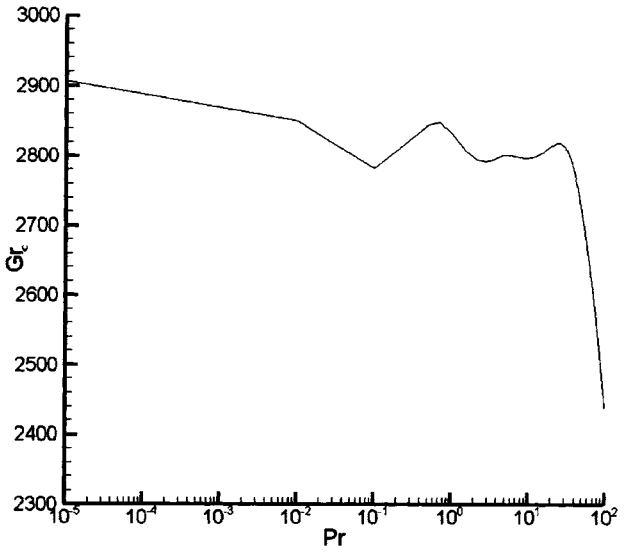

(c)

Fig. 2 (a) The linear neutral curves in the (α,Gr) plane and for various values of the Prandtl number as indicated; (b) the critical wavenumber α_c as a function of the Prandtl number; and (c) the critical Grashof number Gr_c as a function of the Prandtl number. χ=90 deg.

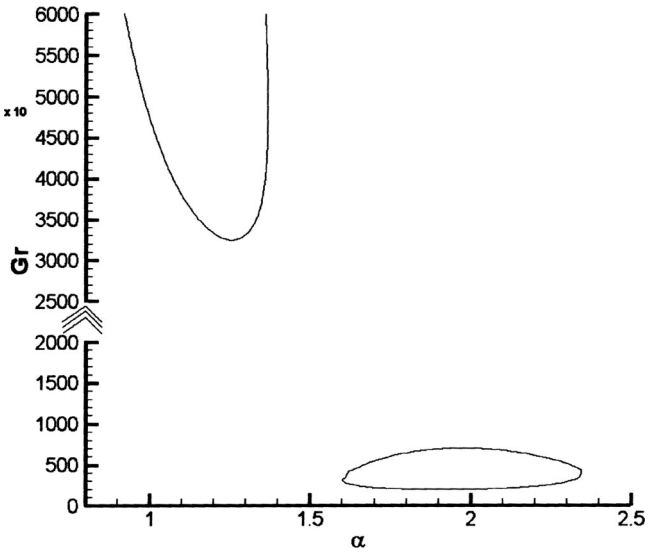

Fig. 3 The critical Grashof number for the primary and the second closed connected neutral curves for transverse roll type perturbations. Pr=7, β=0, and $\chi\approx$4.95 deg

where $\sigma=-i\alpha c$, $\mathbf{x}=(a_0,\ldots,a_N,b_0,\ldots,b_N)^T$, and A and B are $2(N+1)\times 2(N+1)$ complex matrices. The QZ method is utilized to solve Eq. (3.1) with the use of the NAG subroutine F02GJF. The real part of σ, σ_r, defines the rate of damping or amplification of the perturbations. The imaginary part of σ, $\sigma_i=-\alpha\,\mathrm{Re}[c]$, associates with the phase velocity Re[c] of the propagating perturbations in the flow. In order to achieve numerical accuracy of the results a high enough truncation number N must be chosen. It is found that $N\geqslant 35$ is satisfactory.

Figure 2(a) shows the neutral curves in the (α,Gr) plane for various Prandtl numbers in the case of vertical inclination. The neutral curves in Fig. 2(a) always correspond to a Hopf[2] bifurcation. The neutral curve for the case Pr=0 with the critical parameters $(\alpha_c,\mathrm{Gr}_c)=(1.247,2906.3637)$ obtained in [6] is included in the Fig. 2(a). Note that in the limit Pr$\rightarrow$0 Eq. (2.14) with the homogeneous boundary condition for θ gives $\theta\equiv 0$ so that the stability problem of Eq. (3.1) becomes purely hydrodynamic as

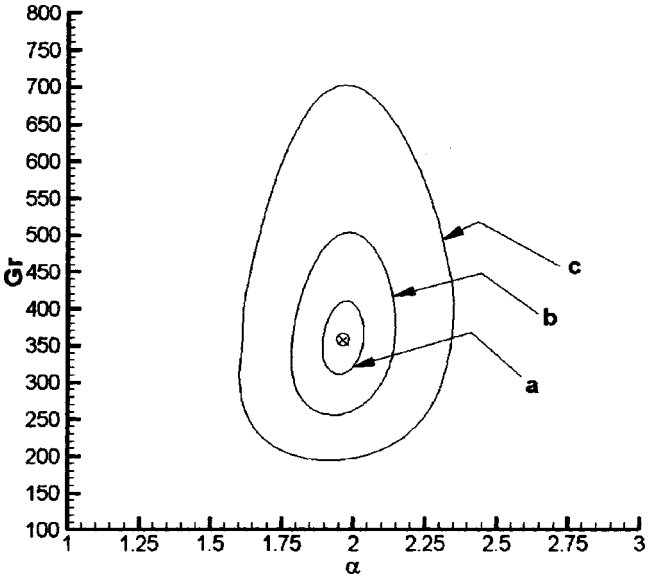

Fig. 4 The closed neutral curves for (a) $\chi\approx$5.121 deg, (b) $\chi\approx$5.085 deg, and (c) $\chi\approx$4.95 deg. Pr=7. ⊗ corresponds to the value $\chi\approx$5.1273 deg.

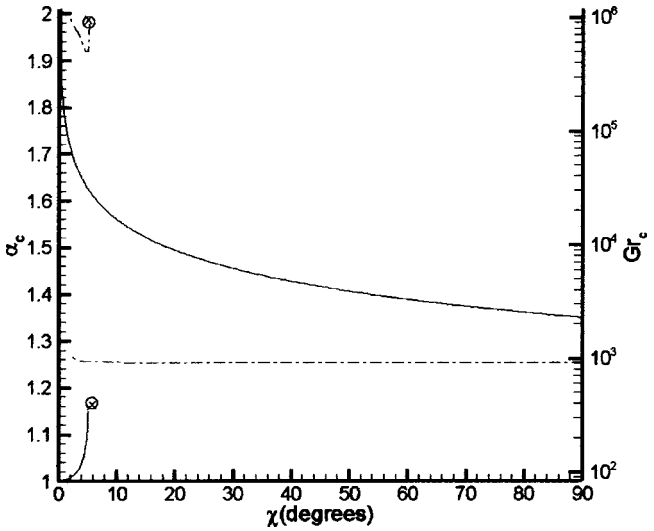

Fig. 5 The critical values of the Grashof number (right scale—continuous curve) and the wavenumber (left scale—dash-dotted curve) against the angle of inclination χ for transverse roll type perturbations (β=0). Pr=7. ⊗ corresponds to the value χ≈5.1273 deg.

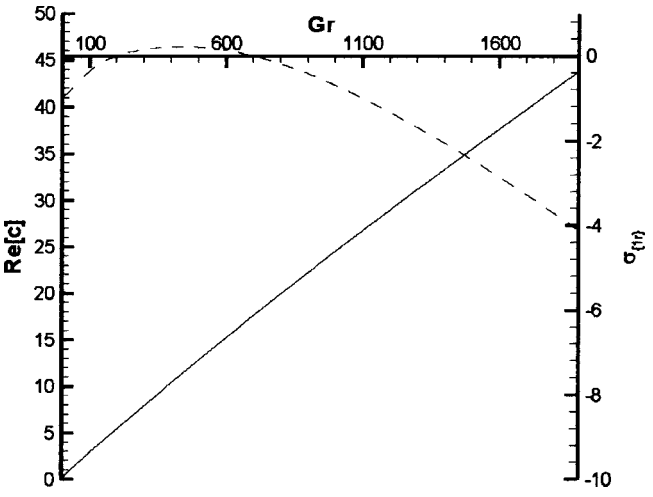

Fig. 7 The phase velocity (continuous curve—left scale) and real part of the leading eigenvalue, σ_{1r}, (dashed curve—right scale) as a function of the Grashof number for the second lower stability curve of Fig. 5 with χ≈4.95 deg and α=2.01, β=0, Pr=7

discussed in [6]. The critical Grashof number and wavenumber are given by $(\alpha_c, Gr_c)=(1.2529, 2848.0201)$ for Pr=0.71 and $(\alpha_c, Gr_c)=(1.2548, 2799.1968)$ for Pr=7. From Fig. 2(a) it is seen that thermal effects have a strong influence on the stability of the basic flow. It is interesting to note that for Pr≥70 the neutral curve consists of two minima with a second minimum developing towards smaller wavenumbers. We find that the same eigenmode is responsible for both minima[3]. As can be seen for Pr=100 in Fig. 2(a) the absolute minimum (that determines Gr_c) is associated with the larger wavenumber. For all values of the Prandtl number examined the phase velocity c of the transverse roll type perturbations is positive, which indicates that transverse roll type perturbations travel opposite to the direction of gravity. Figures 2(b) and 2(c) depict the critical wavenumber and Grashof number, respectively, as a function of the Prandtl number. From Fig. 2(b) we see that the critical wavenumber α_c for 0≤Pr≤25 is only slightly different from the critical wavenumber for the purely hydrodynamic case Pr=0, with $\alpha_c=1.247$. For Pr>25 the value of the critical wavenumber decreases.

Concentrating on Fig. 2(c) we observe that small variations of the value of Pr in the range 0<Pr≤0.1 produce a sizable decrease in the value of the critical Grashof number Gr_c from the value $Gr_c\approx2906$ for Pr=0 to $Gr_c\approx2780$ for Pr=0.1. For 0.1<Pr<35 we observe that the critical Grashof number is within the range $2780<Gr_c<2850$ and for Pr≥35 the value of the critical Grashof number decreases with $Gr_c\approx2440$ at Pr=100.

For the effect of the inclination angle χ on the linear stability the remainder of the linear analysis concentrates on the case Pr=7. We depict two distinct neutral curves for transverse roll type disturbances when χ=4.95 deg in Fig. 3. We observe that there exists a closed neutral curve that lies entirely below the

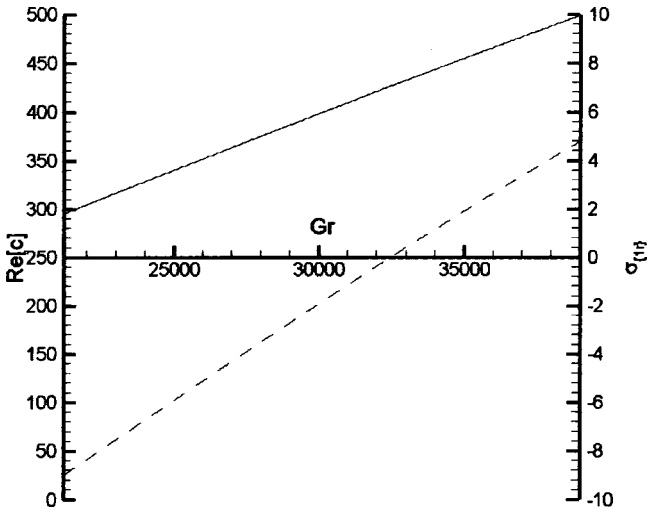

Fig. 6 The phase velocity (continuous curve—left scale) and real part of the leading eigenvalue, σ_{1r}, (dashed curve—right scale) as a function of the Grashof number for the stability curve of Fig. 5 with χ≈4.95 deg and α=1.257, β=0, Pr=7

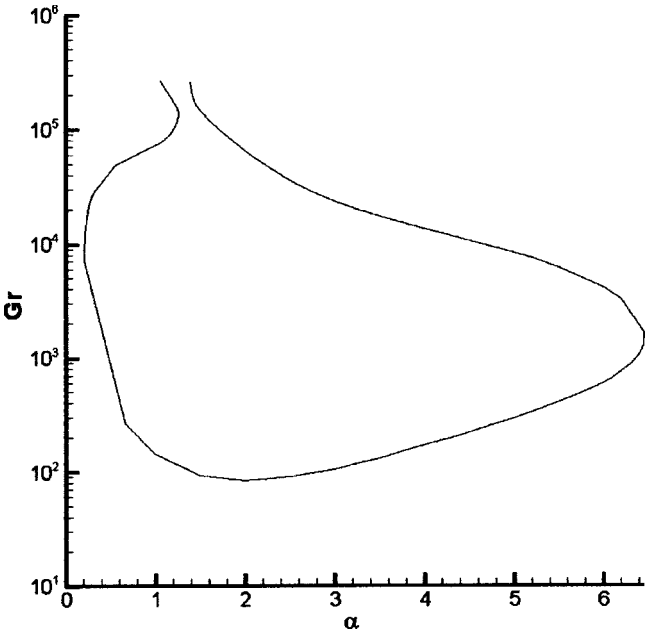

Fig. 8 The neutral curve after the smooth merger of the two neutral curves for χ≈0.9 deg and β=0 with Pr=7

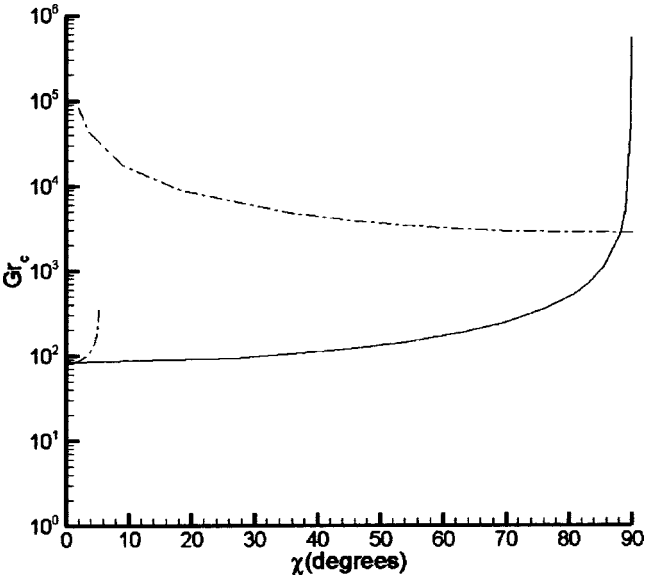

Fig. 9 The critical Grashof number as a function of the angle of inclination for longitudinal roll type perturbations (α=0, continuous curve) and for transverse roll type perturbations (β=0, dash-dotted disconnected curves). Pr=7.

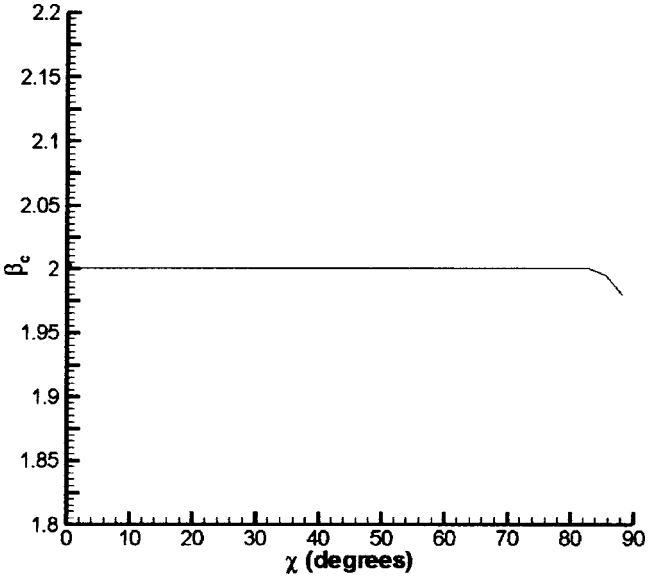

Fig. 10 The critical wavenumber β_c as a function of the angle of inclination χ for longitudinal roll type perturbations (α=0). Pr=7.

primary neutral curve. In Fig. 4 three typical closed neutral curves are given in the sequence of values of the inclination angle χ. The closed neutral curve appears at approximately $\chi \approx 5.1273$ deg (marked with $\otimes$ in Fig. 4) and extends continuously to smaller values of the angle of inclination.

The dependency of the angle of inclination on the critical Grashof number and wavenumber is given in Fig. 5. The observed discontinuity at approximately $\chi \approx 5$ deg in Fig. 5 is due to the appearance of the second closed neutral curve (see Fig. 4) with a much lower critical Grashof number than the one given by the neutral curve of Fig. 2. As can be seen from Fig. 5 there is little change in the value of α_c for 5 deg$\leqslant\chi\leqslant$90 deg. The phase velocity Re$[c]$ as well as the growth rate, σ_r, as a function of the Grashof number, for the primary neutral curve and for the closed neutral curve of Fig. 3 (with χ=4.95 deg) are presented in Figs. 6 and 7, respectively. The closed neutral curve exists over a short range of χ values. It disappears at $\chi \approx 0.9$ deg, where the primary neutral curve and the closed neutral curve merge smoothly as shown in Fig. 8. There is, therefore, one curve below the value $\chi \approx 0.9$ deg.

In order to study the stability of the basic state with respect to longitudinal roll type perturbations ($\partial_x = 0$) we ignore the nonlinear terms in Eqs. (2.12–2.14) and substitute

$$\phi = \exp\{i\beta y + \sigma t\} \sum_{n=0}^{N} a_n f_n(z),$$

$$\psi = \exp\{i\beta y + \sigma t\} \sum_{n=0}^{N} b_n g_n(z),$$

$$\theta = \exp\{i\beta y + \sigma t\} \sum_{n=0}^{N} c_n g_n(z),$$

into the resulting equations. We then follow the method outlined above in order to establish the corresponding eigenvalue problem.

In Fig. 9 the critical Grashof number as a function of the angle of inclination is given for longitudinal roll type perturbations. In the same figure we have provided the critical Grashof number given by transverse roll perturbations for comparison. As is evident from the figure our basic flow becomes unstable to perturbations of the transverse roll type at much lower Gr values than to perturbations of the longitudinal roll type for $\chi \approx 90$ deg, while for all other values of χ longitudinal roll type perturbations are responsible for instability. In the horizontal orientation, however, both longitudinal roll and transverse roll type perturbations share the same value of the critical Grashof number. In Fig. 10 we show the dependency of the critical wavenumber on the angle of inclination for longitudinal roll type perturbations. For the entire spectrum of χ the critical wavenumber, β_c, for longitudinal roll type perturbations (α=0) remains almost constant. Finally, for all values of χ examined the phase velocity of the longitudinal roll type perturbations is zero.

4 Secondary Equilibrium States

4.1 Numerical Method. In this section concentrating, only on the case of vertical orientation χ=90 deg, we calculate the two-dimensional nonlinear TW equilibrium solutions that evolve from transverse roll type perturbations at the neutral curves. Here we ignore the equation for the toroidal part (Eq. (2.13)) ($\psi \equiv 0$) and the spanwise dependency ($\partial_y = 0$). We retain, however, Eqs. (2.12,2.14) and Eqs. (2.15)–(2.16)

$$\frac{\partial}{\partial t}\nabla^2\Delta_2\varphi - \nabla^4\Delta_2\varphi + \hat{U}\partial_x\nabla^2\Delta_2\varphi = \partial_z^2\hat{U}\Delta_2\partial_x\varphi + \partial_x\partial_z\theta - \boldsymbol{\delta}\cdot\{\boldsymbol{\delta}\phi\cdot\nabla\boldsymbol{\delta}\phi\}, \quad (4.1)$$

$$\frac{\partial}{\partial t}\theta = -2\mathrm{Gr}(\mathbf{r}\cdot\hat{\mathbf{k}})\Delta_2\phi + \Delta_2\phi\partial_z\breve{T} - \hat{U}\partial_x\theta - \boldsymbol{\delta}\phi\cdot\nabla\theta + \mathrm{Pr}^{-1}\nabla^2\theta, \quad (4.2)$$

$$\partial_z^2\breve{U} + \breve{T} + \partial_z\overline{\Delta_2\phi(\partial_x\partial_z\phi)} = \partial_t\breve{U}, \quad (4.3)$$

$$\partial_z^2\breve{T} + \mathrm{Pr}\partial_z\overline{(\Delta_2\phi)\theta} = \mathrm{Pr}\partial_t\breve{T}. \quad (4.4)$$

We note that in deriving Eq. (4.3) we have applied the constraint where the vertical pressure gradient is fixed. Eqs. (4.1)–(4.4) are subject to the homogeneous boundary conditions

$$\phi = \partial\phi/\partial z = \breve{U} = \breve{T} = \theta = 0 \quad \text{at } z = \pm 1. \quad (4.5)$$

We expand ϕ and θ in terms of the set of orthogonal functions

Table 1 Values of the l_2-norms, $|l_2^a|$ and $|l_2^b|$, for the poloidal part of the velocity field and for the temperature fluctuations for a sample of the integer range M, N at $\alpha=1.247$ and $Gr=3200$ with Pr=7. The total number Σ of the complex coefficients a_{mn}, b_{mn}, C_n, D_n is also given.

$\lvert l_2^a\rvert(\times 10^2)$	$\lvert l_2^b\rvert(\times 10^3)$	M	N	Σ
0.13049	0.15940	2	19	200
0.06248	0.11541	4	21	396
0.09815	0.12959	4	27	504
0.10103	0.13202	5	37	836
0.10047	0.13155	5	41	924
0.10026	0.13143	5	43	968
0.10033	0.13145	5	45	1012

$$\phi=\sum_{m=-\infty,m\neq 0}^{\infty}\sum_{n=0}^{\infty} a_{mn}\exp\{im\alpha(x-ct)\}f_n(z), \tag{4.6}$$

$$\theta=\sum_{m=-\infty,m\neq 0}^{\infty}\sum_{n=0}^{\infty} b_{mn}\exp\{im\alpha(x-ct)\}g_n(z) \tag{4.7}$$

while we write:

$$\breve{U}=\sum_{\substack{n=\text{even}\\ n=0}}^{\infty} C_n g_n(z), \tag{4.8}$$

$$\breve{T}=\sum_{\substack{n=\text{even}\\ n=0}}^{\infty} D_n g_n(z). \tag{4.9}$$

The factor $(1-z^2)$ has been introduced in the expansions of $\breve{U}$ and $\breve{T}$, so that the conditions of Eqs. (4.5) are satisfied. The symmetry involving ϕ, discussed in [6] for Pr=0, does not change even for the present case with Pr$\neq$0. For θ we impose the reality condition $b_{-mn}=b_{mn}^*$, where * denotes complex conjugate, as well as the additional symmetry $b_{mn}=0$ for $m+n$ odd to the coefficients b_{mn}. After the expressions (4.6)–(4.9) are substituted in Eqs. (4.1)–(4.4) the nonlinear secondary equilibrium solutions are sought numerically with the aid of the Chebyshev collocation point method and the Newton-Raphson iterative method outlined in [6]. Supercritical TW solutions have been obtained for a variety of values of the Grashof number and wavenumber for Pr=0.71 and 7.

4.2 Results. As the measure of the numerical convergence we use the vector l_2-norm of the secondary equilibrium solutions, which is defined by

$$|l_2^a|=\left\{\sum_{n=0}^{N}\sum_{m=-M,m\neq 0}^{M} a_{mn}a_{mn}^*\right\}^{1/2} \tag{4.10}$$

for a_{mn} with a similar expression for $|l_2^b|$ for b_{mn}. We present the vector $|l_2^a|$ and $|l_2^b|$ for various values of m, n in Table 1. The number of unknown coefficients Σ is also presented there. The range Gr$\leqslant$3200 is examined for the numerical convergence. The table shows that a well converged secondary solution is obtained at $N=45$ and $M=5$ for Gr=3200 and Pr=7. These two parameter values are, therefore, retained for the case of Pr=7, while for Pr=0.71 the slightly lower value $N=37$ with $M=5$ is found to be satisfied.

Although numerical convergence of $|l_2^a|$ and $|l_2^b|$ is not examined for Gr$\geqslant$3200 in order to visualize the nature of the steady solutions the disturbance, fluctuating and total flow stream functions, as well as the total temperature are shown for the nonlinear state at $\alpha=1.21$, Gr=23,000, Pr=7 in Fig. 11. From Fig. 11(a) we see that the flow is characterized by a sequence of transverse vortices aligned along the vertical axis as in [6]. The addition of the disturbance $\int \breve{U}dz$ to the fluctuating stream function creates a ''snake''-like wavy motion, meandering between positive and negative values of the horizontal coordinate z as can be seen in Fig. 11(b). This meandering behavior is also present in Fig. 11(c), where the total flow is depicted. Similar characteristic for the total temperature is observed in 11(d), where the hotter fluid meanders along the vertical axis in between islands of colder (lighter shade of the contour) regions. In Fig. 12 we show the distribution of the total mean flow and temperature for the nonlinear equilibrium state of $\alpha=1.21$ for various values of Gr in the case of Pr=7. We confirm that the ''hump''-like structure observed in Fig. 12 for the total mean temperature profile is also present in the case of Pr =0.71.

5 Instabilities of the Secondary Flow

We now study the stability of the secondary flow for $\chi=90$ deg in order to identify possible bifurcation points for the tertiary flow. We superimpose three-dimensional infinitesimal perturbations $\tilde{\mathbf{u}}$ on the secondary flow $\hat{U}\hat{\mathbf{i}}+\breve{\mathbf{u}}$ in the form,

$$\tilde{\mathbf{u}}=\boldsymbol{\delta}\tilde{\phi}+\boldsymbol{\varepsilon}\tilde{\psi}, \tag{5.1}$$

and $\tilde{\theta}$ on the temperature $\hat{T}+\breve{\theta}$ and we seek to evaluate their growth rates numerically.

5.1 Numerical Method. Applying the Floquet theory, we set:

$$\tilde{\phi}=\sum_{m=-\infty}^{\infty}\sum_{n=0}^{\infty}\tilde{a}_{mn}\exp\{i(m\alpha+d)(x-ct)+iby+\sigma t\}f_n(z), \tag{5.2}$$

$$\tilde{\psi}=\sum_{m=-\infty}^{\infty}\sum_{n=0}^{\infty}\tilde{b}_{mn}\exp\{i(m\alpha+d)(x-ct)+iby+\sigma t\}g_n(z), \tag{5.3}$$

$$\tilde{\theta}=\sum_{m=-\infty}^{\infty}\sum_{n=0}^{\infty}\tilde{c}_{mn}\exp\{i(m\alpha+d)(x-ct)+iby+\sigma t\}g_n(z), \tag{5.4}$$

for the complex perturbations $\tilde{\varphi}$, $\tilde{\psi}$, $\tilde{\theta}$ that satisfy the boundary conditions:

$$\tilde{\phi}=\partial\tilde{\phi}/\partial z=\tilde{\psi}=\tilde{\theta}=0 \quad \text{at } z=\pm 1. \tag{5.5}$$

In order to derive the equations for the disturbance field $\{\tilde{\varphi},\tilde{\psi},\tilde{\theta}\}$ we follow [6], arriving at:

$$\begin{aligned}\frac{\partial}{\partial t}\nabla^2\Delta_2\tilde{\varphi}-\nabla^4\Delta_2\tilde{\varphi}+\hat{U}\partial_x\nabla^2\Delta_2\tilde{\varphi}&\\ =\partial_z^2\hat{U}\Delta_2\partial_x\tilde{\varphi}+\partial_x\partial_z\tilde{\theta}+c\partial_x\nabla^2\Delta_2\tilde{\phi}&\\ -\boldsymbol{\delta}\cdot\{(\boldsymbol{\delta}\tilde{\phi}+\boldsymbol{\varepsilon}\tilde{\psi})\cdot\nabla(\boldsymbol{\delta}\phi)+(\boldsymbol{\delta}\phi)\cdot\nabla(\boldsymbol{\delta}\tilde{\phi}+\boldsymbol{\varepsilon}\tilde{\psi})\},&\end{aligned} \tag{5.6}$$

$$\begin{aligned}\frac{\partial}{\partial t}\Delta_2\tilde{\psi}-\partial_y\tilde{\theta}-\nabla^2\Delta_2\tilde{\psi}&\\ =\partial_z\hat{U}\Delta_2\partial_y\tilde{\varphi}-\hat{U}\partial_x\Delta_2\tilde{\psi}+c\partial_x\Delta_2\tilde{\psi}&\\ -\boldsymbol{\varepsilon}\cdot\{(\boldsymbol{\delta}\tilde{\phi}+\boldsymbol{\varepsilon}\tilde{\psi})\cdot\nabla(\boldsymbol{\delta}\phi)+(\boldsymbol{\delta}\phi)\cdot\nabla(\boldsymbol{\delta}\tilde{\phi}+\boldsymbol{\varepsilon}\tilde{\psi})\},&\end{aligned} \tag{5.7}$$

$$\begin{aligned}\frac{\partial}{\partial t}\tilde{\theta}=-2\mathrm{Gr}(\mathbf{r}\cdot\hat{\mathbf{k}})\Delta_2\tilde{\phi}+\Delta_2\tilde{\phi}\partial_z\breve{T}-\hat{U}\partial_x\tilde{\theta}+c\partial_x\tilde{\theta}&\\ -(\boldsymbol{\delta}\tilde{\phi}+\mathbf{e}\tilde{\psi})\cdot\nabla\theta+(\boldsymbol{\delta}\phi+\mathbf{e}\psi)\cdot\nabla\tilde{\theta}+\mathrm{Pr}^{-1}\nabla^2\tilde{\theta}.&\end{aligned} \tag{5.8}$$

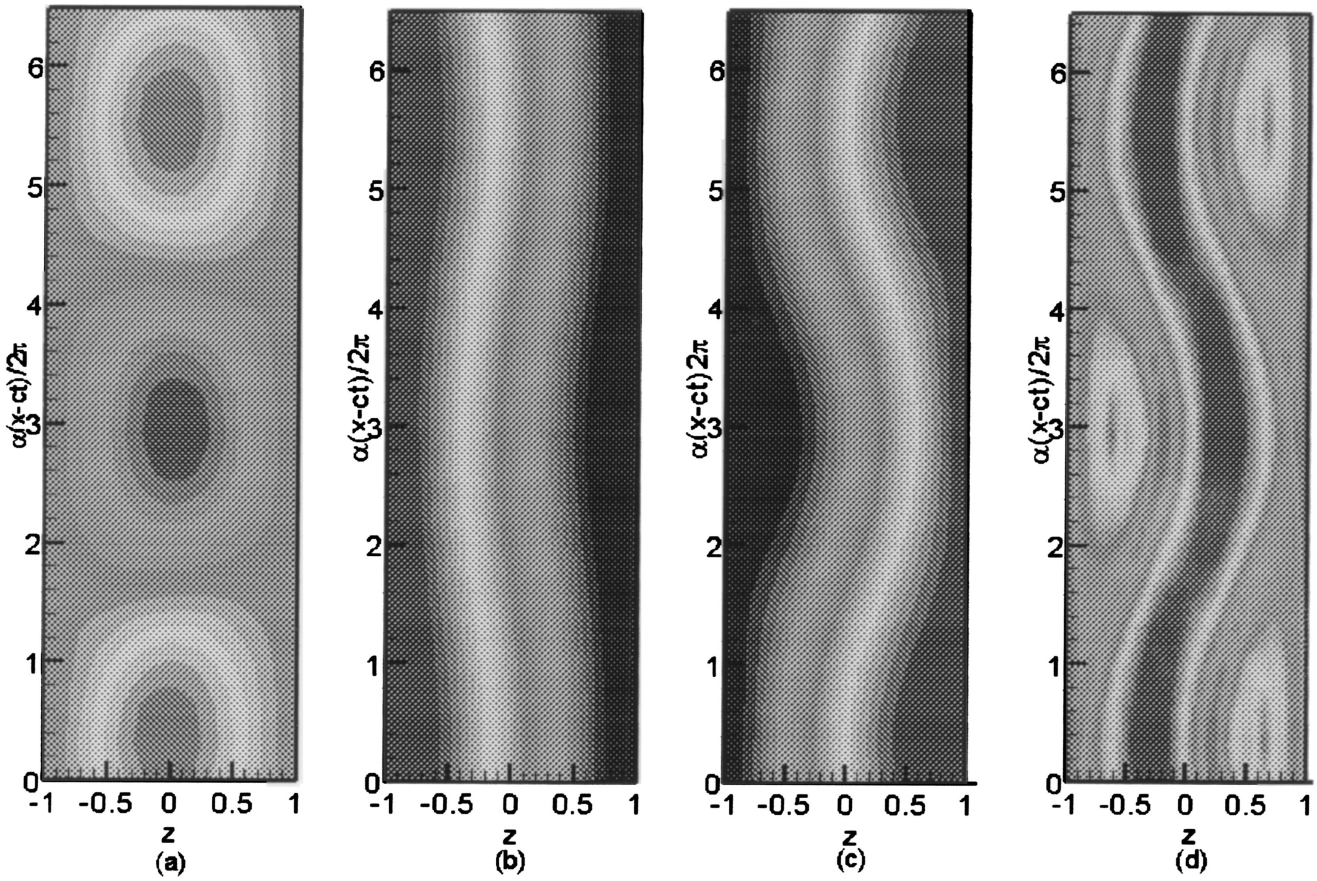

Fig. 11 The stream function of (a) the velocity fluctuations $\partial\phi/\partial x$, (b) the disturbance $\partial\phi/\partial x+\int_{-1}^{z}\check{U}dz$, (c) the total flow, $\partial\phi/\partial x+\int_{-1}^{z}\hat{U}dz$, (d) the total temperature, for the secondary state with α=1.21, Gr=23,000, Pr=7. Colder regions are represented by the lighter shade.

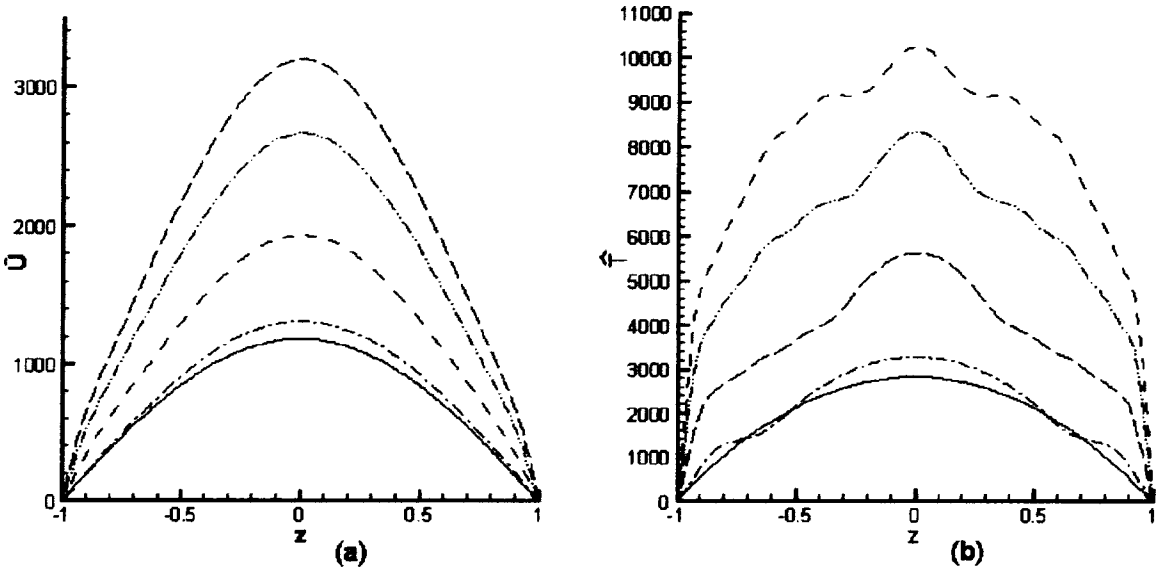

Fig. 12 The total (a) mean flow ($\hat{U}$) profile and (b) mean temperature ($\hat{T}$) profile for various Grashof numbers and for a fixed wavenumber α=1.21. In (a) and (b) the dash-dotted, dashed, dash-dot-dotted and long-dashed curves correspond to Gr=4300, 12,000, 23,000 and 33,000, respectively. The solid curve in both figures represents the basic flow and temperature distributions. Pr=7.

Table 2 Values of the real, σ_{1r}, and imaginary, σ_{1i}, parts of the most dangerous eigenvalue σ_1 for a sample of the integer range $2 \leqslant M \leqslant 8$, $25 \leqslant N \leqslant 45$. Here $\alpha=1.247$, Gr=3200, Pr=7. The value of the parameters $\{d,b\}$ is fixed at $\{\alpha/4, 0.7\}$, respectively. $\tilde{\Sigma}$ represents the total number of the unknown (complex) perturbation coefficients.

$\tilde{\Sigma}$	N	M	σ_{1r}	σ_{1i}
390	25	2	17.138341	−15.327345
1428	27	8	16.796716	−15.634601
1530	29	8	18.067435	−15.735189
1254	37	5	17.430870	−15.646481
1320	39	5	17.160454	−15.576397
1386	41	5	17.292179	−15.612212
1452	43	5	17.237890	−15.596531
1518	45	5	17.257083	−15.602684

As the value of d^2+b^2 is assumed to be different from zero for the rest of the analysis, there are no contributions to the mean flow and the mean temperature. Following the method outlined in [6] the following eigenvalue problem results:

$$A\tilde{\mathbf{x}} = \sigma B\tilde{\mathbf{x}}, \tag{5.9}$$

where $\tilde{\mathbf{x}}$ represents the unknown complex variables $\{\tilde{a}_{mn}, \tilde{b}_{mn}, \tilde{c}_{mn}\}$. The real $3(N+1)(2M+1)$ matrices A and B are functions of the real parameters d, b, Gr, Pr, α and the amplitudes of the steady state solution $\{a_{mn}, b_{mn}, c, C_n, D_n\}$. For Pr=7 we used $N=45$ and $M=5$, while for Pr=0.71 we used the slightly lower value $N=37$ with $M=5$. Equation (5.9) is solved with the use of the NAG subroutine F02GJF. Typically the dimension of the vector $\tilde{\mathbf{x}}$ is 50 percent larger than the dimension of the vector $\mathbf{x}$ representing the steady-state solution for the same truncation level as the comparison between Tables 1 and 2 shows. In Table 2 the behavior of the leading eigenvalue σ_{1r} for a sample of the integer range $2 \leqslant M \leqslant 8$, $25 \leqslant N \leqslant 45$ is given for the secondary state at $\alpha=1.247$, Gr=3200, Pr=7. As can be verified from Table 2 for $N \geqslant 41$ (Pr=7) adequate resolution of the eigenvalue can be achieved. We note that in all cases examined the symmetry relations $\sigma_{1r}(b,d)=\sigma_{1r}(b,\pm d)$, $\sigma_{1r}(b,d)=\sigma_{1r}(\pm b,d)$, are always confirmed. Our results are described in some detail below.

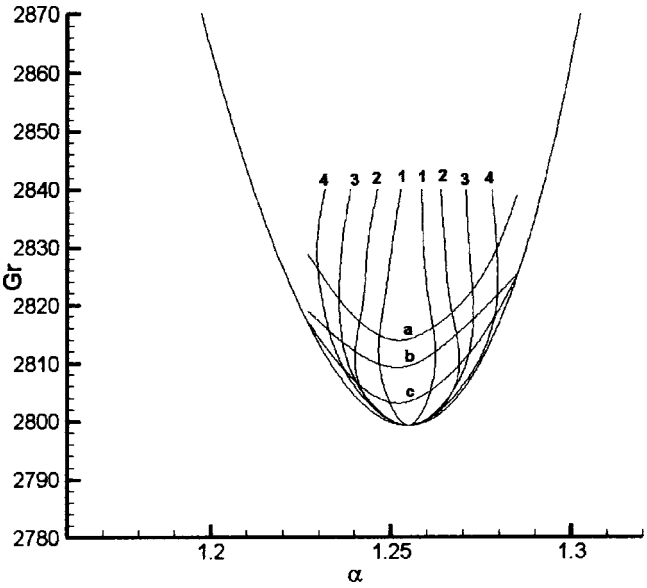

Fig. 14 Instability boundaries of secondary TWs for Pr=7. (1): $d=0.01$, (2): $d=0.02$, (3): $d=0.03$, (4): $d=0.04$, (a): $b=0.2$, (b): $b=0.15$, (c): $b=0.1$. For (1)–(4) $b=0$ and $\sigma_{1i} \neq 0$. For (a)–(c) $d=0$ and $\sigma_{1i}=0$. The outer curve represents the neutral curve.

5.2 Results. In Fig. 13 we provide an example of the behavior of the leading eigenvalue for small values of the parameters b, d when Pr=7 (a similar set of curves exists for Pr=0.71). Here the real part σ_{1r} of the leading eigenvalue σ_1 as a function of the parameter d for four different values of b is given for $\alpha=1.227$, Gr=2817. We recall that $\mathrm{Gr}_c=2816.8898$ for $\alpha=1.227$ by the linear analysis of section 3. As can be seen from Fig. 13 with a fixed value of b as indicated, we observe that as the value of the parameter d varies the real part of σ_{1r} crosses the d/α axis.

As the figure shows σ_{1r} can be positive for perturbations with $b=0.01$ and 0.1 for small d, while σ_{1r} is negative for perturbations with $b=0.005$ and 0.15 for any d. Therefore, there exists a small parameter range $0.01 \leqslant b \leqslant 0.1$ and $d/\alpha \leqslant 0.04$ where the

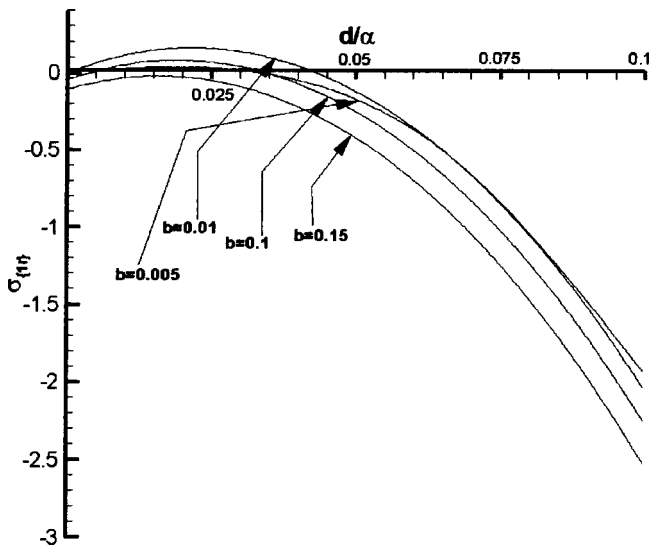

Fig. 13 The real part of the leading eigenvalue as function of d for $\alpha=1.227$, Gr=2817, Pr=7 and for fixed values of the parameter b as indicated. Note that for $\alpha=1.227$, linear stability analysis predicts a value of $\mathrm{Gr}_c=2816.8898$.

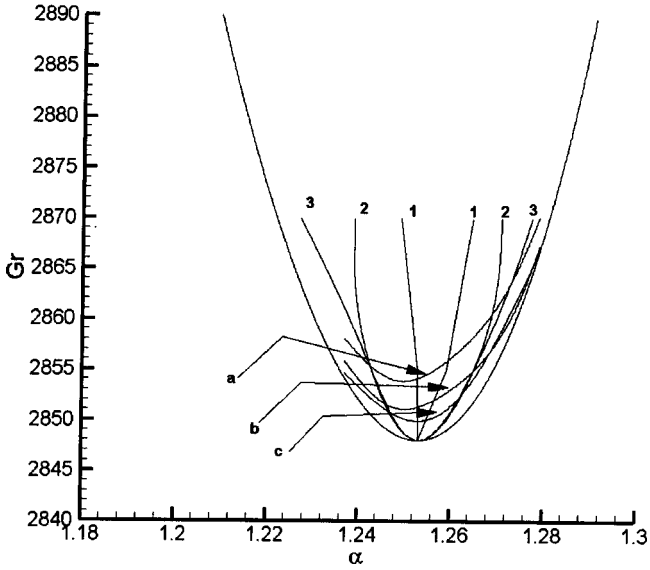

Fig. 15 Instability boundaries of secondary TWs for Pr=0.71. (1): $d=0.01$, (2): $d=0.03$, (3): $d=0.04$, (a): $b=0.2$, (b): $b=0.15$, (c): $b=0.1$. For (1)–(3) $b=0$ and $\sigma_{1i} \neq 0$. For (a)–(c) $d=0$ and $\sigma_{1i} \neq 0$. The outer curve represents the neutral curve.

secondary flow becomes unstable. We find $\sigma_{1r} \leqslant 0$ for any value of b at $d=0$. We also find that σ_{1r} decreases from zero monotonously as b increases from zero for $d=0$ as far as the secondary state is close to the neutral curve, $\mathrm{Gr} \approx \mathrm{Gr}_c$. When the secondary state is away from the neutral curve, however, σ_{1r} increases from zero first and then decreases monotonously for $d=0$ as b increases from zero, having a positive peak value at a small b (this tendency has also been observed in the case Pr=0.71). Similar instabilities for small values of the parameters b and d were also observed in the calculations performed in [13] (monotone B instability) for the case of natural convection in a vertical slot and [14] (zigzag instability) for the case of convection in a horizontal fluid layer heated from below.

We present the stability boundaries of the secondary TW solutions for the vertical orientation of the fluid layer with Pr=7 in Fig. 14 and with Pr=0.71 in Fig. 15. In the case of Pr=0.71 the boundary is formed by the Eckhaus ($b=0$) and Hopf bifurcation ($d=0$) curves while for Pr=7 the boundary is formed by the Eckhaus ($b=0$) and phase-locked bifurcation ($d=0$) curves. Note that for the Hopf bifurcation the real and imaginary parts of the leading eigenvalue σ_1 satisfy $\sigma_{1r}=0$ and $\sigma_{1i} \neq 0$ while for the phase-locked bifurcation they satisfy $\sigma_{1r}=\sigma_{1i}=0$. In Figs. 14 and 15 we provide the boundaries of several Eckhaus curves, depending on the values of the parameter d as indicated.

Our calculations have shown that for Pr=7 the most unstable secondary instability mode is phase-locked with the two-dimensional TW solution, i.e., $\sigma_{1i}=0$ in the frame moving with the phase speed of the TWs. In all cases examined for Pr=0.71 the most unstable secondary instability mode has $\sigma_{1i} \neq 0$ and, therefore, a Hopf bifurcation takes place. This occurrence combined with the underlying two-dimensional TWs shows that for Pr=0.71 the bifurcation is a spatially periodic flow with two frequencies in time (quasi-periodic).

6 Conclusions

In this work we have investigated the nonlinear stability of internally heated flows in a channel by extending the work on the case of a vertical channel with Pr=0 [6] to cases of an inclined channel with nonzero Prandtl numbers. Linear stability analysis for various values of the angle of inclination showed that neutral curves always corresponded to a Hopf bifurcation.

Next, nonlinear secondary equilibrium states were obtained numerically with the aid of the Chebyshev collocation point method and the Newton-Raphson iterative method. For the cases with Pr=0.71 and 7 studied here the secondary equilibrium states for $\chi=90$ deg bifurcate supercritically as for the case with Pr=0 [6]. Nonlinear properties of the secondary flow, such as the spatial structures of the transverse vortices and the mean flow, were analyzed in some detail, although direct comparisons with the experimental work of [5] are not possible as they have allowed for a temperature gradient along the streamwise axis, which was ignored in our studies.

Finally, we studied the stability of the secondary equilibrium state by applying Floquet theory. Traces of the Eckhaus curve were identified and our calculations showed that the bifurcation is quasi-periodic for Pr=0.71 as for Pr=0 [6] while for Pr=7 the bifurcation is phase-locked with the secondary flow. The results of our study also showed that the secondary flow becomes unstable just above the primary neutral curve in the (α,Gr) plane for small values of the parameter d and b (see Figs. 14 and 15). Therefore, the flow pattern likely to be observed is almost two-dimensional with small wavenumber modulation in both the streamwise and the spanwise directions.

Stability results concerning secondary flow were presented for only $\chi=90$ deg in this study. But as is shown in Fig. 9 longitudinal roll type perturbations are more important than transverse roll type perturbations for 0 deg$\leqslant\chi\leqslant$89 deg. Investigations of the transition due to longitudinal roll type perturbations and the competition of transverse roll and longitudinal roll perturbations at $\chi \approx 89$ deg are currently under way and will be reported separately.

References

[1] Horvat, A., Kljenak, I., and Marn, J., 2001, "Two-Dimensional Large-Eddy Simulation of Turbulent Natural Convection Due to Internal Heat Generation," Int. J. Heat Mass Transfer, **44**, pp. 3985–3995.

[2] Nourgaliev, R. R., Dinh, T. N., and Sehgal, B. R., 1997, "Effect of Fluid Prandtl Number on Heat Transfer Characteristics in Internally Heated Liquid Pools With Rayleigh Number Up to 10^{12}," Nucl. Eng. Des., **169**, pp. 165–184.

[3] Worner, M., Schmidt, M., and Grotzbach, G., 1997, "Direct Numerical Simulation of Turbulence in an Internally Heated Convective Fluid Layer and Implications for Statistical Modelling," J. Hydraul. Res., **35**, pp. 773–797.

[4] Arpaci, V. S., 1995, "Buoyant Turbulent Flow Driven by Internal Heat Generation," Int. J. Heat Mass Transfer, **38**, pp. 2761–2770.

[5] Wilkie, D., and Fisher, S. A., 1961, "Natural Convection in a Liquid Containing a Distributed Heat Source," *International Heat Transfer Conference*, Paper 119, University of Colorado, Boulder, pp. 995–1002.

[6] Nagata, M., and Generalis, S., 2002, "Transition in Convective Flows Heated Internally," ASME J. Heat Transfer, **124(4)**, pp. 635–642.

[7] National Engineering Laboratory, 1998, "Prandtl Number for $ZnCl_2$ Solutions," private communication.

[8] Gershuni, G. Z., and Zhukhovitskii, E. M., 1976, *Convective Stability of Incompressible Fluids* (Translated from the Russian by D. Lowish), Keterpress Enterprises, Jerusalem.

[9] Gershuni, G. Z., Zhukhovitskii, E. M., and Yakimov, A. A., 1974, "On Stability of Plane-Parallel Convective Motion Due to Internal Heat Sources," Int. J. Heat Mass Transfer, **17**, pp. 717–726.

[10] Ehrenstein, U., and Koch, W., 1991, "Three-Dimensional Wavelike Equilibrium States in Plane Poiseuille Flow," J. Fluid Mech., **228**, pp. 111–148.

[11] Pugh, J. D., and Saffman, P. G., 1988, "Two-Dimensional Superharmonic Stability of Finite Amplitude Waves in Plane Poiseuille Flow," J. Fluid Mech., **194**, pp. 295–307.

[12] Heiber, C. A., and Gebhart, B., 1971, "Stability of Vertical Natural Convection Boundary Layers: Some Numerical Solutions," J. Fluid Mech., **48**, pp. 625–646.

[13] Chait, A., and Korpela, S. A., 1989, "The Secondary Flow and Its Stability for Neutral Convection in a Tall Vertical Enclosure," J. Fluid Mech., **200**, pp. 189–216.

[14] Busse, F. H., and Glever, R. M., 1979, "Instabilities of Convection Rolls in a Fluid of Moderate Prandtl Number," J. Fluid Mech., **91**, pp. 319–335.

Enhanced Forced Convection Heat Transfer From a Cylinder Using Permeable Fins

Bassam A/K Abu-Hijleh
e-mail: Bassam.Abu-Hijleh@RMIT.edu.au
School of Aerospace,
Mechanical and Manufacturing Engineering,
RMIT University,
Bundoora, Victoria 3083,
Australia

The problem of cross-flow forced convection heat transfer from a horizontal cylinder with multiple, equally spaced, high conductivity permeable fins on its outer surface was investigated numerically. The heat transfer characteristics of a cylinder with permeable versus solid fins were studied for several combinations of number of fins and fin height over the range of Reynolds number (5–200). Permeable fins provided much higher heat transfer rates compared to the more traditional solid fins for a similar cylinder configuration. The ratio between the permeable to solid Nusselt numbers increased with Reynolds number and fin height but tended to decrease with number of fins. This ratio was as high as 4.35 at Reynolds number of 150 and a single fin with a nondimensional height of 3.0. The use of 1–2 permeable fins resulted in much higher Nusselt number values than when using up to 18 solid fins. Such an arrangement has other benefits such as a considerable reduction in weight and cost. [DOI: 10.1115/1.1599371]

Keywords: Computational, Enhancement, Finned Surfaces, Forced Convection, Heat Transfer, Porous Media

Introduction

Laminar forced convection across a heated cylinder is an important problem in heat transfer. It is used to simulate a wide range of engineering applications as well as provide a better insight into more complex systems of heat transfer. Accurate knowledge of the convection heat transfer around circular cylinders is important in many fields, including heat exchangers, hot water and steam pipes, heaters, refrigerators and electrical conductors. Because of its industrial importance, this class of heat transfer has been the subject of many experimental and analytical studies. Though a lot of work has been done in this area, it is still remains the subject of many investigations. Recent economic and environmental concerns have raised the interest in methods of increasing or reducing the convection heat transfer, depending on the application, from a horizontal cylinder. Researchers continue to look for new methods of heat transfer control. The use of porous materials to alter the heat transfer characteristics has been reported by several researchers including Vafai and Huang [1], Al-Nimr and Alkam [2], and Abu-Hijleh [3].

Fins have always been used as a passive method of enhancing the convection heat transfer from cylinders [4–7]. The presence of the solid fins has an effect on both the aerodynamic as well as the thermal characteristics of the flow. The fins tend to obstruct the airflow near the cylinder surface, thus reducing the heat transfer from the cylinder to the surrounding fluid. On the other hand, the fins increase the heat transfer area resulting in an increase in the heat transfer from the cylinder to the surrounding fluid. The net result of these two opposing effects depends on the combination of number of fins, fin height, and Reynolds number. Previous work by the author has shown that increasing the number of uniformly spaced solid fins beyond a Reynolds number dependent value does not increase and can even decrease the Nusselt number [8]. Permeable fins can offer less resistance to the airflow around the cylinder while still offering the increased heat transfer surface area of solid fins. Such fins are expected to offer much enhanced heat transfer rates from a cylinder than solid fins. Stewart and Burns [9] reported enhanced convection heat transfer characteristics in a concentric annulus with heat generating porous media when using a permeable inner boundary. Zhao and Liao [10] and Zhao and Song [11] showed that forced convection heat transfer in a cavity could be significantly enhanced using permeable walls. Previous work by the author has shown that the use of permeable fins to be very effective in the case of natural convection heat transfer from a cylinder [12]. No published work could be located that discusses the use of permeable fins on the forced convection heat transfer from a horizontal cylinder in cross-flow.

This paper details the changes in the Nusselt number due to the use of different number of equally spaced high conductivity permeable fins placed at the cylinder's outer surface. The fluid under consideration is Air. The elliptic momentum and energy equations were solved numerically using the stream function-vorticity method on a stretched grid. This detailed study included varying the Reynolds number (5–200), number of fins (1–18), and the nondimensional fin height (0.15–3.0). This range of values is based on the experience gained from a previous work using uniformly spaced solid fins for the same configuration [8]. Due to symmetry, the computations were carried on half the physical domain making use of the horizontal symmetry plane passing through the center of the cylinder. The number of fins reported herein is that on one half of the cylinder. No fins were located at the symmetry plane.

Mathematical Analysis

The steady-state equations for two-dimensional laminar forced convection over a horizontal cylinder are given by:

$$\frac{1}{r}\frac{\partial(ru)}{\partial r}+\frac{1}{r}\frac{\partial v}{r\partial\theta}=0 \tag{1}$$

$$u\frac{\partial u}{\partial r}+\frac{v}{r}\frac{\partial u}{\partial\theta}-\frac{v^2}{r}=-\frac{1}{\rho}\frac{\partial p}{\partial r}+\nu\left[\frac{\partial^2 u}{\partial r^2}+\frac{1}{r}\frac{\partial u}{\partial r}-\frac{u}{r^2}+\frac{1}{r^2}\frac{\partial^2 u}{\partial\theta^2}-\frac{2}{r^2}\frac{\partial v}{\partial\theta}\right] \tag{2}$$

Contributed by the Heat Transfer Division for publication in the JOURNAL OF HEAT TRANSFER. Manuscript received by the Heat Transfer Division November 27, 2002; revision received May 16, 2003. Associate Editor: K. S. Ball.

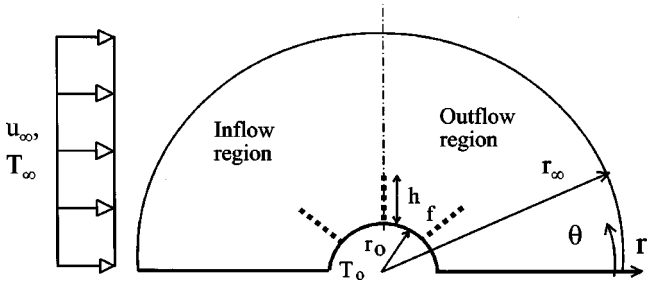

Fig. 1 Schematic diagram of the cylinder with equally spaced permeable fins

$$u\frac{\partial v}{\partial r}+\frac{v}{r}\frac{\partial v}{\partial \theta}+\frac{uv}{r}=-\frac{1}{\rho}\frac{\partial p}{\partial r}+\nu\left[\frac{\partial^2 v}{\partial r^2}+\frac{1}{r}\frac{\partial v}{\partial r}-\frac{v}{r^2}+\frac{1}{r^2}\frac{\partial^2 v}{\partial \theta^2}+\frac{2}{r^2}\frac{\partial u}{\partial \theta}\right] \tag{3}$$

$$u\frac{\partial T}{\partial r}+\frac{v}{r}\frac{\partial T}{\partial \theta}=\alpha\nabla^2 T \tag{4}$$

where,

$$\nabla^2\equiv\left[\frac{\partial^2}{\partial r^2}+\frac{1}{r}\frac{\partial}{\partial r}+\frac{1}{r^2}\frac{\partial^2}{\partial \theta^2}\right]$$

Equations (1–4) are subject to the following boundary conditions:

1. On the cylinder surface, i.e., $r=r_o$; $u=v=0$, and $T=T_o$.
2. Far-stream from the cylinder, i.e., $r\to\infty$; $u\to u_\infty\cos(\theta)$ and $v\to -u_\infty\sin(\theta)$. As for the temperature, the farstream boundary condition is divided into an outflow ($\theta\leqslant 90°$) and an inflow ($\theta>90°$) regions, Fig. 1. The far-stream temperature boundary conditions are $T=T_\infty$ and $\partial T/\partial r=0$ for the inflow and outflow regions, respectively.
3. Plane of symmetry; $\theta=0$ and $\theta=180°$; $v=0$ and $\partial u/\partial\theta=\partial T/\partial\theta=0$.
4. On the surface of solid fin(s); $u=v=0$. On the surface of permeable fin(s); $u=0$. The least restrictive permeable boundary condition is that of no resistance to the velocity normal to the fin surface, i.e., $v=\text{constant}\equiv\partial v/\partial\theta=0$ [9].
5. Since both types of fins are assumed to be very thin and of very high conductivity, the temperature at any point along the fin will be that of the cylinder surface, i.e., $T_f=T_o$. The fins are equally spaced around the perimeter of the cylinder. No fins were placed at the horizontal line of symmetry, i.e., at $\theta=0$ and 180°, see Fig. 2.

The major assumptions made regarding the fins' boundary conditions above are: fin thickness→0, fin thermal conductivity→∞, and fin flow resistance→0. These assumptions we introduced in order to simplify the solution of the problem and will give the ''best case scenario'' effect of using permeable fins. ''Real'' fins will have a finite thickness and thermal conductivity. If this is to be taken into account, the problem will become that of conjugated conduction—convection heat transfer. This will greatly complicate the solution procedure as well as introduce two new parameters that need to be considered, i.e., fin thickness and fin thermal conductivity. Neglecting the fin's flow resistance will only change the velocity gradient boundary condition at the fin but will not affect the computational procedure. Still this will introduce another parameter that needs to be addressed. The inclusion of any of these parameters will greatly increase the number of different cases that need to be simulated and will further expand the size of this paper. Thus as a first attempt at studying the benefits of permeable fins, the author made a conscious decision to introduce the above mentioned simplifying assumptions. With the ''ideal'' performance of permeable fins established, future work can focus on real fin effects such as the fin's flow resistance, thickness, and thermal conductivity.

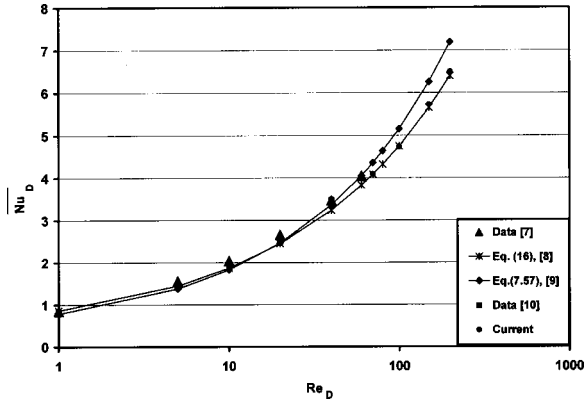

Fig. 2 Comparison of the local Nusselt number for the case of a smooth cylinder. The equations' numbers are from their respective references

The local Nusselt number, based on diameter, on the cylinder surface is given by

$$\mathrm{Nu}_D(\theta)=\frac{Dh(\theta)}{k}=-\frac{D}{(T_o-T_\infty)}\frac{\partial T(r_o,\theta)}{\partial r} \tag{5}$$

The local Nusselt number at fin, based on diameter, is given by

$$\mathrm{Nu}_{D,F}(\theta)=\int_1^{1+h_f}-\frac{D}{(T_o-T_\infty)}\frac{1}{r}\left[\left.\frac{\partial T(r,\theta)}{\partial r}\right|_{\text{top}}+\left.\frac{\partial T(r,\theta)}{\partial r}\right|_{\text{bottom}}\right]dr \tag{6}$$

The effect of adding the fin(s) on the convection heat transfer from the cylinder will be presented in terms of the normalized Nusselt number ($\overline{\mathrm{NU}_{D,F}}$) which shows the relative change in the Nusselt number compared to the case of a smooth cylinder, Eq. (7) below. The ratio of ($\overline{\mathrm{NU}_{D,F}}$) permeable fins to ($\overline{\mathrm{NU}_{D,F}}$) solid fins will be used to gage the enhancement in heat transfer due to the use of permeable fins in place of solid fins, ($\overline{\mathrm{RNU}_{D,F}}$), Eq. (8) below.

$$\overline{\mathrm{NU}_{D,F}}=\overline{\mathrm{Nu}_{D,F}}/\overline{\mathrm{Nu}_{D,o}} \tag{7}$$

$$\overline{\mathrm{RNU}_{D,F}}=(\overline{\mathrm{NU}_{D,F}})_{\text{Permeable}}/(\overline{\mathrm{NU}_{D,F}})_{\text{solid}} \tag{8}$$

Equations (1–4) along with the corresponding boundary conditions were nondimensionalized using the incoming free-stream velocity (u_∞) and cylinder radius (r_o) then solved using the stream function-vorticity method using the finite difference method [12]. A stretched grid in the radial direction was used in order to accurately resolve the boundary layer around the cylinder [12] and [13]. The resulting system of algebraic equations was solved using the hybrid scheme [14]. Such a method proved to be numerically stable for convection-diffusion problems. The finite difference form of the equations was checked for consistency with the original PDEs [14]. The iterative solution procedure was carried out until the error in all solution variables became less than a predefined error level (ϵ). Other predefined parameters needed for the solution method included the placement of the far-stream boundary condition (R_∞) and the number of grid points in both radial and tangential directions, N and M, respectively. Extensive testing was carried out in order to determine the effect of each of these parameters on the solution. This was done to ensure that the

solution obtained was independent of and not tainted by the predefined value of each of these parameters. The testing included varying the value of ϵ from 10^{-3} to 10^{-6}, R_∞ from 5 to 50, N from 100 to 250, and M from 120 to 200. The results reported herein are based on the following combination: $N=210$, $M=180$, $R_\infty=40$, and $\epsilon=10^{-5}$. Increasing any of these parameters resulted in minimal change ($\leqslant 1\%$) in the computed Nusselt number. The current gird resolution is better than most grid resolutions used in published studies of natural [5], forced convection from a heated cylinder [6], and mixed convection at different angles of attack [7]. The large number of grid points in the tangential direction (M) was to ensure that there were sufficient grid points between the fins to properly resolve the flow between the fins, even when using 18 fins. In comparison, the use of 60 points in the tangential direction would have been sufficient to resolve the flow around a smooth cylinder [7]. Figure 2 shows very good agreement between the profiles of the average Nusselt number calculated by the current code and the several results reported in the literature [7–10], for the case of a smooth cylinder with no fins.

In the previous work for uniformly spaced solid fins [12], the number of grid points was varied in the radial ($N=150-163$) and tangential ($M=169-180$) directions in order to insure that all fins coincided with one of the grid's radial lines and that the fins end coincided with one of the grid's tangential lines. The need for the fins to coincide with the grid was also observed in this study but in a different fashion. In order to avoid any changes that might result from using different grids for different combinations of number fin(s) and fin height, a fixed size grid was used for combinations in this study (210×180). In this study the fin's tangential location was varied in 15° increments between 15–165°. Thus using $M=180$ insured that the tangential grid resolution was suitable for all tangential fin locations. The hardest part was adjusting the radial grid resolution to insure that the fin's end coincided with one of the radial grid points. The nominal fin heights (H) used in this study were: 0.15, 0.35, 0.75, 1.5, and 3.0. The combination of $N=210$ and $R_\infty=40$ resulted in a difference of less that 1% between the actual fin height and the nominal fin height used in the current study. The actual height being that of the fin used in the calculation with the fin's end coinciding with the closest radial grid point while using a fixed radial grid resolution ($N=210$). Also in this work, the location of the far-stream boundary (R_∞) was set much further than the previous work for solid fins only ($R_\infty=40$ versus 15 in [12]). The significant increase in R_∞ was needed when using permeable fins. Initial gird testing revealed that long permeable fins resulted in a much bigger wake which extended for a longer distance downstream of the cylinder than when using solid fins, as will be shown later in the results section. This required the use of the larger R_∞ so that the far-stream boundary conditions do not affect the solution. The use of large R_∞ also influenced the radial size of the gird in order to maintain proper grid resolution near the cylinder surface.

Results

The effect of fins on the forced cross-flow heat transfer from a horizontal isothermal cylinder was studied for several combinations of number of fins ($F=1,3,5,8,12,18$), nondimensional fin height ($H=0.15,0.35,0.75,1.5,3.0$), and Reynolds number ($\mathrm{Re}_D=5,10,20,40,70,100,150,200$). All computations and calculations were carried at the eight values of Reynolds number listed above. To save space, only the results of $\mathrm{Re}_D=5$, 20, 70, and 150 will be shown. The results at the other values of Reynolds number had similar trends to the Reynolds number values that will be reported herein. The change in the average Nusselt number, for a given value of Reynolds number, due to the addition of F fin(s) ($\overline{\mathrm{Nu}_{D,F}}$) was normalized by the Nusselt number of a smooth cylinder, no fins, at the same Reynolds number ($\overline{\mathrm{Nu}_D}$). This was done in order to focus on the relative effect of adding the fins. The solid fin cases were re-computed using the current fixed size grid, not the results of the previous work [8], and are intended to show the heat transfer enhancement due to the use of permeable fins. This will be done by looking at the ratio of the normalized Nusselt number for the case of permeable fins to that of solid fins, each with the same number of fins.

Figure 3 shows the change in the normalized average Nusselt number as a function of number of fins at different values of fin height and selected Reynolds numbers. The solid lines correspond to solid fins while the dotted lines correspond to permeable fins. It can be seen that the use of permeable fins results in a significant heat transfer enhancement over solid fins under the same geometric and flow conditions. The advantage of using permeable fins increased with increased Reynolds number and fin height but decreased with increased number of fins. The cause of this will be discussed later when looking at the changes of the local Nusselt number along the cylinder surface due to the addition of solid and permeable fins. The use of a single permeable fin seems to offer the best conditions for enhanced convection heat transfer from the cylinder, particularly as the Reynolds number and/or fin height increases. Under no condition did the use of permeable fins result in a normalized Nusselt number <1.0, as opposed to the case of using a small number of short solid fins and high Reynolds number [8].

Figure 4 shows the shows the ratio of ($\overline{\mathrm{NU}_{D,F}}$) permeable fins to ($\overline{\mathrm{NU}_{D,F}}$) solid fins, $\overline{R\mathrm{NU}_{D,F}}$, for the same values of Reynolds numbers shown in Fig. 3. This figure shows the relative gain in enhanced heat transfer due to the use of permeable versus solid fins. Under no conditions did the use of permeable fins result in a lower Nusselt number than solid fins. The enhancement due to the use of permeable fins was as high as 4.35 for the case of $\mathrm{Re}_D=150$, $F=1$, and $H=3.0$. The advantage of permeable fins tended to decreases with the number of fins for all but the shortest fins. This is due to the different trends in the Nusselt number change when using permeable versus solid fins, Fig. 3.

Figure 5 shows the local Nusselt number distribution along the surface of the cylinder, including that of the fin(s), for the case of $\mathrm{Re}_D=70$ and $H=3.0$ at different number of solid and permeable fin(s). The distribution of the smooth cylinder, no fins, is also shown for comparison. Note that the direction of the x-axis in Fig. 5 is reversed in order to comply with the direction of the angular position shown in Fig. 1. Also there are two charts in Fig. 5 for the case of permeable fins. One with a full range y-axis scale, Fig. 5(b), and the other with a y-axis equal to that of the solid fins, Fig. 5(c). Figure 5(c) is intended to show the different local effects along the cylinder surface when using permeable versus solid fins. Figure 5(a) shows the local increase in the Nusselt number at the location of the solid fins as well as the reduction in the local Nusselt number from the rest of the cylinder surface. This local Nusselt number reduction is caused by the reduction in the air speed ahead of and in the wake of the solid fins. When using more than one solid fin, the downstream fins have a lower contribution to the overall heat transfer than the upstream fins. The exception being for fins that lay in the recirculation zone at the back of the cylinder, e.g., the case of $F=5$. Figure 5(b) shows the significant increase in the local Nusselt number at the location of the permeable fins, which is responsible for the higher heat transfer rates from permeable fins compared to solid fins. The fact that the air can flow through the permeable fins without restriction results in very high convection heat transfer rates. Figure 5(c) shows the cause of the reduction in Nusselt number with increased number of permeable fins seen in Fig. 3. Although permeable fins have a lower effect on the local Nusselt number upstream of the fins, there was almost no heat transfer from the back half of the cylinder ($\theta<90°$), even if there were fins there, i.e., cases of $F=3$ and 5. The high heat transfer rate of the permeable fins caused the air flowing trough them to heat up significantly resulting in a large thermal wake. This will reduce the temperature difference between the downstream fins and the hot incoming air, which in turn translates to reduced convection heat transfer from those fins. The fact that the air was free to flow through the permeable fins im-

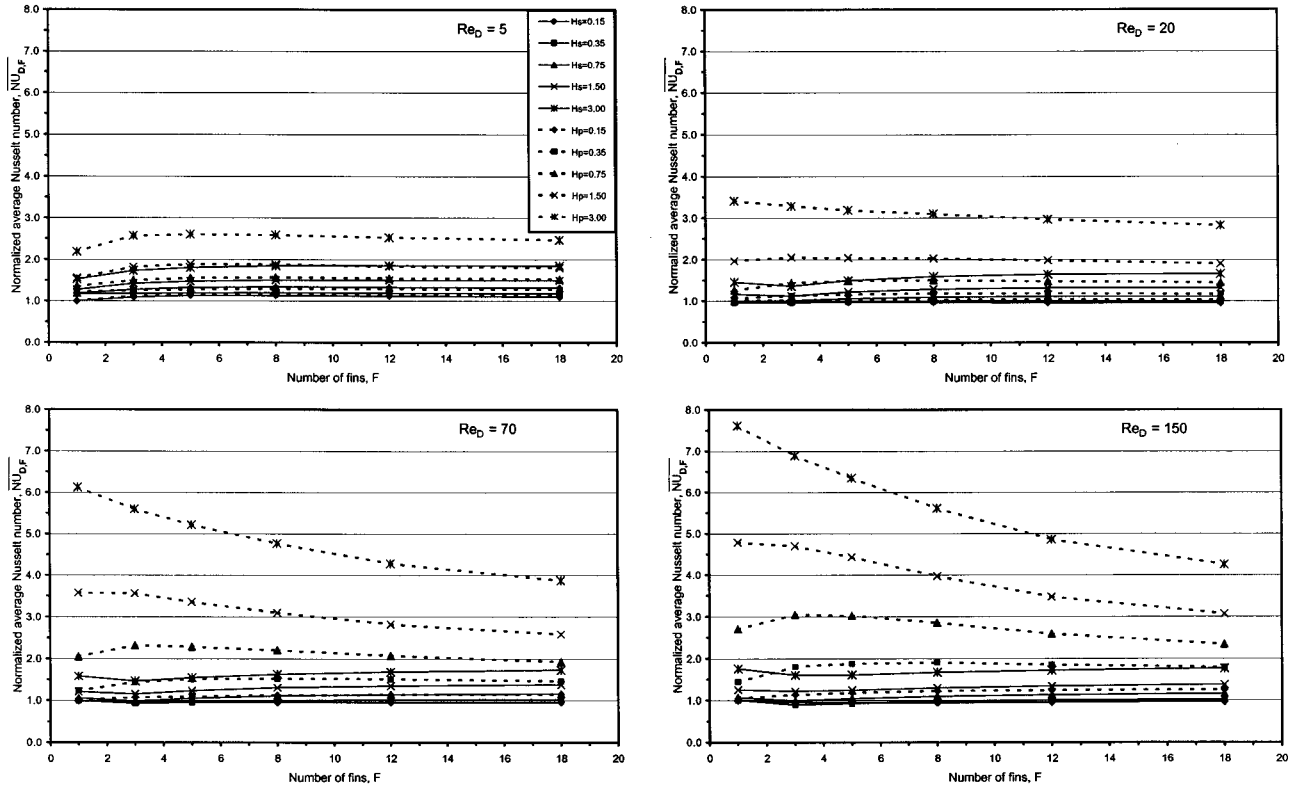

Fig. 3 Change in the normalized Nusselt number of solid fins (solid lines) and permeable fins (dashed lines) as a function of number of fins at different combinations of fin height and Re_D

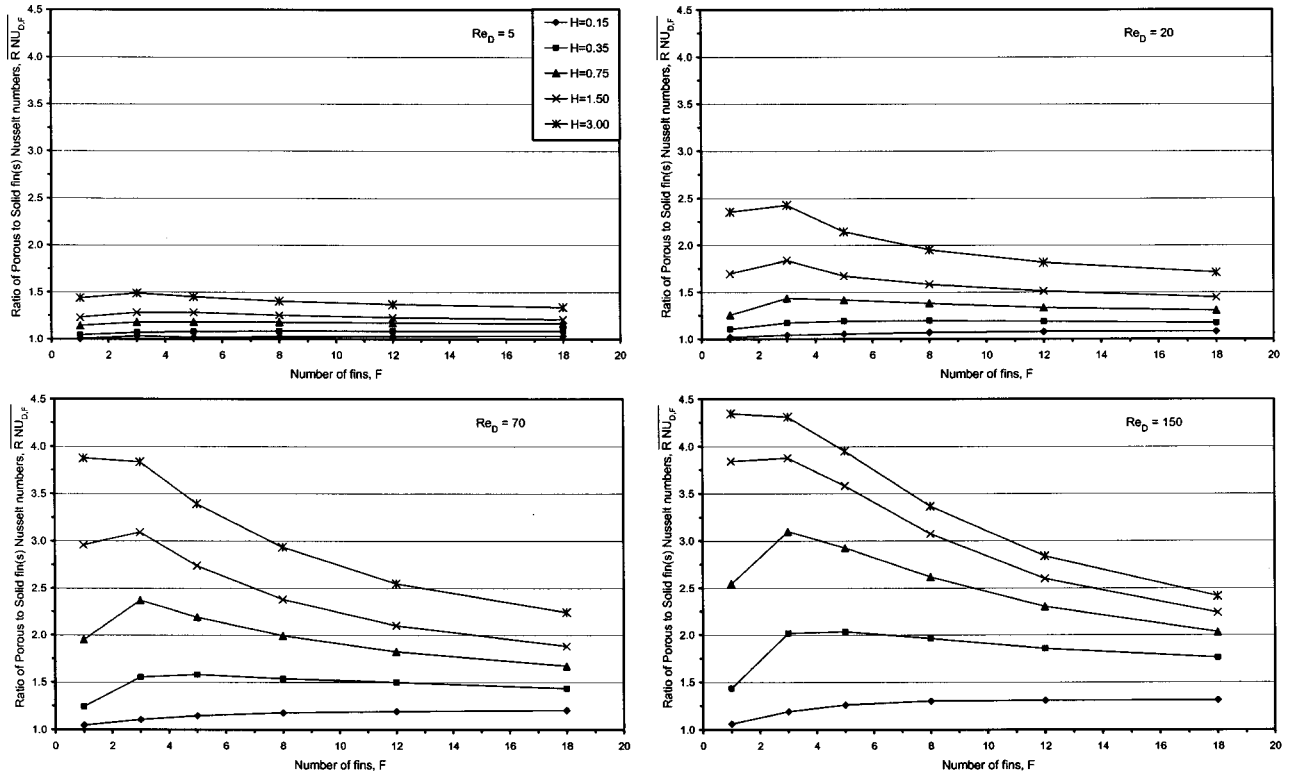

Fig. 4 Change in the ratio of the normalized permeable to solid fins Nusselt number as a function of number of fins at different combinations of fin height and Re_D

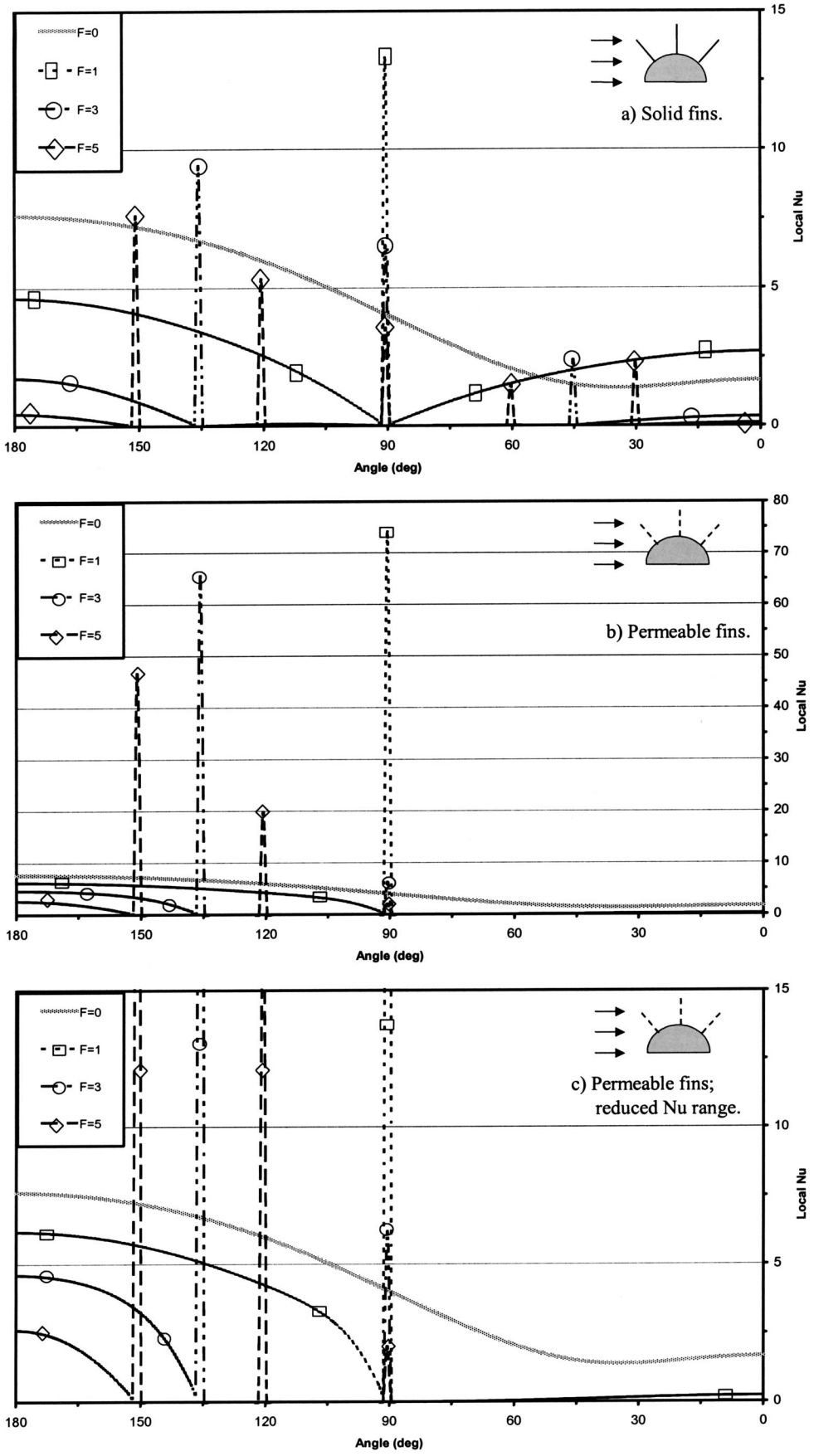

Fig. 5 Variation of the local Nusselt number for the case of Re_D=70 and H=3.0 using solid fins (a) and permeable fins (b and c)

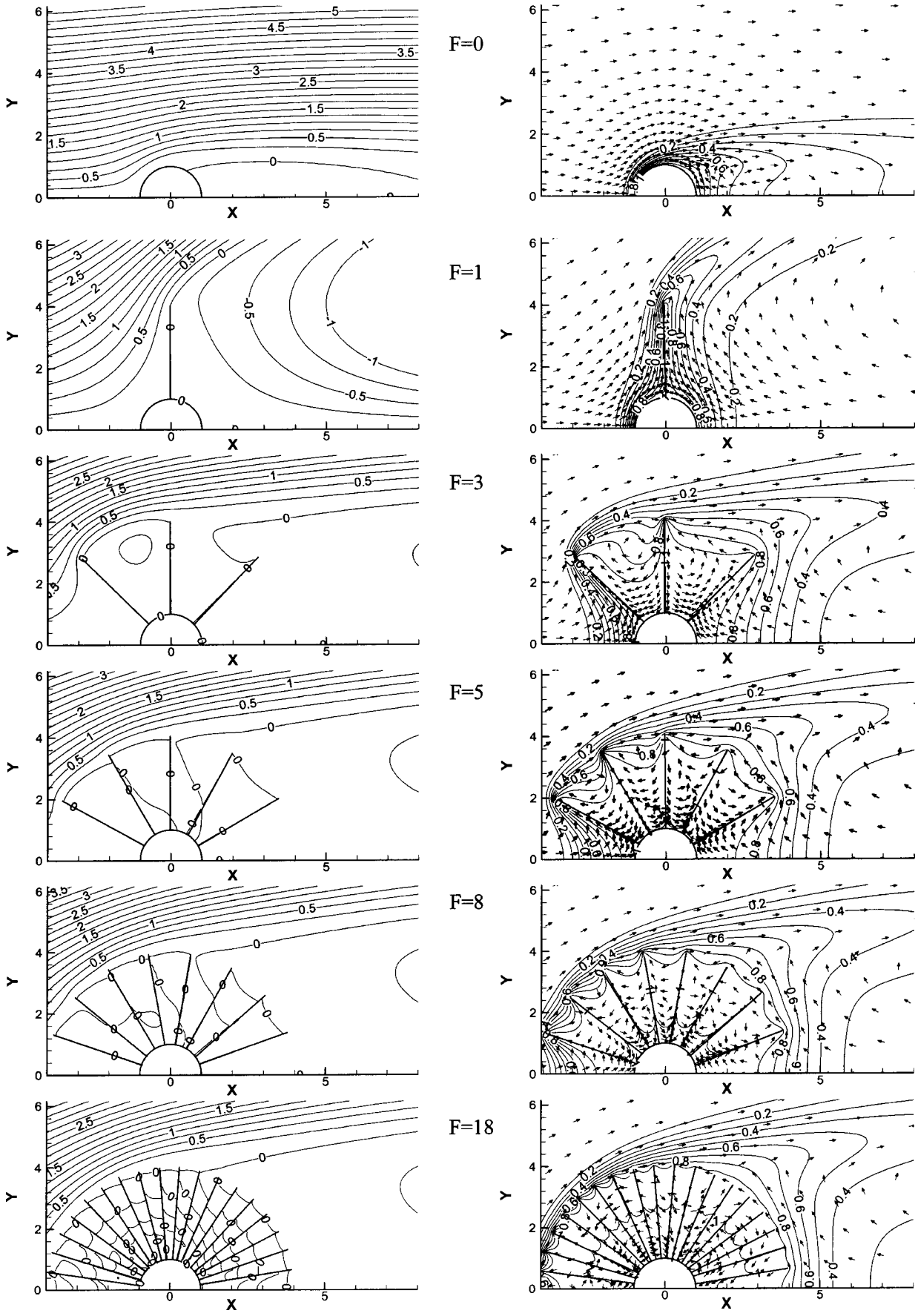

Fig. 6 Streamline contours (left) and isothermal contours and relative velocity vectors (right) using different number of solid fins at Re_D=70 and H=3.0

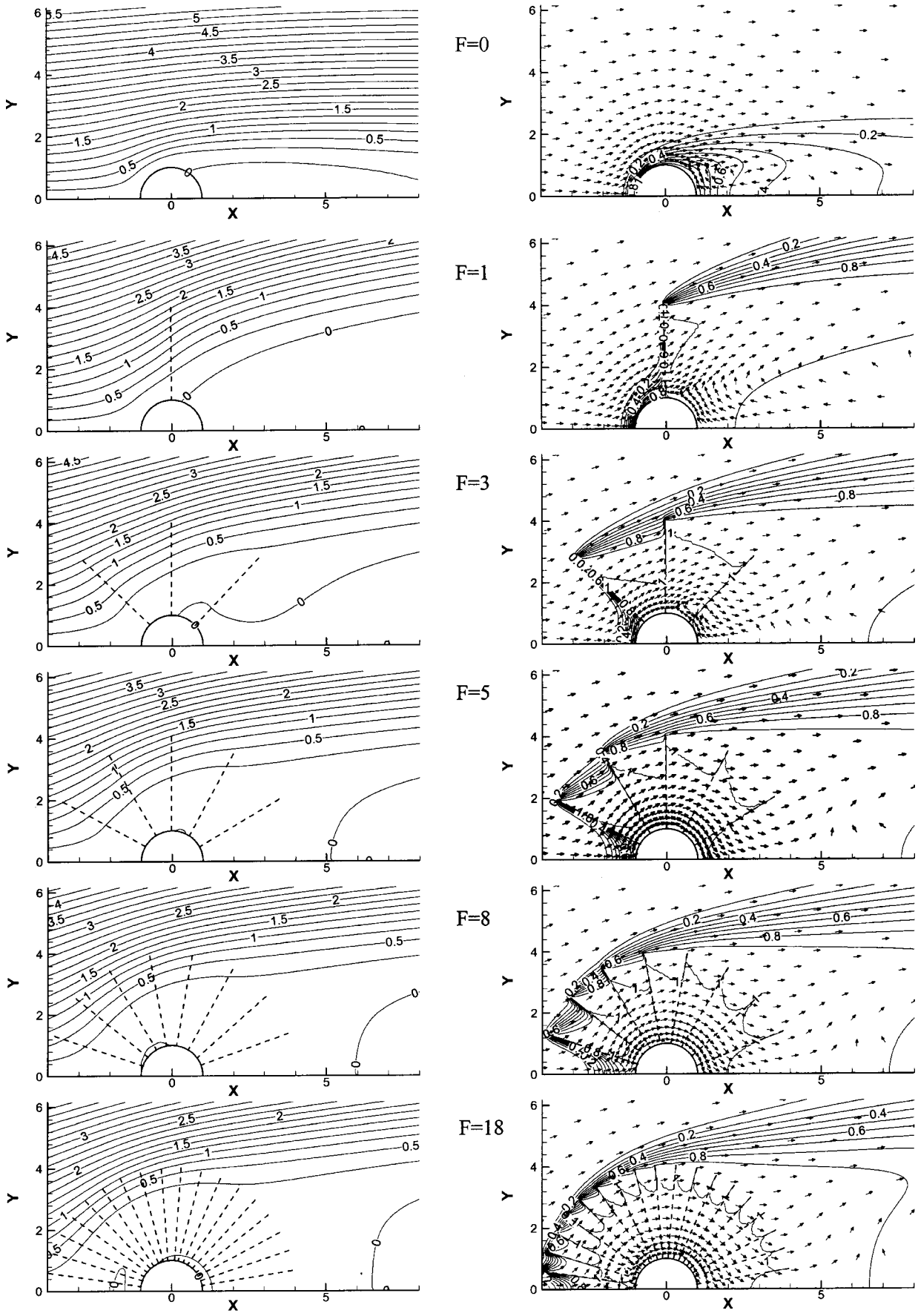

Fig. 7 Streamline contours (left) and isothermal contours and relative velocity vectors (right) using different number of permeable fins at Re_D=70 and H=3.0

plies that no recirculation zones will be formed downstream of the fins, unlike the case of solid fins. The downstream recirculation zones formed by solid fins tend to scavenge some of the cooler free stream air which results in higher temperature difference than that of the case of permeable fins. This can be seen in the streamline and isotherm contours for the case of $Re_D=70$ and $H=3.0$ at different values of solid and permeable fins, Figs. 6 and 7, respectively. The relative velocity vectors are also shown in these figures, i.e., the length of the vector is equivalent of the magnitude of the velocity vector. The big aerodynamic and thermal wakes formed behind the permeable fins are very clear in Fig. 7, especially when compared to those in Fig. 6. This explains the need for placing the far-stream boundary (R_∞) much further away from the cylinder than in the previous study of solid fins only [8], as noted in the preceding Mathematical Analysis section.

Conclusions

The problem of cross-flow forced convection heat transfer from an isothermal horizontal cylinder with high conductivity equally spaced permeable fins was studied numerically. Changes in the normalized average Nusselt number at different combinations of number of fins, fin height, and Reynolds number were reported and compared to those of solid fins. Permeable fins offered a much higher Nusselt number than solid fins, under the same operating conditions. Permeable fins resulted in much larger aerodynamic and thermals wakes which significantly reduced the effectiveness of the downstream fins, especially at $\theta<90°$. A single long permeable fin tended to offer the best convection heat transfer from a cylinder. This has great practical implications in terms of weight and cost of fin(s) needed to achieve a certain level of heat transfer enhancement.

Nomenclature

D = cylinder diameter, $2r_o$ (m)
F = number of equally spaced fins
g = gravity (m/s^2)
H = nondimensional fin height, h_f/r_o
h = local convection heat transfer coefficient (W/m^2 K)
h_f = fin height (m)
k = conduction heat transfer coefficient (W/m K)
M = number of grid points in the tangential direction
N = number of grid points in the radial direction
Nu_D = local Nusselt number based on cylinder diameter
$\overline{\mathrm{Nu}_D}$ = average Nusselt number based on cylinder diameter, no fins
$\overline{\mathrm{Nu}_{D,F}}$ = average Nusselt number based on cylinder diameter, cylinder with F number of fins
$\overline{\mathrm{Nu}_{D,F}}$ = normalized average Nusselt number based on cylinder diameter, cylinder with F number of fins
p = pressure (Pa)
Pr = Prandtl number
r = radius (m)
Re_D = Reynolds number based on cylinder diameter, $U_\infty D/\nu$
$\overline{R\mathrm{NU}_{D,F}}$ = Ratio of the normalized Nusselt number for the case of permeable fins to that of solid fins, each with F number of fins
T = temperature
u = radial velocity (m/s)
v = tangential velocity (m/s)
α = thermal diffusivity (m^2/s)
β = coefficient of thermal expansion (K^{-1})
ϵ = measure of convergence of numerical results
θ = angle (degrees)
ν = kinematic viscosity (m^2/s)
ρ = density (kg/m^3
ψ = stream function

Subscripts

D = value based on cylinder diameter
f = value at fin surface
o = value at cylinder surface
p = permeable fin
s = solid fin
∞ = free stream value

References

[1] Vafai, K., and Huang, P. C., 1994, ''Analysis of Heat Transfer Regulation and Modification Employing Intermittently Emplaced Porous Cavities,'' ASME J. Heat Transfer, **116**, pp. 604–613.
[2] Al-Nimr, M. A., and Alkam, M. K., 1998, ''A Modified Tubeless Solar Collector Partially Filled With Porous Substrate,'' Renewable Energy, **13**, pp. 165–173.
[3] A/K Abu-Hijleh, B., 2001, ''Natural Convection Heat Transfer From a Cylinder Covered With an Orthotropic Porous Layer,'' Numer. Heat Transfer, **40**, pp. 767–782.
[4] Badr, H. M., 1983, ''A Theoretical Study of Laminar Mixed Convection From a Horizontal Cylinder in a Cross Stream,'' Int. J. Heat Mass Transfer, **26**, pp. 639–653.
[5] Saitoh, T., Sajik, T., and Maruhara, K., 1993, ''Benchmark Solutions to Natural Convection Heat Transfer Problem Around a Horizontal Circular Cylinder,'' Int. J. Heat Mass Transfer, **36**, pp. 1251–1259.
[6] Ahmad, R. A., 1996, ''Steady-State Numerical Solution of the Navier-Stokes and Energy Equations Around a Horizontal Cylinder at Moderate Reynolds Numbers From 100 to 500,'' Heat Transfer Eng., **17**, pp. 31–81.
[7] A/K Abu-Hijleh, B., 1999, ''Laminar Mixed Convection Correlations for an Isothermal Cylinder in Cross Flow at Different Angles of Attack,'' Int. J. Heat Mass Transfer, **42**, pp. 1383–1388.
[8] A/K Abu-Hijleh, B., 2003, ''Numerical Simulation of Forced Convection Heat Transfer From a Cylinder With High Conductivity Radial Fins in Cross-Flow,'' Int J. Therm. Sci., **42**(8), pp. 741–748.
[9] Stewart, W. E., and Burns, A. S., 1992, ''Convection in a Concentric Annulus With Heat Generating Porous Media and a Permeable Inner Boundary,'' Int. Commun. Heat Mass Transfer, **19**, pp. 859–868.
[10] Zhao, T. S., and Liao, Q., 2000, ''On Capillary-Driven Flow and Phase-Change Heat Transfer in a Porous Structure Heated by a Finned Surface: Measurements and Modeling,'' Int. J. Heat Mass Transfer, **43**, pp. 1141–1155.
[11] Zhao, T. S., and Song, Y. J., 2001, ''Forced Convection in a Porous Medium Heated by a Permeable Wall Perpendicular to Flow Direction: Analyses and Measurements,'' Int. J. Heat Mass Transfer, **44**, pp. 1031–1037.
[12] A/K Abu-Hijleh, B., 2002, ''Natural Convection Heat Transfer From a Cylinder With High Conductivity Permeable Fins,'' ASME J. Heat Transfer, **125**(2), pp. 282–288.
[13] Anderson, J. D., 1994, *Computational Fluid Dynamics: The Basics With Applications*, McGraw Hill, New York.
[14] Patankar, S. V., 1980, *Numerical Heat Transfer and Fluid Flow*, McGraw Hill, New York.
[15] Incropera, F. P., and DeWitt, D. P., 1996, *Fundamentals of Heat and Mass Transfer*, John Wiley & Sons, New York.

J. Cadafalch
A. Oliva
G. van der Graaf
X. Albets

Centre Tecnològic de Transferència,
de Calor (CTTC),
Lab. de Termotècnia i Energètica,
Universitat Politècnica de Catalunya (UPC),
c/Colom 11, 08222 Terrassa, Spain
e-mail: labtie@labtie.mmt.upc.es

Natural Convection in a Large, Inclined Channel With Asymmetric Heating and Surface Radiation

Finite volume numerical computations are carried out in order to obtain a correlation for free convective heat transfer in large air channels bounded by one isothermal plate and one adiabatic plate. Surface radiation between plates and different inclination angles are considered. The numerical results are verified by means of a post-processing tool to estimate their uncertainty due to discretization. A final validation process is performed by comparing the numerical data to experimental fluid flow and heat transfer data obtained from an ad-hoc experimental setup. [DOI: 10.1115/1.1571845]

Keywords: Channel Flow, Heat Transfer, Natural Convection, Radiation, Ventilation

1 Introduction

Many authors have already studied natural convection between parallel plates for electronic equipment ventilation purposes. In such situations, since channels are short and the driving temperatures are not high, the flow is usually laminar, and the physical phenomena involved can be studied in detail by either experimental or numerical techniques or both. Therefore, a large body of information is available [1–3]. In fact, in vertical channels with isothermal or isoflux walls and for laminar flow, fluid flow and heat transfer can be described by simple equations derived from analytical solutions of natural convection boundary layer in isolated vertical plates and fully developed flow between two vertical plates [1].

Ventilation channels with larger dimensions are frequently encountered in other applications, such as passive solar energy (ventilated facades). These channels involve more complex physical phenomena such as radiative heat transfer between the walls of the channel, turbulent flow, and inclination with respect to the gravity direction. Although the equations developed for simpler situations could in some cases lead to reasonable predictions of the behavior of these channels, work is still required to develop more reliable expressions.

The work presented here is addressed to obtain equations for free convective heat transfer in large air channels with asymmetric isothermal plates (one plate isothermal and the other plate adiabatic). Surface radiation between the plates (radiative coupled plates) and different inclination angles are considered. Correlations of the Nusselt number are obtained from a parametric study carried out by means of computer simulations using finite-volume techniques. The numerical solutions are verified using a post-processing tool based on the Richardson extrapolation theory and on the Grid Convergence Index (GCI) that estimates their uncertainty due to discretization [4,5]. Furthermore, in order to ascertain how far removed the numerical model is from reality, the results of the numerical model are validated by comparison with experimental fluid flow and heat transfer data obtained from an ad-hoc experimental setup.

Contributed by the Heat Transfer Division for publication in the JOURNAL OF HEAT TRANSFER. Manuscript received by the Heat Transfer Division July 17, 2002; revision received February 21, 2003. Associate Editor: S. T. Thynell.

2 Description of the Problem

A schematic of the problem under study is shown in Fig. 1(a). It consists of a large air channel (Pr=0.71) that can be vertical or inclined, with an isothermal wall and an adiabatic wall (upper and lower walls respectively when the channel is inclined). The channel length L varies from $L=1$ m to $L=2$ m and the inter-plate spacing b can vary from $b=0.01$ m to $b=0.04$ m, leading to aspect ratios from $L/b=25$ to $L/b=200$. The inclination of the channel is referenced by the angle θ and varies from $\theta=0$ deg (vertical channel) to $\theta=60$ deg. Radiative heat transfer between the two walls is considered. Both plates have the same emissivity ϵ that can have a value from $\epsilon=0$, corresponding to non-radiating surfaces (white surfaces), to $\epsilon=1$ (black surfaces). The isothermal plate temperature, T_w, reaches values from $T_w=T_a+25°C$ to $T_w=T_a+125°C$, where T_a is the ambient temperature.

In the limiting case of non-radiating plates ($\epsilon=0$), heat transfer is only due to convection at the isothermal plate. In other cases, heat transfer to the air is also due to radiation from the isothermal plate to the adiabatic plate, which transfers the radiating energy to the surrounding air by convection.

The average Nusselt number accounting for natural convection in channels with isothermal walls is typically defined in terms of the inter-plate spacing b as follows:

$$\mathrm{Nu}_b=\left[\frac{Q/A}{(T_w-T_a)}\right]\frac{b}{\lambda} \tag{1}$$

where λ is the air thermal conductivity, Q is the total rate of heat transfer from the plates to the air and A is the surface area of the heat source. In the case under study A represents the surface area of the isothermal plate.

Transition from laminar to turbulent flow in natural convection vertical boundary layers is typically assumed at $\mathrm{Gr}_L=\mathrm{Ra}_L/\mathrm{Pr}=[g\beta(T_w-T_a)L^3/\nu^2]=10^9$ [6], where Gr is the Grashof number, the subindex L means that the channel length is used as geometrical parameter, g is the gravitational acceleration, and β and ν are the volumetric coefficient of thermal expansion and the kinematic viscosity of the air at the film temperature $(T_w+T_a)/2$. However, transition from laminar to turbulent flow in channels is expected to occur at higher values of Gr_L due to the merging effect of the two boundary layers. Most situations under study in this work have a Gr_L number in the order of 10^{10}. Therefore, the assumption of laminar flow may apply. In fact, some numerical experiments not presented here have been carried out using two equations tur-

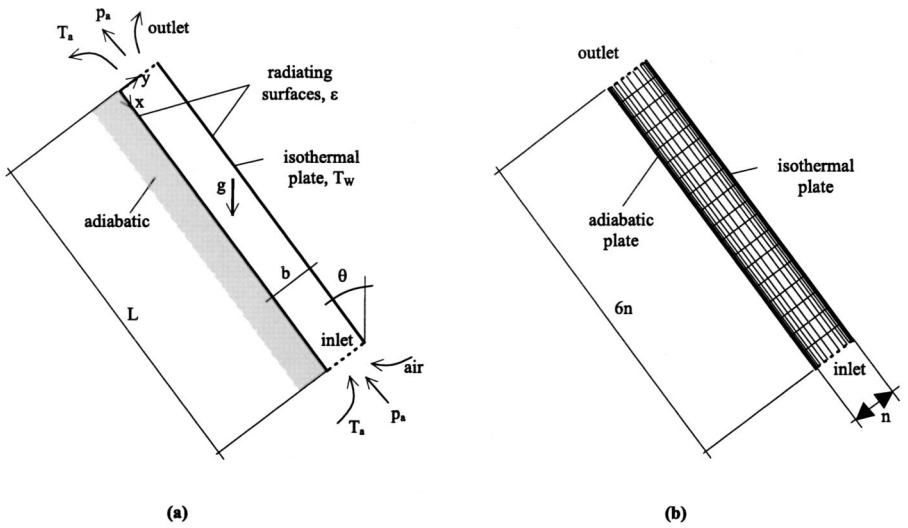

Fig. 1 (a) Schematic of the problem. (b) Mesh and computational domain used in the numerical simulations. The mesh is expressed in terms of the parameter *n*. The solid triangles indicate that the mesh was concentrated near the walls.

bulent models such as those used in [7]. All the solutions obtained indicated that the flow within the channel was laminar.

Numerical works carried out in free convective heat transfer in parallel plates, see for example [2], assume the thermophysical properties of the air to be constant except in the buoyancy terms of the momentum equations, where the Boussinesq equation of state, $\Delta\rho = -\beta\rho\Delta T$, is applied. This approximation is appropriate when the temperature gradients are small [8]. In the work presented here, the temperature differences between the isothermal wall and the ambient are higher than in previous works. Some computations were carried out in order to ensure that the Boussinesq assumption was also appropriate for the modeling of the channels studied in this work. These computations consisted of calculating the heat transfer, the Nusselt number, of cases C and D described in Table 1 assuming the Boussinesq approximation or using temperature dependent physical properties of the air. As indicated in Table 1, in case C the temperature difference between the ambient and the isothermal wall was 75°C and in case D 125°C. The relative differences between the calculated Nusselt with and without assuming the Boussinesq hypothesis were 2.5% and 1.5%, respectively. Therefore, the use of the Boussinesq assumption seems to be also reasonable for the channels under study in this work.

3 Mathematical Model

3.1 Governing Equations. The fluid flow and heat transfer within the channel is assumed to be governed by the two-dimensional Navier-Stokes equations together with the energy equation with the following restrictions: steady state, laminar flow, constant physical properties, density variations relevant only in the buoyancy terms of the momentum equations (Boussinesq approximation), fluid Newtonian behavior, negligible heat friction and influence of pressure on temperature, and radiatively non-participating medium. The corresponding set of differential equations may be written:

$$\frac{\partial u}{\partial x} + \frac{\partial v}{\partial y} = 0 \tag{2}$$

$$\rho u \frac{\partial u}{\partial x} + \rho v \frac{\partial u}{\partial y} = -\frac{\partial p_d}{\partial x} + \rho\nu\left(\frac{\partial^2 u}{\partial^2 x} + \frac{\partial^2 u}{\partial^2 y}\right) - \rho\beta(T - T_o)g_x \tag{3}$$

$$\rho u \frac{\partial v}{\partial x} + \rho v \frac{\partial v}{\partial y} = -\frac{\partial p_d}{\partial y} + \rho\nu\left(\frac{\partial^2 v}{\partial^2 x} + \frac{\partial^2 v}{\partial^2 y}\right) - \rho\beta(T - T_o)g_y \tag{4}$$

$$\rho u \frac{\partial T}{\partial x} + \rho v \frac{\partial T}{\partial y} = \frac{\lambda}{c_p}\left(\frac{\partial^2 T}{\partial^2 x} + \frac{\partial^2 T}{\partial^2 y}\right) \tag{5}$$

where (x,y) are the coordinates in the Cartesian-coordinate system indicated in Fig. 1(a); T is the temperature; T_o the reference temperature; p_d the dynamic pressure; (u,v) and (g_x, g_y) the velocity and the gravitational acceleration vector expressed in the reference system x-y, and the physical properties of the air ρ, ν, β, λ, and c_p are respectively the density, the kinematic viscosity, the thermal expansion coefficient, the thermal conductivity and the specific heat at constant pressure, which are assumed constant (Pr=0.71).

Table 1 Parameters of the cases used for detailed verification purposes: inter-plate spacing (b), channel length (L), inclination angle (θ), isothermal wall temperature (T_w), ambient temperature (T_a=300 K) and emissivity of the plates (ϵ).

case	b [m]	L [m]	θ [deg]	$T_w - T_a$ [°C]	ϵ [−]	$(b/L)\mathrm{Ra}_b \cos\theta$ [−]
A	0.01	1.00	30	25	0.25	$2.0\cdot10^1$
B	0.02	1.50	15	50	0.25	$4.8\cdot10^2$
C	0.03	1.75	45	75	0.50	$2.3\cdot10^3$
D	0.04	2.00	0	125	1.00	$1.5\cdot10^4$

3.2 Boundary Conditions. The temperature of the isothermal plate (upper plate) is T_w. On the other hand, the temperature at the coordinate x of the adiabatic plate results from a surface energy balance considering that the net radiative heat flux arriving at the plate equals the heat flux transferred from the plate to the surrounding air:

$$\frac{\epsilon}{2-\epsilon}\sigma(T_w^4 - T^4)\big|_{(x,y=0)} = -\lambda\left.\frac{\partial T}{\partial y}\right|_{(x,y=0)} \tag{6}$$

where σ is the Stefan-Boltzmann constant and λ is the thermal conductivity of the air. In this energy balance, the radiative heat transfer between the plates (left term of the equality) is modeled assuming a non-participating medium, infinite surfaces, and grey-

diffuse plate surfaces with the identical emissivity value ϵ. The assumption of infinite surface ignores the radiation out of the ends of the channel. This assumption can be acceptable because the aspect ratios of the channels under study are large (in the case with smallest aspect ratio, $L=1$ m and $b=0.04$ m, the diffuse view factor between the plates is larger than 0.96).

The boundary conditions to be assumed at the inlet and outlet are more complicated because an inappropriate formulation of these boundary conditions may lead to a fluid flow and heat transfer that are very different from those under study. Typical assumptions adopted for free convective flow through channels are adopted here [2]. The air is assumed to enter the channel from the surroundings at a temperature equal to T_a (ambient temperature) and with an adiabatic and reversible process, so that dynamic pressure energy in the surrounding air (which is 0) is converted to kinetic energy (i.e., to $1/2\rho\mathbf{v}^2$, where $\mathbf{v}$ is the magnitude of the velocity vector) and dynamic pressure energy at the inlet:

$$T|_{(x=L,y)}=T_a \quad 0=\frac{1}{2}\rho\mathbf{v}^2+p_d\Big|_{(x=L,y)} \tag{7}$$

As in Eq. (7), the magnitude of the velocity vector is used, the flow is not assumed to be uni-directional. Therefore, this boundary condition is according to the characteristics of the flow at the inlet, that can have a considerable curvature which will strongly affect the velocity distribution.

At the outlet, the temperature is assumed to remain constant in the x direction and all the kinetic energy of the air is assumed to be converted to heat, resulting in an outlet dynamic pressure equal to the surrounding air dynamic pressure, i.e., equal to 0:

$$\left.\frac{\partial T}{\partial x}\right|_{(x=0,y)}=0 \quad p_d|_{(x=0,y)}=0 \tag{8}$$

3.3 Governing Dimensionless Groups. A nondimensionalization of the governing equations and boundary conditions shows that Nu_b depends on the Rayleigh number, the aspect ratio, the inclination, the thermal emissivity of the plates and on two radiation numbers, Pl and R, that arise from the adiabatic wall boundary condition when radiative heat transfer is considered. Thus:

$$\mathrm{Nu}_b=\mathrm{Nu}_b(\mathrm{Ra}_b, b/L, \cos\theta, \epsilon, \mathrm{Pl}, R) \tag{9}$$

where the Rayleigh number in terms of the geometrical parameter b is defined as $\mathrm{Ra}_b=[g\beta(T_w-T_a)b^3/\nu^2]\mathrm{Pr}$. The radiation numbers are the Planck number $\mathrm{Pl}=\lambda/b\sigma T_a^3$ and $R=(T_w-T_a)/T_a$, where σ is the Stefan-Boltzmann constant and λ is the thermal conductivity of the air at the film temperature.

4 Numerical Model

The set of coupled partial differential equations and the boundary conditions described in Section 3 are converted to algebraic equations by means of finite-volume techniques using rectangular meshes on a staggered arrangement. Diffusive terms at the boundaries of the control volumes are evaluated by means of second-order central differences, while the convective terms are approximated by means of the high-order SMART scheme [9], with a theoretical order of accuracy between 1 and 3.

The domain where the computations are performed and a schematic of the mesh adopted is shown in Fig. 1(b). The mesh is represented by the parameter n. According to Fig. 1(b), $6n*n$ control volumes are used (for example, when $n=40$ it means that the problem is solved on 240*40 control volumes). The mesh is intensified near the two plates using a tanh-like function with a concentration factor of 1 [7], in order to properly solve the boundary layer. This aspect is indicated in the figure with two solid triangles.

The pressure boundary conditions indicated in Eq. 7 and 8 have been modeled according to [10]. This implementation of the boundary conditions predicts curvature effects in the inlet region with no need to include zones outside the channel in the computational domain.

The resulting algebraic equation system was solved using a pressure-based SIMPLE-like algorithm [11,12], and the iterative convergence procedure was truncated when relative increments of the computed Nusselt number (Eq. 1) in the last 50 iterations dropped below 0.005%.

4.1 Verification of the Numerical Model. The numerical solutions presented here have been calculated adopting a global h-refinement criterion. That is, all the numerical parameters (numerical scheme, numerical boundary conditions, etc.) are fixed, and the mesh is refined to yield a set of numerical solutions. This set of numerical solutions have been post-processed by means of a tool based on the Richardson extrapolation theory and on the concept of the Grid Convergence Index (GCI) [4,5]. When the numerical solutions are free of programming errors, convergence errors and round-off errors, the computational error is due only to the discretization. The tool processes a set of three consecutive solutions in the h-refinement. The main output is an estimate of the uncertainty of the numerical solutions due to discretization, the GCI. Other information also obtained from the tool is the order of accuracy of the numerical solution (apparent or observed order of accuracy) and the percentage of nodes at which it has been possible to calculate the order of accuracy (Richardson nodes [4]). An observed order of accuracy approaching the theoretical value (order of accuracy of the numerical schemes used) and a high percentage of Richardson nodes indicate that the estimator GCI is reliable, and that the solution is free of programming errors, convergence errors and round-off errors.

To show the appropriateness of the numerical parameters adopted in all the numerical solutions of this work, the results of a detailed verification process will be discussed. The numerical parameters to be considered are the grid, the numerical scheme and the convergence criterion.

In order to obtain the final correlation for the Nusselt number, a parametric study of the air channel was carried out involving up to 2500 different cases, see Section 6.1. The data obtained from the post-processing that are presented here, correspond to four of the cases that are representative of the others. Hereafter they will be called as cases A, B, C, and D. Their corresponding parameters (inter-plate spacing b, channel length L, inclination angle θ, difference between isothermal wall temperature and ambient temperature T_w-T_a, and emissivity of the plates ϵ), are presented in Table 1.

For each of the four cases, a set of 5 solutions using the global h-refinement criterion with a refinement ratio of 2 (doubling the mesh) were computed. They correspond to $n=5$, 10, 20, 40, and 80. The post-processing results are given in Table 2 for $n=20$, 40, and 80. Presented are the global observed order of accuracy, p, the percentage of Richardson nodes, Rn, and the global uncertainty due to discretization, GCI, corresponding to the different dependent variables of the problem u, v, and T.

The percentage of Richardson nodes given in the table is high for the cases A and B, but decreases in the cases C and D, where the physical phenomena are more complex. While cases A and B have a value of $(b/L)Ra_b\cos\theta$ below $5*10^2$, the corresponding values for cases C and D are beyond $2*10^3$. On the other hand, most estimates of the order of accuracy, p, approach the theoretical values of the differential scheme used (between 1 and 3). However, they do not tend to an asymptotic value with the mesh. As the GCI is directly calculated from p, GCI increases with the mesh in some situations where p degenerates with the mesh to values close to 1. This means that, for these cases, the calculated uncertainty due to discretization increases when the mesh is refined! This aspect is in accordance with the practical use of the GCI, which indicates that low values of the observed order of accuracy tend to overestimate the uncertainty due to discretization. When dealing with a single case, it may be possible to over-

Table 2 Results from the post-processing tool: Richardson nodes (Rn), global observed order of accuracy (p), and global uncertainty due to discretization normalized by the reference values (GCI*). (Note: * means that the GCIs are normalized using a reference value of $v_{ref}=[Lg\beta(T_w-T_a)\cos\theta]^{1/2}$ for the velocity components and $T_{ref}=T_w-T_a$ for the temperature.)

	case A								
	u			v			T		
grid n	Rn [%]	p	GCI* [%]	Rn [%]	p	GCI* [%]	Rn [%]	p	GCI* [%]
20	89	1.1	.273	87	2.0	.0017	99	1.7	.208
40	97	2.5	.013	91	2.0	.0023	84	3.9	.005
80	96	1.1	.014	89	1.8	.0010	83	1.6	.0120
	case B								
	u			v			T		
grid n	Rn [%]	p	GCI* [%]	Rn [%]	p	GCI* [%]	Rn [%]	p	GCI* [%]
20	75	1.9	.162	71	2.2	.0013	67	2.2	.070
40	82	0.9	.162	71	1.2	.0036	72	1.2	.068
80	91	1.9	.014	79	1.6	.0015	81	1.8	.010
	case C								
	u			v			T		
grid n	Rn [%]	p	GCI* [%]	Rn [%]	p	GCI* [%]	Rn [%]	p	GCI* [%]
20	78	1.3	.568	43	2.1	.0069	77	1.5	.320
40	84	2.1	.063	43	1.9	.0030	58	2.6	.020
80	88	2.0	.014	76	1.9	.0023	74	2.0	.012
	case D								
	u			v			T		
grid n	Rn [%]	p	GCI* [%]	Rn [%]	p	GCI* [%]	Rn [%]	p	GCI* [%]
20	63	1.6	.350	43	1.4	.0213	73	0.9	1.44
40	51	2.1	.087	48	1.6	.0080	59	2.6	.026
80	67	1.2	.087	50	1.3	.0070	59	1.2	.072

come this problem simply by changing the numerical schemes or the discretization of the domain. Though, as in this work up to 2500 different cases are studied, it is not practical to find a specific mesh and scheme for each of them.

All the numerical solutions used in the previous discussion were obtained using the convergence criterion as explained at the beginning of Section 4. This convergence criterion results in a reasonable number of iterations for the convergence procedure, and therefore also in a reasonable CPU time. However, it appears to be a non-restrictive convergence criterion. Several computations were carried out considering various situations, including the four cases analyzed in this section, with a more restrictive convergence criterion. Some small differences were found in the estimates obtained from the post-processing. This indicates that the numerical error of the solutions with the non-restrictive convergence criterion is not totally free of convergence error. However, the general tendency is that whenever the estimates obtained from the verification process indicated that the solution was credible, there were no variations in the value of Nu_b when the convergence criterion was strengthened.

Some of this information is given in Fig. 2. The evolution of the Nu_b with the mesh parameter n for the four cases is shown in Fig. 2(a). Beyond the fourth level of refinement, $n=40$, no significant differences are observed in the Nu_b. The evolution of the Nu_b during the iterative process in terms of the number of iterations is shown in Fig. 2(b). A continuous line is used which turns into a dotted line when the non-restrictive convergence criterion is reached. As can be observed, all the dotted lines are horizontal lines, which indicates that there are no deviations in the Nu_b when the non-restrictive convergence criterion has been reached.

5 Experimental Setup

The experimental setup consists of a channel with two parallel plates 1600 mm long and 800 mm wide with a spacing of 20 mm. A schematic of the setup is shown in Fig. 3. The channel is inclined 45 deg. It is closed at its sides by two lids covered with insulation material on the outside. Two additional adiabatic lids can be mounted at the inlet and the outlet when required to stop the air circulation through the channel. The lower plate is a single plate insulated from the ambient by insulation material. The upper plate consists of eight square modules of 400*400 mm^2. Each module is heated by electrical heaters glued on the upper side. A self-calibrated K-type thermocouple sensor is placed at its center. Heaters of the two modules placed at the same height are connected to an AC controlled power supply, forming four pairs of modules connected to four different power lines. Four glass windows with an observation area of 20*20 mm^2 are mounted on one side wall at 200, 600, 1000, and 1400 mm from the outlet of the channel in order to permit the visualization of the air flow in the channel. The ambient temperature T_a (laboratory temperature) is measured by a self-calibrated PT-100 resistance thermal device. Control, regulation and data acquisition are carried out with an HP VXI series data acquisition unit managed by a software application programmed in HPVEE language.

Measurements of the heat transfer and the velocity field were performed in separate experiments. In heat transfer measurements, the overall heat loss of the setup, P, is measured at some specific isothermal plate temperatures, T_w.

In the fluid flow experiments, for a given T_w and T_a, the velocity field is visualized at a section of the channel parallel to and 200 mm from the side wall with windows. The air is seeded by aerosols of olive oil generated by a Laskin nozzle. The diameter of the aerosols are in the order of 5 μm. The images of the flow are captured using a Digital Particle Image Velocimetry (DPIV) facility from LaVision. The main features of the DPIV device used in the fluid flow experiments are: double-cavity Nd-YAG

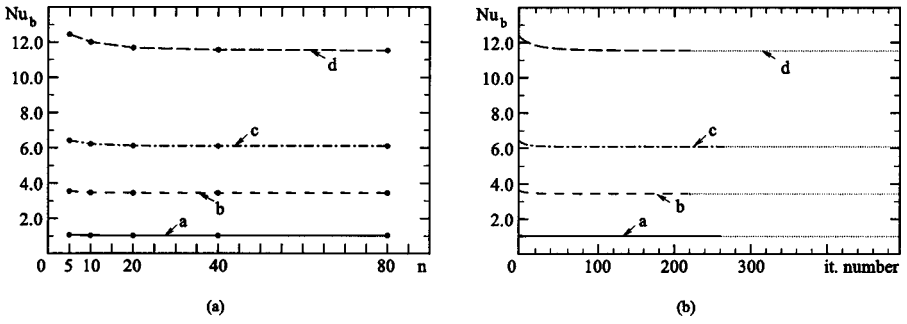

Fig. 2 Verification. (a) Evolution of the Nu_b in terms of the mesh parameter n. (b) Evolution of the Nu_b during the convergence procedure in terms of the number of iterations. A dotted line indicates that the convergence criterion is achieved.

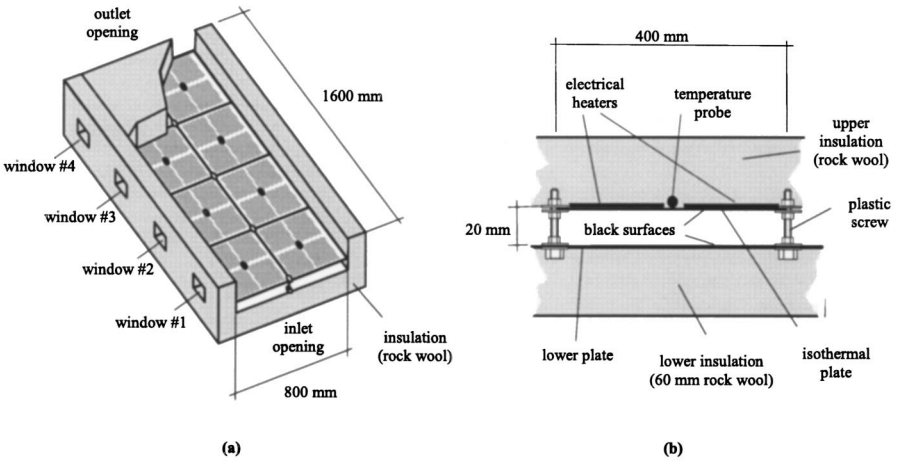

Fig. 3 Schematic of the setup. (a) General view. (b) Detail of the modules that make up the isothermal plate.

(2×35 mJ/pulse) laser from Quantel, optics consisting of one spherical and two cylindrical lenses forming a Galilean telescope to create and focus a light-sheet, a high sensitive (Peltier-element cooled) 12 bit CCD camera with a resolution of 1280*1024 pixels, and a Nikkor camera lens with focal length of 105 mm. Details of the experimental procedures adopted for both the heat transfer and fluid flow measurements are given in the following two subsections.

5.1 Measurement of Heat Transfer. With channel either open or closed, the total heat loss of the setup, P, was measured at different temperatures of the isothermal plate: $T_w = 70$, 100, 125, and 150°C. The total heat loss was obtained by measuring the power that was supplied to the electrical heaters. This was done by means of power transducers with a precision of $\pm[0.5 + 0.02P]$ W. Data were recorded for a period of 15 minutes in intervals of 3 seconds at steady state.

Results from measurements of heat loss with the channel closed were fitted by a least squares method to a second-order equation in terms of the temperature difference $\Delta T = (T_w - T_a)$. This led to a correlation for the heat loss of the setup without heat evacuation through the channel, $Q_{\text{loss}} = (a + b\Delta T)\Delta T$.

Experimental values of the heat removed from the channel, Q, were calculated by subtracting the corresponding Q_{loss} from the overall measured heat loss, P, obtained from the experiments with the channel open. The Nusselt number was calculated from Q according to Eq. (1).

5.2 Measurement of Fluid Flow. Measurements of the velocity field at each window of the channel were obtained at two different temperatures of the isothermal plate: $T_w = 70$°C and $T_w = 150$°C. Each measurement consisted of five series of ten data sets of velocity fields taken at a sample rate of 8 Hz, resulting in 50 data sets of velocity fields. The image analyses showed that the maximum particle image displacements were of the order of 9 pixels. Adaptive interrogation areas from 64*64 to 32*32 pixels with 50% overlapping were applied. The effects of in-plane loss of particle pairs were minimized by zero-offsetting of the interrogation areas. Errors of the measured velocities due to the DPIV device, the data acquisition and the post-processing were expected to be below ±0.03 m/s.

Even if an optimum PIV experiment has been carried out, there is always the probability of erroneous velocity vectors, usually called outliers. Therefore, post-processing of the PIV results is always necessary in order to detect and eliminate as many erroneous vectors as possible [13]. Outliers were detected by the median test performed by a self-written algorithm and substituted by the local mean value of the nine surrounding velocities.

6 Results and Discussion

6.1 Parametric Study. A parametric study was carried out varying channel length L, inter-plate spacing b, inclination angle θ, thermal emissivity of the plates ϵ and isothermal wall temperature T_w and setting the ambient temperature at $T_a = 300$ K. Values for each parameter were fixed within the interval range under study and for equal sized intervals (see Section 2). Four different values for b and five different values for the other parameters were used. This resulted in a total number of 2500 cases. The numerical results obtained for all the cases were calculated with the level of refinement $n = 40$, and using the convergence criterion and numerical schemes as explained in Section 4. These numerical parameters are in accordance with the conclusions of the verification process as discussed in Section 4. The conclusions of this verification process focussed on the analysis of 4 of the 2500 cases under study. Therefore, there was no guarantee that these numerical parameters would lead to results that were free of computational errors for all the situations. Thus, to discard non-credible numerical solutions, all of them were submitted to a verification test. This consisted of two steps. In the first step, the global observed order of accuracy p, the normalized global grid convergence index, GCI*, and the percentage of Richardson nodes, Rn, were calculated by means of the post-processing tool; see Section 4. In the second step, the solutions were filtered according to the post-processing results. The values of acceptance adopted were: p within the interval [1:4], GCI* below 1% and Rn over 40%. This filtering criterion was fulfilled in 1842 cases out of the 2500. Values of the parameters L, b, θ, ϵ, and $T_w - T_a$ for those cases that did not fulfill the criterion were rather random, without clear tendencies. More restrictive filtering led us to discard those solutions with higher values of the number $(b/L)Ra_b \cos\theta$. This was mainly because the convergence with the mesh was more difficult and, as a consequence, the number of Richardson nodes was lower. Differences between the fit of the solutions that passed a more restrictive filtering and the fit of the solutions finally accepted were not significant. Therefore, the given correlation was not expected to be affected by wrongly converged solutions.

Computations were performed on a Beowulf cluster composed by 48 personal computers (AMD K7 CPU at 900 MHz and 512 Mbytes of RAM) running with Debian Linux 2.1 (kernel version 2.7.2.3). Converging cases required between 15 to 30 minutes of

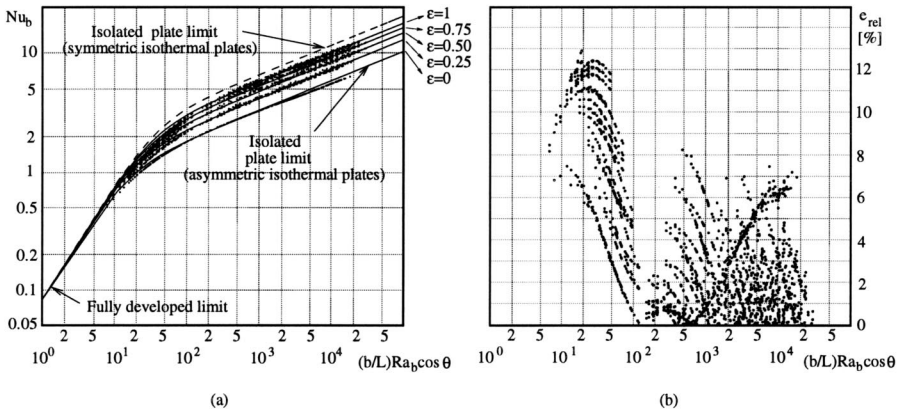

Fig. 4 Results from the fitting process. (a) Nu_b in terms of $(b/L)Ra_b \cos\theta$ and ϵ. Solid lines: heat transfer relation 10 for different values of emissivity of the plates ϵ. Dashed line: relation of Bar-Cohen and Rohsenow [1] for symmetric isothermal vertical plates using the Nu_b number as defined in Eq. 1. Dots: fitted data. (b) Relative errors between the fitted data and the heat transfer relation 10 in terms of $(b/L)Ra_b \cos\theta$.

CPU time (including the three levels of the global *h*-refinement). As initial guess for the coarse grid solution, a uniform map for the temperatures and velocity components fields was assumed ($T = T_a$, $u = -1$ m/s and $v = 0$). The coarse grid solution was used as initial guess for the middle grid solution, and the middle grid solution as the initial guess for the fine grid solution. With this procedure, for most cases, the number of iterations required for the convergence of each solution were about 2000, 1000, and 500 for the coarse, middle and fine grid, respectively. The calculations of the non-converged cases were stopped when 3000 iterations of the converging procedure (in any of the three levels of refinement) were reached resulting in a total "lost" CPU time between 60 to 120 minutes.

6.2 Heat Transfer Relation. From the non-dimensionalization of the governing equations and boundary conditions as discussed in Section 3.3, is found that Nu_b depends on 6 different governing numbers: Ra_b, b/L, $\cos\theta$, ϵ, Pl and R. By using a single group $(b/L)Ra_b \cos\theta$ as a correlating group instead of the three separate groups (b/L), Ra_b and $\cos\theta$, the number of correlating numbers was reduced to 4. This is a widely adopted practice for inclined plates [3]. Furthermore, after an initial first evaluation of the data to be fitted, the influence of the radiating groups (Planck number and R) was shown to be negligible. Therefore, the set of correlating numbers was reduced to 2. Accordingly, data of all the 1842 solutions fulfilling the verification-filtering criterion as described in Section 6.1 were fitted to a heat transfer relation for the Nusselt number, Nu_b, in terms of the groups $(b/L)Ra_b \cos\theta$ and ϵ. The resulting relation reads:

$$Nu_b = \left[\left(\frac{1}{12} (b/L) Ra_b \cos\theta \right)^{-2} + (0.59[(b/L) Ra_b \cos\theta]^{1/4} [1 + \epsilon^{4/5}]^{4/5})^{-2} \right]^{-1/2} \quad (10)$$

The fitting process was carried out minimizing the average of the relative differences between the data and the fitting relation by means of the Powell method [14]. Several fitting procedures were employed using different number of constants. The final fitting process actually adopted was based on fixing all the parameters in Eq. (10), except the two exponents that affect only ϵ. The correlating exponents -2 and $-1/2$ were selected according to Bar-Cohen and Rohsenow [1]. Relation (10) is shown to properly represent all the numerical data. The maximum relative error between the fitted data and the correlation was found to be below 13% and the average relative error below 4%.

One outstanding issue is that in the case of non-radiating surfaces ($\epsilon = 0$), Eq. (10) coincides exactly with the well-known composite-relation proposed by Bar-Cohen and Rohsenow [1] for laminar natural convection in parallel vertical ($\cos\theta = 1$) asymmetric isothermal plates. This relation was based on the analytical solutions for the two limiting situations of fully developed laminar flow and laminar flow along an isolated plate, and it was also validated with experimental data obtained in short channels.

The main results of the fitting process are shown in Fig. 4. The heat transfer relation (10) for the Nusselt number is presented in Fig. 4(a) in terms of the parameter $(b/L)Ra_b \cos\theta$ (abscissas) and ϵ (five different lines corresponding to the values $\epsilon = 1$, 0.75, 0.5, 0.25, and 0).

The composite-relation of Bar-Cohen and Rohsenow for laminar natural convection in parallel vertical asymmetric plates overlaps the curve for $\epsilon = 0$. In addition, the composite-relation for symmetric isothermal plates (both plates isothermal), also given by Bar-Cohen and Rohsenow, is presented in Fig. 4(a) with a dashed line. This relation is used here for convenience with the Nusselt number as defined in Eq. (1), even though this is not the standard definition for symmetric isothermal plates [1].

The limiting situation of fully developed laminar flow (fully developed limit) and laminar flow along an isolated plate (isolated plate limit) are indicated in the figure by an arrow. While Nu_b in the fully developed limit for symmetric or asymmetric isothermal plates is identical, in the isolated plate limit Nu_b of the symmetric isothermal plates is twice as large than that of the asymmetric isothermal plates.

For $(b/L)Ra_b \cos\theta$ values larger than 10^2, the physical phenomenon tends towards the isolated plate limit. For these cases and at a fixed value of $(b/L)Ra_b \cos\theta$, Nu_b increases with the ϵ from the value corresponding to asymmetric plates to the value corresponding to symmetric plates. However, the Nu_b of the symmetric plates situation is never reached. This is explained by the fact that the lower plate is unable to reach the temperature of the isothermal plate along the entire channel even in situations using black surfaces ($\epsilon = 1$).

In the situations studied here $(b/L)Ra_b \cos\theta$ is never below approximately $5*10^0$. In spite of this, the heat transfer relation (10) is also consistent in this zone with the results of Bar-Cohen and Rohsenow (fully developed limit). All the computed Nu_b presented here tend to converge to the fully developed limit solution for low values of $(b/L)Ra_b \cos\theta$, showing no dependency on the emissivity of the plates.

Table 3 Comparison of the Nu_b obtained from the experiment, from the numerical model and from the heat transfer relation 10. Relative differences with respect to the value corresponding to the heat transfer relation are indicated within brackets in percent.

		Nu_b		
$(b/L)Ra_b \cos\theta$	ϵ	experimental	numerical	fit (Eq. 10)
$3.2\cdot10^2$	1	4.18 (2.6%)	4.31 (0.5%)	4.29
$5.1\cdot10^2$	1	5.01 (3.3%)	4.98 (2.7%)	4.85
$6.7\cdot10^2$	1	5.52 (6.1%)	5.40 (3.8%)	5.20
$8.7\cdot10^2$	1	6.09 (9.5%)	5.86 (5.4%)	5.56

The relative errors between the fitted data and the heat transfer relation (10) are pictured in Fig. 4(b) in terms of $(b/L)Ra_b \cos\theta$. Major deviations are observed for $(b/L)Ra_b \cos\theta$ values between $5*10^0$ and 10^2. According to Bar-Cohen and Rohsenow [1], Eq. (10) is a composite relation derived from a linear superposition of two known limiting expressions within which the Nu_b varies smoothly (i.e., the fully developed limit and the isolated plate limit). The zone of greatest observed relative errors coincides with the intermediate zone between the two limiting expressions, where it is more difficult for this type of composite relation to properly accommodate the data. As can be observed, Eq. (10) fits all data fairly accurately (with a maximum relative error below 8%) if $(b/L)Ra_b \cos\theta$ is larger than 10^2.

Fitting errors in the intermediate zone could be reduced by a fitting procedure permitting the variation of the constant that affects the first term of Eq. (10) together with the two exponents affecting ϵ. The following relation was obtained:

$$Nu_b = \left[\left(\frac{2}{29} (b/L) Ra_b \cos\theta \right)^{-2} + (0.59[(b/L) Ra_b \cos\theta]^{1/4}[1+\epsilon^{4/5}]^{4/5})^{-2} \right]^{-1/2} \quad (11)$$

The maximum relative fitting errors of this relation are below 9% and the average relative errors around 2%. However, this relation is not consistent with the solution of the fully developed limit for low values of $(b/L)Ra_b \cos\theta$, as the fitted parameter 2/29 was applied instead of 1/12 (which arises from the analytical solution of the fully developed limit).

6.3 Validation. As a final step to assess the credibility of the heat transfer relation, the results of a validation test are presented in this Section. The direct comparison of solutions of the numerical model to the experimental heat transfer and fluid flow data obtained (see Section 5) are discussed. Numerical solutions used in this validation test were implemented reproducing the experimental conditions.

The numerical and experimental values of the Nusselt numbers are given in Table 3 together with the corresponding values from the heat transfer relation (10). Relative differences between these and the Nu_b derived from the heat transfer relation are also indicated. They remained below 10% in all cases.

The comparison of the numerical and experimental fluid flow data is shown in Fig. 5 and Fig. 6. They correspond to the case of $T_w = 70°C$ and $T_w = 150°C$ respectively. Compared is the u component of the velocity normalized by the reference velocity $v_{ref} = [Lg\beta(T_w - T_a)\cos\theta]^{1/2}$. The upper index * indicates that u was normalized. Both figures contain two sets of data. Velocity profiles at the central vertical section of each observation window are shown at the bottom. At the top there are maps of local differences $\Delta u^*(x,y)$ between the numerical and experimental data in the four observation windows. These maps of differences were obtained by interpolating the experimental and numerical data at the nodes of a regular mesh of 50*50 nodes, and by calculating the differences at each of the nodes. Third-order accurate interpolations were used to minimize additional errors in the data-processing. Apart from a few large local differences in some nodes caused by errors in the experimental data (white gaps close to the top walls), all local differences in the u^* are below 10%. However, the experimental u^*-profiles are not perfectly reproduced by the numerical profiles. Experimental measurements at window # 2 of the case with $T_w = 70°C$ and at windows # 2 and # 3 for $T_w = 150°C$ show an irregular velocity profile close to the bottom wall. There is no clear explanation for these irregularities in the u-profile, and therefore would require further investigation.

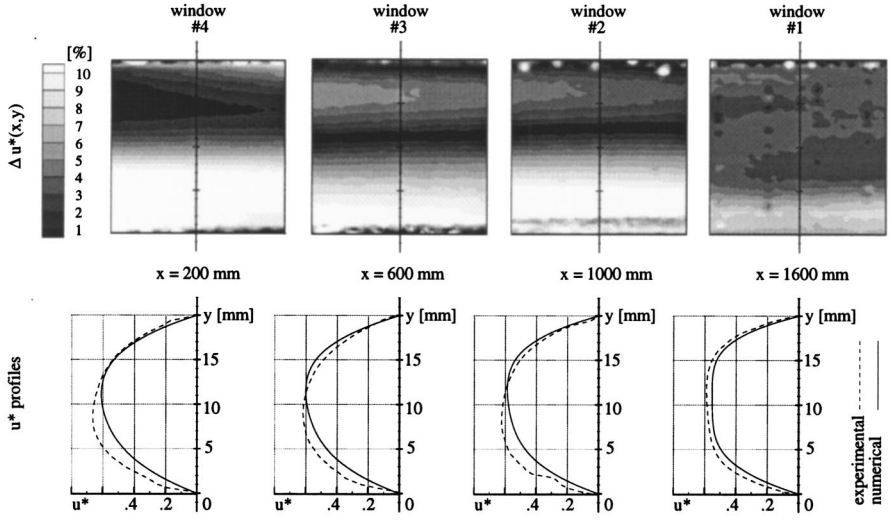

Fig. 5 Comparison of the u-velocity obtained from the experimental setup and from the numerical model for $T_w = 70°C$ and T_a = laboratory temperature. Top: map of differences in the four observation windows. Bottom: profiles at the central vertical section of each observation window. (Note:* means that the u-velocity is normalized by the reference velocity $v_{ref} = [Lg\beta(T_w - T_a)\cos\theta]^{1/2}$.)

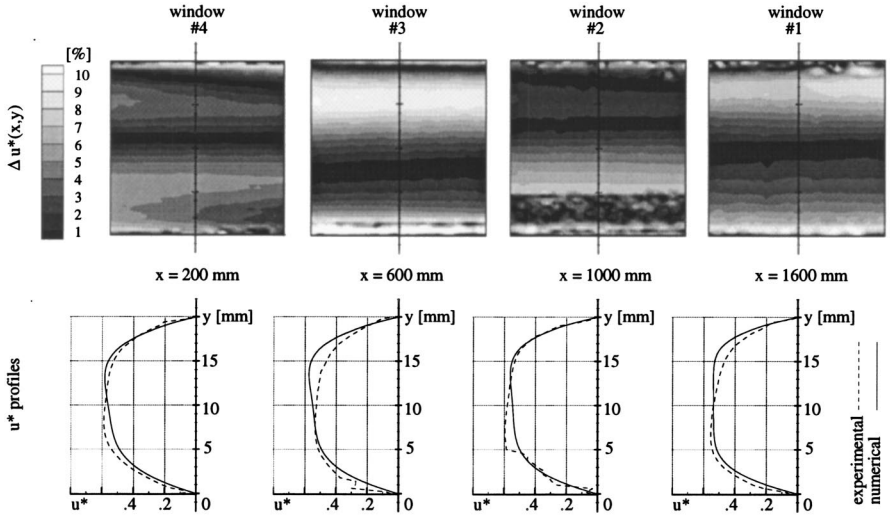

Fig. 6 Comparison of the *u*-velocity obtained from the experimental setup and from the numerical model for T_w=150°C and T_a=*laboratory temperature*. Top: map of differences in the four observation windows. Bottom: profiles at the central vertical section of each observation window. (Note: * means that the *u*-velocity is normalized by the reference velocity $v_{ref}=[Lg\beta(T_w-T_a)\cos\theta]^{1/2}$.)

7 Conclusions

A parametric numerical study was performed to obtain a relation of the Nusselt number for free air (Pr=0.71) convection in large asymmetric radiative coupled isothermal plates. Variations in the channel length, the inter-plate spacing, the inclination of the channel, the emissivity of the plates and the temperature difference between the isothermal wall and the ambient were taken into account. The channels under study were beyond the applicability range of the heat transfer relations already presented by other authors, and that seemingly were limited to small aspect ratios, lower Grashof numbers and did not consider radiation heat transfer.

The parametric study involved 2500 different cases. All the numerical solutions were subjected to a verification process to asses their credibility. Estimates for their numerical uncertainty and order of accuracy were obtained.

The Nusselt numbers of all the credible solutions were fitted to a relation in terms of two numbers: the surface emissivity and a modified Rayleigh number including the channel aspect ratio and the inclination angle. In the case of non-radiating vertical plates, the equation coincides with the previously available composite-relations for lower Grashof numbers.

A final validation test was carried out by comparing numerical data with experimental heat transfer and fluid flow data measured in an ad-hoc experimental setup. The fluid flow was measured by a Digital Particle Image Velocimetry device.

Acknowledgments

This work has been financially supported by the Spanish Comisión Interministerial de Ciencia y Tecnología (project TIC1999-0770), and by the Comissionat per Universitats i Recerca of the Generalitat de Catalunya.

Nomenclature

A = surface area of the isothermal plate m^2
GCI = grid convergence index [5]
Gr = Grashof number
L = channel length, m
Nu_b = average Nusselt number, Eq. (1)
Pr = Prandtl number, $\nu\rho c_p/\lambda$
Pl = Planck number, $\lambda/b\sigma T_a^3$
R = radiation number, $(T_w-T_a)/T_a$
Ra = Rayleigh number, Pr·Gr
Rn = percentage of Richardson nodes [4]
P = total heat loss of the setup, W
Q = total heat transfer rate from the plates to the air, W
Q_{loss} = heat loss of the setup with channel closed, W
T = temperature, K
T_a = ambient temperature, K
T_w = isothermal plate temperature, K
T_o = reference temperature, K
b = inter-plate spacing, m
c_p = specific heat at constant pressure, J/kgK
g = gravitational acceleration, m/s^2
n = parameter used to represent the mesh, see Fig. 1(b)
p = global observed order of accuracy
p_d = dynamic pressure, Pa
u, v = velocity components, m/s
$\mathbf{v}$ = magnitude of the velocity vector, m/s
x, y = Cartesian coordinates, m, see Fig. 1

Greek Symbols

ΔT = temperature difference, K
β = volumetric coefficient of thermal expansion, 1/K
ϵ = emissivity of the plates
λ = thermal conductivity, W/mK
ν = kinematic viscosity, m^2/s
ρ = density, kg/m^3
σ = Stefan-Boltzmann constant, W/m^2K^4
θ = angle of inclination of the channel respect to the gravity direction, deg

Superscripts

* = normalized value

References

[1] Bar-Cohen, A., and Rohsenow, W. M., 1984, "Thermally Optimum Spacing of Vertical, Natural Convection Cooled, Parallel Plates," ASME J. Heat Transfer, **106**, pp. 116–123.
[2] Sparrow, E. M., Chrysle, G. M., and Azevedo, L. F., 1984, "Observed Flow Reversals and Measured-Predicted Nusselt Numbers for Natural Convections in a One-Sided Heated Vertical Channel," ASME J. Heat Transfer, **106**, pp. 325–332.

[3] Azevedo, L. F., and Sparrow, E. M., 1985, ''Natural Convection in Open-Ended Inclined Channels,'' ASME J. Heat Transfer, **107**, pp. 893–901.
[4] Cadafalch, J., Pérez-Segarra, C. D., Cònsul, R., and Oliva, A., 2002, ''Verification of Finite Volume Computations on Steady State Fluid Flow and Heat Transfer,'' ASME J. Fluids Eng., **124**, pp. 11–21.
[5] Roache, P. J., 1994, ''Perspective: A Method for Uniform Reporting of Grid Refinement Studies,'' ASME J. Fluids Eng., **116**, pp. 405–413.
[6] Bejan, A., 1995, *Convection Heat Transfer*, second edition, Wiley, New York, p. 192.
[7] Pérez-Segarra, C. D., Oliva, A., Costa, M., and Escanes, F., 1995, ''Numerical Experiments in Turbulent Natural and Mixed Convection in Internal Flows,'' Int. J. Numer. Methods Heat Fluid Flow, **5**, pp. 13–33.
[8] Gray, D. D., and Giorgini, A., 1975, ''The Validity of the Boussinesq Approximation for Liquids and Gases,'' Int. J. Heat Mass Transf., **19**, pp. 545–551.
[9] Gaskell, P. H. et al., 1988, ''Comparison of Two Solution Strategies for Use with Higher-Order Discretization Schemes in Fluid Flow Simulation,'' Int. J. Numer. Methods Fluids, **8**, pp. 1203–1215.
[10] Marthur, S. R., and Murthy, J. Y., 1997, ''Pressure Boundary Conditions for Incompressible Flow Using Unstructured Meshes,'' Numer. Heat Transfer, Part B, **32**, pp. 283–298.
[11] Patankar, S. V., 1980, *Numerical Heat Transfer and Fluid Flow*, McGraw-Hill.
[12] Van Doormal, J. P., and Raithby, G. D., 1984, ''Enhancements of the Simple Method for Predicting Incompressible Fluid Flows,'' Numer. Heat Transfer, **7**, pp. 147–163.
[13] Westerweel, J., 1994, ''Efficient Detection of Spurious Vectors in Particle Image Velocimetry,'' Exp. Fluids, **16**, pp. 236–247.
[14] Press, W. H., Teukolsky, S. A., Vetterling, W. T., and Flannery, B. P., 1994, *Numerical Recipes in C: The Art of Scientific Computing*, second edition, Cambridge University Press, New York, pp. 412–420.

Self-Preserving Properties of Unsteady Round Buoyant Turbulent Plumes and Thermals in Still Fluids

F. J. Diez

R. Sangras

G. M. Faeth
e-mail: gmfaeth@umich.edu

Department of Aerospace Engineering,
The University of Michigan,
Ann Arbor, Michigan 48109-2140

O. C. Kwon
School of Mechanical Engineering,
Sungkyunkwan University,
Suwon, Kyunggi-do 440-746, Korea

The self-preserving properties of round buoyant turbulent starting plumes and starting jets in unstratified environments. The experiments involved dye-containing salt water sources injected vertically downward into still fresh water within a windowed tank. Time-resolved images of the flows were obtained using a CCD camera. Experimental conditions were as follows: source diameters of 3.2 and 6.4 mm, source/ambient density ratios of 1.070 and 1.150, source Reynolds numbers of 4,000–11,000, source Froude numbers of 10–82, volume of source fluid for thermals comprising cylinders having the same cross-sectional areas as the source exit and lengths of 50–382 source diameters, and streamwise flow penetration lengths up to 110 source diameters and 5.05 Morton length scales from the source. Near-source flow properties varied significantly with source properties but the flows generally became turbulent and then became self-preserving within 5 and 20–30 source diameters from the source, respectively. Within the self-preserving region, both normalized streamwise penetration distances and normalized maximum radial penetration distances as functions of time were in agreement with the scaling relationships for the behavior of self-preserving round buoyant turbulent flows to the following powers: time to the 3/4 power for starting plumes and to the 1/2 power for thermals. Finally, the virtual origins of thermals were independent of source fluid volume for the present test conditions. [DOI: 10.1115/1.1597620]

Keywords: Fire, Heat Transfer, Plumes, Thermal, Turbulence

Introduction

Recent theoretical and experimental studies of the temporal development of round nonbuoyant turbulent starting jets and puffs (the latter due to brief releases of a nonbuoyant source fluid) [1,2], in still environments (denoted starting jets and puffs in the following) were extended to consider the corresponding buoyant flows, e.g., round buoyant turbulent starting plumes and thermals (the latter due to brief releases of a buoyant source fluid), in still and unstratified environments (denoted starting plumes and thermals in the following). Study of these flows is motivated by practical applications to the unconfined and unsteady turbulent flows resulting from the initiation of steady and interrupted buoyant fluid releases caused by process upsets, unwanted fires, and explosions, among others. The general configuration of these flows is illustrated in Fig. 1 for the familiar cases of rising positively-buoyant starting plumes and thermals. Due to their simplicity, the present flows also are of interest as classical buoyant turbulent flows that illustrate the development of unsteady turbulent flows. In addition, due to their well-defined initial and boundary conditions, and their simple geometry, observations of these flows are useful to provide data needed to evaluate detailed methods for predicting the properties of buoyant turbulent flows. Similar to earlier studies of starting jets and puffs of Refs. [1] and [2], the present experiments emphasized conditions far from the source where effects of source disturbances are lost and flow structure is largely controlled by its conserved properties. For such conditions, the flows approximate self-preserving turbulent behavior fixed by their conserved properties and appropriately scaled flow properties are independent of streamwise distance. The advantages of self-preserving turbulent flows are that the properties of this region significantly simplify both the presentation of measurements of these flows, and numerical simulations needed to model these flows, because effects of source disturbances have been lost and flow properties scale in a relatively compact manner.

Past experimental, theoretical and computational studies of steady plumes have been carried out by a number of workers because this flow configuration involves a classical fundamental flow that is characterized by only a few parameters. Early studies and reviews of this work can be found in Rouse et al. [3], Morton et al. [4], Morton [5], Turner [6], Seban and Behnia [7], Yih [8], Yih and Wu [9], George et al. [10], Chen and Chen [11] and List [12]. Most of this early research concentrated on developing the scaling relationships for self-preserving behavior and carrying out measurements to find mean flow properties in terms of self-preserving variables. Subsequent studies of steady plumes sought more detail about the turbulence properties and the development of the flows toward self-preserving conditions, see Papanicolaou and List [13], Papantoniou and List [14], Peterson and Bayazitoglu [15], Dai et al. [16–18], and references cited therein. A surprising feature of the steady plume measurements of Dai et al. [16–18] was that self-preserving behavior was only observed at distances farther from the source than previously thought, e.g., distances greater than roughly 80 source diameters. In contrast, recent studies of starting jets and puffs of Refs. [1] and [2], indicated that these flows reached self-preserving behavior at distances as small as 20–30 source diameters from the source. The reasons for these discrepancies are unknown, although different source exit states, effects of unsteadiness, effects of buoyancy and effects of the parameter being studied, have been suggested as possible mechanisms controlling the approach to self-preserving behavior [1]. Clearly, however, these observations raise concerns about whether existing measurements of the self-preserving be-

Contributed by the Heat Transfer Division for publication in the JOURNAL OF HEAT TRANSFER. Manuscript received by the Heat Transfer Division August 20, 2002; revision received April 10, 2003. Associate Editor: K. S. Ball.

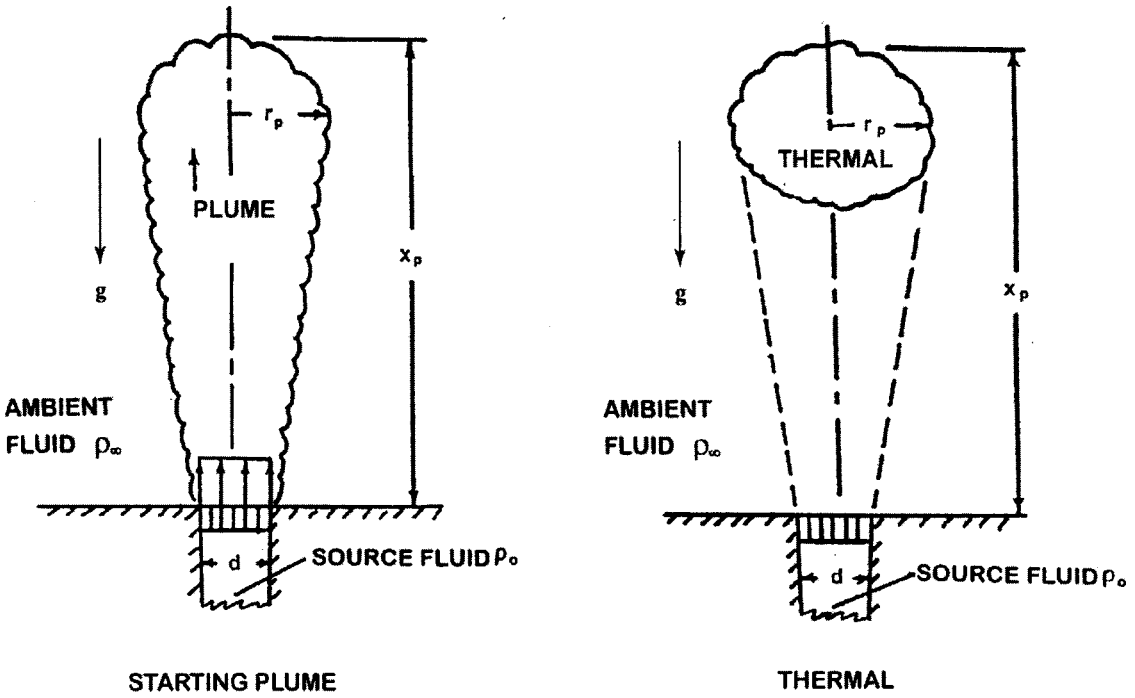

Fig. 1 Sketches of starting plumes and thermals

havior of round buoyant turbulent unsteady flows were carried out far enough from the source to properly observe self-preserving behavior.

Starting plumes and thermals have received less attention than steady plumes. Representative studies include Turner [19], Middleton [20], Delichatsios [21], Pantzloff and Lueptow [22], and references cited therein, for starting plumes, and Scorer [23], Turner [24,25], Fay and Lewis [26], Batt et al. [27], Thompson et al. [28], Turner [29], Morton [30], and references cited therein, for thermals. These studies have provided self-preserving scaling relationships that describe the main features of starting plumes and thermals, however, corresponding measurements of the self-preserving properties of these flows are surprisingly limited and involve concerns about whether self-preserving conditions were actually achieved as mentioned earlier.

In view of the previous discussion, the present investigation considered the self-preserving properties of starting plumes and thermals in still and unstratified environments. The specific objectives of the study were as follows:

1. Measure the streamwise (vertical) and radial penetration properties of these flows as a function of time for various source diameters, source Reynolds numbers, source Froude numbers, source/ambient density ratios and amounts of injected source fluid (the last for thermals).
2. Use the measured penetration properties to evaluate self-preserving scaling and determine the empirical factors needed to correlate the streamwise (vertical) and the radial penetration properties of these flows.

Experimental methods were generally similar to the earlier studies of starting jets and puffs of Refs. [1] and [2], except for the obvious differences needed to consider buoyant flows. Thus, the present experiments involved salt water sources injected vertically downward into a still fresh water bath, with buoyancy levels varied by using sources having different salt concentrations. Penetration properties were measured from flow visualizations consisting of time-resolved video records of dye-containing injected source liquids.

Experimental Methods

Test Apparatus. The experiments involved salt water modeling of buoyant turbulent flows as suggested by Steckler et al. [31]. A sketch of the test apparatus appears in Sangras et al. [1]. The apparatus consisted of a Plexiglass (18 mm thick) tank open at the top. The volume of water inside the tank was rectangular and had inside plan dimensions of 610×720 mm and depth of roughly 400 mm. Water for the tank was obtained from the laboratory water supply but the water was degassed of dissolved air before use by allowing it to heat to room temperature followed by agitation. The dense salt-containing starting plume or thermal liquid settled naturally to the bottom of the tank and was removed after every three tests to prevent the ambient fluid density from increasing more than 0.1% above its nominal value.

The starting plume and thermal source flows were injected into the tank through smooth round tubes having inside diameters of 3.2 and 6.4 mm, with injector passage length/diameter ratios of 100 and 50, respectively, to help insure fully-developed turbulent pipe flow at the injector exit for sufficiently large injector Reynolds numbers [32]. The tubes were mounted vertically and discharged downward, roughly 5 mm below the liquid surface. The tubes passed through a plane horizontal Plexiglass plate (280 ×432 mm plan dimensions×12 mm thick) with a tight fit. The tube (source) exits were mounted flush with the lower surface of the plexiglass plate to provide well-defined entrainment conditions near the source exit. The source liquid was supplied to the tubes using up to two syringe pumps (Harvard Apparatus, PHD 2000, Model 70–2000 Syringe Pump, each with four 150 cc syringes having volumetric accuracies of ±1% and mounted in parallel). The pumps were computer controlled to start, stop and deliver liquid at preselected times and rates. The pumps were calibrated by collecting liquid for timed intervals. The discharge properties of the pumps were found as discussed by Sangras et al. [1]: pump delivery rates were essentially constant with short development periods upon starting and stopping the pump handled by extrapolating the constant delivery portions to the zero flow rate condition and finding equivalent origins for start and stop

times. A plot illustrating the pump flow rate transients when the pumps were started and stopped appears in Sangras et al. [1].

The salt water source liquids were prepared by adding appropriate weights of salt (certified ACS crystal sodium chloride, 100.2% assay) to given volumes (weights) of water based on the tabulation of liquid densities as a function of salt concentration due to Lange [33]. These results were checked satisfactorily using precision hygrometers (Fisher Scientific, Cat. No. 11–583D, having 0.2% accuracies). The absolute viscosities of the test liquids were measured directly using a Cannon/Fenske viscometer; this information was then combined with the known densities to obtain kinematic viscosities for each source liquid considered during the present investigation. Red vegetable dye was added to the source liquid in order to facilitate flow visualization at a concentration of 0.15% dye by volume.

Instrumentation. Measurements of starting plume or thermal dimensions as a function of time were obtained from video records. The water bath was illuminated for these observations using two 650 W quartz lamps (Color Tran. Quartz king dual 650, Model 116-011). The appearance of the dye-containing injected source liquid was recorded as a function of time using a color video CCD camera (Panasonic Model No. WV-CL 352). This camera has a 682×492 pixel array (yielding a resolution of 0.5 mm per pixel for present conditions) with an 8-bit dynamic range, and a 12 mm focal length ×f1.8 lens (WV aspherical-LA/208). Color still photographs of the flows were also obtained using a Nikon FM2 camera having an 85 mm focal length ×f1.4 lens using conventional Fuji-color film.

The video records were analyzed to provide the maximum mean streamwise penetration distances (taken as the average of the largest streamwise distance of injected source liquid from the jet exit) and the mean maximum radial penetration distance as a function of time from the start of injection, and the mean radial penetration distances of the plume-like portion of these flows as a function of distance from the injector exit at various times after the start of injection. These mean values were obtained by averaging the results of three separate tests at a particular jet exit condition. (Note that each test condition provided numerous data points, so that only three tests at each condition provided rather dense plots of the data within the experimental uncertainties noted in the following.) Experimental uncertainties (95% confidence) of the measurements from the video records were similar to Sangras et al. [1], as follows: less than 7% for times from the start of injection, less than 8% for mean maximum streamwise penetration distances and less than 15% for mean maximum radial penetration distances. The experimental uncertainties of the streamwise and radial penetration distances were largely governed by sampling errors due to the irregular turbulent boundaries of the present buoyant turbulent flows but also include fundamental accuracies of distance and time calibrations and measurements.

Test Conditions. Test conditions for the present round buoyant turbulent starting plumes and thermals are summarized in Table 1. The test conditions involved source diameters of 3.2 and 6.4 mm; source passage length/diameter ratios of 100 and 50; source/ambient density ratios of 1.070 and 1.150; source Reynolds numbers of 4000–11,000; source Froude numbers of 10–82; normalized volume of source fluid for thermals, $Q_o/(A_o d)$, of 50–382; streamwise flow penetration lengths, $(x_p - x_o)/d$, up to 110 and, $(x_p - x_o)/\ell_M$, up to 5.05. It should be noted that the present range of source Froude numbers involves values generally larger than the asymptotic value of roughly 5 for steady round turbulent buoyant plumes in the self-preserving region, this implies generally over-accelerated source flows as defined by George et al. [10]. Finally, experimental uncertainties for values of the source Reynolds and Froude numbers are less than 5%.

Table 1 Summary of test conditions for starting plumes and thermals[a]

Parameter	Value
Source diameter, d	3.2 and 6.4 mm
Source passage length/diameter ratio, L/d	50 and 100
Ambient fluid	Water
Source fluid	Salt water mixtures
Ambient fluid density, ρ_∞	998 kg/m^3
Ambient fluid kinematic viscosity, ν_∞	1.0 mm^2/s
Source fluid density, ρ_o	1070 and 1150 kg/m^3
Source fluid kinematic viscosity, ν_o	1.11 and 1.36 mm^2/s
Source flow rate, $\dot{Q}_o$	15–30 cc/s
Source/ambient fluid density ratio, ρ_o/ρ_∞	1.070 and 1.150
Source Reynolds number, $u_o d/\nu_o$	4,000–11,000
Source Froude number, $(\rho_\infty u_o^2/(gd\lvert\rho_o-\rho_\infty\rvert))^{1/2}$	10–82
Source fluid discharged for thermals, $Q_o/(A_o d)$	50–382
Streamwise penetration distance, $(x_p - x_o)/d$	0–110
Streamwise penetration distance, $(x_p - x_o)/\ell_M$	0–5.05
Characteristic flow time, $(t-t_d)/t^*$	0–2,000

[a]Salt water jets injected from round tubes into a still volume of fresh water having dimensions of 610×720×400 (deep) mm at an ambient pressure and temperature of 99±0.5 kPa and 297±0.5 K.

Scaling Methods

Self-Preserving Region. Two parameters that are useful for estimating when round buoyant turbulent flows from steady and interrupted sources become self-preserving are the distance from the virtual origin normalized by the source diameter, $(x-x_o)/d$, and the distance from the virtual origin normalized by the Morton length scale, $(x-x_o)/\ell_M$, see Dai et al. [16]. The first parameter is pertinent to both buoyant and nonbuoyant flows and measures the distance needed to modify distributions of mean and fluctuating properties from conditions within a passage, typical of most sources, to conditions within an unbounded flow, e.g., the distance needed for the transition region required to eliminate source disturbances. The second parameter is only pertinent to buoyant flows and measures the distance needed for buoyancy-induced momentum to dominate the momentum of the source flow (which can be either an excess of this momentum for an over-accelerated source or a deficiency of this momentum for an under-accelerated source [10]). The Morton length scale is defined as follows for steady buoyant turbulent flows from round sources having uniform properties [5,12]:

$$\ell_M/d = (\pi/4)^{1/4}(\rho_\infty u_o^2/(gd\lvert\rho_o-\rho_\infty\rvert))^{1/2} \tag{1}$$

where an absolute value has been used for the density difference in order to account for both rising and falling flows (under the limitation that the source flow is directed accordingly in the rising or falling direction, as opposed to fountains where the source flow is in the direction opposite to the eventual direction of the flow as a result of effects of buoyancy, e.g., the flows considered by Pantzlaff and Lueptow [22] and Baines et al. [34,35]). The source Froude number, Fr_o, is proportional to ℓ_M/d for uniform source properties, as follows [12,16]:

$$\mathrm{Fr}_o = (4/\pi)^{1/4}\ell_M/d \tag{2}$$

The source Froude number is often used to characterize the initial degree of buoyant behavior of a source, e.g., $\mathrm{Fr}_o = 0$ and ∞ represent purely buoyant and purely nonbuoyant sources, respectively. As mentioned earlier, past studies of steady round buoyant turbulent plumes suggest $(x-x_o)/d > 80$ and involved $(x-x_o)/\ell_M > 10$ for self-preserving conditions, based on distributions of mean mixture fractions and streamwise velocities, see Dai et al. [16] and references cited therein. Another important criterion for self-preserving flows is that properties within the flow should not be very different from ambient properties so that property changes are very nearly linear functions of the degree of mixing (i.e., the relative properties of injected and ambient fluid in a sample, see

Dai et al. [16–18] for examples of measurements of the degree of mixing of buoyant turbulent flows). For the present flows, where the main property variation involves the density, this last criterion for self-preserving behavior implies $|\rho_o-\rho_\infty|/\rho_\infty \ll 1$. Present test conditions are limited to maximum values of $|\rho_o-\rho_\infty|/\rho_\infty = 0.150$, see Table 1; therefore, this last criterion was generally satisfied during the present study.

Self-Preserving Scaling. Assuming that the flow is within the self-preserving region, expressions for the streamwise flow penetration distance of the present round buoyant turbulent flows from steady and interrupted sources are available from past work, see Morton et al. [4], Morton [5], Turner [6,19,24,25], George et al. [10], List [12], Delichatsios [21], Pantzlaff and Lueptow [22], Scorer [23], Batt et al. [27], Baines et al. [34], and references cited therein. The configurations of the present starting plumes and thermals are illustrated in Fig. 1. (Note that present flows involve falling negatively-buoyant starting plumes and thermals, however, all images of these flows are inverted to represent them as rising positively-buoyant starting plumes in the following to provide a more familiar flow convention for most readers.) It should be noted that both rising and falling flows involve progressive approach of the flow density to the ambient density with increasing distance from the source so that they have correspondingly similar buoyant flow properties. Initiating a flow from a subsequently steady source leads to the starting plume, whereas initiating a flow from an interrupted source leads to a thermal.

Major assumptions for present considerations are similar to earlier determinations of self-preserving flow scaling as discussed by List [12], as follows: physical property variations in the flows are assumed to be small (i.e., the flows are assumed to be weakly buoyant so that density variations are nearly linear functions of the degree of mixing, as discussed earlier); steady sources are assumed to start instantly and subsequently maintain constant source properties, including constant source flow rates; interrupted sources are assumed to start and stop instantly and maintain constant source properties during the period of flow, including constant source flow rates; extrapolated temporal origins or terminations of flow conditions are used to handle the small transient periods when the pump flows are initiated or terminated as discussed in Ref. [1]; and virtual origins for the streamwise distance are used to maximize conditions where self-preserving behavior is observed. Finally, source flow properties are assumed to be uniform similar to the conditions required for Eqs. (1) and (2) to be correct. This last approximation is not a critical assumption, however, because the details of the conserved properties of the flows are adequately prescribed by mean source properties within the self-preserving regions of the present flows.

Under these assumptions, the temporal variation of the maximum streamwise penetration distance can be expressed as follows within the self-preserving regions of the present unsteady turbulent flows (see Morton et al. [4], Morton [5], and Taylor [6] for examples of the methodology and earlier determinations of scaling relationships for buoyant turbulent flows):

$$(x_p-x_o)/d = C_x((t-t_d)/t^*)^n \tag{3}$$

where t_d is the extrapolated temporal origin of initiation of pump flow to the source that was discussed earlier. The corresponding temporal variation of the maximum radial penetration distance can be expressed most conveniently in terms of the streamwise penetration distance, as follows:

$$r_p/(x_p-x_o) = C_r \tag{4}$$

The values of C_x, C_r, x_o, t_d, t^*, and n vary depending upon the particular unsteady flow that is being considered. The values of C_x and C_r, x_o, and t_d are best-fit empirical parameters of the self-preserving scaling relationships and will be considered later when the measurements are discussed. However, the values of t^* and n follow from the requirements of conserved properties for self-preserving flows and can be expressed as follows for the present unsteady flows:

$$t^* = (d^4/\dot{B}_o)^{1/3}, \quad n = 3/4; \quad \text{starting plume} \tag{5}$$

$$t^* = (d^4/B_o)^{1/2}, \quad n = 1/2; \quad \text{thermal} \tag{6}$$

In these equations, $\dot{B}_o$ is the conserved source specific buoyancy flux in a starting plume and B_o is the conserved source specific buoyancy force in a thermal, which are the properties of these flows that define this self-preserving scaling. Under the present assumptions of uniform source properties, the conserved source specific buoyancy flux for a plume and the source specific buoyancy force for a thermal can be found from source properties, as follows [12]:

$$\dot{B}_o = \dot{Q}_o g|\rho_o-\rho_\infty|/\rho_\infty; \quad \text{starting plume} \tag{7}$$

$$B_o = Q_o g|\rho_o-\rho_\infty|/\rho_\infty; \quad \text{thermal} \tag{8}$$

where an absolute value has been used for the density difference, as before, to account for both rising and falling flows.

The expressions for the vertical penetration distances of starting plumes and thermals, Eqs. (3), (5), and (6), are convenient for illustrating the development of these flows toward self-preserving behavior and the subsequent variation of streamwise penetration distances as functions of time. These formulations are somewhat misleading, however, because they involve the source diameter which is not a relevant variable of self-preserving flows. This is apparent because d cancels out of Eqs. (3) and (5) for starting plumes and out of Eqs. (3) and (6) for thermals at self-preserving conditions to yield the following expressions for the vertical penetration distances of these flows in still environments:

$$(x_p-x_o)/(\dot{B}_o^{1/3}(t-t_d))^{3/4} = C_x; \quad \text{starting plume} \tag{9}$$

$$(x_p-x_o)/(B_o^{1/2}(t-t_d))^{1/2} = C_x; \quad \text{thermal} \tag{10}$$

where the theoretical values for self-preserving starting plumes and thermals, $n = 3/4$ and 1/2, have been used in Eqs. (9) and (10).

To compare present results for starting plumes and thermals with the earlier results of Refs. [1] and [2] for starting jets and puffs, it is useful to have the self-preserving scaling relationships for the nonbuoyant flows. In this case, Eqs. (3) and (4) apply as before for maximum streamwise and radial penetration distances as functions of time. Values of t^* and n, however, differ for the nonbuoyant flows and take on the following values [1,2];

$$t^* = d^2/(\dot{Q}_o u_o)^{1/2}, \quad n = 1/2; \quad \text{starting jet} \tag{11}$$

$$t^* = d^4/(Q_o u_o), \quad n = 1/4; \quad \text{puff} \tag{12}$$

Finally, proceeding in the same manner as before, the source diameter can be factored out of these equations to yield the following self-preserving equations for the streamwise penetration distances [2]:

$$(x_p-x_o)/((\dot{Q}_o u_o)^{1/2}(t-t_d))^{1/2} = C_x; \quad \text{starting jet} \tag{13}$$

$$(x_p-x_o)/((Q_o u_o)(t-t_d))^{1/4} = C_x; \quad \text{puff} \tag{14}$$

where the theoretical values for self-preserving starting jets and puffs, $n = 1/2$ and 1/4, have also been used in Eqs. (13) and (14).

Results and Discussion

Overview. The ranges of Re_o and $(x_p-x_o)/d$ and the values of n, C_x, C_r, and x_o/d for starting jets and plumes are summarized in Table 2. Corresponding ranges of Re_o, $(x_p-x_o)/d$ and $Q_o/(A_o d)$ and the values of n, C_x, C_r, and x_o/d for puffs and thermals are summarized in Table 3. For present measurements, the time delay was subtracted from the original time records to correct for startup conditions.

Table 2 Summary of the properties of starting jets and plumes[a]

Source	Re_o	$(x_p - x_o)/d$[b]	n	C_x	C_r	x_o/d
Starting Jets:						
Diez et al. [2]	3,000–12,000	140	1/2	2.8 (0.06)	0.15 (0.003)	0.0
Starting Plumes:						
Present	4,000–11,000	110	3/4	2.7 (0.09)	0.16 (0.006)	7.0 (1.7)
Turner [19]	···	···	3/4	···	0.18±0.03	···

[a]Injection of starting jets and plumes into still and unstratified environments. Experimental uncertainties (95% confidence) in parenthesis.
[b]Maximum streamwise penetration distances observed.

The virtual origins for each of the present flows were found by plotting $((t-t_o)/t^*)^n$ as a function of x_p/d for every test condition. A linear fit of the far-field data was then developed for each flow so that solution of this fit at time $(t-t_d)=0$ determined the virtual origin, x_o/d. The values of x_o/d were relatively constant for each flow; this will be illustrated later for thermals. As a result, a mean value of x_o/d could be found for each flow and is summarized (along with its experimental uncertainty) with the other self-preserving parameters of each flow in Tables 2 and 3.

Starting Plumes. Video images of a typical starting plume in a still environment at various times after initiation of the source flow are illustrated in Fig. 2. The general appearance of a typical starting plume illustrated in Fig. 2 is qualitatively similar to a typical starting jet illustrated in Sangras et al. [1]. The flow boundary is relatively smooth near the source but becomes roughened and turbulent-like a few diameters from the source exit at small times after initiation of the source flow. The starting plumes generally exhibited roughened surfaces nearer to the jet exit than the corresponding starting jets [1], however, this is consistent with the widely recognized increased instability of plumes compared to jets, e.g., plumes intrinsically involve effects of Rayleigh-Taylor instability near the axis of the flow due to the approach of the flow to the ambient density as the streamwise distance increases (independent of whether the flow is a rising positively-buoyant flow or a falling negatively-buoyant flow) which naturally are absent from nonbuoyant flows, see Dai et al. [16]. The radius of the starting plume is seen to increase smoothly from the source exit to the maximum radius condition near the tip of the plume, with no

Table 3 Summary of the properties of puffs and thermals[a]

Source	Re_o	$(x_p - x_o)/d$[b]	$Q_o/(A_o d)$	n	C_x	C_r	x_o/d
Puffs:							
Diez et al. [2]	3,000–12,000	100	30–191	1/4	2.6(0.06)	0.17(0.005)	8.5(2.0)
Thermals:							
Present:	4,000–11,000	110	50–382	1/2	2.7(0.05)	0.19(0.003)	8.5(0.7)
Scorer [23]	···	···	···	1/2	···	0.26	···
Turner [25]	···	···	···	1/2	···	0.25	···
Thompson et al. [28]	···	···	···	···	···	0.24	···

[a]Injection of puffs and thermals into still and unstratified environments. Experimental uncertainties (95% confidence) in parenthesis.
[b]Maximum streamwise penetration distances observed.

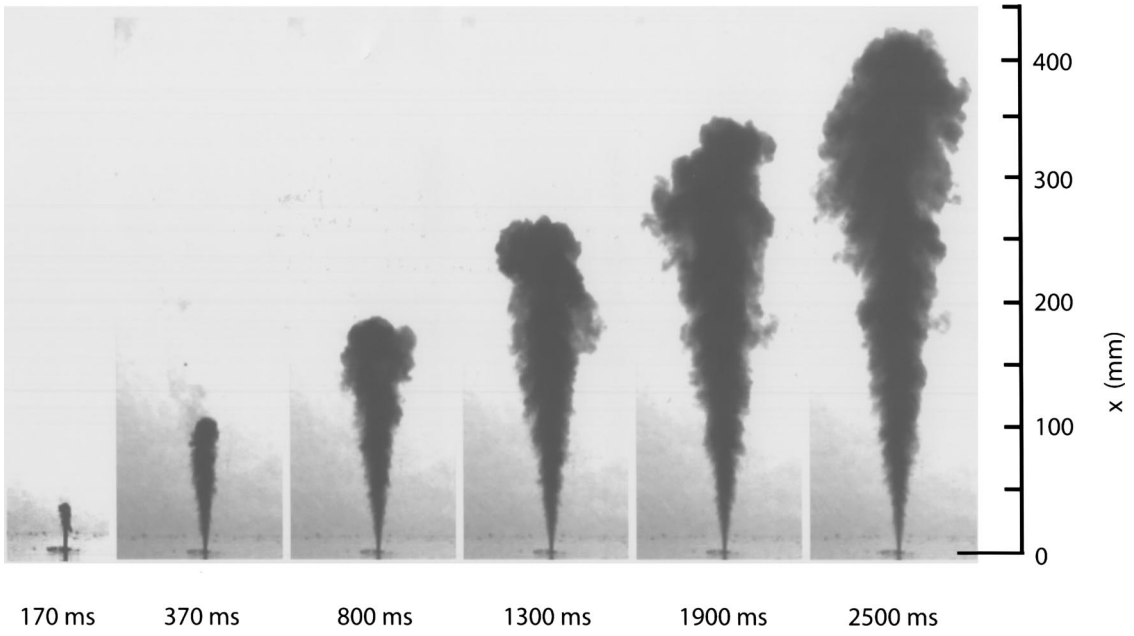

Fig. 2 Visualization of a starting plume ($d=3.2$ mm, $u_o=3700$ mm/s, $\rho_o/\rho_\infty=1.150$, $Re_o=9000$ and $Fr_o=58.5$)

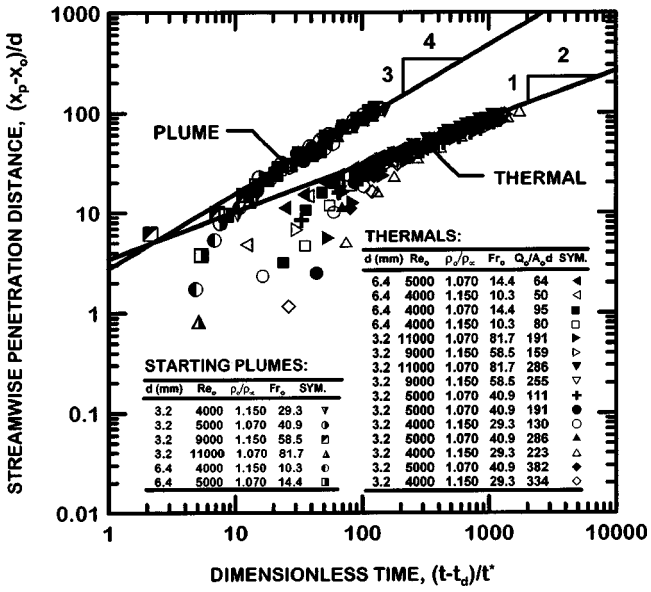

Fig. 3 Streamwise penetration distances of starting plumes and thermals as functions of time

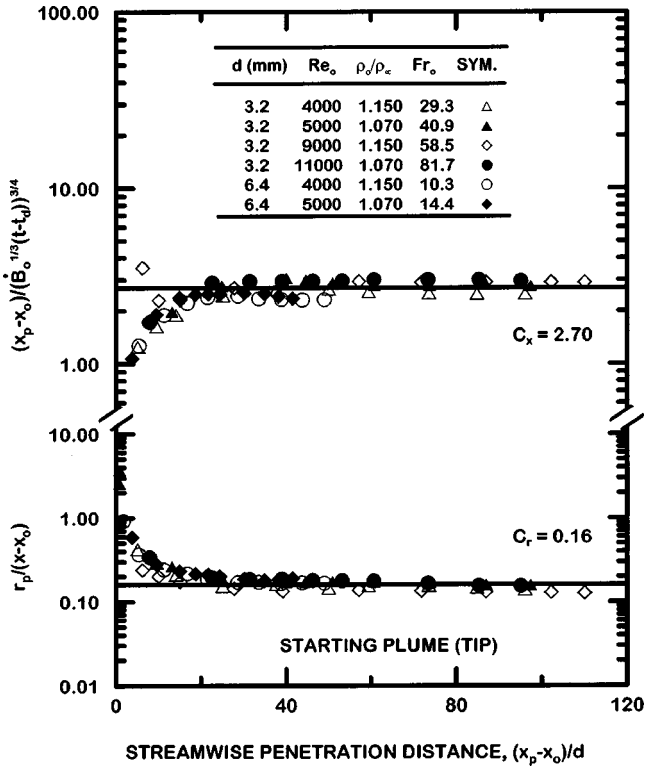

Fig. 4 Streamwise and radial penetration distances of starting plumes as functions of streamwise penetration distance

evidence of a cap-like structure associated with the leading vortex; notably, the general appearance of starting jets was similar, see flow visualizations in Sangras et al. [1] and Pantzlaff and Lueptow [22] for starting jets.

Normalized streamwise (vertical) penetration distances for starting plumes are plotted as a function of dimensionless time, according to the self-preserving scaling of Eqs. (3) and (5), in Fig. 3. However, near-source behavior varies depending upon source properties, present source flows correspond to over-accelerated flows ($\mathrm{Fr}_o > 5$) so that the flows generally decelerate at first before self-preserving conditions are approached. All the measurements for the starting plumes are seen to follow the self-preserving correlation at large dimensionless times, e.g., at $(t-t_d)/t^* > 20$. However, this implies reaching self-preserving distances at scaled times somewhat smaller than was the case for starting jets, where self-preserving behavior was not approached until $(t-t_d)/t^* > 100$ [1]; recall, however, that the definitions of t^* for the two flows differ, see Eqs. (5) and (11). In contrast, streamwise penetration distances needed to approach self-preserving conditions are comparable for starting jets and plumes, $(x_p-x_o)/d > 20-30$, where the normalized penetration distance expression is identical for both flows, see Sangras et al. [1], which is much nearer to the source than the values of $(x-x_o)/d > 80$ needed to reach self-preserving behavior for steady round buoyant turbulent plumes based on measured mean and fluctuating concentration and velocity distributions [16–18]. Reasons for this behavior have been suggested, as follows [1]: stabilities of starting and steady turbulent flows are fundamentally different, and distances needed for self-preserving flow frequently depend upon the property that is observed. For example, the turbulence spectra of streamwise and cross-stream velocity fluctuations approach self-preserving behavior for steady plumes at streamwise distances of $(x-x_o)/d \approx 25$ that are much smaller than streamwise distances required for self-preserving behavior of other properties in these flows [16]. Notably, flow behavior within the self-preserving region is relatively independent of the variations of source diameter, Reynolds number, source/ambient density ratio and source Froude number considered in Fig. 3.

Another interesting observation concerning the self-preserving behavior of starting plumes in Fig. 3 is that $(x_p-x_o)/\ell_M$ is only greater than 0.3 for the range of the present data satisfying self-preserving behavior of starting plumes, which seems relatively small. For example, the experimental range for self-preserving behavior of steady plumes was $(x-x_o)/\ell_M > 10$ for the studies of Dai et al. [16–18], although it should be noted that no attempt was made to find limiting values of $(x-x_o)/\ell_M$ for self-preserving behavior during these studies. One explanation of why $(x_p-x_o)/\ell_M$ can be relatively small for self-preserving behavior of starting plumes is that source velocities decay relatively rapidly for starting jets compared to starting plumes, e.g., the ratio of the penetration velocities of starting-plumes/starting-jets is proportional to $(x_p-x_o)^{2/3}$. Thus, it appears that flow momentum due to effects of buoyancy develops sufficiently rapidly so that effects of source momentum do not disturb self-preserving starting plume behavior when $(x_p-x_o)/d$ is 20–30, even though $(x_p-x_o)/\ell_M$ is as small as 0.3, or Fr_o is as large as 82. Chen and Chen [11] discuss this issue but more study of the combined effects of large $(x_p-x_o)/d$, to control effects of source disturbances, and large $(x_p-x_o)/\ell_M$, to control effects of source momentum, on the self-preserving behavior of starting plumes clearly would be useful.

Measurements of maximum streamwise (vertical) penetration distances of starting plumes are plotted in terms of the dimensionless self-preserving streamwise penetration parameter of Eq. (9) as a function of normalized vertical penetration distance in Fig. 4. Plotted in this manner, it is evident that the self-preserving parameter has a variety of values near the source depending on source properties and distance from the source, however, the self-preserving parameter approaches a constant $C_x = 2.70$ for vertical penetration distances greater than 20–30 source diameters from the source. The fact that C_x is on the order of unity, as expected, is also supportive that physically realistic conditions for self preservation have been identified in Fig. 4.

Normalized maximum radial penetration distances (found near the jet tip as illustrated in Fig. 1) of starting plumes are plotted according to self-preserving scaling based on Eq. (4) in Fig. 4. The normalized maximum radial penetration distance has relatively large values in the region nearest the source where measurements were made; this is expected, however, because this property

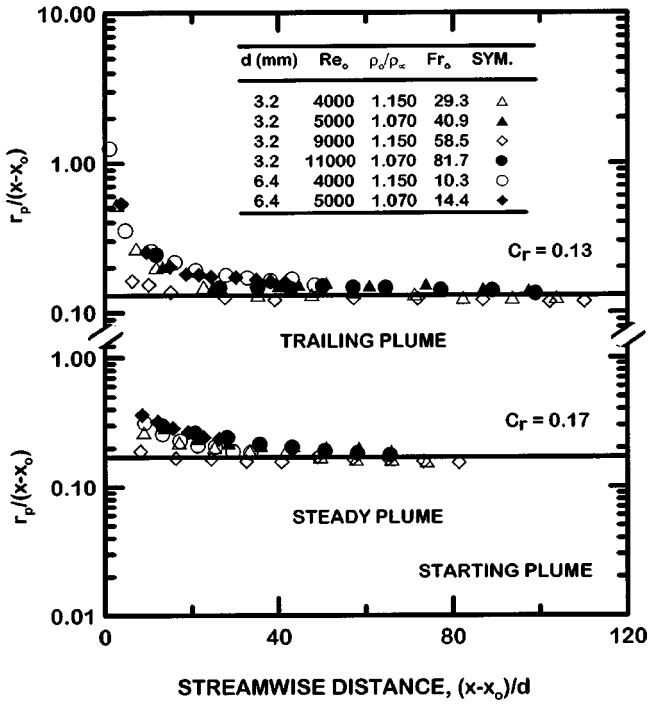

Fig. 5 Radial penetration distances of the trailing and steady plume regions of starting plumes as functions of streamwise distance

becomes unbounded at the virtual origin. The normalized maximum radial penetration distance decreases progressively with increasing streamwise distance and becomes relatively constant in the self-preserving region where $(x_p-x_o)/d>20-30$. This radial flow parameter approaches self-preserving behavior in nearly the same manner as the dimensionless self-preserving streamwise penetration distance that is also plotted in Fig. 4. For self-preserving conditions, $r_p/(x_p-x_o)=C_r=0.16$ for the present measurements. This value is just slightly larger than the corresponding value found for starting jets of $C_r=0.15$ [1]; it is also comparable to the outer boundary of steady round buoyant turbulent plumes based on measurements of mean mixture fraction and velocity distributions [16,17].

Two other parameters were measured to help describe the structure of starting plumes in addition to C_x and C_r. The first, called the trailing plume radius, is plotted in Fig. 5 as a function of streamwise distance. The starting plumes were assumed to consist of a starting vortex and a trailing plume. The starting vortex was assumed to be circular with a radius given by the maximum radial penetration of the tip of the plume. The portion of the plume behind this starting vortex was called the trailing plume (i.e., from the source up to this location). The penetration radii of the trailing plume were measured as a function of both streamwise distance and time. As can be seen from Fig. 5, the dimensionless trailing plume radii eventually reach a mean value of $r_p/(x-x_o)=0.13$ for $(x-x_o)/d>30-40$. This behavior typifies the tendency of radial penetration properties to approach self-preserving behavior somewhat slower than streamwise penetration properties.

The second additional parameter of interest for describing the behavior of starting plumes was the steady plume radius. The starting plume was allowed to run for a time. After the leading vortex passes by, the turbulent plume becomes steady or stationary. The radius of this steady plume was measured as a function of streamwise distance and normalized to obtain values of the reduced steady jet radius that also are illustrated in Fig. 5. This radius decreases with increased streamwise distance from the source for the same reason as the maximum radial penetration distance discussed in connection with Fig. 4. This parameter eventually approaches an asymptotic value of $r_p/(x-x_o)=0.17$ for $(x-x_o)/d>30-40$, which is significantly larger than C_r for the trailing plume in Fig. 5, suggesting gradual radial growth of the trailing plume after the plume tip has passed a given location. However, it should be noted that the present radial penetration distances are visible radii, and are likely to be larger than e^{-1} radii based on reduction of distributions of concentrations of source fluid, mean velocities and turbulence properties, normalized by their centerline values.

A summary of values of n, C_r, C_x, and x_o/d is provided in Table 2, based on the measurements of Diez et al. [2] for starting jets and the measurements of Turner [19] and the present investigation for starting plumes. The results for n from all the studies agree with the expectations of self-preserving scaling and the values of C_r from Ref. [2] for starting jets and from the present study for starting plumes are nearly identical. The values of C_x for the nonbuoyant and buoyant flows also are nearly the same, even though the scaling parameter, t^*, for the two flows is not the

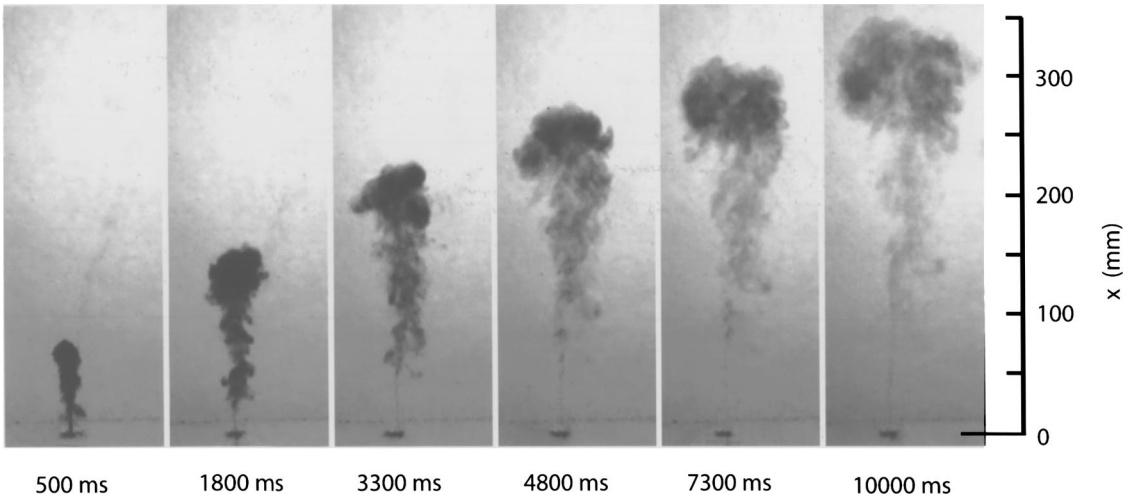

Fig. 6 Visualization of a thermal ($d=3.2$ mm, $u_o=1850$ mm/s, $\rho_o/\rho_\infty=1.150$, Re$_o=4000$, Fr$_o=29.3$ and $Q_o/(A_o d)=130$)

same, see Eqs. (5) and (11). Finally, x_o/d could not be distinguished from zero for the starting jets but had a mean value of $x_o/d=7.0$ for the starting plumes.

Thermals. Video images of a typical thermal at various times after initiation of the flow are illustrated in Fig. 6. The present observations of thermals are qualitatively similar to earlier observations of thermals in the literature due to Turner [19] and Scorer [23], and they also are qualitatively similar to the earlier observations of puffs due to Sangras et al. [1]. The appearance of the thermal in the early stages, when the source flow is maintained, is naturally identical to a starting plume (this involves the first photograph at 300 ms after the start of source flow in Figs. 2 and 6). Once the source flow is terminated, the leading turbulent vortex and the trailing plume continue to penetrate into the still liquid. However, there is an interesting difference, between the near-source properties of thermals and puffs. In particular, buoyancy-induced motion in a thermal causes the stem between the plume-like region of the thermal and the source to disappear relatively rapidly; in contrast, a thin stem connecting the jet-like region of a puff and the source remains as a prominent feature of the flow throughout the period of observation of puffs, see Sangras et al. [1]. The buoyant motion also causes the trailing plume-like region of a thermal to merge relatively rapidly with the leading vortex compared with puffs. The main difference between the motion of the upper regions of a starting plume and a thermal is that the latter has a smaller velocity once the source flow has ended; this is evident from the different scaling rules of starting plumes and thermals from Eqs. (3), (5), and (6), e.g., $(x_p-x_o)\sim(t-t_d)^n$ with $n=3/4$ and 1/2 for starting plumes and thermals, respectively. In addition, continued penetration of the thermal implies continued increases of the volume of the leading vortex; this causes the trailing plume to eventually be engulfed by the leading vortex followed by continued dilution of the leading vortex. Thus, there is significant potential for several different flow regimes during the development and eventual self-preserving flow periods of the lifetime of a thermal; although the general scaling behavior of both thermals and puffs did not exhibit significant changes as the leading vortex engulfed the trailing plume and jet, respectively. Finally, the maximum radial penetration distances are similar for thermals and puffs, whereas both are larger than the corresponding radial penetration distances of starting plumes and jets.

Normalized streamwise (vertical) penetration distances for thermals are plotted as a function of dimensionless time, according to the self-preserving scaling of Eqs. (3) and (6) in Fig. 3. Present measurements agree reasonably well with self-preserving scaling for thermals for $(t-t_d)/t^*>200$, and $(x_p-x_o)/d>20-30$. The value of scaled time for the onset of self-preserving thermal behavior is significantly larger than the corresponding scaled time for the onset of self-preserving starting jet behavior; however, this is not surprising, because the definitions of the t^* for these two flows differ. In contrast, the values of $(x_p-x_o)/d$ for onset of self-preserving behavior for the two flows, where the scaling definitions of the two flows are the same, are nearly the same as well. In addition, there is a tendency for thermals having larger amounts of source fluid, i.e., larger amounts of $Q_o/(A_o d)$, to require somewhat larger scaled times to reach self-preserving behavior, although the streamwise location where the thermals become self-preserving is relatively unaffected by the amount of source fluid used for the present test range. Similar to starting plumes, conditions for self-preserving behavior of thermals in Fig. 3 only involved $(x_p-x_o)/\ell_M>0.3$, which seems small as already discussed in connection with present measurements of starting plumes. Similar to starting plumes and jets, however, ratios of penetration velocities of thermals/puffs increase proportional to $(x_p-x_o)^2$, so that the relatively rapid decay of source momentum allows buoyant momentum to dominate the penetration velocities of thermals at $(x_p-x_o)/d$ of 20–30, even though $(x_p-x_o)/\ell_M$ is as small as 0.3, and Fr_o is as large as 82, for present test conditions. However, also similar to starting plumes, study of the combined effects of large $(x_p-x_o)/d$, to control effects of source disturbances, and large $(x_p-x_o)/\ell_M$ to control effects of source momentum, on the self-preserving behavior of thermals, clearly would be useful.

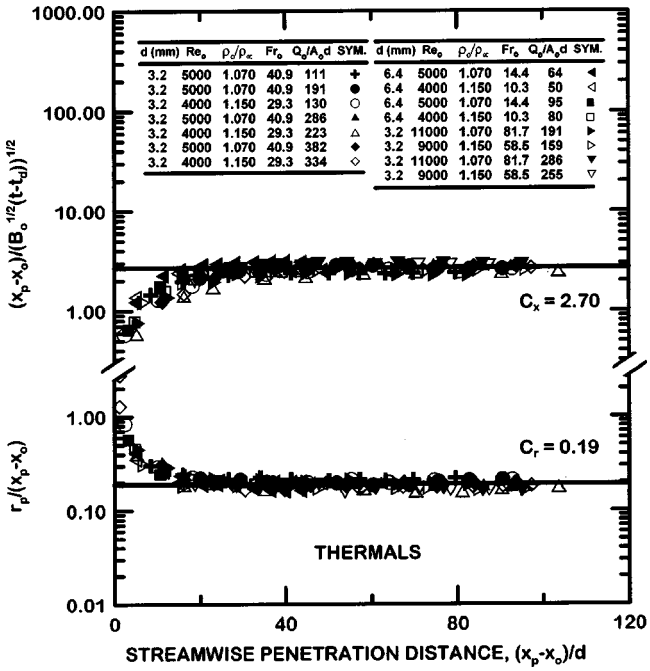

Fig. 7 Streamwise and radial penetration distances of thermals as functions of streamwise penetration distance

Measurements of maximum streamwise (vertical) penetration distances of thermals are plotted in terms of the dimensionless self-preserving streamwise penetration parameter of Eq. (10) as a function of normalized vertical penetration distance in Fig. 7. Plotted in this manner, it is evident that the self-preserving parameter has a variety of values near the source depending on source properties and distance from the source. However, the parameter approaches a constant $C_x=2.70$ for vertical penetration distances greater than 20–30 source diameters from the source. Similar to the observations for starting plumes in connection with Fig. 4, the fact that C_x is on the order of unity is also supportive that physically realistic conditions for self preservation have been identified in Fig. 7.

Normalized maximum radial penetration distances for thermals are plotted according to the self-preserving scaling of Eq. (4) in Fig. 7. The behavior here is qualitatively similar to the results for starting plumes illustrated in Fig. 4. The flow tends to approach self-preserving behavior for the radial penetration distance when $(x_p-x_o)/d>20-30$, which is comparable to distances from the source required for self-preserving behavior of streamwise penetration distances. The main difference between the radial penetration distances of thermals and starting plumes is that the normalized maximum radial penetration distance in the self-preserving region is larger for thermals than for starting plumes, e.g., $r_p/(x_p-x_o)=C_r=0.19$ for thermals as opposed to a value of 0.15 for starting plumes. Somewhat similar behavior was observed by Diez et al. [2] for starting jets and puffs where $r_p/(x_p-x_o)=C_r=0.17$ for puffs as opposed to a value of 0.15 for starting jets.

Present observations of the variation of the virtual origin location as a function of the amount of source fluid injected, $Q_o/(A_o d)$, for thermals are illustrated in Fig. 8. The value of $x_o/d=8.5$ is seen to be independent of the amount of source fluid injected for the range that was considered, $Q_o/(A_o d)=50-382$, even though the thermals for the larger amounts of source fluid considered approach the behavior of self-preserving starting

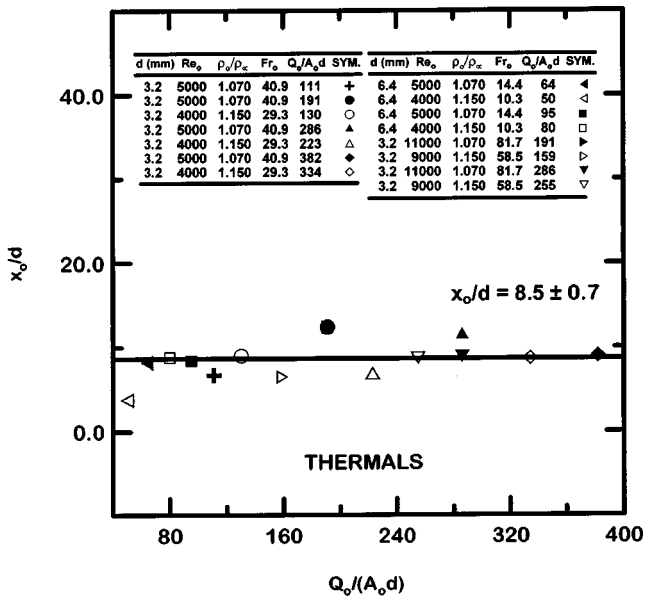

Fig. 8 Virtual origin locations of thermals as a function of the injected source liquid volume

plumes and might be considered to be interrupted plumes. Notably, Diez et al. [2] observed almost the same behavior for puffs, with $x_o/d=8.5$, for $Q_o/(A_o d)=60-320$, even though puffs for the larger amounts of source fluid considered approach the behavior of self-preserving starting jets and might be considered to be interrupted jets.

A summary of values of n, C_r, C_x, and x_o/d is provided in Table 3, based on the measurements of Diez et al. [2] for puffs and the measurements of Scorer [23], Turner [25], Thompson et al. [28] and the present investigation for thermals. Similar to the observations for starting jets and plumes in Table 2, the results for n in Table 3 for puffs and thermals agree with the expectations of self-preserving theory. The values of C_r for the results of Diez et al. [2] and the present investigation are similar but are significantly smaller than the measurements of Scorer [23], Turner [25] and Thompson et al. [28]. Recalling that values of $r_p/(x_p-x_o)=C_r$ progressively decrease until the self-preserving region is reached, where they become constant, see Fig. 7, it is likely that these discrepancies occur because measurements were not obtained far enough from the source in Refs. [23], [25], and [28] for the self-preserving region to be reached. Finally, values of C_x for puffs and thermals are nearly the same in Table 3, similar to the observation that values of C_x for starting jets and plumes are nearly the same in Table 2 (the values of C_x for all four flows only vary in the range 2.6–2.8).

Conclusions

Scaling relationships for the temporal development of starting plumes and thermals were evaluated based on experiments. Conditions far from the source were emphasized where: effects of source disturbances are lost; the momentum of the flow is dominated by effects of buoyancy; the conserved properties of the flow control flow structure; and self-preserving behavior is approximated. The test conditions consisted of dye-containing salt water sources injected into still fresh water with injector passage length/diameter ratios of 50 and 100 and other conditions as follows: source diameters of 3.2 and 6.4 mm, source/ambient density ratios of 1.070 and 1.150, source Reynolds numbers of 4000–11,000, source Froude numbers of 10–82, $Q_o/(A_o d)$ of 50–382 for thermals and streamwise flow penetration lengths up to 110 source diameters and 5.05 Morton length scales from the source. The major conclusions of the study are as follows:

1) The flows became turbulent near the source exit at distances less than 5 diameters from the source. Although near-source behavior varied significantly with source properties and distance from the source, self-preserving behavior generally was observed for $(x_p-x_o)/d>20-30$ and $(x_p-x_o)/\ell_M>0.3$. The latter value, which is surprisingly small, can be explained by the relatively rapid decay of effects of source momentum, compared to effects of source buoyancy, with increasing distance from the source for starting plumes and thermals.

2) Within the self-preserving region, the dimensionless penetration distance, $(x_p-x_o)/d$, generally varied as a function of time in agreement with self-preserving scaling. This implies that maximum penetration distances varied as a function of time to the following powers: 3/4 for starting plumes and 1/2 for thermals.

3) Within the self-preserving region, the normalized maximum radius of the flow generally grew as a function of time in the same manner as the normalized streamwise penetration distance. This implies the following normalized values of the maximum flow radius, $r_p/(x_p-x_o)$: 0.16 for starting plumes and 0.19 for thermals. These maximum radii were observed at the position of the leading vortex.

4) For large values of $Q_o/(A_o d)$ for thermals, self-preserving starting plume behavior is approached before the source flow is terminated and the flow could be characterized as an interrupted plume. Nevertheless, thermals exhibited nearly constant values of $x_o/d=8.5$ for $Q_o/(A_o d)$ as large as 382. This behavior was essentially the same as recent observations for puffs, where $x_o/d=8.5$ for $Q_o/(A_o d)$ as large as 320, even though flows for the larger amounts of source fluid approach interrupted jet behavior [2].

Acknowledgment

This research was supported by the United States Department of Commerce, National Institute of Standards and Technology, Grant Nos. 60NANB8D0081 and 60NANB1D0006, with H. R. Baum of the Building and Fire Research Laboratory serving as Scientific Officer.

Nomenclature

A_o = source cross-sectional area
B_o = source specific buoyancy force, Eq. (8)
$\dot{B}_o$ = source specific buoyancy flux, Eq. (7)
C_r = radial penetration coefficient, Eq. (4)
C_x = streamwise penetration coefficient, Eq. (3)
d = source diameter
Fr_o = source Froude number, Eq. (2)
g = acceleration of gravity
L = source passage length
ℓ_M = Morton length scale, Eq. (1)
n = time exponent, Eqs. (3), (5), (6), (11) and (12)
Q_o = volume of injected source fluid
$\dot{Q}_o$ = volumetric rate of injection of source fluid
Re_o = source Reynolds number, $u_o d/\nu_o$
r = radial distance
t = time
t^* = self-preserving time scale, Eqs. (3), (5), (6), (11) and (12)
u = streamwise velocity
x = streamwise distance

Greek Symbols

ν = kinematic viscosity
ρ = density

Subscripts

d = delay
max = maximum value
p = maximum penetration location

o = initial value or virtual origin location
∞ = ambient value

References

[1] Sangras, R., Kwon, O. C., and Faeth, G. M., 2002, ''Self-Preserving Properties of Unsteady Round Nonbuoyant Turbulent Starting Jets and Puffs in Still Fluids,'' ASME J. Heat Transfer, **124**, pp. 460–469.

[2] Diez, F. J., Sangras, R., Kwon, O. C., and Faeth, G. M., 2003, ''Self-Preserving Properties of Unsteady Round Nonbuoyant Turbulent Starting Jets and Puffs in Still Fluids,'' ASME J. Heat Transfer, **125**, pp. 204–205.

[3] Rouse, H., Yih, C. S., and Humphreys, H. W., 1952, ''Gravitational Convection From a Boundary Source,'' Tellus, **4**, pp. 201–210.

[4] Morton, B. R., Taylor, G. I., and Turner, J. S., 1956, ''Turbulent Gravitational Convection From Maintained and Instantaneous Sources,'' Proc. R. Soc. London, Ser. A, **234**, pp. 1–23.

[5] Morton, B. R., 1959, ''Forced Plumes,'' J. Fluid Mech., **5**, pp. 151–163.

[6] Turner, J. S., 1973, *Buoyancy Effects in Fluids*, Cambridge University Press, Cambridge, London.

[7] Seban, R. A., and Behnia, M. M., 1976, ''Buoyant Turbulent Jets in Unstratified Surroundings,'' Int. J. Heat Mass Transfer, **19**, pp. 1197–1204.

[8] Yih, C.-S., 1977, ''Buoyant Turbulent Plumes,'' Phys. Fluids, **20**, pp. 1234–1237.

[9] Yih, C.-S., and Wu, F., 1981, ''Round Buoyant Laminar and Turbulent Plumes,'' Phys. Fluids, **24**, pp. 823–830.

[10] George, W. K., Jr., Alpert, R. L., and Tamanini, F., 1977, ''Turbulence Measurements in an Axisymmetric Buoyant Plume,'' Int. J. Heat Mass Transfer, **20**, pp. 1145–1154.

[11] Chen, C. J., and Chen, C. H., 1979, ''On Prediction and Unified Correlation for Decay of Vertical Buoyant Jets,'' ASME J. Heat Transfer, **101**, pp. 532–537.

[12] List, E. J., 1982, ''Turbulent Jets and Plumes,'' Annu. Rev. Fluid Mech., **14**, pp. 189–212.

[13] Papanicolaou, P. N., and List, E. J., 1988, ''Investigation of Round Vertical Buoyant Turbulent Jets,'' J. Fluid Mech., **195**, pp. 341–391.

[14] Papantoniou, D., and List, E. J., 1989, ''Large Scale Structure in the Far Field of Buoyant Jets,'' J. Fluid Mech., **209**, pp. 151–190.

[15] Peterson, J., and Bayazitoglu, Y., 1992, ''Measurements of Velocity and Turbulence in Vertical Axisymmetric Isothermal and Buoyant Plumes,'' ASME J. Heat Transfer, **114**, pp. 135–142.

[16] Dai, Z., Tseng, L.-K., and Faeth, G. M., 1994, ''Structure of Round, Fully-Developed, Buoyant Turbulent Plumes,'' ASME J. Heat Transfer, **116**, pp. 409–417.

[17] Dai, Z., Tseng, L.-K., and Faeth, G. M., 1995, ''Velocity Statistics of Round, Fully-Developed Buoyant Turbulent Plumes,'' ASME J. Heat Transfer, **117**, pp. 138–145.

[18] Dai, Z., Tseng, L.-K., and Faeth, G. M., 1995, ''Velocity/Mixture-Fraction Statistics of Round, Self-Preserving Buoyant Turbulent Plumes,'' ASME J. Heat Transfer, **117**, pp. 918–926.

[19] Turner, J. S., 1962, ''The Starting Plume in Neutral Surroundings,'' J. Fluid Mech., **13**, pp. 356–368.

[20] Middleton, J. H., 1975, ''The Asymptotic Behavior of a Starting Plume,'' J. Fluid Mech., **72**, pp. 753–771.

[21] Delichatsios, M. A., 1979, ''Time Similarity Analysis of Unsteady Buoyant Plumes,'' J. Fluid Mech., **93**, pp. 241–250.

[22] Pantzlaff, L., and Lueptow, R. M., 1999, ''Transient Positively and Negatively Buoyant Turbulent Round Jets,'' Exp. Fluids, **27**, pp. 117–125.

[23] Scorer, R. S., 1957, ''Experiments on Connection of Isolated Masses of Buoyant Fluid,'' J. Fluid Mech., **2**, pp. 583–594.

[24] Turner, J. S., 1964, ''The Dynamics of Spheroidal Masses of Buoyant Fluid,'' J. Fluid Mech., **19**, pp. 481–490.

[25] Turner, J. S., 1969, ''Buoyant Plumes and Thermals,'' Annu. Rev. Fluid Mech., **1**, pp. 29–44.

[26] Fay, J. A., and Lewis, D. H., 1976, ''Unsteady Burning of Unconfined Fuel Vapor Clouds,'' Proceedings of the Combustion Institute, **16**, pp. 1397–1405.

[27] Batt, R. G., Brigoni, R. A., and Rowland, D. J., 1984, ''Temperature-Field Structure Within Atmospheric Buoyant Thermals,'' J. Fluid Mech., **141**, pp. 1–25.

[28] Thompson, R. S., Snyder, W. H., and Weil, J. C., 2000, ''Laboratory Simulation of the Rise of Buoyant Thermals Created by Open Detonation,'' J. Fluid Mech., **417**, pp. 127–156.

[29] Turner, J. S., 1957, ''Buoyant Vortex Rings,'' Proc. R. Soc. London, Ser. A, **239**, pp. 61–75.

[30] Morton, B. R., 1960, ''Weak Thermal Vortex Rings,'' J. Fluid Mech., **9**, pp. 107–118.

[31] Steckler, K. D., Baum, H. R., and Quintiere, J. G., 1986, ''Salt Water Modeling of Fire Induced Flows in Multicomponent Enclosures,'' Proceedings of the Combustion Institute, **21**, pp. 143–149.

[32] Wu, P.-K., Miranda, R. F., and Faeth, G. M., 1995, ''Effects of Initial Flow Conditions on Primary Breakup of Nonturbulent and Turbulent Round Liquid Jets,'' Atomization Sprays, **5**, pp. 175–196.

[33] Lange, N. A., 1952, *Handbook of Chemistry*, Handbook Publishers, Sandusky, OH, p. 1160.

[34] Baines, W. D., Turner, J. S., and Campbell, I. H., 1990, ''Turbulent Fountains in an Open Chamber,'' J. Fluid Mech., **212**, pp. 557–592.

[35] Baines, W. D., Corriveau, A. F., and Reedman, T. J., 1993, ''Turbulent Fountains in a Closed Chamber,'' J. Fluid Mech., **255**, pp. 621–646.

Importance of Turbulence-Radiation Interactions in Turbulent Diffusion Jet Flames

Genong Li
e-mail: gnl@fluent.com
Fluent Incorporated,
10 Cavendish Court,
Lebanon, NH 03766

Michael F. Modest
e-mail: mfm6@psu.edu
Fellow ASME
Department of Mechanical Engineering,
The Pennsylvania State University,
University Park, PA 16802

Traditional modeling of radiative transfer in reacting flows has ignored turbulence-radiation interactions (TRI). Radiative fluxes, flux divergences and radiative properties have been based on mean temperature and concentration fields. However, both experimental and theoretical work have suggested that mean radiative quantities may differ significantly from those predictions based on the mean parameters because of their strongly nonlinear dependence on the temperature and concentration fields. The composition PDF method is able to consider many nonlinear interactions rigorously, and the method is used here to study turbulence-radiation interactions. This paper tries to answer two basic questions: (1) whether turbulence-radiation interactions are important in turbulent flames or not; and (2) if they are important, then what correlations need to be considered in the simulation to capture them. After conducting many flame simulations, it was observed that, on average, TRI effects account for about 1/3 of the total drop in flame peak temperature caused by radiative heat losses. In addition, this study shows that consideration of the temperature self correlation alone is not sufficient to capture TRI, but that the complete absorption coefficient-Planck function correlation must be considered.
[DOI: 10.1115/1.1597621]

Keywords: Combustion, Heat Transfer, Jets, Radiation, Turbulence

Introduction

In turbulent reacting flows the turbulent fluctuations of the flow field cause fluctuations of species concentrations and temperature. Consequently, the radiation field, which is determined by species concentration and temperature fields, will fluctuate as well. In a numerical simulation fluctuations in the radiation field interact with the fluctuations of the flow field, causing the so-called turbulent-radiation interactions (TRI). It has been a great challenge to consider these interactions in numerical simulations because they are strongly nonlinear in nature.

For several decades, radiation and turbulence were treated as independent phenomena, and radiative heat fluxes were computed neglecting fluctuations in the radiative intensity and in radiative properties [1]. Some early simple numerical analyses and limited experimental data have indicated the importance of these correlations. Through a Taylor series expansion of the Planck function, Cox [2] estimated that the contribution from temperature fluctuations to radiative emission may dominate the contribution from the mean temperature field when the temperature fluctuation intensity exceeds approximately 40%. Gore et al. [3] showed through experiments that actual radiative fluxes may be two times or more larger than would be expected based on the mean values alone. In the late eighties, some researchers [4–8] performed numerical simulations taking turbulence-radiation interactions (TRI) into account in some simplified fashion, and their predictions were observed to match better with experimental data. In these early studies, either correlations for the turbulent medium or the shape of the PDF had to be assumed. As a result, turbulence-radiation interactions could not be rigorously considered and many claims that were made about TRI need to be further examined.

Probability density function (PDF) methods have the unique feature that many nonlinear interactions can be treated exactly [9], and have been widely used in the modeling of reacting flows in the absence of radiation, in which the chemical reactions, no matter how complicated they are, can be considered exactly [10,11]. Such methods have been introduced to the study of turbulence-radiation interactions by Mazumder and Modest [12] and by Li and Modest [13]. Mazumder and Modest [12] employed the velocity-composition joint PDF method in their simulation of a bluff body combustor and found inclusion of the absorption coefficient-temperature correlation alone may increase radiative heat flux by 40–45%. The inclusion of velocities and time scale information within the PDF, although allowing closure of more terms, adds further mathematical complexities to the modeling of the PDF equation as well as to stability problems in the numerical simulations. For the purpose of capturing TRI, the composition PDF method is as rigorous as the velocity-composition joint PDF method, but computationally more robust and more efficient. Its use in the study of TRI was demonstrated by Li and Modest [13]. By employing the same method, this paper aims to check the importance of turbulence-radiation interactions, and the relative importance of the different contributions to TRI. Since the Planck function is the most nonlinear function in the radiation calculation, it has been hypothesized that consideration of the temperature self correlation alone can capture most of the TRI [14]. If this were the case, one could treat TRI with the traditional Reynolds average approach, constructing the first few higher moments of temperature. Such issues will be discussed in this paper.

Mathematical Formulation

Turbulence-Radiation Coupling. In the presence of radiative heat transfer, the energy equation needs to include a radiative source term,

$$S_{\text{radiation}} = -\nabla \cdot \underline{q}^R = \int_0^\infty \kappa_\eta \left(\int_{4\pi} I_\eta \, d\Omega - 4\pi I_{b\eta} \right) d\eta, \qquad (1)$$

where $\underline{q}^R$ denotes the radiative heat flux; κ_η is the spectral absorption coefficient of the radiating gas, which may be a function of temperature T and species concentrations of the radiating medium $\underline{Y}$; here I_η is the spectral intensity, $I_{b\eta}$ is the spectral blackbody intensity (or Planck function), the subscript η is used to

Contributed by the Heat Transfer Division for publication in the JOURNAL OF HEAT TRANSFER. Manuscript received by the Heat Transfer Division October 31, 2003; revision received April 18, 2003. Associate Editor: S. T. Thynell.

indicate spectral dependence and Ω denotes solid angle. The radiation intensity is governed by the radiative transfer equation (RTE): for an absorbing-emitting but nonscattering gas, the instantaneous radiant energy balance on a pencil of radiation propagating in direction $\vec{s}$ and confined to a solid angle $d\Omega$ is given by [15],

$$(\vec{s}\cdot\nabla)I_\eta=\kappa_\eta(I_{b\eta}-I_\eta), \tag{2}$$

where the first term on the right-hand side represents augmentation due to emission and the second term is attenuation due to absorption.

To include radiation effects in conventional turbulence calculations, Eqs. (1) and (2) need to be time-averaged, resulting in

$$\langle S\rangle_{\text{radiation}}=\int_0^\infty\left[\int_{4\pi}\langle\kappa_\eta I_\eta\rangle d\Omega-4\pi\langle\kappa_\eta I_{b\eta}\rangle\right]d\eta, \tag{3}$$

$$(\vec{s}\cdot\nabla)\langle I_\eta\rangle=\langle\kappa_\eta I_{b\eta}\rangle-\langle\kappa_\eta I_\eta\rangle. \tag{4}$$

Due to the strongly nonlinear dependence of radiative properties on temperature and species concentrations, $\langle\kappa_\eta(T,\underline{Y})I_\eta\rangle$ does not equal $\kappa_\eta(\langle T\rangle,\langle\underline{Y}\rangle)\langle I_\eta\rangle$ and $\langle\kappa_\eta(T,\underline{Y})I_{b\eta}(T)\rangle$ does not equal $\kappa_\eta(\langle T\rangle,\langle\underline{Y}\rangle)I_{b\eta}(\langle T\rangle)$, making these two terms unclosed. $\langle\kappa_\eta I_\eta\rangle$ represents a correlation between the spectral absorption coefficient and the spectral incident intensity, and $\langle\kappa_\eta I_{b\eta}\rangle$ represents a correlation between the spectral absorption coefficient and the spectral blackbody intensity. Complete information of the statistics among the composition variables is needed for their determination. For the convenience of later discussion, these two correlations are loosely defined as ''spectral absorption coefficient–spectral incident intensity correlation'' and ''spectral absorption coefficient–spectral blackbody intensity correlation.''

The time averaging procedure can be applied to any solution technique for radiation calculation and different unclosed terms may arise for different spectral models and solution methods. However, all of them can be categorized as belonging to two groups: (a) correlations that can be calculated from scalars ϕ directly or indirectly, and (b) correlations that cannot. The set of scalars ϕ is defined as

$$\phi=(\underline{Y},T)=(\phi_1,\phi_2,\cdots,\phi_s) \tag{5}$$

where s is the total number of scalar variables (number of species plus one) and the last scalar, ϕ_s, is reserved for temperature (or enthalpy). Variables in the set ϕ are often called the composition variables, since they determine the composition of the mixture.

The unclosed term $\langle\kappa_\eta I_{b\eta}\rangle$ belongs to group (a), since both κ_η and $I_{b\eta}$ are functions of variables in set ϕ only. The unclosed term $\langle\kappa_\eta I_\eta\rangle$ belongs to group (b), because I_η is not a local quantity, i.e., cannot be expressed in terms of the local scalar variables.

One of the most common approximations made in the open literature on turbulence-radiation interactions is the optically thin eddy approximation as described by Kabashnikov and Myasnikova [16]. Kabashnikov suggested that if the mean free path for radiation is much larger than the turbulence length scale, then the local radiative intensity is weakly correlated with the local absorption coefficient, i.e., $\langle\kappa_\eta I_\eta\rangle=\langle\kappa_\eta\rangle\langle I_\eta\rangle$, in which $\langle\kappa_\eta\rangle$ is loosely defined as the ''absorption coefficient self correlation.'' The rationale behind this assumption is that the instantaneous local intensity at a point is formed over a path traversing several turbulent eddies. Therefore, the local intensity is weakly correlated to the local radiative properties. The validity of this assumption depends on the eddy size distribution and the radiation properties of the absorbing gases. In a numerical simulation of combustion chambers, Hartick et al. [8] showed that, although the thin eddy assumption may not be valid over some highly absorbing parts of the spectrum, these spectral zones affect the total radiation exchange only slightly, thus allowing straightforward application of the thin eddy assumption in their simulation. The thin eddy assumption is also employed in the current study. As a result, all correlations needed to capture TRI belong to group (a).

Radiation Submodel. The radiative transfer equation is a spectrally, spatially and directionally dependent integro-differential equation, and is extremely difficult to solve for general, multi-dimensional geometries. Several approaches are available to reduce this equation to a simpler form. Among them, one of the most popular methods is the P_1-approximation, in which the incident radiation, G, is governed by a Helmholtz equation, which is relatively easy to solve. For the vast majority of important engineering problems (i.e., in the absence of extreme anisotropy in the intensity field), the method provides high accuracy at very reasonable computational cost. Another challenge in gas radiation calculations comes from the strong spectral dependence of radiation properties. Although line-by-line calculations provide best accuracy, such calculations are too time-consuming for any practical combustion system. Global methods such as the Weighted-Sum-of-Gray-Gases Model (WSGG) are commonly used [15,17]. Recently, the Full-Spectrum k-Distribution method (FSK) developed by Modest and Zhang [18] has been shown to be superior to the WSGG model, to which it reduces in its crudest implementation. The method is exact within its limitations [gray walls, gray scattering properties, spectral absorption coefficient obeying the so-called scaling approximation, i.e., the spectral and spatial dependence of the absorption coefficient are separable as $\kappa_\eta(\eta,\phi)=k_\eta(\eta)u(\phi)$ where ϕ are the composition variables]. The P_1-approximation in conjunction with the FSK model will be used in this study.

Radiative properties and, consequently, the radiative intensity change dramatically across spectral space. In the FSK method the radiative quantities' spectral dependence has been transformed to a g-dependence, where g is the cumulative distribution function of the absorption coefficient calculated over the whole spectrum and weighted by the Planck function. For example, the source term in the energy equation due to radiative heat transfer is calculated as

$$\begin{aligned}S_{\text{radiation}}&=-\int_0^\infty\kappa_\eta(4\pi I_{b\eta}-G_\eta)d\eta\\&=-\int_0^1 k_g u(4\pi a_g I_b-G_g)dg,\end{aligned} \tag{6}$$

where u is the spatial dependence of the absorption coefficient as mentioned before and a_g is a weight factor introduced during the transformation. The advantage of this transformation lies in the fact that $k_g(g)$ is a smooth, monotonically increasing function of g, thus requiring only a few numerical quadrature points. Readers are referred to [18] for the details about this method. In practical calculations, the integration is replaced by numerical quadrature. If Gaussian quadrature is used, Eq. (6) becomes

$$S_{\text{radiation}}\approx-\sum_{j=1}^{M}w_j k_j u(4\pi a_j I_b-G_j), \tag{7}$$

where M is the total number of quadrature points and the w_j are the quadrature weights. The incident radiation G_j must be determined by solving the P_1-equation, i.e. [15],

$$\nabla\cdot\left(\frac{1}{3k_g u}\nabla G_g\right)=k_g u[G_g-4\pi a_g I_b], \tag{8}$$

subject to the boundary condition,

$$-\frac{2(2-\epsilon)}{3\epsilon}\hat{n}\cdot\nabla G_g=k_g u(4\pi a_g I_b-G_g), \tag{9}$$

where ϵ is surface emittance and $\hat{n}$ is a unit normal at a boundary surface. The values of k_g, $u(\phi)$ and a_g are obtained from a pre-calculated FSK data base.

Reynolds averaging of the radiative source term and the P_1-equation leads to

$$\langle S\rangle_{\text{radiation}}=-\sum_{j=1}^{M}w_j k_j[4\pi\langle u a_j I_b\rangle-\langle u\rangle\langle G_j\rangle], \tag{10}$$

$$\nabla\cdot\left[\frac{1}{3k_j}\frac{1}{\langle u\rangle}\nabla\langle G_j\rangle\right]=k_j\langle u\rangle\langle G_j\rangle-4\pi k_j\langle ua_jI_b\rangle,\quad j=1,\cdots,M, \tag{11}$$

where the optically thin eddy approximation has been employed. As a result of turbulence-radiation interactions two terms, $k_j\langle ua_jI_b\rangle$ and $k_j\langle u\rangle$, representing correlations between dependent variables, need to be modeled.

Composition PDF Methods. The philosophy of the PDF approach is to treat species concentration and temperature as random variables and consider the transport of their PDFs rather than their finite moments. Once that PDF is known, the mean of any quantity can be evaluated exactly from the PDF, as long as it is a function of the species concentrations or/and temperature. For example,

$$\langle u(\phi)a_j(\phi)I_b(\phi)\rangle=\int u(\psi)a_j(\psi)I_b(\psi)f(\psi)d\psi, \tag{12}$$

$$\langle u(\phi)\rangle=\int u(\psi)f(\psi)d\psi. \tag{13}$$

In these equations, ψ represents the composition space variable, $\psi\equiv(\psi_1,\psi_2,\cdots,\psi_s)$, and $f(\psi)$ is defined to be the probability density of the compound event $\phi=\psi$ (i.e., $\phi_1=\psi_1,\phi_2=\psi_2,\cdots,\phi_s=\psi_s$), so that,

$$f(\psi)d\psi=\text{Probability}(\psi\leqslant\phi\leqslant\psi+d\psi). \tag{14}$$

In a general turbulent reacting flow, the composition PDF is also a function of space, x, and time, t. The transport equation for the composition PDF, $f(\psi,x,t)$, can be derived from the conservation laws of scalars, which is

$$\begin{aligned}&\frac{\partial}{\partial t}[\rho f]+\frac{\partial}{\partial x_i}[\tilde{u}_i\rho f]+\frac{\partial}{\partial\psi_\alpha}[S_{\alpha,\text{reaction}}(\psi)\rho f]\\&\quad-\sum_{j=1}^{M}4\pi w_jk_j\frac{\partial}{\partial\psi_s}[ua_jI_bf]\\&\quad=-\frac{\partial}{\partial x_i}[\langle u_i''|\psi\rangle\rho f]+\frac{\partial}{\partial\psi_\alpha}\left[\left\langle\frac{1}{\rho}\frac{\partial J_i^\alpha}{\partial x_i}\middle|\psi\right\rangle\rho f\right]\\&\quad-\sum_{j=1}^{M}w_jk_j\frac{\partial}{\partial\psi_s}[u\langle G_j\rangle f],\end{aligned} \tag{15}$$

where i and α are summation indices in physical space and composition space, respectively and $\langle A|B\rangle$ is the conditional probability of the event A, given that the event B occurs.

On the left-hand side of Eq. (15), the first two terms represent the rate of change of the PDF when following the Favre-averaged mean flow. The third and fourth terms are the divergence of the flux of probability in the composition space due to chemical reaction and radiative emission. The form of this term clearly shows the advantage the PDF method has over moment methods: no matter how complicated and nonlinear these source terms are, they require no modeling. In contrast, the terms on the right-hand side of Eq. (15) need to be modeled. The first term represents transport in physical space due to turbulent convection. Since the compostion PDF does not contain any information on velocity, this term is not closed. Generally, a gradient-diffusion model with information supplied for the turbulent flow field is employed,

$$-\langle u_i''|\psi\rangle\rho f\approx\Gamma_T\frac{\partial(\rho f)}{\partial x_i}, \tag{16}$$

where $\Gamma_T=c_\mu\langle\rho\rangle\sigma_\phi^{-1}k^2/\varepsilon$ is the turbulent diffusivity, and k, ε, c_μ, and σ_ϕ are, respectively, the turbulent kinetic energy, dissipation rate of turbulent kinetic energy, a modeling coefficient in the standard $k-\varepsilon$ turbulence model, and turbulent Schmidt or Prandtl numbers.

The second term represents transport in scalar space due to molecular mixing. Many mixing models such as the interaction-by-exchange-with-the-mean (IEM) model and Pope's particle-pairing model [9] have been proposed. Appropriate mixing model are crucial for combustion problems related to flame ignition or extinction. For flames away from those extreme conditions, numerical results, especially low order moments of the PDF such as temperature and species concentrations, are not very sensitive to mixing models. In this paper the IEM model is used, i.e.,

$$\left\langle\frac{1}{\rho}\frac{J_i^\alpha}{\partial x_i}\middle|\psi\right\rangle\approx\frac{1}{2}C_\phi\omega(\psi_\alpha-\tilde{\phi}_\alpha), \tag{17}$$

where $\omega=\varepsilon/k$ is a turbulence "frequency" and C_ϕ is a model constant.

The third term on the right-hand side of Eq. (15) is closed by invoking the optically thin eddy approximation. As a result, the modeled transport equation for the composition mass density PDF function is closed and contains all necessary information about all scalars. The composition PDF transport equation is a partial differential equation in $(4+s)$ dimensions. Traditional finite volume or finite element methods are very inefficient to solve an equation of such high dimensionality. Instead, the Monte Carlo method is generally used, in which the PDF is represented by a large number of computational particles. Each particle evolves in time and space according to a set of stochastic equations and carries with it all composition variables. The PDF is then obtained approximately as a histogram of the particles' properties in sufficiently small neighborhoods in physical space, and the mean quantities are deduced statistically by sampling the particles.

Chemical Reaction Mechanism

Although PDF methods allow the use of detailed chemical reaction mechanisms in principle, computational intractability has limited their application. Detailed mechanisms are necessary if slow reactions are present or intermediate species are of interest. In practice, reduced mechanisms are often used in the PDF calculations. A wide range of reduced mechanisms of chemical reactions for hydrocarbon fuels is available in the literature [19] and the simplest—a single-step skeletal mechanism—is used in this study. It takes the form

$$CH_4+2O_2\rightarrow CO_2+2H_2O. \tag{18}$$

Westbrook and Dryer [20] provided an Arrhenius relationship for the reaction rate of methane as

$$\frac{d[CH_4]}{dt}=-A\exp(-E_a/R_uT)[CH_4]^a[O_2]^b, \tag{19}$$

where the quantities within square brackets represent molar concentrations; R_u is the universal gas constant, and E_a is the activation energy of the methane. A, a and b are constants in the general Arrhenius equation, which may be obtained from Westbrook and Dryer. For the methane/air flames considered here, the global mechanism is able to predict the correct temperature level and the major species CO_2 and H_2O, i.e., all relevant parameters for the radiation calculation.

Flame Simulations

Flame optical thickness has an important impact on radiative transfer. Three jet flames with different optical thickness have been considered, where flame optical thickness has been defined as

$$\tau=\kappa_PL, \tag{20}$$

where κ_P is an average Planck mean absorption coefficient of the participating medium, i.e., the combustion products of H_2O and CO_2, and L is the flame length. For turbulent jet flames, flame length is approximately a linear function of jet diameter [21] and, in this study, is estimated to be $L=40d_j$. The base flame is San-

Table 1 Computed flame peak temperature

Flames	T_{norad} (K)	T_{noTRI} (K)	T_{TRI} (K)	ΔT_{rad} (K)	ΔT_{TRI} (K)
$\kappa L.1$	2165	2101	2083	−64	−18
$\kappa L.2$	2161	2016	1952	−145	−64
$\kappa L.3$	2169	1842	1725	−327	−117

dia's Flame D [22]. The basic experimental setup of this flame is summarized here. The fuel jet ($d_j = 7.2$ mm) with high velocity ($u_j = 49.6$ m/s) is accompanied by an annular pilot flow ($d_p = 18.4$ mm, $u_p = 11.4$ m/s), which is then surrounded by a slow coflow of air ($u_c = 0.9$ m/s). The fuel is a mixture of air and methane with a ratio of 3:1 by volume. A bank of measured data is available for this flame and, for this reason, has been simulated to validate the code [23]. Satisfactory prediction of CO_2, H_2O concentrations and of temperature fields is a prerequisite if the radiation field is to be reproduced accurately. Comparison of experimental data and computed values of these variables and some quantities related to the radiation field was made and, generally speaking, good agreement between numerical results and experimental data has been obtained. In addition, it was found that the radiation field is more accurately captured if turbulence-radiation interactions are accounted for [23], even for this optically thin flame with an optical thickness of 0.237 by Eq. (20). The other two considered (artificial) flames were derived from Flame D by doubling and quadrupling the jet diameter, and their flame optical thickness is 0.474 and 0.948, respectively. For future reference the three flames will be denoted as $\kappa L.1$, $\kappa L.2$ and $\kappa L.3$, respectively.

To simulate these flames, a rectangular axisymmetric computational domain of $70d_j \times 18d_j$ was used, and a nonuniform grid system of 60×70 was found to be fine enough to give grid-independent solutions in the finite volume code. The global time step used in the PDF/particle code was 2.0 ms, and 4.0 ms and 8.0 ms for flames $\kappa L.1$, $\kappa L.2$, and $\kappa L.3$, respectively. For each simulation a total of approximate 1100 iterations was required to get to a statistically stationary result and about 58,000 particles were used in the simulation, taking about 22 cpu hours on a four processor Silicon Graphics O200 machine. The conventional way to define residual error in finite volume methods is meaningless in the hybrid FV/PDF Monte Carlo simulation because the statistical error is generally larger than the truncation error. In the current study, the overall numerical error for a variable ϕ after the jth iteration is defined as $err = 1/N \Sigma_{i=1}^{N} [\phi_i^j - \phi_i^{j-1}]^2 / [\phi_i^{j-1}]^2$, where N is the total number of nodal points. This error never converges to zero, but rather to a value representative of the statistical fluctuation of the solution when steady state is reached. This level mainly depends on the number of particles in the simulation. If temperature is used to monitor the numerical error, a value on the order of 10^{-4} has been reached in the calculations.

Importance of TRI. In order to study turbulence-radiation interactions, three different scenarios were considered for each flame. In the first scenario, radiation is completely ignored in order to study the importance of radiation in flame simulations in general. In the second and third scenarios, radiation is considered but turbulence-radiation interactions are ignored and considered, respectively. The importance of turbulence-radiation interactions can be assessed by comparing numerical results from these two scenarios. By ignoring turbulence-radiation interactions, it is implied that the two unclosed terms $\langle u \rangle$ and $\langle u a I_b \rangle$ are evaluated based on the cell means; when considering TRI, these two terms are treated exactly.

When comparing numerical results of these three scenarios the most obvious difference is that the flame gets colder and colder as radiation without TRI and radiation with TRI are considered. This is universally true for every flame although the trend is more obvious for flames with large optical thickness. Flame peak temperatures for different flames are tabulated in Table 1. To facilitate the discussion, drops in temperature as a result of considering radiation with/without TRI are also listed in the table. While the peak temperature drops only 64 K and an additional 18 K for a small optical thickness flame, it drops by 145 K and 64 K, respectively, for a medium flame, and by 327 K and 117 K for a large optical thickness flame. While peak temperature applies only to a single point, it usually characterizes the entire temperature field. Figure 1 shows the computed temperature contours for Flame $\kappa L.3$. To examine the differences in more detail, temperature profiles at the axis are shown in Fig. 2. From these figures, it is seen that temperature levels have fallen globally as a result of consideration of radiation and TRI.

From these comparisons, it is clear that radiation cannot just be conveniently ignored in flame simulations, since this would lead to severely overpredicted flame temperatures, which is especially true for large flames, such as Flame $\kappa L.3$. Moreover, turbulence-radiation interactions account for about one third of the total temperature drop due to radiation, and thus turbulence-radiation interactions generally cannot be neglected if radiation is going to be considered in a turbulent flame simulation.

The most important quantity that describes the overall radiation field of a flame is the net radiative heat loss ($\dot{Q}_{net}$) from the flame, and its normalized variable, the "radiant fraction" (f_{rad}), which is defined as the ratio of the net radiative heat loss to the total heat released during combustion, i.e.,

$$f_{rad} \equiv \frac{\dot{Q}_{net}}{\dot{m}_{fuel} \Delta H_{comb}}, \tag{21}$$

where $\dot{m}_{fuel}$ is the mass flow rate of fuel, and ΔH_{comb} is the heat of combustion. In every simulation, these quantities were calculated and the results are shown in Table 2. As the flame's optical thickness is increased, the flame radiant fraction increases quickly and the flame gets colder as discussed earlier. In the current study optical thickness was varied by changing the size of the flame. The total potential chemical energy that a fluid particle can release is fixed. Thus, as the flame gets larger, the flow residence time becomes longer, which implies that an average fluid particle will lose more energy through radiation. As a result, the radiant fraction increases as flame size increases. The radiant fraction is only about 5% for Flame $\kappa L.1$, but as high as 18% for Flame $\kappa L.3$. This also explains why temperature levels drop more significantly in optically thick flames. The table also shows how the turbulence-radiation interactions enhance radiative heat transfer. For Flame $\kappa L.1$, the net radiative heat loss from that flame is increased from 0.534 kW to 0.798 kW, indicating a 49% increase as a result of turbulence-radiation interactions. In contrast, total radiative heat loss increases by 32% for Flame $\kappa L.2$ and by only 4.6% for Flame $\kappa L.3$ as a result of considering turbulence-radiation interactions. As the flame gets optically thicker, the actual values of radiative heat loss, ignoring TRI and considering TRI, become closer and closer. This does not mean that considering turbulence-radiation interactions is less important for optically thick flames. Radiation calculation is strongly dependent on the flame temperature level and the temperature level has greatly decreased as a result of TRI. Thus, comparison of the radiative loss quantities alone would be misleading.

Importance of Different Correlations. The role of turbulence-radiation interactions on radiative heat transfer can be better understood by isolating their effects on the radiation calculations alone. This can be done by freezing the particle field (including particles' locations, particles' species concentrations and their temperatures) at a point in time, and then calculating radiation fields by ignoring and by considering turbulence-radiation interactions, respectively. Since the same particle field is used, differences in the results of two different simulations are caused entirely by turbulence-radiation interactions. From earlier discussion, it is clear that several terms in the time-averaged governing equations are not closed as a result of turbulence-radiation inter-

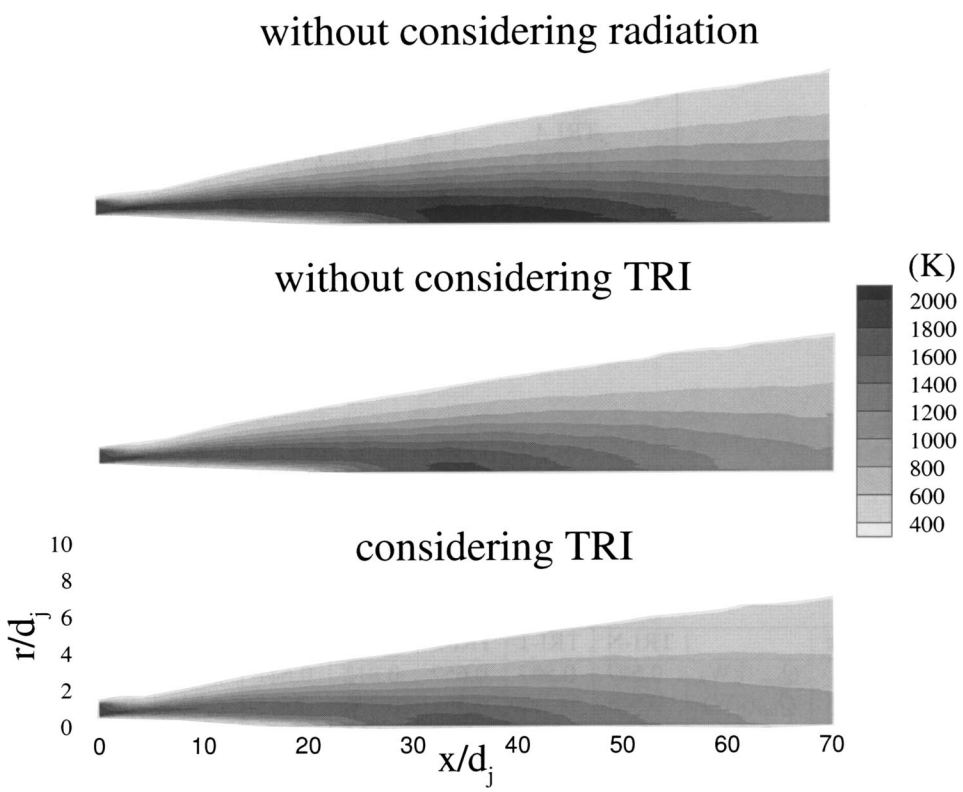

Fig. 1 Temperature structure for Flames $\kappa L.3$

actions. The frozen study can also help to differentiate which correlations making up the full TRI are the most important.

From a mathematical point of view, the importance of turbulence-radiation interactions reflects the importance of correlations of $\langle u \rangle$ and $\langle u a_i I_b \rangle$ in the calculations. To illuminate different facets of turbulence-radiation interactions, seven scenarios have been investigated, namely: TRI-N, TRI-1, TRI-2, TRI-3, TRI-4, TRI-5, and TRI-F as summarized in Table 3, where quantities evaluated simply from the mean composition variables are denoted with an overbar. In TRI-N turbulence-radiation interactions are ignored altogether; in TRI-1 only the absorption coefficient self-correlation in the absorption term is considered, with

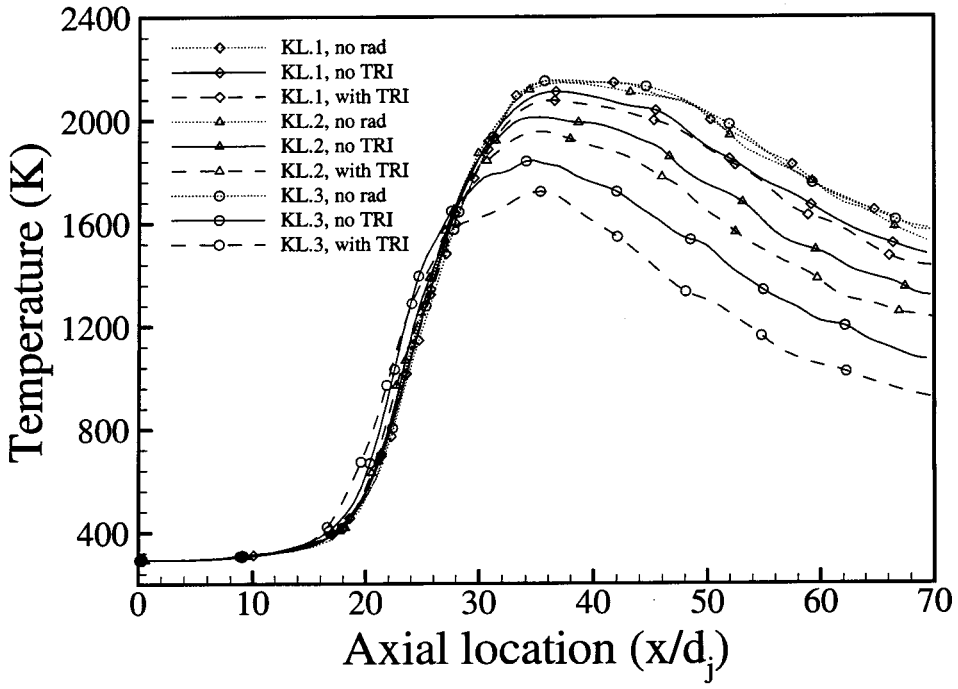

Fig. 2 Centerline temperature profiles for series of κL-Flames

Table 2 Summary of radiation calculation results

Flame	Without TRI $\dot{Q}_{em}$ (kW)	Without TRI $\dot{Q}_{net}$ (kW)	Without TRI f^1_{rad} (%)	With TRI Q_{em} (kW)	With TRI $\dot{Q}_{net}$ (kW)	With TRI f^2_{rad} (%)	$(f^2-f^1)/f^1$ (%)
κL.1	0.624	0.534	3.05	0.928	0.798	4.56	49
κL.2	4.12	2.98	8.51	5.33	3.92	11.2	32
κL.3	21.68	12.12	17.3	20.94	12.68	18.1	4.6

others evaluated at mean property values; in TRI-2 the absorption coefficient self-correlation is considered both in absorption and emission, with the weighted Planck function evaluated at mean property values; in TRI-3 and in TRI-4 the Planck function and the weighted Planck function are considered exactly, respectively (sometimes referred to as ''temperature self-correlation''); and in TRI-5, the effects of absorption coefficient-Planck function correlation on emission are also included (but not on absorption); finally, in TRI-F all TRI terms are considered.

Table 3 Approximations of two TRI terms for different scenarios

Different Scenarios	$k\langle u\rangle$	$k\langle uaI_b\rangle$
TRI-N	$k\overline{u}$	$k\overline{ua}\,\overline{I_b}$
TRI-1	$k\langle u\rangle$	$k\overline{ua}\,\overline{I_b}$
TRI-2	$k\langle u\rangle$	$k\langle u\rangle\overline{aI_b}$
TRI-3	$k\underline{u}$	$k\underline{u}a\langle I_b\rangle$
TRI-4	$k\underline{u}$	$k\underline{u}\langle aI_b\rangle$
TRI-5	$k\overline{u}$	$k\langle uaI_b\rangle$
TRI-F	$k\langle u\rangle$	$k\langle uaI_b\rangle$

The frozen study was performed for every scenario, using particle fields of the fully converged solution for the TRI cases. Table 4 summarizes the results of radiation calculations, including calculated total radiative emission, net radiative heat loss and radiant fraction for each scenario. Comparing results of the cases without TRI and the cases with TRI, the radiant fraction for every flame is increased as a result of considering turbulence-radiation interactions. For example, the radiant fraction is increased by 66%, from 10.9% to 18.1% in Flame κL.3. This is in contrast to the results of the coupled flow-radiation calculations (Table 2), in which these quantities are almost identical. Contours of radiative heat loss for this flame are shown in Fig. 3. In most regions, the local radiative heat loss is increased as a result of turbulence-radiation interactions, mainly because the absorption coefficient and the Planck function are positively correlated. The enhancement of radiative heat loss directly depends on the fluctuations of temperature and species concentration fields. These fluctuations are very large at the flame front, and the increase of radiative heat loss is more prominent there, which can be observed more clearly from their profiles at one cross-section and at the centerline as shown in Fig. 4.

Effects of $\langle u\rangle$. The absorption coefficient self correlation, $k_i\langle u\rangle$, appears in the absorption term of Eq. (10), i.e., $\Sigma\, w_i k_i\langle u\rangle \times\langle G_i\rangle$. Comparing the TRI-N case and the TRI-1 case, the only difference is that the absorption coefficient self-correlation is considered in the absorption term for the TRI-1 case. The computational results in Table 4 show that flame absorption is increased as a result of considering this correlation. This is true for every

Table 4 Comparison of radiation calculation results for series of κL-flames

Flame		TRI-N	TRI-1	TRI-2	TRI-3	TRI-4	TRI-5	TRI-F
	$\dot{Q}_{em}$ (kW)	0.597	0.597	0.657	0.812	0.641	0.928	0.928
κL.1	$\dot{Q}_{net}$ (kW)	0.516	0.507	0.558	0.706	0.555	0.820	0.798
	f (%)	2.94	2.90	3.19	4.03	3.17	4.68	4.56
	$\dot{Q}_{em}$ (kW)	3.42	3.42	3.73	4.59	3.69	5.33	5.33
κL.2	$\dot{Q}_{net}$ (kW)	2.51	2.45	2.68	3.42	2.73	4.02	3.92
	f (%)	7.14	6.98	7.64	9.74	7.78	11.5	11.2
	$\dot{Q}_{em}$ (kW)	12.7	12.7	13.8	17.5	14.2	20.9	20.9
κL.3	$\dot{Q}_{net}$ (kW)	7.63	7.44	8.03	10.6	8.63	13.1	12.7
	f (%)	10.9	10.6	11.5	15.1	12.3	18.7	18.1

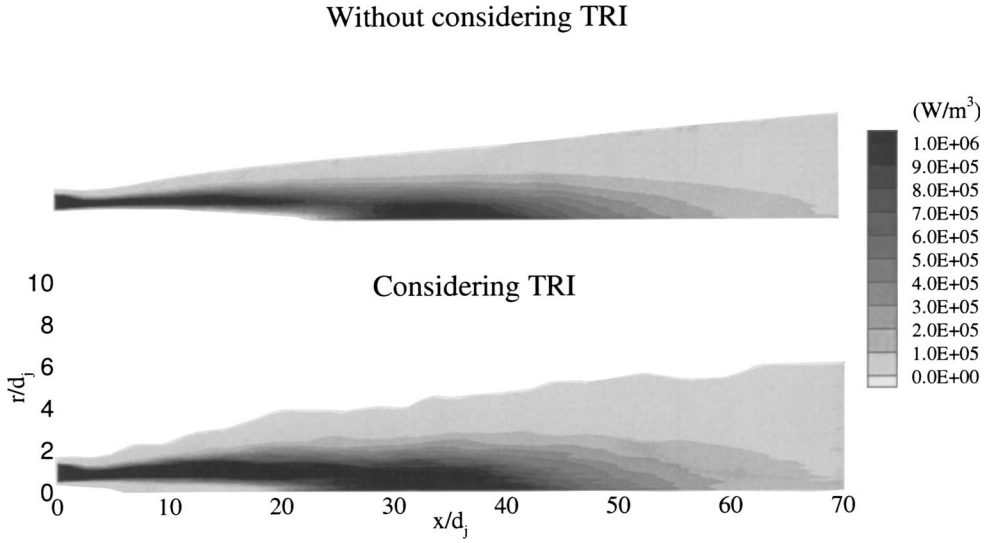

Fig. 3 Contours of radiative heat loss from Flame κL.3

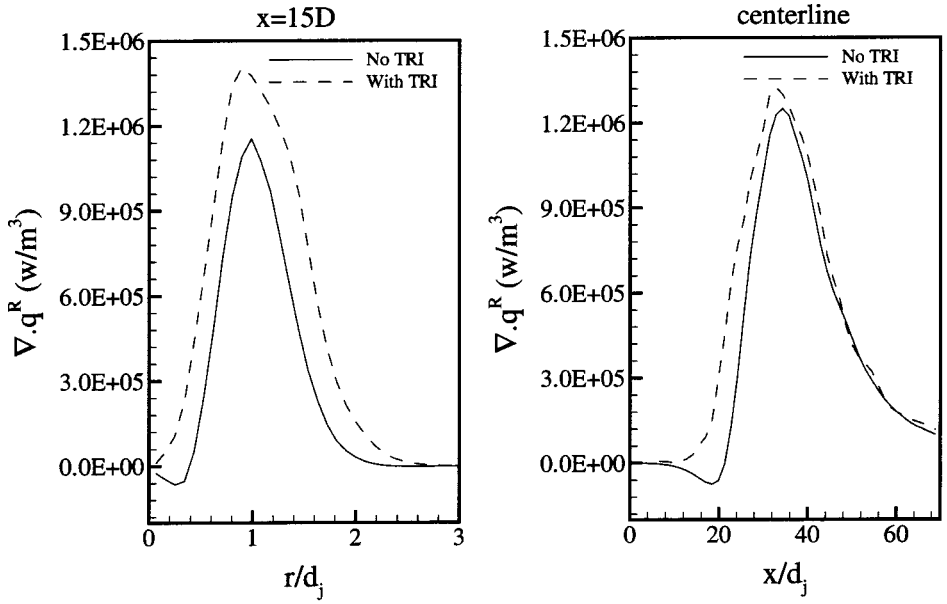

Fig. 4 Profiles of radiative heat loss at one cross-section and at the centerline for Flame κL.3

flame. But the magnitude of change is quite small, e.g., 10% for Flame κL.1, 7% for Flame κL.2 and 4% for Flame κL.3, indicating that the exact consideration of this correlation is not very important. This is expected, since the absorption coefficient is linearly dependent on species concentrations and almost linearly dependent on temperature, so that $\langle u \rangle$ is close to $\bar{u}$. This also explains why TRI-1 and TRI-2, and TRI-5 and TRI-F, respectively, lead to similar results.

Effects of $\langle ua_jI_b \rangle$. The absorption coefficient-Planck function correlation, $\langle ua_iI_b \rangle$, appears in the emission term of Eq. (10), i.e., $\Sigma 4\pi w_i k_i \langle ua_iI_b \rangle$. In the TRI-5 case, only this correlation is considered in the calculations. Comparing the numerical results of this case with those of the TRI-N case, flame emission, absorption and total net heat loss all have increased dramatically, e.g., radiative heat loss has increased by 59% in Flame κL.1, 60% in Flame κL.2 and 72% in Flame κL.3, indicating the importance of this correlation.

The Planck function is the most nonlinear function in the absorption coefficient-Planck function correlation. It has been suggested that consideration of the Planck function self-correlation (or temperature self correlation) alone may be enough to capture the essence of turbulence-radiation interactions. If this were true, only temperature fluctuations would be required to capture turbulence-radiation interactions, since the Planck function depends only on temperature; fluctuations of species concentrations would have no impact, which would greatly simplify the analysis of turbulence-radiation interactions. TRI-3 and TRI-4 cases were designed specifically to answer this question. Comparing the results of TRI-N and TRI-3, the total radiative heat loss is increased about 37%, 36%, and 39%, respectively, for each case as a result of considering the Planck function. For nongray gases, the weighted Planck function should be used in calculation of the temperature self correlation. Comparing results of TRI-3 with those of TRI-4, it is interesting to see that the consideration of $\langle aI_b \rangle$ considerably diminishes the total radiative heat loss. This indicates that turbulence-radiation effects may have less important impact in strongly nongray media than in gray media. Even for a gray case, the Planck function self-correlation accounts for about 60% of total TRI; therefore, considering only this correlation would be insufficient. It is also interesting to note that, although the absorption coefficient self-correlation and the weighted Planck function self correlation are not important, the positive correlation between them makes the absorption coefficient-Planck function correlation very important.

Conclusions

The composition PDF method was used to study radiating reactive turbulent flows. The method is able to treat turbulence-radiation interactions in a rigorous way: many unclosed terms due to TRI in the conventional moment method can be calculated exactly. Effects of turbulence-radiation interactions were investigated by comparing two different simulations of several two-dimensional jet flames: one ignores turbulence-radiation interactions and the other considers them. The simulations show that, by ignoring TRI, radiation heat losses are always severely underpredicted and, consequently, temperature levels are generally substantially overpredicted. This conclusion may be generalized to arbitrary flames, since temperature and concentration of CO_2 and H_2O are always positively correlated, thus always causing an increase in radiative heat loss. In addition, through freezing species concentrations and temperature fields, the importance of different TRI-related correlations were investigated. Numerical results show that, in order to determine turbulence-radiation interactions, consideration of the temperature-self correlation alone is not sufficient (although non-linearity of the Planck function with temperature is the severest among other functions), the absorption coefficient-Planck function correlation must also be considered.

Acknowledgments

The authors are grateful to the National Science Foundation for funding of this research under grant number CTS-9732223.

Nomenclature

a = weight factor in FSK model
C_ϕ = model constant
C_μ = constant in turbulence modeling
d_j = jet diameter, m
f = probability density function
f_{rad} = radiant fraction
G = incident radiation, $=\int_{4\pi} I_y d\Omega$, W/m^2
ΔH_{comb} = heat of combustion, J/kg

I = radiative intensity, W/m^2sr
I_b = Planck function, W/m^2sr
J_i^α = molecular diffusive flux of α-th composition variable
k = spectral dependence part of absorption coefficient, cm^{-1}
k = turbulent kinetic energy, m^2/s^2
L = flame length, m
$\dot{m}_{\text{fuel}}$ = mass flow rate of the fuel, kg/s
$\underline{q}^R$ = radiative heat flux, W/m^2
$\dot{Q}_{\text{em}}$ = radiative emission, W
$\dot{Q}_{\text{net}}$ = net radiative heat loss, W
$\underline{s}$ = directional vector
$S_{\text{radiation}}$ = source due to radiation, W/m^3
T = temperature, K
u = spatial dependence part of absorption coefficient
u_c = coflow air velocity, m/s
u_j = jet velocity, m/s
u_p = pilot flow velocity, m/s
w = numerical quadrature weight
x_i = space variable in ith direction
$\underline{Y}$ = species concentration vector, kg/m^3

Greek

κ = absorption coefficient, cm^{-1}
κ_P = Planck mean absorption coefficient, cm^{-1}
ρ = mixture density, kg/m^3
Ω = solid angle, sr
η = wave number, cm^{-1}
ϕ = composition variables
ψ = sample space of the composition variables
ϵ = surface emittance
ε = turbulent dissipation rate, m^2/s^3
Γ_T = turbulent diffusivity, m^2/s
ω = turbulent mixing frequency, Hz

References

[1] Viskanta, R., and Mengüç, M. P., 1987, "Radiation Heat Transfer in Combustion Systems," Prog. Energy Combust. Sci., **13**, pp. 97–160.
[2] Cox, G., 1977, "On Radiant Heat Transfer From Turbulent Flames," Combust. Sci. Technol., **17**, pp. 75–78.
[3] Faeth, G. M., Gore, J. P., Shuech, S. G., and Jeng, S. M., 1989, "Radiation From Turbulent Diffusion Flames," Annu. Rev. Numer. Fluid Mech. Heat Transfer, **2**, pp. 1–38.
[4] Song, T. H., and Viskanta, R., 1987, "Interaction of Radiation With Turbulence: Application to a Combustion System," J. Thermophys. Heat Transfer, **1**(1), pp. 56–62.
[5] Soufiani, A., Mignon, P., and Taine, J., 1990, "Radiation Effects on Turbulent Heat Transfer in Channel Flows of Infrared Active Gases," *Radiation Heat Transfer: Fundamentals and Applications, ASME, HTD-137*, **137**, pp. 141–148.
[6] Soufiani, A., Mignon, P., and Taine, J., 1990, "Radiation-Turbulence Interaction in Channel Flows of Infrared Active Gases," *Proceedings of International Heat Transfer Conference*, **6**, pp. 403–408.
[7] Hall, R. J., and Vranos, A., 1994, "Efficient Calculations of Gas Radiation From Turbulent Flames," Int. J. Heat Mass Transfer, **37**(17), pp. 2745–2750.
[8] Hartick, J. W., Tacke, M., Fruchtel, G., Hassel, E. P., and Janicka, J.,1996, "Interaction of Turbulence and Radiation in Confined Diffusion Flames," *Twenty-Sixth Symposium (International) on Combustion*, **26**, pp. 75–82.
[9] Pope, S. B., 1985, "PDF Methods for Turbulent Reactive Flows," Prog. Energy Combust. Sci., **11**, pp. 119–192.
[10] Kollmann, W., 1990, "The PDF Approach to Turbulent Flow," Theor. Comput. Fluid Dyn., **1**, pp. 249–285.
[11] Dopazo, C., 1994, "Recent Developments in PDF Methods," in P. A. Libby and F. A. William, eds., *Turbulent Reacting Flow*, Academic Press, San Diego, pp. 375–474.
[12] Mazumder, S., and Modest, M. F., 1998, "A PDF Approach to Modeling Turbulence-Radiation Interactions in Nonluminous Flames," Int. J. Heat Mass Transfer, **42**, pp. 971–991.
[13] Li, G., and Modest, M. F., 2002, "Application of Composition PDF Methods in the Investigation of Turbulence-Radiation Interactions," J. Quant. Spectrosc. Radiat. Transf., **73**, pp. 461–472.
[14] Burns, S. P., 1999, "Turbulence Radiation Interaction Modeling in Hydrocarbon Pool Fire Simulation," *SAND 99-3190*.
[15] Modest, M. F., 2003, *Radiative Heat Transfer*, 2nd ed., Academic Press, New York.
[16] Kabashnikov, V. P., and Myasnikova, G. I., 1985, "Thermal Radiation in Turbulent Flows-Temperature and Concentration Fluctuations," Heat Transfer-Sov. Res., **17**(6), pp. 116–125.
[17] Hottel, H. C., and Sarofim, A. F., 1967, *Radiative Transfer*, McGraw-Hill, New York.
[18] Modest, M. F., and Zhang, H., 2002, "The Full-Spectrum Correlated-k distribution for Thermal Radiation From Molecular Gas-Particulate Mixtures," ASME J. Heat Transfer, **124**(1), pp. 30–38.
[19] Dryer, F. L., and Glassman, I., 1972, "High-Temperature Oxidation of CO and CH_4," *Fourteenth Symposium (International) on Combustion*, pp. 987–1003.
[20] Westbrook, C. K., and Dryer, F. L., 1981, "Simplified Reaction Mechanisms for the Oxidation of Hydrocarbon Fuels in Flames," Combust. Sci. Technol., **27**, pp. 31–43.
[21] Turns, S. R., 2000, *An Introduction to Combustion: Concepts and Applications*, McGraw-Hill, Boston.
[22] Barlow, R. S., and Frank, J. H., 1998, "Effects of Turbulence on Species Mass Fractions in Methane/Air Jet Flames," *Twenty-Seventh Symposium (International) on Combustion*, pp. 1087–1095.
[23] Li, G., and Modest, M. F., 2002, "Investigation of Turbulence-Radiation Interactions in Turbulent Jet Flames," submitted to Combustion and Flame.

Calculation of Direct Exchange Areas for Nonuniform Zones Using a Reduced Integration Scheme

Weixue Tian

Wilson K. S. Chiu
e-mail: wchiu@engr.uconn.edu

Department of Mechanical Engineering,
University of Connecticut,
Storrs, CT 06269-3139

In the zonal method, considerable computational resources are needed to calculate the direct exchange areas (DEA) among the isothermal zones due to integrals with up to six dimensions, while strong singularities occur in the integrands when two zones are adjacent or overlaping (self-irradiation). A special transformation of variables to reduce a double integral into several single integrals is discussed in this paper. This technique was originally presented by Erkku (1959) for calculation of DEA using a uniform zone system in a cylindrical enclosure. However, nonuniform zones are needed for applications with large thermal gradients. Thus we extended this technique to calculate the DEA for nonuniform zones in an axisymmetrical cylinder system. A six-fold reduction in computational time was observed in calculating DEA compared with cases without a variable transformation. It is shown that accuracy and efficiency of estimation of radiation heat flux is improved when using a nonuniform zone system. Reasonable accuracy of all DEA are calculated without resorting to the conservative equations. Results compared well with analytical solutions and numerical results of previous researchers. This technique can be readily extended to rectangular enclosures with similar reduction in computation time expected. [DOI: 10.1115/1.1599368]

Keywords: Heat Transfer, Laser, Numerical Methods, Participating Media, Radiation

1 Introduction

The zonal method, originally developed by Hottel and Cohen [1], is a powerful and rigorous approach for estimating radiative heat transfer in semitransparent media. In this method, the domain of interest, usually an enclosure, is divided into a finite number of isothermal surface areas or volume zones. The radiative heat transfer rate is determined by the emissive power and mutual direct exchange areas (DEA) of each zone in the enclosure. The DEA represent the geometrical and optical relationship of every zone with each other. A detailed description of the zonal method can be found in [2] and [3]. A brief description is given here for clarity of discussion.

Three different types, or more specifically, surface-surface, volume-surface, volume-volume, DEA exist for an enclosure of semitransparent medium. They can be expressed as the following integrals,

$$\overline{s_i s_j} = \int_{A_i}\int_{A_j} \exp(-\beta S)\,\frac{\cos\theta_i \cos\theta_j}{\pi S^2}\,dA_j dA_i \tag{1}$$

$$\overline{g_i s_j} = \int_{V_i}\int_{A_j} \exp(-\beta S)\,\frac{\beta \cos\theta_j}{\pi S^2}\,dA_j dV_i \tag{2}$$

and

$$\overline{g_i g_j} = \int_{V_i}\int_{V_j} \exp(-\beta S)\,\frac{\beta^2}{\pi S^2}\,dV_j dV_i \tag{3}$$

Reciprocity holds for DEA, which indicates the following equations:

$$\overline{s_i s_j} = \overline{s_j s_i} \tag{4}$$

$$\overline{g_i s_j} = \overline{s_j g_i} \tag{5}$$

and

$$\overline{g_i g_j} = \overline{g_j g_i} \tag{6}$$

According to conservation of energy, two additional relationships among the DEA should be satisfied

$$\sum_{j=1}^{N} \overline{s_j s_i} + \sum_{k=1}^{M} \overline{g_k s_i} = A_i \tag{7}$$

and

$$\sum_{j=1}^{N} \overline{s_j g_i} + \sum_{k=1}^{M} \overline{g_k g_i} = 4\beta V_i \tag{8}$$

Evaluation of the DEA is the basis of the zonal method. An alternative definition of the DEA has been given in [4], where the surface-volume and volume-volume DEA is written in terms of volume zone boundary. As shown in Eqs. (1), (2), and (3), it involves the calculation of four, five, and six-dimensional integrals. The integrands have strong singularities when two zones are adjacent, or overlap each other (self-irradiation). High accuracy numerical approximation of these multiple integrals is difficult to achieve [5]. Considerable efforts are devoted to simplify calculation of DEA. For example, Siddall [6] developed a scheme to simplify the multiple integrals, by which the surface-volume and volume-volume DEA were reduced to a large number of single integrals. The DEA of a rectangular enclosure were numerically integrated, correlated and graphed by Tucker [7]. Erkku [8] studied the DEA of a cylindrical enclosure filled with semitransparent media. He developed techniques especially for zones with constant radial and axial distances in a cylindrical system to reduce the severity of the singularities as well as the dimension of inte-

Contributed by the Heat Transfer Division for publication in the JOURNAL OF HEAT TRANSFER. Manuscript received by the Heat Transfer Division January 10, 2003; revision received May 16, 2003. Associate Editor: S. T. Thynell.

grals. In his study, the volume to volume DEA are inferred from Eq. (8), because of limited computational resources. Tabulated results of his study can be found in Hottel and Sarofim [3]. One may use available tables and graphs [3,7,8] to evaluate the DEA of the zonal system. But this approach may cause problems. Equations (7) and (8) are difficult to satisfy due to the accumulation of errors inherent in interpolation of table values or graph lookup [9]. The table or graph also has a limited range of published values. A more serious problem is that the zone geometry is limited to specific zones, i.e., cubic or uni-dimensional zones. Sika [10] recognized the difficulty of the multiple integrals and used a different geometrical approach to calculate DEA in a cylindrical system. Sika expressed the DEA as summation of single or double integrals. But his derivation is complex and complicated to implement. An alternative approach to calculate DEA is the Monte Carlo scheme, as done by Murty [11]. However, Monte Carlo schemes are notoriously computationally intensive. Our goal is to further develop the necessary computational simplifications for the zonal method.

In real physical problems, the zones may not necessarily have constant size ($\Delta r=\Delta z=B$) as studied by Erkku [8]. In applications like laser heating, a high heat flux induced by a laser may cause a large temperature gradient in the heated region [12]. Thus, zones must be small enough so that the isothermal zone assumption is still a good approximation for estimating of radiative heat flux. However, in regions without laser heating, the temperature variation is expected to be much smaller, allowing larger zones. Due to the iterative nature of modeling conjugated heat transfer, significant computational time can be saved by reducing the number of zones, which requires the inversion of a smaller matrix [2]. Thus, nonuniform zones are necessary for these cases.

In this paper, we extend Erkku [8] technique for nonuniform zones. We reduce one integral dimension and the severity of singularities for most DEA. Case studies are performed and compared with analytical solutions as well as numerical solutions obtained by other researchers. It is shown that all DEA, including self irradiation, can be calculated directly using our technique without resorting to the conservative equations. Very good agreement with data provided by previous researchers are achieved. A demonstration case shows that using non-uniform zones may yield higher accuracy over uniform zones with the same number of zones.

2 Formulation of Direct Exchange Areas

2.1 A Preliminary Scenario. A special technique to transform a double integral into two single integrals was developed by Erkku [8]. We extend this transformation to nonuniform grids using an additional argument. Assume we have a double integral as the following:

$$I=\int_0^a\int_0^b f(x-y)dxdy \tag{9}$$

where a and b are constants, and we assume that $b\geqslant a>0$, f is some arbitrary function of $x-y$.

Let $x-y=z-a$, then Eq. (9) is transformed into the following:

$$I=\int_0^a\int_{a-y}^{a+b-y} f(z-a)dzdy \tag{10}$$

On a z−y plane as shown in Fig. 1, the limit of integration can be seen as the shaded areas. Apparently, the integration can be carried out in three regions. Thus we have,

$$I=\int_0^a\int_{a-y}^{a} f(z-a)dzdy+\int_0^a\int_a^b f(z-a)dzdy+\int_0^a\int_b^{a+b-y} f(z-a)dzdy \tag{11}$$

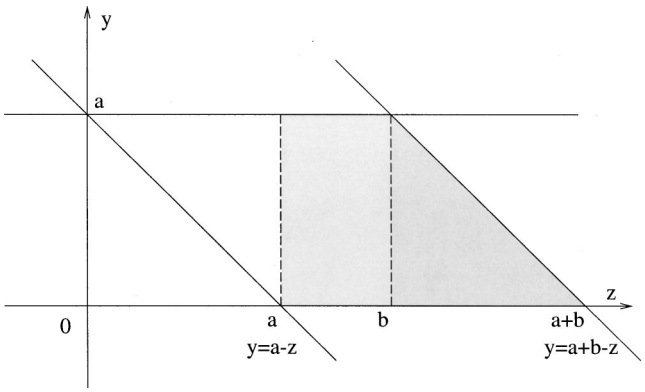

Fig. 1 $z-y$ plane of the integral

The order of integration can be changed to obtain the following equation:

$$I=\int_0^a\int_{a-z}^{a} f(z-a)dydz+a\int_a^b f(z-a)dz+\int_b^{b+a}\int_0^{b+a-z} f(z-a)dydz \tag{12}$$

Since f is a function of z, the integration of y can be carried out directly,

$$I=\int_0^a zf(z-a)dz+a\int_a^b f(z-a)dz+\int_b^{b+a}(b+a-z)f(z-a)dz \tag{13}$$

It is critical to note that when the integrand is not ''smooth,'' requiring a large number of quadrature points to determine I, considerable computation time can be saved using Eq. (13). For example, if M points in each dimension are needed for I, then Eq. (9) needs M^2 points totally to evaluate while Eq. (13) only needs $3M$ points. Thus roughly a factor of $M^2/3M=M/3$ computational time can be saved.

2.2 Application to Direct Exchange Areas. Equation (13) provides two desirable features of multiple integrals: reduction of one order of integration and severity of singularities. We will use the above technique to illustrate a calculation of DEA. Volume to volume DEA are shown in this study as an example to demonstrate the application of the technique. Although the above technique can be easily extended to three-dimensional rectangular enclosures, its usage in cylindrical enclosure is demonstrated in this paper.

Using Eq. (3) for a cylindrical system as shown in Fig. 2, the DEA between zones V_i and V_j are expressed as

$$\overline{g_ig_j}=\int_{r_{i1}}^{r_{i1}+\Delta r_i}\int_{z_{i1}}^{z_{i1}+\Delta z_i}\int_0^{2\pi}\int_{r_{j1}}^{r_{j1}+\Delta r_j}\int_{z_{j1}}^{z_{j1}+\Delta z_j}\int_0^{2\pi} r_ir_j\times\frac{e^{-\beta S}\beta^2}{\pi S^2}d\phi_jdz_jdr_jd\phi_idz_idr_i \tag{14}$$

where S is the distance between the zones,

$$S=\sqrt{r_i^2+r_j^2-2r_ir_j\cos(\phi_i-\phi_j)+(z_i-z_j)^2} \tag{15}$$

Since the enclosure is axisymmetric, Eq. (14) can be simplified as the following:

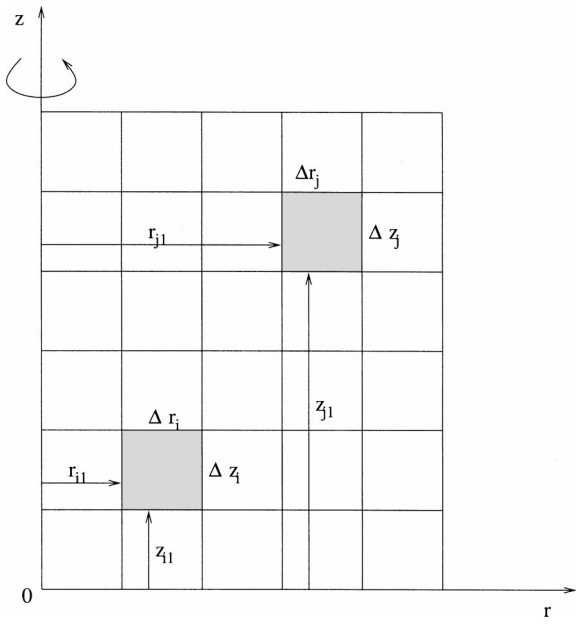

Fig. 2 Schematic of volume-volume zones

$$\overline{g_i g_j} = 4\int_{r_{i1}}^{r_{i1}+\Delta r_i}\int_{z_{i1}}^{z_{i1}+\Delta z_i}\int_{r_{j1}}^{r_{j1}+\Delta r_j}\int_{z_{j1}}^{z_{j1}+\Delta z_j}\int_0^{\pi} r_i r_j \times \frac{e^{-\beta S}\beta^2}{S^2} d\phi dz_j dr_j dz_i dr_i \tag{16}$$

where $\phi = \phi_i - \phi_j$. To facilitate the application of Eq. (13), Eq. (16) can also be written as the following:

$$\overline{g_i g_j} = 4\int_{r_{i1}}^{r_{i1}+\Delta r_i}\int_0^{\pi}\int_{r_{j1}}^{r_{j1}+\Delta r_j}\int_0^{\Delta z_j}\int_0^{\Delta z_i} r_i r_j \times \frac{e^{-\beta S}\beta^2}{S^2} dz_1 dz_2 dr_j d\phi dr_i \tag{17}$$

and

$$S = \sqrt{r_i^2 + r_j^2 - 2r_i r_j \cos\phi + (z_{i1} - z_{j1} + z_1 - z_2)^2} \tag{18}$$

where $z_i = z_{i1} + z_1$ and $z_j = z_{j1} + z_2$. After assuming $\Delta z_j \geqslant \Delta z_i$ and setting $z_1 - z_2 = z - \Delta z_i$, we apply Eq. (13) to get

$$\begin{aligned}\overline{g_i g_j} = {} & 4\int_{r_{i1}}^{r_{i1}+\Delta r_i}\int_0^{\pi}\int_{r_{j1}}^{r_{j1}+\Delta r_j}\int_0^{\Delta z_i} z r_i r_j \frac{e^{-\beta S}\beta^2}{S^2} dz dr_j d\phi dr_i \\ & + 4\int_{r_{i1}}^{r_{i1}+\Delta r_i}\int_0^{\pi}\int_{r_{j1}}^{r_{j1}+\Delta r_j}\int_{\Delta z_i}^{\Delta z_j} (\Delta z_i) r_i r_j \times \frac{e^{-\beta S}\beta^2}{S^2} dz dr_j d\phi dr_i \\ & + 4\int_{r_{i1}}^{r_{i1}+\Delta r_i}\int_0^{\pi}\int_{r_{j1}}^{r_{j1}+\Delta r_j}\int_{\Delta z_j}^{\Delta z_j+\Delta z_i} (\Delta z_j + \Delta z_i - z) r_i r_j 9 \times \frac{e^{-\beta S}\beta^2}{S^2} dz dr_j d\phi dr_i \end{aligned} \tag{19}$$

and

$$S = \sqrt{r_i^2 + r_j^2 - 2r_i r_j \cos\phi + (z_{i1} - z_{j1} + z - \Delta z_i)^2} \tag{20}$$

Thus, we have the reduced form for calculating DEA between zone V_i and V_j. It is straightforward then to derive the ring-ring DEA and volume-ring DEA in the axisymmetrial cylinder, which are given as the following equations:

$$\begin{aligned}\overline{s_i s_j} = {} & 4\int_0^{\pi}\int_0^{\Delta z_i} z \frac{R^4 e^{-\beta S}(1-\cos\phi)^2}{S^4} dz d\phi \\ & + 4\int_0^{\pi}\int_{\Delta z_i}^{\Delta z_j} (\Delta z_i) \frac{R^4 e^{-\beta S}(1-\cos\phi)^2}{S^4} dz d\phi \\ & + 4\int_0^{\pi}\int_{\Delta z_j}^{\Delta z_j+\Delta z_i} (\Delta z_j + \Delta z_i - z) \frac{R^4 e^{-\beta S}(1-\cos\phi)^2}{S^4} dz d\phi \end{aligned} \tag{21}$$

and

$$S = \sqrt{2R^2 - 2R^2\cos\phi + (z_{i1} - z_{j1} + z - \Delta z_i)^2} \tag{22}$$

$$\begin{aligned}\overline{s_i g_j} = {} & 4\int_0^{\pi}\int_{r_{j1}}^{r_{j1}+\Delta r_j}\int_0^{\Delta z_i} z R r_j \frac{(R - r_j\cos\phi)e^{-\beta S}\beta}{S^3} dz dr_j d\phi \\ & + 4\int_0^{\pi}\int_{r_{j1}}^{r_{j1}+\Delta r_j}\int_{\Delta z_i}^{\Delta z_j} (\Delta z_i) R r_j \times \frac{(R - r_j\cos\phi)e^{-\beta S}\beta}{S^3} dz dr_j d\phi \\ & + 4\int_0^{\pi}\int_{r_{j1}}^{r_{j1}+\Delta r_j}\int_{\Delta z_j}^{\Delta z_j+\Delta z_i} (\Delta z_j + \Delta z_i - z) R r_j \times \frac{(R - r_j\cos\phi)e^{-\beta S}\beta}{S^3} dz dr_j d\phi \end{aligned} \tag{23}$$

and

$$S = \sqrt{R^2 + r_j^2 - 2R r_j\cos\phi + (z_{i1} - z_{j1} + z - \Delta z_i)^2} \tag{24}$$

The technique developed is, however, not applicable to DEA with the top and bottom disk surfaces because the integrands for these DEA can not be written in terms of $z_i - z_j$ as in Eq. (15). Nevertheless, the reducable volume-volume DEA have the highest integration order and are much greater in number than surface-volume and surface-surface DEA. Since the volume-volumed DEA are most time consuming to compute, significant time savings in overall DEA calculation is observed after implementing the reduced scheme.

Following the same procedure, reduced forms of DEA of a three-dimensional rectangular enclosure can be derived. For example, the volume to volume DEA between two zones in rectangular enclosure can be reduced from a six dimensional integral to 27 three dimensional integrals. A rough estimation shows that computational time can be saved with a factor of $M^3/27$.

2.3 Numerical Procedure. Analytical solutions are not available for calculating DEA in a cylindrical enclosure except in cases for surface to surface DEA with zero absorption coefficient. In this case, DEA between surfaces are equivalant to view factors: $\overline{s_i s_j} = A_i F_{ij} = A_j F_{ji}$. Thus, the integrals need to be carried out numerically. Gaussian quadrature is used for such multiple dimensional integrals because its capability of achieving a high order of accuracy with a small number of points [5]. The integrals are carried out in such a way that each dimension of integration is calculated using an adaptive 10-point Gaussian quadrature. Then that dimension is subdivided to two regions, and re-calculated using a 10-point Gaussian quadrature. If the results from those two calculations have a percentage difference of less than 10^{-3}, then integration in that dimension stops. Otherwise, that dimension is subdivided into three regions and repeated steps until the

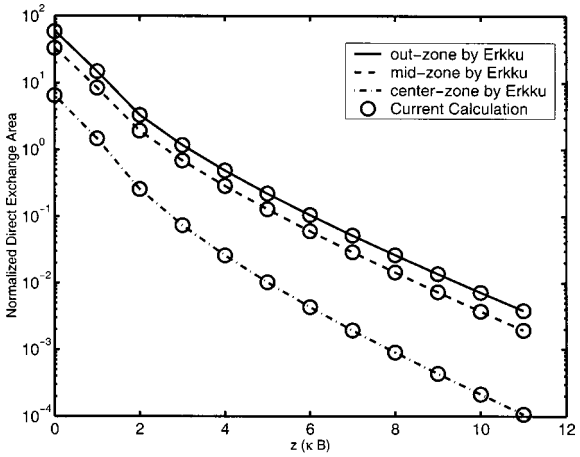

Fig. 3 Comparison of volume-volume DEA with Erkku [8]. The curves, from top to bottom, represent DEA of zones at the centerline, midpoint, and surface of the cylinder, respectively.

percentage difference of last two integration reaches 10^{-3}. A similar scheme is used to calculate the obstructed view factors in [13], where a detailed description is given. To verify the validation of the current scheme, the surface-surface DEA with nonabsorbing media in a cylindrical enclosure was compared with analytical solutions for various geometry sets provided by Siegel and Howell [14]. Almost an exact agreement was observed.

3 Results and Discussion

3.1 Validation of Reduced Integration Order Scheme. The scheme developed in this study will be checked for its validity by comparison with data of Erkku [8]. Erkku studied the DEA of a cylindrical system with up a $5\times12\,\beta B$, where B is the size the volume zone, $\Delta r=\Delta z=B$, and βB can be seen as the optical thickness of the volume zone. The system has 5 volume zones in the radial direction and 12 volume zones in the axial direction. Totally, the system has 60 volume zones and 22 surface area zones. The DEA are then normalized and tabulated in [3] and [8] for various optical thickness. Among all the volume-volume DEA, 180 values are found to be distinct. The comparison with our calculations showed less than 5% difference for βB up to 1.25. A typical comparison of results for volume-volume DEA are shown in Fig. 3 and Fig. 4 with $\beta B=0.5$. The vertical axis of Fig. 3 shows the normalized volume-volume DEA defined as $\overline{g_i g_j}/(\beta B)^2 B^2$, while the horizontal axis is the axial distance between two zones. The three curves from top to bottom show a comparison of the DEA results with data by Erkku for volume zones next to the centerline (center-zone), at the mid-point of the radial direction (mid-zone), and next to the surface (out-zone), respectively. Figure 4 shows the percentage difference of the corresponding data. It can be seen that these two sets of results agree very well with a maximum difference of 3.1%, which is reasonable taking account into the dimensions of integration. Thus, the current scheme is validated. From the calculated data in the current study, normalized DEA can be presented graphically or using a correlation with optical thickness βB, as by Erkku [8] and Tucker [7]. However, we did not pursue this because of two reasons: the uni-dimensional zone may not be an optimized approach for estimating radiation heat flux; the integration of DEA using this current technique is affordable with current computational power.

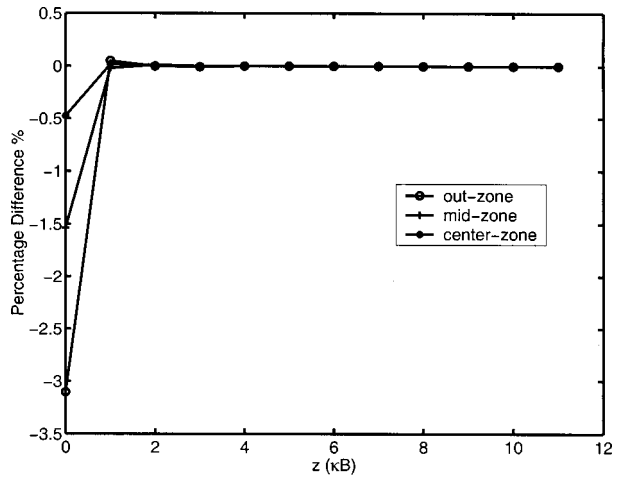

Fig. 4 Percentage of difference of current results and the data by Erkku [8]

It should be noted that although the current calculation has the same origin as that of Erkku [8], the procedures to calculate the DEA are significantly different. Erkku took advantage of the unidimensions of a zone ($\Delta r=\Delta z$) and simplified the expression of surface-surface and volume-surface DEA using an involved mathematical technique, which reduced the computational demands of calculation. But it can only be used for uni-dimensional zones, with significant limitations when applied to other configurations. Erkku's volume-volume DEA are derived from (8) because of limited computational capacity. The current calculation uses Eq. (19) to directly calculate the volume-volume DEA, thereby, the conservation equation can be used to check the accuracy of the calculated DEA.

An alternative and more general validation for the accuracy of calculated DEA is to use conservative Eqs. (7) and (8). After normalized with A_i and $4\beta V_i$ respectively, the right side of the equations becomes unity. This is indeed the case where for $\beta B=0.5$, the sum of normalized DEA to volume zone is within 2% of unity and to surface zone is within 0.5% of unity. Similar accuracy was observed with βB up to 1.25. This again demonstrates the validity of the current approach.

The computational time needed to integrate Eq. (16) is observed to be at least a factor of six more than that of equations derived in this study. This is because the integral is reduced by one dimension, thus fewer quadrature points are needed for the integration. The severity of singularities in the integrand may also be reduced because of a reduction of the integral dimension.

3.2 Nonuniform Zones. This part of the study focuses on using nonuniform zones to accurately estimate radiation heat flux in problems with large temperature gradients. The geometry considered is an infinitely long cylindrical enclosure filled with semitransparent media. Temperature variation exists only in the radial direction. The boundary is assumed to be black with constant temperature T_s. Azad and Modest [15] provided an analytical solution for the radiative heat flux in this cylindrical enclosure. The heat flux at any arbitrary radial direction can be readily expressed as a function of temperature distribution and optical thickness [2,15]. For an infinitely long cylinder, the heat flux at the radial boundary zone can be expressed as following equation using the zonal method:

$$q_{si}=\frac{1}{A_i}\left(\sum_{j=1}^{N}\overline{s_i s_j}e_{bsj}+\sum_{k=1}^{M}\overline{g_k s_i}e_{bgk}-A_i e_{bsi}\right)$$
$$=\frac{1}{A_i}\left(\sum_{k=1}^{M}\overline{g_k s_i}e_{bgk}-\sum_{k=1}^{M}\overline{g_k s_i}e_{bsi}\right) \tag{25}$$

The infinitely long cylinder is approximated by a cylinder enclosure with axial optical thickness of 10, so that the surfaces of the top and bottom disks have a minimal effect on heat flux at the central axial surface zone, which is approximated as the surface

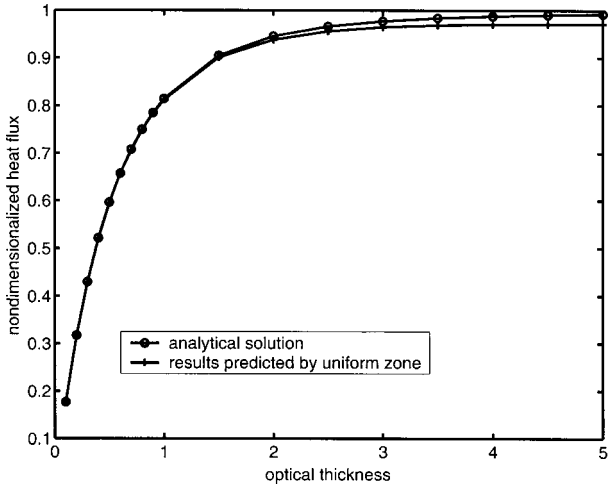

Fig. 5 Comparison of nondimensionalized surface heat flux of an isothermal cylinder using uniform zones with analytical solution [2]

heat flux in the analytical solution. Two temperature distributions in the semitransparent medium described by the following equations are studied.

$$T(r)=T_c \tag{26}$$

and

$$\frac{T(r)-T_c}{T_s-T_c}=\left(\frac{\tau(r)}{\tau_R}\right)^5 \tag{27}$$

where τ_R is the optical thickness of the enclosure defined by the radius and subscript c indicates centerline. For the first temperature distribution, the semitransparent medium in the enclosure is isothermal. The second distribution has large temperature gradient near the surface, while temperature variation around centerline is small.

Figures 5 and 6 show the normalized surface heat flux for the two different temperature distributions. The heat flux is normalized by $q_{si}/\sigma(T_c^4-T_s^4)$. A 6×11 zone system is used in the current study. The heat flux to the surface zone at half length in axial direction is then compared with the analytical heat flux of an infinitely long cylinder. For the nonuniform zone, the Δr of two adjacent zones has a ratio of 0.7 and decreases in the radial direction so that the region with the large temperature gradient has a greater number of zones.

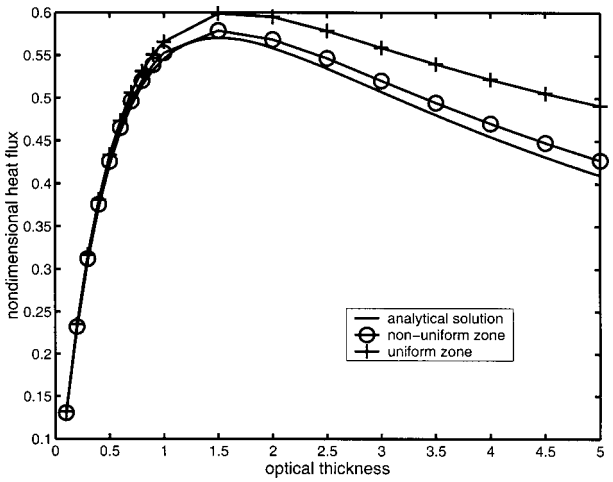

Fig. 6 Comparison of nondimensionalized surface heat flux of a nonisothermal cylindrical enclosure by uniform and nonuniform zones with analytical solution [2]

If the medium in the cylinder enclosure is isothermal, the surface heat flux predicted by the uniform zone system agrees very well with Azad and Modest's analytical solution. This agreement extends over a range optical thickness with less than 2% of error observed. For the nonisothermal case with a small optical thickness, both the uniform and nonuniform zones show good agreement with the analytical solution. This is because the absorption of the semitransparent medium is small with small optical thickness, thus its effect on boundary surface heat flux is small. However, as the radial optical thickness of the enclosure increases to 5, the uniform zone solution has a maximum error of around 20% while non-uniform zone's error is around 5%. This is because as the optical thickness of the enclosure increases, the temperature variation of zones near the boundary becomes larger over a large optical thickness ($\beta\Delta r$), thus the isothermal approximation for each zone becomes less appropriate. The nonuniform grid has a larger number of zones at the boundary to accomodate regions with larger temperature gradients, thus resulting in an improved accuracy. Thus, reasonable accuracy of predicting the radiative heat flux can be achieved using a small number of zones by choosing smaller zones in regions with a large temperature gradient.

4 Conclusion

A variable transformation to reduce the integration order for DEA calculations was discussed. With this technique, the DEA were calculated by direct integration without resorting to the conservative equations. This transformation can reduce the integrals needed for calculating DEA by one order as well as the severity of singularities. A factor of six in saving computational effort was observed in this study when compared with direct integration of DEA. Thus considerable saving of computational time can be achieved using the reduced integration scheme. DEA calculations agree well with published data.

In certain applications, such as laser heating, where a large temperature gradient may exist in a part of the computational domain, nonuniform zone size is desirable in terms of efficiency and accuracy. Nonuniform zone also requires fewer zones to achieve high accuracy. It is demonstrated that with smaller zones at regions where temperature gradients are large, a significantly improvement in model accuracy and robustness was observed. Additionally, the technique can readily be applied to three-dimensional rectangular enclosure with non-uniform zones, similar saving in computation time is expected.

Acknowledgment

Financial support by the National Science Foundation (Grant #CTS-0093544) and the Office of Naval Research (Grant #N0014-01-1-0691) are gratefully acknowledged.

Nomenclature

A = surface area, m^2
e_b = black emissive power, W/m^2
$\overline{g_i g_j}$ = direct exchange area between volume zones i and j, m^2
$\overline{g_i s_j}$ = direct exchange area between volume zone i and surface zone j, m^2
$\overline{s_i s_j}$ = direct exchange area between surface zones i and j, m^2
$F_{i,j}$ = view factor between two surfaces
M = number of volume zones; number of quadrature points
N = number of surface zones
S = distance between two zones, m
V = volume, m^3

Greek Letters

β = extinction coefficient, m^{-1}
ϕ = azimuthal angle, rad
σ = Stefan-Bolzman constant, 5.670×10^{-8} W/m^2 K^4
τ = optical thickness
θ = angle between surface normal and S, rad

References

[1] Hottel, H. C., and Cohen, E. S., 1958, ''Radiant Heat Exchange in a Gas-Filled Enclosure: Allowance for Nonuniformity of Gas Temperature,'' AIChE J., **4**, pp. 3–14.
[2] Modest, M. F., 2003, *Radiative Heat Transfer*, 2nd ed., Academic Press, San Diego, CA.
[3] Hottel, H. C., and Sarofim, A. F., 1967, *Radiative Transfer*, McGraw-Hill Inc., New York.
[4] Goyhénéche, J. M., and Sacadura, J. F., 2002, ''The Zonal Method: A New Explicit Matrix Relation to Calculate the Total Exchange Areas in Anisotropically Scattering Medium Bounded by Anisotropically Reflecting Walls,'' ASME J. Heat Transfer, **124**, pp. 696–703.
[5] Stroud, A. H., 1971, *Approximate Calculation of Multiple Integrals*, Prentice-Hall, Englewood Cliffs, NJ.
[6] Siddall, R. G., 1986, ''Accurate Evaluation of Radiative Direct-Exchange Areas for Rectangular Geometries,'' in *Proceedings of the Eighth International Heat Transfer Conference*, Hemisphere Publishing Corp., Washington, DC, pp. 751–756.
[7] Tucker, R. J., 1986, ''Direct Exchange Areas for Calculating Radiation Transfer in Rectangular Furnaces,'' ASME J. Heat Transfer, **108**, pp. 707–710.
[8] Erkku, H., 1959, ''Radiant Heat Exchange in Gas-Filled Slabs and Cylinders,'' Ph.D. thesis, Massachusetts Institute of Technology, Cambridge, MA.
[9] Larsen, M. E., and Howell, J. R., 1986, ''Least-Squares Smoothing of Direct Exchange Areas in Zonal Analysis,'' ASME J. Heat Transfer, **108**, pp. 239–242.
[10] Sika, J., 1991, ''Evaluation of Direct-Exchange Areas for a Cylindrical Enclosure,'' ASME J. Heat Transfer, **113**, pp. 1040–1044.
[11] Murty, C. V. S., 1993, ''Evaluation of Radiation Reception Factors in a Rotory Kiln Using a Modified Monte-Carlo Scheme,'' Int. J. Heat Mass Transfer, **36**, pp. 119–133.
[12] Tian, W., and Chiu, W. K. S., 2002, ''Numerical Modeling of CO_2 Laser-Heated Moving Glass Rods,'' in *Proceedings of ASME International Mechanical Engineering Congress and Exposition*, CD-ROM, **1**, ASME, New York, Paper No. IMECE-33082.
[13] Walton, G., 2002, ''Calculation of Obstructed View Factors by Adaptive Integration,'' Tech. Rep. NISTIR 6925, NIST.
[14] Siegel, R., and Howell, J., 2002, *Thermal Radiation Heat Transfer*, 4th ed., Taylor & Francis, London.
[15] Azad, F. H., and Modest, M. F., 1981, ''Evaluation of the Radiative Heat Flux in Absorbing, Emitting and Linear-Anisotropically Scattering Cylindrical Media,'' ASME J. Heat Transfer, **103**, pp. 350–356.

Geometric Optimization of Radiant Enclosures Containing Specular Surfaces

K. J. Daun
e-mail: kyle_daun@mail.utexas.edu

D. P. Morton

J. R. Howell

Department of Mechanical Engineering,
The University of Texas at Austin,
1 University Station, C2200,
Austin, TX 78712-0292

This paper presents an optimization methodology for designing radiant enclosures containing specularly-reflecting surfaces. The optimization process works by making intelligent perturbations to the enclosure geometry at each design iteration using specialized numerical algorithms. This procedure requires far less time than the forward "trial-and-error" design methodology, and the final solution is near optimal. The radiant enclosure is analyzed using a Monte Carlo technique based on exchange factors, and the design is optimized using the Kiefer-Wolfowitz method. The optimization design methodology is demonstrated by solving two industrially-relevant design problems involving two-dimensional enclosures that contain specular surfaces. [DOI: 10.1115/1.1599369]

Keywords: Geometry, Heat Transfer, Monte Carlo, Radiation

Introduction

The design of radiant enclosure geometry is a challenging problem often encountered in the field of thermal engineering. Enclosure geometry is an important consideration in almost every design problem involving radiant enclosures, and in particular those that contain specularly-reflecting surfaces. Common examples include solar concentrating collectors and light boxes for illumination applications.

Traditionally, the enclosure geometry is designed using a forward "trial-and-error" methodology. First, the designer poses a candidate enclosure geometry and then evaluates it by performing an analysis. If this enclosure design does not satisfy the problem requirements, the designer modifies the design according to his or her experience and intuition and repeats the analysis. This process continues until a satisfactory solution to the design problem is identified. Usually, this requires many iterations, and consequently a substantial amount of design time. Furthermore, while the final solution may be satisfactory, it is rarely optimal.

Recently, optimization techniques have been adapted to design radiant enclosures. The procedure is as follows: first, an objective (or "cost") function, $F(\Phi)$, is defined so that the minimum of the objective function corresponds to the ideal design outcome. The objective function depends on a set of design parameters contained in the vector Φ that control the enclosure configuration. Specialized numerical algorithms are then employed to minimize the objective function through successive iteration. The total number of iterations required by the design process is limited by making intelligent changes to the design parameters at each step, based on the local objective function curvature. Consequently, far fewer iterations are required to solve the design problem compared with the forward methodology, and the final solution is usually near optimal.

Enclosure geometry is one of the most important considerations when designing enclosures that contain specular surfaces; accordingly, most literature dealing with enclosure geometry design has focused on this class of problem. Non-imaging optics techniques are among the most widely used methods for optimizing the geometry of enclosures containing specular surfaces [1]. The most common of these techniques is the edge-ray method, which uses a complex mathematical procedure based on analytical geometry and calculus to determine the optimal shape of reflector surfaces, and is often applied to design concentrators that have the highest-possible radiant heat flux concentration ratios between entrance and exit apertures. Güven [2] also presented a semi-analytical method for designing collector geometries. In this method, the optimal collector shape is found by deriving an analytical expression for the intercept factor (defined as the fraction of the reflected radiation that reaches the receiver), which is then maximized by taking the derivatives with respect to two geometric parameters and setting these equal to zero. While these techniques are very powerful design tools, they can only be used to treat a narrow class of enclosure geometry and do not account for surfaces properties that have both diffuse and specular components. Moreover, the designer must possess specialized mathematical knowledge in order to carry out these analyses.

Numerical simulation has been extensively used to design radiant enclosures containing specular surfaces. Most simulations are based on a Monte Carlo ray-tracing method, which can treat very complex problems and is also very straightforward to implement. Ryan et al. [3] used a Monte Carlo technique to analyze a cylindrical solar collector, and drew general conclusions about the collector configuration based on a series of univariate parametric studies. Mushaweck et al. [4] calculated optical reflector shapes for non-tracking parabolic trough collectors. The reflector shape was set equal to the idealized edge-ray solution, which in turn is a function of the upper and lower acceptance angles of the reflector. The ideal collector configuration was then found by plotting the average utilizable power over a rectangular domain defined by the maximum and minimum values of the acceptance angles. Although numerical simulation techniques can treat a more extensive set of problems than those based on analytical solutions, both of the above studies relied on primitive optimization algorithms that required a substantial amount of design time and also restricted the number of design parameters that could be considered in the analysis.

A more sophisticated optimization approach is described by Ashdown [5], in which a ray-tracing technique used to simulate illumination within an enclosure is coupled with a genetic algorithm that searches for the globally optimum enclosure geometry. Genetic algorithms mimic natural selection as it occurs in nature. This class of algorithms generates new designs by "mating" pairs of previously generated designs and by "mutating" existing designs. The designs that perform well are favored in the mating process, and after many generations, a near-optimum solution is usually found.

This paper presents an optimization method for determining the

Contributed by the Heat Transfer Division for publication in the JOURNAL OF HEAT TRANSFER. Manuscript received by the Heat Transfer Division December 5, 2002; revision received May 16, 2003. Associate Editor: S. T. Thynell.

enclosure configuration that produces a desired heat flux and temperature distribution over a region of the enclosure surface, called the design surface. This class of problem is commonly encountered when the radiant enclosure is part of a heat treatment process; for example, the design surface may consist of food products that need to be baked or a coated surface that needs to be dried or cured. In this method, a Monte Carlo technique based on exchange factors is used to calculate the boundary conditions over the design surface, while the objective function is minimized using the Kiefer-Wolfowitz method, a gradient-based technique that is well-suited for optimizing stochastic systems in which analytical gradient estimates are not available. Finally, the procedure is demonstrated by applying it to design two two-dimensional radiant enclosures containing both diffuse and specularly reflecting surfaces.

Gradient-Based Optimization

Optimization methods work by solving the well-posed forward (or explicit) design problem through successive iteration. Unlike the ''trial-and-error'' design methodology, which relies solely on the designer's intuition, the optimization methodology uses numerical algorithms to adjust the design configuration at each iteration until the optimum design is identified. In this way, the number of iterations and consequently the time required to design the enclosure is reduced, and the final solution quality is usually much better than that obtained by the trial-and-error design methodology.

The first step of the optimization process is to define an objective function, $F(\Phi)$, which quantifies the ''goodness'' of a particular design configuration, in such a way that the minimum of $F(\Phi)$ corresponds to the optimal design. The objective function is dependant on a set of variables contained in Φ, called design parameters, which completely specify the design configuration. The goal, then, is to identify the set of design parameters that minimize $F(\Phi)$,

$$F(\Phi^*)=\mathrm{Min}[F(\Phi)], \quad \Phi \in \Re^n. \tag{1}$$

Often, it is also necessary to impose design constraints on Φ of the form

$$\begin{aligned} c_i(\Phi)&=0, \quad i=1 \ldots m' \\ c_i(\Phi)&\geq 0, \quad i=m'+1 \ldots m, \end{aligned} \tag{2}$$

which define the domain of Φ in n-space, called the feasible region.

Consider the radiant enclosure design problem shown in Fig. 1. The objective of this problem is to identify the enclosure geometry and heater settings that produce a desired heat flux and temperature distribution over the design surface. This is accomplished by first specifying the temperature distribution over the design surface and then using the heat flux evaluated at N_{DS} discrete locations over the design surface to define the objective function,

$$F(\Phi)=\frac{1}{N_{DS}}\sum_{j=1}^{N_{DS}}[q_{sj}(\Phi)-q_{sj}^{\mathrm{target}}]^2, \tag{3}$$

with the design parameters in Φ specifying the heater settings and enclosure geometry. The heat flux distribution over the design surface that best matches the desired distribution is produced by the design configuration corresponding to Φ^*, which in turn is found by minimizing the objective function defined in Eq. (3). (Alternatively, the heat flux distribution could be specified over the design surface and the temperature distribution could be used to define $F(\Phi)$.) Design constraints could also be imposed to limit the size of the enclosure, and to prevent the heat flux distribution over the heater surface from assuming negative values.

Many different methods have been developed to minimize the objective function. Gradient-based techniques are commonly employed if the feasible region is convex and the defining objective function and constraints in Eqs. (1) and (2) are continuously differentiable. These algorithms find Φ^* iteratively; at the kth iteration, a search direction, $\mathbf{p}_k$, is first chosen based on the objective function curvature at Φ_k. Next, a step size, α_k, is found, usually by performing a ''line'' minimization of $F(\Phi_k+\alpha_k\mathbf{p}_k)$ with respect to α_k using Newton-Raphson, bisection, or golden section routines. Alternatively, the step size can be set equal to a series based on the iteration number, k [6],

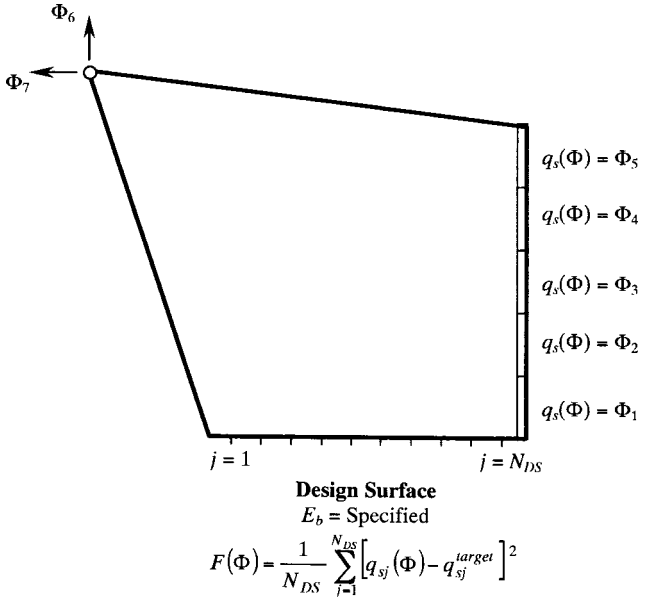

Fig. 1 Example of a radiant enclosure design problem

$$\alpha_k=\frac{\alpha_0}{k^a}, \quad 0\leq a\leq 1. \tag{4}$$

Finally, the new set of design parameters is found by taking a ''step'' in the $\mathbf{p}_k$ direction,

$$\Phi_{k+1}=\Phi_k+\alpha_k\mathbf{p}_k. \tag{5}$$

Gradient-based methods differ on how the search directions are chosen. In the steepest-descent method, the search direction is set equal to the direction of steepest-descent,

$$\mathbf{p}_k=-\frac{g(\Phi_k)}{|g(\Phi_k)|}, \tag{6}$$

where the gradient vector, $g(\Phi_k)$, contains the first-order sensitivities of the objective function to each of the design parameters,

$$g(\Phi_k)=\left\{\frac{\partial F(\Phi_k)}{\partial \Phi_1}, \frac{\partial F(\Phi_k)}{\partial \Phi_2}, \ldots, \frac{\partial F(\Phi_k)}{\partial \Phi_n}\right\}^T. \tag{7}$$

Although this method is the most intuitive of the gradient-based techniques, it is not a popular choice because it only uses first-order curvature information in the calculation of $\mathbf{p}_k$ and accordingly has a slower rate of convergence to Φ^*, compared with other higher-order methods. Nevertheless, this method is widely used to optimize stochastic systems, for reasons that will be presented later in this paper.

Solution of the Heat Flux Distribution

In this application, the heat flux distribution over the design surface is estimated using exchange factors calculated by the Monte Carlo method. The Monte Carlo method has been extensively used to analyze many different radiant enclosure problems, and is especially well suited for analyzing enclosures containing specularly-reflecting surfaces. Although the Monte Carlo method

has been described extensively in the literature, e.g., [7,8], it is presented again here to better demonstrate challenges inherent in stochastic optimization.

The first step of this method is to discretize the enclosure surface into N elements, with the ith element having area ΔA_i. The emissivity ε_i is known over each element, and either the heat flux, q_{si}, or the temperature, T_i, is specified. Assuming a uniform temperature or heat flux distribution over each element and performing an energy balance over the ith element results in the equation

$$q_{si}(\Phi)+\sum_{j=1}^{N}\varepsilon_j E_{bj}(\Phi)\mathfrak{F}_{ji}(\Phi)\frac{\Delta A_j(\Phi)}{\Delta A_i(\Phi)}=\varepsilon_i E_{bi}(\Phi), \tag{8}$$

where $E_{bi}(\Phi)=\sigma T_i^4(\Phi)$ and $\mathfrak{F}_{ji}(\Phi)$ is the exchange factor from the jth to the ith element, equal to the fraction of the radiant energy emitted by the jth element that is absorbed by the ith element. By applying the reciprocity rule for exchange factors, Eq. (8) can be rewritten in a more compact form,

$$\frac{q_{si}(\Phi)}{\varepsilon_i}+\sum_{j=1}^{N}E_{bj}(\Phi)\mathfrak{F}_{ij}(\Phi)=E_{bi}(\Phi). \tag{9}$$

Although the analytical solution of the exchange factor is quite tractable for diffuse-walled enclosure problems, this is not the case for enclosures that contain specular surfaces. The exchange factor, $\mathfrak{F}_{ij}(\Phi)$, can be expressed as the expectation of a random variable $\mathfrak{F}_{ij}(\Phi,\xi)$, where ξ contains the three random variables that specify the emission direction and location of a random bundle leaving the ith surface. Theoretically, $\mathfrak{F}_{ij}(\Phi)$ could be found by integrating over the probability distribution governing each ξ_i, i.e.,

$$\begin{aligned}\mathfrak{F}_{ij}(\Phi)&=E[\mathfrak{F}_{ij}(\Phi,\xi)]\\&=\int_0^1\int_0^1\int_0^1\mathfrak{F}_{ij}(\Phi,\xi)dP_1(\xi_1)dP_2(\xi_2)dP_3(\xi_3).\end{aligned} \tag{10}$$

(This is, in fact, equivalent to the integration used to calculate view factors between diffuse surfaces.) Instead, we use a Monte Carlo simulation to estimate $\mathfrak{F}_{ij}(\Phi)$ in Eq. (10),

$$E[\mathfrak{F}_{ij}(\Phi,\xi)]\approx\widetilde{\mathfrak{F}_{ij}}(\Phi)=\frac{1}{N_{bi}}\sum_{k=1}^{N_{bi}}\mathfrak{F}_{ij}(\Phi,\xi^k)=\frac{N_{bij}}{N_{bi}}, \tag{11}$$

where N_{bi} is the total number of bundles emitted by the ith element, and N_{bij} is the number of those elements that are absorbed by the jth element. Due to the law of large numbers, the Monte Carlo approximation of $E[\mathfrak{F}_{ij}(\Phi,\xi)]$ becomes exact with probability one as N_{bi} approaches infinity. Since we are restricted to using a finite number of bundles, however, $\widetilde{\mathfrak{F}_{ij}}(\Phi)$ contains a random error that propagates throughout the solution.

Assume the elements are renumbered so that T_i is specified for $i=1\ldots m$ and q_{si} is specified for $i=m+1\ldots N$. Equation (9) can then be rewritten as

$$\frac{\tilde{q}_{si}(\Phi)}{\varepsilon_i}+\sum_{j=m+1}^{N}\tilde{E}_{bj}(\Phi)\widetilde{\mathfrak{F}_{ij}}(\Phi)=E_{bi}(\Phi)-\sum_{j=1}^{m}E_{bj}(\Phi)\widetilde{\mathfrak{F}_{ij}}(\Phi) \tag{12}$$

for elements with specified T_i, and

$$\tilde{E}_{bi}(\Phi)-\sum_{j=m+1}^{N}\tilde{E}_{bj}(\Phi)\widetilde{\mathfrak{F}_{ij}}(\Phi)=\frac{q_{si}(\Phi)}{\varepsilon_i}+\sum_{j=1}^{m}E_{bj}(\Phi)\widetilde{\mathfrak{F}_{ij}}(\Phi) \tag{13}$$

for elements where q_{si} is specified. Equations (12) and (13) are arranged so the q_{si} and E_{bi} terms on the right-hand sides are known, while those on the left-hand side remain unknown. Writing Eqs. (12) and (13) for all the elements results in a system of N equations containing N unknowns, which are rearranged into a matrix equation

$$\tilde{\mathbf{A}}\tilde{\mathbf{x}}=\tilde{\mathbf{b}}, \tag{14}$$

where $\tilde{\mathbf{x}}=\{\tilde{q}_{s1},\ldots,\tilde{q}_{sm},\tilde{E}_{bm+1},\ldots,\tilde{E}_{bN}\}^T$. (The dimension of $\mathbf{A}$ can be reduced by excluding equations that correspond to elements where q_s is equal to zero.) The $\tilde{\mathbf{A}}$ matrix is usually well-conditioned, and Eq. (14) can be solved to yield the heat flux distribution over the design surface.

This heat flux distribution is subject to a random error induced by the sampling error in the exchange factors, as well as a "bias" error caused by assuming uniform heat flux and temperature distribution over each surface element. The former error is reduced by increasing the number of bundles emitted by each element, while the latter diminishes with a higher level of grid refinement. Nevertheless, both errors result in a grid-dependent objective function containing a statistical uncertainty, which renders it difficult to optimize.

The magnitude of the random error is estimated by performing a replication procedure. Suppose a total of N_{bundles} bundles is used to calculate the exchange factors throughout the process. A sequence of Monte Carlo simulation is used to estimate p independent sets of the required exchange factors, each using N_{bundles}/p bundles. Each of these sets of exchange factors is then used to find an estimate of the heat flux distribution over the design surface, through Eq. (14). Performing this procedure for each set of exchange factors results in p independent solutions, $\tilde{\mathbf{x}}^k$, $k=1\ldots p$.

The heat flux at each discrete point over the design surface is then approximated by the average of the p independent solutions,

$$\tilde{q}_{si}(\Phi)=\frac{1}{p}\sum_{k=1}^{p}\tilde{q}_{si}^k(\Phi), \tag{15}$$

while the corresponding random error associated with $\tilde{q}_{si}(\Phi)$ is estimated from the sample standard deviation,

$$\sigma_{i,\text{ave}}(\Phi)=\frac{\sigma_i(\Phi)}{\sqrt{p}}, \tag{16}$$

where $\sigma_i^2(\Phi)$ is the sample variance of the p measurements, given by

$$\sigma_i^2(\Phi)=\frac{1}{p-1}\sum_{k=1}^{p}[\tilde{q}_{si}^k(\Phi)-\tilde{q}_{si}(\Phi)]^2. \tag{17}$$

Optimization Procedure

The goal of the optimization process is to minimize the objective function defined by Eq. (3). In this application, however, the heat flux at each discrete point over the design surface, $q_{sj}(\Phi)$, is estimated by $\tilde{q}_{sj}(\Phi)$, which in turn is obtained from the Monte Carlo technique presented in the previous section. Accordingly, the objective function is approximated by

$$F(\Phi)\approx\tilde{F}(\Phi)=\frac{1}{N_{DS}}\sum_{j=1}^{N_{DS}}[\tilde{q}_{sj}(\Phi)-q_{sj}^{\text{target}}]^2. \tag{18}$$

This approximation is subject to a sampling error, $\delta_1(\Phi)$, induced by the statistical uncertainty in $\tilde{q}_{sj}(\Phi)$. The sampling error is estimated by [9]

$$\delta_1(\Phi)\approx\left[\sum_{i=1}^{N_{DS}}\sum_{j=1}^{N_{DS}}\frac{\partial F(\Phi)}{\partial\tilde{q}_{si}}\frac{\partial F(\Phi)}{\partial\tilde{q}_{sj}}\Gamma_{ij}(\Phi)\right]^{1/2}, \tag{19}$$

where the terms of the variance-covariance matrix, $\Gamma(\Phi)$, are defined by

$$\Gamma_{ij}(\Phi)=\frac{1}{p(p-1)}\sum_{k=1}^{p}[\tilde{q}_{si}^{k}(\Phi)-\tilde{q}_{si}(\Phi)][\tilde{q}_{sj}^{k}(\Phi)-\tilde{q}_{sj}(\Phi)]. \tag{20}$$

The uncertainty inherent in the evaluation of $\tilde{F}(\Phi)$ makes the optimization of stochastic systems somewhat more complicated than that of deterministic systems, since the "exact" value of $F(\Phi)$ is unknown.

Many methods used to optimize stochastic systems are based on those used to optimize deterministic systems. The Kiefer-Wolfowitz method [10,11] is a gradient-based technique that is often used when an analytical evaluation of the gradient of $\tilde{F}(\Phi)$ is not possible. This method is based on the steepest-descent algorithm; at the kth iteration, the step size is found from Eq. (4), and the search direction is set equal to

$$\mathbf{p}_k=\frac{-\tilde{g}(\Phi_k)}{|\tilde{g}(\Phi_k)|}, \tag{21}$$

where $\tilde{g}(\Phi_k)$ is the second-order central-difference approximation of the gradient vector of $\tilde{F}(\Phi)$ at Φ_k. The pth term of $\tilde{g}(\Phi_k)$ is given by

$$\tilde{g}_p(\Phi_k)=\frac{\tilde{F}(\Phi_k+\mathbf{e}_p\cdot h_k)-\tilde{F}(\Phi_k-\mathbf{e}_p\cdot h_k)}{2h_k}, \tag{22}$$

where $\mathbf{e}_p$ is the unit vector in the pth direction, and h_k is the interval used in the finite-difference approximation at the kth iteration.

This estimate contains two sources of error: a bias error, $\delta_{2,p,k}(\Phi_k,h_k)$, due to the truncation of higher-order terms in the finite-difference approximation, and a random error, $\delta_{3,p,k}(\Phi_k,h_k)$, induced by the sampling error in $\tilde{F}(\Phi_k)$. (This random error tends to dominate finite difference approximation of higher-order derivatives, which is why steepest-descent is used instead of the Newton and quasi-Newton methods.) The bias error is given by [12]

$$\delta_{2,p,k}(\Phi_k,h_k)=g_p(\Phi_k)-\frac{F(\Phi_k+\mathbf{e}_p\cdot h_k)-F(\Phi_k-\mathbf{e}_p\cdot h_k)}{2h_k}. \tag{23}$$

Since the central difference approximation improves with diminishing step size, $\delta_{2,p,k}(\Phi_k,h_k)$ decreases as h_k becomes small. Assuming independent estimates of $F(\Phi_k+\mathbf{e}_p\cdot h_k)$ and $F(\Phi_k-\mathbf{e}_p\cdot h_k)$, the random error is found from

$$\delta_{3,p,k}(\Phi_k,h_k)=\frac{\sqrt{\delta_1^2(\Phi_k+\mathbf{e}_p\cdot h_k)+\delta_1^2(\Phi_k-\mathbf{e}_p\cdot h_k)}}{2h_k}, \tag{24}$$

and tends to *increase* as h_k becomes small, since decreasing h_k does not necessarily decrease the magnitude of the numerator in Eq. (24). Therefore, it is important to select an intermediate interval length that ensures both $\delta_{2,p,k}(\Phi_k,h_k)$ and $\delta_{3,p,k}(\Phi_k,h_k)$ are sufficiently small. One choice is to reduce h_k with each successive iteration according to a series similar to Eq. (4),

$$h_k=\frac{h_0}{k^b}, \quad 0\leqslant k\leqslant 1. \tag{25}$$

Pflug [12] recommends values of $a=1$ and $b=1/3$ for Eqs. (4) and (25), respectively.

Another way of reducing $\delta_{3,p,k}(\Phi_k,h_k)$ is to use the same sequence of random numbers (common random numbers, [13]) to generate both $\tilde{F}(\Phi+\mathbf{e}_p\cdot h_k)$ and $\tilde{F}(\Phi-\mathbf{e}_p\cdot h_k)$.

Demonstration of Method

The method described in the previous section is demonstrated by applying it to design two radiant enclosures. In both cases, the goal of the design process is to identify an enclosure geometry that produces a uniform heat-flux distribution over the temperature-specified design surface.

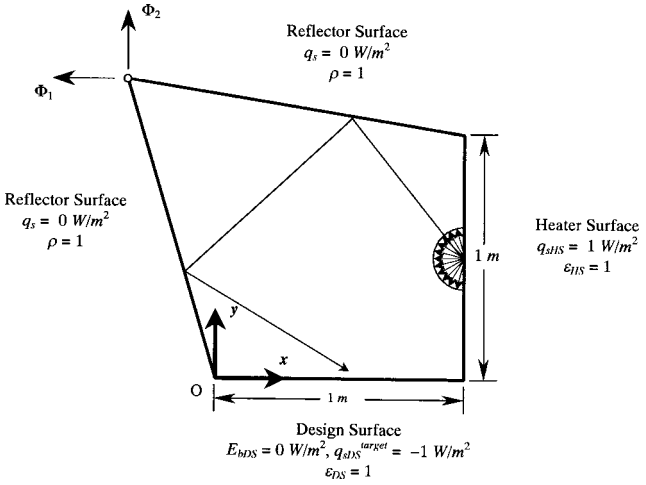

Fig. 2 First radiant enclosure design problem

The first enclosure, shown in Fig. 2, consists of a heater surface, a temperature-specified design surface, and two adiabatic reflector surfaces. The heater and design surfaces are both diffuse and have an emissivity of $\varepsilon=1$, while the adiabatic surfaces are perfectly specular with a reflectivity $\rho=1$. A uniform heat input $q_{sHS}=1\ \mathrm{W/m^2}$ is maintained over the entire heater surface, while the design surface has an emissive power $E_{bDS}=0\ \mathrm{W/m^2}$.

The objective of the problem is to find the enclosure geometry that results in a uniform heat flux of $q_{sDS}=-1\ \mathrm{W/m^2}$ over the design surface, which is done by minimizing the objective function

$$\tilde{F}(\Phi)=\frac{1}{N_{DS}}\sum_{j=1}^{N_{DS}}[\tilde{q}_{sj}(\Phi)+1]^2, \tag{26}$$

where $\Phi=\{\Phi_1,\Phi_2\}^T$ control the x and y-coordinates of the upper left-hand vertex of the enclosure, respectively. The minimum of Eq. (26) is estimated by performing an unconstrained Kiefer-Wolfowitz minimization, starting at $\Phi_0=\{-0.5,0.5\}^T$. A personal computer with a Pentium III™ 600 MHz processor and 130 MB of RAM was used to perform the minimization.

As previously mentioned, assuming a uniform heat flux and emissive power distribution over each surface element produces discretization errors in the values of $\tilde{q}_{sj}(\Phi)$, and accordingly in $\tilde{F}(\Phi)$, that diminish with increasing levels of grid refinement. Therefore, it is necessary to perform a grid refinement study prior to the optimization process in order to estimate the discretization error in $\tilde{F}(\Phi)$, and to ensure that enough surface elements are used in the analysis. (This also helps the designer to choose a suitable convergence criterion, since seeking a value of $\tilde{F}(\Phi^*)$ smaller than the discretization error is computationally expensive and does not provide further improvement in solution quality.)

A grid-refinement study performed at $\Phi_0=\{-0.5,0.5\}^T$ is shown in Fig. 3. A constant ratio of bundles to elements, $N_{\mathrm{bundles}}/N=2\times10^5$, was used to obtain approximately the same sampling error at every level of refinement. An estimate of the grid-independent solution is obtained from the highest level of grid refinement, $\tilde{F}_\infty(\Phi_0)\approx\tilde{F}_{2048}(\Phi_0)=0.1690$. The discretization error at the next highest level of grid refinement, $N=1024$, is then estimated as -2.74×10^{-4}, or -1.6 percent of the grid-independent solution.

Next, the effect of the number of bundles on the random error, $\delta_1(\Phi)$, is demonstrated by systematically increasing the number

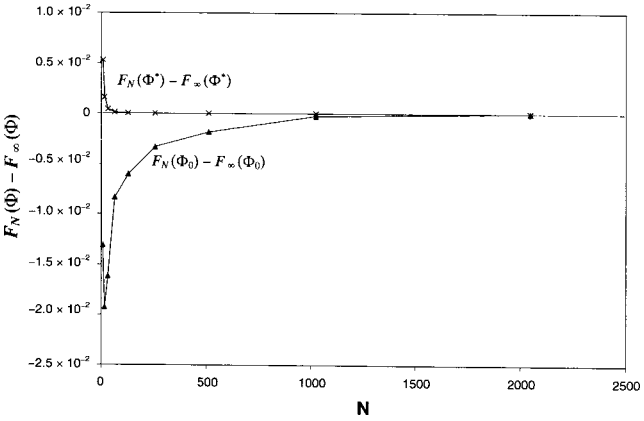

Fig. 3 Grid refinement study for the design problem of Fig. 2

of bundles used to calculate $\tilde{F}(\Phi_0)$ for an enclosure with $N=1024$ discrete surface elements. As shown in Fig. 4, a power-law relationship exists between the number of bundles and the random error,

$$\delta_1(\Phi_0) = 1.4320\, N_{\text{bundles}}^{-0.5272}, \tag{27}$$

which is consistent with the $1/\sqrt{N_{\text{bundles}}}$ trend predicted by the central limit theorem.

Based on the above results, the Kiefer-Wolfowitz minimization was carried out using $N=1024$ elements. In order to decrease $\delta_1(\Phi_k)$ as Φ_k approaches Φ^*, the number of bundles used in the simulation was increased with each successive iteration according to

$$N_{\text{bundles}} = A \log_{10} k + B, \tag{28}$$

where $A=160\times10^6$ and $B=20\times10^6$, chosen based on the results of the grid and bundle refinement studies. The minimization procedure is stopped when

$$|\tilde{F}(\Phi_k) - \tilde{F}(\Phi_{k-1})| < 1\times10^{-4}. \tag{29}$$

The resulting solution path is shown in Fig. 5. Eight steps, corresponding to 22 hours of CPU time, were required to identify a local minimum at $\Phi^* = \{0.0034, 0.8547\}^T$, with $\tilde{F}(\Phi^*) = 2.26\times10^{-4}$. The enclosure geometries corresponding to Φ_0 and Φ^* are shown in Fig. 6, while the heat flux distributions over the design surface are shown in Fig. 7. A grid refinement study performed on $\tilde{F}(\Phi^*)$ is also shown in Fig. 3, which demonstrates that a sufficient number of elements were used to identify the local minimum.

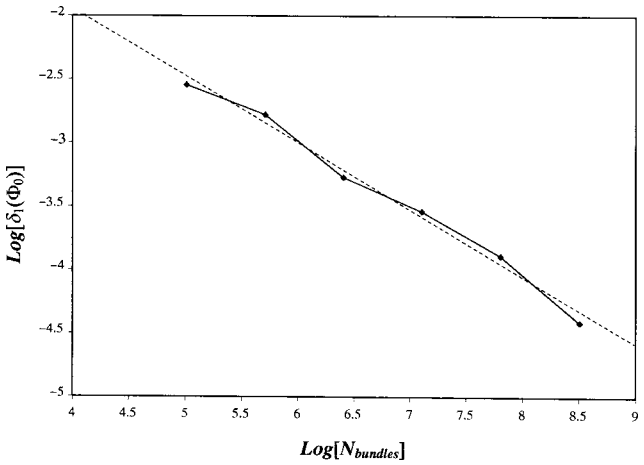

Fig. 4 Effect of number of bundles on $\delta_1(\Phi_0)$ for the design problem of Fig. 2

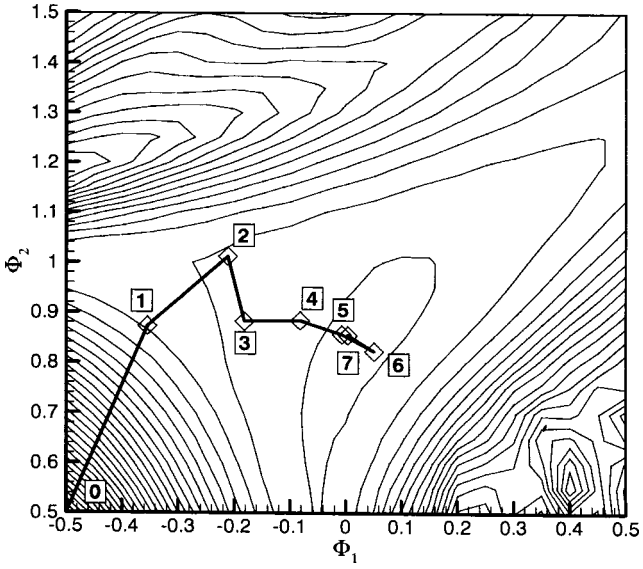

Fig. 5 Minimization path for design problem of Fig. 2

The second design problem is shown in Fig. 8, and is similar to the imaging furnace described by Maruyama [14]. The enclosure consists of a cylindrical heating element surrounded by six reflecting surfaces and a design surface. The heater surface is black and

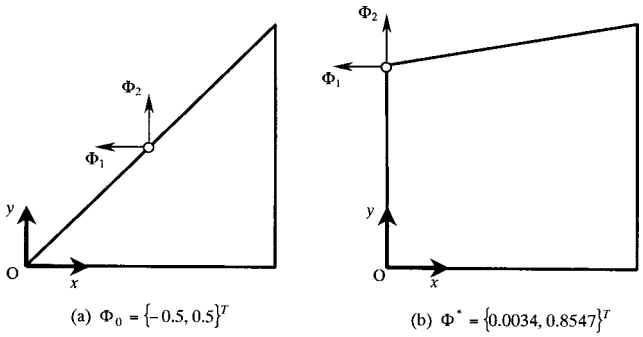

Fig. 6 Initial and final enclosure geometries for the design problem of Fig. 2

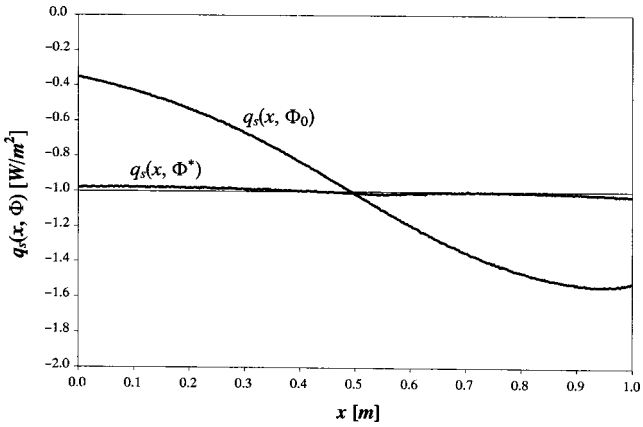

Fig. 7 Initial and final design surface heat flux distributions for the design problem of Fig. 2

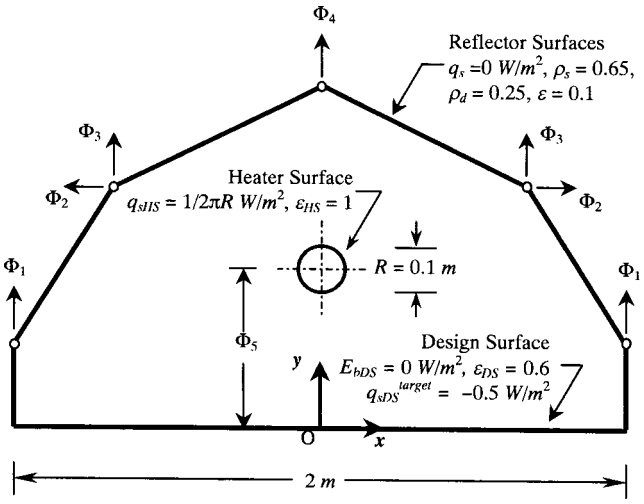

Fig. 8 Second radiant enclosure design problem

diffuse, and has a specified heat flux of $q_{sHS}=1/2\pi R$ W/m^2, where the radius of the heater element is $R=0.1$ m. The design surface has a specified emissive power $E_{bDS}=0$ W/m^2 and an emissivity of $\varepsilon_{DS}=0.6$. The reflecting surfaces are adiabatic and are specular-diffuse having the optical properties of polished nickel, with $\rho_s=0.65$, $\rho_d=0.25$, and $\varepsilon=0.1$ [15].

The objective of the design problem is to identify the enclosure configuration that most closely produces a heat flux of $q_{sDS}^{\text{target}}=-0.5$ W/m^2 over the design surface. The enclosure configuration is governed by five design parameters; Φ_1 through Φ_4 control the orientation of the reflector surfaces, while Φ_5 specifies the height of the heater element over the design surface. The optimal configuration is again determined by performing an unconstrained Kiefer-Wolfowitz minimization, starting from $\Phi_0=\{0.25, 0.75,0.75,1.25,0.5\}^T$. The minimization was carried out on a PC workstation with a Pentium OHM™ 2 GHz processor and 1000 MB of RAM.

Based on the results of a grid refinement study performed at Φ_0, 1024 surface elements were again used throughout the minimization process. A bundle refinement study performed at Φ_0 was used to select values for A and B in Eq. (27) equal to 6×10^6 and 5×10^5, respectively. The minimization procedure was stopped when

$$|\tilde{F}(\Phi_k)-\tilde{F}(\Phi_{k-1})|<1\times10^{-6}. \tag{30}$$

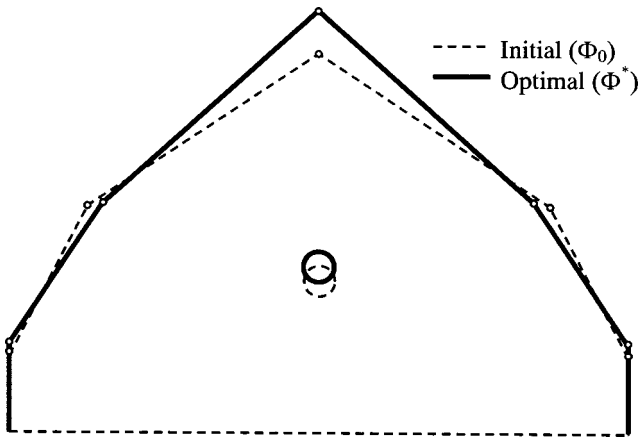

Fig. 9 Initial and final enclosure geometries for the design problem of Fig. 9

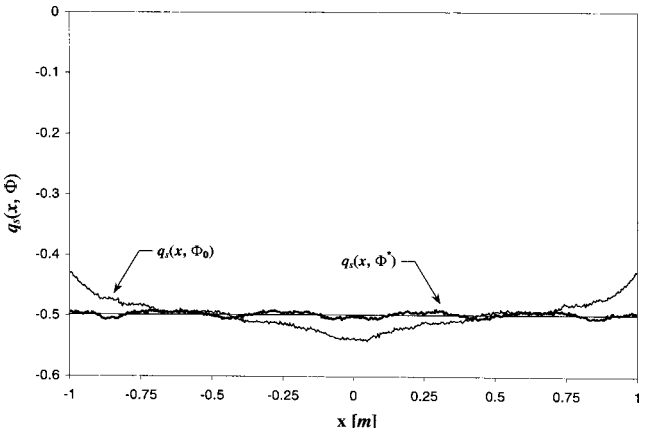

Fig. 10 Initial and final design surface heat flux distributions for the design problem of Fig. 9

Eighteen steps and forty hours of CPU time were required to identify a local minimum at $\Phi^*=\{0.2982,0.6980,0.7600,1.3935, 0.5588\}^T$ with $\tilde{F}(\Phi^*)=7.87\times10^{-5}$. The initial and final enclosure configurations are shown in Fig. 9, while the corresponding heat flux distributions are shown in Fig. 10.

One of the drawbacks of gradient-based minimization is that only one local minimum can be detected during a single minimization process. For example, it is clear from Fig. 5 that multiple local minima exist, and an alternate local minimum might have been detected if a different set of initial design parameters were chosen. The simplest remedy to this problem is to carry out multiple minimizations, each time starting from a different Φ_0. Although sophisticated multistart heuristic algorithms use this approach in an attempt to locate the global minimum (e.g., [16]), the CPU time associated with performing multiple local minimizations in this setting makes their application computationally intractable.

Conclusions and Future Work

Until recently, radiant enclosure geometry has almost exclusively been designed using a forward ''trial-and-error'' design methodology. This work describes an optimization methodology that facilitates the design of radiant enclosures containing specular surfaces; it requires far less design time, and the solution quality is usually much better than that obtained using the forward design methodology. In the optimization methodology, the primal problem is solved using a Monte Carlo technique based on exchange factors, and the optimization is carried out using the Kiefer-Wolfowitz method. The latter method is specialized for optimizing stochastic systems and is well suited to accommodate the random error inherent in the Monte Carlo technique. This methodology was successfully implemented to design the geometry of two two-dimensional radiant enclosures containing specularly-reflecting surfaces.

Acknowledgments

This work was supported by National Science Foundation Grants CTS 70545, DMI 9702217, and DMI 0217927, and the Natural Sciences and Engineering Research Council of Canada.

Nomenclature

a = step size coefficient, Eq. (4)
$\mathbf{A}$ = coefficient matrix for heat flux equation, Eq. (13)
A = coefficient for determining $N_{\text{bundles},k}$, Eq. (27)
b = interval length coefficient, Eq. (23)
$\mathbf{b}$ = right-hand vector for heat-flux equation
B = constant for determining $N_{\text{bundles},k}$, Eq. (27)

c_i = design constraint
$\mathbf{e}_p$ = unit vector in the pth direction
$E[\ ]$ = expectation function
E_{bi} = σT_i^4, W/m^2
$\%EI$ = energy imbalance, Eq. (25)
$F(\Phi)$ = objective function
$\mathfrak{F}_{ij}$ = exchange factor between ith and jth surface elements
$g(\Phi)$ = gradient vector
h_k = interval length for central-difference approximation at the kth iteration
k = iteration number
n = number of design parameters
N = number of finite surface elements
N_{bundles} = number of bundles used in Monte Carlo simulation
N_{DS} = number of surface elements on design surface
p = number of independent solutions used to estimate δ_1
$\mathbf{p}$ = search direction
q_s = heat flux, W/m^2
T = temperature, K
x = vector containing unknown values of q_{si} and E_{bi}

Subscripts and Superscripts

k = iteration number
$\tilde{}$ = value subject to statistical uncertainty

Greek Symbols

α = step size
$\delta_1(\Phi)$ = random error in $\tilde{F}(\Phi)$, Eq. (18)
$\delta_2(\Phi,h)$ = bias error in $g(\Phi)$ due to finite-difference approximation, Eq. (21)
$\delta_3(\Phi)$ = random error in $g(\Phi)$ due to δ_1, Eq. (22)
ε = surface emissivity
Φ = vector containing design parameters
Φ^* = design parameters corresponding to optimal solution
Φ_p = pth design parameter
Γ = variance-covariance matrix
ρ = surface reflectivity
σ = Stefan-Boltzmann constant
$\sigma_{i,ave}$ = random error associated with $\tilde{q}_{si}(\Phi)$, Eq. (15)
σ_i^2 = variance of samples obtained by stratified sampling, Eq. (16)
ξ = vector containing random variables used to find exchange factors

References

[1] Winston, R., 1991, ''Nonimaging Optics,'' Sci. Am., **264**, pp. 76–81.
[2] Güven, H. M., 1994, ''Optimization of Parabolic Trough Collector Design for Varying Manufacturing Tolerances Using a Closed-Form Expression for Intercept Factor,'' ASME J. Sol. Energy Eng., **116**, pp. 164–166.
[3] Ryan, J. P., Miller, J. A., and Burns, P. J., 1998, ''Development and Use of a Monte Carlo Code to Conduct a Parametric Study of Cylindrical Solar Collector Arrays,'' *Proceedings of the 1998 International Solar Energy Conference*, Albuquerque, NM, June 14th–17th.
[4] Muschaweck, J., Spirkl, W., Timinger, A., Benz, N., Dörfler, M., Gut, M., and Kose, E., 2000, ''Optimized Reflectors for Non-Tracking Solar Collectors With Tubular Absorbers,'' Sol. Energy, **68**, pp. 151–159.
[5] Ashdown, I., 1994, ''Non-Imaging Optics Design Using Genetic Algorithms,'' J. Illum. Eng. Soc., **23**, pp. 12–21.
[6] Bertsekas, D. P., 1999, *Nonlinear Programming 2nd ed.*, Athena Scientific, Belmont, MA, pp. 32–33.
[7] Modest M. F., 1993, *Radiative Heat Transfer*, McGraw-Hill Inc., New York, NY, pp. 669–702.
[8] Siegel, R., and Howell, J. R., 1992, *Thermal Radiation Heat Transfer, 3rd ed.*, Hemisphere Publishing Company, Washington D.C., pp. 480–504.
[9] Hammersely, J. M., and Handscomb, D. C., 1992, *Monte Carlo Methods*, Chapman and Hall, London, pp. 14.
[10] Kiefer, J., and Wolfowitz, J., 1952, ''Stochastic Estimation of the Maximum of a Regression Function,'' Ann. Math. Stat., **23**, pp. 462–466.
[11] Kushner, H. J., and Clark, D. S., 1978, *Stochastic Approximation Methods for Constrained and Unconstrained Systems*, Springer, New York, NY.
[12] Pflug, G. C., 1996, *Optimization of Stochastic Models: The Interface Between Simulation and Optimization*, Kluwer Academic Publishers, Boston, MA, pp. 281–288.
[13] Morton, D. P., and Popova, E., 2001, ''Monte Carlo Simulations for Stochastic Optimization,'' *Encyclopedia of Optimization*, C. A. Floudas and P. M. Pardalos, eds., Kluwer Academic Publishers, Boston, MA, pp. 439–447.
[14] Maruyama, S., 1993, ''Uniform Isotropic Emission Form an Involute Reflector,'' ASME J. Heat Transfer, **115**, pp. 492–495.
[15] Birkebak, R. C., Sparrow, E. M., Eckert, E. R. G., and Ramsey, J. W., 1964, ''Effect of Surface Roughness on the Total Hemispherical and Specular Reflectance on Metallic Surfaces,'' ASME J. Heat Transfer, **C87**, pp. 429–435.
[16] Ugray, Z., Lasdon, L., Plummer, J., Glover, F., Kelly, J., and Marti, R., 2002, ''A Mulitstart Scatter Search Heuristic for Smooth NLP and MINLP Problems,'' INFORMS J. Comput., in press.

Evaporation Heat Transfer and Pressure Drop of Refrigerant R-410A Flow in a Vertical Plate Heat Exchanger

Y. Y. Hsieh

T. F. Lin

Department of Mechanical Engineering,
National Chaio Tung University,
Hsinchu, Taiwan, R.O.C.

Experiments are carried out here to measure the evaporation heat transfer coefficient h_r and associated frictional pressure drop ΔP_f in a vertical plate heat exchanger for refrigerant R-410A. The heat exchanger consists of two vertical counterflow channels which are formed by three plates whose surface corrugations have a sine shape and a chevron angle of 60 deg. Upflow boiling of refrigerant R-410A receives heat from the hot downflow of water. In the experiments, the mean vapor quality in the refrigerant channel is varied from 0.10 to 0.80, the mass flux from 50 to 100 kg/m^2s, and the imposed heat flux from 10 to 20 kW/m^2 for the system pressure fixed at 1.08 and 1.25 MPa. The measured data indicate that both h_r and ΔP_r increase with the refrigerant mass flux except at low vapor quality. In addition, raising the imposed heat flux is found to significantly improve h_r for the entire range of the mean vapor quality. However, the corresponding friction factor f_{tp} is insensitive to the imposed heat flux and refrigerant pressure. Based on the present data, empirical correlations are provided for h_r and f_{tp}, for R-410A in the plate heat exchanger. [DOI: 10.1115/1.1518498]

Keywords: Boiling, Evaporation, Heat Transfer, Heat Exchangers

1 Introduction

Over the past decades the HCFC (hydrochlorofluorocarbon) refrigerant R-22 has been used as the working fluid in many refrigeration and air-conditioning systems. But it will be phased out in a short period of time (before 2020) since the chlorine it contains has an ozone depletion potential (ODP) of 0.055 and comparatively high global warming potential (GWP) of 1500 based on the time horizons of 100 years [1,2]. As a result, the search for a replacement for R-22 has been intensified in recent years. Owing to the fact that there are no single-component hydrofluorocarbons (HFCs) that have thermodynamic properties close to those of R-22, binary or ternary refrigerant mixtures have been introduced. The technical committee for the Alternative Refrigerants Evaluation Program (AREP) has proposed an updated list of the potential alternatives to R-22 [2]. Some of the alternatives on the AREP's list are R-410A, R-410B, R-407C and R-507. Currently, R-134a is extensively used in many systems. A number of investigations have been reported in the literature dealing with the phase change heat transfer of R-134a in ducts of various geometries. However, the two-phase boiling and condensation heat transfer characteristics for R-410A, R-410B, and R-407C have not been studied extensively. It should be mentioned here that refrigerant R-410A is a mixture of R-32 and R-125 (50 percent by mass) which exhibits azetropic behavior with a temperature glide of about 0.1°C.

A number of studies have been reported in the open literature on the R-22 evaporation heat transfer in various enhanced ducts such as microfin tubes [3,4], internally-fin tubes [5], and axially grooved tubes [6]. The measured data were compared with other common refrigerants. Recently, Sami and Poirier [7] compared the evaporation and condensation heat transfer data inside an enhanced tubing for several refrigerant blends proposed as substitutes for R-22, including R-410A, R-410B, R-507 and the quanternary mixture R-32/125/143a/134a. They showed that the two phase heat transfer coefficient and pressure drops all increased with the refrigerant mass flux. In a continuing study [8] they showed that in a double fluted tube for the refrigerant Reynolds number higher than 4.2×10^6, R-410A had better evaporation heat transfer than R-507. Wang et al. [9] compared the measured data for R-22 and R-410A flowing in a horizontal smooth tube and indicated that the heat transfer coefficients for R-410A were 10–20 percent higher than those for R-22 and the pressure drop of R-410A was about 30–40 percent lower than that of R-22. This outcome was attributed to the higher latent heat of vaporization, thermal conductivity and specific heat, and lower liquid viscosity for R-410A. In a similar study Ebisu and Torikoshi [10] indicated that the evaporation heat transfer coefficient of R-410A was 20 percent higher than that of R-22 up to the vapor quality of 0.4, while the heat transfer coefficients for both R-410A and R-22 became almost the same at the quality of 0.6. Furthermore, the pressure drop for R-410A was about 30 percent lower than that of R-22 during evaporation. The quantitative differences in the pressure drops between R-410A and R-22 were mainly attributed to the lower vapor density for R-410A. Wijaya and Spatz [11] reached a similar conclusion.

Plate heat exchangers (PHEs) have been widely used in food processing, chemical reaction processes and many other industrial applications due to their high effectiveness, compactness, flexibility, and cost competitiveness. Furthermore, they have been introduced to the refrigeration and air conditioning systems as evaporators or condensers. Recently, a number of investigations on PHEs were reported in the open literature. Unfortunately, these studies were mainly focused on the single-phase liquid-to-liquid heat transfer [12–15]. In view of this scarcity in the two-phase heat transfer data for PHEs, Yan and Lin [16] recently investigated the evaporation of R-134a in a vertical plate heat exchanger. They showed that that evaporation heat transfer for R-134a flowing in the PHE was much higher than that in circular tubes, particularly in high vapor quality convection dominated regime. Both the evaporation heat transfer coefficient and pressure drop increased

Contributed by the Heat Transfer Division for publication in the JOURNAL OF HEAT TRANSFER. Manuscript received by the Heat Transfer Division April 24, 2001; revision received July 25, 2002. Associate Editor: M. K. Jensen.

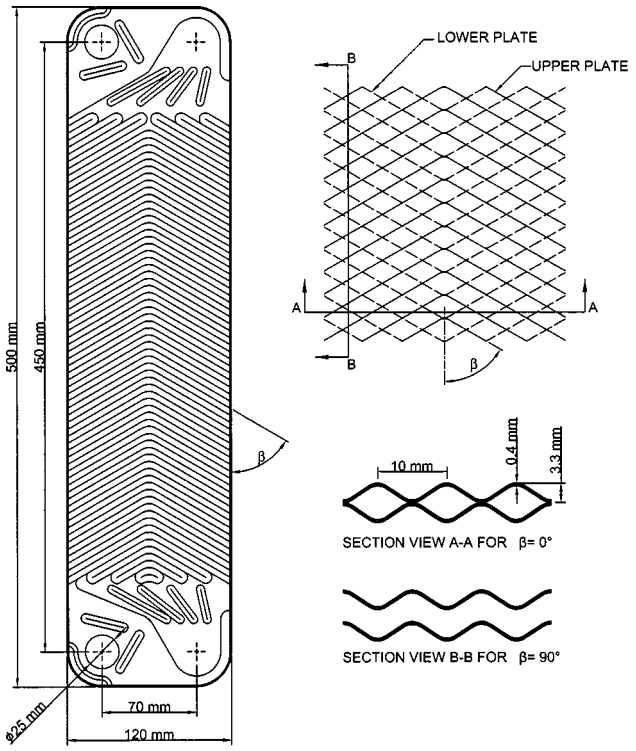

Fig. 1 Schematic diagram of the plate

with the refrigerant mass flux and vapor quality. Moreover, the rise in the heat transfer coefficient with the quality was larger than that in the pressure drop.

The above literature review clearly reveals that although R-410A is one of the most possible substitutes for R-22, the two-phase heat transfer data for R-410A are still scarce especially for PHEs. To complement our previous study on the two-phase heat transfer in the PHE [16], the evaporation heat transfer of R-410A in a vertical PHE is investigated in this study.

2 Experimental Apparatus and Procedures

The experiment apparatus established previously to explore the R-134a evaporation in a PHE [16] is used here to investigate the evaporation heat transfer and associated frictional pressure drop of R-410A in a vertical PHE. It includes a refrigerant loop, two water loops (one for preheater and the other for the test section), and a cold water-glycol loop. R-410A is circulated in the refrigerant loop. In order to control various test conditions of R-410A in the test section, we need to control the temperature and flow rate in the other three loops. The detailed description of the apparatus is available from our earlier study [16]. The refrigerant flow rate is measured by an accurate mass flux meter manufactured by Mircomotion (Type UL-D-IS) with a reading accuracy of ± 1 percent. Here only the test section employed in the experiment is described in some detail.

Three commercial SS-316 plates manufactured by the Kaori Heat Treatment Co. Ltd., Taiwan, form the plate heat exchanger (test section). The plate surfaces are pressed to become grooved with a corrugated sinusoidal shape and 60 deg of chevron angle β. The detailed configuration of the PHE can be seen in Fig. 1. The corrugated grooves on the right and left outer plates have a V shape but those in the middle plate have a contrary V shape on both sides. This arrangement allows the flow stream to be divided into two different flow directions along the plates. Thus, the flow moves mainly along the grooves in each plate. Due to the contrary V shapes between two neighbor plates the flow streams near the two plates cross each other in each channel. This cross flow results in significant flow unsteadiness and randomness. In the PHE the upflow of R-410A in one channel is heated by the downflow of the hot water in the other channel. The heat transfer rate in the test section is calculated by measuring the total water temperature drop in the water channel and the water flow rate.

In each test the system pressure at the test section is first maintained at a specified level. Then, the vapor quality of R-410A at the test section inlet is kept at the desired value by adjusting the temperature and flow rate of the hot water loop for the preheater. Next, the heat transfer rate between the counterflow channels in the test section can be varied by changing the water temperature and flowrate in the water loop for the tests section. Meanwhile, the R-410A mass flow rate in the test section is maintained at a desired value.

In the test any changes of the system variables will lead to fluctuations in the temperature and pressure of the refrigerant flow. It takes about 20–100 minutes for the system to reach a statistically stable state at which variations of the time-average inlet and outlet temperatures are both less than ± 0.2°C, and the variations of the pressure and imposed heat flux are within 1 percent and 4 percent, respectively. Then the data acquisition unit is initiated to scan all the data channels for ten times in 50 sec. The mean value of the data for each channel is used to calculate the evaporation heat transfer coefficient and the associated frictional pressure drop. Additionally, the flow rate of water in the test section should be high enough to have turbulent flow in the water side so that the associated single-phase heat transfer in it is high enough for balancing the evaporation heat transfer in the refrigerant side.

Before examining the R-410A evaporation heat transfer characteristics, a preliminary test for single-phase water-to-water convective heat transfer in the vertical PHE is performed. The Wilson's method [17] is adopted to calculate the relation between the single-phase heat transfer coefficient and the flow rate from these data. The result obtained can then be used to analyze the data acquired from the evaporation heat transfer experiments.

The uncertainties of the experimental results are analyzed by the procedures proposed by Kline and McClintock [18]. This analysis indicates that the uncertainties for the data of the imposed heat flux q, mass flux G, pressure P, pressure drop ΔP, average vapor quality X_m single phase heat transfer coefficient h_w, evaporation heat transfer coefficient h_r, and friction factor f_{tp} are respectively ± 6.5 percent, ± 2 percent, ± 1 percent, ± 1.5 percent, ± 8 percent, ± 11 percent, ± 14.5 percent, and ± 16.5 percent.

3 Data Reduction

The data reduction analysis detailed in our earlier study for R-134a evaporation [16] is also used here to deduce the R-410A evaporation heat transfer coefficient and associated frictional pressure drop from the measured raw data. Specifically, the data from the single-phase water-to-water heat transfer tests are analyzed by the modified Wilson plot [17]. The single phase convection heat transfer coefficient in a PHE, suggested by Shah and Focke [12], can be expressed empirically as

$$h_w = C \cdot \left(\frac{k}{D_h}\right) \cdot \mathrm{Re}^n \cdot \mathrm{Pr}^{1/3} \cdot \left(\frac{\mu}{\mu_{\mathrm{wall}}}\right)^{0.14} \tag{1}$$

Here the constants C and n can be determined from the Wilson plot.

To evaluate the evaporation heat transfer coefficient of the refrigerant flow, the total heat transfer rate Q_w between the counter flows in the PHE is calculated first from the hot water side. Then, the refrigerant vapor quality at the test section inlet is evaluated from the energy balance for the preheater. The change in the refrigerant vapor quality in the test section is then deduced from the total heat transfer rate to the refrigerant in the test section,

$$\Delta X = \frac{Q_w}{W_r \cdot i_{fg}} \tag{2}$$

The determination of the overall heat transfer coefficient for the evaporation of refrigerant R-410A in the PHE is based on the heat transfer between the counter-flow channels and is expressed as

$$U = \frac{Q_w}{A \cdot \mathrm{LMTD}} \tag{3}$$

The log-mean temperature difference (LMTD) is determined from the inlet and exit temperatures in the two channels. According to the thermal resistances for heat transfer across the channel, the evaporation heat transfer coefficient in the flow of R-410A is evaluated from the equation

$$\left(\frac{1}{h_r}\right) = \left(\frac{1}{U}\right) - \left(\frac{1}{h_w}\right) - R_{\mathrm{wall}} \cdot A \tag{4}$$

where h_w is calculated from the single-phase water-to-water heat transfer test.

In order to obtain the friction factor associated with the R-410A evaporation in the refrigerant channel in the vertical PHE, the frictional pressure drop ΔP_f is calculated by subtracting the acceleration pressure drop, the pressure losses at the test section inlet and exit manifolds and ports, and the elevation pressure rise from the measured total pressure drop in the refrigerant channel. The acceleration pressure drop and elevation pressure rise are estimated by the homogeneous model for two phase gas-liquid flow [19]. The pressure drop in the inlet and outlet manifolds and ports was empirically suggested by Shah and Focke [12]. Based on the above estimation, the acceleration pressure drop and the pressure losses at the test section inlet and exit manifolds and ports are found to be rather small. In fact, the summation of these two pressure losses ranges from 1 percent to 3 percent of the total pressure drop. The pressure drop due to the elevation difference between the inlet and outlet ports of the PHE is smaller than 1 percent of the total pressure drop. According to the definition

$$f_{tp} = -\frac{\Delta P_f \cdot D_h}{2G^2 \cdot v_m \cdot L} \tag{5}$$

the friction factor for the evaporation of R-410A in the PHE is obtained

4 Results and Discussion

The single phase water-to-water convection heat transfer coefficient for the present vertical plate heat exchanger deduced from the modified Wilson plot can be correlated as

$$h_w = 0.2092 \cdot \left(\frac{K_1}{D_h}\right) \cdot \mathrm{Re}^{0.78} \cdot \mathrm{Pr}^{1/3} \cdot \left(\frac{\mu_m}{\mu_{\mathrm{wall}}}\right)^{0.14} \tag{6}$$

with the regression accuracy of 0.997. Here the viscosities μ_m and μ_{wall} are, respectively, based on the average bulk water and wall temperatures estimated by averaging the measured inlet and outlet temperatures in the hot and cold sides. The present single-phase heat transfer data well agree with Eq. (18) in the study of Muley and Manglik [13], as is clear from Fig. 2.

Effects of the refrigerant mass flux, imposed heat flux and system pressure on the evaporation heat transfer of R-410A in the vertical PHE are illustrated in Fig. 3 by presenting the changes of the R-410A evaporation heat transfer coefficient with the refrigerant vapor quality at the imposed heat fluxes $q=10$ and 20 kw/m^2 for refrigerant mass fluxes $G=50$ to 100 kg/m^{2}s, system pressures $P=1.08$ and 1.25 MPa ($T_{\mathrm{sat}}=10$°C and 15°C). In these plots X_m denotes the mean R-410A vapor quality in the PHE. The total change in the vapor quality ΔX in the test section for the present study ranges from 0.126 and 0.337. The data in Fig. 3 clearly indicate that a given heat flux, mass flux and system pressure the evaporation heat transfer coefficient increases noticeably with the mean vapor quality of the refrigerant in the PHE. For example, at $G=75$ kg/m^{2}s, $P=1.08$ MPa, and $q=10$ kW/m^2 the evaporation heat transfer coefficient at X_m of 0.8 is about 60 percent higher than that at 0.1 (Fig. 3(*a*)).This significant increase of h_r with X_m obviously results from the fact that in the high vapor quality regime, intense evaporation at the liquid-vapor interface diminishes the thickness of the liquid film on the plate surface to a noticeable degree. This, in turn, reduces the resistance of heat transfer from the channel surface to the refrigerant. Furthermore, the data also show that a rise in the refrigerant mass flux always produces an evident increase in the evaporation heat transfer coefficient except at the low vapor quality regime. In fact, at low vapor quality ($X_m<.20$) the evaporation heat transfer coefficient is insensitive to the refrigerant mass flux. This can be ascribed to the fact that the interfacial evaporation of the liquid film on the plate is largely suppressed at low vapor quality. Moreover, the evaporation heat transfer coefficient for the higher mass flux rises more quickly with the vapor quality than that for the lower mass flux. This larger increase in h_r with X_m at a higher G is considered to result from the more intense turbulence in the flow for a higher G. Similar results were noted for other system pressures. The results in Fig. 3 further show that the evaporation heat transfer coefficient increases significantly with the imposed heat flux for both pressures. For example, at $G=75$ cg/m^{2}s and $P=1.08$ MPa the quality-average evaporation heat transfer coefficients at 20 kW/m^2 is about 32 percent higher than that at 10 KW/m^2. This large increase in the evaporation heat transfer coefficient is ascribed to the higher wall superheat and thinner liquid film on the plate surface for a higher imposed heat flux. It is also noted that the evaporation heat transfer is slightly better at the lower pressure for a higher vapor quality ($X_m>0.6$). At the low vapor quality for $X_m<0.5$ the effects of the pressure on the evaporation heat transfer is insignificant except for $q=20$ kW/m^2 and $G=100$ kg/m^{2}s (Fig. 3(*b*)). This is attributed to the fact that the density of the R-410A vapor is lower at a lower saturated pressure, which causes the vapor flow to move in a higher speed and hence the higher evaporation heat transfer coefficient.

We also compare the present data for the R-410A evaporation heat transfer in the PHE with those for R-134A in the same PHE

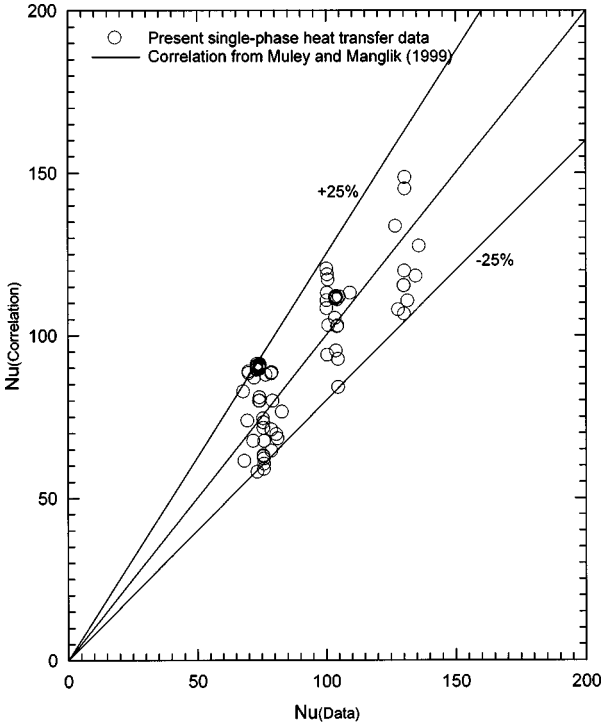

Fig. 2 Comparison of the present single-phase water convection heat transfer data with the correlation from Muley and Manglik [13]

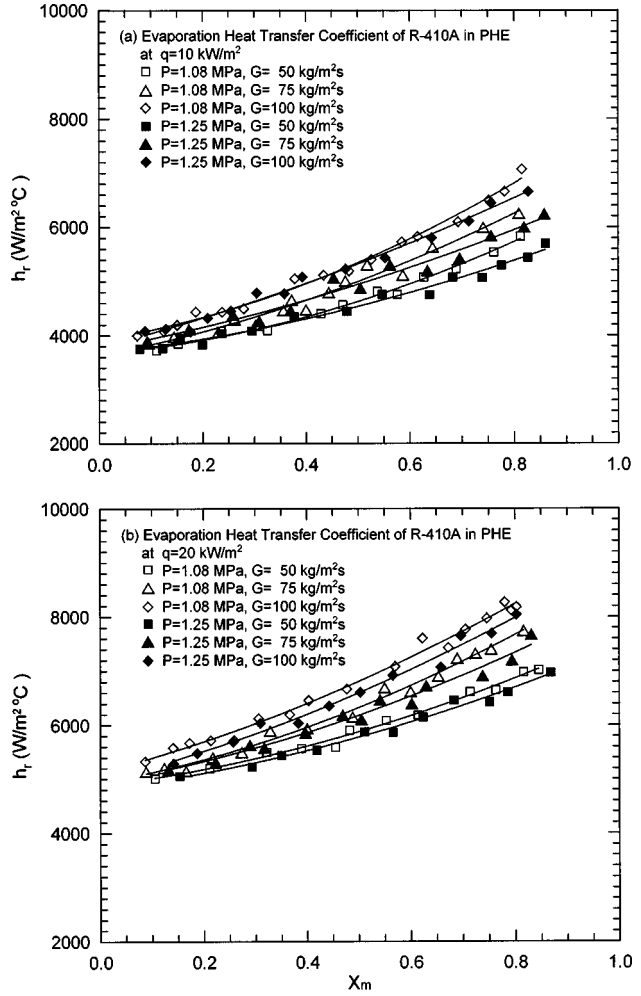

Fig. 3 Variations of evaporation heat transfer coefficient with mean vapor quality for various system pressures and refrigerant mass fluxes at (*a*) $q=10$ kW/m^2 and (*b*) $q=20$ kW/m^2

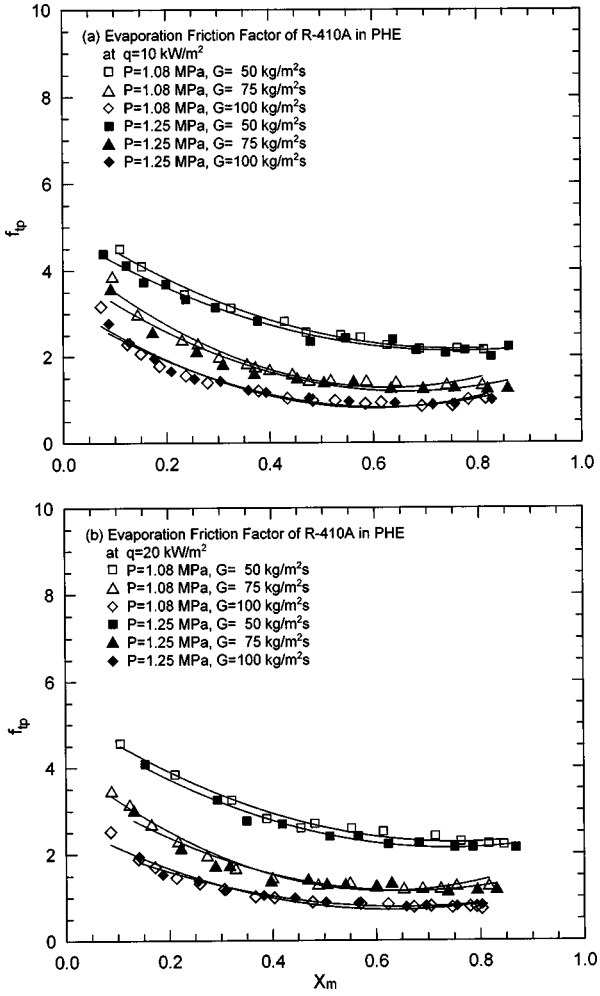

Fig. 4 Variations of friction factor with mean vapor quality for various system pressures and refrigerant mass fluxes at (*a*) $q=10$ kW/m^2 and (*b*) $q=20$ kW/m^2

reported by Yan and Lin [16] and with those for R-410A in a horizontal smooth pipe collected by Ebisu and Torikoshi [10]. This comparison indicates that the R-410A evaporation heat transfer coefficient is higher than that for R-134a in the PHE to a noticeable degree except at high vapor quality for $X_m > 0.75$. More specifically, at high X_m the R-134a evaporation is more effective. These opposite trends in different vapor quality ranges are attributed mainly to the different thermal conductivities of the two refrigerants for the liquid and vapor phases. Specifically, the liquid thermal conductivity for R-410A is higher than that for R-134a by about 20 percent. However, the vapor thermal conductivity for R-410A is lower than that for R-134a. Hence, at lower quality the evaporation heat transfer coefficient for R-410A is higher than that for R-134a. The results suggest that the evaporation heat transfer in the PHE is dominated by the heat transfer associated with the liquid film evaporation. The comparison also shows that for R-410A the evaporation heat transfer coefficient in the PHE is substantially higher than that in a horizontal smooth tube.

The friction factor, defined in Eq. (5), associated with the R-410A evaporation in the PHE obtained in the present study are presented in Fig. 4. The results indicate that the friction factor significantly decreases with the increase in the refrigerant mass flux. For example, at $P=1.08$ MPa, $G=100$ kg/m^{2}s, and $q=10$ kW/m^2, the quality-average fraction factor is respectively about 50 percent and 30 percent lower than those for $G=50$ and 75 kg/m^{2}s (Fig. 4(*a*)). Besides, the friction factor decreases significantly with the increase in the mean vapor quality at low vapor quality ($X_m < 0.4$). At high vapor quality for $X_m < 0.5$, the effect of the vapor quality on the friction factor is insignificant. It is of interest to note that the friction factor is not affected to a noticeable degree by the imposed heat flux and refrigerant pressure. We also note that for $X_m > 0.5$ the frictional pressure drop of R-410A evaporation in the PHE is substantially lower than that for R-134a in the same PHE, but is much higher than in a smooth horizontal pipe for all X_m. The lower frictional pressure drop for R-410A evaporation can be attributed to the fact that the densities and viscosities of R-410A vapor and liquid are lower than those of R-134a.

Correlation equations for the heat transfer coefficient and friction factor associated with the R-410A evaporation in the vertical PHE are important for thermal design of evaporators in various air conditioning and refrigeration systems. Based on the present data, an empirical correlation for the evaporation heat transfer coefficient is proposed by considering the convective and nucleate boiling contributions [20]. It is expressed as

$$h_r = E \cdot h_1 + S \cdot h_{\text{pool}}, \quad \text{for} \quad 2000 < \text{Re} < 12{,}000 \quad \text{and} \quad 0.0002 < \text{Bo} < 0.0020 \tag{7}$$

Here h_1 and h_{pool} are respectively given by the Dittus-Boelter Eq. [21] and Cooper [22] as

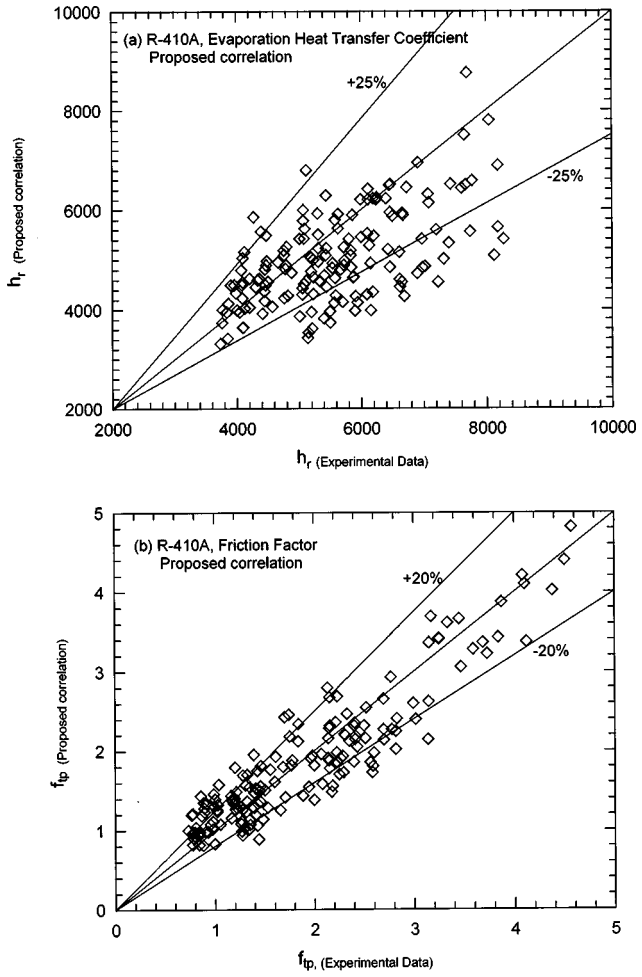

Fig. 5 Comparison of the proposed correlations with the present data for (*a*) the heat transfer coefficient and (*b*) the friction factor

$$h_1 = 0.023 \cdot \mathrm{Re}_1^{0.8} \cdot \mathrm{Pr}^{0.4} \cdot (k_1/D_h) \tag{8}$$

$$h_{\mathrm{pool}} = 55 \cdot P_r^{0.12} \cdot (-\log_{10} P_r)^{-0.55} \cdot M^{-0.5} \cdot q^{0.67} \tag{9}$$

Besides, E and S respectively represent the enhancement and suppression factors, which are dependent on the boiling number Bo, the Martnelli parameter X_{tt} and liquid Reynolds number Re_1. The expressions for E and S are

$$E = 1 + 24{,}000 \cdot \mathrm{Bo}^{1.16} + 1.37\left(\frac{1}{X_{tt}}\right)^{0.86} \tag{10}$$

$$S = (1 + 1.15 \times 10^{-6} \cdot E^2 \cdot \mathrm{Re}_1^{1.17})^{-1} \tag{11}$$

The friction factor is correlated as

$$f_{tp} = 23{,}820 \cdot \mathrm{Re}_{\mathrm{eq}}^{-1.12}, \quad \text{for} \quad 2000 < \mathrm{Re} < 12{,}000 \quad \text{and} \quad 0.0002 < \mathrm{Bo} < 0.0020 \tag{12}$$

where $\mathrm{Re}_{\mathrm{eq}}$ is the equivalent Reynolds number and is defined as

$$\mathrm{Re}_{\mathrm{eq}} = \frac{G_{\mathrm{eq}} \cdot D_h}{\mu_1} \tag{13}$$

in which

$$G_{\mathrm{eq}} = G\left[(1 - X_m) + X_m \cdot \left(\frac{\rho_1}{\rho_g}\right)^{1/2}\right] \tag{14}$$

Here G_{eq} is an equivalent mass flux which is a function of the R-410A mass flux, mean vapor quality and densities at the saturated conditions. Figure 5 shows that more than 74 percent of the present experimental data for h_r fall within ± 25 percent of Eq. (7), and the average deviation between the present data for f_{tp} and the proposed correlation is about 18 percent.

5 Concluding Remarks

Experiments have been carried out here to investigate the evaporation heat transfer and the associated frictional pressure drop for the ozone friendly refrigerant R-410A in a vertical plate heat exchanger. The effects of the refrigerant mass flux, imposed heat flux, system pressure and vapor quality of R-410A on the evaporation heat transfer coefficient and friction factor were examined in detail. A summary of the major findings is given in the following.

1. The evaporation heat transfer coefficient and frictional pressure drop normally increases with the refrigerant mass flux and vapor quality. It is also noted that the evaporation heat transfer coefficient is only slightly affected by the refrigerant mass flux at low vapor quality. Furthermore, the increase of the frictional pressure drop with the vapor quality is more evident than the rise of the heat transfer.
2. A rise in the imposed heat flux results in a significant increase in the evaporation heat transfer coefficient. Nevertheless the influences of the imposed heat flux and system pressure on the friction factor are rather slight.
3. Empirical correlation for the R-410A evaporation heat transfer coefficient and friction factor in the PHE were provided to facilitate the design in various thermal systems.

Acknowledgments

The financial support of this study by the engineering division of National Science Council of Taiwan, R.O.C. through the contract NSC 85-2221-E-009-06 is greatly appreciated

Nomenclature

A = heat transfer area of the plate, m^2
Bo = boiling number, $\mathrm{Bo} = q/G \cdot i_{fg}$, dimensionless
c_p = specific heat, J/kg°C
D_h = hydraulic diameter, $D_h = 2b, m$
E, S = enhancement and suppression factors
f_{tp} = two-phase friction factor
G = refrigerant mass flux, kg/m^2s
G_{eq} = equivalent all liquid mass flux in Eqs. (13, 14)
h = heat transfer coefficient, $W/m^2°C$
i_{fg} = enthalpy of evaporation, J/kg
k = conductivity, W/m°C
L = plate length from center of inlet port to center of exit port, m
LMTD = log mean temperature difference, °C
M = molecular weight
Nu = Nusselt number, $\mathrm{Nu} = h_w \cdot D_h/k_1$, dimensionless
P = pressure, Pa
Pr = Prandtl number, $\mathrm{Pr} = \mu \cdot c_p/k$, dimensionless
Q_w = total heat transfer rate, W
q = imposed heat flux, W/m^2
R_{wall} = thermal resistance of the wall
Re = Reynolds number, $\mathrm{Re} = G \cdot D_h/\mu$, dimensionless
$\mathrm{Re}_{\mathrm{eq}}$ = equivalent all liquid Reynolds number in Eqs. (12, 13)
U = overall heat transfer coefficient, $W/m^2°C$
v_m = specific volume of the vapor-liquid mixture, m^3/kg
W = mass flow rate, kg/s
X_m = mean vapor quality
X_{tt} = Martinelli parameter, dimensionless

Greek Symbols

ΔP_f = frictional pressure drop
ΔX = total quality change in the exchanger
β = chevron angle
μ = viscosity, Ns/m^2
ρ = density, kg/m^3

Subscripts

g = vapor phase
l = liquid phase
m = mean value for the two-phase mixture in the exchanger
pool = pool boiling
r = reduced, refrigerant
w = water
wall = wall/fluid near the wall

References

[1] Newman, P. A., 1988, ''Preserving Earth's Stratosphere,'' Mech. Eng. (Am. Soc. Mech. Eng.), **120**, pp. 88–91.
[2] Gopalnarayanan, S., 1998, ''Choosing the Right Refigerant,'' Mech. Eng. (Am. Soc. Mech. Eng.), **120**, pp. 92–95.
[3] Chamra, L. M., and Webb, R. L., 1996, ''Advanced Micro-Fin Tubes for Evaporation,'' Int. J. Heat Mass Transf., **39**, pp. 1827–1838.
[4] Schlager, L. M., Pate, M. B., and Bergles, A. E., 1990, ''Evaporation and condensation Heat Transfer and Pressure Drop in Horizontal 12.7-mm Microfin Tubes With Refrigerant 22,'' ASME J Heat Transfer, , **112**, pp. 1041–1047.
[5] Kubanek, G. R., and Miletti, D. L., 1979, ''Evaporative Heat Transfer and Pressure Drop Performance of Internally-Finned Tubes With Refrigerant 22,'' ASME J. Heat Transfer, , **101**, pp. 447–452.
[6] Liu, X., 1997, ''Condensing and Evaporating Heat Transfer and Pressure Drop Characteristics of HFC-134a and HCFC-22,'' ASME J. Heat Transfer, , **119**, pp. 158–163.
[7] Sami, S. M., and Poirier, B., 1997, ''Comparative Study of Heat Transfer Characteristics of New Alternatives to R-22,'' ASHRAE Trans., **103**, pp. 824–829.
[8] Sami, S. M., and Poirier, B., 1998, ''Two Phase Flow Heat Transfer of Binary Mixtures Inside Enhanced Surface Tubing,'' Int. Commun. Heat Mass Transfer, **25**, pp. 763–773.
[9] Wang, C. C., Yu, J. G., Lin, S. P., and Lu, D. C., 1998, ''An Experimental Study of Convective Boiling of Refrigerant R-22 and R-410A,'' ASHRAE Trans., **104**, pp. 1144–1150.
[10] Ebisu, T., and Torikoshi, K., 1998, ''Heat Transfer Characteristics and Correlations for R-410A Flowing Inside a Horizontal Smooth Tube,'' ASHRAE Trans., **104**, pp. 556–561.
[11] Wijaya, H., and Spatz, M. W., 1995, ''Two-Phase Flow Heat Transfer and Pressure Drop Characteristics of R-22 and R-32/R125,'' ASHRAE Trans., **101**, pp. 1020–1027.
[12] Shah, R. K., and Focke, W. W., 1988, ''Plate Heat Exchangers and their Design Theory,'' *Heat Transfer Equipment Design*, R. K. Shah, E. C. Subbarao, and Mashelkar, R. A., eds. Hemisphere, Washington, pp. 227–254.
[13] Muley, A., and Manglik, R. M., 1999, ''Experimental Study of Turbulent Flow Heat Transfer and Pressure Drop in a Plate Heat Exchanger With Chevron Plates,'' ASME J. Heat Transfer, , **121**, pp. 110–117.
[14] Muley, A., Manglik, R. M., and Metwally, H. M., 1999, ''Enhanced Heat Transfer Characteristics of Viscous Liquid Flows in a Chevron Plate Heat Exchanger,'' ASME J. Heat Transfer, , **121**, pp. 1011–1017.
[15] Thonon, B., Vidil, R., and Marvillet, C., 1995, ''Recent Research and Developments in Plate Heat Exchangers,'' J. of Enhanced Heat Transfers, **2**, pp. 149–155.
[16] Yan, Y. Y., and Lin, T. F., 1999, ''Evaporation Heat Transfer and Pressure Drop of Refrigerant R-134a in a Plate Heat Exchanger,'' ASME J. Heat Transfer, , **121**, pp. 118–127.
[17] Wilson, E. E., 1915, ''A Basic for Traditional Design of Heat Transfer Apparatus,'' Trans. ASME, **37**, pp. 47–70.
[18] Kline, S. J., and McClintock, F. A., 1953, ''Describing Uncertainties in Single-Sample Experiments,'' Mech. Eng. (Am. Soc. Mech. Eng.), **75**, pp. 3–12.
[19] Collier, J. G., 1981, *Convective Boiling and Condensation*, 2nd ed., McGraw-Hill, New York, pp. 26–69.
[20] Gungor, K. E., and Winterton, R. H. S., 1986, ''A General Correlation for Flow Boiling in Tubes and Annuli,'' Int. J. Heat Mass Transf., **29**, pp. 351–358.
[21] Incropera, F. P., and Dewitt, D. P., 1981, *Fundamentals of Heat Transfer*, John Wiley & Sons, New York, p. 406.
[22] Cooper, M. G., 1984, ''Saturation Nucleate Pool Boiling: A Simple Correlation,'' 1st U.K. National Conference on the Heat Transfer, **2**, pp. 785–793.

Short-Time-Transient Surfactant Dynamics and Marangoni Convection Around Boiling Nuclei

Vivek M. Wasekar

Raj M. Manglik
Mem. ASME
e-mail: Raj.Manglik@uc.edu

Thermal-Fluids and Thermal Processing Laboratory,
Department of Mechanical, Industrial and Nuclear Engineering,
University of Cincinnati,
Cincinnati, OH 45221-0072

The effects of surfactant concentration on the initial short-time-scale Marangoni convection around boiling nuclei in aqueous solutions have been computationally investigated. The model consists of a hemispherical bubble (1–100 μm radius) on a downward-facing constant-temperature heated wall in a fluid pool with an initial uniform temperature gradient. Time-dependent transport of liquid mass, momentum, energy, and surfactant bulk and surface convection along with the adsorption kinetics are considered. Conditions for bubble sizes, surfactant bulk concentrations, and wall heat flux levels are represented by a range of thermocapillary and diffusocapillary Marangoni numbers ($6 \leqslant Ma_T \leqslant 10^3$, $0 \leqslant Ma_S \leqslant 8.6 \times 10^5$) over a micro-scale time period (1 μs–1 ms). With a surfactant in solution, a surface concentration gradient develops at the bubble interface that tends to oppose the temperature gradient and reduce the overall Marangoni convection. The maximum circulation strength, which is dependent on the bubble size, corresponds to a characteristic surfactant adsorption time. This, when scaled by a ratio of bubble radius, is found to depend solely on the surfactant bulk concentration. Moreover, the interfacial surfactant adsorption does not display a stagnant cap behavior for the range of parameters and time scales covered in this study. [DOI: 10.1115/1.1599367]

Keywords: Additives, Bubble Growth, Heat Transfer, Interface, Microscale, Thermocapillary

Introduction

Boiling heat transfer in water and the attendant ebullient behavior is altered considerably when surfactants are present in solution [1]. Depending upon the additive bulk concentration, the heat transfer is usually enhanced with an optimum increase occurring at or around the critical micelle concentration (c.m.c.) of the surfactant [2–4]; the c.m.c. is described by the state where colloid-sized clusters or micelar aggregates in bulk-phase are formed in solutions [5]. Of the different mechanisms that come into play [1,6], the transport of surfactant molecules from the bulk solution towards the growing vapor-bubble interface is possibly the most critical to the modification of the bubble dynamics during boiling in aqueous surfactant solutions. While the variation in temperature along the bubble interface induces thermocapillary convection in the surrounding fluid, the presence of concentration gradients due to non-uniform surfactant adsorption at the vapor-liquid interface lead to diffusocapillary convection. Both these types of Marangoni convection may play a significant role in the heat removal process during nucleate boiling.

In one of the early studies, McGrew et al. [7] identified the mechanism of thermo-capillary convection at the bubble interface in nucleate boiling of water. Their observations are further supported by the experimental findings of Huplik and Raithby [8], Straub et al. [9], Arlabosse et al. [10], Baranenko and Chichkan [11], and Straub [12] for microgravity boiling, and Marek and Straub [13] for subcooled pool boiling. Thermocapillary convection is generally characterized by a strong jet-type flow that projects outward from the bubble crown with cooler liquid being drawn inward toward the heater surface and the bubble base. The temperature nonuniformity along the bubble surface during these flows, with peak temperature gradients of 55 to 115 K/mm, has been shown in several holographic and interferometric studies [14,15]. Also, increasing temperature gradients and decreasing bubble diameters tend to increase the resultant intensity of thermal convection.

Air-bubble studies, despite their adiabatic conditions and utility in non-boiling applications, have provided a controlled method to understand the mechanism of Marangoni convection during boiling. Several experimental [16–18] and numerical [19–24] investigations are reported in the literature that address thermocapillary convection around nongrowing air bubbles in both terrestrial and microgravity conditions. Relatively few studies [8,21] have considered the effects of surfactant additives on Marangoni convection. For steady-state computations, Kao and Kenning [21] assumed a stagnant cap, similar to that observed on drops and bubbles moving in surfactant solutions [25], and found an overall suppression of convection. Stagnant cap behavior refers to an immobile portion of the bubble interface, which is modeled by the no-slip boundary condition while the rest of the interface allows slip. However, boiling is a dynamic process, where typical bubble life times are about 15 to 50 ms [26–34] (see Table 1) and, with surfactant diffusion times of 5 to 10 ms [35–37], a stagnant cap may not be formed. Furthermore, surfactant-specific adsorption kinetics, which is generally dependent upon the additive's molecular structure, ionic nature, and molecular weight, among other factors, governs the surface excess concentrations [38–40], which in turn drive diffusocapillary flows.

In macro-surface boiling, surface tension forces become appreciably important at small length and time scales, when bubble growth tends to be influenced by the short-time-transient heat transfer mechanism associated with the temperature-gradient-driven Marangoni convection around the boiling nuclei. The nucleating cavity sizes for water typically range from 1–100 μm (Table 1), which effectively represent the length scale of incipient bubbles. In surfactant solutions, the surface tension is depressed considerably and relatively smaller cavities tend to nucleate. Also, with somewhat comparable time scales for surfactant diffusion in water and bubble growth, and the nonuniform surfactant adsorption at the vapor-liquid interface, a concentration gradient devel-

Contributed by the Heat Transfer Division for publication in the JOURNAL OF HEAT TRANSFER. Manuscript received by the Heat Transfer Division September 18, 2002; revision received May 16, 2003. Associate Editor: V. P. Carey.

Table 1 Typical ranges of cavity sizes and bubble growth times for saturated boiling of pure water and aqueous surfactant solutions

Cavity sizes $\sim r_b$ [μm]		Bubble growth times [ms]	
	Pure water		
10–100	Hsu [26]	25–30	Dergarabedian [27]
3–30	Kenning and Cooper [28]	15–20	Han and Griffith [29]
1–10	Gaddis [20]	15–25	Hahn and Ribeiro [30]
12–100	Kant and Weber [31]	20–50	Son et al. [32]
	Aqueous surfactant solutions		
5–10	Wu et al. [33]	10–30	Wu and Yang [34]
		5–20	Wu et al. [33]

ops around the bubble that induces diffusocapillary flows in the surrounding bulk fluid. The combined influence of thermocapillary and diffusocapillary convection lends to a rather complex flow field in the bubble vicinity.

This study computationally investigates the mechanism of Marangoni convection, driven by both temperature and concentration gradients, in low-concentration (0–500 wppm), aqueous solutions of sodium dodecyl sulphate (SDS), an anionic surfactant, around a fixed-size, hemispherical-shaped vapor bubble, located on the underside of a heated wall maintained at uniform temperature; in pool boiling with large diameter ($\gg 2r_b$) cylindrical heaters, bubbles mostly originate from its underside [2,6]. Computations are carried out for different bubble sizes ($1 \leqslant r_b \leqslant 100\ \mu$m), which are typical of boiling nuclei in water and aqueous surfactant solutions (Table 1) for varying heat flux and surface cavity conditions. This model is consistent with the early-time-transient, post-inception, experimental observations of Dergarabedian [27] that nucleated bubbles can maintain their size for a significant period of time ($\sim O[10]$ ms), and it is thus a first-order characterization for very short time transients ($1\ \mu\text{s} \leqslant \bar{t} \leqslant 1$ ms; $\bar{t} \ll$ average bubble-growth time). The critical cavity sizes for such viable bubbles in saturated nucleate boiling and the presence of superheated boundary layer with $100 \leqslant q''_w \leqslant 1000\ \text{kW/m}^2$, are in the 3–50 μm range [41,42]. Their hemispherical shape, typical of early-transient bubble dynamics [43], represents a contact angle of 90 deg, nominally found in boiling of water on copper surfaces [44,45]; the contact angle variation for low-concentration aqueous SDS solutions tends to be quite small [34], and the hemisphere provides a first-order simulation of experimentally observed shapes [2,4]. The convection behavior in very short time-transients (which are critical to the early stages of incipience boiling) around the nucleated bubble for a broad range of thermocapillary and diffusocapillary Marangoni numbers is delineated, and the influence of surfactant additives on the Marangoni convection in their dilute premicelar aqueous solutions is highlighted.

Mathematical Formulation

The physical model and coordinate system for the hemispherical bubble on a uniformly heated, downward-facing, high-conductivity heater surface in a liquid pool of aqueous SDS solution is shown in Fig. 1(a). At the time of bubble inception ($\bar{t}=0$), the initial condition is given by a uniform temperature gradient in the viscous, incompressible Newtonian liquid. For laminar axisymmetric flows around the nondeformable bubble, a vorticity-stream function formulation in two-dimensional spherical coordinates is employed. Thus, by invoking the Boussinesq approximation to account for the body forces, the conservation equations for stream function, vorticity, energy, surfactant bulk, and surfactant surface transport, can be stated as

$$\bar{E}^2\bar{\psi} = \bar{\omega}\bar{r}\sin\theta \tag{1}$$

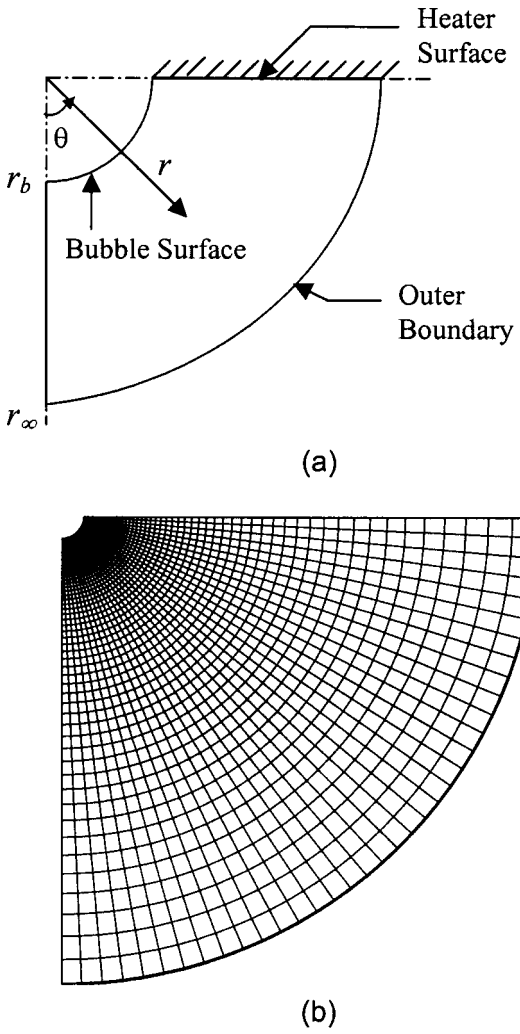

Fig. 1 Vapor bubble and surrounding liquid field: (a) physical domain, and (b) typical computational grid

$$\frac{\partial\bar{\omega}}{\partial t} + \sin\theta\left[\bar{u}\bar{r}\frac{\partial}{\partial\bar{r}}\left(\frac{\bar{\omega}}{\bar{r}\sin\theta}\right) + \bar{v}\frac{\partial}{\partial\theta}\left(\frac{\bar{\omega}}{\bar{r}\sin\theta}\right)\right] = \frac{\nu}{\bar{r}\sin\theta}\bar{E}^2(\bar{\omega}\bar{r}\sin\theta) + \beta g\left(\sin\theta\frac{\partial\bar{T}}{\partial\bar{r}} + \frac{\cos\theta}{\bar{r}}\frac{\partial\bar{T}}{\partial\theta}\right) \tag{2}$$

$$\frac{\partial\bar{T}_l}{\partial t} + \bar{u}\frac{\partial\bar{T}_l}{\partial\bar{r}} + \frac{\bar{v}}{\bar{r}}\frac{\partial\bar{T}_l}{\partial\theta} = \alpha\bar{\nabla}^2\bar{T}_l \tag{3}$$

$$\frac{\partial\bar{C}}{\partial t} + \bar{u}\frac{\partial\bar{C}}{\partial\bar{r}} + \frac{\bar{v}}{\bar{r}}\frac{\partial\bar{C}}{\partial\theta} = D\bar{\nabla}^2\bar{C} \tag{4}$$

$$\frac{\partial\bar{\Gamma}}{\partial t} + 2\frac{\bar{u}\bar{\Gamma}}{r_b} + \frac{1}{r_b\sin\theta}\frac{\partial}{\partial\theta}(\sin\theta\bar{v}\bar{\Gamma}) = D_s\left[\frac{1}{r_b^2\sin\theta}\frac{\partial}{\partial\theta}\left(\sin\theta\frac{\partial\bar{\Gamma}}{\partial\theta}\right)\right] + D\left.\frac{\partial\bar{C}}{\partial\bar{r}}\right|_{\bar{r}=r_b} \tag{5}$$

Here the stream function and vorticity are defined as

$$\bar{u} = -\frac{1}{\bar{r}^2\sin\theta}\frac{\partial\bar{\psi}}{\partial\theta}, \quad \bar{v} = \frac{1}{\bar{r}\sin\theta}\frac{\partial\bar{\psi}}{\partial\bar{r}}, \quad \bar{\omega} = \frac{1}{\bar{r}}\left[\frac{\partial}{\partial\bar{r}}(\bar{r}\bar{v}) - \frac{\partial\bar{u}}{\partial\theta}\right] \tag{6}$$

and the differential operators are given by

$$\overline{E^2}=\frac{\partial^2}{\partial \overline{r}^2}+\frac{\sin\theta}{\overline{r}^2}\frac{\partial}{\partial\theta}\left(\frac{1}{\sin\theta}\frac{\partial}{\partial\theta}\right),$$

$$\overline{\nabla}^2=\frac{1}{\overline{r}^2}\left[\frac{\partial}{\partial \overline{r}}\left(\overline{r}^2\frac{\partial}{\partial \overline{r}}\right)+\frac{1}{\sin\theta}\frac{\partial}{\partial\theta}\left(\sin\theta\frac{\partial}{\partial\theta}\right)\right] \tag{7}$$

With symmetry conditions at $\theta=0$ deg, Eqs. (1) through (5) are subject to the following initial and boundary conditions: zero flow, uniform temperature gradient and bulk concentration, and zero surface concentration at $\overline{t}=0$; zero flow, uniform temperature gradient and bulk concentration at far field; no slip, constant temperature, and zero θ-direction concentration gradient on the heater surface; zero radial velocity and temperature gradient, subsurface concentration, and zero θ-direction surface-excess concentration gradients at $\theta=0$ deg and 90 deg on the bubble surface.

Furthermore, special attention is required for the tangential velocity (or shear stress) and subsurface concentration boundary conditions at the bubble surface. The spatial variation in σ due to non-uniformities in temperature and concentration gives rise to a tangential force. In addition, the interface itself has surface shear and surface dilation viscosities, which give rise to corresponding forces [25]. Considering only the surface tension force, the shear stress balance at the bubble surface therefore yields

$$-\mu\left[\overline{r}\frac{\partial}{\partial \overline{r}}\left(\frac{\overline{v}}{\overline{r}}\right)+\frac{1}{\overline{r}}\frac{\partial \overline{u}}{\partial\theta}\right]=\frac{1}{\overline{r}}\left[\left.\frac{\partial\sigma}{\partial \overline{T}}\right|_{\overline{\Gamma}}\frac{\partial \overline{T}}{\partial\theta}+\left.\frac{\partial\sigma}{\partial \overline{\Gamma}}\right|_{\overline{T}}\frac{\partial \overline{\Gamma}}{\partial\theta}\right] \tag{8}$$

In the present analysis, $(\partial\sigma/\partial \overline{T})_{\overline{\Gamma}}$ is taken from the experimentally determined adsorption isotherms for SDS solutions [37]. Whereas $(\partial\sigma/\partial \overline{\Gamma})_{\overline{T}}$ is obtained from the Langmuir isotherm, which relates surface tension σ with surface-excess concentration $\overline{\Gamma}$ at equilibrium under constant temperature conditions and can be expressed as

$$\sigma=\sigma_0+nR_0\overline{T}\Gamma_m\ln[1-(\overline{\Gamma}/\Gamma_m)] \tag{9}$$

Thus, assuming $\overline{T}=T_{\text{sat}}$ for pure water at atmospheric pressure yields

$$(\partial\sigma/\partial \overline{\Gamma})_{\overline{T}}=-nR_0T_{\text{sat}}[\Gamma_m/(\Gamma_m-\overline{\Gamma})] \tag{10}$$

Surfactants in aqueous solutions diffuse towards the vapor/liquid interface and subsequently get adsorbed on it. This is a time-dependent process and in the early transients lends to a dynamic surface tension, which reduces to an equilibrium value after a long time [37]. While the adsorption stage involves transfer of molecules between the surface and the subsurface layer of few molecular diameters thickness below the surface, the bulk convection and diffusion of surfactant molecules involves transfer from bulk to the subsurface layer and takes place over much larger distances than the thickness of the adsorption layer [38]. An equilibrium adsorption isotherm relates the surface excess concentration $\overline{\Gamma}$ at equilibrium with the subsurface concentration $\overline{C_s}$. Under dynamic conditions (or nonequilibrium adsorption), however, aqueous surfactant systems show diffusion controlled, kinetic controlled, or mixed diffusion-kinetic controlled adsorption [38–40]. In the present study, the modified Langmuir-Hinshelwood (L-H) kinetics [38] that represents the mixed-kinetic adsorption is used to describe the dynamic adsorption of the surfactant (SDS). The kinetic expression is consistent with the Langmuir isotherm at equilibrium and has the form,

$$D\left.\frac{\partial \overline{C}}{\partial \overline{r}}\right|_{\overline{r}=r_b}=k_a\overline{C_s}\left(1-\frac{\overline{\Gamma}}{\Gamma_m}\right)\exp\left(-B\frac{\overline{\Gamma}}{\Gamma_m}\right)-k_d\overline{\Gamma}\exp\left(-B\frac{\overline{\Gamma}}{\Gamma_m}\right) \tag{11}$$

where k_a, k_d, and B are, respectively, the adsorption rate, desorption rate, and an empirical parameter. This expression indicates that the adsorption rate depends not only on the subsurface concentration $\overline{C_s}$, but also on the fraction of the uncovered surface $(1-\overline{\Gamma}/\Gamma_m)$. The exponential multiplier in both the adsorption and desorption rate terms accounts for the effects due to a more pronounced decrease of the adsorption rate with increasing surface coverage. Computations have been carried out for three different concentrations of SDS, for which k_a, k_b, and B were obtained from Chang and Franses [38] and these values are listed in Table 2.

Table 2 Langmuir-Hinshelwood (L-H) kinetics parameters for various concentrations of SDS at 25°C (Chang and Franses [38]; $\Gamma_m=10\times10^{-6}$ mol/m^2)

C_∞ [mol/m^3 (wppm)]	k_a [m/s]	k_d [s^{-1}]	B
1.7 (490.11)	5.5×10^{-4}	500	52
3.3 (951.39)	9.0×10^{-4}	818	22
8.1 (2335.2)	3.0	2.73×10^{6}	32

To render the governing equations dimensionless, the following variables are introduced:

$$r=\overline{r}/r_b,\quad t=(\alpha\overline{t})/r_b^2 \tag{12}$$

$$u=(r_b\overline{u}/\alpha),\quad v=(r_b\overline{v}/\alpha),\quad \psi=(\overline{\psi}/r_b\alpha),\quad \omega=(r_b^2\omega/\alpha), \tag{13}$$

$$T=[(T_w-\overline{T})k/r_bq_w''],\quad C=(\overline{C}/\overline{C}_\infty),\quad \Gamma=(\overline{\Gamma}/\Gamma_m)$$

$$E^2=r_b^2\overline{E^2},\quad \nabla^2=r_b^2\overline{\nabla}^2 \tag{14}$$

Thus, by setting $D=D_s$, the conservation equations take the form,

$$E^2\psi=\omega r\sin\theta \tag{15}$$

$$\frac{\partial\omega}{\partial t}+\sin\theta\left[ur\frac{\partial}{\partial r}\left(\frac{\omega}{r\sin\theta}\right)+v\frac{\partial}{\partial\theta}\left(\frac{\omega}{r\sin\theta}\right)\right]=\frac{\text{Pr}}{r\sin\theta}E^2(\omega r\sin\theta)-\text{Ra}\cdot\text{Pr}\left[\sin\theta\frac{\partial T}{\partial r}+\frac{\cos\theta}{r}\frac{\partial T}{\partial\theta}\right] \tag{16}$$

$$\frac{\partial T}{\partial t}+u\frac{\partial T}{\partial r}+\frac{v}{r}\frac{\partial T}{\partial\theta}=\nabla^2T \tag{17}$$

$$\frac{\partial C}{\partial t}+u\frac{\partial C}{\partial r}+\frac{v}{r}\frac{\partial C}{\partial\theta}=\frac{D}{\alpha}\nabla^2C \tag{18}$$

$$\frac{\partial\Gamma}{\partial t}+2u\Gamma+\frac{1}{\sin\theta}\frac{\partial}{\partial\theta}(\sin\theta v\Gamma)=\frac{1}{\text{Le}}\left[\frac{1}{\sin\theta}\frac{\partial}{\partial\theta}\left(\sin\theta\frac{\partial\Gamma}{\partial\theta}\right)+\frac{1}{\delta}\left.\frac{\partial C}{\partial r}\right|_{r=1}\right] \tag{19}$$

where, the Lewis number $\text{Le}=\alpha/D$, and the non-dimensional adsorption length $\delta=\overline{\Gamma}_m/r_b\overline{C}_\infty$. The corresponding initial and boundary conditions in terms of the dimensionless variables are:

Initial $(t=0)$: $\psi=0$, $\omega=0$, $T=r\cos\theta$,

$C=1$, and $\Gamma=0$

Far field: $\psi=0$, $\omega=0$, $T=r_\infty\cos\theta$, and $C=1$

Heater surface: $\psi=0$, $\omega=(1/r^3)(\partial^2\psi/\partial\theta^2)$,

$T=0$, and $(\partial C/\partial\theta)=0$

Symmetry surface: $\psi=0$, $\omega=0$,

$(\partial T/\partial\theta)=0$, and $(\partial C/\partial\theta)=0$

Bubble surface: $\psi=0$,

$$\omega=\left[\frac{2}{\sin\theta}\frac{\partial\psi}{\partial r}-\mathrm{Ma}_T\frac{\partial T}{\partial\theta}+\mathrm{Ma}_S\frac{n\delta}{(1-\Gamma)}\frac{\partial\Gamma}{\partial\theta}\right],\quad (\partial T/\partial r)=0,$$

$$\left.\frac{\partial C}{\partial r}\right|_{r=1}=\frac{k_a r_b}{D}\left[C_s(1-\Gamma)\exp(-B\Gamma)-\frac{\Gamma}{\mathrm{La}}\exp(-B\Gamma)\right],\quad \text{and}$$

$$(\partial\Gamma/\partial\theta)_{\theta=0,90}=0$$

where the thermocapillary and diffusocapillary Marangoni numbrers, and Langmuir number, respectively, are defined as

$$\mathrm{Ma}_T=\frac{-(d\sigma/d\overline{T})r_b^2 q_w''}{k\alpha\mu},\quad \mathrm{Ma}_S=\frac{R_0\overline{T}_\infty\overline{C}_\infty r_b^2}{\alpha\mu},\quad \text{and}$$

$$\mathrm{La}=\frac{k_a\overline{C}_\infty}{k_d\Gamma_m}\tag{20}$$

Here the liquid thermo-physical properties are evaluated at the saturation bulk temperature (100°C), and $(d\sigma/d\overline{T})$ is taken from the experimental $\sigma(T)$ measurements [37].

Computational Procedure and Validation

The governing differential equations were discretized using the forward-time, central-space differencing scheme, except the convective terms for which a hybrid scheme given by Manglik and Bergles [46] was used. Explicit time marching was employed for its accuracy in small transients and simplicity of use, and numerical solutions were obtained by using successive-over-relaxation by lines with a maximum relative error of 10^{-5}. The location of the far field boundary condition, which is influenced by Marangoni number and transient time [19,21–22], required a trial and error procedure and was set at 10-to-20 times the bubble radius.

To ensure a finer mesh near the bubble surface, the coordinate transformation $r=e^z$ was employed with $\Delta z=0.0023$. A uniform grid of $\Delta\theta=2$ deg in the θ-direction was used and this has been shown to be sufficient [47–48] for this type of computational problem. A typical grid structure in the computational domain is shown in Fig. 1(b). Because of the constraint on Δt imposed by the explicit method, the maximum Δt was set as 10^{-5} with increasingly smaller time steps ($\Delta t\leqslant 10^{-6}$) required for higher Marangoni numbers and larger time periods. Computations were carried out for the initial transients up to 1 ms, which corresponds to the time scale for the existence of boiling nuclei before their growth. The validity of the numerical solutions and grid refinement were established by comparing the results for purely thermocapillary convection in water with those of Jabardo [22]. The excellent agreement between the two is seen in Fig. 2, where the maximum stream function $|\psi_m|$ values are graphed for the conditions of uniform wall heat flux q_w'' and initial bulk temperature T_∞ everywhere. Furthermore, as listed in Table 3, there is good agreement with the steady state results of Kao and Kenning [21] for the conditions of constant wall temperature and initial uniform bulk temperature gradient. It may be noted that Kao and Kenning essentially solve a conjugate problem involving conduction inside the heated wall, and this may perhaps explain the slight variations between the two results. Additional details of the computational procedures and grid refinement can be found in Ref. [48].

Table 3 Comparison of computed steady-state results for water (T_w=constant) with those of Kao and Kenning [21]

		$\lvert\psi_m\rvert$	
Ma_T	Bi	Present study	Ref. [21]
500	0	17.2	15.9
500	11.3	1.97	1.95
2050	11.3	5.11	6.9
2250	11.3	6.96	7.9

Results and Discussion

Computational results for different combinations of a broad range of controlling parameters ($1\leqslant r_b\leqslant 100\,\mu$m, $10^4\leqslant q_w''\leqslant 10^6$ W/m^2, $0\leqslant\overline{C}_\infty\leqslant 8.1$ mol/m^3, $6\leqslant\mathrm{Ma}_T\leqslant 1000$, and $0\leqslant\mathrm{Ma}_S\leqslant 8.6\times10^5$) are presented. These are representative and typical of nucleate boiling in water with or without surfactant additives. Also, the buoyancy effects represented by Rayleigh number are

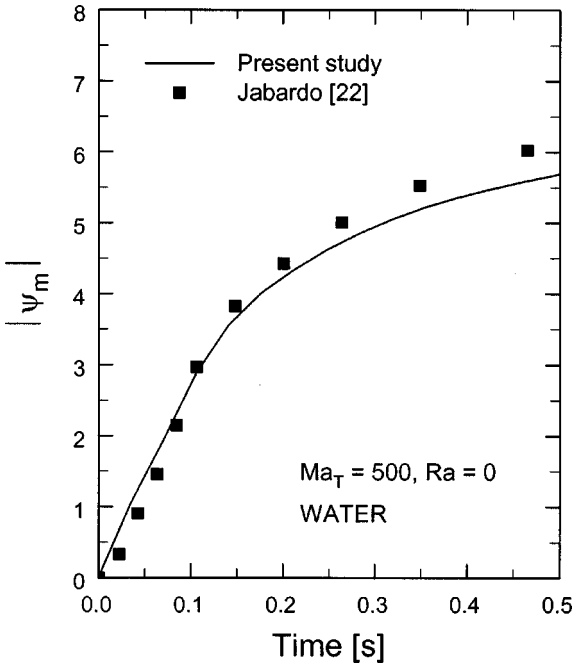

Fig. 2 Comparison of computed transient variation of $|\psi_m|$ for pure water with the results of Jabardo [22]

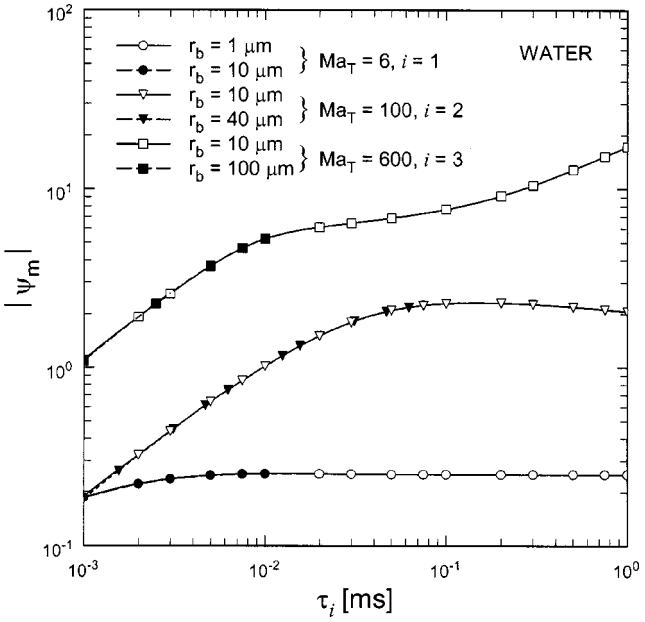

Fig. 3 Effect of Ma_T and r_b on the transient variation of $|\psi_m|$ for pure water

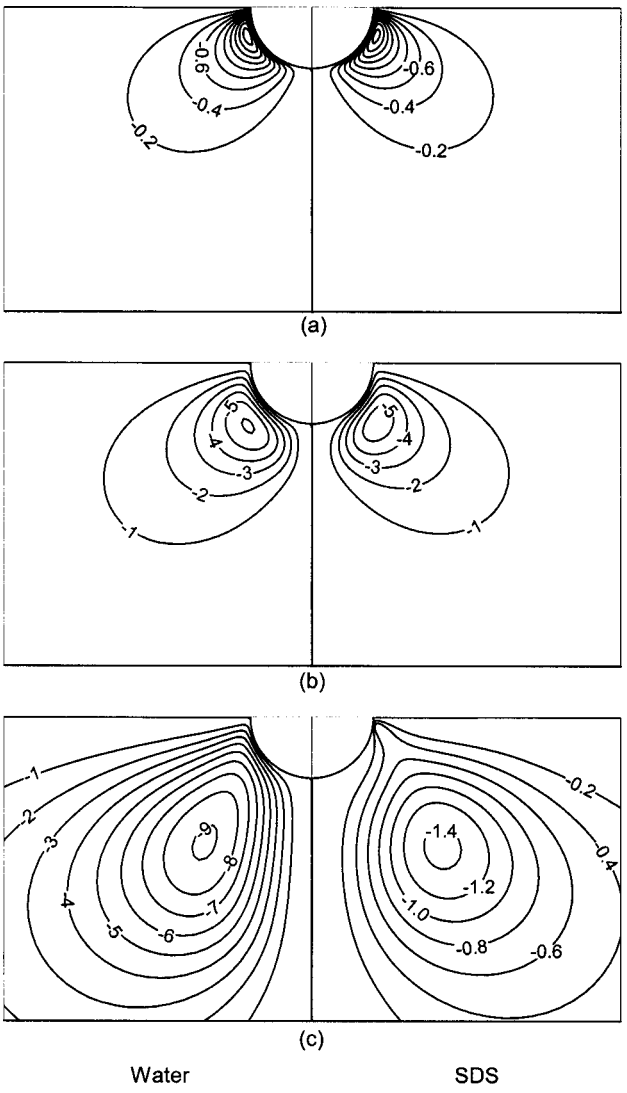

Fig. 4 Dimensionless stream function distribution for Marangoni convection in pure water and aqueous SDS solution ($\bar{C}_\infty = 1.7$ mol/m^3, $Ma_S = 1.1\times10^4$) for $r_b = 10\ \mu$m, and $Ma_T = 600$ at (a) 2 μs, (b) 20 μs, and (c) 200 μs

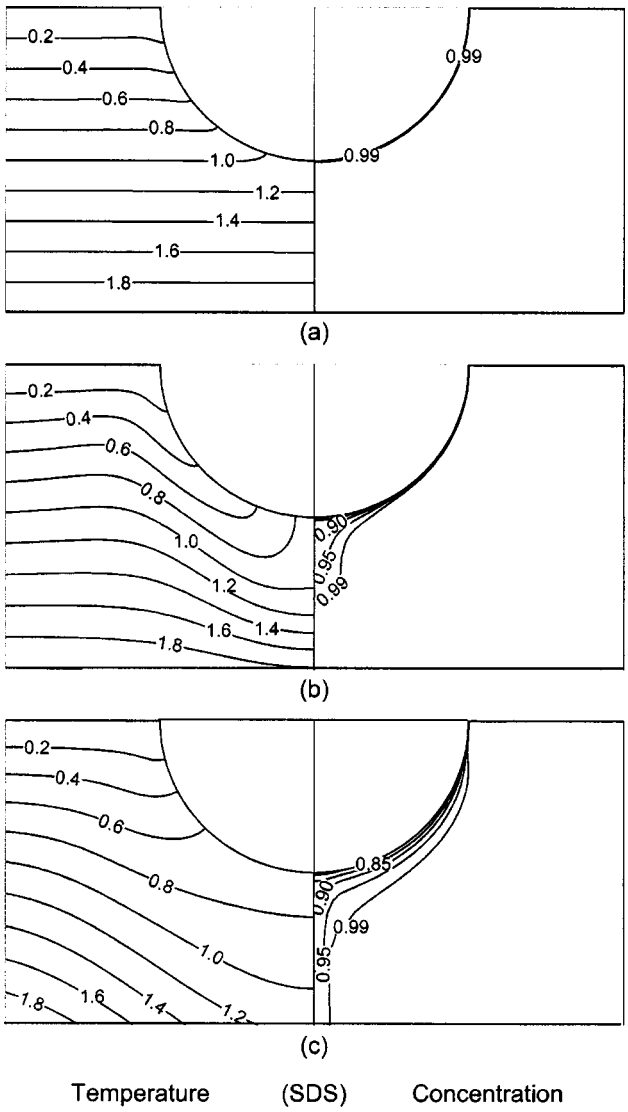

Fig. 5 Dimensionless temperature and concentration contours for $r_b = 10\ \mu$m, $Ma_T = 600$, and $Ma_S = 1.1\times10^4$ at (a) 2 μs, (b) 20 μs, and (c) 200 μs

negligible for these nuclei (1~100 μm), and the results are therefore applicable to most conditions ranging from zero to earth gravity.

Figure 3 gives the magnitude of the maximum dimensionless stream function $|\psi_m|$ values in the vortex core of thermocapillary convection in pure water ($Ma_S = 0$, $6 \leqslant Ma_T \leqslant 600$) over a 1-ms period for varying bubble sizes. Here the abscissa represents a normalized time that is scaled by the square of the ratio of bubble radii as follows:

$$\tau_i = \bar{t}(\bar{r}_i/r_b)^2; \quad \bar{r}_1 = 1\ \ \mu\text{m}, \quad \text{and} \quad \bar{r}_2 = \bar{r}_3 = 10\ \ \mu\text{m} \tag{21}$$

In general, it is seen that the circulation strength is higher for larger Ma_T, which, for water with constant properties, depends solely upon r_b and q''_w [see Eq. (20)]. However, when time is scaled by the ratio $(\bar{r}_i/r_b)^2$, the flow development around the vapor bubble is seen to be independent of the wall heat flux q''_w. This is amply illustrated by the $|\psi_m|$ values graphed in Fig. 3 for thermocapillary Marangoni numbers of 6, 100, and 600. More significantly, these results imply that thermocapillary convection in pure water has similarity solutions with respect to the bubble radius, and the results for a single bubble can be adequately extrapolated for other bubble sizes under the influence of same Ma_T.

The transient stream function distributions for water and SDS solution ($r_b = 10\ \mu$m, $q''_w = 10^6$ W/m^2, $\bar{C}_\infty = 1.7$ mol/m^3, $Ma_T = 600$, $Ma_S = 1.1\times10^4$) at $t = 2$, 20, and 200 μs, are depicted in Fig. 4. It is seen that with progressing time, a bulk fluid vortex cell (anti-clockwise circulation) sets in motion near the bubble interface. It brings the cold liquid from the bulk pool towards the bubble base and circulates it back in jet streams at the bubble crown. In the early transients (2–20 μs), the circulation pattern and its strength are the same in both water and SDS solution. At longer time (200 μs), however, only a fraction of the bubble interface remains active in the aqueous surfactant solution, and the overall circulation strength is reduced significantly with the vortex cell no longer remaining symmetric but skewed towards the bubble base. The corresponding transient temperature and concentration contours in the aqueous SDS solution are shown in Fig. 5, where the bulk convection in the fluid region two-times the bubble radius around the interface is mapped. The penetration of flow in the stagnant bulk fluid as well as the development of concentration sublayer around the bubble interface, and the progressive

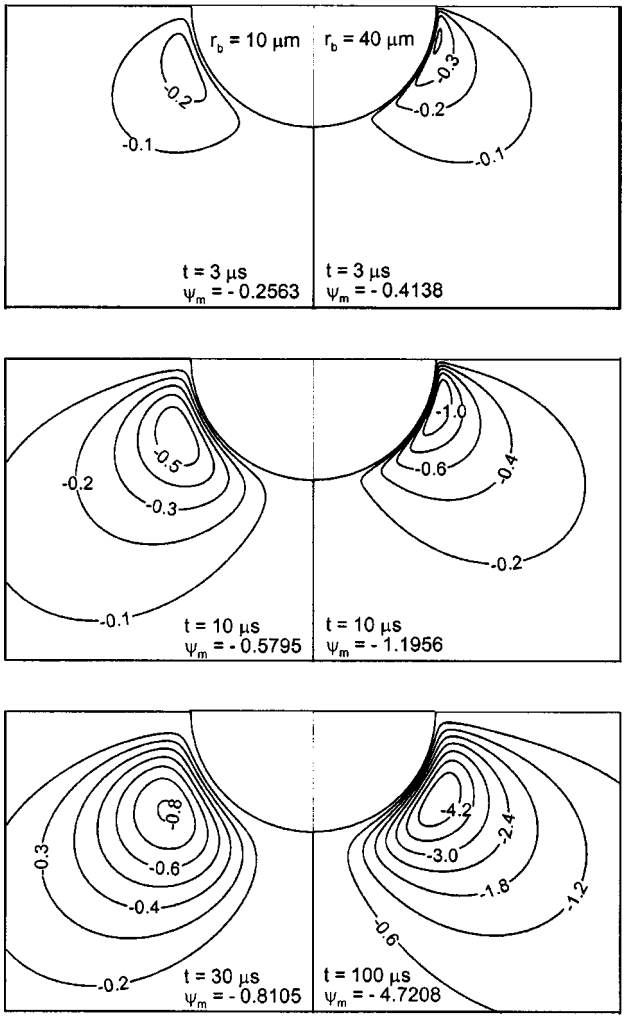

Fig. 6 Dimensionless stream function distributions in aqueous SDS solution at $q''_w = 100$ kW/m^2 and $\bar{C}_\infty = 1.7$ mol/m^3 around bubbles (with normalized radial coordinates) of different sizes: (a) 10-μm, $Ma_T = 60$, $Ma_S = 1.1\times10^4$, and (b) 40-μm, $Ma_T = 1000$, $Ma_S = 1.8\times10^5$

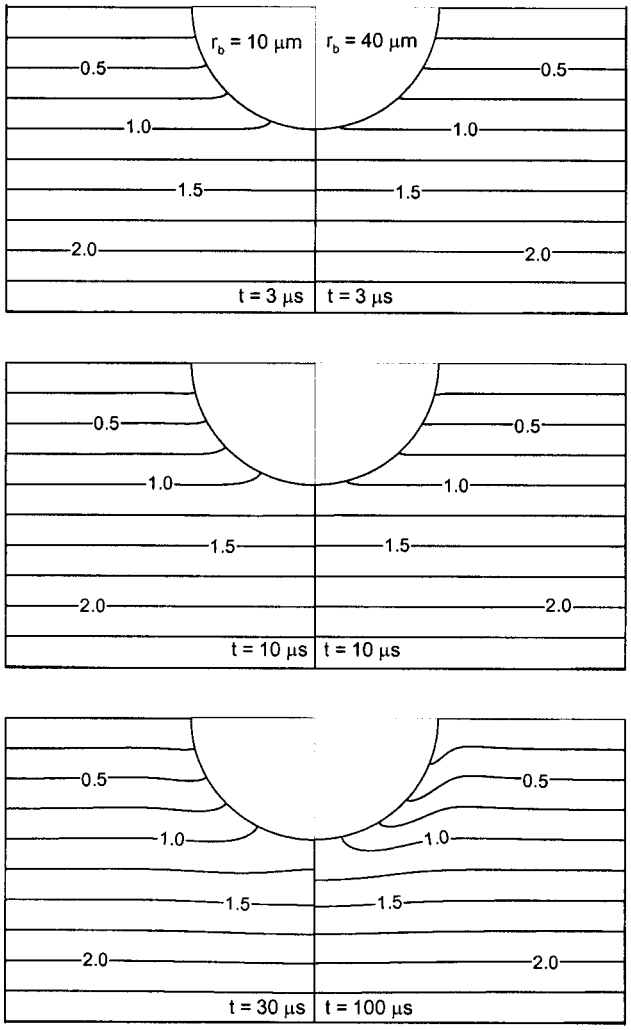

Fig. 7 Dimensionless temperature distributions in aqueous SDS solution at $q''_w = 100$ kW/m^2 and $\bar{C}_\infty = 1.7$ mol/m^3 around bubbles (with normalized radial coordinates) of different sizes: (a) 10-μm, $Ma_T = 60$, $Ma_S = 1.1\times10^4$, and (b) 40-μm, $Ma_T = 1000$, $Ma_S = 1.8\times10^5$

increase in its thickness, is seen clearly from the changing nature of isotherms. With progression of time, the thickness of the concentration sublayer becomes considerably nonuniform along the bubble surface and increases from the bubble base to the bubble crown. Moreover, the liquid jet, issuing at the bubble crown, also tends to distribute the surfactant over larger distances in the bulk fluid.

For a constant wall heat flux and surfactant bulk concentration, the combined thermocapillary and diffusocapillary Marangoni convection is found to be dependent upon the bubble size. This is evident from Figs. 6 and 7, where dimensionless stream function and temperature contours at three different time steps are graphed for two bubble sizes (10 and 40 μm); the radial coordinates in both figures are normalized with the respective bubble radius so as to magnify the flow and temperature development in the bubble vicinity. For a fixed time evolution, the larger bubble tends to have higher circulation strength owing to a larger value of Ma_T (Fig. 6). Also, in this case, the eye of the vortex is comparatively nearer the bubble interface and towards the heater surface. For times that correspond to the peaking in the maximum value of stream function in the core of the vortex (30 μs for a 10-μm bubble, and 100 μs for a 40-μm bubble), the fluid circulation becomes more symmetric with the center of the vortex around the 40-μm bubble being comparatively closer to the interface than that around the 10-μm bubble. The isotherms in Fig. 7 show the corresponding variations in the fluid temperature close to the bubble surface, and indicate a relatively stronger jet effect away from the bubble crown for the larger bubble.

Further insights into the surfactant adsorption behavior and its influence on the interfacial flow dynamics are obtained from Figs. 8 and 9. The variation in $|\psi_m|$ with time shows well-defined maximum values for surfactant solutions of all concentrations and bubble sizes. The characteristic time corresponding to this peak $|\psi_m|$ value represents the time at which surfactant effects start dominating over the temperature effects in the development of overall fluid circulation. The adsorption of surfactants at the vapor-liquid interface of the bubble creates a surface excess concentration gradient, which acts in the opposite direction to the imposed temperature gradient. This is also implied from the vorticity boundary condition at the bubble surface, and it results in the reduction of thermocapillary convection around the bubble. For time periods smaller than the characteristic time, the circulation strength in surfactant solutions is approximately same as that of pure water. However, at higher times, $|\psi_m|$ values drop considerably, indicating a significantly weak circulation. The characteristic time for a given r_b is independent of q''_w (or Ma_T), and it

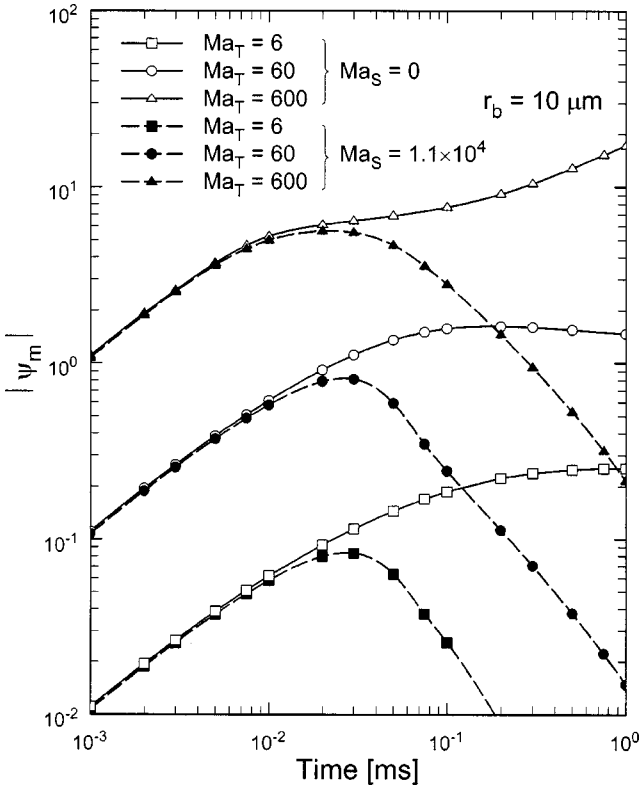

Fig. 8 Effect of surfactant additive on the transient variation of $|\psi_m|$ for different Ma_T

depends solely on the surfactant concentration $\overline{C}_\infty$ (Figs. 8 and 9). Furthermore, at a fixed value of q''_w (or Ma_T), this dependency on $\overline{C}_\infty$ (or Ma_S) is seen in Fig. 9 to have a progressively decreasing trend with corresponding increase in $\overline{C}_\infty$.

The characteristic time behavior noted above may perhaps have a correlation with the nature of surfactant adsorption at the bubble interface. Diffusion of surfactants through the bulk fluid towards the interface leads to the development of a concentration sublayer, with the bulk convection promoting surfactant transport. Based upon the nature of their adsorption kinetics, surfactant molecules adsorb from this sublayer on to the bubble surface. The characteristic time could then be taken as a measure of surfactant adsorption for the given bulk concentration, and should thus be independent of q''_w and r_b. This interpretation is very well supported by the results in Fig. 10, where the $|\psi_m|$ values for various combinations of Ma_T and r_b at a fixed value of $\overline{C}_\infty$ (1.7 mol/m^3) are graphed against a modified time τ (with r_b in μm) that is defined as,

$$\tau = \overline{t}(\overline{r}_0/r_b); \quad r_0 = 1\ \mu\text{m} \tag{22}$$

Figure 10 clearly shows that all the curves peak around the same value of τ ($\sim$25–30 μs) for the SDS concentration of 1.7 mol/m^3 in water. Similar values of τ for other $\overline{C}_\infty$ values can be expected on the lines of those presented in Fig. 9.

Additional features of the adsorption behavior of surfactants at the interface can be ascertained from the transient plots of surface-excess concentration Γ along the bubble surface that are given in Fig. 11. Results for 10 and 40-μm-radius bubbles and SDS concentrations of 1.7 and 3.3 mol/m^3 are presented. With the growth of concentration boundary layer, the surface concentration of sur-

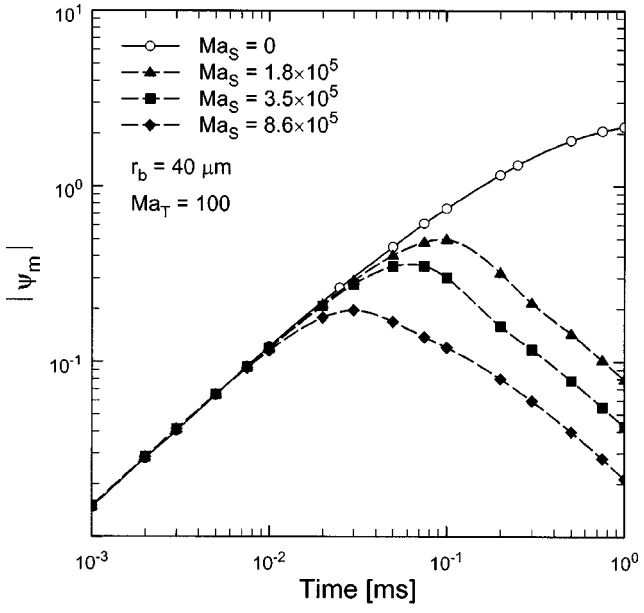

Fig. 9 Effect of surfactant concentration on the transient variation of $|\psi_m|$ for $r_b = 40\ \mu$m and $Ma_T = 100$

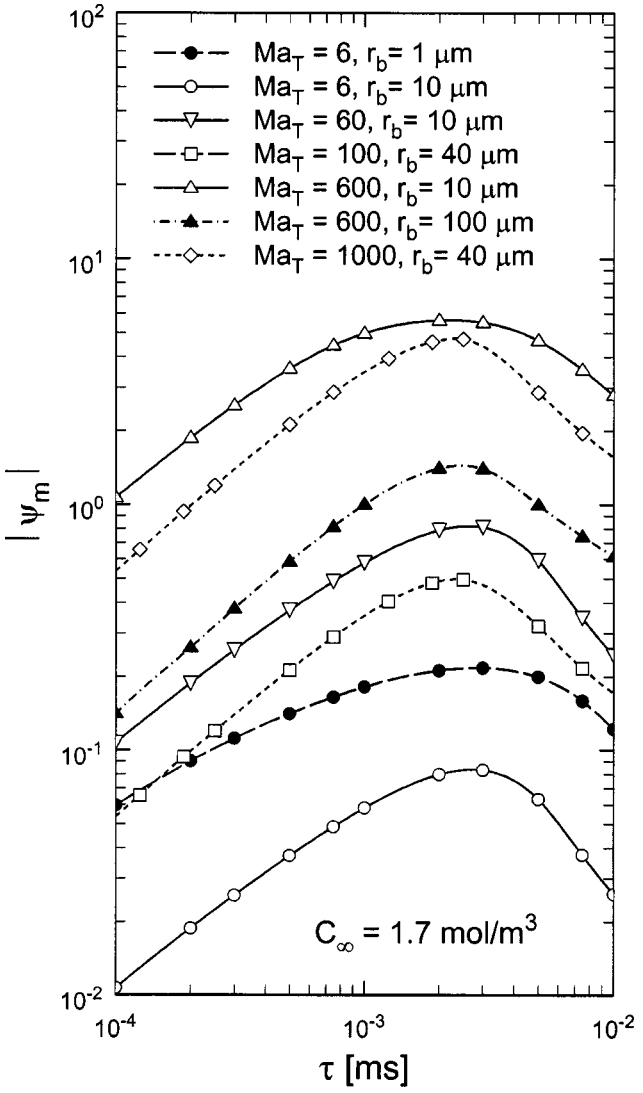

Fig. 10 Concentration-based generalized adsorption behavior of SDS in water

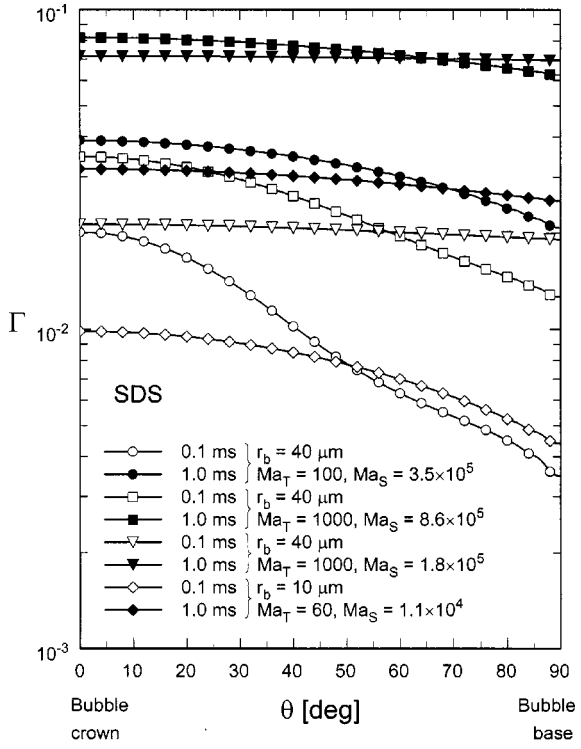

Fig. 11 Transient variation of dimensionless surface excess concentration Γ along the bubble surface

factant increases with time. All the profiles typically show a maximum value of Γ at the bubble crown with progressively decreasing values towards the bubble base. This occurs due to the surface convection of SDS molecules from the bubble base to the crown, in addition to their self-diffusion. The concentration gradients that are thus developed oppose the temperature gradients, resulting in reduced convection (Figs. 8 and 9). Moreover, in the short transient-time-period scales considered in this study, no stagnant cap behavior is observed for the range of parameters investigated.

Conclusions

For the constant-size hemispherical bubble nuclei ($1 \leqslant r_b \leqslant 100\ \mu$m) located on the underside of a heater surface in a stable stratified water pool, the thermo-capillary convection yields similarity solutions for a given Ma_T. Correspondingly, the results for a single bubble can be extended for other sizes by the appropriate time scaling given by Eq. (21). When surfactants are present in water, there is generally a reduction of the overall or combined thermocapillary and diffusocapillary Marangoni convection. Also, the circulation strength, as represented by the maximum stream function value for a given q''_w (or Ma_T) and $\overline{C}_\infty$ (or Ma_S), is dependent upon the bubble size; larger bubbles have stronger circulation. The reduction in Marangoni convection, in aqueous surfactant solutions, is seen to be quite significant after a characteristic surfactant adsorption time, which corresponds to the time period for the development of maximum or peak fluid circulation. By using a modified time τ (scaled by a ratio of bubble radius), this characteristic adsorption time has been shown to be solely dependent upon the bulk concentration of surfactant ($\overline{C}_\infty$ or Ma_S). Furthermore, for the investigated range of parameters and time scales, the surfactant adsorption at the interface is not characterized by the presence of a stagnant cap.

Acknowledgments

This study was supported in part by the National Science Foundation CAREER Award (Grant No. CTS-9502128), and the University Research Council. Also, the valuable advice of Professor M. A. Jog and the assistance given by Mr. Juntao Zhang are gratefully acknowledged.

Nomenclature

B = empirical parameter, Eq. (11) and Table 2 [−]
$\overline{C}, C$ = dimensional and dimensionless concentration [mol/m^3, −]
D = apparent bulk diffusion coefficient [m^2/s]
D_s = apparent surface diffusion coefficient [m^2/s]
g = acceleration due to gravity [m/s^2]
k = thermal conductivity [W/m K]
k_a = adsorption rate parameter [m/s]
k_d = desorption rate parameter [s^{-1}]
La = Langmuir number, Eq. (20) [−]
Le = Lewis number, $=\alpha/D$ [−]
Ma_T = thermocapillary Marangoni number, Eq. (20) [−]
Ma_S = diffusocapillary Marangoni number, Eq. (20) [−]
n = counter-ions adsorption factor [−]
Pr = Prandtl number, $=\nu/\alpha$ [−]
q''_w = wall heat flux [W/m^2]
Ra = Raleigh number, $=(g\beta q''_w r_b^4/k\alpha\nu)$ [−]
R_0 = universal gas constant [J/mol·K]
$\overline{r}, r$ = dimensional and dimensionless radial coordinate [m,−]
r_b = bubble radius [μm or m]
$\overline{T}, T$ = dimensional and dimensionless temperature [K,−]
$\overline{t}, t$ = dimensional and dimensionless time [s,−]
$\overline{u}, u$ = dimensional and dimensionless radial velocity [m/s,−]
$\overline{v}, v$ = dimensional and dimensionless tangential velocity [m/s,−]
z = dimensionless transformed r-coordinate [−]

Greek symbols

α = thermal diffusivity [m^2/s]
β = coefficient of thermal expansion [1/K]
δ = dimensionless adsorption length, $=\Gamma_m/r_b C_\infty$ [−]
$\overline{\Gamma}, \Gamma$ = dimensional and dimensionless surface-excess concentration [mol/m^2,−]
μ = dynamic viscosity [N s/m^2]
ν = kinematic viscosity [m^2/s]
θ = angular (or tangential) coordinate [deg]
σ = surface tension [N/m]
τ = modified time, Eq. (22) [ms]
$\overline{\omega}, \omega$ = dimensional and dimensionless vorticity [s^{-1},−]
$\overline{\psi}, \psi$ = dimensional and dimensionless stream function [m^3/s,−]

Subscript

m = maximum
s = subsurface
sat = at saturation conditions
w = at heater surface
∞ = bulk, far field condition

References

[1] Wasekar, V. M., and Manglik, R. M., 1999, "A Review of Enhanced Heat Transfer in Nucleate Pool Boiling of Aqueous Surfactant and Polymeric Solutions," J. Enhanced Heat Transfer, **6**(2–4), pp. 135–150.
[2] Wasekar, V. M., and Manglik, R. M., 2000, "Pool Boiling Heat Transfer in Aqueous Solutions of an Anionic Surfactant," ASME J. Heat Transfer, **122**(4), pp. 708–715.
[3] Hetsroni, G., Zakin, J. L., Lin, Z., Mosyak, A., Pancallo, E. A., and Rozenblit, R., 2000, "The Effect of Surfactants on Bubble Growth, Wall Thermal Patterns

and Heat Transfer in Pool Boiling,'' Int. J. Heat Mass Transfer, **44**, pp. 485–497.
[4] Zhang, J., and Manglik, R. M., 2003, ''Pool Boiling Heat Transfer in Aqueous Solutions of a Cationic Surfactant,'' Paper No. TED-AJ03-248, *Proceedings of 6th AMSE-JSME Thermal Engineering Joint Conference*, ASME, New York.
[5] Myers, D., 1999, *Surfaces, Interfaces, and Colloids*, 2nd Edition, Wiley-VCH, New York, NY.
[6] Wasekar, V. M., and Manglik, R. M., 2002, ''The Influence of Additive Molecular Weight and Ionic Nature on the Pool Boiling Performance of Aqueous Surfactant Solutions,'' Int. J. Heat Mass Transfer, **45**(3), pp. 483–493.
[7] McGrew, J. L., Bamford, F. L., and Rehm, T. R., 1966, ''Marangoni Flow: An Additional Mechanism in Boiling Heat Transfer,'' Science, **153**(3740), pp. 1106–1107.
[8] Huplik, V., and Raithby, G. D., 1972, ''Surface-Tension Effects in Boiling From A Downward-Facing Surface,'' ASME J. Heat Transfer, **94**, pp. 403–409.
[9] Straub, J., Picker, G., Winter, J., and Zell, M., 1997, ''Effective Cooling of Electronic Components by Boiling Phase Transition in Microgravity,'' Acta Astronaut., **40**, pp. 119–127.
[10] Arlabosse, P., Tadrist, H., Pantaloni, J., and Tadrist, L., 1998, ''Experimental Study of Marangoni Convection Around A Bubble: Application to the Boiling Heat Transfer Under Microgravity Conditions,'' *Heat Transfer 1998*, **2**, KSME, Seoul, Korea, pp. 371–376.
[11] Baranenko, V. I., and Chichkan, L. A., 1980, ''Thermocapillary Convection in the Boiling of Various Fluids,'' Heat Transfer-Sov. Res., **12**(2), pp. 40–44.
[12] Straub, J., 2000, ''Microscale Boiling Heat Transfer Under 0 g and 1 g Conditions,'' Int. J. Therm. Sci., **39**, pp. 490–497.
[13] Marek, R., and Straub, J., 2001, ''The Origin of Thermocapillary Convection in Subcooled Nucleate Pool Boiling,'' Int. J. Heat Mass Transfer, **44**, pp. 619–632.
[14] Beer, H., 1979, ''Interferometry and Holography in Nucleate Boiling,'' in *Boiling Phenomena*, S. Van Stralen and R. Cole, Eds., **2**, Hemisphere, New York, NY, pp. 821–843.
[15] Ilyin, I. N., Grivtsov, V. P., and Yaundalders, S. R., 1982, ''Holographic Interferometry Studies of Temperature Profiles in Thermal Boundary Layer in Free Convection and Bubble Boiling,'' *Heat Transfer 1982*, U. Grigull et al., Eds., **4**, München, Germany, pp. 55–59.
[16] Raake, D., Siekmann, J., and Chun, C.-H., 1989, ''Temperature and Velocity Fields due to Surface Tension Driven Flow,'' Exp. Fluids, **7**, pp. 164–172.
[17] Wozniak, G., Wozniak, K., and Bergelt, H., 1996, ''On the Influence of Buoyancy on the Surface Tension Driven Flow Around Bubble on A Heated Wall,'' Exp. Fluids, **21**, pp. 181–186.
[18] Rashidnia, N., 1997, ''Bubble Dynamics on A Heated Surface,'' J. Thermophys. Heat Transfer, **11**, pp. 477–480.
[19] Larkin, B. K., 1970, ''Thermocapillary Flow Around Hemispherical Bubble,'' AIChE J., **16**, pp. 101–107.
[20] Gaddis, E. S., 1972, ''The Effects of Liquid Motion Induced By Phase Change and Thermocapillarity on the Thermal Equilibrium of A Vapor Bubble,'' Int. J. Heat Mass Transfer, **15**, pp. 2241–2250.
[21] Kao, Y. S., and Kenning, D. B. R., 1972, ''Thermocapillary Flow Near A Hemispherical Bubble on A Heated Wall,'' J. Fluid Mech., **53**, pp. 715–735.
[22] Jabardo, J. M. S., 1981, ''Investigation of Thermocapillary Flows Around Hemispherical Bubbles,'' Ph.D. thesis, University of Illinois at Urbana-Champaign, IL.
[23] Straub, J., Betz, J., and Marek, R., 1994, ''Enhancement of Heat Transfer by Thermocapillary Convection Around Bubbles–A Numerical Study,'' Numer. Heat Transfer, Part A, **25**, pp. 501–518.
[24] Arlabosse, P., Lock, N., Medale, M., and Jaeger, M., 1999, ''Numerical Investigation of Thermocapillary Flow Around A Bubble,'' Phys. Fluids, **11**, pp. 18–29.
[25] Sadhal, S. S., Ayyaswami, P. S., and Chung, J. N., 1997, *Transport Phenomena with Drops and Bubbles*, Springer, New York, NY.
[26] Hsu, Y. Y., 1962, ''On the Size Range of Active Nucleation Sites on a Heating Surface,'' ASME J. Heat Transfer, **84**, pp. 207–216.
[27] Dergarabedian, P., 1960, ''Observations on Bubble Growths in Various Superheated Liquids,'' J. Fluid Mech., **9**, pp. 39–48.
[28] Kenning, D. B. R., and Cooper, M. G., 1965, ''Flow Patterns Near Nuclei and the Initiation of Boiling During Forced Convection Heat Transfer,'' *Proceedings of the Institution of Mechanical Engineers 1965–66*, Vol. 180, Pt. 3C, Paper 11, pp. 112–123.
[29] Han, C.-H., and Griffith, P., 1965, ''The Mechanism of Heat Transfer in Nucleate Pool Boiling—Part I: Bubble Initiation, Growth and Departure,'' Int. J. Heat Mass Transfer, **8**, pp. 887–904.
[30] Hahne, E., and Ribeiro, R., 1998, ''Single Bubble Heat Transfer in Nucleate Pool Boiling,'' *Heat Transfer 1998*, **2**, KSME, Seoul, Korea, pp. 503–508.
[31] Kant, K., and Weber, M., 1994, ''Stability of Nucleation Sites in Pool Boiling,'' Exp. Therm. Fluid Sci., **9**, pp. 456–465.
[32] Son, G., Dhir, V. K., and Ramanujapu, N., 1999, ''Dynamics and Heat Transfer Associated With a Signle Bubble During Nucleate Boiling on a Horizontal Surface,'' ASME J. Heat Transfer, **121**, pp. 613–631.
[33] Wu, W. T., Yang, Y. M., and Maa, J. R., 1999, ''Pool Boiling Incipience and Vapor Bubble Growth Dynamics in Surfactant Solutions,'' Int. J. Heat Mass Transfer, **42**, pp. 2483–2488.
[34] Wu, W. T., and Yang, Y. M., 1992, ''Enhanced Boiling Heat Transfer by Surfactant Additives,'' in *Pool and External Flow Boiling*, ASME, New York, NY, pp. 361–366.
[35] Dushkin, C. D., and Iliev, Tz. H., 1994, ''Dynamic Surface Tension of Micellar Solutions Studied by the Maximum Bubble Pressure Method: 2. Theory of the Solutions Below CMC,'' Colloid Polym. Sci., **272**, pp. 1157–1165.
[36] Ferri, J. K., and Stebe, K. J., 2000, ''Which Surfactants Reduce Surface Tension Faster? A Scaling Argument for Diffusion-Controlled Adsorption,'' Adv. Colloid Interface Sci., **85**, pp. 61–97.
[37] Manglik, R. M., Wasekar, V. M., and Zhang, J., 2001, ''Dynamic and Equilibrium Surface Tension of Aqueous Surfactant and Polymeric Solutions,'' Exp. Therm. Fluid Sci., **25**(1–2), 55–64.
[38] Chang, C.-H., and Franses, E. I., 1995, ''Adsorption Dynamics of Surfactants at the Air/Water Interfaces: A Critical Review of Mathematical Models, Data, and Mechanisms,'' Colloids Surf., A, **100**, pp. 1–45.
[39] Dukhin, S. S., Kretzschmar, G., and Miller, R., 1995, *Dynamics of Adsorption at Liquid Interfaces*, Elsevier, Amsterdam.
[40] Eastoe, J., and Dalton, J. S., 2000, ''Dynamic Surface Tension and Adsorption Mechanisms of Surfactants at the Air-Water Interface,'' Adv. Colloid Interface Sci., **85**, pp. 103–144.
[41] Hewitt, G. F., 1998, ''Boiling,'' in *Handbook of Heat Transfer*, W. M. Rohsenow, J. P. Hartnett, and Y. I. Cho, eds., 3rd Edition, McGraw-Hill, New York, NY, Chpt. 15.
[42] Davis, E. J., and Anderson, G. H., 1966, ''The Incipience of Nucleate Boiling in Forced Convection Flow,'' AIChE J., **12**, p. 774.
[43] Kenning, D. B. R., and Toral, H., 1977, ''On the Assessment of Thermocapillary Effects in Nucleate Boiling of Pure Fluids,'' *Proceedings of International Conference on Physicochemical Hydrodynamics*, **1**, Oxford, UK, pp. 653–665.
[44] Shakir, S., Thome, J. R., and Lloyd, J. R., 1985, ''Boiling of Methanol-Water Mixtures on Smooth and Enhanced Surfaces,'' in *Multiphase Flow and Heat Transfer*, HTD—Vol. 47, ASME, New York, NY, pp. 1–6.
[45] Wang, C. H., and Dhir, V. K., 1992, ''Effect of Surface Wettability on Active Nucleation Site Density During Pool Boiling of Water on A Vertical Surface,'' ASME J. Heat Transfer, **115**, pp. 659–669.
[46] Manglik, R. M., and Bergles, A. E., 1994, ''Fully Developed Laminar Heat Transfer in Circular-Segment Ducts With Uniform Wall Temperature,'' Numer. Heat Transfer, Part A, **26**, pp. 499–519.
[47] Cuenot, B., Magnaudet, J., and Spennato, B., 1997, ''The Effects of Slightly Soluble Surfactants on the Flow Around A Spherical Bubble,'' J. Fluid Mech., **339**, pp. 25–53.
[48] Wasekar, V. M., and Manglik, R. M., 2001, ''Nucleate Pool Boiling Heat Transfer in Aqueous Surfactant Solutions,'' Report No. TFTPL-4, Thermal-Fluids & Thermal Processing Laboratory, University of Cincinnati, Cincinnati, OH.

Binary Fluid Mixture and Thermocapillary Effects on the Wetting Characteristics of a Heated Curved Meniscus

David M. Pratt
United States Air Force,
Wright-Patterson AFB, OH 45433-7542

Kenneth D. Kihm
Department of Mechanical Engineering,
Texas A&M University,
College Station, TX 77843-3123

An investigation has been conducted into the interactions of binary fluid mixtures (pentane [C_5H_{12}] coolant and decane [$C_{10}H_{22}$] additive) and thermocapillary effects on a heated, evaporating meniscus formed in a vertical capillary pore system. The experimental results show that adding decane, the secondary fluid that creates the concentration gradient, actually decreases the meniscus height to a certain level, but did increase the sustainable temperature gradient for the liquid-vapor interface, so did the heat transfer rate, delaying the onset of meniscus instability. The results have demonstrated that interfacial thermocapillary stresses arising from liquid-vapor interfacial temperature gradients, which is known to degrade the ability of the liquid to wet the pore, can be counteracted by introducing naturally occurring concentration gradients associated with distillation in binary fluid mixtures. Also theoretical predictions are presented to determine the magnitudes of both the thermocapillary stresses and the distillation-driven capillary stresses, and to estimate the concentration gradients established as a result of the distillation in the heated pore. [DOI: 10.1115/1.1599372]

Keywords: Binary, Evaporation, Heat Transfer, Thermocapillary, Thin Films

Introduction

Heat transport devices capable of dissipating high intensity heat energy as high as 200 W/cm^2 are required for cooling electronics; hypersonic and re-entry vehicles; satellites; propulsion and thermal energy recovery systems; cryoprobes; permafrost stabilizers; and roadway deicers among others. Of the heat transport devices presently under consideration in this regime, most utilize the latent heat of vaporization via liquid-vapor phase change. Relevant to the present research are passive capillary-driven phase change devices [1]. In these devices, the phase change occurs in a liquid-saturated porous or grooved media where capillary forces provide the driving potential for the liquid flow from the condenser to the evaporator. Ultimately for low temperature devices, the rate at which the condenser can re-supply liquid to the evaporator limits the heat transport. In practice, however, this capillary heat transport limitation is rarely achieved [2]. One possible explanation is that design predictions over-predict the wetting characteristics since they are based on a 'maximum capillary potential' which presumes that the liquid within the porous structure is perfectly wetting and static conditions exist at the evaporating menisci. Dynamic effects, other than those due to viscous flow losses, are not considered.

The speculation here is that the dynamics associated with fluid motion and heat transport in the vicinity of the evaporating meniscus can detrimentally affect the driving capillary potential by degrading the wetting ability of the working fluid [3,4]. The change in wetability is the result of non-isothermal liquid-vapor interfacial temperatures near the contact line arising from both non-uniform substrate wall temperatures and non-uniform evaporation. Either or both of these influences yield surface tension gradients on the liquid-vapor interface, with positive slope toward a cooler region of the interface. For example, if the pore wall is heated, the relatively cooler pore center region, with higher surface tension, can act to pull down the evaporating, hotter thin film region with lower surface tension. Therefore, these surface tension gradients result in thermocapillary stresses, or the pulling action, acting near the contact line which can degrade the wetability of the liquid as has been seen in many published works [5–8].

Ehrhard and Davis [5] showed that the spreading of a drop on a surface in the direction of increased wall temperature is retarded relative to the spreading of a similar drop on an isothermal surface. Furthering this work, Hocking [6] showed that the advancement or spreading of an evaporating drop is retarded due to the evaporation process. Sen and Davis [7] showed that, for a slot configuration, surface tension gradients create a fluid surface flow field, which also affects the liquid wetability. Anderson and Davis [8] analytically demonstrated that the flow field was coupled to the temperature field through the thermocapillarity as discussed by Sen and Davis [7].

Recent studies of rewetting of liquids along inclined heated plates by Ha and Peterson [9] and Chan and Zhang [10] showed that the maximum wicking height measured was beneath that predicted using the typical Laplace-Young equation by as much as thirty percent. Pratt and Hallinan [4] established and experimentally verified the relationship between the liquid-vapor interfacial temperature gradient and the wetting characteristics of a liquid within small pores. They showed that thermocapillary stresses acting near the contact line of the advancing liquid front inhibit the wetting of the liquid thereby reducing the wicking height.

The predicted degradation leads to a reduction in the capillary pumping potential in capillary heat transfer devices and thus a reduction in their ability to transport energy [2]. Thus the question arises as to how to minimize this reduction. The degradation arises from thermocapillary stresses along the liquid-vapor interface due to the reduction in surface tension with an increase in temperature. One possible solution to counteract the degradation is the introduction of a small amount of a relatively high surface-free-energy, less volatile fluid (additive) into the volatile or relatively low surface-free-energy working fluid. This would result in an increase in the concentration of the less volatile fluid with an increase in temperature or the preferred evaporation of the lower

Contributed by the Heat Transfer Division for publication in the JOURNAL OF HEAT TRANSFER. Manuscript received by the Heat Transfer Division November 22, 2002; revision received May 16, 2003. Associate Editor: G. P. Peterson.

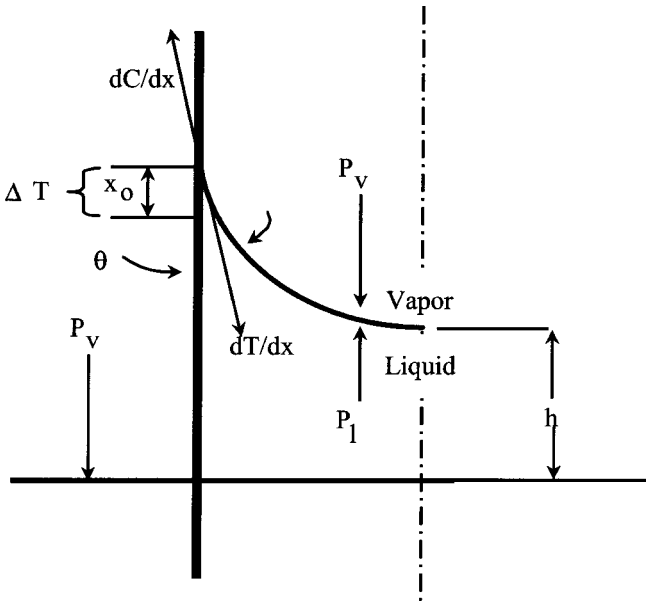

Fig. 1 Liquid-vapor interface of a binary mixture working fluid with heated pore wall

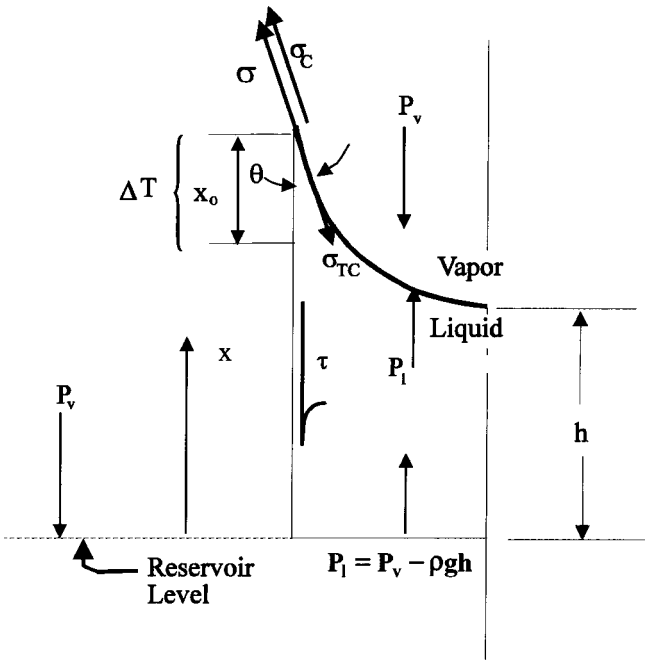

Fig. 2 Binary mixture meniscus inside a capillary tube with an induced temperature gradient by wall heating and a concentration gradient by distillation of a more volatile working fluid

surface-free-energy fluid. This would thus result in a concentration gradient for additive in the opposite direction to the temperature gradients (see Fig. 1), and the additive concentration gradient is consistent with the surface tension gradient of the mixture, so-called distillation effect [11], which counteracts the thermocapillary surface tension gradient.

The distillation effects of binary mixtures for the case of superheated or pool boiling cases have been examined by several researchers [12–14]. Reddy and Lienhard [12] presented an observation of the presence of induced subcooling because of composition differences that makes the liquid bulk temperature lower than the vapor temperature. Avedisian and Purdy [13] reported the critical boiling heat flux for pentane-heptane and pentane-propanol binary mixtures under different saturation pressures. Parks and Wayner [11] presented an anlytical model to predict the meniscus profiles near the contact line for a binary mixture and showed an experimental validation. Their model also showed that the single most important mechanism for flow in the microscale evaporating meniscus region of 1 to 10 μm thickness is the distillation-driven capillary stress resulting from preferential evaporation of the more volatile component. Reyes and Wayner [14] presented an interfacial model to predict the critical heat flux for various binary mixtures and to compare their predictions with published experimental data.

The present paper reports an experimental investigation that was designed so that macroscopic wetting characteristics could be observed for a heated and evaporating meniscus within a simple capillary pumped loop. Specifically, it was designed to determine the effects of binary fluid mixtures (pentane [C_5H_{12}] coolant and decane [$C_{10}H_{22}$] additive) on the thermocapillary stresses arising near the contact line of evaporating menisci, within capillary pores, by measuring the capillary pumping potential or the meniscus height differentials between the evaporator and condenser cores. In addition, a preliminary analysis has been conducted to examine the range of the parametric requirements to ensure an ideal counter-balancing between the thermocapillary stress and the distillation-driven capillary stress.

Analysis

Analysis is presented to qualitatively explain the experimental results, rather than as a rigorous solution to the problem herein discussed. The most easily measurable macroscopic wetting characteristic of a liquid in a pore is the wicking height. For static interfacial conditions, it can be predicted with the Young-Laplace equation [15].

$$P_v - P_l = \sigma K \tag{1}$$

The reduced liquid pressure at the meniscus causes the liquid to wick to a height h (Fig. 2), which for an axisymetric pore of radius r and a condenser of radius R gives rise to the following expression

$$\rho g h = \frac{2\sigma(R-r)}{rR}\cos\theta \tag{2}$$

where θ is the apparent contact angle and σ is the surface tension of the mixture. When the meniscus is heated via wall heating, dynamic effects can alter this wicking height.

One effect of heating is to produce a liquid-vapor interfacial temperature gradient near the contact line, with a negative slope toward the pore center. This temperature gradient gives rise to a thermocapillary stress (σ_{TC}) emanating from the contact line if the contact line region is hotter than the remainder of the meniscus. Additionally, the evaporative transport from the meniscus due to the heat transfer induces liquid flow from the bulk pore region. Associated with this flow are viscous losses (τ) along the wall of the pore. The use of a binary fluid mixture gives rise to an additional stress along the interface resulting from the naturally occurring concentration gradient which tends to counteract the thermocapillary stress, because of the aforementioned distillation effect. While, both the thermocapillary and the flow loss effects can reduce the wicking height, the concentration effect acts to negate these effects.

A vertical force balance is applied to the control volume defined by the liquid column in the pore shown in Fig. 2 to determine the thermocapillary and flow loss effects on capillary potential. This results are in the following equilibrium condition.

$$(P_l - P_v)\pi r^2 + (\sigma - \sigma_{TC} + \sigma_C)2\pi r\cos\theta - \Delta P_{\text{flow}}\pi r^2 - \sigma 2\pi R\cos\theta = 0 \tag{3}$$

with $P_l - P_v = -\rho g h$. Dividing by πr^2 and substituting yields

$$\rho g h = \frac{2(\sigma - \sigma_{TC} + \sigma_C)}{r}\cos\theta - \frac{2\sigma R}{r^2}\cos\theta - \Delta P_{\text{flow}} \tag{4}$$

Elementary momentum analysis assuming fully-developed laminar pipe flow of radius r gives an expression for the pressure differential for the flow length L_{flow} measured from the bottom of the capillary tube to the meniscus as,

$$\Delta P_{\text{flow}} = \frac{8\mu\langle V\rangle}{r^2} L_{\text{flow}} \tag{4a}$$

Considering the energy balance between the heat input to meniscus Q_M and the evaporative mass flow rate $\dot{m}_{\text{evap}}$, the average flow velocity $\langle V\rangle$ is expressed as,

$$\langle V\rangle = \frac{Q_M}{\rho A[h_{fg} + c_p \Delta T]} \tag{4b}$$

where the cross-sectional area $A \equiv \pi r^2$ and the temperature differential, $\Delta T \equiv T_{\text{sat}} - T_r$, is set between the saturation condition at the evaporating interface and the reservoir condition at the bottom of the capillary bulk. Combining Eqs. (4*a*) and (4*b*) gives

$$\Delta P_{\text{flow}} = \frac{8\mu L_{\text{flow}}}{\rho\pi r^4} \frac{Q_M}{h_{fg} + c_p(T_{\text{sat}} - T_r)} \tag{4c}$$

Substituting Eq. (4*c*) into Eq. (4) yields

$$\rho g h = \frac{2(\sigma - \sigma_{TC} + \sigma_C)}{r}\cos\theta - \frac{2\sigma R}{r^2}\cos\theta - \frac{8\mu L_{\text{flow}}}{\rho\pi r^4} \frac{Q_M}{h_{fg} + c_p(T_{\text{sat}} - T_r)} \tag{5}$$

This modified version of the capillary pumping potential incorporates yet undefined thermocapillary and concentration forces that can be determined by examining the effects of liquid-vapor interfacial temperature gradients on the surface tension. Assuming the mixture surface tension is linearly contributed by the mixture concentration,

$$\sigma = C(\sigma_{oD} - \gamma_D T) + (1 - C)(\sigma_{oP} - \gamma_P T) \tag{6}$$

so that letting

$$\sigma_C - \sigma_{TC} = \frac{\partial \sigma}{\partial x} x_o \tag{7}$$

and differentiation of Eq. (6) with respect to x gives,

$$\frac{\partial \sigma}{\partial x} = \frac{\partial C}{\partial x}(\sigma_{oD} - \gamma_D T - \sigma_{oP} + \gamma_P T) - \frac{\partial T}{\partial x}[C\gamma_D + (1 - C)\gamma_P] \tag{8}$$

Finally expressions for the thermocapillary and concentration forces are obtained from combining Eqs. (7) and (8) as,

$$\sigma_{TC} = \frac{\partial T}{\partial x}[C\gamma_D + (1 - C)\gamma_P] x_o \tag{9}$$

and

$$\sigma_C = \frac{\partial C}{\partial x}[(\sigma_{oD} - \gamma_D T) - (\sigma_{oP} - \gamma_P T)] x_o \tag{10}$$

The thermocapillary stress, Eq. (9), is of the same form as that which was shown to exist by Pratt and Hallinan [4].

For an ideal case, the thermocapillary stress (Eq. (9)) can be completely counteracted by the distillation-driven capillary stress (Eq. (10)), i.e.,

Table 1 Decane concentration at the meniscus top (C_T) for complete counteraction of the distillation-driven capillary to the thermocapillary drive: for different decane concentrations at the meniscus bottom, (C_B), and for different temperature gradients along the meniscus, ($\partial T/\partial x$) = 10^2, 10^3, 10^4, 3×10^4 and 6×10^4.

$\partial T/\partial x$ (K/m)	Decane Concentration at the Meniscus Bottom or Bulk Mixture (C_B)			
	0.01	0.03	0.05	0.1
10^2	0.01145	0.03145	0.05145	0.10145
10^3	0.0245	0.0445	0.0645	0.1145
10^4	0.155	0.175	0.195	0.245
3×10^4	0.445	0.465	0.485	0.535
6×10^4	0.867	0.887	0.907	0.957

$$\frac{\sigma_{TC}}{\sigma_C} = \frac{\dfrac{\partial T}{\partial x}[C\gamma_D + (1 - C)\gamma_P]}{\dfrac{\partial C}{\partial x}[(\sigma_{oD} - \gamma_D T) - (\sigma_{oP} - \gamma_P T)]} = 1 \tag{11}$$

where the ratio of the temperature gradient to the concentration gradient must be ensured as,

$$\Re_{T-C} \equiv \frac{\dfrac{\partial T}{\partial x}}{\dfrac{\partial C}{\partial x}} = \frac{[(\sigma_{oD} - \gamma_D T) - (\sigma_{oP} - \gamma_P T)]}{[C\gamma_D + (1 - C)\gamma_P]} \tag{12}$$

Note that the required ratio $\Re_{T-C}$ varies with the mixture temperature T and decane concentration C.

Assuming a linear change in the decane concentration from C_B at the meniscus bottom point, or equivalent to the bulk mixture concentration, to C_T at the meniscus upper end,

$$C_T = \left(\frac{\partial C}{\partial x}\right) r + C_B \tag{13}$$

For a specified ($\partial T/\partial x$), ($\partial C/\partial x$) is given from Eq. (12) and the concentration differential $C_T - C_B$ can be calculated from Eq. (13). Table 1 shows example calculations for C_T for different C_B for the range of ($\partial T/\partial x$) from 10^2 to 6×10^4, where a constant value of $\Re_{T-C} = 70.0$ is used assuming $T = 290$ K. To be shown later in Results Section, temperature gradient along the meniscus surface, $\partial T/\partial x$ for the present experiment spans up to 10^4 or less for all cases of C_B. Note that the decane concentration differential $C_T - C_B$ increases linearly with increasing $\partial T/\partial x$, as expected.

Experiment

To accomplish the goal of the research, a single pore capillary pumped heat transfer device was constructed as shown in Fig. 3. The test specimen shown is a closed, single pore evaporator capillary pumped loop consisting of a pore evaporator of 2 mm diameter with 10 mm diameter pore condensers. This idealized and enlarged evaporator was designed to study some basic physics that can be extracted for potential applications to the meniscus development in an individual pore of a porous structure of heat pipes and capillary pumps.

Heat is introduced via electrical resistance heating elements mounted on the outer diameter of the evaporator pore. To minimize convection losses and isolate the test specimen, shown in Fig. 3, from ambient conditions, it was placed in a vacuum chamber (Fig. 4). The chamber was equipped with feed-throughs for thermocouples, pressure transducers, heater power connections, and cooling fluid lines.

A roughing vacuum pump was used to evacuate the loop system and the vacuum chamber. The filling of the test loop system uti-

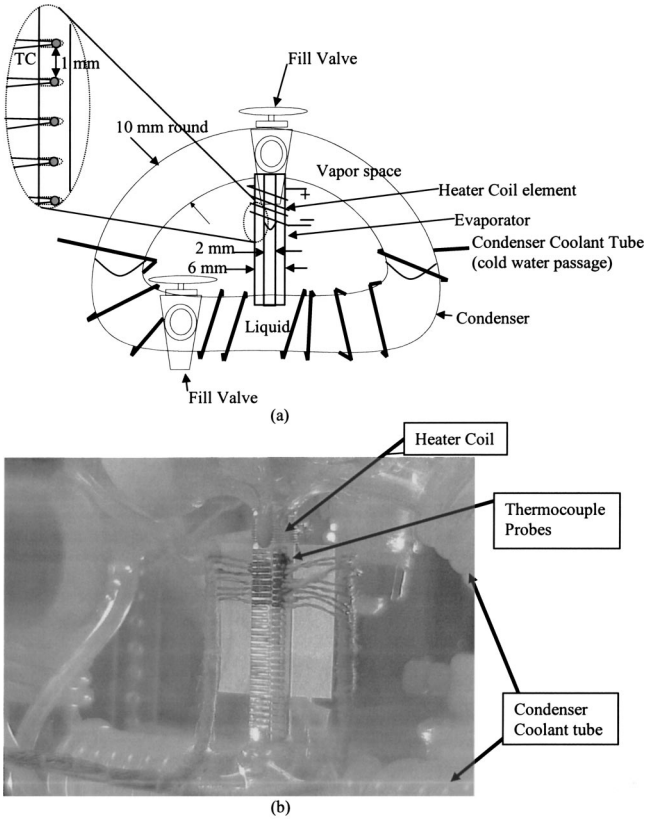

Fig. 3 Schematic of the single pore capillary pumped loop

lizes a large fluid reservoir filled with the appropriate ratio of working fluids. This reservoir is connected to the test specimen and a vacuum pump through complex plumbing that allows vacuum to be pulled from the specimen and the reservoir and regulation of the fluid fill to the specimen. All of these processes are controlled independently so that the amount of charging can be adjusted. The working fluid consisted of a binary fluid mixture of n-pentane and decane. The properties for which are presented in Table 2. Concentrations of 0, 3, 5, and 10% by volume of decane were examined. To control the temperature of the condenser region, a refrigerated circulator was used to pump a constant temperature cooling fluid through the coolant tube wrapped around the exterior of the condenser region.

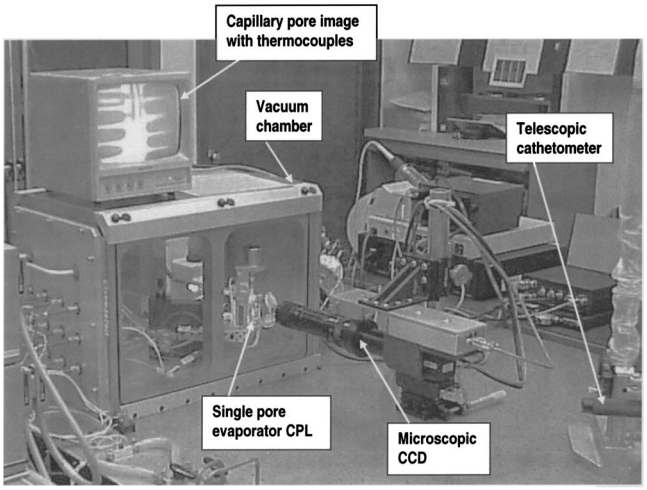

Fig. 4 Experimental setup of the single pore evaporator capillary pumped loop (CPL) placed in a vacuum chamber

Table 2 Properties of Pentane and Decane

Pentane (C_5H_{12}) (Working fluid)	Decane ($C_{10}H_{22}$) (Additive)
$M=72.15$	$M=142.28$
$\sigma=0.0155$ N/m (at 20°C)	$\sigma=0.0234$ N/m (at 20°C)
$\sigma_{op}=0.04835$ N/m	$\sigma_{od}=0.05079$ N/m
$\gamma_p=0.0001102$ N/m·K	$\gamma_d=0.00009197$ N/m·K
Refractive index (n) $=1.3545$ at 20°C	Refractive index (n) $=1.4102$ at 20°C
$T_{BOIL}=36.1$°C at 1 atm	$T_{BOIL}=174.1$°C at 1 atm
$\rho=621.4$ kg/m^3	$\rho=726.4$ kg/m^3

The capillary tube was heated using a fine Nichrome heater wire (spirally wrapped around the tube at the top) having a resistance of 1 Ω/cm. It was connected to a precision DC power supply capable of producing up to three amps at thirty volts. A shunt resistor connected in series with the heating element allowed for the current flowing through the heater to be determined by measuring the voltage drop across it.

Calibrated thermocouples were used to measure the wall temperature of the capillary tube and to measure the temperature of the vapor path and liquid reservoir at the condenser. To determine the temperature distribution of the evaporator region, thermocouples with 0.25 mm bead size were positioned at 0.5 mm intervals along the capillary pore. This was accomplished by creating two rows of thermocouples 180 deg apart. Each row had thermocouples placed longitudinally every millimeter and the two rows have a longitudinal offset of 0.5 mm. Data were recorded using an A/D board interfaced to a Pentuim III—500 PC. The associated errors in the temperature readings were ±0.3°C with a 95% confidence interval. A video microscope system was used to image the meniscus profile so that the contact angle could be estimated. It consisted of a long distance microscope connected to a Hi-8 resolution black and white camera. This image was recorded using an SVHS video recorder. The meniscus was back lit with a high intensity white light source, filtered to allow transmission of light in the green spectrum only and to block transmission of much of the thermal radiation in the infrared spectrum.

The refrigerated circulator temperature was used to set the liquid reservoir (condenser) temperature at 5, 15, and 25°C. Tests were run for each of these system states for variable heat input. The test conditions and power input for the tests are summarized in Table 3. The data presented in this table includes the bulk liquid reservoir temperature and the range of the considered power input.

Table 3 Experimental test conditions

Volume concentration of Decane (%)	Condenser temperature (°C)	Heat input (W)
0	5	0–1.4
	15	0–1.4
	25	0–1.4
3	5	0–2.7
	15	0–2.6
	25	0–3
5	5	0–2.1
	15	0–2.4
	25	0–2.4
10	5	0–1.8
	15	0–3
	25	0–3

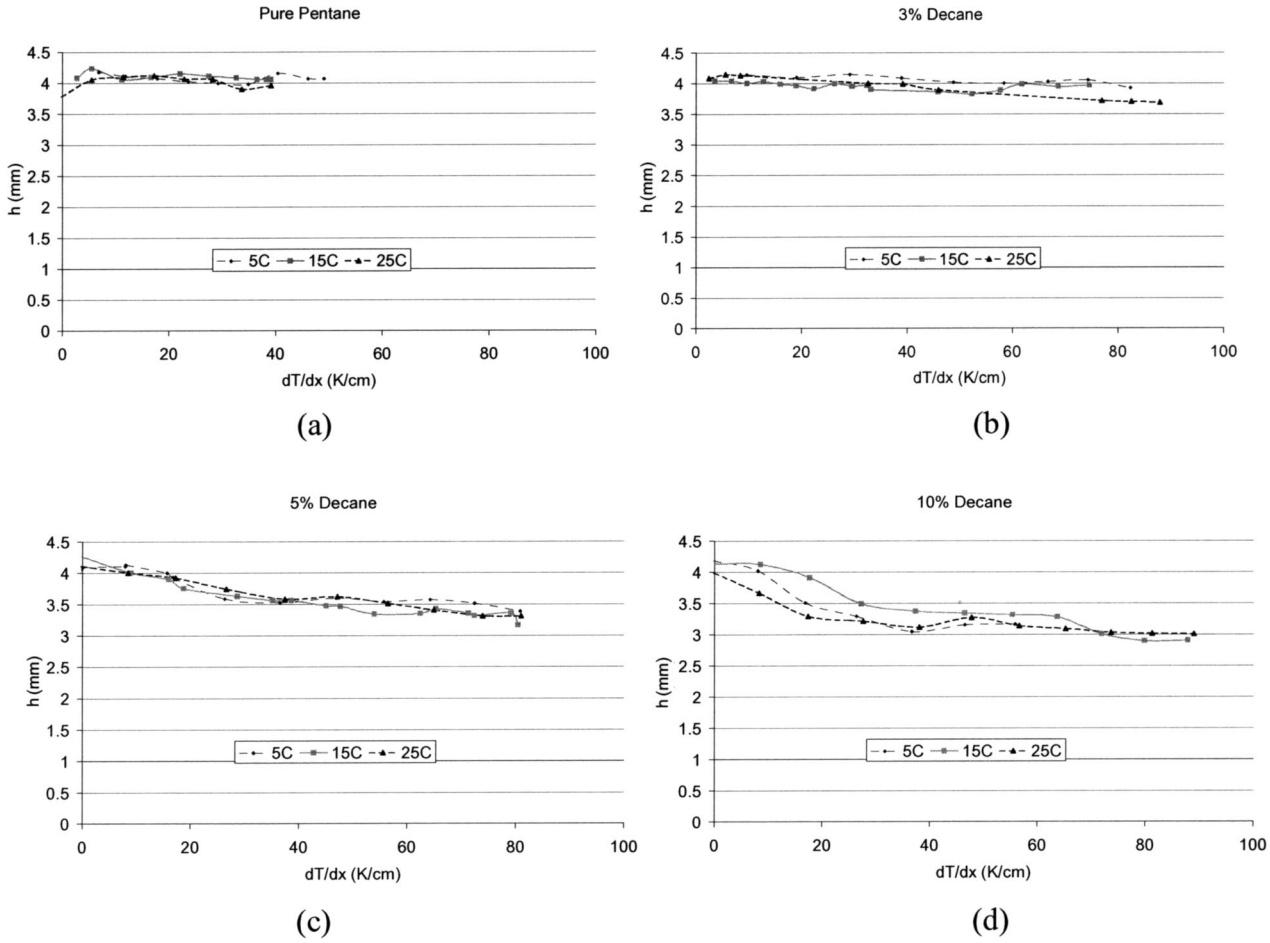

Fig. 5 Capillary pumping potential versus wall temperature gradient: (a) Pure pentane, (b) 3% decane, (c) 5% decane, and (d) 10% decane in volume in the mixture with pentane.

Results

For full examination of the experimentally determined wetting characteristics, data is presented for the conditions detailed in Table 3. This presented data includes the steady-state wicking height versus wall temperature gradient for concentrations of 0, 3, 5, and 10% decane in volume in the mixture with pentane. The capillary pumping potential, or equivalent to the wicking height differential between the evaporator and condenser pores, was measured by a cathetometer that essentially consists of a small telescope with a horizontal hairline to be adjusted in height with the meniscus bottom location and has a digital meter with minimum reading resolution of ± 5 μm. For each measurement condition, up to thirty (30) readings were averaged to alleviate the uncertainties associated with the potentially subjective reading variations through the cathetometer.

Tests were conducted until the temperature nearest to the heating element exceeded 110°C or for the pure pentane case, the system became dynamically unstable. The *x*-axis on all plots is set to the same scale to assist in comparisons. Total errors associated with these plots are $\pm 2.7\%$ with a 95% confidence interval for the capillary pumping potential measurements, and $\pm 8.5\%$ at a 95% confidence interval for the temperature gradient assessment.

Figure 5 is a presentation of capillary pumping potential versus wall temperature gradient at the meniscus for 0 (pure pentane), 3, 5, and 10% decane in volume. All binary mixtures show significantly extended temperature gradients with the onset of meniscus instability deferred in that meniscus said to be unstable when oscillatory motion occurs. The temperature gradient dT/dx is determined from the thermocouple readings that are located closest to the meniscus so that it can be approximated to be comparable to the temperature gradient along the interface [16,17]. Note that the measurements were stopped once any of the thermocouple readings reached 110°C to prevent thermally induced cracking of the glass pore and the stable operation ranges could span farther allowing higher temperature gradients than presented. It shows that there is little variation in wicking height with subcooling of the condenser temperature for all the cases examined.

In Fig. 6 the same data sets are re-grouped and re-plotted so that the effect of the decane concentration on the capillary pumping potential can be more exclusively observed. These show that for low concentrations of decane the capillary pumping potential is not deleteriously affected. However for high concentrations of decane the wicking height, i.e., capillary pumping potential is drastically reduced, whereas their stable operational ranges have been significantly extended. This is a result of the distillation process near the contact line where decane is the primary component and thus dominates the wetting characteristics or contact angles. To understand the significance of this assumption, examination of the contact angle is required.

Figure 7 is a semi-empirical plot of contact angle versus liquid temperature. The values presented were obtained by measuring the wicking height of a single pore placed within a large liquid reservoir held at a known temperature and calculating the contact angle using Eq. (14).

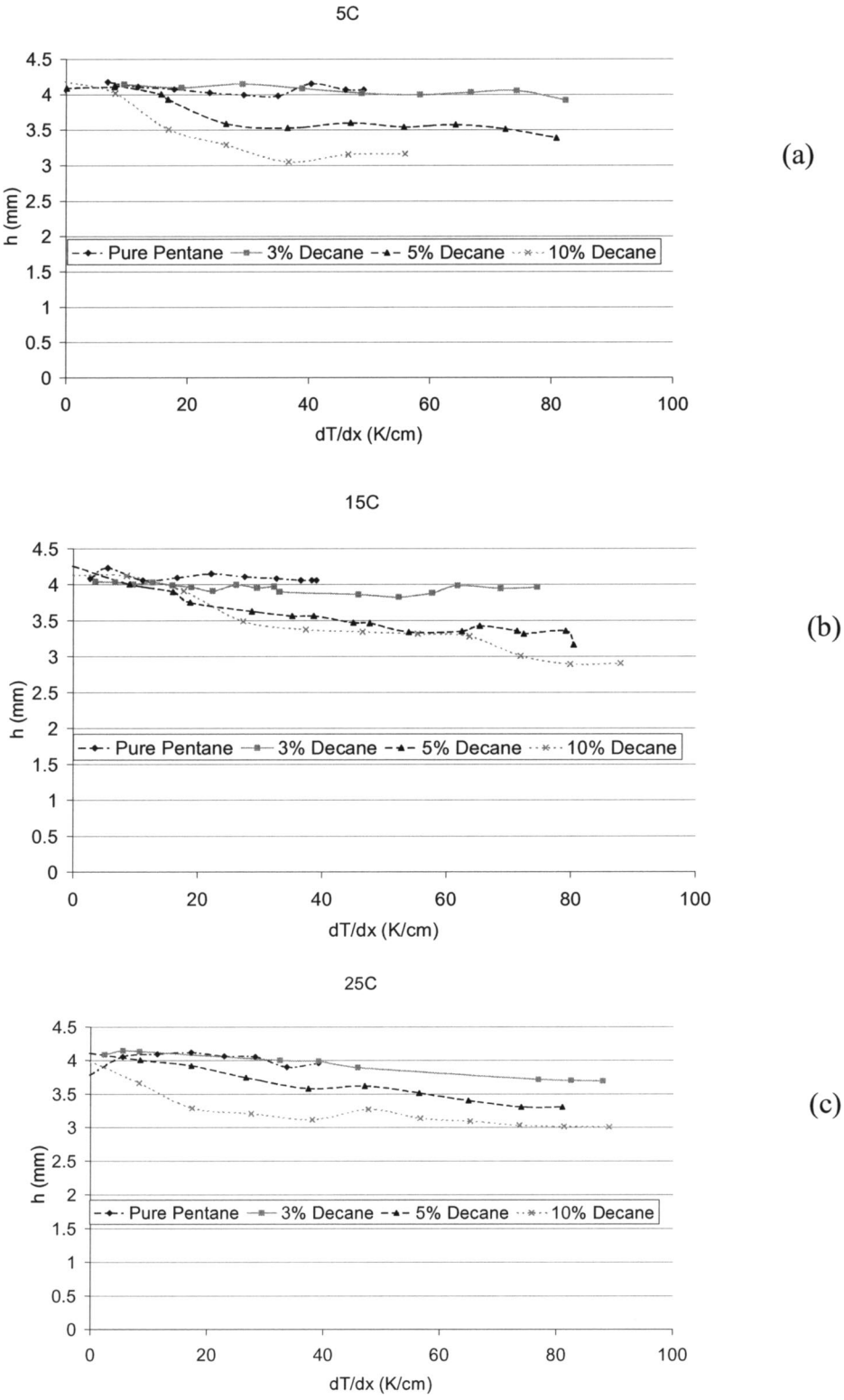

Fig. 6 Capillary pumping potential versus wall temperature gradient for decane concentrations: (a) condenser temperature at 5°C, (b) 15°C, and (c) 25°C.

$$\theta = \cos^{-1} \frac{\rho g h r}{2\sigma} \tag{14}$$

Then the Young-Dupre' equation (Eq. (15)) was applied to determine the variation in contact angle with temperature by assuming that the numerator was approximately constant with temperature for the tested range and allowing the denominator to vary.

$$\cos\theta = \frac{\sigma_{sv} - \sigma_{sl}}{\sigma} \tag{15}$$

The produced contact angle data was then used in Eq. (2) to examine the variation in wicking height due solely to bulk liquid temperature variations for pure pentane, and a decane in pentane mixture where a decane dominated contact angle is expected (Fig.

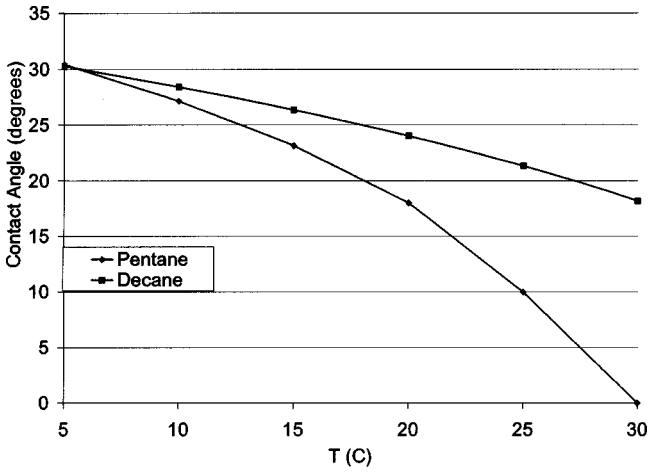

Fig. 7 Contact angle versus liquid temperature for pure pentane and pure decane

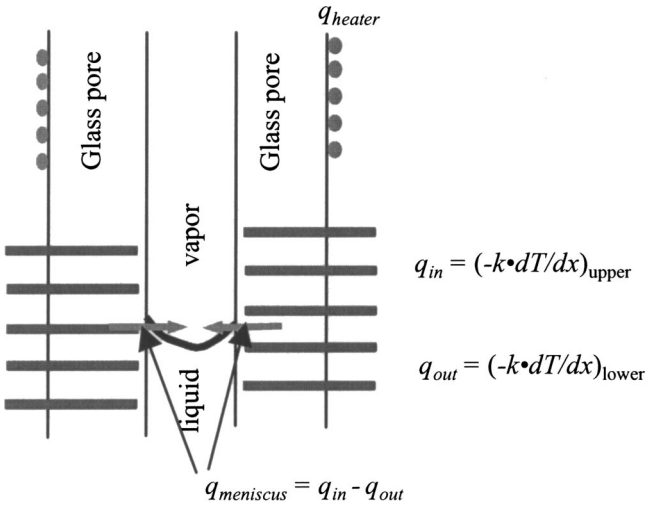

Fig. 10 Energy balance at the meniscus to estimate the amount of heat transfer into the meniscus

8). For pure pentane, the contact angle calculated for pentane was used, and for the mixture, the contact angle measured for decane was used because of the distillation effect is prevalent near the heated wall. The results show similar variations in wicking height as those seen during testing. Thus the assumption that for high decane concentration mixtures, the decane controls the contact angle, seems to be substantiated. This also supports the model developed and presented in Eqs. (8) to (10) because if the wicking height variation is due to changes in contact angle, no net interfacial stress exists. This is apparent if the model is examined. It shows that the thermocapillary stress is balanced by the stress arising from the concentration gradient along the liquid-vapor interface. This balance would yield no net interfacial stress.

Finally, consideration must be made as to how if at all the addition of decane to the working fluid affects heat transfer. To do this two variables must be examined, (1) the rate of energy consumed for evaporation at the meniscus, and (2) the temperature of the meniscus. Figure 9 shows the power input into the meniscus versus the total power provided for the electric heater versus 0, 3, 5, and 10% decane in volume in the mixture with pentane and for a fixed 25°C condenser temperature. This figure shows that the addition of decane into the pentane has no degrading effect on the energy transferred into the meniscus. The heat transferred into the meniscus is calculated by applying a simple energy balance at the meniscus location from the thermocouple data, as illustrated in Fig. 10. This may represent a slightly overestimated heat transfer rate to the meniscus in that the direct heating from the glass inner pore wall to the vapor and to the bulk liquid regions is not accounted for. However, those direct or convective heating magni-

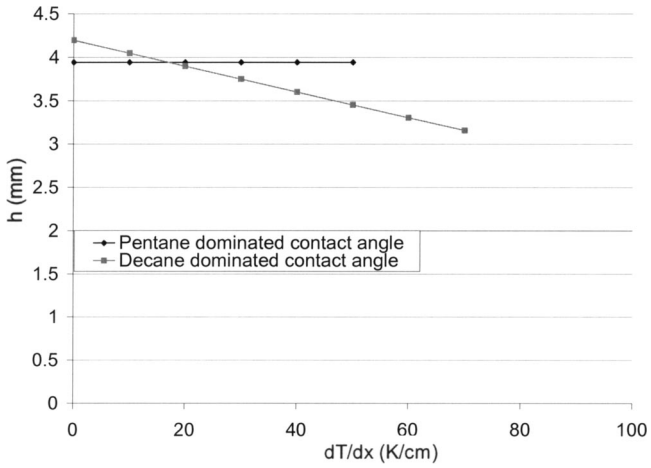

Fig. 8 Capillary pumping potential versus wall temperature gradient

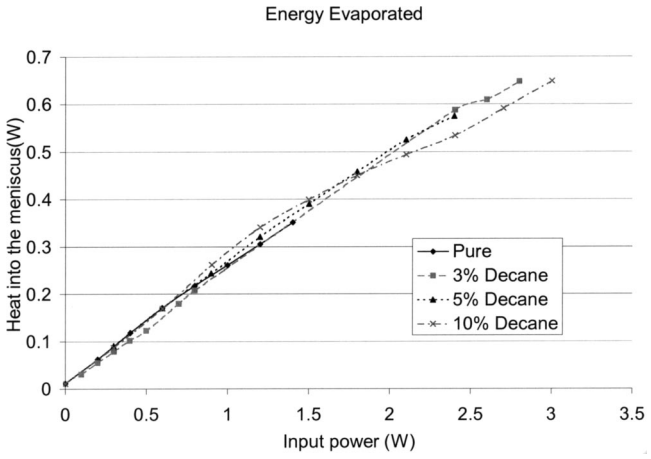

Fig. 9 Heat transferred into the meniscus versus total heat input for a fixed condenser temperature of 25°C

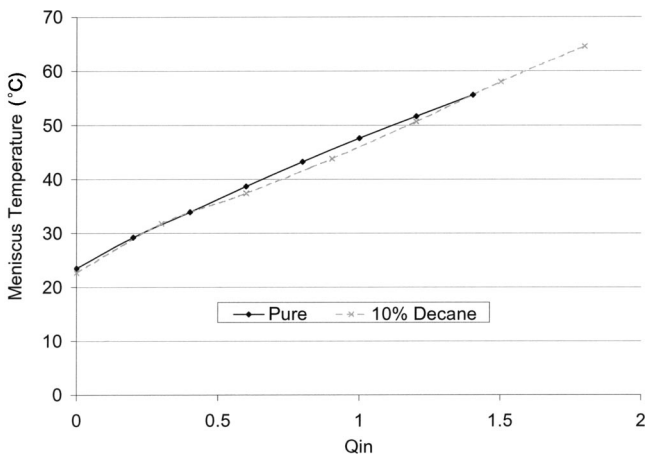

Fig. 11 Temperature at the meniscus versus input power-condenser temperature is 25°C

tudes will not be substantial because of small temperature differentials at the solid-bulk liquid and solid-vapor interfaces and the majority of heat transfer is taking place in the meniscus region under evaporation.

To further substantiate this conclusion, examination of the aforementioned second variable, the meniscus temperature is necessary. Figure 11 is a presentation of the temperature of the thermocouple closest to the intrinsic meniscus for the two limiting cases of pure pentane and 10% decane in pentane. Figure 11 shows that there is no significant variation in the temperature at the meniscus for the two limiting cases. This in conjunction with Fig. 9 demonstrates that the heat transfer characteristics of the system are not necessarily depreciated due to the addition of decane, while the range of stable establishment of its capillary pumping potential is significantly extended in terms of the temperature gradient at the meniscus.

Conclusions

Analysis describing a novel method of negating the deleterious effects of thermocapillary stress on capillary driven phase change devices has been presented and preliminary experiments have been completed, showing its validity. The data revealed that added concentrations of decane in pentane warrant that the onset of meniscus instability is noticeably prolonged with no degradation in heat transfer. This improvement is attributed to concentration-driven capillary gradient due to the distillation of the pentane in the near contact line region, which counteracts the degrading thermocapillary pulling actions, along the meniscus. However, for high concentrations of decane in pentane, substantial reductions in wicking height were observed due to the higher surface-free-energy as decane dominates the contact angle characteristics. Nevertheless, neither the rate of heat input to meniscus nor the meniscus temperature shows any noticeable degradation with the wicking height reduction.

Acknowledgment

This material is based on the work partially supported by the National Research Council-Summer Faculty Fellow Program (SFFP) for Dr. K. D. Kihm and by the Air Force Office of Scientific Research Laboratory Research Initiation Request. Any opinions, findings, and conclusions or recommendations expressed in this publication are those of the authors and do not necessarily reflect the view of the NRC or the AFOSR.

Nomenclature

C = volumetric concentration of decane
c_p = constant pressure specific heat (J/kg-K)
g = acceleration due to gravity (m/s^2)
h = wicking height (m)
h_{fg} = latent heat of vaporization (J/kg)
K = curvature (1/m)
L = length (m)
M = molecular mass
n = index of refraction
P = pressure (Pa)
r = radius of the capillary tube (m)
R = radius of the condenser (m)
T = temperature (°C)
V = average liquid velocity (m/s)
x = cartesian coordinate parallel to thin film (m)
$\Re_{T-C}$ = ratio of the temperature gradient to the concentration gradient [Eq. (12)]
γ = slope of surface tension (N/m-K)
μ = absolute viscosity (Pa-s)
θ = contact angle (degrees)
ρ = density (kg/m^3)
σ = surface tension (N/m)

Subscripts

B = bottom of meniscus
C = concentration
D = decane
flow = flow
l = liquid
o = reference
P = pentane
r = reservoir
sat = saturation
sl = solid-liquid
sv = solid-vapor
T = top of meniscus
TC = thermocapillary
v = vapor

References

[1] Chang, W. S., and Hager, B. G., 1990, ''Advance Two-Phase Thermal Management in Space,'' *National Heat Transfer Conference*, Minneapolis, MN.
[2] Pratt, D. M., Chang, W. S., and Hallinan, K. P., 1998, ''Effects of Thermocapillary Stresses on the Capillary Limit of Capillary-Driven Heat Transfer Devices,'' *Proc. 11th International Heat Transfer Conference*, Kyongju, Korea.
[3] Ma, H. B., Pratt, D. M., and Peterson, G. P., 1998, ''Disjoining Pressure Effect on the Wetting Characteristics in a Capillary Pore,'' Microscale Thermophys. Eng., **2**(4), pp. 283–297.
[4] Pratt, D. M., and Hallinan, K. P., 1997, ''Thermocapillary Effects on the Wetting Characteristics of a Heated Curved Meniscus,'' J. Thermophys. Heat Transfer, **11**(4), pp. 519–525.
[5] Ehrhard, P., and Davis, S. H., 1991, ''Non-Isothermal Spreading of Liquid Drops on Horizontal Plates,'' J. Fluid Mech., **229**, pp. 365–388.
[6] Hocking, L. M., 1995, ''On Contact Angles in Evaporating Liquids,'' Phys. Fluids, **7**(12), pp. 2950–2955.
[7] Sen, A. K., and Davis, S. H., 1982, ''Steady Thermocapillary Flows in Two-Dimensional Slots,'' J. Fluid Mech., **121**, pp. 163–186.
[8] Anderson, D. M., and Davis, S. H., 1994, ''Local Fluid and Heat Flow Near Contact Lines,'' J. Fluid Mech., **268**, pp. 231–265.
[9] Ha, J. M., and Peterson, G. P., 1994, ''Analytical Prediction of the Axial Dryout Point for Evaporating Liquids in Triangular Microgrooves,'' ASME J. Heat Transfer, **116**(2), pp. 498–503.
[10] Chan, S. H., and Zhang, W., 1994, ''Rewetting Theory and the Dryout Heat Flux of Smooth and Grooved Plates With a Uniform Heating,'' ASME J. Heat Transfer, **116**(1), pp. 173–179.
[11] Parks, C. J., and Wayner, Jr., P. C., 1987, ''Surface Shear Near the Contact line of a Binary Evaporating Curved Thin Film,'' AIChE J., **33**(1), pp. 1–10.
[12] Reddy, R. P., and Lienhard, J. H., 1989, ''The Peak Boiling Heat Flux in Saturated Ethanol-Water Mixtures,'' ASME J. Heat Transfer, **111**, pp. 480–486.
[13] Avedisian, C. T., and Purdy, D. J., 1993, ''Experimental Study of Pool Boiling Critical Heat Flux of Binary Fluid Mixtures on an Infinite Horizontal Surface,'' *Proceedings of 1993 ASME International Electronics Packaging Conference*, **2**, pp. 909–915.
[14] Reyes, R., and Wayner, P. C., 1997, ''Interfacial Models for the Critical Heat Flux Superheat of a Binary Mixture,'' National Heat Transfer Conference, HTD-Vol., 342, pp. 187–194.
[15] Carey, V. P., 1999, *Statistical Thermodynamics and Microscale Thermophysics*, Cambridge University Press, Cambridge, UK, Chap. 10.
[16] He, O., 1996, ''Novel Microscale Flow Field Measurement Technique for Extracting Fundamental Physics of Dynamic Thin Films,'' Ph.D. dissertation, Dept. of Mechanical and Aerospace Engineering, Univ. of Dayton, Dayton, OH.
[17] Pratt, D. M., Brown, J. R., and Hallinan, K. P., 1998, ''Thermocapillary Effects on the Stability of a Heated, Curved Meniscus,'' ASME J. Heat Transfer, **120**, pp. 220–226.

Determination of the Thermal Dispersion Coefficient During Radial Filling of a Porous Medium

Mylene Deleglise[1]
Pavel Simacek
Christophe Binetruy
Suresh Advani
e-mail: advani@udel.edu

Department of Mechanical Engineering and
Center for Composite Materials, 201
Spencer Laboratory, University of Delaware
Newark, DE 19716-3144

Resin Transfer Molding is one of the Liquid Composite Molding processes in which a thermoset resin is infiltrated into a fibrous porous media in a closed mold. To reduce the curing time of the resin, the mold may be heated, influencing other filling parameters such as the resin viscosity. Analysis of the non-isothermal effects during filling will help to understand the manufacturing process. One of the issues of non-isothermal filling in porous media is the variation of the velocity profile at the micro scale level, which as it is averaged, cannot be included in the convective term. To account for it, the thermal conductivity tensor is modified and a thermal dispersion coefficient K_d *is introduced to model the micro convection effects. In this paper, we explore the temperature profile under non-isothermal conditions for radial injection during Resin Transfer Molding in order to determine the thermal dispersion coefficient. An approximate solution is derived from the series solution and validated with a numerical method. Experiments using carbon fibers and polyester resin were conducted. The thermal dispersion coefficient is determined by comparing experimental results with the steady state analytical solution. The comparison between radial and linear injection results shows that the same degree of dispersion is present in isotropic fibrous porous media.* [DOI: 10.1115/1.1599366]

Keywords: Experimental, Flow, Heat Transfer, Porous Media

Introduction

Liquid Composite Molding injection processes are widely used in the aerospace and automotive industries. The process consists of injecting a resin into a fiber preform placed in a one or two-sided closed mold. Resin Transfer Molding is one of these processes. The materials used are glass, carbon or aramid fibers, through which a thermoset resin is forced to flow. Thermoset resins involve a curing stage that can last more than half of the cycle time. In order to reduce this step, the mold is heated, as the curing reaction can be catalyzed by heat, and cold resin (room temperature) is injected. Heat conducts through the mold walls and is convected by the resin as it flows through the stationary preform. The temperature of the resin rises in the mold cavity, influencing the cure kinetics and thus the resin viscosity, complicating the manufacturing process. Although at the macro-scale the resin velocity profile can be considered as uniform, at the micro-scale and because of the structure of the preform, the resin flow separates before the fibers and reattaches behind them.

This phenomenon is taken into account in the energy balance equation through the thermal dispersion coefficient. This coefficient is expected to depend on the velocity of the flow front, on the porosity and structure of the media and on the thermal characteristics of the materials [1–5].

The objective of the paper is to characterize and measure the dispersion coefficient in a radial injection. By comparing the experimental data with the analytical solution, we can relate the dispersion coefficient with the initial velocity of the resin. An analytical solution derived from the energy balance equation for the steady state and a numerical simulation taking into account the transient term are developed. The thermal dispersion coefficient can then be calculated for the radial flow case and compared with the values found for linear injection cases.

Background

It is necessary to include a dispersion coefficient in the energy balance equation in order to take into account the micro-scale convection around the fibers that cannot be included in the Darcy's velocity [1–15]. Heat transfer in porous media is described through the energy balance equation written for the two phases. The dispersion coefficient is included in the conductive term through a modified thermal conductivity tensor. Two models are found in the literature, the one-equation model or local thermal equilibrium model (LTE), and the two-equation model, or non-local thermal equilibrium model (NLTE).

When NLTE model is used, a heat transfer coefficient between the fibers and the preform has to be defined [16–20]. Experimentally, this coefficient is difficult to determine, for the temperature of the two phases at the interface needs to be measured. Numerical experiments show that almost no temperature difference existed when non-metallic materials are considered, thus that the local thermal equilibrium assumption is not an unreasonable one for LCM processes [21].

The LTE uses volume averaging on the domain and states that the averaged temperatures of the preform and of the resin are equal at the interface, as expressed below:

$$\langle T_s \rangle_s = \langle T_f \rangle_f = \langle T \rangle \tag{1}$$

This assumption is valid under certain conditions. For instance, the temperature gradient between the two phases must be negligible, thus that the ratio of the thermal conductivities should be approximately unity. The one-equation model breaks down also when high injection velocities are used or when a significant heat generation occurs in one of the two phases [21–24]. When using the LTE model, the energy balance equation is written for the

[1]Current Address: Ecole des Mines de Douai, Technology of Polymers and Composites Department, 941 Rue Charles Bourseul, 59508 Douai, France

Contributed by the Heat Transfer Division for publication in the JOURNAL OF HEAT TRANSFER. Manuscript received by the Heat Transfer Division May 16, 2002; revision received May 12, 2003. Associate Editor: P. S. Ayyaswamy.

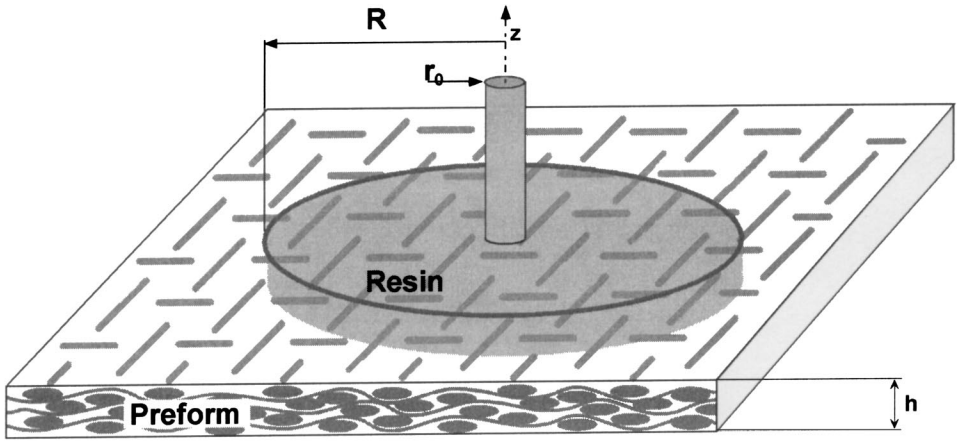

Fig. 1 Schematic of a radial injection

resin or fluid phase and for the preform or solid phase. For the fluid phase, a convective term that accounts for the motion of the fluid, and a heat generation term due to curing reaction are included as shown below.

$$(\rho C_p)_f \frac{\partial T_f}{\partial t} + (\rho C_p)_f \nabla \cdot (\mathbf{v}_f T_f) = \nabla \cdot (k_f \cdot \nabla T_f) + \phi \dot{s} \tag{2}$$

$$(\rho C_p)_s \frac{\partial T_s}{\partial t} = \nabla \cdot (k_s \nabla T_s) \tag{3}$$

where the subscripts f and s stand for the fluid and solid phase respectively.

Applying the LTE assumption (Eq. (1)) and using the volume averaging method [1–5], the governing equation is obtained.

$$(\phi(\rho C_p)_f + (1-\phi)(\rho C_p)_s) \frac{\partial \langle T \rangle}{\partial t} + (\rho C_p)_f \langle \mathbf{v}_f \rangle \cdot \nabla \langle T \rangle = \nabla \cdot ((\mathbf{k}_e + \mathbf{k}_D) \cdot \nabla \langle T \rangle) \tag{4}$$

The resulting model shown in Eq. (4) assumes that no curing reaction is involved. By applying the volume average method, the local variations of the velocity [5] can be introduced in the thermal conductivity tensor $\mathbf{k}$ by adding a thermal dispersion tensor $\mathbf{k}_D$ to the effective thermal conductivity.

$$\mathbf{k} = \mathbf{k}_e + \mathbf{k}_D \tag{5}$$

The effective conductivity tensor $\mathbf{k}_e$ is also called the stagnant conductivity and may be estimated as the average of the materials thermal conductivities:

$$\mathbf{k}_e = \phi \mathbf{k}_f + (1-\phi)\mathbf{k}_s \tag{6}$$

In order to determine the dispersion coefficient, one must conduct experiments. The investigations found in the literature prove that the thermal dispersion coefficient depends on the injection velocity, on the volume fraction of the preform, and on the thermal conductivities of the materials [1–3].

The dependence of the dispersion coefficient with the velocity was studied in the linear injection case in order to establish a relation between the thermal dispersion and the Peclet number:

$$\mathrm{Pe} = \frac{\langle \mathbf{v}_f \rangle d}{\alpha_f} \tag{7}$$

or Pe=Pr Re,

where d is the diameter of the fiber tows and α_f is the thermal diffusion of the fluid phase. The results found in the literature show that the dispersion coefficient varies with Pe^n, where n ranges between 1 [21,23,25–28] and 2 [29–32], and may be different if high or low Peclet numbers are considered [23].

Only one investigation on the Peclet number-dependence of the dispersion coefficient can be found in the radial experimental case [5], although the radial injection scheme is widely used in the industry for various reasons. While in the linear injection case, the flow velocity can be modeled as constant during the injection, in the radial case; the velocity depends on the position of the flow front in the radius direction. A schematic of radial injection is shown in Fig. 1.

Assuming radial symmetry, the flow velocity is

$$\langle v_f \rangle_{flow\ \ front} = \langle v_0 \rangle \frac{r_0}{R} \tag{8}$$

where R is the position of the flow front and $\langle v_f \rangle$ the corresponding velocity, $\langle v_0 \rangle$ and r_0 are respectively the initial velocity and radius of the inlet. As $\mathbf{k}_d = f(\mathrm{Pe}) = f(\langle v_f \rangle)$, the dispersion coefficient will also be a function of the radius [25].

We propose to consider the radial injection scheme by deriving an analytical solution in the cylindrical coordinate system in order to study the variation of the dispersion coefficient with the Peclet number.

Analytical Method

The analytical solution is derived under the assumption that the inlet injection flow rate remains constant throughout the injection, no curing reaction is initiated, the materials used are isotropic in the in-plane directions, and that the viscosity does not directly depend on the temperature, which is a valid assumption as far as thermoset resins are concerned provided that no curing reaction is initiated. Moreover, the dispersion along the in-plane directions can usually be neglected, as the thickness is at least 10 times smaller than the in-plane dimensions [13–14].

We will assume that the transverse component of dispersion tensor, k_{Dzz}, depends linearly on local Peclet number Pe. This correlates well with the measurements carried out previously [1]. This means (Eqs. (7) and (8)):

$$k_{Dzz} = A \cdot \mathrm{Pe}(r) = A \cdot \frac{d}{\alpha_f} \cdot \frac{\langle v_0 \rangle \cdot r_0}{r} = \frac{D_{zz} \cdot R}{r} \tag{9}$$

where A and D_{zz} are constant coefficients.

Under the assumptions listed above, the energy balance is then expressed in a cylindrical coordinate system in Eq. (10).

$$\frac{\partial T^*}{\partial t^*} + \xi Gz \frac{1}{r^*} \frac{\partial T^*}{\partial r^*} = \xi k_{zz}^* \frac{\partial^2 T^*}{\partial z^{*2}} \tag{10}$$

Table 1 Governing equation parameters

Parameter	Description
T^*	$\frac{T-T_{in}}{T_{wall}-T_{in}}$
r^*	$\frac{r}{R}$
r_0^*	$\frac{r_0}{R}$
z^*	$\frac{z}{h}$
ξ	$\frac{\rho_f Cp_f}{\phi\rho_f Cp_f+(1-\phi)\rho_s Cp_s}$
G_z (Graetz Number)	$\frac{\rho_f Cp_f\langle v_0\rangle h^2}{k_e R}$
A	$\xi Gz\frac{r_0}{R}$
B	$\xi\frac{k_{zz}}{k_e}$
C	$\xi\frac{D_{zz}}{k_e}$

where k_{zz}^* (nondimensionalized modified thermal conductivity in the thickness direction) is defined by

$$k_{zz}^*=\frac{k_e+k_{Dzz}}{k_e}=1+\frac{D_{zz}}{k_e r^*} \tag{11}$$

The description of the nondimensional parameters is given in Table 1.

Moreover, the convection only takes place in the radial direction as the volume averaged flow velocity develops in this direction because of radial symmetry. The variations of the velocity profile phenomena are included in the thermal dispersion tensor, $\mathbf{k}_D$, of which only the k_{Dzz} component in the z-direction is considered. The steady state case of Eq. (10) can be written as

$$\frac{A}{r^*}\frac{\partial T^*}{\partial r^*}=B\frac{\partial^2 T^*}{\partial z^{*2}}+\frac{C}{r^*}\frac{\partial^2 T^*}{\partial z^{*2}} \tag{12}$$

Table 2 Materials properties

Characteristics	Symbol	Units	Polyester resin	Carbon fibers
Viscosity	μ	Pa·s	0.08	N/A
Density	ρ	Kg/m^3	1020	1600
Thermal conductivity	k	W/m·K	0.417	1.03
Specific heat capacity	C_p	J/KgK	1800	1000

A, B, and C are constants and are functions of the initial velocity $\langle v_0\rangle$, and of the thermal properties of the materials (see Table 2). The thermal dispersion term D_{zz} (Eq. (9)) is included in the constant C. The temperature profile can thus be derived using the method of separation of variables, using the following boundary conditions:

- the inlet temperature at $r=r_0$ is constant
- the mold walls temperature are held constant

The analytical solution is written for the mid-plane temperature profile, at $z=h/2$, as follows [14]:

$$T^*=1-\frac{4}{\pi}\sum_{n=0}^{\infty}\frac{(-1)^n}{2n+1}\exp\left(\frac{-(2n+1)^2\pi^2 C}{A}(r^*-r_0^*)\right)$$
$$\times\exp\left(\frac{-(2n+1)^2\pi^2 B}{2A}(r^{*2}-r_0^{*2})\right) \tag{13}$$

This solution allows us to evaluate the steady-state temperature along mold mid-plane dependent on heat dispersion magnitude, given by D_{zz}.

Experimental Setup

Experiments are necessary to determine the dispersion coefficient. The aim of the experiments is to monitor the temperature profile in the mid-plane of a mold and along the flow front direction. This temperature profile can then be compared with the analytic solution (Eq. (13)) and the dispersion coefficient in the analytic solution can be varied until the steady state values of the experiment match the analytic solutions values. The carbon fiber preforms used have a quadri-axial structure (0 deg, 45 deg, 90 deg, −45 deg) produced by SAERTEX, as shown in Fig. 2. The four plies are stitched together.

A low viscosity polyester resin from Reichhold, named polylite 31532-02, catalyzed by 1% of peroxide (Norpol 3 from Reichhold), is used.

Table 2 lists the rheological and thermal characteristics of the materials.

The mold used is made of aluminum. It is mounted on a press and a channel was drilled on the mid-thickness of the upper plate in order to access the central injection point. The mold schematic and its dimensions are reported in Fig. 3. K-type thermocouples, with a deviation of 1°C at 100°C are placed in the mid-plane, at the center of the preform, regularly spaced along a radial direction, as shown in Fig. 4.

The mold is placed on a press platen, and thermocouples are connected to a National Instrument acquisition card. The injection unit has a capacity of 12 liters, and a hydraulic pump with a maximum power of 100 bars assured constant flow rate injections. The injection unit was controlled by a numerical command programmed in ISO language (Fig. 5).

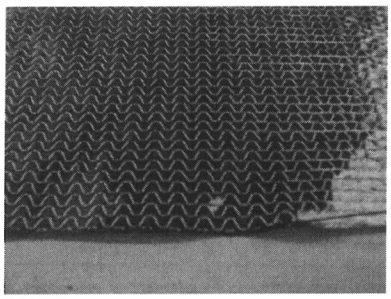

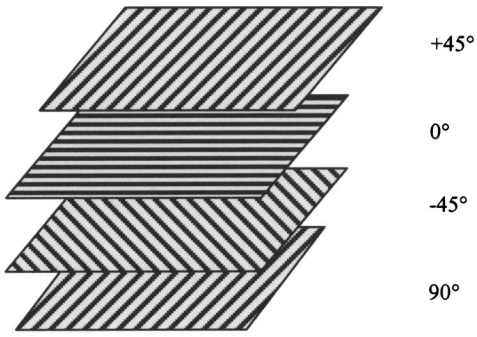

Fig. 2 Carbon fabrics

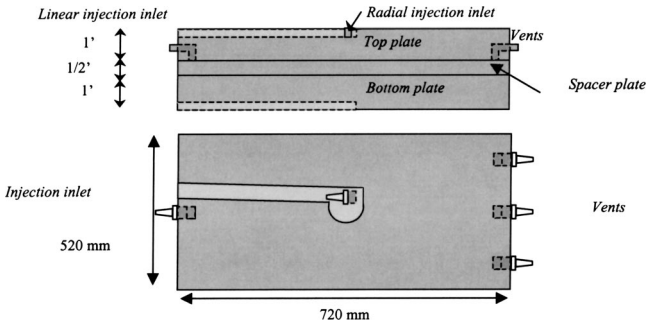

Fig. 3 Schematic of the mold used for resin injections in a mold containing fiber preform. Top and side view.

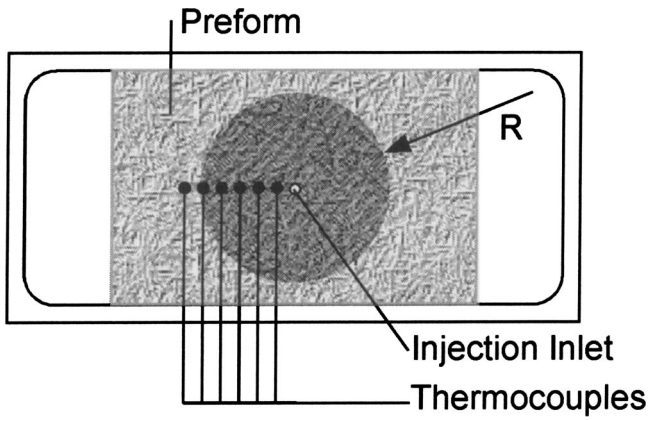

Fig. 4 Thermocouples placement as shown with solid dots

The resin is kept at room temperature while the mold platens are heated to 51°C by using electrical power. The mold plate's thickness insures that the temperature of the mold walls is kept constant. The injection starts when the preform temperature has equilibrated and reached a constant temperature.

Data Analysis

As the flow front advances in a circular shape and encapsulates a thermocouple, the thermocouple temperature drops instantly. At this moment, we can record the time at which the drop occurs and knowing the positions of the thermocouples, calculate the average flow front velocity.

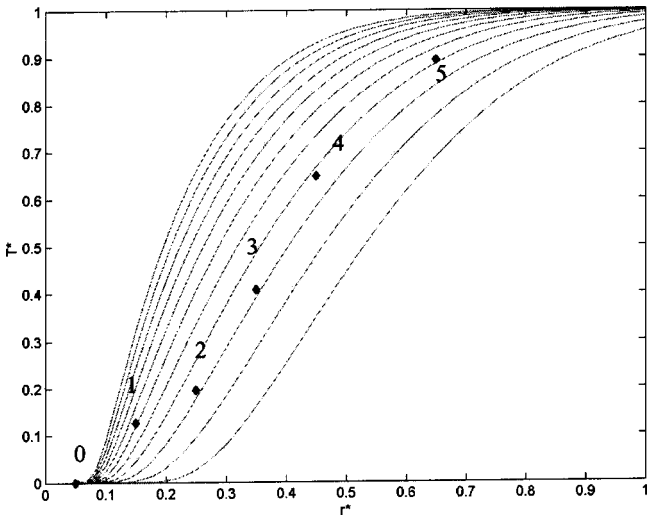

Fig. 6 Comparison between analytical profiles with different dispersion coefficient with experimental data $\langle v_0 \rangle = 0.0180$ m/s, D_{zz} varying from 0 to 10 (increments of 1)

For the radial injection, the velocity varies with the radius of the flow front. For the calculation, only the initial velocity is needed as the velocity at each radius can be expressed in terms of the inlet flow front velocity.

The steady-state temperature at each sensor location is recorded and nondimensionalized as $T^* = (T - T_{in})/(T_{wall} - T_{in})$. The inlet temperature T_{in} is the temperature of the first thermocouple placed at the inlet. The data needed for the determination of the dispersion coefficient are the fiber volume fraction, the thermal properties of the materials, and the mold walls temperature. The inputs that may vary from one experiment to another are the inlet temperature, the thermocouples location and the corresponding steady state temperature, and the velocity of the flow front.

These parameters are set into a Matlab code that calculates the analytical steady state temperature profile along the mold, in the flow front direction. An iterative subroutine allows the dispersion coefficient to vary in an incremental fashion over a predictable scale of values. For every incremental value of the dispersion coefficient an analytical profile is calculated and is compared with the experimental steady state temperature profile. The curve that gives the ''best match'' with the experimental results defines the dispersion coefficient corresponding to that experiment (Figs. 6, 7).

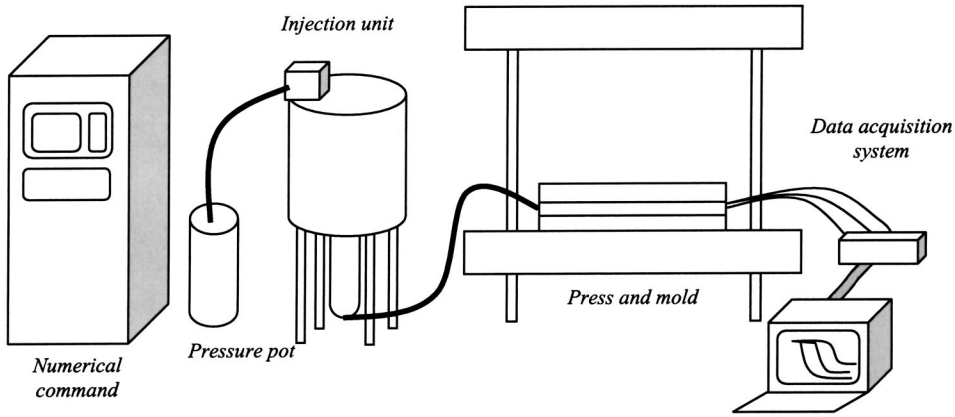

Fig. 5 Experimental setup

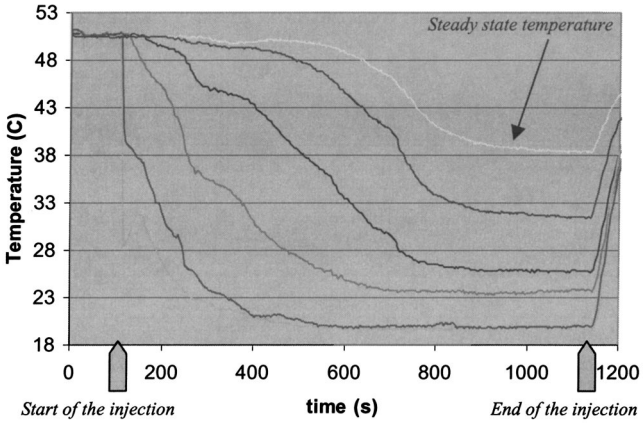

Fig. 7 Experimental time history of the thermocouples as the resin flows across them in a radial mold

Results and Discussion

Experiments were performed with a 49% volume fraction carbon preform at different injection flow rates. The reference velocity used here is the velocity at the inlet. The experimental results are reported in Table 3.

The dispersion coefficient relation with the Peclet number is shown in Fig. 8. The linear relation is expressed as follows:

$$\frac{D_{zz}}{k_e} = 0.0241\mathrm{Pe} + 0.85 \tag{14}$$

This relation can be compared with the relation found in the linear case as follows:

$$\frac{D_{zz}}{k_e} = 0.0211\mathrm{Pe} - 0.303 \tag{15}$$

Table 3 Dispersion Coeficients at Different Injection Velocities calculated by matching the steady state analytic solution with the steady state experimental profile

Experiment	Injection velocity $\langle v_0 \rangle$ m/s	Dispersion coefficient D_{zz} W/mK
0311r20	0.00723	0.4
0301r50	0.0180	2.8
0313r87	0.00314	3.2
0304r125	0.0452	3.7
0227r150	0.0543	3.8
0312r200	0.0724	6.4

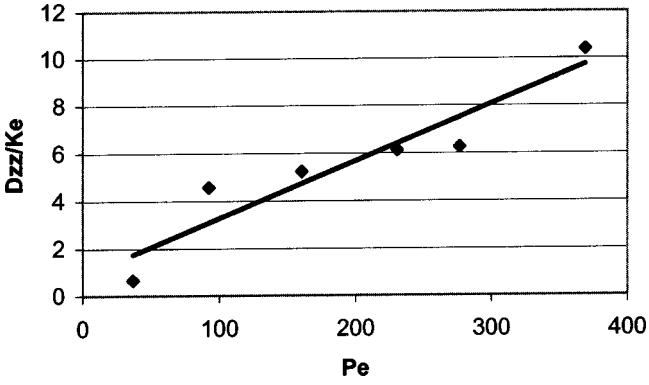

Fig. 8 Dependence of the dispersion coefficient on the Peclet number for the radial case

where k_e is the effective thermal conductivity, $k_e = 0.613$ W/mK and same experimental setup and materials were used for the linear injection as well.

We notice that the relation between the dispersion coefficient and the Peclet number does not go through the origin. Actually, when very low injection velocities are considered, the creeping flow effects become important, affecting the dispersion coefficient as well. As the radius dependence on the dispersion coefficient and on the velocity are already accounted for in the energy balance equation, it makes sense that the dispersion coefficient factor for the linear and the radial injection cases are similar. The range of the values obtained agrees well with the values found in the literature, although the focus in literature has been on the use of glass fibers to represent the fibrous porous media.

Conclusions

An analytical exact solution for the steady state temperature profile was derived from the energy balance equation written for the radial case and validated by a numerical code. The dispersion coefficient was calculated from the comparison between the analytical solution and experimental steady state temperature profile. The dependence of the thermal dispersion coefficient with the injection velocity was studied. Comparison with linear injection experiments conducted with the same materials and in the same experimental set-up validates the results obtained in the radial injection case.

Dispersion coefficient is a property of a material and more widely of a fluid/resin system. The structure of the materials and their thermal properties are important as well as the porosity of the preform and the injection velocity. Once the thermal dispersion is known, non-isothermal numerical simulations become more reliable. Further investigations on the dependence of the thermal dispersion coefficient for different fiber architectures, and a predictive model to estimate it, is a key to modeling nonisothermal flow in which dispersion will be significant.

Acknowledgment

This work was supported by NSF under the grant number 971352 and by ONR under contract number N00014-00-C-0333. Experiments were performed at the Polymers and Composites Technology Department of the Ecole des Mines de Douai, 59500 Douai, France.

Nomenclature

Cp = specific heat at constant pressure
h = reference thickness
$\mathbf{k}$, k = thermal conductivity (tensor, component)
$\mathbf{k}_e$, k_e = effective thermal conductivity (tensor, component)
$\mathbf{k}_D$, k_D = dispersion coefficient (tensor, component)
L = reference length
T = temperature
t = time
$\langle \mathbf{v}_f \rangle$ = volume average flow velocity
ρ = density
ϕ = porosity
$\mathbf{K}$ = permeability tensor
P = pressure
η = viscosity
α = thermal diffusivity
d = fiber tow diameter
r = radial coordinate
R = outer radius of the part

Subscripts and Superscripts

f = fluid
s = solid
$*$ = nondimensional parameters

References

[1] Hsiao, K. T., Laudorn, H., and Advani, S. G., 2001, ''Experimental Investigation of Thermal Dispersion Due to Impregnation of Viscous Fluids in Heated Fibrous Porous Media During Composites Processing,'' ASME J. Heat Transfer, **123**, pp. 178–187.

[2] Advani, S. G., Bruschke, M. V., and Parnas, R. S., 1994, ''Resin Transfer Molding Flow Phenomena in Polymeric Composites,'' *Flow and Rheology in Polymer Composites Manufacturing*, S. G. Advani, ed., Elsevier, Amsterdam, pp. 465–515.

[3] Zhang, W., and Advani, S. G., 1994, ''Heat Dispersion in Stationary Fiber Beds,'' *Mechanics in Materials Processing and Manufacturing*, ASME AMD, **194**, pp. 335–352.

[4] Tucker III, C. L., and Dessenberger, R. B., 1994, ''Governing Equations for Flow and Heat Transfer in Stationary Fiber Beds,'' *Flow and Rheology in Composites Manufacturing*, Suresh G. Advani, ed., Elsevier, Amsterdam, pp. 257–323.

[5] Bruschke, M. V., and Advani, S. G., 1990, ''A Finite Element/Control Volume Approach to Mold Filling in Anisotropic Porous Media,'' Polym. Compos., **11**, pp. 398–405.

[6] Bruschke, M. V., and Advani, S. G., 1991, ''RTM: Filling Simulation of Complex Three-Dimensional Shell-Like Structures,'' SAMPE Q., **23**(1), pp. 2–11.

[7] Bruschke, M. V., and Advani, S. G., 1994, ''A Numerical Approach to Model Non-Isothermal, Viscous Flow With Free Surfaces Through Fibrous Media,'' Int. J. Numer. Methods Fluids, **19**, pp. 575–60.

[8] Liu, B., and Advani, S. G., 1995, ''Operator Splitting Scheme for 3-D Temperature Solution Based on 2-D Flow Approximation,'' Computational Mechanics, **38**, pp. 74–82.

[9] Liu, B., Bickerton, S., and Advani, S. G., 1996, ''Modeling and Simulation of RTM: Gate Control, Venting and Dry Spot Prediction,'' Composites, Part A, **27**, pp. 135–141.

[10] Maier, R. S., Rohaly, T. F., Advani, S. G., and Fickie, K. D., 1996, ''A Fast Numerical Method for Isothermal Resin Transfer Mold Filling,'' Int. J. Numer. Methods Eng., **39**, pp. 1405–1422.

[11] Bickerton, S., Simacek, P., Guglielmi, S., and Advani, S. G., 1997, ''Investigation of Draping and its Effects on the Mold Filling Process During Manufacturing of a Compound Curved Composite Part,'' Composites, Part A, **28A**, pp. 801–816.

[12] Simacek, P., and Advani, S. G., 2001, ''An Analytic Solution for the Temperature Distribution in Flow Through Porous Media in Narrow Gaps: I—Linear Injection,'' Heat Mass Transfer, **1–2**, pp. 25–33.

[13] Simacek, P., and Advani, S. G., 2001, ''An Analytic Solution for the Temperature Distribution in Flow Through Porous Media in Narrow Gaps: II—Radial Injection,'' Heat Mass Transfer, **6**, pp. 497–505.

[14] Simacek, P., and Advani, S. G., 2003, ''Approximate Numerical Method for Prediction of Temperature Distribution in Flow Through Narrow Gaps,'' accepted in Journal of Computational Mechanics.

[15] Yang, J. H., and Lee, S. L., 1998, ''Effect of Anisotropy on Transport Phenomena in Anisotropic Porous Media,'' Int. J. Heat Mass Transfer, **42**, pp. 2673–2681.

[16] Lee, S. L., and Yang, J. H., 1998, ''Modelling of Effective Thermal Conductivity for a Non-Homogeneous Anisotropic Porous Medium,'' Int. J. of Heat and Mass Transfer, **41**(6–7), pp. 931–937.

[17] Lin, R., Lee, L. J., and Liou, M., 1993, ''Mold Filling and Curing Analysis Liquid Composite Molding,'' Polym. Compos., **14**(1), pp. 71–81.

[18] Hunt, M. L., and Tien, C. L., 1988, ''Effects of Thermal Dispersion on Forced Convection in Fibrous Media,'' Int. J. Heat Mass Transfer, **31**(2), pp. 301–309.

[19] Quintard, M., and Whitaker, S., 1995, ''Local Thermal Equilibrium for Transient Heat Conduction: Theory and Comparison With Numerical Experiments,'' Int. J. Heat Mass Transfer, **38**(15), pp. 2779–2796.

[20] Jiang, P. X., Ren, Z. P., and Wang, B. X., 1999, ''Numerical Simulation of Forced Convection Heat Transfer in Porous Plate Channels Using Thermal Equilibrium and Non-Isothermal Equilibrium Models,'' Numer. Heat Transfer, Part A, **35**, pp. 99–113.

[21] Kuwahara, F., and Nakayama, A., 1999, ''Numerical Determination of Thermal Dispersion Coefficients Using a Periodic Porous Structure,'' ASME J. Heat Transfer, **121**, pp. 160–167.

[22] Hsu, C. T., and Cheng, P., 1990, ''Thermal Dispersion in a Porous Medium,'' Int. J. Heat Mass Transfer, **33**(8), pp. 1587–1597.

[23] Winterberg, M., Tsotas, E., Krischke, A., and Vortmeyer, D., 2000, ''A Simple and Coherent Set of Coefficients for Modeling of Heat and Mass Transport With and Without Chemical Reaction in Tube Filled With Spheres,'' Chem. Eng. Sci., **55**, pp. 967–979.

[24] Amiri, A., and Vafai, K., 1998, ''Transient Analysis of Incompressible Flow Through a Packed Bed,'' Int. J. Heat Mass Transfer, **41**, pp. 4259–4279.

[25] Lebrun, G., and Gauvin, R., 1995, ''Heat Transfer Analysis in a Heated Mold During the Impregnation Phase of the Resin Transfer Molding Process,'' J. Mater. Process. Manuf. Sci., **4**(2), pp. 81–104.

[26] Adnani, P., Catton, I., and Abdou, M. A., 1995, ''Non-Darcian Forced Convection in Porous Media With Anisotropic Dispersion,'' ASME J. Heat Transfer, **117**, pp. 447–451.

[27] Quintard, M., Kaviany, M., and Whitaker, S., 1997, ''Two-Medium Treatment of Heat Transfer in Porous Media: Numerical Results for Effective Properties,'' Adv. Water Resour., **20**, pp. 77–94.

[28] Zanotti, F., and Carbonell, R. G., 1984, ''Development of Transport Equations for Multiphase Systems-III, Application to Heat Transfer in Packed Beds,'' Chem. Eng. Sci., **39**(2), pp. 299–311.

[29] Young, W. B., 1995, ''Thermal Behavior of the Resin and Mold in the Process of Resin Transfer Molding,'' J. Reinf. Plast. Compos., **14**(4), p. 310.

[30] Koch, D. L., and Brady, J. F., 1987, ''The Symmetry of the Effective Diffusivity Tensor in Anisotropic Porous Media,'' Phys. Fluids, **30**, pp. 642–650.

[31] Koch, D. L., and Brady, J. F., 1985, ''Dispersion in Fixed Bed,'' J. Fluid Mech., **154**, pp. 399–427.

[32] Yuan, Z. G., Somerton, W. H., and Udell, K. S., 1991, ''Thermal Dispersion in Thick-Walled Tubes as a Model of Porous Media,'' Int. J. Heat Mass Transfer, **34**(11), pp. 2715–2726.

Li Shi
e-mail: lishi@mail.utexas.edu
Department of Mechanical Engineering,
Center for Nano and Molecular Science and Technology,
University of Texas at Austin, TX 78712

Deyu Li
Department of Mechanical Engineering,
University of California, Berkeley, CA 94720

Choongho Yu
Department of Mechanical Engineering,
Center for Nano and Molecular Science and Technology,
University of Texas at Austin, TX 78712

Wanyoung Jang
Department of Physics,
Department of Mechanical Engineering,
University of California, Berkeley, CA 94720

Dohyung Kim
Department of Mechanical Engineering,
Center for Nano and Molecular Science and Technology,
University of Texas at Austin, TX 78712

Zhen Yao
Department of Physics,
Department of Mechanical Engineering,
University of California, Berkeley, CA 94720

Philip Kim
Department of Physics,
Columbia University, New York

Arunava Majumdar
Materials Science Division,
Lawrence Berkeley National Laboratory,
Department of Mechanical Engineering,
University of California, Berkeley, CA 94720

Measuring Thermal and Thermoelectric Properties of One-Dimensional Nanostructures Using a Microfabricated Device

We have batch-fabricated a microdevice consisting of two adjacent symmetric silicon nitride membranes suspended by long silicon nitride beams for measuring thermophysical properties of one-dimensional nanostructures (nanotubes, nanowires, and nanobelts) bridging the two membranes. A platinum resistance heater/thermometer is fabricated on each membrane. One membrane can be Joule heated to cause heat conduction through the sample to the other membrane. Thermal conductance, electrical conductance, and Seebeck coefficient can be measured using this microdevice in the temperature range of 4–400 K of an evacuated Helium cryostat. Measurement sensitivity, errors, and uncertainty are discussed. Measurement results of a 148 nm and a 10 nm-diameter single wall carbon nanotube bundle are presented. [DOI: 10.1115/1.1597619]

Keywords: Heat Transfer, Measurement Techniques, Microscale, Nanoscale, Thermoelectric

Introduction

One-dimensional (1D) nanostructures such as nanotubes, nanowires, and nanobelts have unique thermophysical properties very different from those of their bulk counter parts. In general, as these materials are confined to low dimensions with a size comparable to the scattering mean free paths, the thermal conductivity is often reduced due to increased boundary scattering and modified phonon dispersion [1,2]. An exception to this scaling trend is carbon nanotubes (CNs). Due to the unique crystalline structure, boundary scattering is nearly absent in CNs, giving rise to super high thermal and electrical conductivity that makes the CN an ideal candidate for nanoelectronic applications. Furthermore, a single wall (SW) CN is an ideal system to study quantum thermal conduction phenomena. For example, a (10,10) SWCN has a series of phonon sub-bands near the zone center [3]. The small diameter (d_t) of the nanotube causes relatively large sub-band splitting between the acoustic and the optical modes. For a temperature $T \ll 2hv/(k_B d_t)$, where h, v, k_B, d_t are Planck constant, phonon group velocity, Boltzmann constant, and tube diameter, respectively, only four acoustic modes are occupied, and the thermal conductance of a SWCN is expected to show linear temperature dependence with a maximum possible value $G_{th}=4g_0$. Here, $g_0=\pi^2 k_B^2 T/3h=(9.46\times10^{-13})T$ (W/K) is the universal quantum of thermal conductance [4].

The potential applications and intriguing nanoscale thermal conduction physics has inspired several groups to measure Seebeck coefficient [5], specific heat [6,7], and thermal conductivity [8,9] of CN bundles and mats. Hone et al. measured the thermal conductivity [7,8] and Seebeck coefficient [5] of millimeter size mat samples made of CNs. The measured thermal conductance shows linear temperature dependence below 25 K and extrapolates to zero at zero temperature. The measurement results have advanced our understanding of thermal conduction in CNs. However, it is difficult to extract the thermal conductivity of a single tube from such measurements because the sample consists of numerous micrometer-long tubes connected into a millimeter-size mat. As such, there exist large contact thermal resistances at the junctions between individual tubes in the mat. Further, the filling factor or density of the tubes in the mat is unknown. As the consequence, the estimated room-temperature thermal conductivity of

Contributed by the Heat Transfer Division for publication in the JOURNAL OF HEAT TRANSFER. Manuscript received by the Heat Transfer Division October 14, 2002; revision received April 8, 2003. Associate Editor: G. Chen.

the mat is about 250 W/m-K, one order of magnitude lower than theoretical predictions [10–12]. In addition, the measured thermal conductance increases with temperature for the entire temperature range of 8–350 K, showing no signature of Umklapp phonon-phonon scattering. This indicates that the dominant scattering mechanism is phonon scattering by defects and boundaries. Yi et al. [6] used a self heating 3ω method to measure the specific heat and thermal conductivity of a suspended millimeter-long aligned multi-wall (MW) CN bundle with an apparent cross section of 10^{-10} to 10^{-8} m^2. The measured specific heat exhibits linear temperature dependence in a temperature range of 10–300 K, showing a different behavior from the results obtained by Hone et al. In addition, because of the large thermal resistance at the defects and at the contacts between individual tubes, the measured thermal conductivity is about 20 W/m-K at room temperature, two orders of magnitude lower than theoretical predictions for a single defect-free tube.

It is necessary to investigate the intrinsic thermal transport properties of individual CNs by eliminating the influences from contact thermal resistances at the junctions between individual tubes and from phonon scattering between adjacent tubes. This is also the case for other nanostructures including a variety of nanotubes, nanowires, and nanobelts. Of particular interest, nanowires of Bi and Bi_2Te_3 may exhibit significant enhancement of the thermoelectric figure of merit, and have potential applications in efficient thermoelectric energy conversion [13,14]. Currently, there have been few measurement data of thermal properties of individual nanotubes, nanowires, and nanobelts. This is because conventional techniques for thin film thermal property measurements, such as the 3ω method [15], cannot be used readily for these nanostructures due to the small sample size. In order to concurrently measure thermal conductance, electrical conductance, and Seebeck coefficient of CNs, we and our collaborators developed a suspended microdevice in a previous work [16,17]. We used the device for measuring thermal conductivity and Seebeck coefficient of an individual suspended MWCN and obtained results in agreement with theory [17]. Here, we further optimize device design and fabrication process, improve the measurement method, and employ the technique for thermal property measurements of a variety of one-dimensional nanostructures. The following sections discuss the design, fabrication, measurement method, sensitivity, errors, and uncertainty of the technique. As a demonstration of the technique, the measurement results of two SWCN bundles are presented.

Experimental Methods

Device Design and Fabrication. Figure 1 shows a scanning electron micrograph (SEM) of the microdevice. The device is a suspended structure consisting of two adjacent 14 μm×25 μm low stress silicon nitride (SiN_x) membranes suspended with five 0.5-μm-thick, 420-μm-long and 2-μm-wide silicon nitride beams. One 30-nm-thick and 300-nm-wide platinum resistance thermometer (PRT) coil is designed on each membrane. The PRT is connected to 200 μm×200 μm Pt bonding pads on the substrate via 1.8 μm wide Pt leads on the long SiN_x beams. An additional 1.8 μm wide Pt electrode is designed on each membrane next to each other, providing electrical contact to the sample.

The device is batch fabricated using a wafer-stage microfabrication process, as shown in Fig. 2. First, a 0.5-μm-thick low-stress SiN_x film is deposited on a 100-mm-diameter wafer using a low pressure chemical vapor deposition (LPCVD) method, as shown in Fig. 2(a). A 30 nm-thick Pt film is then deposited on the SiN_x film by radio-frequency (RF) sputtering. A 300-nm-thick low temperature silicon dioxide (LTO) is grown on the Pt film using LPCVD. A photoresist is spun on the LTO film and patterned using an I-line wafer stepper. Combined with an oxygen plasma etching technique, the wafer stepper can produce photoresist patterns with a line width below 0.4 μm. The photoresist pattern is then transferred to the LTO film using reactive ion etching (RIE).

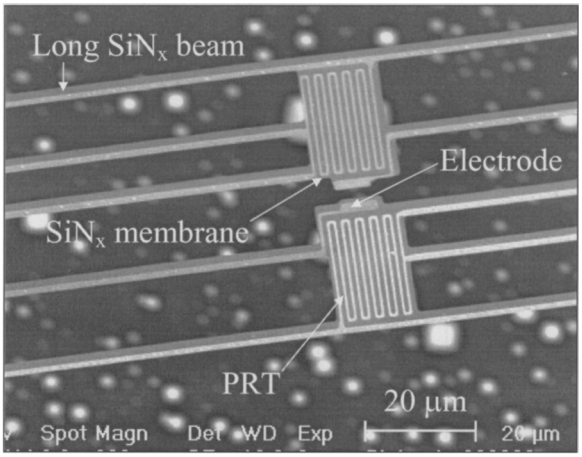

Fig. 1 SEM micrograph of a microdevice for thermal property measurements of nanostructures

Using the patterned LTO as a mask, the unprotected Pt film is etched using ion milling or sputter etching to make serpentine PRT lines (Fig. 2(b)). After the photoresist and LTO are stripped, a 300-nm-thick LTO is deposited on the wafer. A photolithography and wet etching step is then used to open contact windows to the Pt contact pads for wire bonding, and to the 1.8 μm wide Pt electrode near the PRT. This Pt electrode is used for making electrical contact to the sample. A photoresist film is then spun on the wafer and patterned (Fig. 2(c)). The pattern is transferred to the SiN_x film by RIE. After the photoresist is stripped, tetramethylammonium hydroxide (TMAH) is used to etch the exposed Si region and the suspended structure is released when the Si substrate is etched away, as shown in Fig. 2(e). The etching pit in the Si substrate is usually about 100–200 μm deep, and as such the

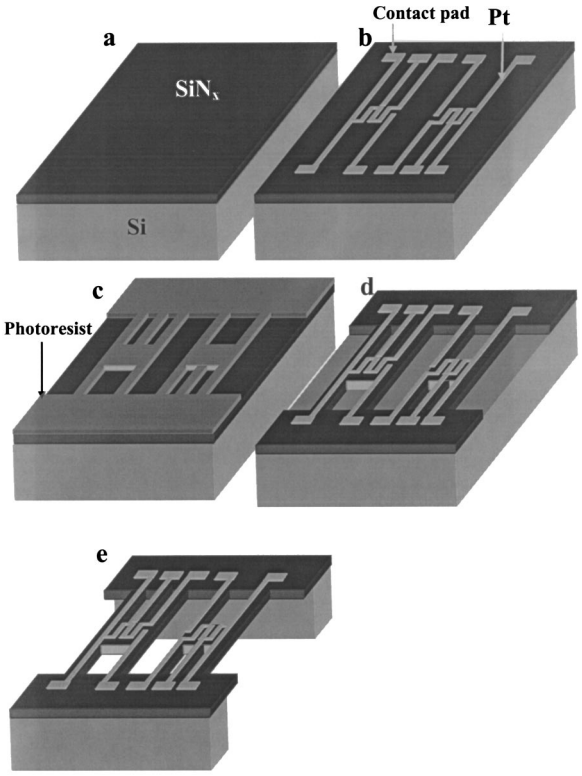

Fig. 2 Fabrication process of the microdevice

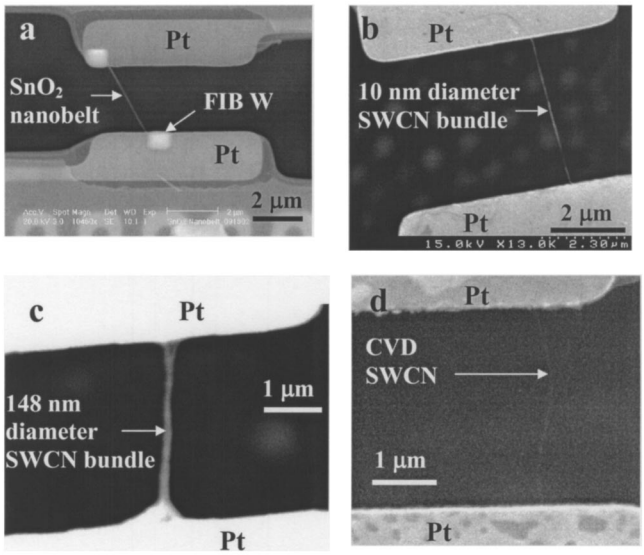

Fig. 3 SEM image of a SnO_2 nanowire (a), a 10 nm diameter SWCN bundle (b), a 148 nm diameter SWCN bundle (c), and a CVD-grown SWCN (d) connecting two Pt electrodes on two suspended membranes

suspended structure does not collapse to the substrate even without the use of a critical point dryer. Using this wafer-stage fabrication technique, about 2000 densely packed suspended structures can be made on a 100 mm diameter wafer.

A nanotube, nanowire, or nanobelt can be placed between the two suspended membranes by several methods. One way is to use a sharp probe to pick up a sample, and then manipulate the probe using a probe station to place the sample between the two membranes. The process requires a high-resolution optical microscope. This method was employed in our previous work for placing MWCN bundles and individual MWCNs between two membranes [17].

The probe manipulation method is a tedious process. In view of this, we have developed two different approaches for trapping a nanostructure sample between the two membranes. In the first approach, a solution containing the nanostructures is dropped and spun on a wafer containing many suspended devices. We have found that the nanostructures are often adsorbed on the two Pt electrodes. Figures 3(a–c) show a SnO_2 nanobelt, a 10 nm diameter SWCN bundle, and a 148 nm diameter SWCN bundle adsorbed on the two membranes, respectively, by this wet deposition method. To improve the thermal and electrical contact between the sample and the Pt electrode, we usually anneal the device at 300°C for a few hours. Further, a small tungsten or Pt pad can be deposited on top of the sample-electrode contact using a focused ion beam technique, as shown in Fig. 3(a). Alternatively, an amorphous carbon film can be deposited on top of the sample-electrode contact region. To do that, the electron beam of a SEM is focused on the contact region with a high magnification of 200,000 or larger. Because of organic contamination in the SEM chamber, the electron beam induces the deposition of a carbon film on the focused region. This can further improve the contact.

In the second approach, we employ a chemical vapor deposition (CVD) method to grow individual SWCNs bridging the two membranes. To do that, we first spin a solution containing catalyst nano-particles made of Fe, Mo, and Al_2O_3 on the suspended membranes. This yields many catalyst nano-particles deposited on the Pt electrodes. The suspended device is then placed in a 900°C CVD tube with flowing methane resulting in individual SWCNs grown between two catalyst particles on the two Pt electrodes. Figure 3(d) shows a SWCN synthesized by this method. The sample-electrode contact is annealed in the high-temperature growth process, leading to low contact resistances.

Measurement Method

Thermal Conductance. Figure 4 shows the schematic diagram of the experimental setup for measuring the thermal conductance of the sample. The suspended structure is placed in a cryostat with a vacuum level better than 1×10^{-5} Torr. The two suspended membranes are denoted as the heating membrane and sensing membrane, respectively. A dc current (I) flows to one of the two PRTs. A Joule heat $Q_h=I^2R_h$ is generated in this heating PRT that has a resistance of R_h. The PRT on each membrane is connected to the contact pads by four Pt leads, allowing four-probe resistance measurement. The resistance of each Pt lead is R_L, which is about half of R_h. A Joule heat of $2Q_L=2I^2R_L$ is dissipated in the two Pt leads that supply the dc current to the heating PRT. We assume that the temperature of the heating membrane is raised to a uniform temperature T_h. This assumption can be justified because the internal thermal resistance of the small membrane is much smaller than the thermal resistance of the long narrow beams thermally connecting the membrane to the silicon chip at temperature T_0. A certain amount of the heat (Q_2) is conducted through the sample from the heating membrane to the sensing one, raising the temperature of the latter to T_s. In vacuum and with a small $\Delta T_h(\equiv T_h-T_0<6$ K), the heat transfer between the two membranes by air conduction and radiation is negligible compared to Q_2, as discussed below. The heat flow in the amount of Q_2 is further conducted to the environment through the five beams supporting the sensing membrane. The rest of the heat, i.e., $Q_1=Q_h+2Q_L-Q_2$, is conducted to the environment through the other five beams connected to the heating membrane.

The five beams supporting each membrane are designed to be identical. It can be shown that below 400 K, the radiation and air conduction heat losses from the membrane and the five supporting beams to the environment are negligible compared to conduction heat transfer through the five beams. Hence, the total thermal conductance of the five beams can be simplified as $G_b=5k_lA/L$, where k_l, A, and L are the thermal conductivity, cross

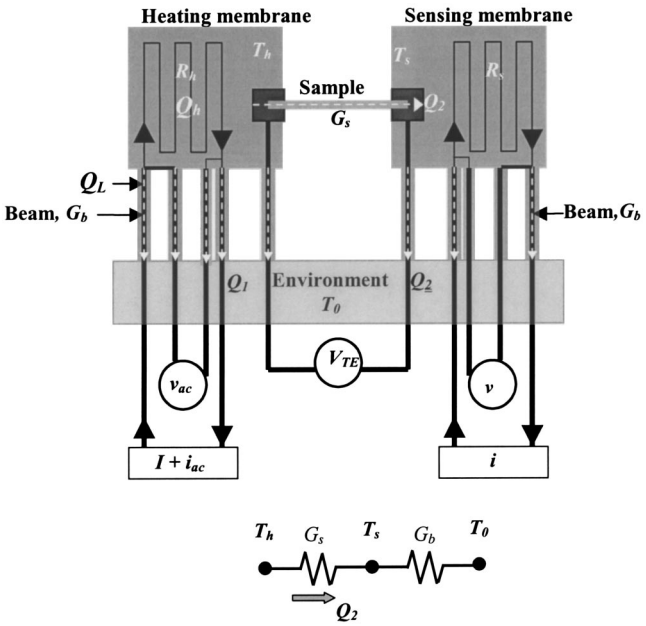

Fig. 4 Schematic diagram and thermal resistance circuit of the experimental setup

sectional area, and length of each beam, respectively. We can obtain the following equation from the thermal resistance circuit shown in Fig. 4,

$$Q_2 = G_b(T_s - T_0) = G_s(T_h - T_s), \tag{1}$$

where G_s is the thermal conductance of the sample and consists of two components, i.e.,

$$G_s = (G_n^{-1} + G_c^{-1})^{-1} \tag{2}$$

where $G_n = k_n A_n / L_n$ is the intrinsic thermal conductance of the nanostructure, k_n, A_n, and L_n are the thermal conductivity, cross sectional area, and length of the free-standing segment of the sample between the two membranes, respectively. G_c is the contact thermal conductance between the nanostructure and the two membranes. Because the temperature excursion ΔT_h is small, G_s, G_b, and G_c are assumed to be constant as ΔT_h is ramped.

Considering one-dimensional heat conduction, one can obtain temperature distribution in the ten beams supporting the two membranes. A Joule heat of Q_L is generated uniformly in each of the two Pt leads supplying the heating current, yielding a parabolic temperature distribution along the two beams; while linear temperature distribution is obtained for the remaining eight beams without Joule heating. The heat conduction to the environment from the two Joule-heated beams can be derived as $Q_{h,2} = 2(G_b \Delta T_h/5 + Q_L/2)$; while that from the remaining three beams connected to the heating membrane is $Q_{h,3} = 3G_b \Delta T_h/5$, and that from the five beams connected to the sensing membrane is $Q_{s,5} = G_b \Delta T_s$, where $\Delta T_s \equiv T_s - T_0$. Considering energy conservation, i.e., $Q_{h,2} + Q_{h,3} + Q_{s,5} = Q_h + 2Q_L$, one obtains

$$G_b = \frac{Q_h + Q_L}{\Delta T_h + \Delta T_s}, \tag{3a}$$

and

$$G_s = G_b \frac{\Delta T_s}{\Delta T_h - \Delta T_s}. \tag{3b}$$

Q_h and Q_L can be calculated readily from the dc current and the voltage drops across the heating PRT and the Pt leads. ΔT_h and ΔT_s are calculated from the measured resistance of the two PRTs and their temperature coefficient of resistance (TCR $\equiv (dR/dT)/R$). The four-probe differential electrical resistance R_s of the sensing PRT is measured using a SR830 lock-in amplifier with a 250–500 nA, 199 Hz sinusoidal excitation current. The temperature rise ΔT_s of the sensing membrane depends on the DC current I of the heating PRT, and is related to R_s according to the following equation

$$\Delta T_s(I) = \frac{\Delta R_s(I)}{\dfrac{dR_s(I=0)}{dT}}; \quad \Delta R_s(I) \equiv R_s(I) - R_s(I=0) \tag{4}$$

The differential resistance R_h of the heating PRT can be obtained by one of the two following methods. In the first method, the $I-V$ curve is measured as the dc current (I) is slowly ramped up to a value in the range of 4–10 μA depending on T_0. One ramping cycle typically takes 15 minutes. The *differential* resistance of the PRT heater is calculated as $R_h = dV/dI$. For a slow voltage ramp rate, it can be shown that the temperature rise in the heating membrane is

$$\Delta T_h(I) = \frac{\Delta R_h(I)}{3\dfrac{dR_h(I=0)}{dT}}; \quad \Delta R_h(I) \equiv R_h(I) - R_h(I=0) \tag{5}$$

Here, we use the differential resistance instead of the average resistance ($\equiv V/I$) because the former offers better sensitivity for temperature measurement.

Alternatively, a 250–500 nA sinusoidal current (i_{ac}) with a frequency f can be coupled to the much larger dc heating current I. A SR830 lock-in amplifier is used to measure the first harmonic component (v_{ac}) of the voltage drop across the heating PRT, yielding the differential resistance $R_h = v_{ac}/i_{ac}$. For R_h obtained by this method, it can be shown that

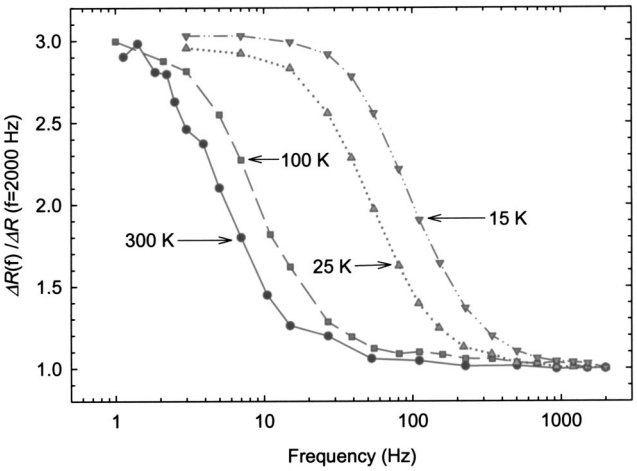

Fig. 5 Normalized first harmonic component of the measured resistance rise of the heating PRT as a function of the frequency of an ac current coupled to the dc heating current

$$\Delta T_h(I) = \frac{\Delta R_h(I)}{3\dfrac{dR_h(I=0)}{dT}}, \quad \text{for } f \ll 1/(2\pi\tau) \tag{6a}$$

$$\Delta T_h(I) = \frac{\Delta R_h(I)}{\dfrac{dR_h(I=0)}{dT}}, \quad \text{for } f \gg 1/(2\pi\tau) \tag{6b}$$

where τ is the thermal time constant of the suspended device, and is estimated to be on the order of 10 ms. The difference between these two solutions origins from a first harmonic modulated heating component, i.e., $2i_{ac}IR_h$. At a very low (high) frequency compared to $1/(2\pi\tau)$, the modulated heating yields a nontrivial (trivial) first harmonic component in T_h. This further causes a nontrivial (trivial) first harmonic oscillation in R_h. This effect gives rise to the factor of 3 difference between Eq. 6(a) and Eq. 6(b). In addition, τ is proportional to C/k, where C and k are the heat capacity and thermal conductivity, respectively. According to the kinetic theory, k is proportional to Cl, where l is the phonon mean free path and increases with decreasing temperature. Hence, τ is proportional to $1/l$ and decreases with decreasing temperature. Therefore, the transition between Eq. 6(a) and Eq. 6(b) occurs at a higher frequency as the temperature is lowered. This frequency dependence has been confirmed by an experiment conducted at four different temperatures, namely 15 K, 25 K, 100 K, and 300 K, as shown in Fig. 5. In the experiment, ΔR_h was measured at different f for the same I (thus the same ΔT_h). The measurement results exhibit a factor of 3 difference between the low and high frequency limits, as expected from Eq. 6. In practice, we use $f > 700$ Hz, for which Eq. 6(b) is valid in the temperature range of 4−400 K. We confirmed that the lock-in method yields the same result as the fitting method. The lock-in method is preferred in our measurements because it is more sensitive than the fitting one.

Electrical Conductance. The electrical conductance of the sample can be measured using the two Pt electrodes contacting the two ends of the sample. As mentioned above, a FIB method can be used to deposit a metal line on top of the sample-electrode contact to reinforce the electrical contact and minimize the contact

electrical resistance. The FIB deposition can break through the oxide layer of a semiconductor nanowire and reduce the contact resistance.

Seebeck Coefficient. The temperature difference of the two membranes yields a thermoelectric voltage that can be measured using the two Pt electrodes contacting the nanostructure, i.e., $V_{TE}=(S_s-S_{Pt})(T_h-T_s)$. The Seebeck coefficient (S_{Pt}) of the Pt electrode can be calibrated separately. By measuring T_h, T_s, and V_{TE}, the Seebeck coefficient (S_s) of the sample can be obtained.

Measurement Sensitivity. The sensitivity of thermal conductance measurement determines the minimum or noise-equivalent sample thermal conductance that can be measured using the microdevice. Usually $\Delta T_h \gg \Delta T_s$ in our measurements. Hence, from Eq. 3(b), the noise-equivalent thermal conductance (NEG_s) of the sample is proportional to the noise-equivalent temperature rise (NET) of the sensing membrane, i.e.

$$\mathrm{NEG}_s = G_b \frac{\mathrm{NET}}{\Delta T_h - \Delta T_s} \tag{7}$$

NET is further related to the noise equivalent resistance (NER) in the R_s measurement

$$\mathrm{NET} = \frac{\mathrm{NER}/R_s}{\mathrm{TCR}} \tag{8}$$

For the resistance measurement method using a lock-in amplifier,

$$\frac{\mathrm{NER}}{R_s} = \frac{\delta v}{v} + \frac{\delta i}{i} \tag{9}$$

where δv and δi are the noises in the ac voltage measurement and that of the current source, respectively. At 300 K, δv is dominated by the thermal or Johnson noise to be $\delta v = \sqrt{4k_B T R_s \Delta f} \approx 4$ nV for a noise bandwidth of $\Delta f \approx 0.3$ Hz. Therefore

$$\frac{\delta v}{v} = \frac{4\ \mathrm{nV}}{2\ \mathrm{mV}} = 2\times 10^{-6} \tag{10}$$

The current source $i = v_{\mathrm{out}}/R$, where v_{out} is a sinusoidal 199 Hz output voltage from the lock-in amplifier and R is the 10 MΩ resistance of a 10 ppm/K precision resistor that is coupled to the sinusoidal voltage output of the lock-in amplifier for converting a constant ac voltage source to a constant ac current source. Therefore,

$$\frac{\delta i_{ac}}{i_{ac}} = \frac{\delta v_{\mathrm{out}}}{v_{\mathrm{out}}} + \frac{\delta R}{R} \tag{11}$$

The relative noise in the ac voltage output from the lock-in amplifier ($\delta v_{\mathrm{out}}/v_{\mathrm{out}}$) is about 4×10^{-5}. The resistance fluctuation ($\delta R/R$) of the 10 MΩ precision resistance is about 2×10^{-6} for a 0.2 K fluctuation of room temperature. Therefore, $\delta i_{ac}/i_{ac} \sim 4.2 \times 10^{-5}$. The noise in the current source is the dominant noise source. From Eqs. 9–11, we can write

$$\frac{\mathrm{NER}}{R_s} \approx 5\times 10^{-5} \tag{12}$$

This has been confirmed by measuring the noise level using a 2 KΩ precision resistor to replace the PRT. The measured resistance noise is about 100 mΩ, indicating $\mathrm{NER}/R_s \approx 5\times 10^{-5}$.

$R_s(I=0)$ is measured in the temperature range of 10–400 K, as shown in Fig. 6. Above 30 K, $R_s(I=0)$ increases linearly with temperature. Typically, the TCR of the PRT is in the range of 1.8×10^{-3}–3.6×10^{-3} K^{-1} and 3.5×10^{-3}–7.2×10^{-3} K^{-1} at 300 K and 30 K, respectively, depending on the thin film deposition condition. Thus, NET of the lock-in measurement is in the range of 13–27 mK and 6–13 mK at 300 K and 30 K, respectively. Below 30 K, the TCR becomes smaller, leading to a larger NET.

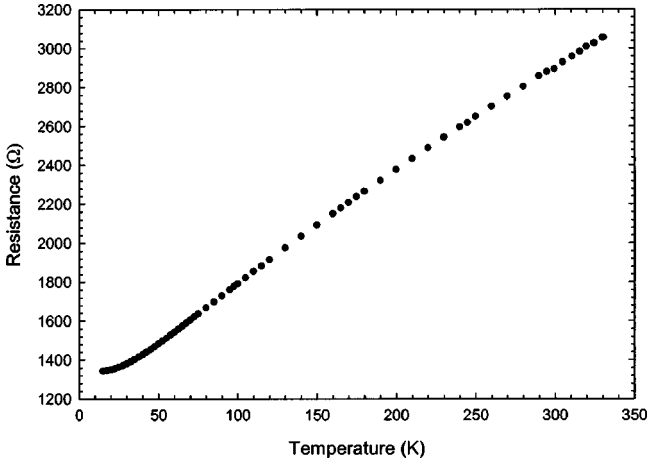

Fig. 6 The resistance ($R_s(I=0)$) of the PRT as a function of temperature

This NET value was found to be comparable or slightly below the temperature fluctuation of the cryostat, which can be controlled to be within 25 mK for $T_0 > 100$ K and 10 mK for $T_0 < 100$ K. Therefore,

$$\mathrm{NET} \approx 25\ \mathrm{mK} \quad \text{for } T_0 = 300\ \mathrm{K};$$
$$\mathrm{NET} \approx 10\ \mathrm{mK} \quad \text{for } T_0 = 30\ \mathrm{K} \tag{13}$$

The thermal conductance (G_b) of the five beams has been calculated from the measured ΔT_h and ΔT_s according to Eq. 3(a). The measured ΔT_h is shown in the inset of Fig. 7 as a function of I, and the calculated G_b is shown in Fig. 7. At 300 K, G_b is about 9.4×10^{-8} W/K, in agreement with the value of 9.0×10^{-8} W/K that is obtained based on the geometry of the five beams as well as the room temperature thermal conductivity values of SiN_x and Pt films, i.e., $k_{\mathrm{SiNx}} = 5.5$ W/m-K and $k_{\mathrm{Pt}} = 70$ W/m-K [16]. Therefore, from Eqs. 7 and 13, the noise equivalent thermal conductance at 300 K is $NEG_s \approx 1\times 10^{-9}$ W/K for a temperature excursion $\Delta T_h - \Delta T_s = 2$ K. At 30 K, $G_b \approx 3\times 10^{-8}$ W/K, and $NEG_s \approx 1.5 \times 10^{-10}$ W/K for the same temperature excursion. If only the four acoustic phonon modes are filled up for a (10,10) SWCN at 30 K, the maximum possible thermal conductance would be $G_{SWCN} = 4g_0 = 4\times 30\times 9.46\times 10^{-13}\ \mathrm{W/K} = 1.1\times 10^{-10}$ W/K. This is in

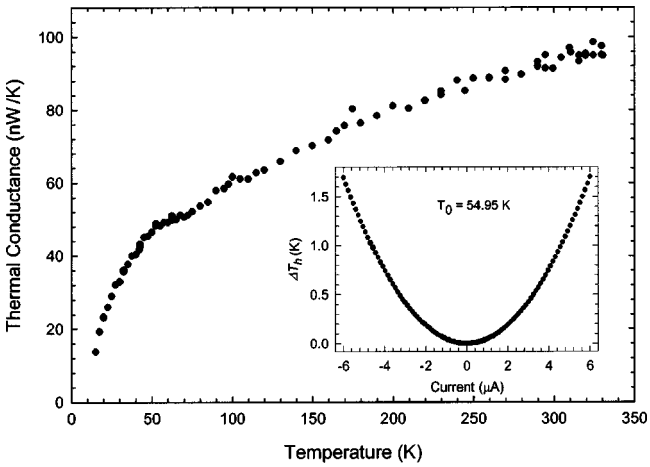

Fig. 7 Thermal conductance of the five beams supporting one membrane of the microdevice as a function of temperature. Inset: temperature rise in the heating membrane as a function of the dc heating current at $T_0 = 54.95$ K.

the vicinity of the measurement sensitivity. To increase the signal to noise ratio, two or more individual SWCNs can be grown between the two suspended membranes using the CVD method, or an Nb doped Si resistance thermometer with a larger TCR [18] can be used to replace the PRT.

Measurement Errors. One error source of the measurement is due to heat transfer between the two membranes via radiation and air conduction. The radiation thermal conductance can be estimated as

$$G_{h-s\_\mathrm{rad}}=\sigma(T_s+T_h)(T_s^2+T_h^2)F_{h-s}A \tag{14}$$

where F_{h-s} and A are the view factor between the two adjacent membranes and the surface area of one membrane, respectively. It can be shown that $F_{h-s}A\approx 12\ \mu\mathrm{m}^2$. Thus $G_{h-s\_\mathrm{rad}}=8\times10^{-14}$ and 7×10^{-11} W/K at $T=30$ K and 300 K, respectively. These values are well below the measurement sensitivity.

The thermal conductance of air can be written as $G_{h-s\_\mathrm{air}}=k_aA_{eq}/D$, where k_a is the thermal conductivity of the residual air molecules in the evacuated cryostat, A_{eq} and D are the equivalent surface area of the membrane and the distance between the two membranes, respectively. For a vacuum pressure of 1×10^{-5} Torr, the mean free path of air molecules is of the order of 1 m and is much larger than D. Under such circumstance, according to the kinetic theory,

$$k_a=\frac{CvD}{3}\quad\text{and}\quad G_{h-s\_\mathrm{air}}=\frac{CvA_{eq}}{3} \tag{15}$$

where C and v are the heat capacity and velocity of air molecules. From Eq. 15, it can be estimated that $G_{h-s\_\mathrm{air}}=2\times10^{-12}$ W/K at $T=300$ K, well below the measurement sensitivity of 1×10^{-9} W/K.

We have measured the thermal conductance due to air conduction and radiation at different temperatures using a bare device without a nanostructure sample bridging the two membranes. No signal above the noise level can be detected by the sensing PRT as the temperature of the heating membrane is raised. The measurement confirms that air conduction and radiation do not introduce noticeable errors in our measurements.

A major error source in the measurement is the contact thermal resistance (G_c^{-1}). To decrease G_c^{-1}, as discussed in the previous section, one can deposit a small Pt or W pad on top of the sample-electrode contact so that the sample is sandwiched between two metal layers. Alternatively, amorphous carbon can be deposited on the contact area using a SEM. Note that the contact area between the sample and the electrode is proportional to the diameter of the nanostructure sample; while the thermal conductance of the sample is proportional to the square of the diameter. Therefore, as a general trend, the ratio of G_c to G_n is larger as the diameter of the sample becomes smaller. For this reason, the contact thermal resistance causes a smaller error at nanoscale than at macroscale.

In a measurement of Si nanowires, we estimated the error introduced by the contact thermal resistance. In that measurement, amorphous carbon was deposited on the contact area. The conductance of one of the contacts can be expressed as k_cA_c/δ_a, where k_c is the thermal conductivity of the amorphous carbon; A_c is the contact area and is of the order of $2\pi rL_c$, where L_c is the length of the carbon deposit (about 2 μm), and r is the radius of the nanowire; δ_a is the average distance between the nanowire surface and Pt electrode, which is of the order of r. Using $k_c=0.1$ W/m-K, the lower limit of inorganic solid materials, and $k_n=47$ W/m-K, the room temperature measurement value of a 100 nm diameter Si nanowire, we estimated that $G_c/G_n=6.8$. Hence, the two contacts together yielded an error less than 15 percent for the 100 nm Si nanowire. This error is expected to be smaller for nanowires with a smaller diameter.

Nevertheless, it is desirable to quantify the contact thermal resistance G_c. A conventional method is to measure a collection of samples with the same diameter and different lengths. The contact thermal resistance can be estimated from the length-dependence of the sample thermal conductance (G_s) provided that thermal conduction in the sample is diffusive.

Table 1 Uncertainty of thermal conductance (G_s) data shown in Fig. 8

Temperature (K)	300	160	30
148 nm diameter SWCN bundle	9%	14%	36%
10 nm diameter SWCN bundle	36%	57%	⋯

Measurement Uncertainty. For the case when $\Delta T_h\gg\Delta T_s$ the uncertainty of the measured thermal conductance of the sample can be written as

$$\frac{\delta(G_s)}{G_s}=\frac{\delta(Q)}{Q}+\frac{\delta(\Delta T_s)}{\Delta T_s}+2\frac{\delta(\Delta T_h)}{\Delta T_h} \tag{16}$$

where $\delta(x)$ is the uncertainty in x. Since $\Delta T_h\gg\Delta T_s$, the dominant term in the left hand side of Eq. 16 is $\delta(\Delta T_s)/\Delta T_s$. With $\mathrm{d}R_s(\mathrm{I}=0)/\mathrm{d}T$ obtained from Fig. 6 and considering a 1 percent gain accuracy of the lock-in amplifier, we estimated from Eq. 4 that the upper limit of $\delta(\Delta T_s)$ is 36 mK. Further, ΔT_s depends on G_s/G_b. When measuring the 148 nm diameter SWCN bundle shown in Fig. 3(c), we increased ΔT_h up to 2 K. It was found that $G_s\approx0.2G_b$ at 300 K. Hence, $\Delta T_s(\approx\Delta T_hG_s/G_b)$ was as high as 0.4 K, and $\delta G_s/G_s\approx\delta(\Delta T_s)/\Delta T_s\approx9$ percent at 300 K. At 30 K, $G_s\approx0.05G_b$, so that $\Delta T_s\approx0.1$ K. This results in $\delta G_s/G_s\approx\delta(\Delta T_s)/\Delta T_s\approx36$ percent at 30 K. For the 10 nm diameter SWCN bundle shown in Fig. 3(b), we increased ΔT_h up to 6 K in order to keep the uncertainty $\delta G_s/G_s$ below 36 percent and 57 percent at 300 K and 160 K, respectively. These uncertainty values, as summarized in Table 1, represent the upper bound because they are estimated using the upper limit of $\delta(\Delta T_s)$.

To obtain the thermal conductivity, one needs to measure the length and diameter of the sample. The length of the sample can be measured using a SEM with a uncertainty of 10 nm. Thus, for a 2 μm long sample, $\delta(L)/L=0.5$ percent. To obtain the diameter, we used a tapping mode atomic force microscope to measure the sample segment that is located on top of the Pt electrode. The uncertainty of the diameter measurement was about 0.3 nm. For the 10 nm (or 148 nm) diameter SWCN bundle, this introduces an additional uncertainty of 6 percent (or 0.4 percent) to the calculated thermal conductivity. These uncertainty values are usually smaller than that introduced by the uncertainty of G_s. However, the calculated thermal conductivity (k) does not take into account of the contact thermal resistance (G_c), and thus represents the lower bound of k.

Measurement Results and Discussion

Using the microdevice, a variety of nanostructure samples have been measured. These include MWCNs [17], SWCNs, nanowires made of Si [19] and Bi_2Te_3 [20], and SnO_2 nanobelts [21]. It exceeds the scope of this paper to include all the measurement results. For appropriate nanostructures of interest, the readers are referred to the appropriate papers cited in the reference section.

As an example, Figs. 8–10 show the measurement results of thermal conductance, electrical conductance, and Seebeck coefficient of a 10 nm diameter and 4.2 μm long SWCN bundle (see Fig. 3(b)) and another 148 nm diameter, 2.66 μm long SWCN bundle (see Fig. 3(c)). For the 148 nm diameter bundle, the thermal conductance exhibits a $T^{1.5}$ dependence between 20 K and 100 K. This is different from the quadratic temperature dependence observed for individual MWCNs [17] as well as the linear dependence observed by Hone et al. for a SWCN mat below 25 K. To verify the expected linear behavior expected for SWCNs at low temperatures, we will need to measure individual SWCNs grown by the CVD method in order to eliminate the influences

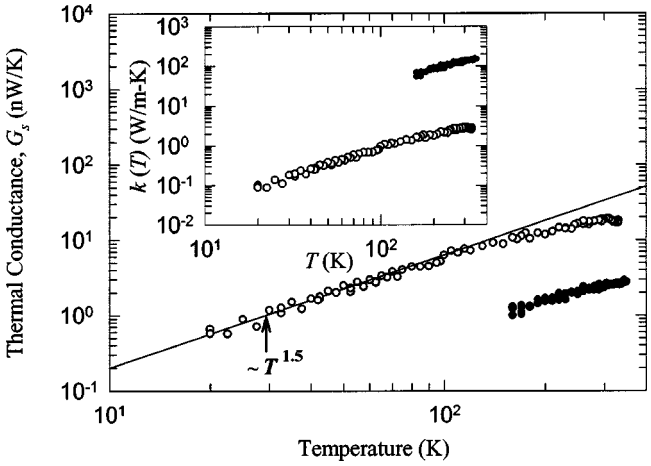

Fig. 8 Thermal conductance of two SWCN bundles as a function of temperature. Inset: Thermal conductivity (k) as a function of temperature (T). Solid and open circles represent the measurement results of the 10 nm and the 148 nm diameter SWCN bundle, respectively.

from phonon scattering at contacts between individual tubes in a bundle. The inset to Fig. 8 shows the calculated thermal conductivity values of the two bundles, which are much lower than the results that we previously obtained for an individual MWCN. We have measured very high room-temperature thermal conductivity of individual SWCNs grown by the CVD method (see Fig. 3(d)), and the measurement results will be reported elsewhere.

Figure 9 shows the measured electrical conductance of the two SWCN bundles. For the 10 nm diameter bundle, the electrical conductance shows a power law dependence of $T^{1.7}$ with temperature. On the other hand, the electrical conductance of the 148 nm bundle can be fitted using two different power law dependences, i.e., $\sim T^{1.5}$ below 60 K and $\sim T$ above. These behaviors are different from those obtained by Bockrath et al. [22] and Yao et al. [23], where a single $T^{0.6}$ dependence was observed for smaller metallic SWCN bundles in the range of 4–400 K. The $T^{0.6}$ behavior was thought to be caused by the tunneling resistance from the metal electrodes to the nanotube according to the Luttinger-Liquid model [22]. We expect that there are many defects and contacts in the two relatively large bundles that we have measured. The electrical resistance is thus dominated by scattering inside the bundle instead of tunneling from the metal contact into the SWCN.

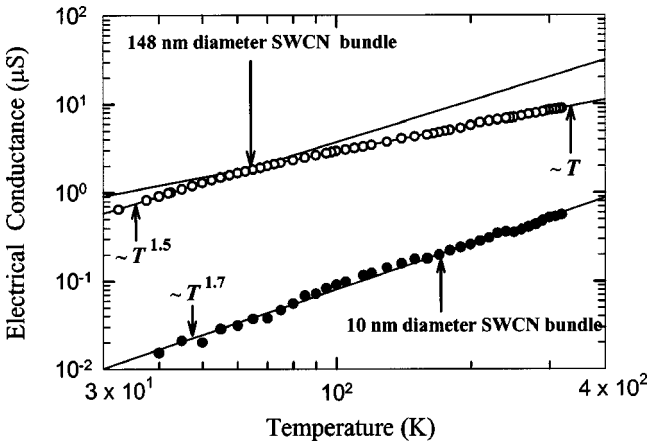

Fig. 9 Electrical conductance of two SWCN bundles as a function of temperature

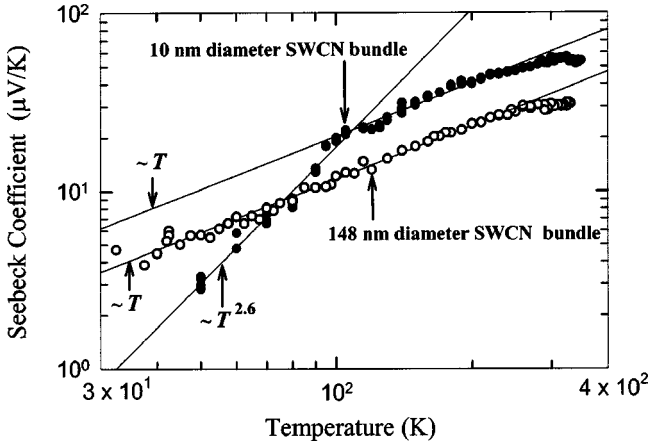

Fig. 10 Seebeck coefficient of two SWCN bundles as a function of temperature

As discovered by Collins et al. [24], the electrical conductance and Seebeck coefficient of SWCN bundles are very sensitive to oxygen exposure. Oxygen doping can result in enhanced electrical conductance of semiconducting SWCNs and hole-type majority carriers of a bundle, which usually consists of both metallic and semiconducting SWCNs. The hole doping further results in positive values of Seebeck coefficient that are much larger than that of a metal. As SWCN bundles were deoxygenated in high vacuum (10^{-6} to 10^{-8} Torr), negative values of Seebeck coefficient with smaller magnitudes than those of oxygenated samples were found [24,25].

Because large and positive values of Seebeck coefficient were observed in our measurement, as shown in Fig. 10, it is possible that the SWCN bundles were still oxygen doped, despite the fact that they were kept in vacuum for a few hours before the measurement. Note that Fig. 10 plots the difference in Seebeck coefficient between the sample and the Pt electrode, i.e., $S_s - S_{Pt}$. The magnitude of S_{Pt} is typically 5 μV/K at 300 K and decreases linearly with temperature [26], much smaller than the measurement result of $S_s - S_{Pt}$. Thus, $S_s - S_{Pt} \approx S_s$.

For the 148 nm diameter bundle, the measured Seebeck coefficient shows linear temperature dependence in the temperature range of 30–250 K, and saturates above 250 K. This bears some similarity to the measurement result of oxygen-exposed SWCN mats by Hone et al. [3], where the saturation temperature was about 100 K. The linear dependence, which is expected for a metallic sample, is also observed for the 10 nm SWCN bundle in

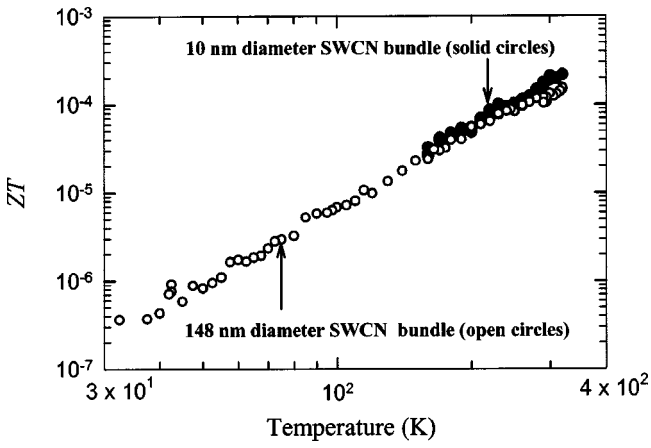

Fig. 11 Thermoelectric figure of merit (ZT) of two SWCN bundles as a function of temperature

the temperature range of 100 K to 250 K. In addition, the Seebeck coefficient for this bundle also saturates above 250 K. However, below 100 K, a power law dependence of $T^{2.6}$ is observed, indicating a departure from the metallic behavior. These observations will be analyzed elsewhere.

The thermoelectric figure of merit ($ZT \equiv S^2/RG$, where S, R, and G are Seebeck coefficient, electrical resistance, and thermal conductance of the sample) is calculated from the measurement results, and is plotted in Fig. 11. The ZT is small for the two SWCN bundles.

Conclusions

We have batch-fabricated a microdevice for measuring the thermal conductance, electrical conductance, and Seebeck coefficient of one-dimensional nanostructures including nanotubes, nanowires, and nanobelts. The measurements are performed with the sample placed in an evacuated liquid helium cryostat spanning a temperature range of 4–400 K. The sensitivity in thermal conductance measurement is estimated to be on the order of 10^{-10} and 10^{-9} W/K at 30 and 300 K, respectively. Errors due to radiation are estimated to be less than 8×10^{-14} and 7×10^{-11} W/K at 30 K and 300 K, respectively; while conduction through residual gas molecules contributes to less than 2×10^{-12} W/K at 300 K. The TCR of the PRT becomes smaller at temperatures below 30 K. To reduce the measurement uncertainty at low temperatures, one needs to use other high-TCR materials such as Nb doped Si to replace the PRT.

The measurement results of a 10 nm and a 148 nm-SWCN bundle are presented. Due to phonon scattering at many defects and contacts in the bundles, the observed thermal conductivity is low compared to that of an individual MWCN. For the 148 nm bundle, the thermal conductivity exhibits a $T^{1.5}$ in the temperature range of 20–100 K. To verify the expected linear temperature dependence of the thermal conductance of SWCNs at low temperatures, we will need to measure individual SWCNs grown by the CVD method in order to eliminate the influences from phonon scattering at contacts between individual tubes in a bundle.

Acknowledgments

For this work, LS, CY, and DK are supported by a CAREER award and an instrumentation grant from the Division of Chemical and Transport System of NSF. DL and AM are supported by the NSF NIRT program and by the Basic Energy Science program of DOE. The SnO_2 sample is provided by Prof. Z. L. Wang's group at Georgia Institute of Technology. We thank the Welch foundation for partial financial support to the Center for Nano and Molecular Science and Technology, University of Texas at Austin.

Nomenclature

A = area [m^2]
C = specific heat [J/K-m^3]
D = distance between the two membranes [m]
G = thermal conductance [W/K]
I, i = current [A]
k = thermal conductivity [W/m-K]
L = length [m]
Q = heat [W]
R = differential electrical resistance [Ω]
S = Seebeck coefficient [V/K]
T = temperature [K]
V, v = voltage [V]
σ = Stefan-Boltzmann's constant [W/m^2-K^4]

Subscripts

a = air
0 = environment
b = beam
c = contact
eq = equivalent
h = heating membrane
L = Pt lead
n = nanostructure sample
s = sensing membrane

References

[1] Volz, S. G., and Chen, G., 1999, "Molecular Dynamics Simulation of Thermal Conductivity of Silicon Nanowires," Appl. Phys. Lett., **75**, pp. 2056–2058.
[2] Khitun, A., Balandin, A., and Wang, K. L., 1999, "Modification of the Thermal Conductivity in Silicon Quantum Wires Due to Spatial Confinement of Acoustic Phonons," Superlattices Microstruct., **26**, pp. 181–193.
[3] Dresselhaus, M. S., and Eklund, P. C., 2000, "Phonons in Carbon Nanotubes," Adv. Phys., **49**(6), pp. 705–814.
[4] Schwab, K., Henriksen, E. A., Worlock, J. M., and Roukes, M. L., 2000, "Measurement of the Quantum of Thermal Conductance," Nature (London), **404**, pp. 974–976.
[5] Hone, J., Ellwood, I., Muno, M., Mizel, A., Cohen, M. L., Zettl, A., Rinzler, A. G., and Smalley, R. E., 1998, "Thermoelectric Power of Single-Walled Carbon Nanotubes," Phys. Rev. Lett., **80**, pp. 1042–1045.
[6] Yi, W., Lu, L., Zhang, D. L., Pan, Z. W., and Xie, S. S., 1999, "Linear Specific Heat of Carbon Nanotubes," Phys. Rev. B, **59**, pp. R9015–9018.
[7] Mizel, A., Benedict, L. X., Cohen, M. L., Louie, S. G., Zettl, A., Budraa, N. K., and Beyermann, W. P., 1999, "Analysis of the Low-Temperature Specific Heat of Multiwalled Carbon Nanotubes and Carbon Nanotube Ropes," Phys. Rev. B, **60**, pp. 3264–3270.
[8] Hone, J., Whitney, M., Piskoti, C., Whitney, M., and Zettl, A., 1999, "Thermal Conductivity of Single-Walled Carbon Nanotubes," Phys. Rev. B, **59**, pp. R2514–2516.
[9] Hone, J., Llaguno, M. C., Nemes, N. M., Johnson, A. T., Fischer, J. E., Walters, D. A., Casavant, M. J., Schmidt, J., and Smalley, R. E., 2000, "Electrical and Thermal Transport Properties of Magnetically Aligned Single Wall Carbon Nanotube Films," Appl. Phys. Lett., **77**, pp. 666–668.
[10] Berber, S., Kwon, Y.-K., and Tomanek, D., 2000, "Unusually High Thermal Conductivity of Carbon Nanotubes," Phys. Rev. Lett., **84**, pp. 4613–4616.
[11] Che, J., Cagin, T., and Goddard, W. A., 2000, "Thermal Conductivity of Carbon Nanotubes," Nanotechnology, **11**, pp. 65–69.
[12] Osman, M., and Srivastava, D., 2001, "Temperature Dependence of the Thermal Conductivity of Single-Wall Carbon Nanotubes," Nanotechnology, **12**, pp. 21–24.
[13] Lin, Y.-M., Sun, X., and Dresselhaus, M. S., 2000, "Theoretical Investigation of Thermoelectric Transport Properties of Cylindrical Bi Nanowires," Phys. Rev. B, **62**, pp. 4610–4623.
[14] Heremans, J. P., Thrush, C. M., Morelli, D. T., and Wu, M.-C., 2002, "Thermoelectric Power of Bismuth Nanocomposites," Phys. Rev. Lett., **88**, p. 216801.
[15] Cahill, D. G., 1990, "Thermal Conductivity Measurement From 30–750 K: The 3ω Method," Rev. Sci. Instrum., **61**, pp. 802–808.
[16] Shi, L., 2001, "Mesoscopic Thermophysical Measurements of Microstructures and Carbon Nanotubes," Ph.D. dissertation, University of California, Berkeley.
[17] Kim, P., Shi, L., Majumdar, A., and McEuen, P. L., 2001, "Thermal Transport Measurements of Individual Multiwalled Carbon Nanotubes," Phys. Rev. Lett., **87**, p. 215502.
[18] De Vecchio, D., Taborek, P., and Rutledge, J. E., 1995, "Matching the Resistivity of Si:Nb Thin Film Thermometers to the Experimental Temperature Range," Rev. Sci. Instrum., **66**, pp. 5367–5368.
[19] Li, D., Wu, Y., Kim, P., Shi, L., Mingo, N., Liu, Y., Yang, P., and Majumdar, A., 2003, "Thermal Conductivity of Individual Silicon Nanowires,"submitted.
[20] Li, D., Prieto, A. L., Wu, Y., Martin-Gonzalez, M. S., Stacy, A., Sands, T., Gronsky, R., Yang, P., and Majumdar, A., 2002, "Measurement of Bi_2Te_3 Nanowire Thermal Conductivity and Seebeck Coefficient," Proc. 21st International Conference on Thermoelectrics, IEEE, pp. 333–336.
[21] Shi, L., Hao, Q., Yu, C., Kim, D., Farooqi, R., Mingo, N., Kong, X., and Wang, Z. L., 2003, "Thermal Conductivity of SnO_2 Nanobelts," in preparation.
[22] Bockrath, M., Cobden, D. H., Lu, J., Rinzler, A. G., Smalley, R. E., Balents, L., and McEuen, P. L., 1999, "Luttinger-Liquid Behavior in Carbon Nanotubes," Nature (London), **397**, pp. 598–601.
[23] Yao, Z., Postma, H. W. Ch., Balents, L., and Dekker, C., 1999, "Carbon Nanotube Intramolecular Junctions," Nature (London), **402**, pp. 273–280.
[24] Collins, P. G., Bradley, K., Ishigami, M., and Zettl, A., 2000, "Extreme Oxygen Sensitivity of Electrical Properties of Carbon Nanotubes," Science, **287**, pp. 1801–1804.
[25] Bradley, K., Jhi, S.-H., Collins, P. G., Hone, J., Cohen, M. L., Louie, S. G., and Zettl, A., 2000 "Is the Intrinsic Thermoelectric Power of Carbon Nanotubes Positive?" Phys. Rev. Lett., **85**, pp. 4361–4364.
[26] Rowe, D. M., 1995, *CRC Handbook of Thermoelectrics*, CRC Press, New York.

Fully-Developed Thermal Transport in Combined Pressure and Electro-Osmotically Driven Flow in Microchannels

D. Maynes
e-mail: maynes@byu.edu

B. W. Webb

Department of Mechanical Engineering,
Brigham Young University,
Provo, UT 84602

Thermally fully-developed heat transfer has been analyzed for combined electro-osmotic and pressure driven flow in a circular microtube. The two classical thermal boundary conditions of constant wall heat flux and constant wall temperature were considered. Such a flow is established by the combination of an imposed pressure gradient and voltage potential gradient along the length of the tube. The induced flow rate and velocity profile are functions of the imposed potential gradient, electro-osmotic mobility of the fluid, the ratio of the duct radius to the Debye length, the established streamwise pressure gradient, and the fluid viscosity. The imposed voltage gradient results in Joule heating in the fluid, with an associated distributed volumetric source of energy. For this scenario, the solution for the fully developed, dimensionless temperature profile and corresponding Nusselt number have been determined. The fully-developed Nusselt number is found to depend on the duct radius/Debye length ratio (termed the relative duct radius), the dimensionless volumetric source, and a dimensionless parameter that characterizes the relative strengths of the two driving mechanisms. This parameter can take on both positive and negative values, depending on the signs of the streamwise voltage and pressure gradients imposed. Analytical results are presented and discussed for a range of the governing dimensionless parameters. [DOI: 10.1115/1.1597624]

Keywords: Channel Flow, Convection, Heat Transfer, Laminar, Microscale

Introduction

Transport phenomena have recently found importance in novel technologies in micropower generation, chemical separation processes, cell analysis instrumentation, and other biomedical diagnostic techniques. At the microscale, where channel cross-sections are of the order of 100 μm, generating fluid motion is a formidable challenge. Conventional pressure driven flow technology at these physical scales requires significant pressures. Whereas micropumps capable of delivering such pressures are available [1–3], their manufacture and maintenance are difficult [1], and they lack the precise control that is often needed in such microfluidic applications [4]. Electro-osmotically generated flow presents a viable alternative to pressure driven flow in liquid delivery systems, featuring better flow control and no moving parts. Several previous studies have reported on successful demonstration of electro-osmotic pumping systems [5–8].

Electro-osmosis is the bulk movement of liquid relative to a stationary surface due to an externally applied electric field, and was first observed and reported by Reuss nearly two centuries ago [9]. The physics of this unique flow phenomenon have been described in detail previously [10,11]. The resulting electro-osmotic flow velocity distribution is a function of the ratio of the capillary radius to the Debye length, where the Debye length characterizes the penetration of non-neutral charge into the fluid medium [10]. When the capillary radius is much greater than the Debye length, the resulting velocity profile is nearly uniform (characterized by slug flow). At the other extreme, when the capillary radius is of the same order as the Debye length, the flow exhibits a velocity distribution more nearly like that of classical pressure driven flow.

The liquid flow rates induced by electro-osmotic potentials are typically small, with average velocities of the order of a few mm/s. Therefore, even small pressure differences imposed along a microtube may result in velocity distributions and corresponding flow rates that depart from the purely electro-osmotic case. While it may not be likely that combined pressure and electro-osmotic forces would be intentionally imposed, pressure differences may result if one reservoir becomes pressurized as a result of the pumping or due to some other means, or if variations in the wall zeta potential exist [12,13]. When both electro-osmotic and traditional pressure forces are present, the resulting velocity profile is the superimposed effect of both phenomena [10]. It should further be noted that the pressure force may either assist or oppose the electro-osmotic driving force, depending on the relative signs of the applied pressure gradient and voltage gradient.

Since the fluid dynamics of combined pressure and electro-osmotically generated flow are significantly different from either traditional pressure driven flow or purely electro-osmotically induced flow, the thermal transport dynamics are expected to be quite different as well. Two elements of this combined flow scenario result in departure from traditional pressure driven flow heat transfer.

1. The velocity profile in the tube will be a strong function of the relative strengths of the pressure driven and electro-osmotically driven character of the flow, and is dependent on the capillary radius-to-Debye length ratio. The resulting velocity profile in the tube will influence the temperature distribution and resulting heat transfer.
2. The applied voltage gradient and its induced electric current establishes Joule heating in the fluid, resulting in a volumetric energy generation therein. The magnitude of the thermal energy source has significant influence on the temperature distribution and heat transfer.

Due to the small physical scale of microtubes with typical di-

Contributed by the Heat Transfer Division for publication in the JOURNAL OF HEAT TRANSFER. Manuscript received by the Heat Transfer Division November 22, 2002; revision received May 9, 2003. Associate Editor: H. Bau.

ameters of the order of 100 μm, the hydrodynamic and thermal entrance regions are expected to be only a few millimeters in length. Therefore, fully developed flow may prevail over the majority of the tube length in a given microfluidic application. An understanding of the thermal transport characteristics for such fully developed flows is therefore needed, and is the objective of this work.

Classical fully developed pressure driven flow and heat transfer are well understood, and analytical treatments can be found in any undergraduate heat transfer text. Several analytical studies have appeared in the literature describing the hydrodynamics of fully developed electro-osmotic flow through circular and rectangular channels [14–16]. More recent hydrodynamic studies have explored the effects of streamwise gradients in the electrical conductivity [17], and variations in the wall zeta potential [12,13] on the velocity field. Additionally, some experimental studies have reported on velocity profile measurements associated with electro-osmotic flows in circular and rectangular channels [18–21].

With regards to characterization of the convection heat transfer associated with electro-osmotic flow, relatively little prior work has appeared in the literature. Li et al. have explored electrokinetic effects induced in a pressure driven flow on the frictional and heat transfer characteristics for both round and rectangular microchannels [22,23]. They report that the resulting induced electrokinetic potential results in a reduced flow rate, a greater friction factor, and a reduced Nusselt number from the classical laminar pressure driven flow scenario. There exists also some related early work exploring the effect of volumetric energy dissipation on thermal development in channels under pressure driven flow conditions [24]. In a recent study the convective heat transport characteristics for purely electro-osmotically driven, fully developed flow, with its unique combination of complex velocity distribution and fluid Joule heating, was presented [25]. These results show that the Nusselt number is strongly dependent on the magnitude of the volumetric generation, and the ratio of the tube or channel diameter to the Debye length. However, there appear to be no studies reported in the literature treating convective heat transfer for combined pressure and electro-osmotically driven flow. This study presents solutions for thermally (and hydrodynamically) fully developed combined flow in circular tubes for constant wall heat flux and constant wall temperature boundary conditions. The heat transfer behavior is investigated parametrically for a range of problem scenarios relevant to combined pressure and electro-osmotic flow in microtubes.

Analysis

Consider fully developed flow of an incompressible fluid with constant thermophysical properties in a circular microtube of radius a induced by combined pressure and voltage potential gradients. The limiting case of low wall potentials is considered here where the Debye-Hückel linearization is applicable [11]. If one defines a dimensionless radial coordinate as $R=r/a$, and a duct relative radius (ratio of tube radius to Debye length) as $Z=a/\lambda$, the normalized steady, fully developed velocity distribution can be expressed as [10]

$$U(R)=1-\frac{I_0(ZR)}{I_0(Z)}+\Gamma(1-R^2) \tag{1}$$

where $U=u/u_{eo}$, and u_{eo} is the maximum possible electro-osmotic velocity for a given applied potential field, given by $(-\varepsilon\zeta/\mu)d\Phi/dx$. Φ is the applied voltage potential field, and the grouping $\varepsilon\zeta/\mu$ is often termed the electro-osmotic mobility, μ_{eo}, of the liquid [15]. The properties μ, ε, and ζ are the viscosity, dielectric constant, and wall zeta potential, respectively. In general, these properties can be temperature dependent and for situations where significant variation exists, the momentum and energy equations are coupled and simultaneous solution of both equations using a numerical approach is requisite. However, for the sake of generality the present analysis focuses on the limiting case of constant properties, where the momentum and energy equations are uncoupled. This case provides a baseline from which flows with highly variable properties will deviate, depending on the degree of variability experienced. The parameter Γ in Eq. (1) is the ratio of pressure to electro-osmotic driving forces, $\Gamma=(a^2/4\varepsilon\zeta)\times[(dp/dx)/(d\Phi/dx)]$. For constant fluid properties Γ is also constant provided $(dp/dx)/(d\Phi/dx)$ is invariant as well, which is the scenario considered here. The fluid normalized average velocity, defined as $\overline{U}=\overline{u}/u_{eo}$ where $\overline{u}$ is the average fluid velocity, is determined by integration of Eq. (1) over the tube cross-sectional area, which yields

$$\overline{U}=1+\frac{\Gamma}{2}-\frac{2I_1(Z)}{ZI_0(Z)} \tag{2}$$

For $\Gamma\to\infty$, pressure forces dominate the momentum transport (for any value of Z), and a classical laminar Poiseuille flow parabolic profile is recovered from Eq. (1). For $\Gamma\to 0$, the momentum transport is dominated by electro-osmotic forces, and the velocity profile is governed solely by the relative duct radius Z. For $Z\to\infty$ (and $\Gamma=0$), Eq. (1) reduces to the classical Helmoltz-Smoluchowski equation $u/u_{eo}=1$ [10]. For situations where the pressure force opposes the electro-osmotic force ($\Gamma<0$), regions of both negative and positive velocity may occur in the tube. Negative velocities arise first on the tube centerline, and are found when $\Gamma<[1/I_0(Z)-1]$. This criterion results only when Γ is negative, with a magnitude such that the opposing pressure force results in retardation of, and ultimately reverse flow in the tube core, while electro-osmosis drives positive velocities near the tube wall. This relation reveals that the value of Γ for which negative flow occurs decreases from a value of $\Gamma=-0.21$ at $Z=1$ to an asymptotic value of -1 at large Z, reaching a value of $\Gamma=-0.99$ at $Z=6$. Of course, for $-\Gamma\to\infty$, pressure driven flow in the reverse direction dominates.

Thermal Transport—Constant Wall Heat Flux

Consider steady, hydrodynamically fully developed transport in a circular tube with constant thermophysical properties and uniform volumetric energy generation. Under these conditions, with an imposed constant wall heat flux, q''_w, the energy equation and associated boundary conditions are

$$\frac{u}{\alpha}\frac{\partial T}{\partial x}=\frac{\partial^2 T}{\partial x^2}+\frac{1}{r}\frac{\partial}{\partial r}\left(r\frac{\partial T}{\partial r}\right)+\frac{s}{k} \tag{3}$$

$$\left.\frac{\partial T}{\partial r}\right|_{r=0}=0 \qquad \text{and} \qquad \left.k\frac{\partial T}{\partial r}\right|_{r=a}=q''_w \tag{4}$$

T is the local temperature, α and k are the fluid thermal diffusivity and conductivity, and s is the volumetric generation due to the combined effect of resistance heating arising from the applied potential gradient and viscous heating.

The local volumetric source consists of Joule and viscous heating components and has a magnitude $s=i_e^2\sigma+\mu(\partial u/\partial r)^2$. The term i_e is the so-called conduction current density (Amps/m^2) established by the applied potential [11], σ is the liquid electrical resistivity (Ω-m), and $\partial u/\partial r$ is the gradient of the streamwise velocity. For low zeta potentials the conduction current is essentially uniform across the tube cross section [14,16]. However, the viscous heating is dependent on the radial coordinate. For small values of Z large velocity gradients do not exist and viscous dissipation is not expected to be significant. However, as the capillary radius-to-Debye length ratio exceeds 100, although the velocity across much of the tube is uniform with essentially no velocity gradient, a large velocity gradient exists near the tube wall. Volumetric generation due to viscous dissipation for such flows may be significant, but its relative influence depends on the magnitudes of the imposed heat flux and Joule heating, the tube radius-to-Debye-length ratio, the fluid properties, and the physical size of the cap-

illary of interest. An order-of-magnitude analysis suggests that the total energy added to the fluid per capillary length is of the order $\mu(u_{eo}/\delta_e)^2\pi a\lambda$ where δ_e is the characteristic length over which a velocity gradient exists. For $Z\to\infty$, δ_e is of the same order as the Debye length, λ, whereas for small values of Z it is of the order of the capillary radius a. The total energy added to the fluid per capillary length due to Joule heating is $(i_e^2\sigma)\pi a^2$. Recall that $u_{eo}=(\mu_{eo})d\Phi/dx$, and by use of Ohm's law $i_e=(d\Phi/dx)/\sigma$. Thus, the ratio of Joule heating to viscous heating is of the order $(a\lambda)/(\mu\sigma\mu_{eo}^2)$. For distilled water at standard conditions, this ratio will be approximately 4×10^3 for a 100 μm diameter capillary [13]. Consequently, for the present analysis, we neglect the viscous heating contribution, and consider only the limiting case of uniform volumetric generation due to the conduction current, $s\approx i_e^2\sigma$.

The classical definition of a thermally fully developed flow requires that the ratio $(T-T_w)/(T_m-T_w)$ be invariant with x [26], where T_w and T_m are the local wall and fluid mixed-mean temperatures, respectively. Under an imposed constant heat flux boundary condition ($q_w''=$constant), this requires $\partial T/\partial x = dT_m/dx=$constant, and $\partial^2T/\partial x^2=0$. Furthermore, an overall energy balance on the fluid yields

$$\frac{dT_m}{dx}=\frac{2q_w''+sa}{\rho\overline{u}ac_p} \tag{5}$$

In Eq. (5) above, ρ and c_p are the fluid density and specific heat, respectively. Substituting Eq. (5) into Eq. (3) and introducing the dimensionless temperature $\theta=(T-T_m)/(q_w''a/k)$, yields the nondimensional energy equation and boundary conditions for uniform wall heat flux

$$\frac{1}{R}\frac{\partial}{\partial R}\left(R\frac{\partial\theta}{\partial R}\right)+2\left[S-(1+S)\frac{U(R)}{\overline{U}}\right]=0 \tag{6}$$

$$\left.\frac{\partial\theta}{\partial R}\right|_{R=0}=0 \quad \text{and} \quad \left.\frac{\partial\theta}{\partial R}\right|_{R=1}=1 \tag{7}$$

The dimensionless volumetric source is defined as $S=s\overline{a}/2q_w''$, and the dimensionless local and mean velocities, U and $\overline{U}$, were defined previously.

Equation (6) may be integrated subject to its boundary conditions, Eq. (7), yielding an expression for the fully developed temperature distribution in the tube as an implicit function of the unknown Nusselt number

$$\theta(R)=\frac{2}{\mathrm{Nu}}-2Sf(R)+\frac{2(S+1)}{\overline{U}}g(R) \tag{8}$$

where 2/Nu is the as-yet unknown tube wall temperature, θ_w, and the functions $f(R)$ and $g(R)$ are given as

$$f(R)=\frac{R^2-1}{4} \tag{9a}$$

and

$$g(R)=f(R)+\frac{1}{Z^2}\left[1-\frac{I_0(ZR)}{I_0(Z)}\right]+\Gamma\left(\frac{R^4}{16}-\frac{R^2}{4}+\frac{3}{16}\right) \tag{9b}$$

Closure in the solution of Eq. (8) comes from the definition of the dimensionless mean temperature,

$$\frac{2}{U}\int_0^1 U(R)\theta(R)RdR=0 \tag{10}$$

Substituting the normalized velocity $U(R)$ from Eq. (1) (for a particular value of Z and Γ), and the temperature $\theta(R)$ from Eq. (8), the integral of Eq. (10) may be evaluated, yielding the unknown Nusselt number Nu:

$$\mathrm{Nu}=\frac{\overline{U}^2/2}{S\overline{U}\int_0^1 f(R)U(R)RdR-(S+1)\int_0^1 g(R)U(R)RdR} \tag{11}$$

In practice, the integrations of Eqs. (10) and (11) were carried out numerically using the trapezoidal rule for a specified S, Z, and Γ. A nonuniform grid with 1000 node points was employed in the integration, with cell clustering near the walls where the velocity gradients were the greatest. A grid size study was conducted for combined flow conditions yielding the largest velocity gradient ($Z=500$, $\Gamma=-1$), and the results indicate only 0.7% change in predicted Nusselt number when the number of node points was decreased to 200. Further, the numerical integration was validated by comparison with the classical solutions for no volumetric heating ($S=0$): Poiseuille flow ($\Gamma\to\infty$) with no volumetric heating ($S=0$) yields Nu=4.36; slug flow ($\Gamma=0$, $Z\to\infty$) yields Nu=8.0 [26]. The numerical integration agreed with the exact solutions to within 0.1%.

Thermal Transport—Constant Wall Temperature

The differential equation governing thermal transport with uniform wall temperature is identical to that for the imposed constant wall heat flux, Eq. (3). However, the boundary condition at the tube wall is $T(r=a)=T_w$. For constant wall temperature the asymptotic condition at a point downstream occurs when all energy generated volumetrically by Joule heating in the fluid is dissipated convectively at the channel wall (resulting in fluid cooling with $q_w''<0$). The energy balance of Eq. (5) thus yields $dT_m/dx=0$, corresponding to the conditions $S=sa/2q_w''=-1$. This situation is similar to fully developed Poiseuille flow in a tube with imposed constant wall temperature and viscous dissipation, studied by Ou and Cheng [27], where all viscous heating was dissipated by wall convection with an axially constant mean fluid temperature exceeding the wall temperature. Since the volumetric energy generation in the fluid is assumed independent of axial position in the channel, an overall energy balance requires that there be axially uniform cooling of the fluid. Thus, for an imposed constant wall temperature with volumetric heating in the fluid, the asymptotic condition requires also a constant (negative) wall heat flux. The solution for the fully developed temperature and Nusselt number for the $T_w=$constant thermal boundary condition is therefore identical to the constant wall flux solution, Eqs. (8)–(11), with $S=-1$. Note that the terms which vanish in Eq. (6) are those associated with dT_m/dx. In other words for the scenario presented here, the fully developed constant wall temperature case is also a constant wall flux solution.

The solution for the fully developed temperature distribution and corresponding Nusselt number for constant imposed channel wall temperature may be found by integrating Eq. (6) analytically for the case $dT_m/dx=0$ to determine the temperature distribution. The resulting solution for the Nusselt number is identical to the solution for the constant wall heat flux boundary condition with $S=-1$, requiring that fluid convective cooling at the wall be balanced by the volumetric generation. These solutions are not repeated here, since they may be derived from Eqs. (8) and (11) by specifying $S=-1$.

The dependence of normalized temperature profiles and Nusselt number on S, Z, and Γ will be explored over their relevant ranges in sections to follow, where for the present paper only velocity profiles exhibiting no negative (reverse) flow are considered. Thermal boundary conditions departing from the constant wall heat flux or constant wall temperature conditions discussed will result in Nusselt number behavior that is bounded by that predicted for these two limiting case boundary conditions.

Results and Discussion

At this point an examination of the relevant range of the dimensionless source S is warranted. Recall the definition of the source $S=sa/2q_w''$, or $S=a(d\Phi/dx)^2/2\sigma q_w''$. A reasonable upper limit

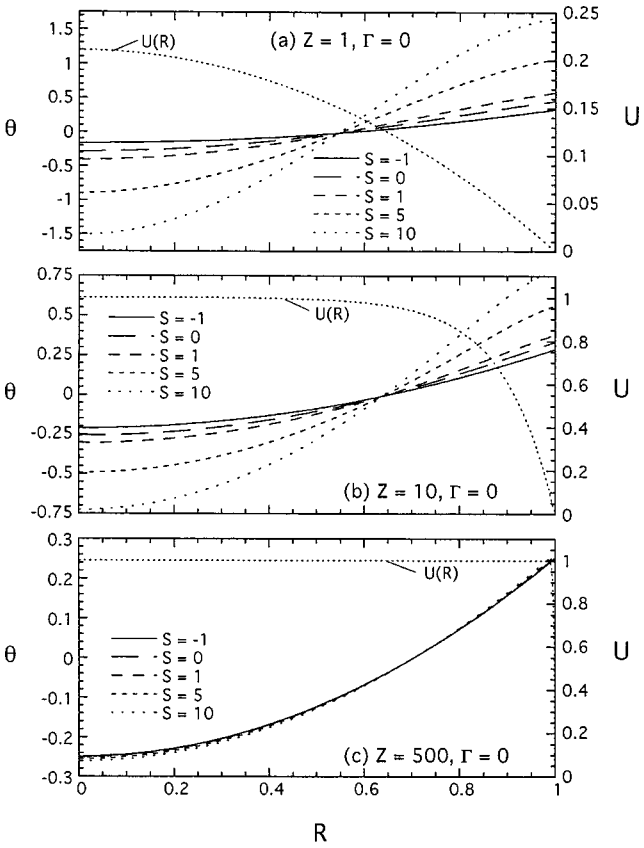

Fig. 1 Fully developed temperature and velocity distributions for purely electro-osmotic flow ($\Gamma=0$), three relative duct radii, and five values of *S*

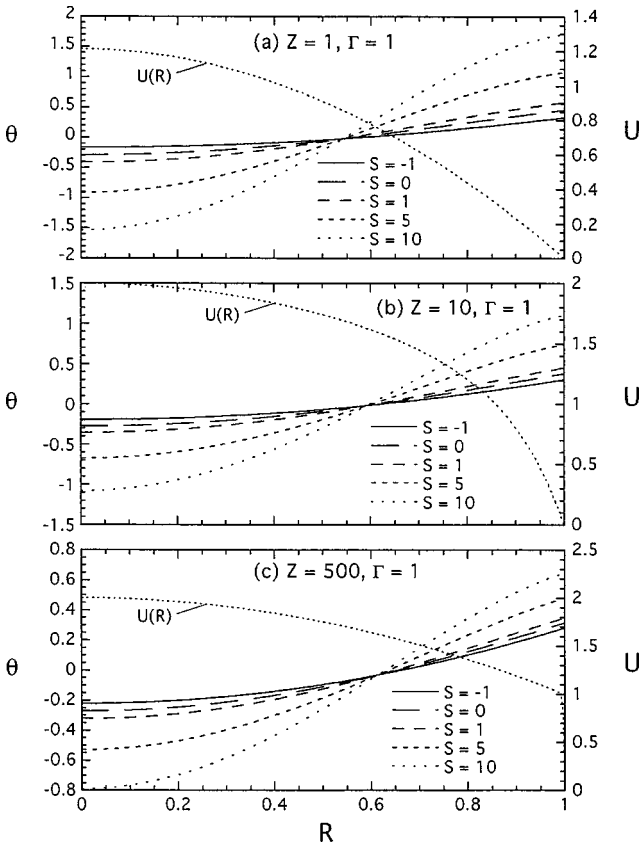

Fig. 2 Fully developed temperature and velocity distributions for pressure assisted flow ($\Gamma=1$), three relative duct radii, and five values of *S*

on the applied potential gradient $d\Phi/dx$ is 10^5 V/m, and the electrical resistivity of distilled water represents an approximate upper bound of $\sigma=10^4\ \Omega$-m. The wall heat flux may vary between large values (for applied heating) to nearly adiabatic conditions. Free convection to a microtube with a 1 cm thick insulating layer and a 10°C temperature difference yields a lower bound on the imposed heat flux to be $q''_w=3$ W/m^2. Thus, with a representative microtube radius $a=50\ \mu$m, the maximum dimensionless source S is of order 10. Lower positive values of S would result for finite wall heating.

Figures 1, 2, and 3, respectively, illustrate the fully developed normalized temperature distribution in the duct for values of $\Gamma=0$ (purely electro-osmotic flow), $\Gamma=1$ (pressure-assisted flow), and $\Gamma=-1$ (pressure-opposed flow) for values of Z spanning the range 1 to 500. (The parameter combination $\Gamma=-1$, $Z=1$ yields negative tube core velocities as shown by the reverse flow criterion discussed previously, so only two values of Z are shown for this case.) Each panel shows temperature profiles for five values of the dimensionless source S (-1, 0, 1, 5, and 10). Recall $S=-1$ corresponds to the constant wall temperature scenario (with fluid cooling).

The normalized velocity profiles are also shown in Figs. 1–3. The velocity profiles show that for purely electro-osmotic flow ($\Gamma=0$ in Figs. 1(a–c)), as Z is increased from a value of unity to a value of 500, the velocity profile changes from a near-Poiseuille flow distribution to a near-slug flow. The corresponding dimensionless temperature profiles for $\Gamma=0$ show a dependence on source S, with increasing S yielding greater variation in θ over the tube cross-section. The dependence of temperature on S diminishes with increasing Z; for $Z=500$ (Fig. 1(c)), temperature profiles for all magnitudes of S are nearly identical. Indeed, for slug flow ($Z\rightarrow\infty$), $U(R)/\bar{U}=1$, and Eq. (6) shows that the normalized temperature is independent of source magnitude. For this case of purely electro-osmotic flow, the maximum dimensionless temperature always occurs at the wall, $R=1$, and for finite Z, the wall temperature magnitude increases with increasing S. Also, for a

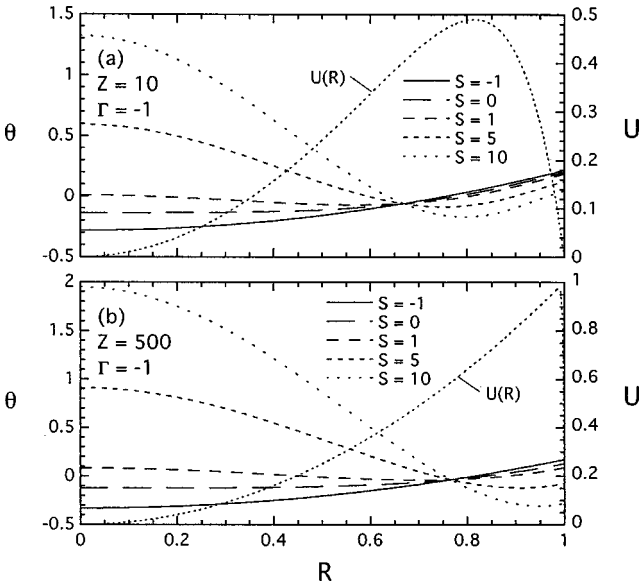

Fig. 3 Fully developed temperature and velocity distributions for pressure opposed flow ($\Gamma=-1$), two relative duct radii, and five values of *S*

uniform surface heating, the wall temperature gradient, $\partial\theta/\partial R|_{R=1}$, is constant (as can be observed in the temperature profiles for all cases in this study). Since the fully developed Nusselt number is inversely proportional to the normalized wall temperature ($\mathrm{Nu}=2/\theta_{R=1}$), increasing S yields lower Nusselt number.

For the pressure-assisted flow scenario ($\Gamma=1$) illustrated in Figs. 2(a–c), the velocity profiles exhibit flow qualitatively similar to classical pressure-driven tube flow except for $Z=500$, for which a very thin hydrodynamic boundary layer is observed at the tube wall due to the electro-osmotic body force in that region. The maximum velocity in the tube always occurs at the centerline, $R=0$. The temperature profiles show that, unlike the purely electro-osmotic flow case of Fig. 1, for combined electro-osmotic and pressure-assisted flow the normalized temperature is a function of S for all values of Z. Interestingly, for $Z=1$ and $\Gamma=1$ the velocity distribution is quite similar to its $\Gamma=0$ counterpart, as are the corresponding temperature profiles. As Z increases, however, the velocity profiles for the purely electro-osmotic and the combined pressure-assisted cases are quite different due to the additive effect of both fluid driving mechanisms. Consequently, the temperature profiles exhibit greater variation between tube centerline and wall extremes. These differences are more pronounced for $Z\rightarrow\infty$.

Hydrodynamic behavior for combined, pressure-opposed flow, illustrated in Figs. 3(a,b), is radically different from either of the two cases previously discussed. Recall that for $\Gamma=-1$ (at large Z), the pressure opposing the electro-osmotic driving force is sufficiently high to yield vanishing centerline velocity, according to Eq. (1). Thus, while a thin hydrodynamic boundary layer continues to exist at the wall for this pressure-opposed case, the maximum velocity is found near the wall rather than at the tube centerline, and a nearly stagnant central core exists. Further, the velocity gradient at the tube wall increases with increasing Z. As Z decreases, so also does the maximum velocity, and the position of the maximum is shifted slightly toward the duct centerline. Normalized temperature profiles for this pressure-opposed condition also exhibit behavior radically different from the $\Gamma=0$ and $\Gamma=1$ cases. For $S=0$, θ is approximately constant over much of the duct cross-section, rising to a maximum at the wall, regardless of the magnitude of Z. For positive values of S, the temperature profiles exhibit a local minimum. Further, for increasing S the maximum dimensionless temperature occurs at the duct centerline rather than the wall. Thus, the nearly stagnant core can reach temperatures significantly higher than at the wall. The implication is that the dimensional mean temperature, T_m, may exceed the wall temperature, T_w. Thus, the predicted dimensionless wall temperatures for sufficiently large S may be negative, and the heat transfer coefficient as classically defined will also be negative. This unusual behavior is more pronounced for increasing values of Z. Another interesting implication is that for some unique value of S (dependent on Γ and Z), the fully developed dimensional mean and wall temperatures may be identical. Consequently, for the uniform wall heating boundary considered here, $\mathrm{Nu}\rightarrow\infty$.

Figures 4(a–c) show, respectively, the fully developed Nusselt number as a function of Γ for $1\leqslant Z\leqslant 500$ for $S=0$ (limiting case of no volumetric heating), $S=1$, and $S=-1$. The minimum value of Γ plotted for a specified Z corresponds to that value of Γ which results in a negative core flow condition (i.e., $\Gamma_{\min}=[1/I_0(Z)-1]$). Generally speaking, the Nusselt number is a maximum at $\Gamma_{\min}$, and it is in this range of Γ that Nu is most strongly dependent on Z. The Nusselt number increases with increasing relative duct radius Z for a given value of Γ. As $\Gamma\rightarrow\infty$, pressure forces dominate, and the Nusselt number decreases asymptotically to the respective Poiseuille flow limits $\mathrm{Nu}=4.36$ for no volumetric heating, $S=0$, $\mathrm{Nu}=3.43$ for $S=1$, and $\mathrm{Nu}=6.0$ for $S=-1$. The Nusselt number for pressure-opposed flow may reach a magnitude nearly six times that for the purely pressure-driven flow limit. The maximum in Nusselt number, occurring at $\Gamma=-1$, results from

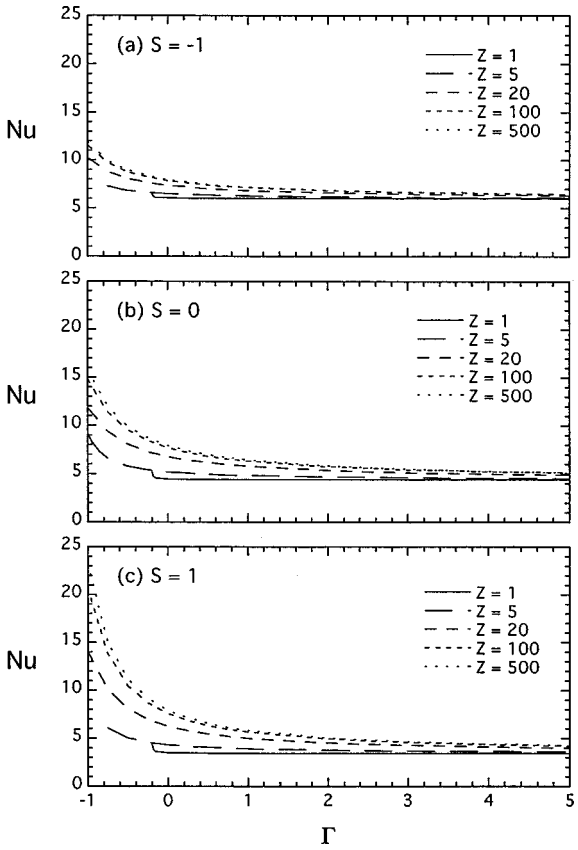

Fig. 4 Fully developed Nusselt number variation as a function of Γ for five relative duct radii and dimensionless source magnitudes of -1, 0, and 1.

the decreasing dimensional mean temperature due to the stagnating core flow, as seen qualitatively in Fig. 3. It is also interesting to note that for the same magnitude of wall heat flux $|S|=1$, the Nusselt number for the constant wall temperature scenario ($S=-1$, fluid cooling) is nearly double that for the constant heat flux boundary condition ($S=1$, fluid heating).

The fully developed Nusselt number is plotted versus Γ for $S=10$ and a range of Z in Fig. 5. For this value of S the asymptotic Nusselt number at large Γ is 1.17. At moderate values of Z the maximum Nusselt number occurs at the minimum allowable value of Γ. However, as Z increases the Nusselt number exhibits a singularity wherein $\mathrm{Nu}\rightarrow\pm\infty$ at a critical (negative) value of Γ. For Γ less than this critical value the Nusselt number, as classically defined, is negative. As illustrated previously in Fig. 3, this occurs when the volumetric source is sufficiently high to cause temperatures in the stagnant core (for $\Gamma<0$) to exceed the wall temperature, with the resulting dimensional mean temperature exceeding the wall temperature. In general, this critical value of Γ is a function of both Z and S, and occurs principally for larger magnitudes of both parameters. Further, for a fixed value of S, the critical value of Γ which yields this singularity in Nu shifts toward -1 as Z decreases, and the singularity vanishes for sufficiently small Z.

Presented in Fig. 6 are fully developed Nusselt number predictions as a function of S at $Z=500$ for a range of Γ corresponding to pressure-assisted flow. Predictions are shown for S values ranging from 0.1 to 100 to fully illustrate the behavior, although values of $S>10$ are not likely. Also tabulated in the figure are fully developed Nusselt numbers corresponding to each value of Z for the constant wall temperature solution, denoted $\mathrm{Nu}_{S=-1}$. Predictions for other values of Z (not shown) reveal that the qualitative Nusselt number behavior shown in Fig. 6 is similar for all Z, differing primarily in magnitude. As $S\rightarrow\infty$, $\mathrm{Nu}\rightarrow 0$ for all Γ. This

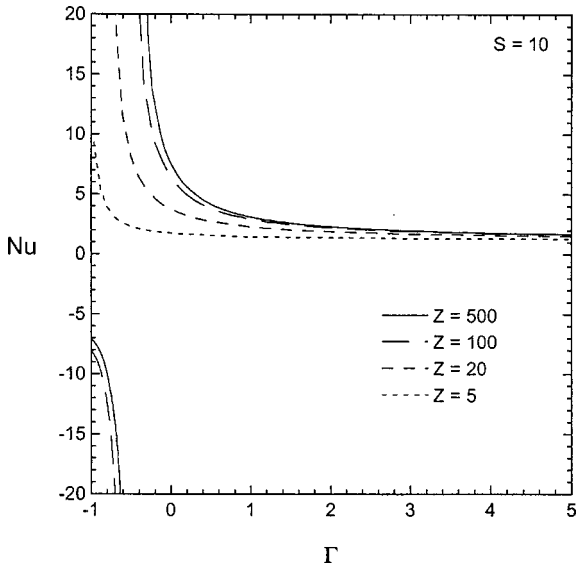

Fig. 5 Fully developed Nusselt number as a function of Γ for a dimensionless source of 10 and four relative duct radii

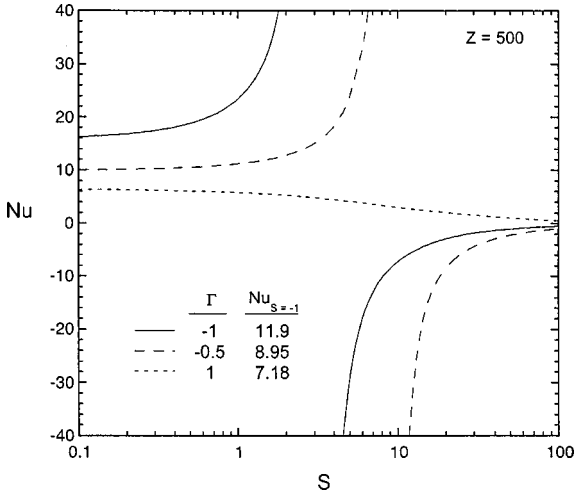

Fig. 7 Fully developed Nusselt number as a function of *S* for large relative duct radius (*Z*=500) with Γ=−1, −0.5, and 1. Corresponding Nusselt numbers for the constant wall temperature scenario (*S*=−1) are also shown.

may be explained by examination of the definition of the dimensionless source, which reveals that the scenario described by $S \rightarrow \infty$ is equivalent to vanishingly small imposed wall heat flux. Previous work by Tyagi et al. has described the Nusselt number dependence on S for purely pressure-driven flow [28]. Predictions carried out here for $\Gamma \rightarrow \infty$ are identical to these previously reported data. As Γ decreases such that the electro-osmotic driving potential becomes more significant, the Nusselt number increases. Note that the constant wall temperature boundary condition ($S=-1$) yields the maximum Nusselt number for a given value of Γ in pressure-assisted flow.

The Nusselt number singularity observed in Fig. 5 is further explored in Fig. 7, where Nu is plotted as a function of S for $Z=500$ and three values of Γ (−1, −0.5, and 1). Again the magnitudes for the $S=-1$ scenario are shown. For $\Gamma<0$ the predicted Nusselt number magnitudes for the constant wall temperature condition are smaller than the condition of uniform fluid heating. This is of course in contrast to the behavior noted in the preceeding paragraph. The figure further illustrates that, defined in the classical fashion, the Nusselt number may exhibit singular behavior and take on negative values for combined electro-osmotic and pressure-opposed flow. Figure 7 shows that this singularity in Nu occurs at larger S as Γ increases, and vanishes completely for $\Gamma>0$.

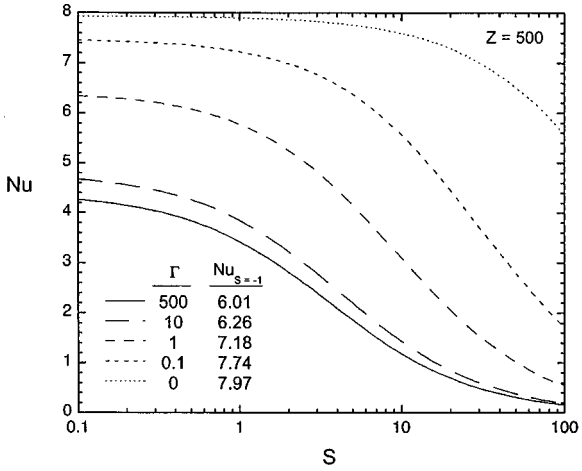

Fig. 6 Fully developed Nusselt number as a function of *S* for large relative duct radius (*Z*=500) and five values of Γ≥0. Corresponding Nusselt numbers for the constant wall temperature scenario (*S*=−1) are also shown

Conclusions

Thermally fully developed, heat transfer has been analyzed for combined electro-osmotic and pressure driven flow in a circular microtube. The two classical boundary conditions of constant heat flux and constant wall temperature were explored. The fully developed Nusselt number has been found to depend on the relative duct radius, the dimensionless volumetric source, and the dimensionless ratio of driving potentials, Γ. This ratio can take on both positive and negative values, depending on the signs of the streamwise voltage and pressure gradients imposed. For negative values of Γ, the velocity distribution exhibits a slow-moving central core with an accompanying local minimum at the duct centerline. When $\Gamma_{min}<\Gamma<0$, the Nusselt number as traditionally defined may be negative under certain conditions (dependent on the magnitudes of Γ, S, and Z). This occurs when the source is large enough that the mixed-mean temperature exceeds the wall temperature. In general, the Nusselt number decreases for increasing S and decreasing Z.

Nomenclature

a = tube radius
c_p = fluid specific heat
h = convective heat transfer coefficient
i_e = conduction current density
k = thermal conductivity
Nu = Nusselt number ($2ha/k$)
p = static pressure
r = radial coordinate
R = normalized radial coordinate (r/a)
q''_w = wall heat flux
s = volumetric energy generation
S = normalized energy generation ($sa/2q''_w$)
T = absolute temperature
T_m = mixed mean temperature
T_w = channel wall temperature
u = local fluid velocity
u_{eo} = maximum possible electro-osmotic velocity

$\overline{u}$ = average velocity
U = normalized local velocity (u/u_{eo})
$\overline{U}$ = ratio of mean velocity to maximum electro-osmotic velocity ($\overline{u}/u_{eo}$)
x = streamwise coordinate
Z = ratio of capillary radius to Debye length (a/λ)

Greek Symbols

α = thermal diffusivity
ε = fluid dielectric constant
Φ = applied potential field
Γ = ratio of pressure to electro-osmotic driving force $(a^2/4\varepsilon\zeta)[(dp/dx)/(d\Phi/dx)]$
λ = Debye length
μ = absolute viscosity
μ_{eo} = electro-osmotic mobility ($\varepsilon\zeta/\mu$)
ν = kinematic viscosity
ρ = fluid density
σ = liquid electrical resistivity
θ = normalized temperature
θ_w = normalized wall temperature
ζ = wall zeta potential

References

[1] Gravensen, P., Branebjerg, J., and Jensen, O. S., 1993, ''Microfluidics—A Review,'' J. Micromech. Microeng., **3**, pp. 168–182.
[2] Shoji, S., Nakagawa, S., and Esashi, M., 1990, ''Micropump and Sample Injector for Integrated Chemical Analysis Systems,'' Sens. Actuators, **21**, pp. 189–1192.
[3] van der Schoot, B. H., van den Berg, A., Jeanneret, S., and de Rooij, N. F., 1991, ''A Miniaturized Chemical Analysis System Using Two Silicon Micro Pumps,'' *Transducers '91*, Proceedings of the 1991 Int. Conference on Solid State Sensors and Actuators, IEEE, Piscataway, NJ, pp. 789–791.
[4] Bousse, L., Cohen, C., Nikiforov, T., Chow, A., Kopf-Sill, A. R., Dubrow, R., and Parce, J. W., 2000, ''Electrokinetically Controlled Microfluidic Analysis Systems,'' Annu. Rev. Biophys. Biomol. Struct., **29**, pp. 155–181.
[5] Arulanandam, S., and Li, D., 2000, ''Liquid Transport in Rectangular Microchannels by Electroosmotic Pumping,'' Colloids Surf., **161**, pp. 29–102.
[6] Culbertson, C. T., Ramsey, R. S., and Ramsey, J. M., 2000, ''Electro-osmotically Induced Hydraulic Pumping on Microchips: Differential Ion Transport,'' Anal. Chem., **72**, pp. 2285–2291.
[7] Dasgupta, P. K., and Shaorong, L., 1994, ''Electroosmosis: A Reliable Fluid Propulsion System for Flow Injection Analysis,'' Anal. Chem., **66**, pp. 1792–1798.
[8] Polson, N. A., and Hayes, M. A., 2000, ''Electro-Osmotic Flow Control of Fluids on a Capillary Electrophoresis Microdevice Using an Applied External Voltage,'' Anal. Chem., **72**, pp. 1088–1092.
[9] Reuss, F. F., 1809, ''Charge-Induced Flow,'' *Proceedings of the Imperial Society of Naturalists of Moscow*, **3**, pp. 327–344.
[10] Probstein, R. F., 1994, *Physicochemical Hydrodynamics*, 2nd ed., Wiley, New York.
[11] Rice, C. L., and Whitehead, R., 1965, ''Electrokinetic Flow in a Narrow Cylindrical Capillary,'' J. Phys. Chem., **69**, pp. 4017–4024.
[12] Ren, L., and Li, D., 2001, ''Electroosmotic Flow in Hetrogeneous Microchannels,'' J. Colloid Interface Sci., **243**, pp. 255–261.
[13] Gleeson, J. P., 2002, ''Electroosmotic Flows With Random Zeta Potential,'' J. Colloid Interface Sci., **249**, pp. 217–226.
[14] Hunter, R. J., 1981, *Zeta Potential in Colloid Science*, Academic Press, London.
[15] Valko, T. E., Siren, H., and Riekkola, M., 1999, ''Characteristics of Electro-Osmotic Flow in Capillary Electropheresis in Water and in Organic Solvents Without Added Ionic Species,'' J. Microcolumn Sep., **11**, pp. 199–208.
[16] Burgreen, D., and Nakache, F. R., 1964, ''Electrokinetic Flow in Ultrafine Capillary Slits,'' J. Phys. Chem., **68**, pp. 1084–1091.
[17] Sounart, T. L., and Baygents, J. C., 2001, ''Electrically-Driven Fluid Motion in Channels With Streamwise Gradients of the Electrical Conductivity,'' Colloids Surf., A, **95**, pp. 59–75.
[18] Paul, P. H., Garguilo, M. G., and Rakestraw, D. J., 1998, ''Imaging of Pressure and Electrokinetically Driven Flows Through Open Capillaries,'' Anal. Chem., **70**, pp. 2459–2467.
[19] Taylor, J. A., and Yeung, E. S., 1993, ''Imaging of Hydrodynamic and Electrokinetic Flow Profiles in Capillaries,'' Anal. Chem., **65**, pp. 2928–2932.
[20] Ross, D., Johnson, T. J., and Locascio, L. E., 2001, ''Imaging of Electro-Osmotic Flow in Plastic Microchannels,'' Anal. Chem., **73**, pp. 2509–2515.
[21] Cummings, E. B., 1999, ''PIV Measurement of Electro-Osmotic and Pressure Driven Flow Components in Microfluidic Systems,'' *Microelectromechanical Systems (MEMS)*, MEMS-Vol. 1, ASME, New York, pp. 377–382.
[22] Yang, C., Li, D., and Masliyah, J. H., 1998, ''Modeling Forced Liquid Convection in Rectangular Microchannels With Electrokinetic Effects,'' Int. J. Heat Mass Transfer, **41**, pp. 4229–4249.
[23] Mala, G. M., Li, D., and Dale, J. D., 1997, ''Heat Transfer and Fluid Flow in Microchannels,'' Int. J. Heat Mass Transfer, **40**, pp. 3079–3088.
[24] Tao, L. N., 1962, ''The Second Fundamental Problem in Heat Transfer of Laminar Forced Convection,'' ASME J. Appl. Mech., **29**, pp. 415–420.
[25] Maynes, D., and Webb, B. W., 2003, ''Fully-Developed Electro-Osmotic Heat Transfer in Microchannels,'' Int. J. Heat Mass Transfer, **46**, pp. 1359–1369.
[26] Burmeister, L. C., 1983, *Convective Heat Transfer*, Wiley and Sons, New York.
[27] Ou, J. W., and Cheng, K. C., 1974, ''Viscous Dissipation Effects on Thermal Entrance Heat Transfer in Laminar and Turbulent Pipe Flows With Uniform Wall Temperature,'' ASME Paper No. 74-HT-50.
[28] Tyagi, V. P., 1966, ''Laminar Forced Convection of a Dissipative Fluid in a Channel,'' ASME J. Heat Transfer, **88**, pp. 161–169.

Simulation of Unsteady Small Heat Source Effects in Sub-Micron Heat Conduction

Sreekant V. J. Narumanchi

Jayathi Y. Murthy

School of Mechanical Engineering,
Purdue University,
585 Purdue Mall,
West Lafayette, IN 47907

Cristina H. Amon

Institute for Complex Engineered Systems and
Department of Mechanical Engineering,
Carnegie Mellon University,
5000 Forbes Ave,
Pittsburgh, PA 15213

In compact transistors, large electric fields near the drain side create hot spots whose dimensions are smaller than the phonon mean free path in the medium. In this paper, we present a study of unsteady hot spot behavior. The unsteady gray phonon Boltzmann transport equation (BTE) is solved in the relaxation time approximation using a finite volume method. Electron-phonon interaction is represented as a heat source term in the phonon BTE. The evolution of the temperature profile is governed by the interaction of four competing time scales: the phonon residence time in the hot spot and in the domain, the duration of the energy source, and the phonon relaxation time. The influence of these time scales on the temperature is investigated. Both boundary scattering and heat source localization effects are observed to have considerable impact on the thermal predictions. Comparison of BTE solutions with conventional Fourier diffusion analysis reveals significant discrepancies. [DOI: 10.1115/1.1603774]

Keywords: Computational, Conduction, Heat Transfer, Microscale, Nanoscale

1 Introduction

In recent years, the extreme miniaturization of integrated circuits has led to increasing concerns about the steady and unsteady thermal performance of micro-electronic devices. It is now well established that conventional Fourier analysis leads to erroneous thermal predictions when the mean free path of heat carriers is comparable to or larger than the characteristic domain size. This is also true when the time scale of interest is smaller than the relaxation time of the carriers [1,2]. When the system length scale is comparable to the carrier mean free path 1, but larger than the carrier wavelength λ, the Boltzmann transport equation in the relaxation time approximation can be employed [3–5]. Phonons, which are quantized lattice vibrations [6,7], are the predominant energy carriers in semiconductors at room temperature. Currently, in typical devices, the region of strongest electron-phonon interaction (i.e., heat generation region) is of the order of 10–30 nm and is much smaller than the mean free path of phonons, which is approximately 300 nm in silicon at room temperature [8].

Studies illustrating non-local spatial [9–11] and temporal [12,13] effects have been reported. Studies have also been performed to examine Joule heating effects in semiconductor devices. Sverdrup et al. [14] report steady one-dimensional results of the temperature distribution in the presence of a localized heat source in a silicon-on-insulator (SOI) device. Their results indicate that Fourier law underpredicts the maximum temperature rise substantially due to heat source localization effects. Another study by Sverdrup et al. [15] focuses on peak temperature rise in submicron devices under electrostatic discharge (ESD) conditions [16]. Sverdrup [17] and Sverdrup et al. [18] have performed a two-dimensional study of temperature distribution in a NMOS transistor using the phonon BTE. They divided phonons into propagating and reservoir modes [19,20]. The propagating mode is responsible for energy transport, while the reservoir mode functions in a purely capacitative mode and does not contribute to thermal transport. Their results indicate considerable discrepancy between BTE and Fourier solutions. Sverdrup et al.[21] have also experimentally demonstrated the localized heat source and nonequilibrium effects in the vicinity of a hot spot.

Two-dimensional simulations of concurrent electrical and thermal transport in semiconductor devices (GaAs MESFETs and Si MOSFETs) have been reported [22–25]. The approach is to consider hydrodynamic equations for electron transport [26] and energy conservation equations for electrons and the different phonon modes. The equations are derived by taking moments of the Boltzmann equation and are hence lower-order approximations. Additionally, an important simplifying assumption in these studies is that heat propagation by acoustic phonons is assumed to be through diffusion (Fourier law).

Most published work in this area addresses steady state behavior. The focus of the present work is the unsteady behavior of small heat sources. We consider an unsteady hot spot in a thin layer and examine the interaction of phonon residence time, hot spot duration, boundary scattering time scales and relaxation time constants in determining peak temperature rise and the rate of temperature decay. For clarity, only a single phonon mode representative of all three phonon branches is considered, and dispersion effects are neglected. By using this simplified model, the intent is to clarify fundamental mechanisms for thermal transport, and to explain the departure between Fourier predictions and those using the BTE. The results may help explain the behavior of more complex models for unsteady sub-micron thermal transport, including multiple phonon branches, dispersion effects and electron-phonon coupling.

2 Formulation

2.1 Governing Equations. The calculation domain is shown in Fig. 1. Only one quarter of the domain is simulated due to symmetry. The length L and width d are chosen so that $d/l < 1$; also $L/\lambda > 1$ and $d/\lambda > 1$, where l is the phonon mean free path and λ is the phonon wavelength. The heat source, represented by the shaded portion in Fig. 1, occupies a square of side d in the computational domain. It is turned on at $t=0$ and stays on with a magnitude q till a time t_q, after which it is turned off. This heat pulse is representative of the electron-phonon interaction, which deposits energy to the phonon system. Sverdrup et al. [18] argue that since the electron-phonon interaction time scales are approximately two orders of magnitude smaller than the phonon-phonon interaction times, the energy transfer from the electrons to the phonons can be incorporated via a heat source term in the phonon BTE; a similar practice is adopted here. Along $y=d$, diffusely

Contributed by the Heat Transfer Division for publication in the JOURNAL OF HEAT TRANSFER. Manuscript received by the Heat Transfer Division July 17, 2002; revision received June 3, 2003. Associate Editor: G. Chen.

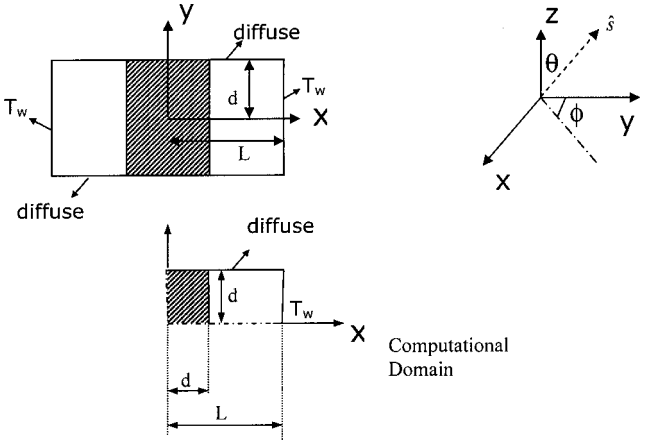

Fig. 1 Computational domain and coordinate system

reflecting boundaries are chosen to model the interface between the device layer and adjacent material; similar assumptions have been made in [14,18] to capture the size effect. At $x=L$, a constant wall temperature is chosen, representing a heat sink.

The phonon BTE in the relaxation time approximation can be written as

$$\frac{\partial f_w}{\partial t}+\vec{v}_w\cdot\nabla f_w=\frac{f_w^0-f_w}{\tau_{s,w}}+q_w$$

where $f_w(\vec{r},t)$ is the phonon distribution function, $\vec{v}_w$ is the phonon velocity vector, $\tau_{s,w}$ is the phonon relaxation time, f_w^0 is the Bose-Einstein equilibrium distribution function of the phonons and is given by

$$f_w^0=\frac{1}{(e^{\hbar w/k_BT}-1)}$$

We define phonon intensity [5] as

$$I=\sum_P\frac{1}{4\pi}\int_0^{w_D}v_w f_w\hbar w D(w)dw$$

where the sum is over the three phonon polarizations p, w is the phonon frequency, w_D is the cutoff frequency, and $D(w)$ is the phonon density of states [7]. We neglect phonon dispersion effects and represent all phonon polarizations with a single velocity v. Defining dimensionless variables

$$t^*=\frac{tv}{L};\quad \tau_q=\frac{t_q v}{L};\quad \tau_L=\frac{L}{v\tau_s};\quad \tau_d=\frac{d}{L}$$

$$I^*=\frac{I-I_w}{qL/v};\quad I^{0*}=\frac{1}{4\pi}\int_{4\pi}I^*d\Omega=\frac{I^0-I_w}{qL/v} \tag{1}$$

where τ_s is the phonon relaxation time and I^0 is the equilibrium intensity. The quantity q is to be understood as the total energy deposited over all frequencies, i.e., the integral over q_w.

The dimensionless equation for gray phonon radiative transfer can be written as

$$\frac{\partial I^*}{\partial t^*}+\nabla\cdot(\hat{s}I^*)=\tau_L(I^{0*}-I^*)+S(t^*) \tag{2}$$

$$\text{for}\quad 0<x^*<\tau_d$$

$$S(t^*)=1\quad \text{for}\quad t^*\leqslant\tau_q$$

$$=0\quad \text{for}\quad t^*>\tau_q$$

$$\text{for}\quad x^*\geqslant\tau_d\quad S(t^*)=0.$$

Here, $I_w=\sigma T_w^4/\pi$ and σ is the Stefan Boltzmann constant for phonons. The expression for σ(T) under the Debye model for energy density is [7]

$$\sigma(T)=\frac{3}{8\pi^2v^2\hbar^3}k_B^4\int_0^{\theta_D/T}\frac{x_3}{(e^x-1)}dx \tag{3}$$

Under the limit $\theta_D/T\gg1$, σ is independent of temperature and reduces to $(\pi^2k_B^4)/(40\hbar^3v^2)$ [5]. The assumption $\theta_D/T\gg1$ is used in the present study for simplicity and also since it permits comparison with solutions from radiative transport literature. Nonetheless, it should be noted that under the Debye model for energy density in a solid, the assumption of $\theta_D/T\gg1$ is not appropriate for silicon at room temperature, though it is appropriate for diamond at room temperature [5].

The phonon direction vector $\hat{s}$ is in Fig. 1 and can be expressed as $\hat{s}=\sin\theta\sin\phi\hat{i}+\sin\theta\cos\phi\hat{j}+\cos\theta\hat{k}$. An equivalent temperature may be computed from the angular average of the intensity as

$$T=\left(\frac{\pi I^0}{\sigma}\right)^{1/4} \tag{4}$$

The dimensionless parameters governing the problem are: τ_L, the acoustic thickness of the domain, which is a ratio the phonon residence time in the domain to the phonon scattering time scale; τ_d, the ratio of the phonon residence time in the hot spot to that in the domain; τ_q, the ratio of the heat source duration to the phonon residence time in the domain.

2.2 Boundary Conditions

Specularly Reflecting Boundaries. For a boundary with outward-pointing normal $\hat{n}$, the intensity for directions entering the domain $(\hat{s}\cdot\hat{n}<0)$ is given by

$$I_b^*(\hat{s})=I_b^*(\hat{s}_r)$$

where

$$\hat{s}_r=\hat{s}-2(\hat{s}\cdot\hat{n})\hat{n}$$

For directions incoming to the boundary $(\hat{s}\cdot\hat{n}\geqslant0)$:

$$\nabla\cdot(\hat{s}I^*)=0$$

Diffusely Reflecting Boundaries. For directions leaving the boundary and entering the domain $(\hat{s}\cdot\hat{n}<0)$

$$I_b^*(\hat{s})=\frac{1}{\pi}\int_{\hat{s}\cdot\hat{n}>0}I^*(\hat{s})\hat{s}\cdot\hat{n}d\Omega$$

For directions incoming to the boundary $(\hat{s}\cdot\hat{n}\geqslant0)$:

$$\nabla\cdot(\hat{s}I^*)=0$$

Given-Temperature Boundaries. For directions leaving the boundary and entering the domain $(\hat{s}\cdot\hat{n}<0)$

$$I_b^*=0$$

For directions incoming to the boundary $(\hat{s}\cdot\hat{n}\geqslant0)$:

$$\nabla\cdot(\hat{s}I^*)=0$$

2.3 Numerical Method. The finite volume method [27–29] is employed to solve the two-dimensional equation for phonon radiative transfer (EPRT). The spatial domain is discretized into rectangular control volumes, while the angular domain at any spatial point is discretized into non-overlapping control angles; the centroid of each control angle is denoted by the direction vector $\hat{s}$. Each octant is divided into $N_\theta\times N_\phi$ control angles. The details of the discretization procedure are described in [28,29]. The transient term in Eq. (2) is treated using a fully implicit scheme, while the step scheme [28] is used to treat the convective term. Each discrete angular direction results in a linear set of algebraic equa-

tions, which are solved using the tridiagonal matrix algorithm [27]. The directions themselves are solved sequentially using Picard iteration.

2.4 Calculations of Fourier Conduction. Computations of Fourier conduction in the presence of an unsteady hot spot are also done for comparison. In all the computations presented in this paper, the specific heat is computed under the assumption $\Theta_D/T \gg 1$ [7], consistent with the assumption for computation of σ, so that

$$C = \frac{4\pi^2}{10}\frac{k_B^4 T^3}{\hbar^3 \nu^3} = \frac{16\sigma T^3}{\nu} \tag{5}$$

C is evaluated for all Fourier conduction computations at T_w. The thermal conductivity is computed from kinetic theory

$$k = Cv^2\tau_s/3 \tag{6}$$

The corresponding dimensionless thermal conductivity used in the Fourier computations is $(k/L)/(4\sigma T_w^3) = 2.39$. Using a temperature dependent C and k does not alter the nondimensional results by more than 3%. The equivalent volumetric heat source used is

$$q''' = \frac{4\pi q}{\nu}$$

The boundary at $y^* = d/L$ is treated as an adiabatic boundary. Numerical simulations are done using the finite volume scheme described in [30], with a fully implicit scheme for time stepping.

3 Results and Discussion

Non-dimensional results for temperature are presented in terms of the variable $\Theta = (T^4 - T_w^4)/(\pi q L/\sigma v)$ for a range of acoustic thicknesses $\tau_L = 0.0558 - 5.58$. The hot spot size τ_d is fixed nominally at 0.1, though variations about this value are also computed. The duration of the hot spot is varied in the range $\tau_q = 0.01 - 20$. Both specular and diffuse boundaries are considered at $y^* = d/L$. The specular boundary condition denotes a one-dimensional problem in the x direction. The diffuse boundary condition models phonon confinement because of boundary scattering.

3.1 Numerical Accuracy. Unless otherwise mentioned, the results presented here are computed using a baseline spatial mesh of 100×10 cells, an angular mesh of $N_\theta \times N_\phi = 8 \times 8$ in the octant, and a time step $\Delta t^* = \Delta t/(L/v) = 0.001$. A number of simulations were carried out with finer spatial and angular discretizations, as well as a smaller time step. The predicted maximum temperatures at representative time instants did not vary by more than 2% with respect to the results obtained with the baseline mesh. A mesh of 100×10 and a time step $\Delta t^* = 0.001$ is used for the Fourier calculations. Comparisons with calculations on finer meshes indicate that the maximum temperature is accurate to well within 0.1%.

Comparisons are also made between the steady state solution to the EPRT and the published literature [31] for the problem of one-dimensional radiation between plane slabs. Two infinite black parallel plates are maintained at two different constant temperatures T_1 and T_2 and contain an absorbing and emitting medium in between them. The solution to the one-dimensional gray radiation problem in radiative equilibrium is the same as that for the EPRT. Figure 2 shows the non-dimensional results for a range of acoustic thicknesses. The numerical solution matches well with the exact solution [31] for the entire range of acoustic thicknesses.

3.2 Asymptotic Behavior. The overall temporal behavior of the system may be understood by examining its behavior in the limits of τ_q. Averaging the BTE over the angular space 4π yields

$$\frac{\partial I^{0*}}{\partial t^*} + \nabla \cdot \vec{q} = S \tag{7}$$

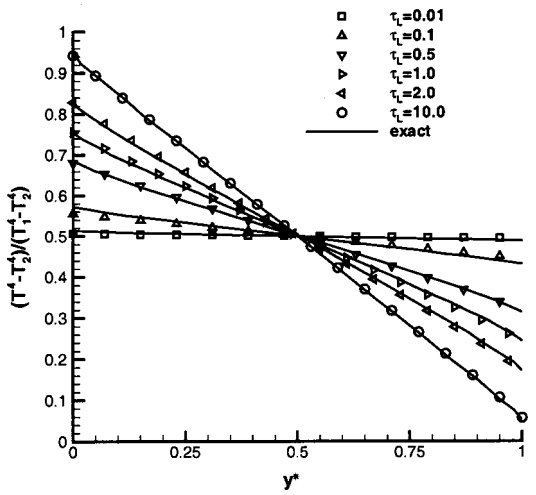

Fig. 2 Comparison of predicted temperature profiles with solution from [31] for radiative heat transfer between black parallel plates enclosing gray absorbing emitting medium

where $\vec{q}$ is the dimensionless heat flux vector

$$\vec{q} = \frac{1}{4\pi}\int_{4\pi} \hat{s} I^* d\Omega \tag{8}$$

For $t^* \ll \tau_d$, phonons originating in the hot spot have not had time to leave the hot spot and ballistic effects are negligible. Thus the flux term in Eq. (7) is negligible. Since the initial conditions are isotropic, the phonon intensity within the hot spot is also isotropic. The BTE in this limit may be approximated as:

$$\frac{\partial I^*}{\partial t^*} = \frac{\partial I^{0*}}{\partial t^*} = S \quad \text{for} \quad x^* \leq \tau_d$$
$$= 0 \quad \text{for} \quad x^* \geq \tau_d \tag{9}$$

Thus, the solution for $t^* \ll \tau_d$ is $I^* = I^{0*} = t^*$ inside the hot spot, and a linear rise in T^4 with time is expected. Outside the hot spot, the intensity solution is $I^* = I^{0*} = 0$, since phonons originating in the hot spot have not yet left it. Thus, for $t^* \ll \tau_d$, the heat-up is purely capacitative.

Case $\tau_q < \tau_d$. For this case, the hot spot duration is smaller than the travel time required by the phonon to cross the hot spot. For $t^* < \tau_q$, the temperature rises linearly until $t^* = \tau_q$. Once the heat source is turned off, the intensity in the hot spot region is expected to remain constant in time until phonons leaving the hot spot enter the cold channel. For an acoustically thin hot spot ($\tau_d \tau_L \ll 1$), this occurs over a time scale $\sim \tau_d (= (d/v)/(L/v))$. Thus, for $\tau_d > t^* > \tau_q$, the intensity and the temperature are expected to remain constant. The peak temperature corresponds to $\Theta = \tau_q$. Beyond $t^* > \tau_d$, ballistic transport of phonons from the hot spot region causes the hot spot intensity to fall. Heat released in the hot spot reach the cold boundary at time scales $t^* \sim O(1)$ if the intervening material is acoustically thin, i.e., $\tau_L \ll 1$. These trends are clearly visible in Fig. 3 which shows the variation of Θ versus t^* for $\tau_q = 0.01$ at a point in the hotspot ($x^* = x/L = 0.015, y^* = y/L = 0.045$) for an acoustic thicknesses $\tau_L = 5.58$ and $\tau_d = 0.1$, for both specular and diffuse top walls. Since ballistic transport is not important for $t^* < \tau_d$, there is little difference between the two boundary conditions for small t^*; boundary confinement effects only begin to manifest themselves for $t^* > \tau_d$ once phonons have had to time to encounter the boundary. Calculations using the Fourier conduction model show that for $t^* \ll \tau_d$, heat-up is again predominantly capacitative. However, the infinite wave speed of the Fourier conduction equation implies

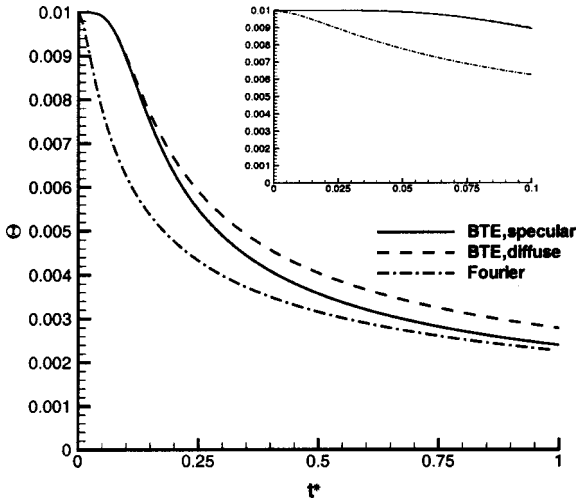

Fig. 3 Variation of temperature with time at point (0.015,0.045) for $\tau_d=0.1$, $\tau_q=0.01$, and $\tau_L=5.58$

that the temperature of the hot spot begins to fall instantaneously for $t^*>\tau_q$, as seen in the inset in Fig. 3, unlike for the BTE. Since the channel acoustic thickness τ_L is relatively high, the Fourier and BTE responses are not significantly different.

Case $\tau_q>\tau_d$. The behavior for large τ_q is presented in Fig. 4 which shows the variation of Θ with time for the point (0.015, 0.045) for $\tau_d=0.1$, $\tau_L=0.558$ and $\tau_q=20$. Here again, for $t^* \ll \tau_d$, the variation of Θ versus t^* is linear, but is not visible on the scale of the figure. For $\tau_q>t^*>\tau_d$, the temperature continues to rise, but at a reduced rate, as phonon transport removes heat from the hot spot; the curves approach the steady state values asymptotically for $t^*<\tau_q$. The steady state value is dictated by the balance of heat generation within the hot spot and its loss through phonon transport from the hot spot to the cold wall. Thus,

$$q'''V \sim A\Psi_b \sigma(T^4 - T_w^4) \tag{10}$$

Here, T is the average temperature of the hot spot, V is the volume of the hot spot, and A is the surface area through which the hot spot loses energy. Ψ_b is a measure of the acoustic conductance due to channel length. Thus $\Theta \sim 4\tau_d/\Psi_b$ at steady state. For a specular boundary at $y^*=d/L$ and $t^* \gg 1$, Ψ_b may be estimated from the theory of steady radiative heat transfer between parallel

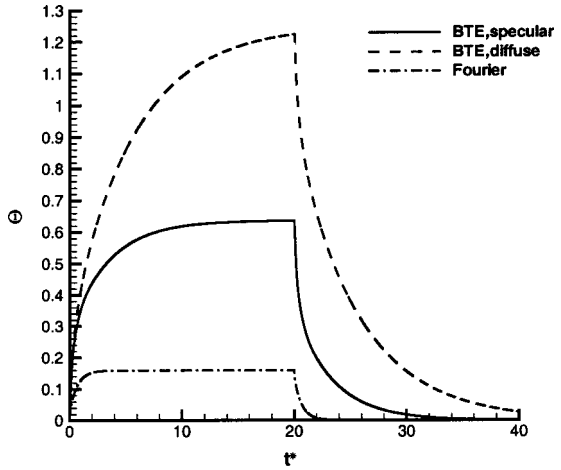

Fig. 4 Variation of temperature with time at point (0.015,0.045) for $\tau_d=0.1$, $\tau_q=20.0$, and $\tau_L=0.558$

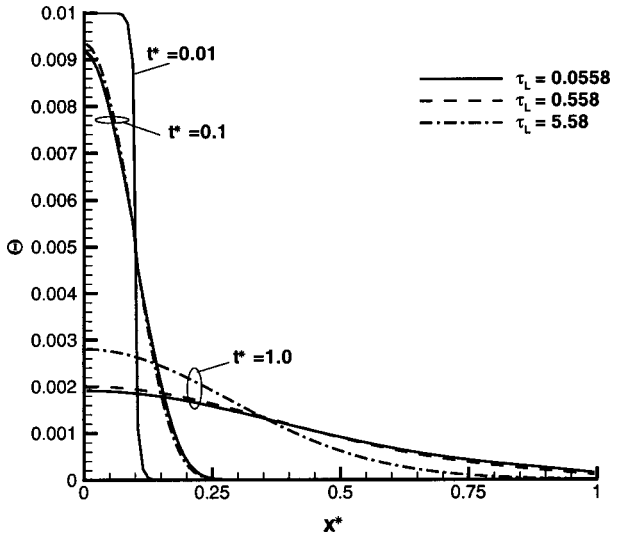

Fig. 5 Spatial variation of temperature with x^* along $y^*=0.045$ for different acoustic thicknesses, for $\tau_d=0.1$ and $\tau_q=0.01$

black plates containing a gray absorbing and emitting medium [31]. For the parameters associated with Fig. 4, $\Psi_b \sim 0.72$, and a steady state value of $\Theta \sim 0.56$ may be computed, which matches the computed value closely. Once the hot spot is turned off, the temperature falls, as expected. Computations using the Fourier law show a faster response time than those using the BTE, a trend also noted in [32]. The steady state value of Θ is also substantially lower. The steady-state Fourier value may be estimated from a balance of heat generation and conduction away from the hot spot

$$q'''V \sim kA(T - T_w)/L \tag{11}$$

Using $k=Cv^2\tau_s/3$, a value of $\Theta \sim 3\tau_d\tau_L \sim 0.17$ may be deduced, consistent with the plateau for Fourier conduction in Fig. 4. This asymptote can also be derived from the acoustically thick limit of Eq. (10) using $\Psi_b=4/3\tau_L$ [31]. Assuming small temperature differences, the equivalent conductivity implied by Eq. (10) for the BTE is $k_{\text{eff}} \sim 4\sigma T_w^3 \Psi_b L$. Thus, assigning a conductivity to the channel from kinetic theory overestimates the equivalent conductance by a factor of $4/(3\tau_L\Psi_b)$. The time constant for the Fourier case is $\sim L^2C/k$; the corresponding dimensionless value is $3\tau_L$. A similar value for the specular BTE may be estimated from L^2C/k_{eff}, resulting in a dimensionless time constant of $4/\Psi_b$. Thus the Fourier time constant for the transient would be smaller by a factor of approximately $3\tau_L\Psi_b/4$. The ratio of the Fourier to specular BTE time constant in Fig. 4 (for $t^*>20$) is approximately 0.24; the estimate of $3\tau_L\Psi_b/4$ is approximately 0.3.

3.3 Influence of Interior Scattering. The influence of interior scattering may be discerned from Figs. 5–7. It is worth mentioning that even with the diffuse boundary condition, the results are practically one-dimensional; hence in subsequent plots only results along a line in the x-direction are shown. Figure 5 shows the spatial variation of Θ for different acoustic thicknesses τ_L for $\tau_d=0.1$ and $\tau_q=0.01$. Figure 6 shows the variation for $\tau_q=1.0$. Both figures assume a diffuse boundary at $y^*=d/L$. For $t^* < \tau_d$, we see that there is no dependence on acoustic thickness. This is in keeping with Eqs. (7) and (9); because ballistic effects are negligible for small t^* and since the scattering term does not appear in Eq. (9), there is no dependence on τ_L. The Θ profile for $t^*<\tau_d$ shows a characteristic ''square'' profile in the hot spot, corresponding to the linear rise of Θ with t^*; a value $\Theta \sim t^*$ is achieved everywhere in the hot spot. Beyond $t^*>\tau_d$, phonon transport from the hot spot causes the profile to become more parabolic. For $\tau_L<1$, boundary scattering overwhelms interior

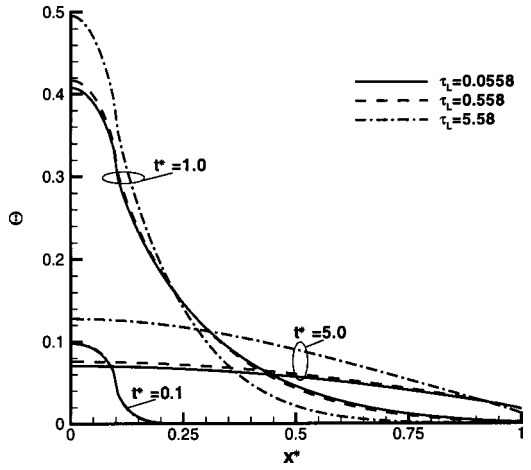

Fig. 6 Spatial variation of temperature with x^* along $y^*=0.045$ for different acoustic thicknesses, for $\tau_d=0.1$ and $\tau_q=1.0$

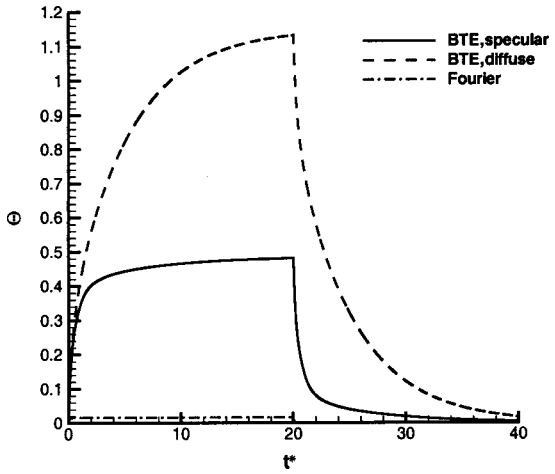

Fig. 8 Variation of temperature with time at point (0.015, 0.045) for $\tau_d=0.1$, $\tau_q=20.0$, and $\tau_L=0.0558$

scattering, as discussed in the next section; hence the curves for $\tau_L=0.0558$ and 0.558 are seen to be nearly coincident. The curve for $\tau_L=5.58$ is markedly different from the other two; this difference begins to manifest itself over time scales $t^*>1/\tau_L$, corresponding to the phonon scattering time. As expected, the greater acoustic impedance associated with $\tau_L=5.58$ leads to higher hot spot temperatures and a slower approach to steady state.

Figure 7 shows the variation of Θ for the point (0.015, 0.045) for the same parameters as in Fig. 4 but with $\tau_L=5.58$. Here again, for $t^*\ll\tau_d$, the variation of Θ versus t^* is linear, but is not visible on the scale of the figure. The overall behavior is similar to that described for Fig. 4; however, the lower acoustic conductance of the channel ($\Psi_b\sim0.2$ [31]) implies a higher asymptotic steady-state value for the specular BTE of $\Theta=4\tau_d/\Psi_b\sim2.0$. The dimensionless time constant of the transient for the specular BTE calculation may be estimated as $\sim4/\Psi_b\sim8$. This is comparable to τ_q. As a result the steady state asymptotic value is not achieved before the hot spot is turned off. For this relatively high acoustic thickness, the Fourier results are similar to specular BTE results.

3.4 Boundary Scattering Effects. The influence of diffuse boundary scattering may be discerned from Figs. 3–4 and 7–8. A lower bound on the time scale for boundary scattering is $\sim d/v$; a corresponding upper bound on the equivalent acoustic thickness of the domain may be computed by considering interior and boundary scattering to be parallel scattering processes. Using Mathiessen's rule [7], the equivalent domain acoustic thickness $\tau_{L,\mathrm{eq}}$ may be computed as

$$\tau_{L,\mathrm{eq}}=L/d+\tau_L=1/\tau_d+\tau_L \tag{12}$$

The influence of diffuse boundary scattering is therefore to increase the equivalent acoustic thickness, resulting in higher acoustic impedance and slower transients. Diffuse scattering causes back scattering of phonon energy into the hot spot, which results in higher temperature rise and a longer phonon residence time in the domain. Under specularly reflecting boundary conditions, there is no back scattering of phonons, and phonons from the hot spot reach the cold wall much sooner. The differences between specular and diffuse boundaries manifest themselves on time scales $t^*>\tau_d$, once the phonons leaving the hot spot have had a chance to encounter the diffuse boundary, as seen in Fig. 3.

From Eq. (12) it is clear that the effects of diffuse boundary scattering are felt more strongly for $\tau_L\ll1/\tau_d$. In this limit $\tau_{L,\mathrm{eq}}\sim1/\tau_d$. For $\tau_d=0.1$, the equivalent acoustic thickness is dominated by boundary scattering for $\tau_L<1$. Hence the curves for $\tau_L=0.0558$ and 0.558 are virtually coincident in Figs. 5 and 6. For $\tau_d\ll1$, the lower bound on the acoustic conductance Ψ_b is $\sim4/(3\tau_{L,\mathrm{eq}})\sim4\tau_d/3$ [31], and is independent of τ_L. Thus, the maximum temperature in the hot spot and the transient response are expected to be nearly identical for $\tau_L\ll1/\tau_d$, other parameters being equal. This is evident from an examination of diffuse boundary scattering cases in Figs. 4 and 8, which show that the Θ plateau value is nearly the same for $\tau_L=0.0558$ ($\Theta_{\max}\sim1.13$) and 0.558 ($\Theta_{\max}\sim1.22$). Also the transient time constants for $\tau_L=0.0558$ and 0.558 are similar, and are approximately 3.9 and 4.2, respectively.

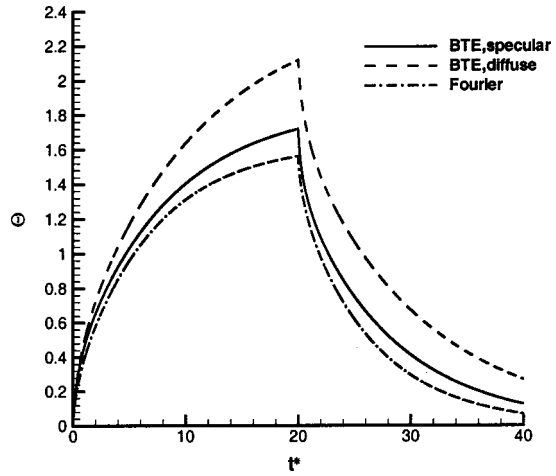

Fig. 7 Variation of temperature with time at point (0.015,0.045) for $\tau_d=0.1$, $\tau_q=20.0$, and $\tau_L=5.58$

3.5 BTE-Fourier Temperature Rise Comparison. It is illustrative to compare the temperature rise predictions obtained from the BTE solutions to those predicted by the Fourier diffusion theory. Figures 9 and 10 compare BTE and Fourier conduction results for $\tau_L=0.0558$ and 5.58 respectively; $\tau_q=1.0$ and $\tau_d=0.1$ are assumed for both cases. Diffuse boundary conditions are used for the BTE at $y^*=d/L$. The non-dimensional temperature difference is defined as $\Phi=(T_{\mathrm{BTE}}-T_F)/(\pi qd/(4\sigma vT_w^3))$ and is plotted along the line $y^*=0.045$. At the start of the calculation, both the BTE and Fourier solutions start with the same initial condition and the temperature difference is zero; similarly, as $t^*\to\infty$, both temperatures tend to the wall temperature and the temperature difference tends to zero. The temperature differences in between depend on the transient response time of the two models.

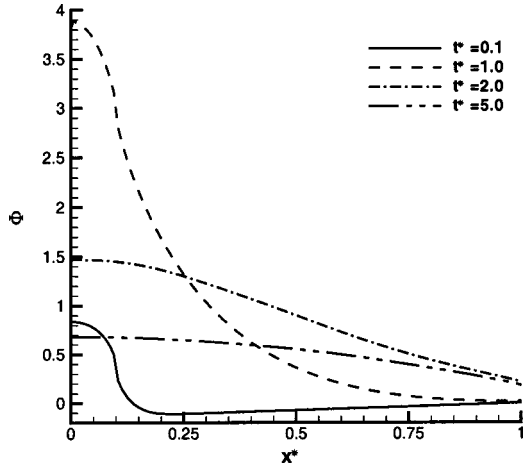

Fig. 9 Spatial variation of temperature difference between BTE and Fourier solutions, along $y^*=0.045$, with time for $\tau_q=1.0$, $\tau_d=0.1$, and $\tau_L=0.0558$

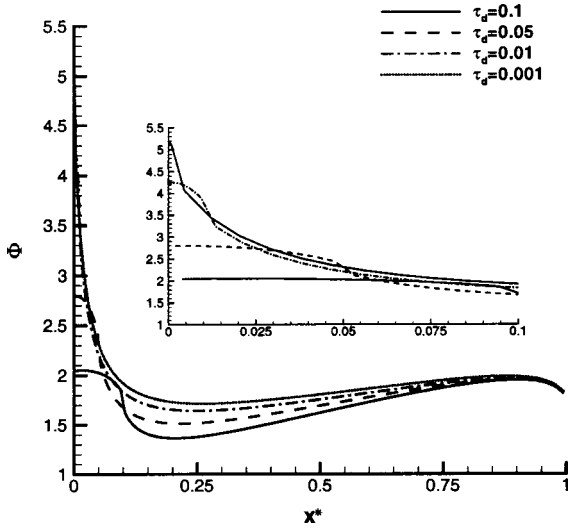

Fig. 11 Spatial variation of temperature difference between BTE and Fourier solutions, along $y^*=0.045$, for steady heat source and specular boundaries at $y^*=d/L$ for $\tau_L=5.58$

In the hot spot, the BTE predicts higher temperatures at all times since the BTE has an effective thermal conductivity that is lower than for the Fourier equation. However, outside the hot spot, BTE predictions may be lower than those produced by the Fourier equation, especially at small t^*. This is because the faster response of the Fourier equation transports heat into the channel region more quickly. For higher values of t^*, the Fourier equation may already reach steady state while the BTE is still evolving, resulting in the positive temperature differences for $t^*>0.1$ in Fig. 9. Higher values of τ_L result in smaller temperature differences between the BTE and Fourier computations; for $\tau_L\rightarrow\infty$ both equations are expected to yield the same answer [5,32]. Figure 11 shows the predicted temperature difference along $y^*=0.045$ for a steady heat source for $\tau_L=5.58$. Since the effective conductivity of the Fourier equation is higher than that implied by the BTE, the Fourier solution underpredicts the temperature over the whole domain compared to the BTE.

3.6 Heat Source Localization Effects. As the size of the hot spot becomes small compared to the phonon mean free path, the predicted temperature departs substantially from Fourier predictions because of ballistic phonon effects [4,14,17,18,21]. Phonons originating in the cold wall and entering the hot spot do not have time to gain energy from the heat source because the scattering time scale is much larger than their residence time in the hot spot ($\tau_d\tau_L<1$). To demonstrate this heat source localization effect, both steady as well as transient simulations are performed. The boundary condition at $y^*=d/L$ is made specular for the BTE so as to remove phonon boundary scattering effects. Furthermore, τ_L is held at 5.58 to keep the channel fairly thick acoustically. Thus, differences between the BTE and Fourier calculations are largely due to the ballistic nature of phonon transport in the hot spot. Figures 11–13 show the variation of Φ along the line $y^*=0.045$. The definition of Φ accounts for the reduction in the amount of heat generation as the hot spot size is decreased. Figure 11 shows the effect of varying the hot spot thicknesses τ_d in the range 0.001–0.1 for the case of a steady heat source. Substantial departures from the Fourier solution are found as $\tau_d\rightarrow 0$. Figures 12 and 13 show the same behavior for unsteady state for $\tau_d=0.1$ and 0.001, respectively. As in the previous section, the hot spot temperature is always higher using the BTE, though locations outside the hot spot may be colder due to the slower evolution of the thermal wave. For $\tau_d=0.001$, the solutions at $t^*=0.1$ and 1.0

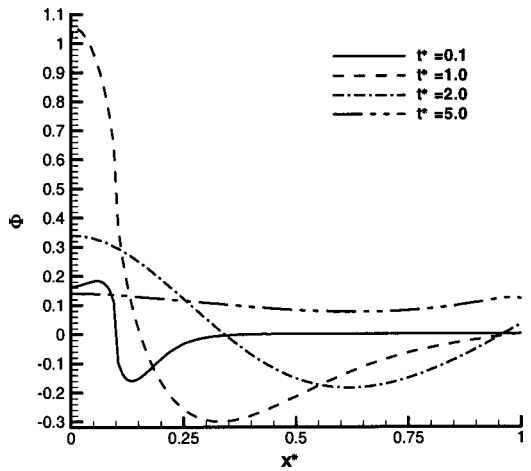

Fig. 10 Spatial variation of temperature difference between BTE and Fourier solutions, along $y^*=0.045$, with time for $\tau_q=1.0$, $\tau_d=0.1$, and $\tau_L=5.58$

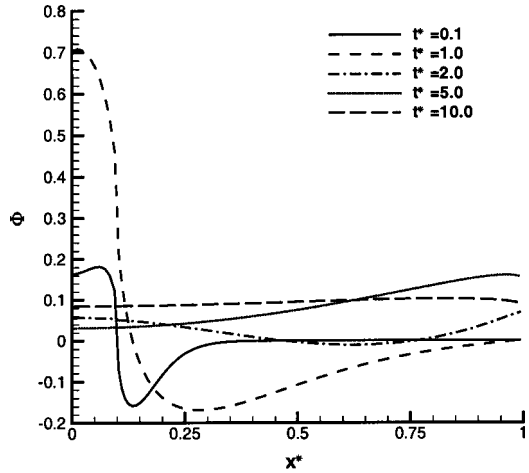

Fig. 12 Spatial variation of temperature difference between BTE and Fourier solutions, along $y^*=0.045$, with specular boundaries at $y^*=d/L$ for $\tau_L=5.58$, $\tau_d=0.1$, and $\tau_q=1.0$

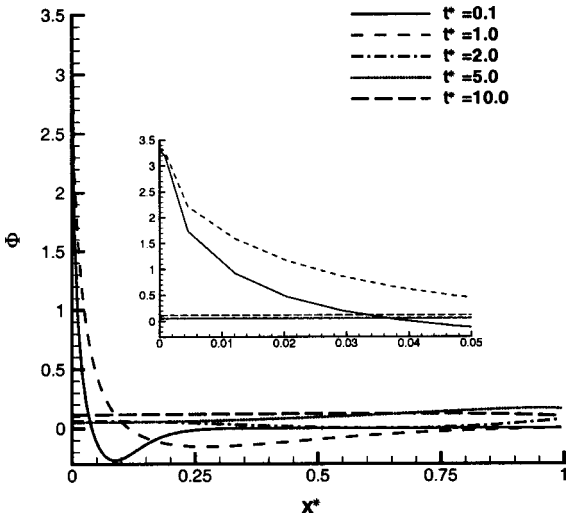

Fig. 13 Spatial variation of temperature difference between BTE and Fourier solutions, along $y^*=0.045$, with specular boundaries at $y^*=d/L$ for $\tau_L=5.58$, $\tau_d=0.001$, and $\tau_q=1.0$

are nearly identical in the hot spot. This is because $\tau_q \gg \tau_d$, and a quasi-equilibrium situation occurs in the hot spot as the heat generation balances the rate of heat removal.

4 Conclusions

In this study, the problem of a small hot spot is studied by solving the two-dimensional transient phonon BTE in the relaxation time approximation using a finite volume method. The interaction of competing time scales in determining the maximum hot spot temperature and the response time have been analyzed. Significant differences between BTE and Fourier solutions have been demonstrated both in the hot spot temperature and the response time.

The formulation in this paper has neglected phonon dispersion, and has represented all phonon polarizations by a single BTE with a constant velocity. Introduction of phonon dispersion, either through approximate two-fluid models [19,20] or through a more faithful representation of dispersion curves and phonon polarizations, is necessary to delineate the unsteady response more precisely. Phonon confinement effects on dispersion relations [33] must be considered for emerging nanoscale devices.

Acknowledgments

The support of NSF Grant CTS 0103082 is gratefully acknowledged.

Nomenclature

C = specific heat per unit volume
$D(w)$ = phonon density of states
d = width of hot spot in the x-direction
f_w = phonon distribution function
f_w^0 = equilibrium (Bose-Einstein) phonon distribution function
$\hbar$ = reduced Planck constant, 1.054×10^{-34} Js
$\hat{i}, \hat{j}, \hat{k}$ = unit vectors in the coordinate directions
I = phonon intensity
I^0 = angular average of phonon intensity
I^* = nondimensionalized phonon intensity
I^{0*} = nondimensionalized angular averaged phonon intensity
I_w = phonon boundary intensity corresponding to T_w
I_b = boundary intensity
k_B = Boltzmann constant, 1.38×10^{-23} J/K
k = thermal conductivity
l = phonon mean free path
L = length of domain in x-direction
$\hat{n}$ = normal direction to the boundaries
N_θ, N_ϕ = number of polar and azimuthal divisions in octant
q = magnitude of heat pulse
q''' = volumetric heat source
q_w = magnitude of heat pulse on frequency basis
$\vec{q}$ = heat flux vector
$\hat{s}$ = ray direction
t = time
t^* = nondimensionalized time
T = temperature
T_w = wall temperature at $x=L$
T_{BTE} = temperature computed using BTE
T_F = temperature computed using Fourier conduction equation
v = phonon velocity
$\vec{v}$ = phonon velocity vector
w = phonon frequency
w_D = cut off frequency
x, y, z = Cartesian coordinates
x^*, y^*, z^* = nondimensionalized coordinates
Ω = solid angle
Δt = time step
Δt^* = nondimensionalized time step
ϕ = Azimuthal angle
Φ = dimensionless temperature difference between BTE and Fourier calculations, $(T_{\mathrm{BTE}}-T_F)/(\pi q d/(4\sigma v T_w^4))$
Ψ_b = acoustic conductance for parallel black plates
σ = Stefan-Boltzmann constant for phonons
τ_d = nondimensionalized width of hot spot
τ_L = acoustic thickness of the medium
$\tau_{L,\mathrm{eq}}$ = equivalent acoustic thickness of the medium
τ_q = nondimensionalized heat pulse duration
τ_s = phonon relaxation time
$\tau_{s,w}$ = frequency dependent relaxation time
θ = polar angle
θ_D = Debye temperature
Θ = dimensionless temperature, $(T^4-T_w^4)/(\pi q L/(\sigma v))$

References

[1] Flik, M. I., Choi, B. I., and Goodson, K. E., 1992, "Heat Transfer Regimes in Microstructures," ASME Journal of Heat Transfer, **114**, pp. 666–674.
[2] Majumdar, A., 1998, "Microscale Energy Transport in Solids," *Microscale Energy Transport*, C. L. Tien et al., eds., Taylor & Francis, Chap. 1.
[3] Chen, G., 1998, "Phonon Wave Effects on Heat Conduction in Thin Films," *AIAA/ASME Joint Thermophysics and Heat Transfer Conference*, ASME, New York, **3**, pp. 205–213.
[4] Chen, G., 2000, "Particularities of Heat Conduction in Nanostructures," J. Nanopart. Res., **2**, pp. 199–204.
[5] Majumdar, A., 1993, "Microscale Heat Conduction in Dielectric Thin Films," ASME Journal of Heat Transfer, **115**, pp. 7–16.
[6] Kittel, C., 1996, *Introduction to Solid State Physics*, seventh edition, John Wiley & Sons, Chaps. 4,5.
[7] Ashcroft, N. W., and Mermin, N. D., 1976, *Solid State Physics*, Saunders College Publishing, Chaps. 22,23.
[8] Ju, Y. S., 1999, "Microscale Heat Conduction in Integrated Circuits and Their Constituent Films," Ph.D. thesis, Stanford University, Stanford, CA.
[9] Mahan, G. D., and Claro, F., 1988, "Nonlocal Theory of Thermal Conductivity," Phys. Rev. B, **38**(3), pp. 1963–1969.
[10] Claro, F., and Mahan, G. D., 1989, "Transient Heat Transport in Solids," J. Appl. Phys., **66**(9), pp. 4213–4217.
[11] Chen, G., 1996, "Nonlocal and Nonequilibrium Heat Conduction in the Vicinity of Nanoparticles," ASME Journal of Heat Transfer, **118**, pp. 539–545.
[12] Qiu, T. Q., and Tien, C. L., 1993, "Heat Transfer Mechanisms During Short-Pulse Laser Heating of Metals," ASME Journal of Heat Transfer, **115**, pp. 835–841.
[13] Qiu, T. Q., and Tien, C. L., 1994, "Femtosecond Laser Heating of Multi-Layer Metals: 1—Analysis," Int. J. Heat Mass Transfer, **37**(17), pp. 2789–2797.
[14] Sverdrup, P. G., Ju, Y. S., and Goodson, K. E., 1999, "Impact of Heat Source

Localization on Conduction Cooling of Silicon-On-Insulator Devices,'' *Proceedings of International Conference on Modeling and Simulation of Microsystems, Semiconductors, Sensors and Actuators*, Integrated Syst. Eng., Intellisense Corp., pp. 399–402.
[15] Sverdrup, P. G., Banerjee, K., Dai, C., Shih, W., Dutton, R. W., and Goodson, K. E., 2000, ''Sub-Continuum Thermal Simulations of Deep Sub-Micron Devices Under ESD Conditions,'' *International Conference on Simulation Semiconductor Processes and Devices*, IEEE Electron Devices Society, pp. 54–57.
[16] Amerasekera, A., and Duvvury, C., 1995, *ESD in Silicon Integrated Circuits*, John Wiley & Sons.
[17] Sverdrup, P. G., 2000, ''Simulation and Thermometry of Sub-Continuum Heat Transport in Semiconductor Devices,'' Ph.D. thesis, Stanford University, Stanford, CA.
[18] Sverdrup, P. G., Ju, Y. S., and Goodson, K. E., 2001, ''Sub-Continuum Simulations of Heat Conduction in Silicon-on-Insulator Transistors,'' ASME Journal of Heat Transfer, **123**, pp. 130–137.
[19] Armstrong, B. H., 1981, ''Two-Fluid Theory of Thermal Conductivity of Dielectric Crystals,'' Phys. Rev. B, **23**(2), pp. 883–899.
[20] Armstrong, B. H., 1985, ''N processes, the relaxation-time approximation, and lattice thermal conductivity,'' Phys. Rev. B, **32**(6), pp. 3381–3390.
[21] Sverdrup, P. G., Sinha, S., Asheghi, M., Uma, S., and Goodson, K. E., 2001, ''Measurement of Ballistic Phonon Conduction Near Hotspots in Silicon,'' Appl. Phys. Lett., **78**(21), pp. 3331–3333.
[22] Majumdar, A., Fushinobu, K., and Hijikata, K., 1995, ''Effect of Gate Voltage on Hot-Electron and Hot-Phonon Interaction and Transport in a Submicrometer Transistor,'' J. Appl. Phys., **77**(12), pp. 6686–6694.
[23] Fushinobu, K., Hijikata, K., and Majumdar, A., 1995, ''Heat Generation in Sub-Micron GaAs MESFETs,'' Proceedings of International Intersociety Electronic Packaging Conference, ASME, New York, EEP-Vol. 10-2, *Advances in Electronic Packaging*, pp. 897–902.
[24] Fushinobu, K., Majumdar, A., and Hijikata, K., 1995b, ''Heat Generation and Transport in Submicron Semiconductor Devices,'' ASME Journal of Heat Transfer, **117**, pp. 25–31.
[25] Lai, J., and Majumdar, A., 1996, ''Concurrent Thermal and Electrical Modeling of Sub-Micrometer Silicon Devices,'' J. Appl. Phys., **79**(9), pp. 7353–7361.
[26] Blotekjaer, K., 1970, ''Transport Equations for Electrons in Two-Valley Semiconductors,'' IEEE Trans. Electron Devices, **ED-17**, No. 1, pp. 38–47.
[27] Patankar, S. V., 1980, *Numerical Heat Transfer and Fluid Flow*, Taylor & Francis, Chaps. 2–5.
[28] Chai, J. C., Lee, H. S., and Patankar, S. V., 1994, ''Finite Volume Method for Radiation Heat Transfer,'' J. Thermophys. Heat Transfer, **8**(3), pp. 419–425.
[29] Murthy, J. Y., and Mathur, S. R., 1998, ''Finite Volume Method for Radiative Heat Transfer Using Unstructured Meshes,'' J. Thermophys. Heat Transfer, **12**(3), pp. 313–321.
[30] Mathur, S. R., and Murthy, J. Y., 1997, ''A pressure Based Method for Unstructured Meshes,'' Numer. Heat Transfer, Part B, **31**(2), pp. 195–216.
[31] Modest, M. F., 1993, *Radiative Heat Transfer*, McGraw-Hill, Chap. 12.
[32] Joshi, A. A., and Majumdar, A., 1993, ''Transient Ballistic and Diffusive Phonon Transport in Thin Films,'' J. Appl. Phys., **74**(1), pp. 31–49.
[33] Balandin, A., and Wang, K. L., 1998, ''Significant Decrease in the Lattice Thermal Conductivity Due to Phonon Confinement in a Free-Standing Semiconductor Quantum Well,'' Phys. Rev. B, **58**(3), pp. 1544–1549.

An Improved Computational Procedure for Sub-Micron Heat Conduction

J. Y. Murthy
e-mail: jmurthy@ecn.purdue.edu
School of Mechanical Engineering,
Purdue University,
West Lafayette, IN 47907

S. R. Mathur
e-mail: sm@fluent.com
Fluent Inc.,
10 Cavendish Court,
Lebanon, NH 03766

Popular numerical techniques for solving the Boltzmann transport equation (BTE) for sub-micron thermal conduction include the discrete ordinates method and the finite volume method. However, the finite wave speed associated with the BTE can cause large errors in the prediction of the equivalent temperature unless fine angular discretizations are used, particularly at low acoustic thicknesses. In this paper, we combine a ray-tracing technique with the finite volume method to substantially improve the predictive accuracy of the finite volume method. The phonon intensity is decomposed into ballistic and in-scattering components. The former is solved using a ray tracing scheme, accounting for finite wave speed; the latter is solved using an unstructured finite volume method. Comparisons between this new technique and traditional finite volume formulations are presented for a range of acoustic thicknesses, and substantial improvement is demonstrated.
[DOI: 10.1115/1.1603775]

Keywords: Conduction, Heat Transfer, Microscale, Nanoscale, Numerical Methods

Introduction

In recent years there has been a great deal of interest in understanding the physics of sub-micron heat conduction because of its importance to microelectronics, ultrafast laser processing, microscale energy systems and to a host of emerging technologies. When the domain length scale is of the order of the mean free path, but greater than the phonon wavelength, conduction in semiconductors and dielectrics can be modeled using the phonon Boltzmann transport equation (BTE) in the relaxation time approximation [1,2]. An analogy between the phonon BTE and the radiative transfer equation (RTE) in thermal radiation has long been recognized [1]. This similarity has been exploited by researchers in developing numerical methods for solving the BTE. Kumar et al. [3] developed a differential discrete ordinates method whereby the angular domain was discretized using techniques similar to the conventional discrete ordinates method [4]. Majumdar and coworkers [1,2] also used a discrete ordinates method combined with an explicit first-order time-stepping scheme. Sverdrup et al. [5] developed a similar methodology to study the problem of electro-static discharge (ESD) in microelectronics. Narumanchi et al. [6] computed unsteady sub-micron conduction in the presence of a time-dependent hot spot using a finite volume method in conjunction with an implicit time-stepping scheme.

The finite volume and discrete ordinates methods originate in the thermal radiation and neutron transport literature and employ a discretization of the angular dimension as well as spatial dimensions. The radiative transfer equation (RTE) is solved in each angular direction over the spatial domain. Inadequate spatial resolution leads to the phenomenon of *false scattering* whereby spatial smearing of the energy distribution is caused purely by numerical diffusion; this type of error has been extensively investigated in the thermal radiation literature [7]. In addition to spatial error, angular discretization leads to another type of error, the *ray effect*. Since the angular space is divided into finite control angles, small scale spatial variations in intensity are in effect averaged over the control angle. This error is especially noticeable at low optical thicknesses in problems with variations in boundary intensity. It may be alleviated by adequate resolution of the angular domain. Coelho [8] has shown how angular and spatial discretization errors tend to compensate each other, so that coarse discretizations of both sometimes yield more accurate solutions than fine discretizations of either space or angle individually.

Our interest is in the solution of the unsteady BTE. In the ballistic limit (zero acoustic thickness), the BTE in any direction is a linear wave equation. Under the relaxation time approximation, phonon scattering leads to the addition of an isotropic scattering term. There have been a variety of higher-order methods developed to address the spatial and time resolution of the linear wave equation for both structured and unstructured meshes [9]. However, special issues with respect to accuracy arise for the unsteady BTE. In addition to inadequate spatial resolution of boundary conditions, the ray effect results in additional errors because of finite wave speed. The phonon travel time from the boundary to the interior is inadequately resolved for coarse angular discretizations. Thus, temperature predictions, which represent angular averages of the phonon intensity, are found to exhibit nonphysical spatial wiggles [10]. This occurs even when individual directional intensities are accurately computed.

Recently, a number of studies have appeared in the thermal radiation literature which address the ray effect for the steady RTE using the modified discrete ordinates method (MDOM) [11,12,13,8]. The idea, originally suggested by Olfe [14] and Modest [15], was applied to two-dimensional rectangular enclosures containing absorbing, emitting and isotropically scattering media by Ramankutty and Crosbie [11]. Here, the radiative intensity is divided into two parts: one which represents the transmission and out-scattering of boundary intensity, and another which redistributes the transmitted energy through in-scattering. An extension to include the effects of sharp changes in temperature within the volume has been published in [8]. The intensity component associated with the boundary contribution is solved by an analytical angular integration of the boundary emission; the other component is typically solved using the discrete ordinates method or a diffuse approximation is made. Substantial improvements to accuracy have been reported over conventional discrete ordinates. Chen [16] employed a similar idea in developing ballistic-diffusive heat conduction approximations to the BTE. However, the in-scattering component of intensity was approximated using a diffusion approximation to facilitate fast turnaround. In this paper, we extend the MDOM idea to the solution of the unsteady BTE

Contributed by the Heat Transfer Division for publication in the JOURNAL OF HEAT TRANSFER. Manuscript received by the Heat Transfer Division June 26, 2002; revision received June 4, 2003. Associate Editor: G. Chen.

with finite wave speed. We consider two different decompositions of the phonon intensity and integrate the scheme with a finite volume method. We present comparisons of accuracy and performance for the two decompositions, and also compare the performance of the new scheme with results from a conventional finite volume scheme.

Governing Equations

For clarity, we consider the gray phonon BTE under the relaxation time approximation [2]

$$\frac{1}{v}\frac{\partial I}{\partial t}+\nabla\cdot(\mathbf{s}I)=\frac{I^0-I}{v\tau} \tag{1}$$

Here $I(\mathbf{r},\mathbf{s},t)$ is the phonon intensity, v is the phonon velocity, and I^0 is given by

$$I^0=\frac{1}{4\pi}\int_{4\pi} I d\Omega \tag{2}$$

where Ω denotes solid angle. The direction vector $\mathbf{s}$ is given by

$$\mathbf{s}=(\sin\theta\sin\phi\mathbf{i}+\sin\theta\cos\phi\mathbf{j}+\cos\theta\,\mathbf{k}) \tag{3}$$

The relaxation time τ is assumed constant. We also assume $T/\theta_D\ll 1$ for simplicity, though this is not essential to the development. We may define an equivalent temperature $T(\mathbf{r},t)$ as a measure of the phonon energy

$$T(\mathbf{r},t)=(\pi I_0(\mathbf{r},t)/\sigma)^{1/4} \tag{4}$$

The Stefan-Boltzmann constant for phonons is taken to be [1]

$$\sigma=\frac{\pi^2 k_B^4}{40\hbar^3 v^2}$$

Though the formulation has been done using the intensity form of the BTE, the numerical issues addressed in this paper apply equally to the energy form such as that used in [17]. The relationship between I_0 and T adopted in Eq. (4), is valid only for low temperatures. However, it does not change the numerical issues underlying the solution of the BTE or the remedies presented here since the recovery of temperature is only a post-processing step.

Initial and Boundary Conditions

The initial condition assumes the initial equilibrium temperature T_i to be given everywhere and that the intensity distribution is the same in all angular directions:

$$I(\mathbf{r},\mathbf{s},t\leq 0)=I_i(\mathbf{r})=\frac{\sigma T_i^4(\mathbf{r})}{\pi}$$

Though a variety of boundary conditions may be considered, in this paper, we consider two conditions which we will use in our test cases.

Thermalizing Boundaries. Here the intensity of outgoing phonons from the boundary is determined from a given temperature T_w. Assuming the boundaries to be completely absorbing and diffusely emitting, the outgoing phonon intensity for $t\geq 0$ is given by

$$I_w(\mathbf{r}_w,\mathbf{s},t)=\frac{\sigma T_w^4(\mathbf{r}_w,t)}{\pi} \tag{6}$$

for all directions $\mathbf{s}\cdot\mathbf{n}<0$. Here $\mathbf{n}$ is the boundary normal pointing out of the domain.

Symmetry Boundaries. Symmetry boundaries are assumed to be specularly reflecting. Thus, at a boundary with an outward-pointing normal $\mathbf{n}$, the intensity in the outgoing direction $\mathbf{s}$ is given by

$$I(\mathbf{r}_w,\mathbf{s},t)=I(\mathbf{r}_w,\mathbf{s}_r,t) \tag{7}$$

where

$$\mathbf{s}_\mathbf{r}=\mathbf{s}-2(\mathbf{s}\cdot\mathbf{n})\mathbf{n}$$

Finite Volume Method

A detailed description of the basic method is available in our previously published papers [18,10]; we summarize it here for completeness. The spatial domain is discretized into arbitrary convex polyhedral control volumes. The angular space 4π at any spatial location is discretized into discrete non-overlapping control angles Ω_i, the centroids of which are denoted by the direction vector $\mathbf{s_i}$, and the polar and azimuthal angles θ_i and ϕ_i. Each octant is discretized into $N_\theta\times N_\phi$ solid angles. The angles θ and ϕ are measured with respect to the global Cartesian system (x, y, z). The angular discretization is uniform; the control angle extents are given by $\Delta\theta$ and $\Delta\phi$. For each discrete direction i Eq. (1) is integrated over the volume $\Delta\mathcal{V}$, the solid angle Ω_i and the time step Δt to yield a balance of phonon energy in the direction i. The spatial derivatives are discretized using the QUICK scheme [19] with a min-mod limiter. Time derivatives are a second-order backward Euler scheme. A few calculations have been done using first-order discretizations of space and time for comparison. The intensity equations result in a set of coupled nominally linear algebraic equations at each discrete time instant. Different directions are coupled together through the I_0 term. At any given time step, the intensities in all directions are solved sequentially and iteratively, with an algebraic multigrid scheme to solve each nominally linear set.

Modified Finite Volume Method

The phonon intensity I is decomposed into two parts:

$$I(\mathbf{r},\mathbf{s},t)=I_1(\mathbf{r},\mathbf{s},t)+I_2(\mathbf{r},\mathbf{s},t)$$

The intent is to have the I_2 problem address the transport of boundary intensity, while the I_1 problem addresses in-scattering. Since the I_1 intensity is expected to vary relatively benignly with angle, a conventional finite volume scheme is sufficient to solve it. The I_2 problem is solved using ray-tracing to accurately capture angular intensity variation. Two different decompositions are evaluated in this paper. These are described below.

Decomposition A. Here I_2 is chosen to satisfy

$$\frac{1}{v}\frac{\partial I_2}{\partial t}+\nabla\cdot(\mathbf{s}I_2)=0 \tag{8}$$

with boundary conditions

$$I_2(\mathbf{r}_w,\mathbf{s},t)=I_w(\mathbf{r}_w,t)-I_i(\mathbf{r}_w) \tag{9}$$

Here, $\mathbf{s}\cdot\mathbf{n}<0$, where $\mathbf{n}$ is the outward-pointing wall normal. I_2 satisfies the initial condition

$$I_2(\mathbf{r},\mathbf{s},t\leq 0)=0 \tag{10}$$

The solution to the I_2 problem is given by

$$I_2(\mathbf{r},\mathbf{s},t)=I_{w2}(\mathbf{r}-(s-s_w)\mathbf{s},t-(s-s_w)/v) \tag{11}$$

where

$$I_{w2}(\mathbf{r},t>0)=I_w(\mathbf{r},t)-I_i(\mathbf{r})$$

$$I_{w2}(\mathbf{r},t\leq 0)=0$$

and $(s-s_w)$ is the ray length from the location $\mathbf{r}$ to the boundary. Eq. 11 is essentially the solution to a unsteady linear advection equation with modified initial and boundary conditions given by Eqs. 9 and 10. The intensity I_{w2} at the intersection of the ray and the boundary is advected at a finite speed v into the domain in the direction $\mathbf{s}$. Therefore, the intensity $I_2(\mathbf{r},\mathbf{s},t)$ is the value at the upwind boundary evaluated at an appropriately retarded time. When $t-(s-s_w)/v\leq 0$, the initial intensity of $I_{w2}=0$ at the upwind boundary applies.

If I_2 satisfies Eq. 8 and the stated initial and boundary conditions, the remaining intensity I_1 must satisfy:

$$\frac{1}{v}\frac{\partial I_1}{\partial t}+\nabla\cdot(\mathbf{s}I_1)=\frac{I_1^0-I_1}{v\tau}+\frac{I_2^0-I_2}{v\tau} \tag{12}$$

Here, I_1^0 and I_2^0 are defined analogously to Eq. 2. I_1 must satisfy the following boundary and initial conditions

$$I_1(\mathbf{r}_w,\mathbf{s},t>0)=I_i(\mathbf{r}_w)$$

$$I_1(\mathbf{r},\mathbf{s},t\leqslant 0)=I_i(\mathbf{r})$$

Decomposition B. Here the idea is to include the outscattering in the I_2 problem in addition to ballistic transport. I_2 is chosen to satisfy

$$\frac{1}{v}\frac{\partial I_2}{\partial t}+\nabla\cdot(\mathbf{s}I_2)=-\frac{I_2}{v\tau} \tag{13}$$

The boundary and initial conditions are chosen to be the same as for decomposition A.

The solution to the I_2 problem is given by

$$I_2(\mathbf{r},\mathbf{s},t)=I_{w2}(\mathbf{r}-(s-s_w)\mathbf{s},t-(s-s_w)/v)\exp\left(-\int_{s_w}^{s}\frac{ds}{v\tau}\right) \tag{14}$$

where

$$I_{w2}(\mathbf{r},t>0)=I_w(\mathbf{r},t)-I_i(\mathbf{r})$$

$$I_{w2}(\mathbf{r},t\leqslant 0)=0$$

The intensity I_1 must satisfy

$$\frac{1}{v}\frac{\partial I_1}{\partial t}+\nabla\cdot(\mathbf{s}I_1)=\frac{I_1^0-I_1}{v\tau}+\frac{I_2^0}{v\tau} \tag{15}$$

I_1 satisfies the same boundary and initial conditions as in decomposition A.

Numerical Method

The finite volume method described above is used to solve the I_1 problem. As before, the spatial domain is discretized into unstructured convex polyhedra, and the angular domain into $N_\theta \times N_\phi$ control angles per octant. The I_1 equation for either decomposition is integrated over the control volume and control angle in the manner described in Mathur and Murthy [10]. In addition, each control angle is subdivided into $n_\theta \times n_\phi$ pixels, associated with a pixel solid angle $\delta\Omega_{in}$; here i is the index of the control angle and n is the pixel index. The I_2 problem is solved assuming a ray direction associated with each pixel center, and using either Eq. 11 or Eq. 14. For decomposition A, the source term due to I_2 in the I_1 problem, $-I_2/v\tau$, must be evaluated (see Eq. 12). In keeping with the finite volume formulation, the integral of I_2 term over the control volume and control angle is written as

$$\frac{1}{v\tau}\int_{\Delta\mathcal{V}}\int_{\Omega_i} I_2 d\Omega d\mathcal{V}=\frac{1}{v\tau}\sum_n I_{2,in}\delta\Omega_{in}\Delta\mathcal{V} \tag{16}$$

Here, $I_{2,in}$ denotes the I_2 intensity associated with the nth pixel in the control angle i. Both Ω_i and $\delta\Omega_{in}$ are computed analytically, as explained in Mathur and Murthy [18]. For both decompositions, the integral of I_2 over 4π is required to find I_2^0. Decomposition B only requires this total integral; the value for each individual control angle is not required. The integral over 4π found using

$$\frac{1}{v\tau}\int_{\Delta\mathcal{V}}\int_{4\pi} I_2 d\Omega d\mathcal{V}=\frac{1}{v\tau}\sum_i\sum_n I_{2,in}\delta\Omega_{in}\Delta\mathcal{V} \tag{17}$$

Discussion

The I_2 problem is solved by ray tracing. Ramankutty and Crosbie [11] converted the integration in Eq. 17 into a surface area integral for their steady RTE computation and computed it analytically. For the unsteady BTE, numerical (rather than analytical) integration of the boundary contribution is necessary because different parts of the boundary contribute different intensities at different times; numerical integration of this type is also necessary for complex thermal boundary conditions and complex geometries. By using pixelation, it is possible to solve the I_2 problem to far greater accuracy than necessary for the I_1 problem; nesting the ray directions inside the control angles ensures conservative transfer of phonon energy from the I_2 problem to the I_1 problem. The formulation ensures that the ballistic limit is captured to the accuracy of the pixelation.

Both schemes require the storage of I_2^0. Decomposition A requires the evaluation in Eq. 16 for each control angle i. This may be done on the fly each iteration if storing I_2 over all control angles is onerous. In our implementation, we store I_2, and compute it only once per time step. This effectively doubles storage requirements over the original finite volume scheme, but reduces the computational time substantially. Decomposition B does not require this extra storage.

Decomposition B requires the computation of attenuation, as in Eq. 14. When $v\tau$ is constant over space, this computation is straightforward and involves minimal extra cost over decomposition A. However, when $v\tau$ varies spatially, the ray tracing scheme must account for this variation. In general τ is a function of temperature, which varies from cell to cell. Thus the ray tracer must find the intersection of each ray with the background mesh. For realistic problems this operation would account for most of the computational cost. Both decompositions must of course account for the existence of blockages and obstacles during ray tracing.

Results

For clarity, we consider a simple rectangular computational domain of length L bounded by walls at the left and right boundaries and symmetry conditions on the top and bottom, leading to a one-dimensional problem. Thus, Eq. (6) is used to specify boundary intensities. The top and bottom boundary conditions are described by Eq. (7), and are specularly reflecting. The initial equilibrium temperature is assumed known at T_C, and is spatially constant. At $t=0$, the temperature associated with outgoing phonons at the left wall is raised to T_H. The acoustic thickness of the domain, $\beta=L/v\tau$, is varied to span the range from purely ballistic to acoustically thick. The objective is to compute the temperature as a function of time and compare the performance of the new scheme with that of the conventional finite volume scheme. The baseline spatial mesh consists of 100 equal cells in the x-direction and is one cell thick. The baseline time step is $\Delta t^*=10^{-3}$. The QUICK scheme with a min-mod limiter and the second-order backward Euler implicit scheme are used for the I_1 problem for both decompositions.

The exact solution to the problem is easily determined for the ballistic problem ($L/v\tau=0$). We define G as

$$G=\frac{1}{4}\int_{4\pi} I d\Omega$$

The solution of $t^*\leqslant 1$ is given by

$$G(x^*,t^*)=\begin{cases} G_C(1-\xi)+G_H\xi & \text{if } x^*\leqslant t^* \\ G_C & \text{otherwise}\end{cases}$$

where $\xi=(1-x^*/t^*)/2$, $x^*=x/L$, $G_H=\sigma T_H^4$ and $G_C=\sigma T_C^4$. The equivalent temperature is $T=(G/\sigma)^{1/4}$ and its nondimensionalized value is $T^*\equiv(T-T_C)/(T_H-T_C)$.

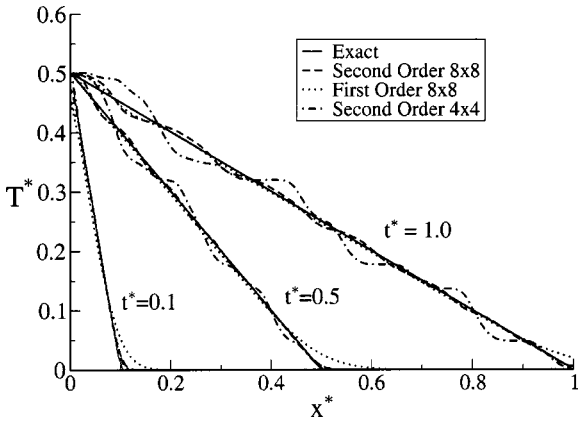

Fig. 1 Finite volume scheme: temperature variation at three different time instants for $\beta=0$

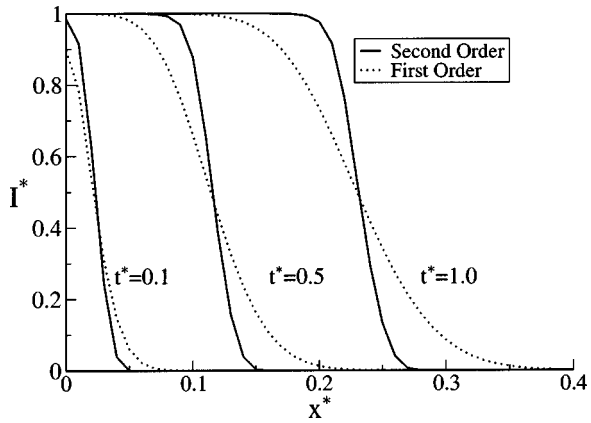

Fig. 2 Finite volume scheme: intensity variation at three different time instants in the direction $s=0.231i+0.189j+0.952k$ for $\beta=0$

Behavior of Conventional Finite Volume Scheme. The finite volume scheme is used to compute the temperature field using two different schemes (i) a first-order step scheme for spatial differencing, and a first-order fully-implicit scheme for time marching, and (ii) a second-order QUICK scheme with a min-mod limiter for spatial differencing with a second-order backward Euler implicit scheme for time marching. The baseline spatial mesh and time step are used for both cases. An 8×8 angular discretization of the octant is used unless otherwise stated. A few calculations done with a 4×4 angular discretization per octant are shown in Fig. 1 and Table 1.

T^* is presented as a function of the dimensionless time $t^*=tv/L$ for the conventional finite volume scheme in Fig. 1 using the first- and second-order schemes. We see that spurious wiggles in the temperature are computed, and are especially evident for the 4×4 angular discretization at $t^*=1.0$. R.m.s errors with respect to the exact solution are shown in Table 1. The r.m.s. error is defined as:

$$\frac{\left(\frac{1}{N}\sum_{N}(T_e^*-T_c^*)^2\right)^{1/2}}{(T_{e,\max}^*-T_{e,\min}^*)}$$

Here, N is the number of cells, T_e^* is the exact solution and T_c^* is the computed solution. The error is scaled to the range of T_e^* at the time instant of interest. Interestingly, the second-order scheme performs worse than the first-order scheme for $t^*=1.0$, with larger excursions in temperature. However, the larger error in the second-order solution should not be attributed to the spatial oscillations sometimes encountered using higher-order schemes. This is borne out by Fig. 2 which shows the dimensionless intensity in the ray direction $\mathbf{s}=0.231\mathbf{i}+0.189\mathbf{j}+0.952\mathbf{k}$ at $t^*=0.1$, 0.5 and 1.0 for the two schemes. The first-order scheme diffuses the intensity profile far more than the second-order scheme, as expected; both schemes show bounded results with no overshoots and undershoots. Despite the boundedness of individual intensities, their angular average, embodied in the temperature, shows significant overshoots and undershoots about the exact solution. This is a direct result of the erroneous estimation of travel time in the finite volume scheme due to the finite angular discretization. The error can be mitigated if finer control angles are used, but at a higher cost. Resolving the spatial or temporal domain further will not solve this problem. Indeed, the loss of error cancellation mechanisms can sometimes lead to worse answers, as seen in Fig. 1 and Table 1. Better results are obtained for higher acoustic thicknesses, as shown in Fig. 3, but some artifacts resulting from this type of error are still visible even at $\beta=1.0$, regardless of the order of spatial and temporal discretization.

Modified Finite Volume Method: Decomposition A. Results for decomposition A for the ballistic problem are shown in Fig. 4 at three different time instants. For 4×4 angular discretization of the octant and a 20×20 pixelation of each control angle, the computed results match the exact solution very closely, and do not exhibit any discernible wiggles. The I_2 problem yields the exact result for any given direction, and the angular average can be made accurate if sufficient pixelation is used. The I_1 solution is zero everywhere for this decomposition and the accuracy of the finite volume method is therefore not an issue. The results produced by this modified finite volume scheme are substantially more accurate than the conventional finite volume scheme, by an order of magnitude at $t^*=1.0$. Also the error does not grow with time.

Next we examine the behavior of the scheme for non-zero acoustic thicknesses. Figures 5 and 6 show plots of T^* versus x^* for $\beta=0.1$ and $\beta=10$ for four different angular discretizations: 8×8 with 20×20 pixelation, 8×8 with 5×5 pixelation, 4×4 with 20×20 pixelation, and 4×4 with 5×5 pixelation. The computed results match each other quite well. For $\beta=10$, decomposition A is found to produce small wiggles in temperature near $T^*=0$. These are not easily visible on the scale of Fig. 6; details are shown in the inset. In this thick limit, these wiggles decrease in amplitude as the control angle discretization becomes finer, and are relatively insensitive to the pixelation. The negative tempera-

Table 1 Percentage R.M.S. error with respect to exact solution for $\beta=0$ for conventional and modified finite volume schemes. Modified schemes employ a 4×4 angular discretization with 20×20 pixelation

Time	Finite Volume First Order 4×4	Finite Volume Second Order 4×4	Finite Volume First Order 8×8	Finite Volume Second Order 8×8	Decompositions A & B
0.1	1.859%	0.540%	1.940%	0.448%	0.193%
0.5	1.655%	2.167%	1.312%	0.646%	0.108%
1.0	2.273%	3.564%	0.982%	1.179%	0.086%

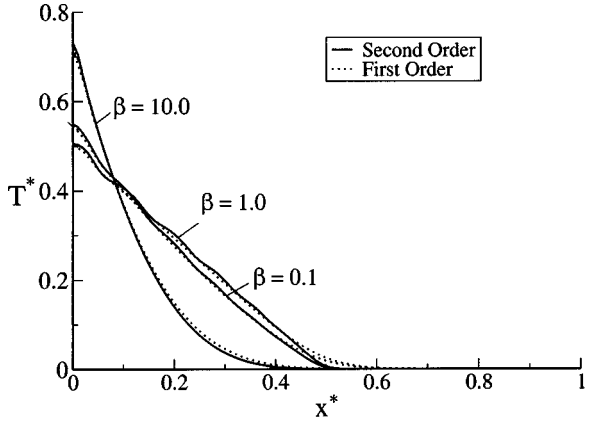

Fig. 3 Finite volume scheme: temperature variation for different acoustic thicknesses at $t^*=0.5$

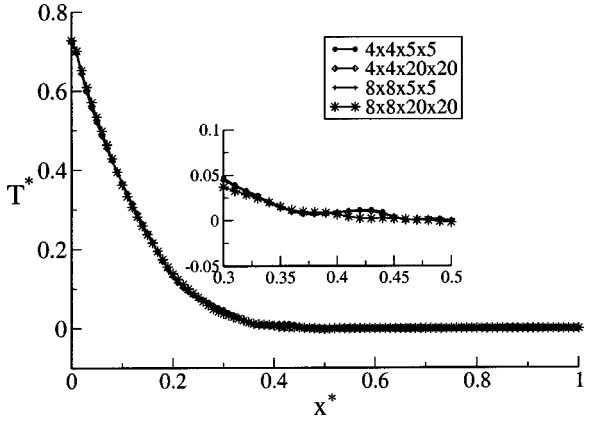

Fig. 6 Decomposition A: temperature variation for $\beta=10.0$ at $t^*=0.5$ for various control angles and pixelations

tures are caused by the I_2 source term in Eq. 12. The I_1 source term is guaranteed not to produce negative I_1 values if the source discretization procedures outlined in [18] are used. However, the I_2 source term can be negative, and can result in values of I_1 which are out of range. Disparities in the angular resolution of the I_1 and I_2 problems can cause the computed total I to be unphysical. This can result in the average total intensity I^0 falling outside the range of the boundary intensities, leading to negative T^*.

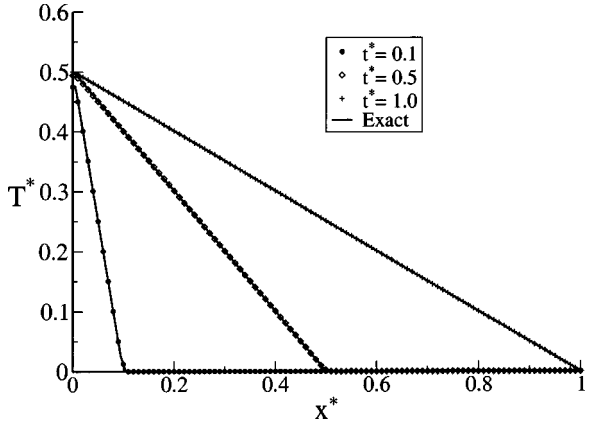

Fig. 4 Decomposition A: temperature variation for $\beta=0$ at $t^*=0.1$, 0.5 and 1.0 for $N_\theta\times N_\phi=4\times4$ and $n_\theta\times n_\phi=20\times20$

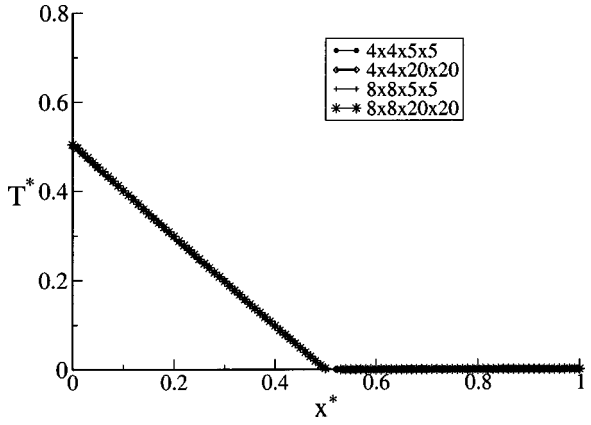

Fig. 5 Decomposition A: temperature variation for $\beta=0.1$ at $t^*=0.5$ for various control angles and pixelations

For low acoustic thicknesses ($\beta=0.1$), the accuracy of decomposition A is governed in large part by the number of ray directions used to discretize the sphere. Thus coarse angular discretizations with fine pixelation or fine angular discretizations with coarse pixelation will serve equally well. The I_1 problem contributes little to the total intensity in this limit, and hence the fineness of the control angle discretization does not matter *per se*.

For very coarse angular discretizations and pixelations, decomposition A can yield solutions that are substantially more inaccurate than any produced by the conventional finite volume scheme, as seen in Fig. 7. For low β, the coarse discretization of the sphere causes wiggles in the predicted temperature because of inadequate representation of the time lag due to the finite wave speed. For high β, coarse angular discretization leads to inaccurate solutions of the I_1 problem, and the disparate accuracies of the I_1 and I_2 problems lead to large errors in the predicted temperature. Thus, decomposition A must be used with care; it can yield more accurate solutions than the finite volume scheme as long as moderate to fine angular discretizations and pixelations are used.

Decomposition B. In the ballistic limit ($\beta=0$) decompositions A and B produce identical results. The variation of temperature with x^* at different time instants is given by Fig. 4. For low (but non-zero) acoustic thicknesses, decompositions A and B perform similarly, as seen from Fig. 8. For high β, the spurious wiggles seen using decomposition A are not seen with decomposition B. The I_2 contribution to the I_1 solution is always positive, as seen from Eq. 15, and cannot cause undershoots. Figure 9

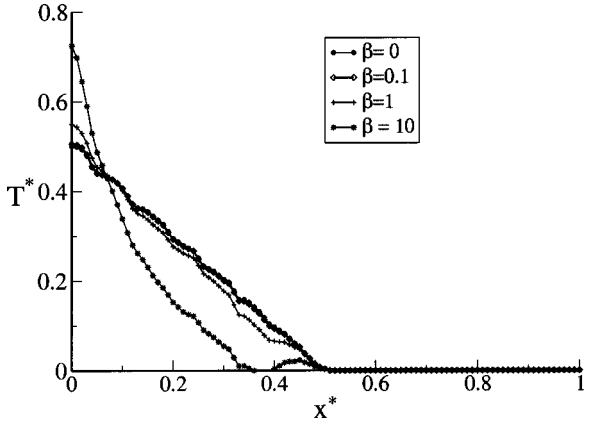

Fig. 7 Decomposition A: temperature variation for various acoustic thicknesses at $t^*=0.5$ for $N_\theta\times N_\phi=2\times2$ and $n_\theta\times n_\phi=5\times5$

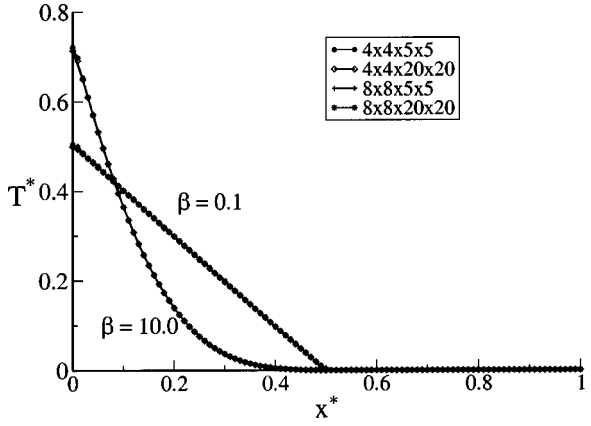

Fig. 8 Decomposition B: temperature variation for $\beta=0.1$ and 10.0 at $t^*=0.5$ for various control angles and pixelations

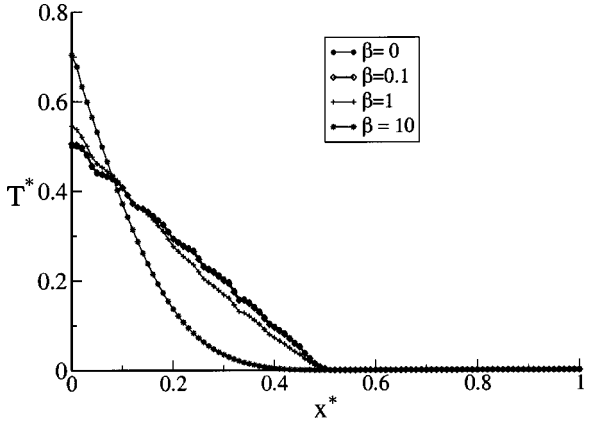

Fig. 10 Decomposition B: temperature variation for various acoustic thicknesses at $t^*=0.5$ for $N_\theta\times N_\phi=2\times2$ and $N_\theta\times n_\phi=5\times5$

shows a comparison of the conventional finite volume and the two decompositions for $\beta=10$ for an angular discretization of 8×8; the two decompositions employ a 20×20 pixelation. We see that the conventional scheme performs comparably to the modified scheme in the thick limit.

Figure 10 shows a plot of T^* versus x^* for a coarse angular discretization of 2×2 and a pixelation of 5×5. The plots are made at $t^*=0.5$ for different acoustic thicknesses. As with decomposition A, the plots for lower β exhibit wiggles resulting from an inadequate resolution of the travel time for coarse angular discretizations. However, the behavior for high β is markedly different from decomposition A. The wiggles exhibited in Fig. 7 for $\beta=10$ are absent in Fig. 10.

Timing. Table 2 shows a comparison of CPU time for the conventional finite volume method using second-order discretization and for the two different decompositions. The calculations are done for $\beta=1.0$ for the baseline mesh of 100 cells and a time step of $\Delta t^*=10^{-3}$. A laptop personal computer with an Intel Pentium 3 chip running at 800 MHz is used. The reported CPU times are for 10 time steps. The solution at each time step is assumed converged when the normalized residual for I_1 falls to 10^{-10}. For the same number of control angles, the modified finite volume method is comparable to the conventional finite volume method for coarse pixelations. Here, the extra cost of ray tracing is offset by convergence being achieved in fewer iterations per time step. Decomposition A performs better than decomposition B in terms of CPU time. For finer pixelations, both decompositions are more expensive than the conventional scheme due to ray-tracing cost, but by factors considerably smaller than $n_\theta\times n_\phi$. This is because the ray tracing is only done once per time step; the rest of the cost is the solution of the I_1 problem, which is common to all the schemes. These results suggest that a medium-grained control angle resolution with moderate-to-fine pixelation would achieve accurate results across the spectrum of acoustic thicknesses without too great a CPU penalty over the conventional finite volume method. However, more complex geometries with obstructions, spatially varying β, and other complexities in the ray tracing scheme may increase the ray tracing cost substantially.

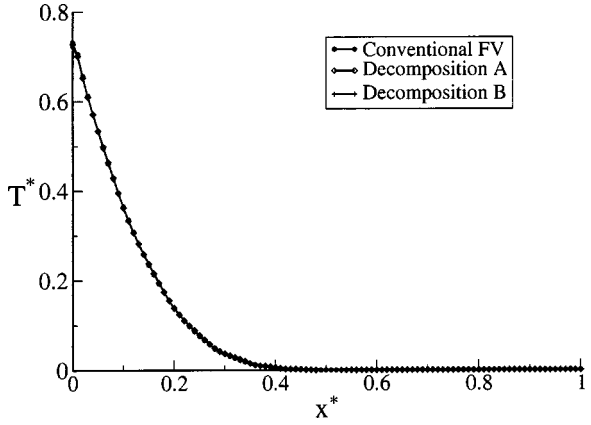

Fig. 9 Temperature variation for $\beta=10$ at $t^*=0.5$ for $N_\theta\times N_\phi=8\times8$. The modified schemes employs a pixelation of $n_\theta\times n_\phi=20\times20$

Closure

A modified finite volume method has been developed for the solution of the unsteady Boltzmann transport equation in the relaxation time approximation. The method decomposes the intensity into two components, with a ray tracing scheme to resolve the ballistic part accurately. Though decomposition B requires more complex ray tracing operations for cases when the relaxation time is spatially varying, it is found to yield more accurate solutions than decomposition A. Both decompositions produce more accurate results than the conventional finite volume scheme for low to moderate β. The computational cost of the modified method relative to the conventional one depends entirely on the complexity of the ray tracing operation. For the simple problem considered here, one time step of the modified method is generally more expensive than the conventional finite volume method for the same angular discretization for moderate to fine pixelations. However, it is difficult to obtain the same accuracy with the conventional scheme, especially for low acoustic thicknesses.

Table 2 Computational times (seconds) for the conventional and modified finite volume schemes ($n_\theta\times n_\phi$ in parentheses)

Case	Finite Volume	Decomposition A	Decomposition B
2×2	1.26	0.78 (5×5)	1.03 (5×5)
		2.79 (20×20)	5.05 (20×20)
4×4	3.42	2.3 (5×5)	3.28 (5×5)
		13.67 (20×20)	22.3 (20×20)
8×8	12.2	8.68 (5×5)	12.34 (5×5)
		53.84 (20×20)	88.13 (20×20)

Acknowledgments

We wish to acknowledge the use of Fluent Inc.'s solver FLUENT/UNS, in which the modified finite volume scheme was implemented.

Nomenclature

h = Planck constant
$\hbar$ = $h/2\pi$
I = phonon intensity
I_1, I_2, = phonon intensity components
I^0 = angular average of intensity
k_B = Boltzmann constant
L = domain length
$\mathbf{n}$ = unit normal vector
N = number of cells
N_θ, N_ϕ = polar and azimuthal control angles per octant
n_θ, n_ϕ = polar and azimuthal pixelation of control angle
$\mathbf{s}$ = ray direction vector
s = path length along $\mathbf{s}$
$\mathbf{r}$ = position vector
$\mathbf{r}_w$ = wall position vector
t = time
t^* = dimensionless time tv/L
T = temperature
T_i = initial temperature
T_H, T_C = boundary temperatures
T^* = dimensionless temperature $(T-T_C)/(T_H-T_C)$
v = phonon velocity
x = coordinate direction
x^* = dimensionless coordinate x/L
β = acoustic thickness $L/v\tau$
$\Delta\mathcal{V}$ = volume of control volume
Ω = solid angle
$\delta\Omega$ = solid angle associated with pixelation
θ = polar angle
θ_D = Debye temperature
τ = relaxation time constant
ϕ = azimuthal angle
σ = Stefan Boltzmann constant

References

[1] Majumdar, A., 1993, "Microscale Heat Conduction in Dielectric Thin Films," ASME J. Heat Transfer, **115**, pp. 7–16.
[2] Joshi, A., and Majumdar, A., 1993, "Transient Ballistic and Diffusive Phonon Heat Transport in Thin Films," J. Appl. Phys., **74**, pp. 31–39.
[3] Kumar, S., Majumdar, A., and Tien, C., 1990, "The Differential Discrete-Ordinates Method for Solutions of the Equation of Radiative Transfer," ASME J. Heat Transfer , **112**, pp. 424–429.
[4] Modest, M. F., 1993, *Radiative Heat Transfer*, Series in Mechanical Engineering, McGraw Hill, New York, NY.
[5] Sverdrup, P., Banerjee, K., Dai, K., Shih, W., Dutton, R., and Goodson, K., 2000, "Sub-Contiuum Simulations of Deep Sub-Micron Devices under ESD Conditions," *Proceedings of the International Conference on Simulation of Semiconductor Processes and Devices*, IEEE, Piscataway, NJ., pp. 54–57.
[6] Narumanchi, S. V. J., Murthy, J. Y., and Amon, C. H., 2003, "Simulation of Unsteady Small Heat Source Effects in Sub-Micron Heat Conduction," ASME Journal of Heat Transfer, to appear.
[7] Chai, J., Lee, H., and Patankar, S., 1993, "Ray Effects and False Scattering in the Discrete Ordinates Method," Numer. Heat Transfer, Part B, **24**, pp. 373–389.
[8] Coelho, P., 2002, "The Role of Ray Effects and False Scattering on the Accuracy of the Standard and Modified Discrete Ordinates Methods," J. Quant. Spectrosc. Radiat. Transf., **73**, pp. 231–238.
[9] Laney, C., 1998, *Computational Gas Dynamics*, Cambridge University Press, Cambridge, U.K.
[10] Murthy, J. Y., and Mathur, S. R., 2002, "Computation of Sub-Micron Thermal Transport Using an Unstructured Finite Volume Method," ASME Journal of Heat Transfer, **124**(6), pp. 1176–1181.
[11] Ramankutty, M., and Crosbie, A., 1997, "Modified Discrete Ordinates Solution of Radiative Transfer in Two-Dimensional Rectangular Enclosures," J. Quant. Spectrosc. Radiat. Transf., **57**(1), pp. 107–140.
[12] Sakami, M., and Charette, A., 2000, "Application of a Modified Discrete Ordinates Method to Two-Dimensional Enclosures of Irregular Geometry," J. Quant. Spectrosc. Radiat. Transf., **64**, pp. 275–298.
[13] Sakami, M., Kasmi, A. E., and Charette, A., 2001, "Analysis of Radiative Heat Transfer in Complex Two-Dimensional Enclosures with Obstacles Using Modified Discrete Ordinates Method," ASME J. Heat Transfer, **123**, pp. 892–900.
[14] Olfe, D., 1970, "Radiative Equilibrium of a Gray Medium Bounded by Non-Isothermal Walls," Prog. Astronaut. Aeronaut., **23**, pp. 295–317.
[15] Modest, M., 1989, "The Modified Differential Approximation for Radiative Transfer in General Three Dimensional Media," J. Thermophys. Heat Transfer, **3**(3), pp. 283–288.
[16] Chen, G., 2001, "Ballistic-Diffusive Heat Conduction Equations," Phys. Rev. Lett., **86**(11), pp. 2297–2300.
[17] Sverdrup, P., Ju, Y., and Goodson, K., 1998, "Sub-Continuum Simulations of Heat Conduction in Silicon-on-Insulator Devices," ASME J. Heat Transfer, **120**, pp. 30–36.
[18] Murthy, J., and Mathur, S., 1998, "Finite Volume Method for Radiative Heat Transfer Using Unstructured Meshes," J. Thermophys. Heat Transfer, **12**(3), pp. 313–321.
[19] Leonard, B., 1979, "A Stable and Accurate Convective Modeling Procedure Based on Quadratic Upstream Interpolation," Comput. Methods Appl. Mech. Eng., **19**, pp. 59–98.

Maximum Attainable Performance of Stirling Engines and Refrigerators

P. C. T. de Boer
Mem.ASME
Graduate School Professor of Mechanical and Aerospace Engineering,
Upson Hall,
Cornell University,
Ithaca, NY 14853

The flow through the regenerator of a Stirling engine is driven by differences of pressure in the compression and expansion spaces. These differences lead to power dissipation in the regenerator. Using linearized theory, it is shown that this dissipation severely limits the maximum attainable thermal efficiency and nondimensional power output. The maximum attainable values are independent of the value of the regenerator conductance. For optimized nondimensional power output, the thermal efficiency equals only half the Carnot value. The power dissipated in the regenerator is removed as part of the heat withdrawn at the regenerator's cold side. Analogous results are presented for the Stirling refrigerator. At optimized nondimensional rate of refrigeration, its coefficient of performance is less than half the Carnot value. [DOI: 10.1115/1.1597618]

Keywords: Cryogenics, Engines, Heat Transfer, Refrigeration, Regenerators

1 Introduction

As noted by Walker in his classic treatise on Stirling engines [1] and emphasized recently by Organ [2], ideal Stirling engines do not work on the Stirling cycle. The gas in an ideal Stirling engine does not execute either the two constant volume processes or the two constant temperature processes with heat transfer that constitute the Stirling cycle. A model for the operation of the ideal Stirling engine was devised by Schmidt [3]. In Schmidt's model, the volumes of the compression and expansion spaces are taken to vary sinusoidally in time. The heat transfer processes in these spaces are assumed to occur at constant temperature. The pressure in the engine is taken to be spatially uniform; i.e., the pressure difference across the regenerator is neglected. Schmidt's theory provides simple analytical results, and has become the classic model for ideal Stirling engine operation. Because it does not take account of any dissipation, the predicted thermal efficiency equals the Carnot efficiency $\eta_{\text{Carnot}}=1-T_c/T_h$. A detailed review of the Schmidt analysis with applications to several geometries is presented in the book by Reader and Hooper [4]. The Schmidt analysis was generalized by Finkelstein [5], who allowed for irreversible heat exchange with the walls of the compression and expansion spaces. The corresponding compression and expansion processes are not isothermal. As a consequence, there arise temperature discontinuities at the working space interfaces, which lead to additional irreversible heat transfer. Due to the irreversibilities, the predicted thermal efficiency is below the Carnot efficiency. The Finkelstein model does not yield simple analytical results. Its solution is accomplished numerically, using nodal analysis. The Schmidt and Finkelstein models have served as the basis for modern analyses of the Stirling engine. These modern analyses make extensive use of numerical computations and account for many additional phenomena of importance. Detailed accounts of modern developments are presented in [1–12].

The present paper considers the basic limitations on performance of Stirling engines and refrigerators that result from the pressure differences across the regenerator. Without these pressure differences there would be no flow through the regenerator, and the power output would be zero. Hence these differences are essential to the operation of the engine. The pressure oscillations in the compression and expansion spaces are taken to be sinusoidal in time. The ratio π_c of the amplitudes of these pressure oscillations, and the phase difference δ between them depend on the piston motion. These quantities are considered to be adjustable variables. The analysis is carried out using linearized theory. The frequency of oscillation is assumed to be sufficiently low to allow taking the pressures in the compression and expansion spaces as uniform. In Section 2, the nondimensional power output P and the thermal efficiency η of the corresponding ideal Stirling engine cycle are found as function of π_c, δ, and the temperature ratio T_c/T_h. The maximum attainable value of P is determined by optimizing with respect to π_c and δ. In Section 3 it is shown that the power P_{reg} dissipated in the regenerator is the product of the cold side temperature T_c and the rate $\langle\dot{\sigma}\rangle$ at which entropy is generated in the regenerator. By determining the entropy flow, it is found that P_{reg} is removed as part of the heat Q_c withdrawn at the cold side. Section 4 concerns the Stirling refrigerator. The analysis in this section is similar to that presented in a recent note on the maximum attainable performance of pulse tube refrigerators [13].

2 Power Output and Thermal Efficiency

The analysis is based on the one-dimensional model sketched in Fig. 1. The regenerator is taken to be thermally perfect, and to have zero void volume. Friction of the pistons as well as heat losses to the walls are neglected. The flow in the high and low temperature spaces is assumed to be isentropic. Heat is supplied at the rate $\dot{Q}_h$ at the high temperature side of the regenerator, and is withdrawn at the rate $\dot{Q}_c$ at the low temperature side. Important results follow from the rate of energy balance for open systems

$$\frac{dU}{dt}=\dot{m}_c h_c-\dot{m}_h h_h+\dot{Q}-\dot{W}. \tag{1}$$

Since the void volume of the regenerator is taken to be zero, $\dot{m}_c=\dot{m}_h\equiv\dot{m}$. Application to the control volume just surrounding the exit plane h of the regenerator, as well as to the control volume just enclosing the expansion space yields

$$\langle\dot{W}_h\rangle=\langle\dot{Q}_h\rangle=\langle\dot{m}h_h\rangle=c_p\langle\dot{m}T_h''\rangle, \tag{2}$$

where T_h'' is the time-varying part of the temperature just outside the exit plane h. The brackets denote average over a cycle. Use was made of the conditions $\langle\dot{m}\rangle=0$ and $T=T_h=$constant just inside the exit plane h. A similar application at the low temperature side yields

Contributed by the Heat Transfer Division for publication in the JOURNAL OF HEAT TRANSFER. Manuscript received by the Heat Transfer Division August 26, 2002; revision received April 1, 2003. Associate Editor: G. P. Peterson.

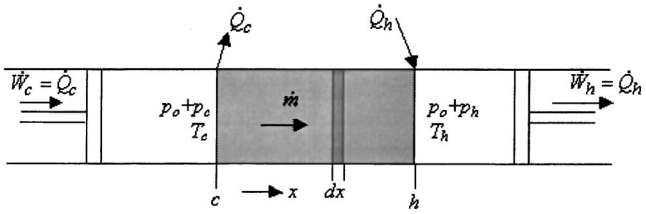

Fig. 1 Sketch of model used for Stirling engine. The high temperature space is the expansion space, the low temperature one is the compression space.

$$\langle \dot{W}_c \rangle = \langle \dot{Q}_c \rangle = c_p \langle \dot{m} T_c'' \rangle. \tag{3}$$

These expressions are evaluated by linearizing the pressures and mass flow rates

$$p_h = p_o + p_h' = p_o + \Delta p_h \sin(\omega t) \quad (p_h' \ll p_o) \tag{4}$$

$$p_c = p_o + p_c' = p_o + \Delta p_c \sin(\omega t + \delta) \quad (p_c' \ll p_o) \tag{5}$$

$$\dot{m} = \rho_h \dot{V}_h = \rho_c \dot{V}_c = \rho_{av} C_r [p_c'(t) - p_h'(t)]. \tag{6}$$

The primes indicate first order quantities, while ρ_{av} is an appropriate average density. The unperturbed pressure p_o is constant throughout the two spaces and the regenerator. The linearized isentropic relation between temperature and pressure is

$$T_h' = \frac{\gamma - 1}{\gamma} \frac{T_h}{p_o} p_h' \quad (T_h' \ll T_h). \tag{7}$$

As shown in the Appendix

$$\langle \dot{W}_h \rangle = \langle \dot{Q}_h \rangle = \langle p_h' \dot{V}_h \rangle, \tag{8}$$

$$\langle \dot{W}_c \rangle = \langle \dot{Q}_c \rangle = \langle p_c' \dot{V}_c \rangle. \tag{9}$$

Working out these expressions leads to

$$\langle \dot{W}_h \rangle = \langle \dot{Q}_h \rangle = \frac{1}{2} C_r \Delta p_h^2 \frac{T_h}{T_{av}} [\pi_c \cos(\delta) - 1], \tag{10}$$

$$\langle \dot{W}_c \rangle = \langle \dot{Q}_c \rangle = \frac{1}{2} C_r \Delta p_h^2 \frac{T_c}{T_{av}} \pi_c [\pi_c - \cos(\delta)]. \tag{11}$$

Here, $\pi_c \equiv \Delta p_c / \Delta p_h (>1)$ is the ratio of pressure amplitudes in the two spaces. The corresponding power output of an ideal Stirling engine is

$$\tilde{P} = \langle \dot{W}_h \rangle - \langle \dot{W}_c \rangle = \frac{1}{2} C_r \Delta p_h^2 \frac{T_h}{T_{av}} P(\pi_c, \delta), \tag{12}$$

where the nondimensional power output P equals

$$P(\pi_c, \delta) = \pi_c \cos(\delta) \left(1 + \frac{T_c}{T_h}\right) - \left(1 + \frac{T_c}{T_h} \pi_c^2\right). \tag{13}$$

The corresponding value of the thermal efficiency is

$$\eta \equiv 1 - \frac{\langle \dot{Q}_c \rangle}{\langle \dot{Q}_h \rangle} = 1 - \frac{T_c}{T_h} \pi_c \frac{\pi_c - \cos(\delta)}{\pi_c \cos(\delta) - 1}. \tag{14}$$

Since the coefficient of $\cos(\delta)$ in Eq. (13) is positive, optimization of P with respect to δ requires $\cos(\delta) = 1$. Optimization with respect to π_c then yields

$$P_{\max} = (1/4)(\sqrt{T_h/T_c} - \sqrt{T_c/T_h})^2 \tag{15}$$

for $\pi_c = (1 + T_h/T_c)/2$. The corresponding value of the thermal efficiency is

$$\eta(P = P_{\max}) = (1 - T_c/T_h)/2 = \eta_{\text{Carnot}}/2. \tag{16}$$

Figure 2 shows P and $\eta/\eta_{\text{Carnot}}$ as function of the pressure amplitude ratio π_c at $T_h/T_c = 4$ for the two cases $\cos(\delta) = 1$ and $\cos(\delta) = 0.9$. It is seen that both power output and thermal efficiency are quite sensitive to the value of $\cos(\delta)$. For $\cos(\delta) < 1$, the power output is negative for values of π_c near 1 and near T_h/T_c. Note that the maximum value of the thermal efficiency $\eta_{\text{Carnot}} = 1 - T_c/T_h$ is reached only for the case $\delta = 0$ and $\pi_c = 1$, in which case the power output $P = 0$. Note also that the results shown in Fig. 2 are independent of the regenerator conductance C_r. The underlying reason is that the work and heat flow rates given by Eqs. (8) and (9) all are proportional to volume flow rate, and, hence, to C_r (cf. Eq. (6)). It must be concluded that Schmidt's result for η at infinitely large C_r ([3,9], $\eta = \eta_{\text{Carnot}} = 1 - T_c/T_h$ for arbitrary π_c and δ) represents a singular case.

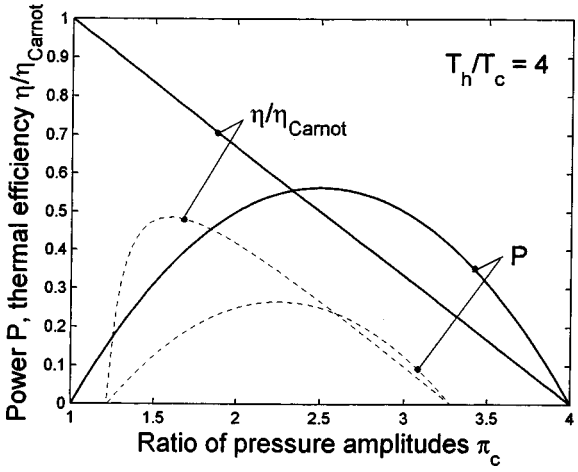

Fig. 2 Nondimensional power output P and thermal efficiency $\eta/\eta_{\text{Carnot}}$ as function of ratio of pressure amplitudes π_c. Solid curves are for $\cos(\delta) = 1$, dotted curves for $\cos(\delta) = 0.9$.

3 Power Flow in the Regenerator

The power output of a Stirling engine without energy dissipation would be $\tilde{P}_{\text{Carnot}} = \eta_{\text{Carnot}} \langle \dot{Q}_h \rangle$. Using Eq. (10), this is can be expressed as

$$\tilde{P}_{\text{Carnot}} = \frac{1}{2} C_r \Delta p_h^2 \frac{T_h}{T_{av}} P_{\text{Carnot}}, \tag{17}$$

$$P_{\text{Carnot}} = \left(1 - \frac{T_c}{T_h}\right) [\pi_c \cos(\delta) - 1]. \tag{18}$$

The difference between Eq. (17) and the actual power output $\tilde{P}$ given by Eq. (12) is the power $\tilde{P}_{\text{reg}}$ dissipated in the regenerator

$$\tilde{P}_{\text{reg}} = \frac{1}{2} C_r \Delta p_h^2 \frac{T_h}{T_{av}} P_{\text{reg}}, \tag{19}$$

$$P_{\text{reg}} = \frac{T_c}{T_h} [\pi_c^2 - 2\pi_c \cos(\delta) + 1] \quad \text{(engine)}. \tag{20}$$

The nondimensional powers P_{Carnot} and P are shown in Fig. 3. The difference between the two is the nondimensional power P_{reg} dissipated in the regenerator.

The power $\tilde{P}_{\text{reg}}$ is removed as part of the heat flow $\langle \dot{Q}_c \rangle$. This can be shown by applying the rate of entropy balance equation

$$\frac{dS}{dt} = \int \frac{d\dot{Q}}{T} + \dot{m}(s_c - s_h) + \dot{\sigma} \tag{21}$$

to the control volume just surrounding the regenerator. Averaging over a cycle yields

$$\frac{\langle \dot{Q}_c \rangle}{T_c} = \frac{\langle \dot{Q}_h \rangle}{T_h} + \langle \dot{\sigma} \rangle. \tag{22}$$

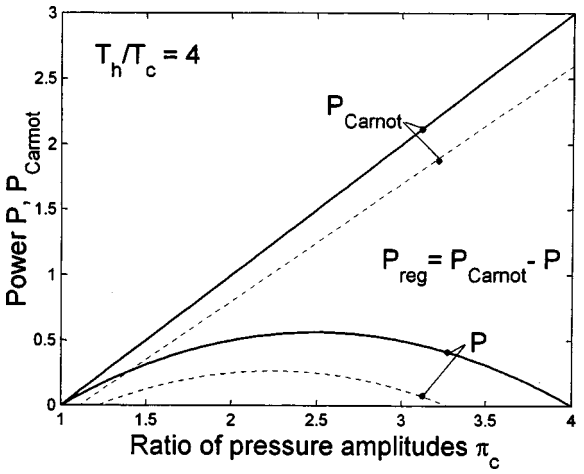

Fig. 3 Nondimensional power outputs P_{Carnot} and P as function of ratio of pressure amplitudes π_c. Solid curves are for $\cos(\delta)=1$, dotted curves for $\cos(\delta)=0.9$.

The term $\dot{m}(s_c-s_h)$ does not contribute to this result because the flows in the compression and expansion spaces are isentropic, and because $\langle\dot{m}\rangle=0$.

Entropy enters the regenerator at the rate $\langle\dot{Q}_h\rangle/T_h$ on the hot side, and increases in value due to dissipation at the rate $\langle\dot{\sigma}\rangle$ while flowing to the cold side. It leaves the cold side at the rate $\langle\dot{Q}_c\rangle/T_c$ which is the sum of the rate entering and the aggregate rate of dissipation.

The value of $\langle\dot{\sigma}\rangle$ can be determined by applying Eq. (21) to an elementary slice dx of the regenerator (see Fig. 1). Upon averaging over a cycle this yields, to first order,

$$\langle d\dot{\sigma}\rangle=\langle\dot{m}ds\rangle=\left\langle\dot{m}\left(c_p\frac{dT}{T}-R\frac{dp}{p}\right)\right\rangle=-\frac{\langle\dot{V}_c dp\rangle}{T_c}. \quad (23)$$

Use was made of the circumstance that the temperature difference dT between the two sides of the slice is constant. Use was also made of the relations $\dot{m}=\rho_c\dot{V}_c$ and $p_o=\rho_c RT_c$. Since $\dot{V}_c$ is independent of x, integration of Eq. (23) over the length of the regenerator yields

$$\langle\dot{\sigma}\rangle=-\frac{1}{T_c}\int_c^h\langle\dot{V}_c dp\rangle=\frac{1}{T_c}\langle\dot{V}_c(p_c'-p_h')\rangle. \quad (24)$$

Evaluating the right hand side of this equation by using Eqs. (4)–(6) results in

$$\langle\dot{\sigma}\rangle=\frac{1}{2}C_r\Delta p_h^2\frac{1}{T_{av}}[\pi_c^2-2\pi_c\cos(\delta)+1]. \quad (25)$$

Comparison with Eqs. (19) and (20) shows that $\tilde{P}_{\text{reg}}=T_c\langle\dot{\sigma}\rangle$, and hence that

$$\langle\dot{Q}_c\rangle=\langle\dot{Q}_h\rangle\frac{T_c}{T_h}+\tilde{P}_{\text{reg}}. \quad (26)$$

It follows that $\tilde{P}_{\text{reg}}$ arises from the rate at which entropy is generated by irreversibilities in the regenerator.

Analysis of the Stirling Refrigerator. The analysis of the Stirling refrigerator is nearly identical to that of the Stirling engine. The major difference is that the directions as well as the relative magnitudes of the heat flows are reversed (see Fig. 4). As a consequence, the sign in Eq. (6) must be reversed: $\dot{m}=\rho_{av}C_r(p_h'-p_c')$. Another difference is that in this case $\pi_c\equiv\Delta p_c/\Delta p_h<1$. The rate of cooling at T_c is given by

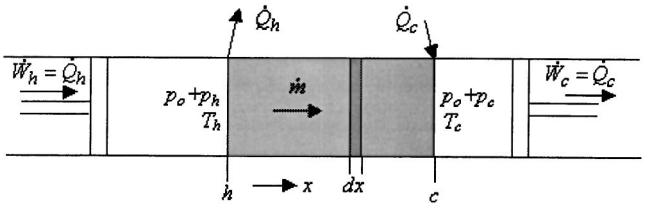

Fig. 4 Sketch of model used for Stirling refrigerator

$$\langle\dot{Q}_c\rangle=\langle\dot{W}_c\rangle=\frac{1}{2}C_r\Delta p_h^2\frac{T_h}{T_{av}}\langle\dot{H}_c\rangle, \quad (27)$$

$$\langle\dot{H}_c\rangle=\frac{T_c}{T_h}\pi_c[\cos(\delta)-\pi_c], \quad (28)$$

the rate of heat withdrawal at T_h by

$$\langle\dot{Q}_h\rangle=\langle\dot{W}_h\rangle=\frac{1}{2}C_r\Delta p_h^2\frac{T_h}{T_{av}}\langle\dot{H}_h\rangle, \quad (29)$$

$$\langle\dot{H}_h\rangle=1-\pi_c\cos(\delta). \quad (30)$$

It follows that

$$\text{COP}\equiv\frac{\langle\dot{Q}_c\rangle}{\langle\dot{Q}_h\rangle-\langle\dot{Q}_c\rangle}=\frac{T_c}{T_h}\frac{\pi_c[\cos(\delta)-\pi_c]}{1+\pi_c^2T_c/T_h-(1+T_c/T_h)\pi_c\cos(\delta)}. \quad (31)$$

Optimization of $\langle\dot{H}_c\rangle$ requires $\cos(\delta)=1$ and $\pi_c=1/2$, yielding $\langle\dot{H}_c\rangle_{\max}=(T_c/T_h)/4$ and

$$\text{COP}(\langle\dot{H}_c\rangle=\langle\dot{H}_c\rangle_{\max})=\frac{1}{2T_h/T_c-1}. \quad (32)$$

Figure 5 shows $\langle\dot{H}_c\rangle T_h/T_c$ and $\text{COP}/\text{COP}_{\text{Carnot}}\equiv\text{COP}(T_h/T_c-1)$ as function of π_c at $T_h/T_c=4$ for the two cases $\cos(\delta)=1$ and $\cos(\delta)=0.9$.

The nondimensional power input to the Stirling refrigerator is

$$\langle\dot{H}_h\rangle-\langle\dot{H}_c\rangle=1+\frac{T_c}{T_h}\pi_c^2-\left(1+\frac{T_c}{T_h}\right)\pi_c\cos(\delta). \quad (33)$$

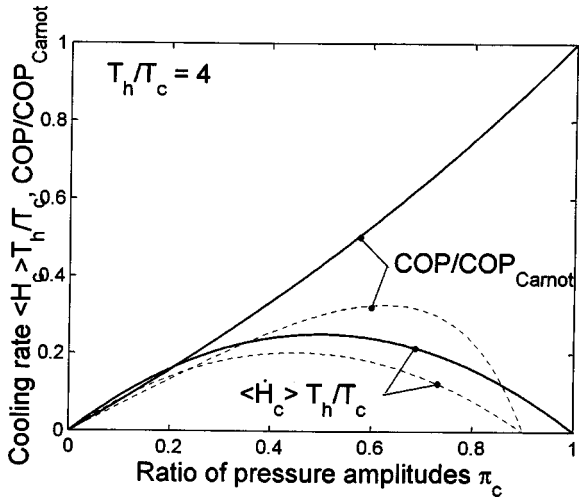

Fig. 5 Nondimensional cooling rate $\langle\dot{H}_c\rangle T_h/T_c$ and coefficient of performance COP/COP_{Carnot} as function of ratio of pressure amplitudes π_c. Solid curves are for $\cos(\delta)=1$, dotted curves for $\cos(\delta)=0.9$.

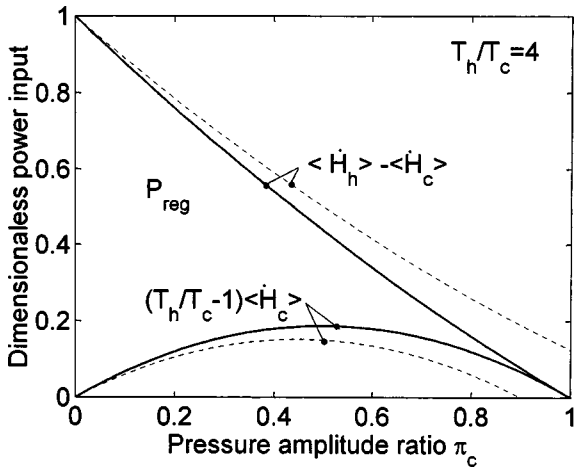

Fig. 6 Nondimensional power inputs $\langle\dot{H}_h\rangle-\langle\dot{H}_c\rangle$ and $(T_h/T_c-1)\langle\dot{H}_c\rangle$ as function of ratio of pressure amplitudes π_c. Solid curves are for $\cos(\delta)=1$, dotted curves for $\cos(\delta)=0.9$.

The corresponding power input to a Stirling refrigerator without energy dissipation would be

$$\left(\frac{T_h}{T_c}-1\right)\langle\dot{H}_c\rangle=\left(1-\frac{T_c}{T_h}\right)\pi_c[\cos(\delta)-\pi_c]. \tag{34}$$

The difference between these two quantities is the nondimensional power dissipated in the regenerator

$$P_{\text{reg}}=1-2\pi_c\cos(\delta)+\pi_c^2 \quad \text{(refrigerator)}. \tag{35}$$

The nondimensional power inputs are shown in Fig. 6 as function of the pressure amplitude ratio π_c at $T_h/T_c=4$ for $\cos(\delta)=1$ and 0.9. In the case of the Stirling refrigerator, the entropy flow is from the cold to the hot side (see also [13]), and

$$\langle\dot{Q}_h\rangle=\langle\dot{Q}_c\rangle\frac{T_h}{T_c}+\tilde{P}_{\text{reg}}. \tag{36}$$

5 Conclusion

The flow in the regenerator of a Stirling engine is driven by differences of pressure in the compression and expansion spaces. Taking account of the resulting energy dissipation leads to severe limitations on maximum attainable thermal efficiency η and nondimensional power output P. These limitations are independent of the regenerator conductance C_r. It is concluded that Schmidt's result $\eta=\eta_{\text{Carnot}}$ [3,9] obtained with $C_r=\infty$ represents a singular case. The thermal efficiency is independent of C_r because the relevant work and heat flow rates all are proportional to volume flow rate (Eqs. (8) and (9)), and hence to C_r (Eq. (6)). Optimum results are obtained at phase angle $\delta=0$. At this phase angle, $\eta/\eta_{\text{Carnot}}$ is a linear function of the pressure amplitude ratio π_c. The value of $\eta/\eta_{\text{Carnot}}$ goes from 1 at $\pi_c=0$ to 0 at $\pi_c=T_h/T_c$ (Fig. 2). The corresponding dependence of P on π_c is parabolic, with $P=0$ at $\pi_c=0$ and at $\pi_c=T_h/T_c$. The maximum value of P is $P_{\max}=(\sqrt{T_h/T_c}-\sqrt{T_c/T_h})^2/4$. At $P=P_{\max}$, the value of the thermal efficiency is $(1-T_c/T_h)/2$ (half the Carnot value). Inasmuch as engines are designed primarily for maximum power output, this constitutes a severe practical limitation. As a consequence, it is not surprising that actual Stirling engines have thermal efficiencies typically not exceeding 40% (see, e.g., [8], Table 5.3, and [9], Fig. 45).

The power $\tilde{P}_{\text{reg}}$ dissipated in the regenerator equals the product of the cold side temperature T_c and the rate $\langle\dot{\sigma}\rangle$ at which entropy is generated in the regenerator. $\tilde{P}_{\text{reg}}$ is removed as part of the heat $\langle\dot{Q}_c\rangle$ withdrawn at the cold side (Eq. 26). The nondimensional power P_{reg} increases with π_c (Fig. 3).

The nondimensional rate of refrigeration $\langle\dot{H}_c\rangle$ of a Stirling refrigerator has a parabolic dependence on π_c (Eq. (27) and Fig. 5). The maximum value of $\langle\dot{H}_c\rangle$ is $(T_c/T_h)/4$, achieved at $\pi_c=1/2$. The corresponding value of the coefficient of performance COP is $1/(-1+2T_h/T_c)$, which is less than half of the Carnot value $1/(-1+T_h/T_c)$. In the case of the Stirling refrigerator, $\tilde{P}_{\text{reg}}$ is removed as part of the heat $\langle\dot{Q}_h\rangle$ withdrawn at the warm side (Eq. 36), and P_{reg} decreases as π_c increases (Fig. 6). The coefficient of performance is independent of C_r because the relevant heat and work flow rates all are proportional to volume flow rate, and hence to C_r (Eqs. (27) and (29)).

The results obtained represent dissipation losses that are unavoidable when a regenerator is used to obtain mechanical power or refrigeration. Losses due to all other non-idealities have been neglected. While the discussion has been focused on Stirling engines and Stirling refrigerators, the conclusions apply equally well to all engines and refrigerators based on the principle of regeneration. These include, for example, Ericsson engines and Gifford-McMahon refrigerators.

Nomenclature

A = cross sectional area (m^2)
C_r = conductance of regenerator (m^4s/kg)
c_p = specific heat at constant pressure [J/(kg K)]
COP = coefficient of performance
$\dot{H}$ = enthalpy flow rate (J/s)
h = specific enthalpy (J/kg)
L = distance (m)
$\dot{m}$ = mass flow rate (kg/s)
P = nondimensional power
$\tilde{P}$ = power (W)
p_o = average pressure (Pa)
p = pressure (Pa)
$\dot{Q}$ = rate of heat flow (W)
S = entropy (J/K)
s = specific entropy [J/(kg K)]
T = temperature (K)
t = time (s)
U = internal energy (J)
$\dot{V}$ = volume flow rate (m^3/s)
$\dot{W}$ = rate of work done (W)
$\langle\ \rangle$ = denote average over a cycle

Greek Symbols

Δ = denotes amplitude of first order quantity
δ = phase angle
η = thermal efficiency
γ = ratio of specific heats
π_c = ratio of pressure amplitudes, $\Delta p_c/\Delta p_h$
ρ = density (kg/m^3)
$\dot{\sigma}$ = rate of entropy generation [J/(sK)]
τ = ωt, nondimensional time
ψ = phase angle of volume flow rate
ω = angular frequency (s^{-1})

Subscripts

av = average (see Eq. 6)
c = cold
h = hot

5 Appendix

In this appendix the expression $\langle \dot{W}_h \rangle = c_p \langle \dot{m} T_h'' \rangle$ appearing in Eq. (2) is evaluated. The evaluation is analogous to that described in [14] for the enthalpy flow toward the warm heat exchanger of a pulse tube.

Without loss of generality, the volume flow rate at h can be written

$$\dot{V}_h = \Delta V_h \sin(\tau + \psi), \tag{A1}$$

where $\tau \equiv \omega t$. During the outflow part of the cycle ($\dot{V}_h > 0$), the temperature equals T_h and hence $T_h'' = 0$. The pressure of a fluid particle leaving plane h at time τ_{out} is $p_o + \Delta p_h \sin(\tau_{\text{out}})$. Until returning at time τ_{in} the temperature of the particle follows the isentropic relation Eq. (7). Hence, to first order its temperature when returning equals

$$T'' = T' = \frac{\gamma - 1}{\gamma} \frac{T_h}{p_o} [p_h'(\tau_{\text{in}}) - p_h'(\tau_{\text{out}})]$$

$$= \frac{\gamma - 1}{\gamma} \frac{T_h}{p_o} \Delta p_h [\sin(\tau_{\text{in}}) - \sin(\tau_{\text{out}})]. \tag{A2}$$

The relation between τ_{out} and τ_{in} follows from considering the rate of change in position of the particle at time τ when it is at distance $L(\tau)$ from plane h. This rate is the sum of the rate of outflow and the rate of change of L due to compression

$$\frac{dL}{d\tau} = \frac{\Delta V_h}{A\omega} \sin(\tau + \psi) - \frac{L}{\gamma p_o} \frac{dp_h}{d\tau}. \tag{A3}$$

The last term on the right hand side is of second order and drops out. Integrating and using the condition $L(\tau_{\text{out}}) = 0$ yields

$$L(\tau) = \frac{\Delta V_h}{A\omega} [\cos(\tau + \psi) - \cos(\tau_{\text{out}} + \psi)]. \tag{A4}$$

It follows from the condition $L(\tau_{\text{in}}) = 0$ that $\tau_{\text{out}} = 2\pi - \tau_{\text{in}} - 2\psi$, and hence that $\sin(\tau_{\text{in}}) - \sin(\tau_{\text{out}}) = 2 \sin(\tau_{\text{in}} + \psi) \cos(\psi)$. The range of inflow is given by $\pi - \psi \leqslant \tau_{\text{in}} \leqslant 2\pi - \psi$. Hence,

$$\langle \dot{W}_h \rangle = c_p \langle \dot{m} T_h'' \rangle$$

$$= \Delta p_h \Delta V_h \frac{\cos(\psi)}{\pi} \int_{\pi - \psi}^{2\pi - \psi} [\sin(\tau_{\text{in}} + \psi)]^2 d\tau_{\text{in}}$$

$$= \frac{1}{2} \Delta p_h \Delta V_h \cos(\psi), \tag{A5}$$

where use was made of the ideal gas law $p_o = \rho_h R T_h$ as well as the relation $\dot{m} = \rho_h \dot{V}_h$.

It is noted that the right hand side of Eq. (A5) also is obtained by substituting

$$T_h'' = T_h' = \frac{\gamma - 1}{\gamma} \frac{T_h}{p_o} p_h' \tag{A6}$$

in Eq. (2). This substitution is equivalent to setting $\langle \dot{W}_h \rangle = \langle p_h' \dot{V}_h \rangle$, where the average is taken over the entire cycle:

$$\langle p_h' \dot{V}_h \rangle \equiv \frac{1}{2\pi} \int_0^{2\pi} p_h' \dot{V}_h d\tau = \frac{1}{2} \Delta p_h \Delta V_h \cos(\psi). \tag{A7}$$

It is concluded that setting $\langle \dot{W}_h \rangle = \langle p_h' \dot{V}_h \rangle$, while formally incorrect, nevertheless provides the correct result. Similarly, setting $\langle \dot{W}_c \rangle = \langle p_c' \dot{V}_c \rangle$ provides the correct result.

References

[1] Walker, G., 1980, *Stirling Engines*, Clarendon Press, Oxford, UK.
[2] Organ, A. J., 1997, *The Regenerator and the Stirling Engine*, Mechanical Engineering Publications Limited, London and Bury St. Edmunds, UK (Section 3.9).
[3] Schmidt, G., 1871, "Theorie der Lehrmanschen Calorischen Maschine," Z. Ver. Dtsch. Ing., **15**(1), pp. 1–12, **15**(2), pp. 97–112.
[4] Reader, G. T., and Hooper, C., 1983, *Stirling Engines*, E. & F. N. Spon, London and New York (Appendix A).
[5] Finkelstein, T., 1960, "Generalized Thermodynamic Analysis of Stirling Engines," SAE Paper 118 B.
[6] Urieli, I., and Berchowitz, D. M., 1984, *Stirling Cycle Analysis*, Adam Hilger Ltd., Bristol, UK.
[7] Walker, G., and Senft, J. R., 1985, *Free Piston Stirling Engines*, Springer-Verlag, Berlin, Germany.
[8] West, C. D., 1986, *Principles and Applications of Stirling Engines*, Van Nostrand Reinhold Company, New York, NY.
[9] Hargreaves, C. M., 1991, *The Philips Stirling Engine*, Elsevier Science Publishers, Amsterdam, The Netherlands.
[10] Organ, A. J., 1992, *Thermodynamics and Gas Dynamics of the Stirling Cycle Machine*, Cambridge University Press, Cambridge, UK.
[11] Senft, J. R., 1993, *Ringborn Stirling Engines*, Oxford University Press, Oxford, UK.
[12] Finkelstein, T., and Organ, A. J., 2001, *Air Engines, the History, Science and Reality of the Perfect Engine*, The American Society of Mechanical Engineers, New York, NY.
[13] de Boer, P. C. T., 2002, "Maximum Attainable Performance of Pulse Tube Refrigerators," Cryogenics, **42**, pp. 123–125.
[14] de Waele, A. T. A. M., Steijaart, P. P., and Koning, J. J., 1998, "Thermodynamic Aspects of Pulse Tubes II," Cryogenics, **38**, pp. 329–335.

Cooling Enhancements in Thin Films Supported by Flexible Complex Seals in the Presence of Ultrafine Suspensions

A.-R. A. Khaled
Department of Mechanical Engineering,
The Ohio State University,
Columbus, OH 43210

K. Vafai
Department of Mechanical Engineering,
University of California, Riverside,
Riverside, CA 92521

Flow and heat transfer inside thin films supported by flexible soft seals having voids of a stagnant fluid possessing a large coefficient of volumetric thermal expansion β_T are studied in the presence of suspended ultrafine particles. The study is conducted under periodically varying thermal load conditions. The governing continuity, momentum and energy equations are non-dimensionalized and reduced to simpler forms. The deformation of the seal is related to the internal pressure and lower plate's temperature based on the theory of linear elasticity and a linearized model for thermal expansion. It is found that enhancements in the cooling are achieved by an increase in the volumetric thermal expansion coefficient, thermal load, thermal dispersion effects, softness of the supporting seals and the thermal capacitance of the coolant fluid. Further, thermal dispersion effects are found to increase the stability of the thin film. The noise in the thermal load is found to affect the amplitude of the thin film thickness, Nusselt number and the lower plate temperature however it has a negligible effect on their mean values.
[DOI: 10.1115/1.1597612]

Keywords: Cooling, Enhancement, Film, Heat Transfer, Seals

1 Introduction

Thin films are widely used in cooling of many heating sources such as electronic components. These elements use thin films in their cooling systems as in flat heat pipes (Moon et al. [1]) or microchannel heat sinks (Fedorov and Viskanta [2], Zhu and Vafai [3]). Many ideas are proposed to enhance the cooling load of thin films. For example, Bowers and Mudawar [4] showed that two phase flow in minichannel is capable of removing maximum heat fluxes generated by electronic packages yet the system may become unstable near certain operating conditions. Further, the use of porous medium in cooling of electronic devices (Hadim [5]) was found to enhance heat transfer due to increases in the effective surface area. However, the porous medium creates a substantial increase in the pressure drop inside the thin film.

Khaled and Vafai [6] showed that cooling effects achieved by having thin films supported by soft seals are more than when these seals are stiff. This is due to an increase in the thickness resulting from pressure forces when soft seals are used. Additional cooling can be achieved if the thin film thickness is allowed to increase by an increase in the thermal load which will cause the coolant flow rate to increase. This task can be reached if the sealing assembly supporting the plates of the thin film is composed of the following: soft seals and voids of a stagnant fluid having a large value of the volumetric thermal expansion coefficient β_T. This proposed sealing assembly will be named a ''flexible complex seal'' and will be used regularly in the text. It is worth noting that the enhancement in the cooling when flexible complex seals are used is expected to be apparent at larger thermal loads for stagnant liquids while it is prominent at lower temperatures for stagnant gases, especially ideal gases. This is because the volumetric thermal expansion coefficient increases for liquids and decreases for gases as their temperatures increases.

In the presence of periodic external thermal loads, the thickness of a thin film supported by a flexible seal containing voids of a fluid having a large β_T value is expected to be periodic. This is because the stagnant fluid expands during maximum thermal load intervals allowing for a relaxation in the thin film thickness which causes a flooding of the coolant. On the other hand, the thin film is squeezed during minimum thermal load intervals due to the contraction in the stagnant fluid in the sealing assembly voids. Several authors have considered flow inside squeezed thin films like Langlois [7] who performed an analytical study for flow inside isothermal oscillatory squeezed films having the fluid density varying with pressure. However, only few of them have analyzed heat transfer inside squeezed thin films such as Hamza [8], Bhattacharyya et al. [9] and Debbaut [10]. In these works, the squeezing was not of an oscillatory type. All of these works considered a predetermined squeezing effect at the plates of the thin film. Recently, Khaled and Vafai [11] considered flow and heat transfer inside incompressible oscillatory squeezed thin films.

One of the advantages of using flexible complex seals is that the increase in the coolant flow rate because of thermal expansion effects produces an additional cooling in the presence of suspended ultrafine particles (Li and Xuan [12]). This is because the chaotic movement of the ultrafine particles, the thermal dispersion, increases with the flow where it is modeled in the energy equation by introducing an effective thermal conductivity of the coolant (Xuan and Roetzel [13]). Further, large fluctuation rates that can be generated in the flow during severe squeezing conditions tend to increase the chaotic motions of the particles in the fluid which increases the energy transport in the coolant.

In this work, the enhancement in the cooling process inside thin films supported by flexible complex seals in the presence of suspended ultrafine particles is investigated. The lower plate of the examined thin film is considered to be under a periodically varying heat flux. The thin film thickness is related to the thermal load and the internal pressure through the volumetric thermal expansion coefficient of the stagnant fluid and the theory of linear elasticity applied to the supporting seals. The governing equations for flow and heat transfer are properly non-dimensionalized and reduced into simpler equations for low Reynolds numbers. The re-

Contributed by the Heat Transfer Division for publication in the JOURNAL OF HEAT TRANSFER. Manuscript received by the Heat Transfer Division November 26, 2002; revision received May 9, 2003. Associate Editor: H. Bau.

sulting equations are then solved numerically to determine the effects of the thermal load, volumetric thermal expansion coefficient of the stagnant fluid, the softness of the seal, thermal capacitance of the working fluid and the squeezing number on the dynamics and thermal characteristic of the thin films supported by flexible complex thin films.

2 Problem Formulation

Figure 1 shows a thin film having a flexible complex seal. It is composed of the coolant flow, the working fluid, passage and the sealing assembly. This assembly contains closed voids filled with a stagnant fluid having relatively a large coefficient of volumetric thermal expansion. The sealing assembly contains also soft seals in order to allow the thin film to expand. A candidate for the soft seal is the closed cell rubber foam [14]. Any excessive heat increases the temperature of the hot plate thus the stagnant fluid becomes warmer and expands. The seals are soft enough so that the expansion results in an increase in the separation between the lower and the upper plates. Accordingly, the flow resistance of the working fluid passage decreases causing a flooding of the coolant. As a result, the excessive heating from the source is removed. It is worth noting that the soft seals can be placed between special guiders as shown in Fig. 1(*b*). As such, side expansion of the seals can be minimized and the transverse thin film thickness expansion is maximized.

The analysis is concerned with a thin film that has a small thickness h compared to its length B and its width D. Therefore, a two-dimensional flow is assumed. The x-axis is taken along the axial direction of the thin film while y-axis is taken along its thickness as shown in Fig. 1(*a*). Further, it is assumed in this work that the film thickness is independent of the axial coordinate. For example, this occurs in two main cases: symmetric thin films hav-

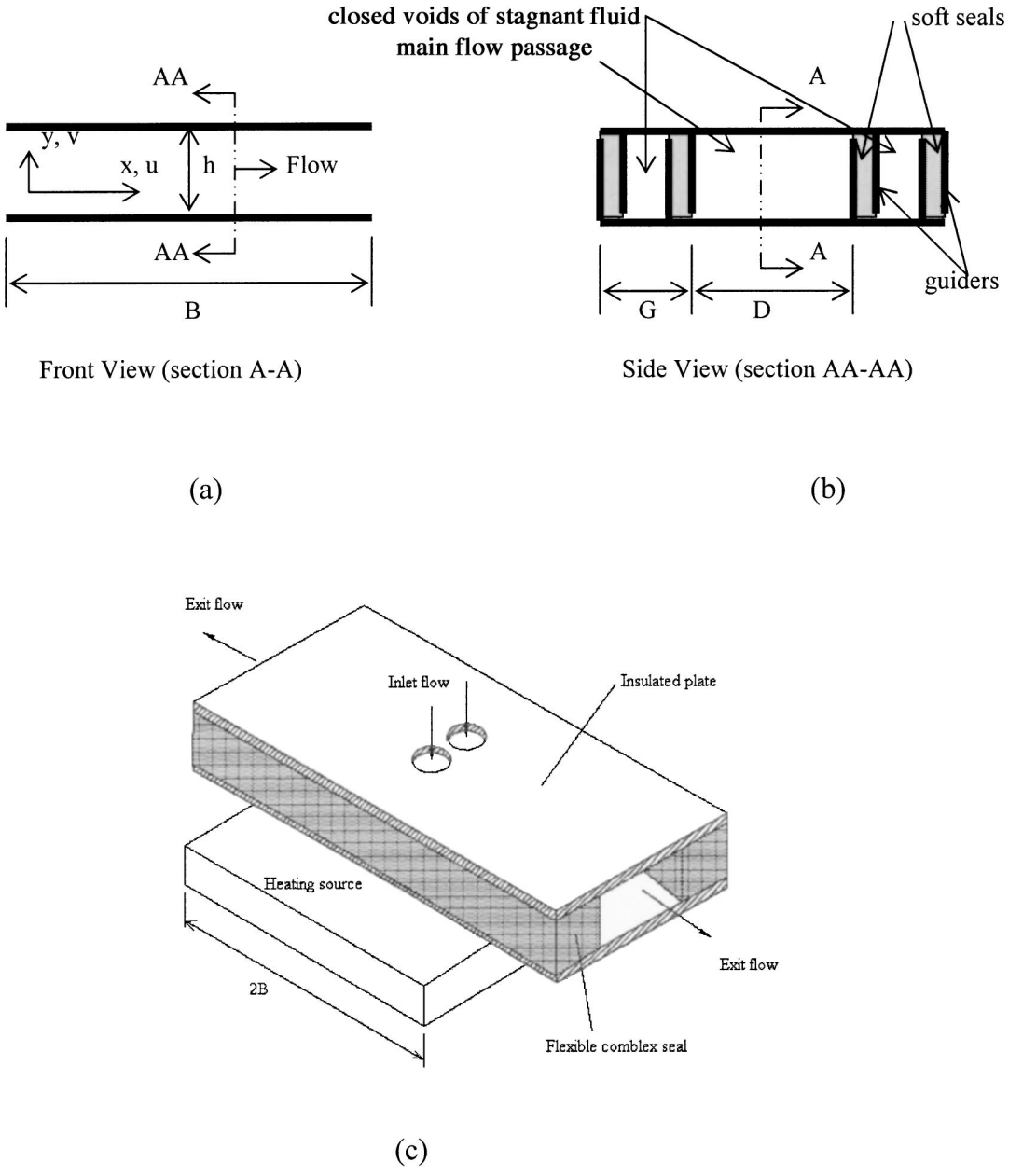

Fig. 1 Schematic diagram for a thin film with flexible complex seal and the corresponding coordinate system: (*a*) front view, (*b*) side view, and (*c*) a three dimensional diagram

ing a fluid injected from the center as shown in Fig. 1(*c*) and in multiple passages thin films having alternating coolant flow directions.

The lower plate of the thin film is assumed to be fixed to a heating source while the upper plate is attached to the lower plate by flexible complex seals allowing it to expand. The motion of the upper plate due to both internal variations in the stagnant fluid temperature and the induced internal pressure pulsations as a result of oscillating thermal loads is expressed according to the following relation:

$$H \equiv \frac{h}{h_o} = (1 + H_T + H_p) \tag{1}$$

where h, h_o, and H are the thin film thickness, a reference film thickness and the dimensionless thin film thickness, respectively. The variables H_T and H_p are the dimensionless motion of the upper plate due to the thermal expansion of the stagnant fluid and the dimensionless motion of the upper plate as a result of the deformation of seals due to the average internal pressure of the working fluid, respectively. It is assumed that the fluid is Newtonian having constant average properties except for the thermal conductivity.

The general two-dimensional continuity, momentum and energy equations for a laminar flow of the working fluid inside the thin film are given as

$$\frac{\partial u}{\partial x} + \frac{\partial v}{\partial y} = 0 \tag{2}$$

$$\rho\left(\frac{\partial u}{\partial t} + u\frac{\partial u}{\partial x} + v\frac{\partial u}{\partial y}\right) = -\frac{\partial p}{\partial x} + \mu\left(\frac{\partial^2 u}{\partial x^2} + \frac{\partial^2 u}{\partial y^2}\right) \tag{3}$$

$$\rho\left(\frac{\partial v}{\partial t} + u\frac{\partial v}{\partial x} + v\frac{\partial v}{\partial y}\right) = -\frac{\partial p}{\partial y} + \mu\left(\frac{\partial^2 v}{\partial x^2} + \frac{\partial^2 v}{\partial y^2}\right) \tag{4}$$

$$\rho c_p\left(\frac{\partial T}{\partial t} + u\frac{\partial T}{\partial x} + v\frac{\partial T}{\partial y}\right) = \frac{\partial}{\partial x}\left(k\frac{\partial T}{\partial x}\right) + \frac{\partial}{\partial y}\left(k\frac{\partial T}{\partial y}\right) \tag{5}$$

where T, u, v, ρ, p, μ, c_p, and k are temperature, dimensional axial velocity, dimensional normal velocity, average density, pressure, average dynamic viscosity, average specific heat and the thermal conductivity, respectively. The previous fluid properties are for the pure working fluid in the case where the fluid is free from any suspensions. In the presence of suspended ultrafine particles, the previous properties will be for an approximated new continuum fluid composed from the mixture of the pure fluid and the suspensions (Xuan and Roetzel [13]). The new properties are related to the fluid and the particle properties through the volume fraction of the suspended particles inside the thin film and the thermal dispersion parameter. These relations are found in the literature (e.g., Xuan and Roetzel [13]).

The following dimensionless variables will be utilized to nondimensionalize Eqs. (2)–(5):

$$X = \frac{x}{B} \quad Y = \frac{y}{h_o} \tag{6a,b}$$

$$\tau = \omega t \tag{6c}$$

$$U = \frac{u}{(\omega B + V_o)} \quad V = \frac{v}{h_o \omega} \tag{6d,e}$$

$$\Pi = \frac{p - p_e}{\mu\left(\omega + \frac{V_o}{B}\right)\varepsilon^{-2}} \tag{6f}$$

$$\theta = \frac{T - T_1}{(q_o h_o)/k_o} \tag{6g}$$

where ω, T_1, p_e, q_o, and V_o are the reference frequency of thermal load, inlet temperature of the fluid, a constant representing the exit pressure, reference heat flux and a constant representing a reference dimensional velocity, respectively. The term k_o corresponds to the working fluid thermal conductivity in the absence of any suspensions while it is the stagnant thermal conductivity, free from the dispersion term, for the dilute mixture between the fluid and the ultrafine suspensions. The stagnant thermal conductivity has usually an enhanced value when compared to that of the pure fluid for metallic particles (Eastman et al. [15]).

It is assumed that the upper plate is insulated to simplify the analysis and that the lower plate is subjected to a periodically varying wall heat flux q_L condition according to the following relation:

$$q_L = q_o(1 + \beta_q \sin(\gamma\omega t)) \tag{7}$$

where β_q and γ are the dimensionless amplitude of the lower plate's heat flux and a dimensionless frequency, respectively. The variables X, Y, τ, U, V, Π, and θ are the dimensionless forms of x, y, t, u, v, p, and T variables, respectively. The parameter ε appearing in Equation (6*f*) is the perturbation parameter, $\varepsilon = h_o/B$.

For the thin film shown in Fig. 1(*c*), the displacement of the upper plate due to internal pressure variations is related to the average dimensionless pressure of the working fluid, Π_{AVG}, through the theory of linear elasticity by the following relation:

$$H_p = F_n \Pi_{\mathrm{AVG}} \tag{8}$$

This is based on the fact that the upper plate is assumed to be rigid and that the applied force on an elastic material (the soft seal is assumed to behave as an elastic material) is proportional to the elongation of this material (Norton [16]). The parameter F_n is referred to as the fixation parameter and it is a measure of the softness of the seal, soft seals have large F_n values. It is equal to

$$F_n = \frac{\mu(V_o + \omega B)}{E\varepsilon^2 d_s}, \tag{9}$$

where E and d_s are the effective modulus of elasticity for the complex seal and a characteristic parameter which depends on the seal's dimensions and the thin film width D, respectively. The quantity d_s is equal to the effective dimension of the seal's cross section times the ratio of the total length of the seal divided by the thin film width D. The seal is considered to have isotropic properties. Further, the effective dimension of the seals times their total length represents the contact area between the seals and the upper or lower plates when the seals have a rectangular cross section as shown in Fig. 1. Other than this, the effective diameter requires a theoretical determination.

In this work, the analysis is performed for relatively small thermal load frequencies in order to ascertain that squeezing generated flows have relatively small Reynolds numbers. For these frequencies, Eq. (8) is applicable and the inertia effect of the upper plate is negligible. Moreover, the increase in the thickness due to a pressure increase in the thin film causes a reduction in the stagnant fluid pressure. This action stiffens the sealing assembly. Therefore, the parameter E is considered to be the effective modulus of elasticity for the sealing assembly not for the seal itself. Practically, the void width G is assumed to be large enough such that a small increase in the stagnant fluid pressure due to the expansion can support the associated increase in the elastic force on the seal.

The dimensionless displacement of the upper plate due to thermal expansion is related to the dimensionless average temperature of the lower plate, $(\theta_W)_{\mathrm{AVG}}$, by the following linearized model:

$$H_T = F_T(\theta_W)_{\mathrm{AVG}} \tag{10}$$

where F_T is named the dimensionless thermal expansion parameter. It is equal to

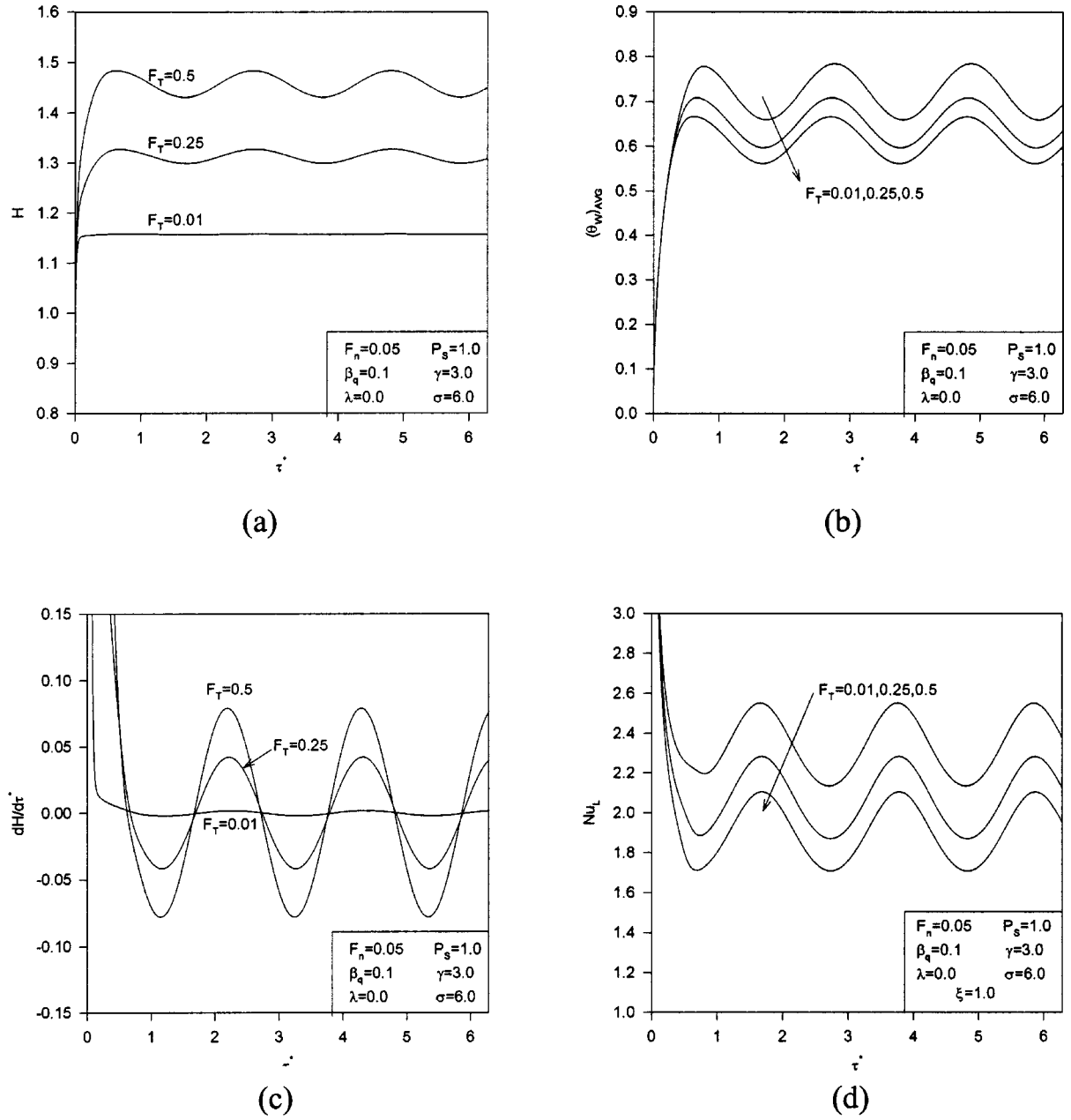

Fig. 2 Effects of the dimensionless thermal expansion parameter F_T on (*a*) dimensionless thin film thickness H, (*b*) dimensionless average lower plate temperature $(\theta_W)_{AVG}$, (*c*) $dH/d\tau$, and (*d*) exit Nusselt number Nu_L

$$F_T = A^* \frac{\beta_T q_o h_o}{k_o} C_F \tag{11}$$

where A^* is a constant depending on the voids dimensions and geometry. The parameter β_T is the volumetric thermal expansion coefficient of the stagnant fluid in its approximate form:

$$\beta_T \approx (1/V_{so})[(V_s - V_{s1})/(T_s - T_1)]|_{p_{s1}}$$

evaluated at the pressure p_{s1} corresponding to the stagnant fluid pressure at the inlet temperature T_1. The quantities V_{s1} and V_s represent the void volumes at normal operating conditions when the stagnant fluid is at T_1 and at the present stagnant fluid temperature T_s, respectively. The parameter V_{so} represents the void volume at the reference condition. The factor C_F represents the volumetric thermal expansion correction factor. This factor is introduced in order to account for the increase in the stagnant pressure due to the increase in the elastic force in the seal during the expansion which tends to decrease the effec-tive volumetric thermal expansion coefficient. It approaches one as the void width G increases and it needs to be determined theoretically.

The parameter F_T is enhanced at elevated temperatures for liquids and at lower temperature for gases because β_T increases for liquids and decreases for gases as the stagnant temperature increases. Dimensionless thermal expansion parameter is also enhanced by a decrease in k_o, an increase in q_o, an increase in F_n or by increases in h_o. It is worth noting that Eq. (10) is based on the assumption that the stagnant fluid temperature is similar to the lower plate temperature since entire void surfaces are considered insulated except that facing the lower plate. Furthermore, the heat flux of the heating source is applied on the portion of the lower plate that is facing the working fluid. The other portion which faces the seals is taken to be isolated from the heating source and

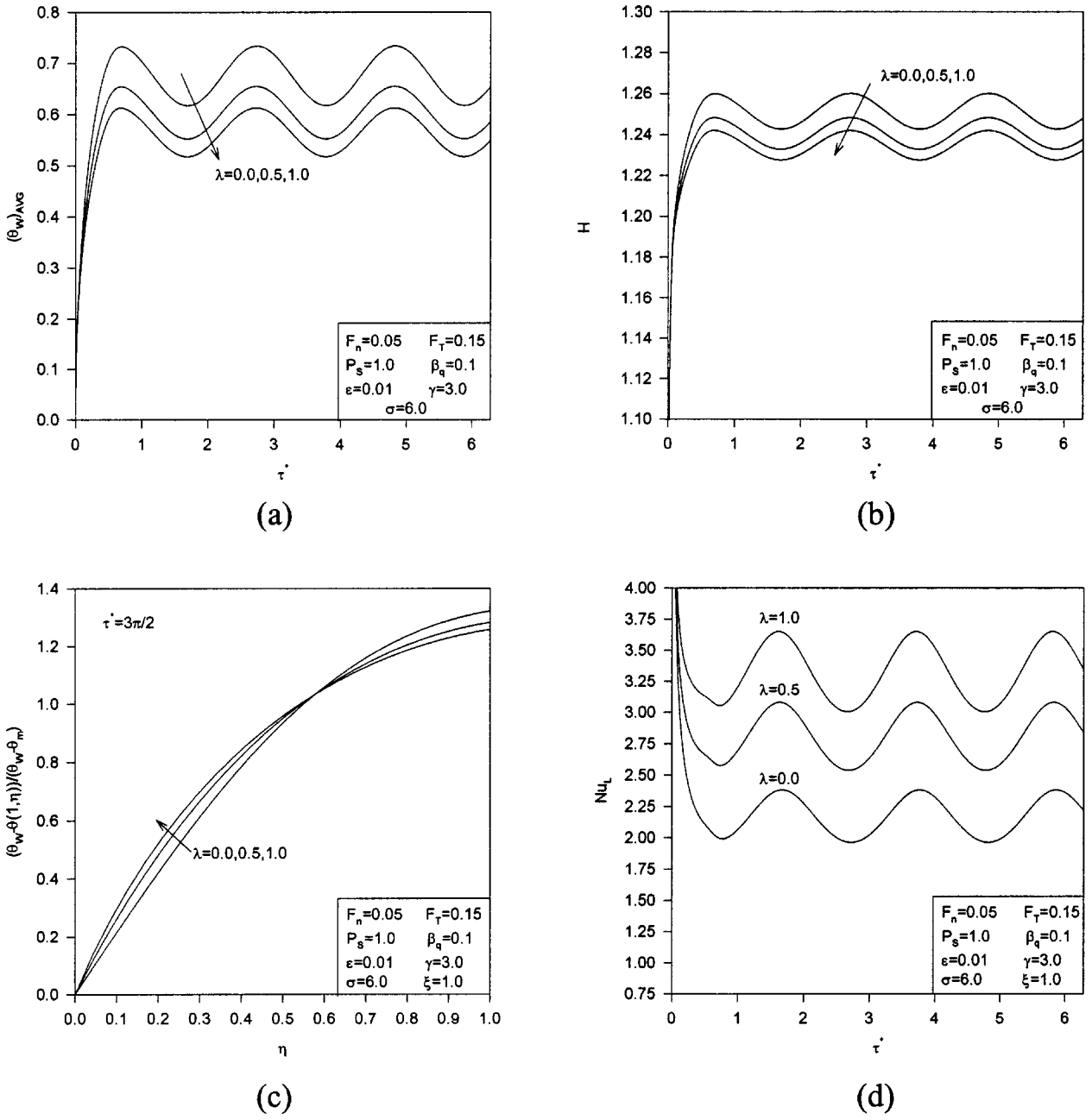

Fig. 3 Effects of the dimensionless thermal dispersion parameter λ on (*a*) dimensionless average lower plate temperature $(\theta_W)_{AVG}$, (*b*) dimensionless thickness *H*, (*c*) temperature Profile, and (*d*) exit Nusselt number Nu_L

the environment to minimize the variation in the lower plate temperature along the width direction.

In the presence of suspended ultrafine particles in the working fluid, the thermal conductivity of the working fluid composed from the pure fluid and suspensions is expected to vary due to the thermal dispersion (Xuan and Roetzel [13]). To account for these variations, the following model which is similar to Xuan and Roetzel [13] model that linearly relates the effective thermal conductivity of the working fluid to the fluid speed is utilized:

$$k(X,Y,\tau)=k_o(1+\lambda\sqrt{U^2(X,Y,\tau)+\Lambda^2V^2(X,Y,\tau)})=k_o\phi(X,Y,\tau) \tag{12}$$

where λ and Λ are the dimensionless thermal dispersion coefficient and the reference squeezing to lateral velocity ratio. They are

$$\lambda=C^*(\rho c_p)h_o(V_o+\omega B) \tag{13a}$$

$$\Lambda=\frac{\varepsilon\sigma}{12} \tag{13b}$$

where C^* is the coefficient of the thermal dispersion which depends on the diameter of the ultrafine particles, its volume fraction (ratio of the particles volume to the total thin film volume), and both fluid and ultrafine particles properties.

It is worth noting that the term ultrafine suspensions indicate that the particle is extremely small compared with the thickness of the thin film. The coefficient C^* is expected to increase by an increase in the diameter of the particles, their volume fraction, their surface roughness and the working fluid Prandtl number, $\Pr=(\rho c_p\upsilon)/k_o$. On the other hand, the stagnant thermal conductivity k_o increases with an increase in both the volume fraction and the surface area of the particles (Xuan and Roetzel [13]). In the

work of Li and Xuan [12], they showed experimentally that dilute mixture of ultrafine suspensions and water produced no significant change in the pressure drop compared to pure water which reveals that the viscosity is a weak function of the fluid dispersion for a dilute mixture.

Generally, flows inside thin films are in laminar regime and could be creep flows as in lubrication. Therefore, the low Reynolds numbers (the modified lateral Reynolds number $\mathrm{Re}_L=(V_o h_o)\varepsilon/\upsilon$ and the squeezing Reynolds number $\mathrm{Re}_S=(h_o^2\omega)/\upsilon$) flow model is adopted here. This model neglects the transient and convective terms in momentum equations, Eqs. (3) and (4). These terms become incomparable to the pressure gradient and diffusive terms for small squeezing frequencies and reference velocities. The application of this model to Eqs. (2)–(4) and the outcome of the dimensionalization of the energy equation, Eq. (5), result in the following reduced non-dimensionalized equations:

$$U=\frac{1}{2}\frac{\partial \Pi}{\partial X}H^2\left(\frac{Y}{H}\right)\left(\frac{Y}{H}-1\right) \tag{14}$$

$$V=\frac{dH}{d\tau}\left(3\left(\frac{Y}{H}\right)^2-2\left(\frac{Y}{H}\right)^3\right) \tag{15}$$

$$\frac{\partial}{\partial X}\left(H^3\frac{\partial \Pi}{\partial X}\right)=\sigma\frac{\partial H}{\partial \tau} \tag{16}$$

$$P_S\left(\frac{\partial \theta}{\partial \tau}+\frac{12}{\sigma}U\frac{\partial \theta}{\partial X}+V\frac{\partial \theta}{\partial Y}\right)=\frac{\partial}{\partial Y}\left(\phi\frac{\partial \theta}{\partial Y}\right) \tag{17}$$

Note that Eq. (17) is based on the assumption that the axial conduction is negligible when compared to the transverse conduction. The parameters σ and P_S are referred to as the squeezing number and the thermal squeezing parameter, respectively. They are defined as

$$\sigma=\frac{12}{1+\dfrac{V_o}{\omega B}} \qquad P_S=\frac{\rho c_p h_o^2\omega}{k_o} \tag{18}$$

Both inlet and exit dimensionless pressures are assumed constant and the following relationship is obtained between the inlet dimensionless pressure and the squeezing number based on the assumption that the reference velocity V_o represents the average velocity in the thin film at zero values of F_T and F_n:

$$\Pi_i=12-\sigma \tag{19}$$

Accordingly, the dimensionless pressure gradient, the dimensionless pressure and the average dimensionless pressure Π_{AVG} inside the thin film are related to the squeezing number through the following equations:

$$\frac{\partial \Pi(X,\tau)}{\partial X}=\frac{\sigma}{H^3}\frac{dH}{d\tau}\left(X-\frac{1}{2}\right)-(12-\sigma) \tag{20}$$

$$\Pi(X,\tau)=\frac{\sigma}{2H^3}\frac{dH}{d\tau}(X^2-X)-(12-\sigma)(X-1) \tag{21}$$

$$\Pi_{\mathrm{AVG}}(\tau)=-\frac{\sigma}{12H^3}\frac{dH}{d\tau}+\frac{(12-\sigma)}{2} \tag{22}$$

Thermal Boundary Conditions. The dimensionless thermal boundary conditions for the previously defined problem are taken as follows:

$$\theta(X,Y,0)=0, \quad \theta(0,Y,\tau)=0,$$

$$\frac{\partial \theta(X,0,\tau)}{\partial Y}=-(1+\beta_q\sin(\gamma\tau)), \quad \frac{\partial \theta(X,H,\tau)}{\partial Y}=0 \tag{23}$$

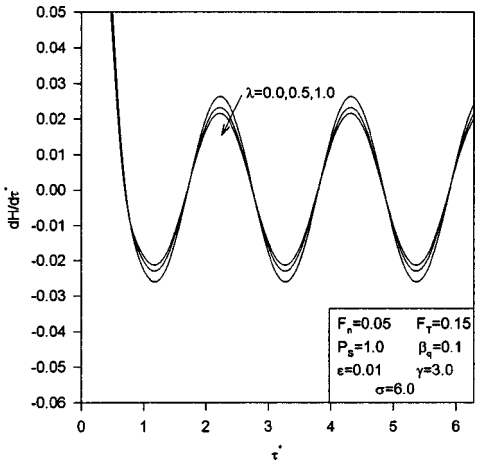

Fig. 4 Effects of the dimensionless dispersion parameter λ on the time variation of the dimensionless thin film thickness $dH/d\tau$

Based on the physical conditions, the Nusselt number is defined as

$$\mathrm{Nu}_L(X,\tau)\equiv\frac{h_c h_o}{k}=\frac{1}{\theta(X,0,\tau)-\theta_m(X,\tau)}=\frac{1}{\theta_W(X,\tau)-\theta_m(X,\tau)} \tag{24}$$

The parameter θ_m is the dimensionless mean bulk temperature. It is given as

$$\theta_m(X,\tau)=\frac{1}{U_m(X,\tau)H}\int_0^H U(X,Y,\tau)\,\theta(X,Y,\tau)\,dY$$
$$U_m(X,\tau)=\frac{1}{H}\int_0^H U(X,Y,\tau)\,dY \tag{25}$$

where U_m is the dimensionless average velocity at a given section.

3 Numerical Procedure

The procedure for the numerical solution is summarized as follows:

1) Initially, a value for H_T is assumed.

2) At the present time, the dimensionless thickness of the thin film H is determined by solving Eqs. (1), (8), (9), and (22), simultaneously, using an explicit formulation. The velocity field, U and V, is then determined from Eqs. (14), (15), and (20).

3) At the present time, the reduced energy equation Eq. (17) is transferred into one with constant boundaries using the following transformations: $\tau^*=\tau$, $\xi=X$ and $\eta=Y/H$. A tri-diagonal solution (Blottner [17]) was implemented along with a marching scheme. Backward differencing was chosen for the axial convective and transient terms and central differencing was selected for the derivatives with respect to η. The values of 0.008, 0.03, 0.001 were chosen for $\Delta\xi$, $\Delta\eta$, and $\Delta\tau^*$, respectively.

4) H_T is updated from Eq. (10) and steps (2)–(4) are repeated until

$$\left|\frac{(H_T)_{\mathrm{new}}-(H_T)_{\mathrm{old}}}{(H_T)_{\mathrm{new}}}\right|<10^{-6} \tag{26}$$

5) The converged solution for the flow and heat transfer inside the thin film is determined at the present time.

6) Time is advanced by $\Delta\tau^*$ and steps (1)–(5) are repeated.

Numerical investigations were performed using different mesh sizes and time steps to assess and ascertain grid and time step independent results. It was found that any reduction in the values of $\Delta\xi$, $\Delta\eta$ and $\Delta\tau^*$ below $\Delta\xi=0.008$, $\Delta\eta=0.03$, and $\Delta\tau^*=0.001$ results in less than 0.2% error in the results.

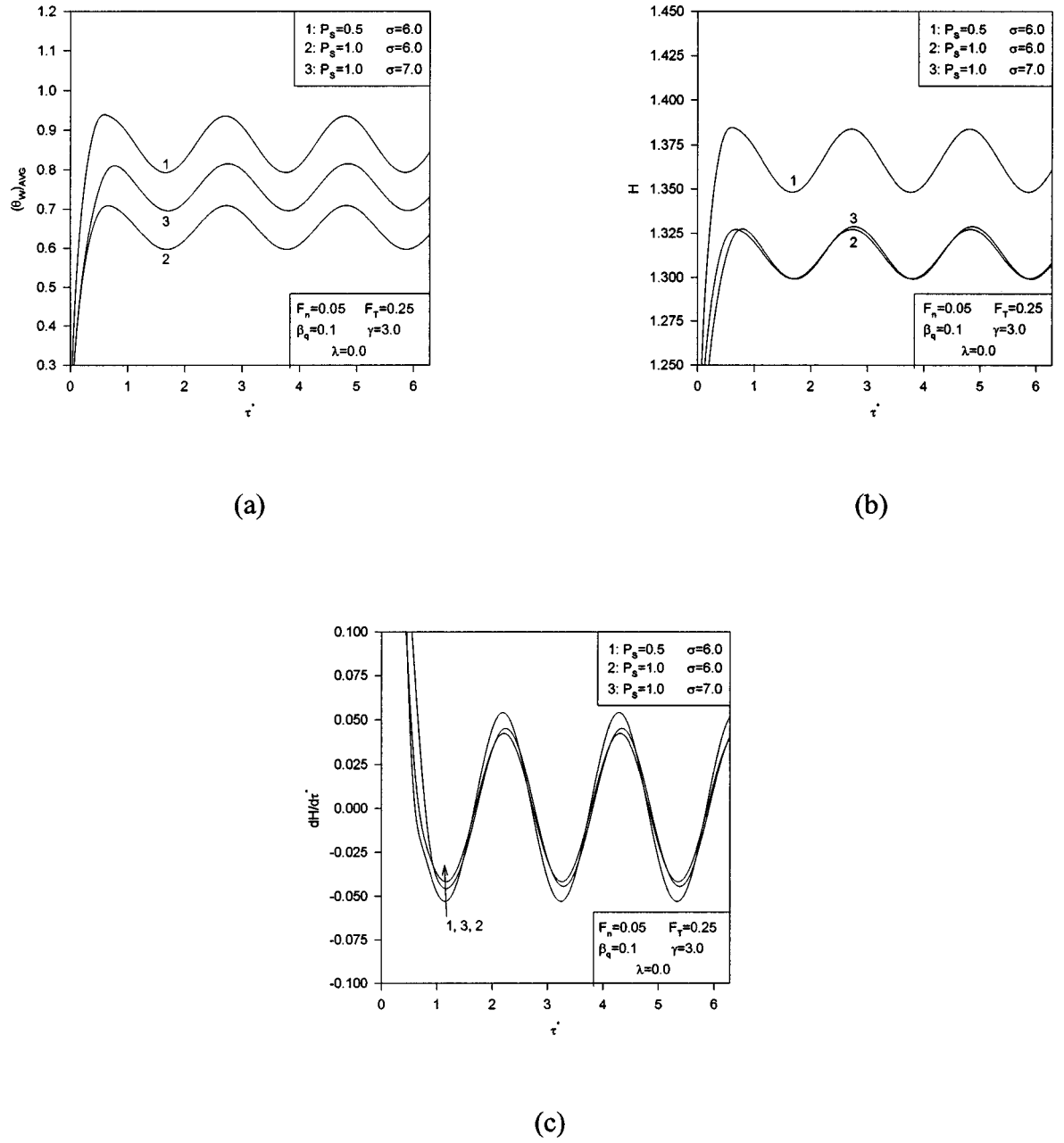

Fig. 5 Effects of the thermal squeezing parameter P_S and the squeezing number σ on (a) dimensionless average lower plate temperature $(\theta_W)_{AVG}$, (b) dimensionless thin film thickness H, and (c) $dH/d\tau$

In the results, the maximum value of the parameters P_S is chosen to be 1.0. Beyond this value, the error associated with the low Reynolds number model will increase for moderate values of the dimensionless thermal expansion parameter, fixation parameter, and the Prandtl number. As an example, the order of transient and convective terms in the momentum equations were found to be less 1.0% that of the diffusive terms for $P_S=1.0$, $\mathrm{Pr}=6.0$, $F_n=0.05$, $F_T=0.25$, $\beta_q=0.1$, and $\sigma=6.0$. The parameters correspond, for example, to a thin film filled with water and having $B=D=60\,\mathrm{mm}$, $h_o=0.3\,\mathrm{mm}$, $d_s=0.5\,\mathrm{mm}$, $\omega=2.0\ \mathrm{s}^{-1}$, $V_o=0.12\,\mathrm{m/s}$, and $E=1.6(10^5)$ pa.

4 Results and Discussions

Ideal gases produce a 15% increase in the void volume at room conditions for a 45°C maximum temperature difference. Further, Li and Xuan [12] reported a 60% increase in the convective heat transfer coefficient for a volume fraction of copper ultrafine particles of 2.0%. Accordingly, the parameters F_T and λ were varied until comparable changes have been attained in the dimensionless thin film thickness and the Nusselt number.

4.1 Effects of Dimensionless Thermal Expansion Parameter. Figure 2(*a*) illustrates the effects of the dimensionless thermal expansion parameter F_T on the dimensionless thickness H of the thin film. The parameter F_T can be increased either by an increase in the volumetric thermal expansion coefficient of the stagnant fluid or by an increase in dimensional reference temperature $(q_o h_o)/k_o$. Both factors make the flexible complex seal softer thus dimensionless thickness H is increased as F_T increases as shown in Fig. 2(*a*). This allows more coolant to flow causing reductions in the average dimensionless lower plate's temperature

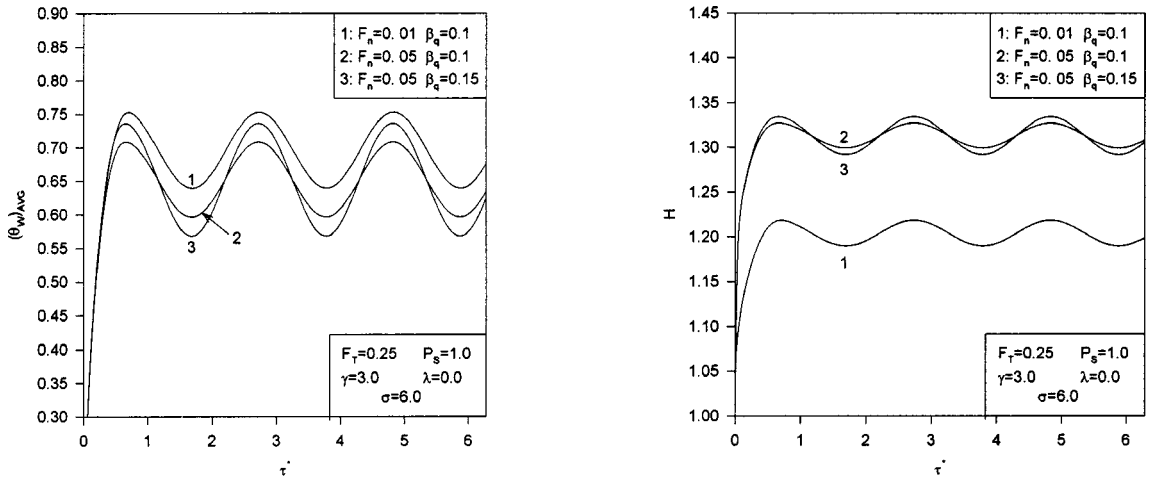

Fig. 6 Effects of the fixation parameter F_n and the dimensionless thermal load amplitude β_q on (a) dimensionless average lower plate temperature $(\theta_W)_{AVG}$, and (b) dimensionless thin film thickness H

$(\theta_W)_{AVG}$ as clearly seen in Fig. 2(*b*) which can provide additional cooling to any heated surface such as surfaces of electronic components.

Figure 2(*b*) can be also read as follows: as thermal load increases, the average lower plate's temperature increases however this increase can be reduced by using a flexible complex seal. This additional cooling is obtained with no need for external controlling devices which provides extra safety for an electronic component, as an example for a heated surface, when their thermal loads increase over the projected capacity. The fluctuation rate at the upper plate, $|dH/d\tau|$, is noticed to increase as F_T increases as shown in Fig. 2(*c*). This could be an advantage for the cooling process especially at high levels of fluctuation rates since it will enhance the thermal dispersion in the coolant when suspended ultrafine particles are present. The Nusselt number is decreased as F_T increases as shown in Fig. 2(*d*) because it is inversely proportional to H. This is the reason for the fact that the percentage decrease in lower plate temperatures is lower than the percentage increase in the thin film thickness as F_T increases.

4.2 Effects of Dimensionless Thermal Dispersion Parameter. Figure 3(*a*) describes the effects of the dimensionless thermal dispersion parameter λ of the coolant fluid on the average lower plate's temperature of the thin film. This parameter can be increased either by increasing the diameter of the ultrafine particles or increasing the roughness of these particles while keeping a fixed volume fraction inside the coolant. This insures that thermal squeezing parameter remains constant. Figure 3(*a*) physically shows that the thermal dispersion can provide additional cooling to a heated element, thus it causes an additional reduction in the average dimensionless lower plate temperature $(\theta_W)_{AVG}$. Part of this cooling is due to the expansion process since it results in flooding of the working fluid which increases the irregularity and the random motion of the particles. This causes additional enhancements in the energy exchange rate. Another Part for the enhancement in the cooling is attributed to the fact that the noise in the thermal load, especially those having heterogeneous fluctuation rates, produces additional squeezing due to the velocities that appear in Eq. (12).

Due to the reduction in the lower plates temperatures as λ increases, the dimensionless thin film thickness decreases as λ increases as depicted in Fig. 3(*b*). It is worth noting that additional enhancements in the thermal dispersion effect are expected as both the perturbation parameter and the squeezing number increase as suggested by Eqs. (12) and (13). Both effects result in a magnification in the fluctuation rates in the flow which causes additional increases in the cooling process. In our example, the perturbation parameter and the fluctuation rates are small and their effects are not noticeable.

The reduction in thermal resistance across the transverse direction when λ increases causes the temperature profiles to be more flattened as λ increases as seen in Fig. 3(*c*). Accordingly, the Nusselt number increases as λ increases as seen in Fig. 3(*d*). It can be seen in Fig. 4 that the fluctuation rate at the upper plate, $|dH/d\tau|$, decreases as λ increases. As a result, ultrafine particle suspensions inside thin films supported by flexible complex seals not only cause enhancements in heat transfer but also make these thin films dynamically more stable. In this example, an increase in λ between zero and unity cause a reduction in the average lower temperature by dimensionless temperature of 0.12 and an increase in the Nusselt number by 50%.

4.3 Effects of Thermal Squeezing Parameter and the Squeezing Number. Figure 5(*a*) shows the effects of the thermal squeezing parameter P_S and the squeezing number σ on the average dimensionless lower plate temperature $(\theta_W)_{AVG}$. It is clearly seen that the lower plate temperature decreases as P_S increases and as σ decreases. Both effects tend to increase thermal convection which decreases the lower plate temperature. The increase in P_S means an increase in the thermal capacitance of the working fluid and a decrease in σ indicates an increase in the reference velocity. Accordingly, the dimensionless thickness H decreases as P_S increases as shown in Fig. 5(*b*). In addition, the pressure force inside the thin film increases as σ decreases causing an increase in H_p while H_T decreases as σ decreases due to the enhancement in the cooling. As a result, the thin film thickness is noticed to vary slightly when σ decreases as illustrated in Fig. 5(*b*). As seen in Fig. 5(*c*), the fluctuation rate at the upper plate is found to increase as σ increases while it decreases as P_S increases. Also, the fluctuation rate at the upper plate is shown to more pronounced to P_S more than to σ.

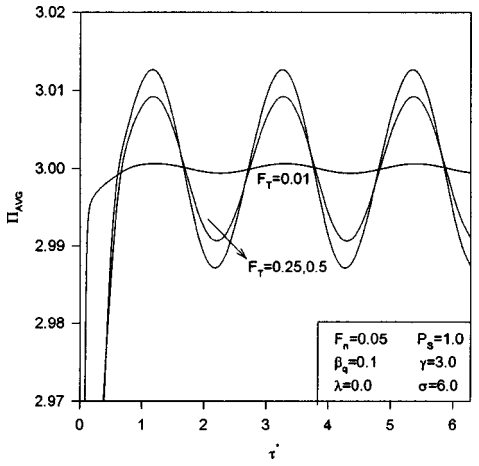

Fig. 7 Effects of the dimensionless thermal expansion parameter F_T on the average dimensionless pressure inside the thin film Π_{AVG}

4.4 Effects of the Fixation Parameter and the Amplitude of the Thermal Load. Figure 6(*a*) shows the effects of the fixation parameter F_n and the dimensionless amplitude of the thermal load β_q on the average dimensionless lower plate temperature $(\theta_W)_{\mathrm{AVG}}$. Since soft seals possess large F_n values, H increases and lower plate temperature decreases as F_n increases as shown in Figs. 6(*a*) and 6(*b*). Further, these figures show that an increase in the amplitude of the heat flux results in an increase in the fluctuation rate at the upper plate and the lower plate temperature but their mean values are almost unaffected.

4.5 Effects of Dimensionless Thermal Expansion Parameter on Average Pressure. Figure 7 shows the effects of F_T on the average dimensionless pressure inside a thin film supported by a flexible complex seal. The periodic behavior of the heat flux results in a periodic variation in the average pressure inside the thin film. The fluctuation in the pressure increases as F_T increases as seen in Fig. 7. Further, it is noticed that the thermal load exceeding the internal pressure by a phase shift approximately equal to $\pi/(2\gamma)$. According to Fig. 7, the induced pressure pulsation can be used as a measurable quantity in order to read, diagnose or for feedback to control the heating source.

5 Conclusions

Flow and heat transfer inside thin films supported by soft seals separating voids of stagnant fluid having a large value the volumetric thermal expansion coefficient have been analyzed in this work in the presence of suspended ultrafine particles in the coolant fluid. The thermal load was taken to be periodic. The governing continuity, momentum and energy equations were nondimensionalized and reduced to proper forms for small Reynolds numbers and negligible axial conduction. The deformation of the seal was related to the internal pressure and lower plate's temperature by theory of elasticity and a linearized model for thermal expansion. The velocity field and the solution of the energy equation were found using an iterative scheme and a marching technique in both the axial direction and time domains.

Increases in the coefficient of thermal expansion, dispersion parameter, fixation parameter and thermal squeezing parameter were found to cause enhancements in the cooling process. The thermal dispersion parameter was found to increase the stability of the thin film by decreasing fluctuation rates in the flow. The noise in the thermal load was found to affect the amplitude of the thin film thickness, Nusselt number and the lower plate temperature as well as their variations rate. However, it has a negligible effect on their mean values. Finally, flexible complex seals are useful in enhancing the cooling and can be used for additional purposes such as for diagnosing functions for heating sources as long as they possess large thermal expansion coefficient.

Acknowledgments

We acknowledge partial support of this work by DOD/DARPA/DMEA under grant number DMEA90-02-2-0216.

Nomenclature

A^* = a void dimension parameter
B = thin film length
C_F = volumetric thermal expansion correction factor
C^* = coefficient of thermal dispersion
c_p = average specific heat of the working fluid or the dilute mixture
D = width of the thin film
d_s = characteristic parameter of the seal
E = effective modulus of elasticity for the sealing assembly
G = width of the void
F_n = fixation parameter
F_T = dimensionless thermal expansion parameter
H, h, h_o = dimensionless, dimensional and reference thin film thicknesses
h_c = convective heat transfer coefficient
k = thermal conductivity of the working fluid or the dilute mixture
k_o = reference thermal conductivity of the fluid
Nu_L = lower plate's Nusselt number
P_S = thermal squeezing parameter
p = fluid pressure
q_o = reference heat flux at the lower plate
T, T_1 = temperature in fluid and the inlet temperature
t = Time
V_o = reference axial velocity
U, u = dimensionless and dimensional axial velocities
V, v = dimensionless and dimensional normal velocities
X, x = dimensionless and dimensional axial coordinates
Y, y = dimensionless and dimensional normal coordinates

Greek Symbols

β_q = dimensionless amplitude of the thermal load
β_T = coefficient of volumetric thermal expansion of the stagnant fluid
ε = perturbation parameter
γ = dimensionless frequency
μ = averaged dynamic viscosity of the working fluid or the dilute mixture
θ, θ_m = dimensionless temperature and dimensionless mean bulk temperature
θ_W = dimensionless temperature at the lower plate
ρ = averaged density of the working fluid or the dilute mixture
υ = averaged kinematic viscosity of the working fluid or the dilute mixture
τ, τ^* = dimensionless time
σ = squeezing number
ω = reciprocal of a reference time (reference squeezing frequency)
η = variable transformation for the dimensionless Y-coordinate
λ = dimensionless thermal dispersion parameter
Π = dimensionless pressure
Π_i = dimensionless inlet pressure
Λ = reference lateral to normal velocity ratio

References

[1] Moon, S. H., Yun, H. G., Hwang, G., and Choy, T. G., 2000, ''Investigation of Packaged Miniature Heat Pipe for Notebook PC Cooling,'' Int. J. Microcircuits Electron. Packag., **23**, pp. 488–493.

[2] Fedorov, A. G., and Viskanta, R., 2000, ''Three-Dimensional Conjugate Heat Transfer in the Microchannel Heat Sink for Electronic Packaging,'' Int. J. Heat Mass Transfer, **43**, pp. 399–415.

[3] Zhu, L., and Vafai, K., 1999, ''Analysis of a Two-Layered Micro Channel Heat Sink Concept in Electronic Cooling,'' Int. J. Heat Mass Transfer, **42**, pp. 2287–2297.

[4] Bowers, M. B., and Mudawar, I., 1994, ''Two-Phase Electronic Cooling Using Mini-Channel and Micro-Channel Heat Sink,'' ASME J. Electron. Packag., **116**, pp. 290–305.

[5] Hadim, A., 1994, ''Forced Convection in a Porous Channel With Localized Heat Sources,'' ASME J. Heat Transfer, **116**, pp. 465–472.

[6] Khaled, A.-R. A., and Vafai, K., 2002, ''Flow and Heat Transfer Inside Thin Films Supported by Soft Seals in the Presence of Internal and External Pressure Pulsations,'' Int. J. Heat Mass Transfer, **45**, pp. 5107–5115.

[7] Langlois, W. E., 1962, ''Isothermal Squeeze Films,'' Q. Appl. Math., **20**, pp. 131–150.

[8] Hamza, E. A., 1992, ''Unsteady Flow Between Two Disks With Heat Transfer in the Presence of a Magnetic Field,'' J. Phys. D, **25**, pp. 1425–1431.

[9] Bhattacharyya, S., Pal, A., and Nath, G., 1996, ''Unsteady Flow and Heat Transfer Between Rotating Coaxial Disks,'' Numer. Heat Transfer, Part A, **30**, pp. 519–532.

[10] Debbaut, B., 2001, ''Non-Isothermal and Viscoelastic Effects in the Squeeze Flow Between Infinite Plates,'' J. Non-Newtonian Fluid Mech., **98**, pp. 15–31.

[11] Khaled, A. R. A., and Vafai, K., 2003, ''Flow and Heat Transfer Inside Oscillatory Squeezed Thin Films Subject to a Varying Clearance,'' Int. J. Heat Mass Transfer, **46**, pp. 631–641.

[12] Li, Q., and Xuan, Y., 2002, ''Convective Heat Transfer and Flow Characteristics of Cu-Water Nanofluid,'' Sci. China, Ser. E: Technol. Sci., **45**, pp. 408–416.

[13] Xuan, Y., and Roetzel, W., 2000, ''Conceptions for Heat Transfer Correlation of Nanofluids,'' Int. J. Heat Mass Transfer, **43**, pp. 3701–3707.

[14] Friis, E. A., Lakes, R. S., and Park, J. B., 1988, ''Negative Poisson's Ratio Polymeric and Metallic Materials,'' J. Mater. Sci., **23**, pp. 4406–4414.

[15] Eastman, J. A., Choi, S. U. S., Li, S., Yu, W., and Thompson, L. J., 2001, ''Anomalously Increased Effective Thermal Conductivities of Ethylene Glycol-based Nanofluids Containing Copper Nanoparticles,'' Appl. Phys. Lett., **78**, pp. 718–720.

[16] Norton, R. L., 1998, *Machine Design; An Integrated Approach*, Prentice-Hall, New Jersey.

[17] Blottner, F. G., 1970, ''Finite-Difference Methods of Solution of the Boundary-Layer Equations,'' AIAA J., **8**, pp. 193–205.

A Study of Fin Effects in the Measurement of Temperature Using Surface-Mounted Thermocouples

T. C. Tszeng

V. Saraf[1]

Thermal Processing Technology Center,
Department of Mechanical,
Materials and Aerospace Engineering,
Illinois Institute of Technology,
Chicago, IL 60616

The present study addresses the effects of thermocouples on the measured temperature when such thermocouples are mounted directly on the surface of the object. A surface-mounted thermocouple is a very convenient way of measuring the surface temperature. However, the heat conduction into/from the thermocouple wire changes the local temperature at the thermocouple junctions along with the immediate vicinity of the thermocouple. As a consequence, the emf appearing at the thermocouple terminals does not correspond to the actual surface temperature. In this paper, we first discuss the general characteristics of the enhanced heating/cooling due to the so-called "fin effects" associated with the surface-mounted thermocouples. An embedded computational model is then developed so that the model can be used in conjunction with a regular FEM model for the multidimensional calculation of the heating or cooling of a part. The embedded computational model is shown to offer very accurate calculation of the temperature at the junction of thermocouple wire. The developed computational model is further used in the inverse heat transfer calculation for a Jominy end quench experiment. [DOI: 10.1115/1.1597622]

Keywords: Heat Transfer, Measurement Techniques, Numerical Methods, Thermocouples

Introduction

Temperature is one of the controlling parameters in many thermal processing technologies of metals. It is crucial to have knowledge of the changing temperature in the part being processed so that the target product quality can be achieved. In general, the knowledge of changing temperature in the part can be used in two broad areas. In the first area, temperature is used as a signal for process control. In the second area, the temperature is used as a parameter to infer the part property/quality at the end of processing. Usually, this is carried out in the stage of process design and development. For example, FEM (finite element method) based computational analyses have been performed intensively to study the temperatures in the part for better understanding and control of the product properties (Majorek et al. [1], Wallis and Craighead [2], Schroder [3], Zhou and Tszeng [4]). In experimental study, the parts may be instrumented with temperature sensors, and go through the actual process. Collected temperature histories are then used for further improvement of the process being developed.

Thermocouples are one of the most commonly used temperature sensing techniques for monitoring the part temperature in thermal processing of metals, among many other applications. If there is a need to know the temperature inside the part, the junction of thermocouple wires has to be embedded in a hole that is drilled into the part. Practical difficulties do exist that can prevent the accurate and reliable reading of the interior temperatures (Park et al. [5], Cross et al. [6], Saraf [7]). In some applications, thermocouples are employed to acquire the temperatures at locations very close to the surface so that the temperature histories will be used in the inverse heat transfer calculation for determining the surface heat transfer coefficients (Cross et al. [6], Saraf [7], Tszeng [8], Beck and Osman [9], Beck et al. [10]). The requirement of using surface temperature for inverse calculation is based on the fact that better solution stability can be achieved (Cross et al. [6], Tszeng [8], Beck et al. [10], Gummadam and Tszeng [11]). Thermocouple placed in a hole drilled from the opposite side of the surface can never reach to the actual surface. Further, it is very difficult to know the exact location of the thermocouple junction. Even a small error in the thermocouple location under the surface can lead to a large temperature difference between the surface and the thermocouple junction in the situations when large temperature gradient exists.

While infrared technique is available for the measurement of surface temperature, it is limited to the situations that the medium is transparent to the infrared light. Many industrial thermal processing for metals are carried out in the opaque media including water, oil, polymer, etc. For such applications, thermocouples are still the commonly used technique for temperature measurement.

When thermocouple wires are mounted directly on the object surface (usually by spot weld), the temperature appearing at the thermocouple junction is thought to be the surface temperature. However, among other difficulties in chemical and mechanical origins, there are important issues needed to be resolved for the surface-mounted thermocouples to render accurate temperature sensing. In order to facilitate the discussion, it is important to recognize the different types of surface-mounted thermocouples. Thermocouples can be installed on the surface in at least two common configurations. For the bead-type junctions, the two dissimilar thermocouple wires (e.g., Alumel and Chromel for K-type thermocouples) first form a junction by welding. The junction is then attached to the object surface by spot welding. A schematic is shown in Fig. 1. The generated emf is uniquely related to the temperature that appears at the bead junction. Because of the finite volume of the bead and the possibly large temperature gradient under the surface, the temperature at the junction may not be exactly the same as that on the undisturbed surface of the object.

The second type of junction is called intrinsic junction, because the material whose temperature is to be measured forms a part of the thermoelectric circuit. Usually two dissimilar thermocouple

[1]Current address: Computer Aided Engineering Group, Ladish Company, Inc., Cudahy, WI 53110.

Contributed by the Heat Transfer Division for publication in the JOURNAL OF HEAT TRANSFER. Manuscript received by the Heat Transfer Division January 15, 2002; revision received April 22, 2003. Associate Editor: A. F. Emery.

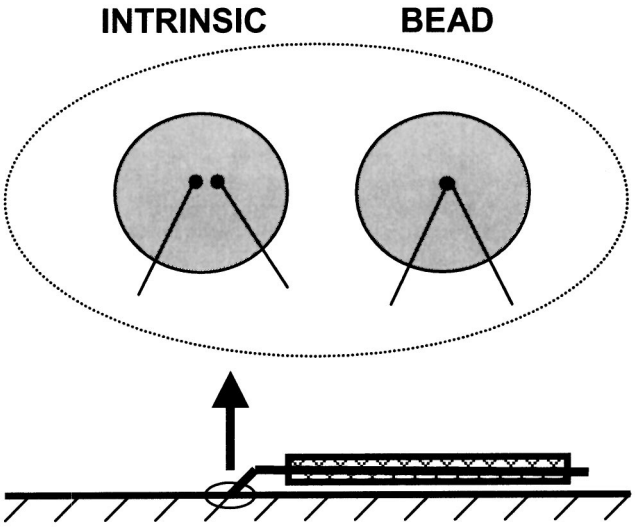

Fig. 1 Two types of junction for installing surface-mounted thermocouples

wires are separately spot welded to the surface directly; with the spacing between the two wires ranges between one to two wire diameters (Park et al. [5], Saraf [7]). A schematic of the installation is shown in Fig. 1. Park et al. [5] theorized that the generated emf in intrinsic junctions is corresponding to a ''virtual junction'' that lies at a location somewhere between the two physical junctions. Based on this postulation, there is a need for them to know the temperature at the virtual junction although its location is not known. However, according to the law of homogeneous thermocouple circuit [12,13], the homogeneous metal connecting the two junctions (referring to the object material between the two junctions) of same temperature in the electric circuit does not contribute to the generated emf, even there is temperature gradient in the connecting metal. Contrary to that stated in Park et al. [5], the generated emf is only related to the temperatures at the two junctions where the thermocouple wires meet the object. In the situations when there is a temperature difference between the two junctions during rapid cooling/heating, a three-wire thermocouple circuit may become needed [13].

Since the junctions lie on the object surface for intrinsic junctions, the temperature appearing at the thermocouple junction would be very close to the actual surface temperature. There are many factors that can contribute to the errors involved with the surface temperature measurement using intrinsic junctions [14]. For example, heat conduction into or from the attached thermocouple wires can alter the temperature at the thermocouple junction as well as its immediate vicinity. This problem is also common to the bead-type junction mentioned earlier. A number of methods and simplifying assumptions have been utilized in modeling the transient response of thermocouples [14–18]. Hennecke and Sparrow [14] first developed the analytical solution of the temperature distribution in a semisolid when a circular heat sink is present at the surface. Then the solution to the problems of surface-mounted thermocouples was obtained by matching the heat flux at the thermocouple junction. In that study, the lateral heat loss per unit length of the thermocouple was determined by the temperature difference at surface and the thermal resistance which was assumed to be known. In fact, the thermal resistance on the surface of thermocouple wire should be formulated as [15,16]

$$R = \frac{1}{2\pi r h} + \frac{\ln(r_o/a)}{2\pi k_i}, \tag{1}$$

where r is the radius of thermocouple wire, r_o and k_i are the outer radius and thermal conductivity of the insulation layer, and h is the heat transfer coefficient on the outer surface. Therefore, the thermal resistance can not be considered as a known variable. Keltner and Beck [16] derived several analytical relationships for error corrections based on Laplace transforms for simple measured response like step or ramp temperature changes. Litkouhi and Beck [17] developed a multimode unsteady surface element method due to step change in substrate temperature. Segall [18] modified the method of Keltner and Beck [16] by using Duhamel's integral to include intrinsic thermocouples with a measured response that can be approximated by an arbitrary third-order polynomial. All of the above-mentioned solution methods assumed the thermal properties to be temperature-independent. Park et al. [5] examined this subject by numerical calculation using FEM, and concluded that significant error can be introduced into the measured temperature signals by the fin effects associated with the direct attachment of thermocouple wires to the surface. The two-dimensional numerical model used in the work of Park et al. [5] requires the thermocouple wire to lie along the center axis of the coordinate system. Because of this constraint, only one thermocouple is allowed on an object in a two-dimensional axisymmetric model. An industrial-scale study on the thermal processing of a critical part usually requires multiple thermocouples on the part. In this situation, three-dimensional models are needed. Given the fact that a thermocouple wire can be as small as 0.02 mm in diameter for better response time, FEM meshing involving two length scales in three dimensions can be difficult and impractical.

In this paper, we first discuss the general characteristics of the enhanced heating/cooling due to the so-called ''fin effects'' associated with the surface-mounted thermocouples. An embedded computational model is then developed so that the multiple thermocouples can be used in conjunction with a regular FEM model for the multidimensional calculation of the heating or cooling of a part. We examine the solution accuracy and its sensitivity to the element size in the parent object. The developed computational model is further used in the inverse heat transfer calculation for a Jominy end quench experiment.

Temperature Affected by Surface-Mounted Thermocouples

The effects of surface-mounted thermocouple on the object temperature are first examined in detail. Although the thermocouple junction considered in this section is of the intrinsic type, with some modification to the wire size, the model can be used to analyze the bead-type junctions. The computational model is based on the FEM. A simple model is shown in Fig. 2(a) that depicts an axisymmetric object with a thermocouple wire mounted at the center of the top surface. The model considers that the thermocouple wire is exposed to the environment without any insulation or protective sleeve. Due to the symmetry, only half of the objects need to be modeled. The elements are four nodes linear element. Detailed background information about the thermal model by FEM can be found in reference [19]. The thermocouple wire is 0.4 mm in diameter and 10 mm in length. The length of 10 mm in the model is considered to be the exposed portion of the thermocouple wire. The FEM mesh is much finer in the region close to the junction so that enough spatial resolution is provided. It is understood that there are actually two junctions with a spacing of about one or two wire diameters for intrinsic junction. For the time being, we assume that there is no interaction between the two junctions. This assumption will be examined in a later part of this paper.

The top surface of the parent object and the thermocouple wire surface are exposed to the environment; all other surfaces are assumed to have zero heat flux (insulated). Since the thermocouple wire in the model is relatively long compared with its diameter, the thermal boundary condition at its far end can be

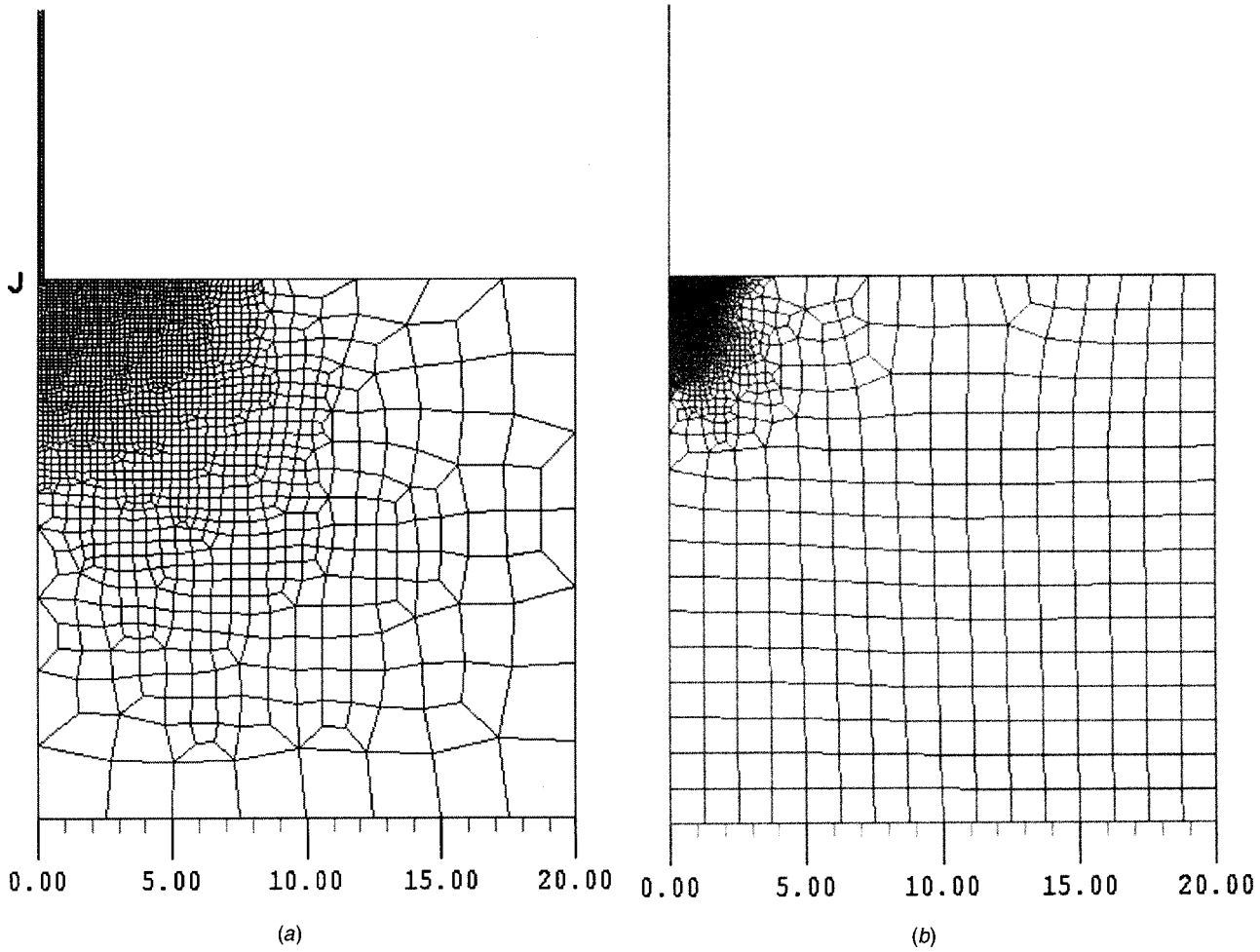

Fig. 2 The simple two-dimensional axisymmetric model and FEM mesh for surface-mounted thermocouple on an object. The mesh only represents symmetric half of the domain. The top surface of the parent object and the thermocouple wire surface are exposed to the environment; all other surfaces are assumed to have zero heat flux (insulated). (a) Thermocouple wire diameter=0.4 mm; (b) Wire diameter=0.04 mm.

assumed to be insulted [14]. However, the reality is that such boundary condition does not have great effects on the resulted temperature field. The interfacial heat transfer between the object and the environment is governed by the equation, $q=h(T_s-T_\infty)$, in which, q is the surface heat flux, h is the heat transfer coefficient, T_s is the surface temperature, and T_∞ is the environment temperature. Note that the convective and radiation heat transfer are both accounted for in the global heat transfer coefficient, h. In the present case, a constant heat transfer coefficient $h=2$ kW/m^2/K is applied throughout the top surface of the object including the thermocouple. The environment temperature remains constant at 20°C. The initial temperature distribution is assumed to be uniformly at 945°C in the object. While the FEM allows different thermophysical properties for each material in the model, the same thermophysical properties are assumed for the object and the thermocouple, of which the thermal conductivity $k=15$ W/m/K and heat capacity $\rho c=5\times10^6$ J/m^3/K. Note that these data are used here mainly for the purpose of illustration, the actual properties are not only different between thermocouple wire and the object material, but also temperature dependent. This issue will be discussed in a later part of this paper.

The temperature picked up by the thermocouple is corresponding to the temperature at the object-thermocouple junction. The junction has a cross section same as that of the thermocouple; it is possible that there is some temperature variation at the junction. Since the emf is related to the temperature at the junction, it is therefore interesting to know the distribution of temperature at the junction. We will examine the actual temperature variation at the junction in a later part of this paper. The computation is carried out by the FEM package HOTPOINT [19]. The calculated temperature distribution in the vicinity of thermocouple junction at 0.1 second in quenching is shown in Fig. 3. At that time, the temperature is about 830°C at the thermocouple junction, compared with the undisturbed surface temperature of about 870°C. Apparently, the installation of thermocouple enhances the local cooling in the vicinity of junction by conducting heat from the surface into the thermocouple and then dissipating in the environment.

The temperature picked up by the thermocouple is corresponding to the temperature at the object-thermocouple junction. The junction has a cross section the same as that of the thermocouple. According to Fig. 3, the temperature is not evenly distributed in the plane of the thermocouple junction. It is interesting to examine the variation of the temperature at the junction. The histories of temperature respectively corresponding to the center and the edge of the junction are shown in Fig. 4. In the earlier stage (the first 0.04 second), the edge of the junction is cooled faster that that at the center. Afterward, the temperature at the center drops much faster. The temperature difference between the center and the edge nonetheless keeps mostly constant later in the quenching. The same figure also shows the undisturbed surface temperature at a location 5 mm from the center of the junction. At one second in

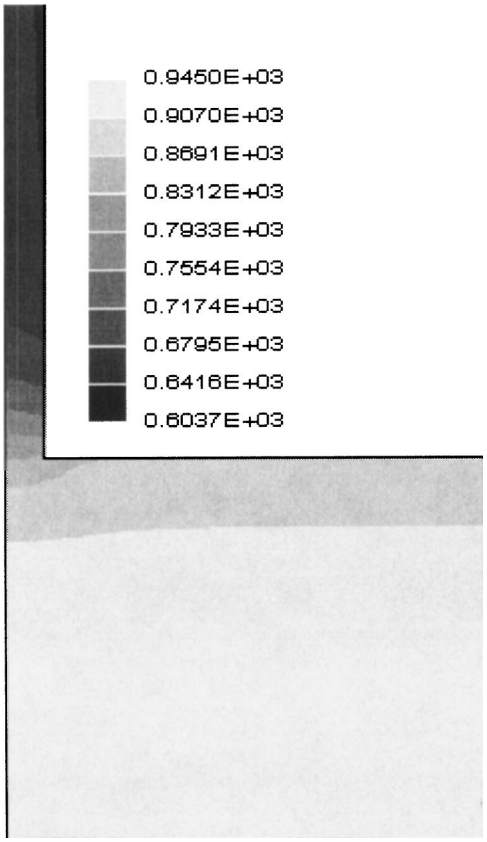

Fig. 3 Distribution of temperature in the vicinity of thermocouple junction at 0.1 second in quenching. Initial temperature is 945°C. Wire diameter=0.4 mm

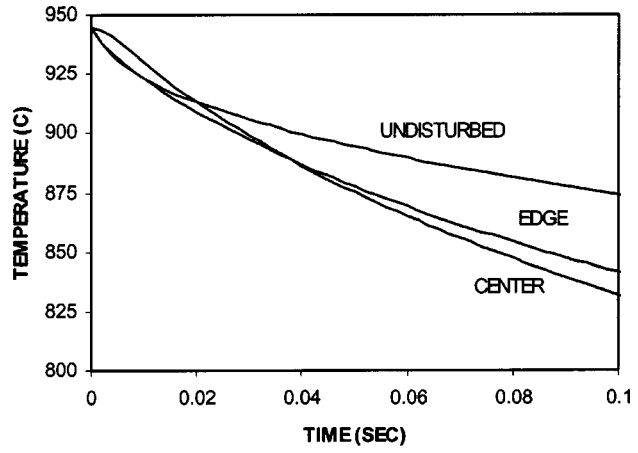

(*a*)

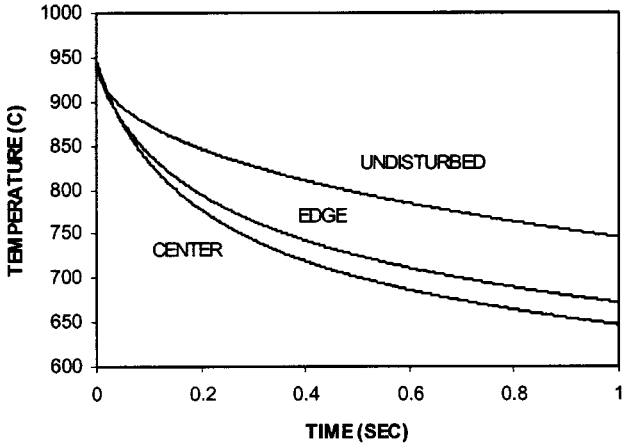

(*b*)

Fig. 4 Temperature histories at the center and at the edge of the thermocouple junction, respectively. Wire diameter=0.4 mm. Also shown is the undisturbed temperature at the surface (at a location 5 mm from the center of the junction). (a) In the first 0.1 second; (b) In the first one second.

the quenching, the difference between the temperature at the center of the junction and the undisturbed surface temperature enlarges to about 100°C.

In the following case, the effects of thermocouple wire diameter is examined. All other parameters remain the same as that of the previous case. The FEM mesh is shown in Fig. 2(b). The histories of temperature respectively corresponding to the center and the edge of the junction are shown in Fig. 5. Similar to the previous case corresponding to a thermocouple wire diameter of 0.4 mm, the center of the junction is cooled faster that that at the edge. The temperature difference between the center and the edge nonetheless keeps mostly constant later in the quenching. The same figure also shows the undisturbed surface temperature at a location 5 mm from the center of the junction. Again, the difference between the temperature at the center of the junction and the undisturbed surface temperature is very significant.

A brief comparison between the effects of thermocouple wire diameter is given in Fig. 6. In this figure, the temperatures at the center of the junction for both cases are shown. While both cases indicate the significance of the fin effects due to surface-mounted thermocouples, the smaller wire diameter brings less overall impact to the junction temperature. The less fin effect corresponding to a smaller wire diameter is mainly due to the smaller cross-sectional area for heat conduction through the junction. Theoretically, it can be postulated that the effect of thermocouple should diminish to nil when the wire diameter approaches to zero.

Figure 6 indicates that the temperature at the junction of thermocouple with smaller wire diameter decreases faster in the earlier stage of quenching. Experimentally, Saraf [7] measured the temperatures from intrinsically mounted thermocouples of two wire diameters (0.32 mm versus 0.038 mm) on a 4142 steel disk of 66.8 mm-diameter×9.52 mm-height immersed horizontally in

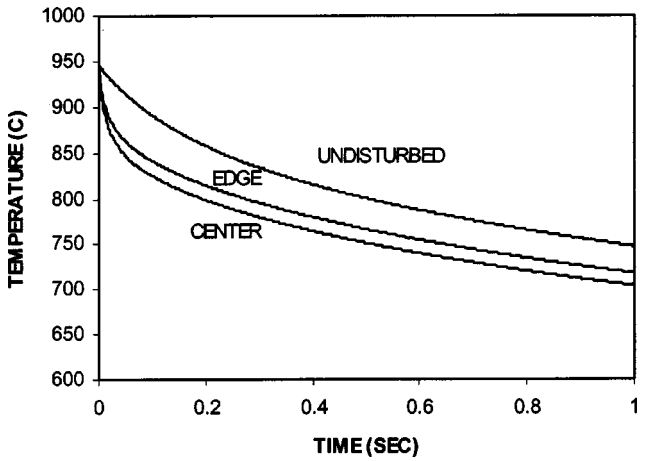

Fig. 5 Temperature histories at the center and at the edge of the thermocouple junction, respectively. Wire diameter=0.04 mm. Also shown is the undisturbed temperature at the surface (at a location 5 mm from the center of the junction).

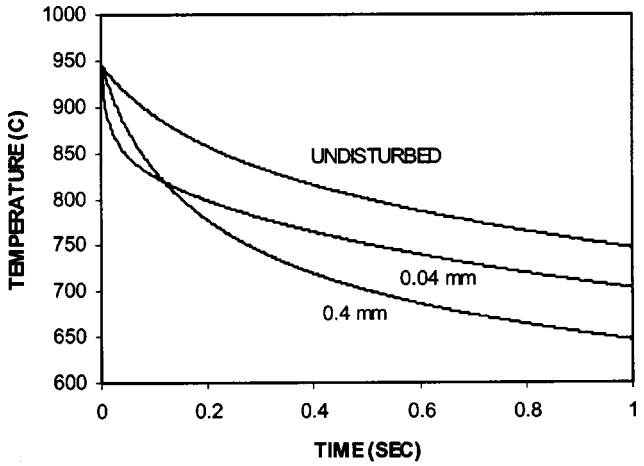

Fig. 6 Comparison of the fin effects between thermocouples of different wire diameter. The temperatures at the center of the junction for both cases are shown.

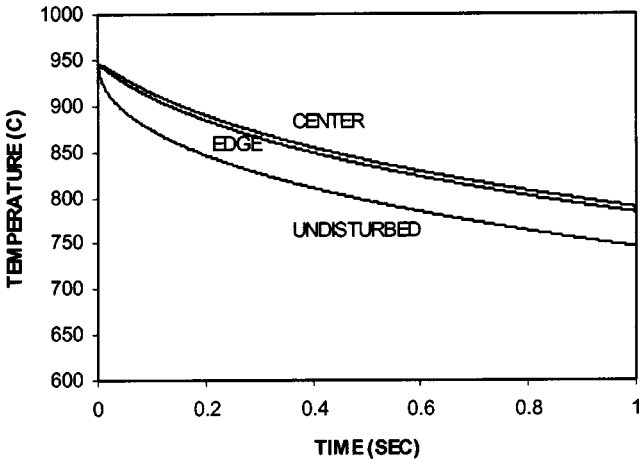

Fig. 8 Temperature histories at the center and at the edge of the insulated thermocouple junction, respectively. Wire diameter $d=0.4$ mm. Also shown is the undisturbed temperature at the surface (at a location 5 mm from the center of the junction).

water at 22°C. The exact location of the junctions is 6.38 mm from the circumference on the diametrically opposite sides from the bottom center. The results are shown in Fig. 7, which indicate the same trend that the temperature at the junction of smaller wire diameter decreases faster in the earlier stage of quenching.

In many applications, thermocouple wires are insulated thermally and electrically except at the junction leads. In order to examine how the thermal insulation can affect the temperature appearing at the junction, one should use the actual boundary condition on the surface of the thermocouple wire as that of Eq. (1). Nonetheless, we simply examine the extreme situations when the thermocouple wire is perfectly insulated although it is understood that the actual insulation materials, e.g., oxides or other superalloys, used as the sleeves for the thermocouple wires are never perfect thermal insulator. For this extreme case, the same model of Fig. 2(a) is used except the thermocouple wire is insulated. The histories of temperature respectively corresponding to the center and the edge of the junction are shown in Fig. 8, together with the undisturbed surface temperature. A total reversal is found in the effect of thermocouple on the temperature; the junction temperature drops more slowly than that on the undisturbed surface. Thus, thermocouple wire acts as a thermal shield for the junction. Similar observation has also been made by Hennecke and Sparrow [14]. According to the forgoing cases involved with exposed thermocouple wires and insulated wires, the degree of influence of surface-mounted thermocouples on the surface temperature also depends on the actual heat transfer between the thermocouple wire and the medium.

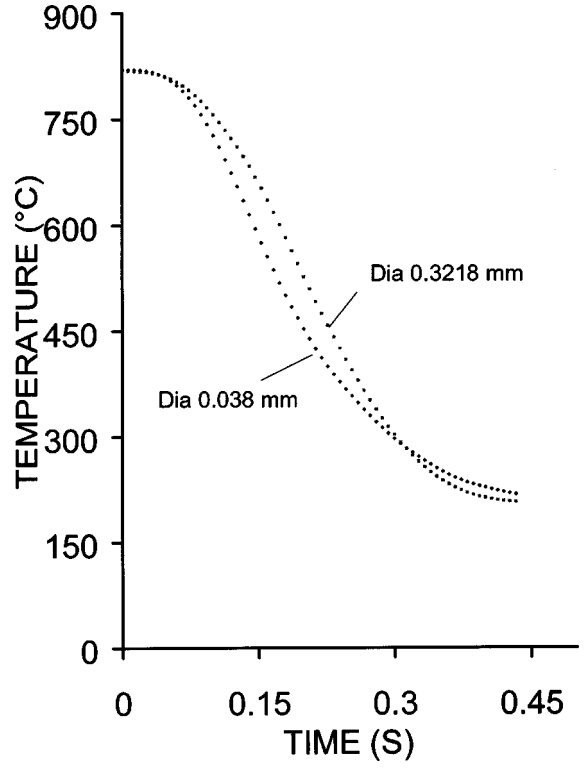

Fig. 7 Experimental results from two surface-mounted K-type thermocouples on a 4142 steel disk with two different wire diameters of 0.32 mm and 0.038 mm, respectively

Embedded Computational Model for Surface-Mounted Thermocouples

The FEM model represented in Fig. 2 considers the complete heat transfer system consisting of the object and the thermocouple wire. In that model, the thermocouple has to lie along the center line of the object. In practical applications, there are multiple thermocouples installed at different locations on the object. Since each thermocouple wire is a three-dimensional object, it is not possible to construct the model similar to that of Fig. 2 in a two-dimensional analysis. In this section, we describe the development of an embedded computational model that can be used in conjunction with a regular FEM model for the multidimensional calculation of the heating or cooling of a part with thermocouples attached on the surface.

The embedded computational model is a submodel of smaller length scale that is used to calculate the local temperature field in the thermocouple wire and its vicinity in the parent object. The concept is based on the fact that the thermocouple wire is usually very thin compared to the radius of curvature on the parent object's surface. Consequently, an axisymmetric model is a good approximation to the heat transfer phenomena in the thermocouple wire and the material in the vicinity of thermocouple junction. The axisymmetric submodel with the FEM mesh is depicted in Fig. 9. The model consists of two portions; the first one is the body of thermocouple wire that is exposed to the environment. The second portion is a finite volume of the object in the vicinity of the junction. The dimensions of the submodel are normalized so that the size of the object portion is unity. The actual size of the domain is

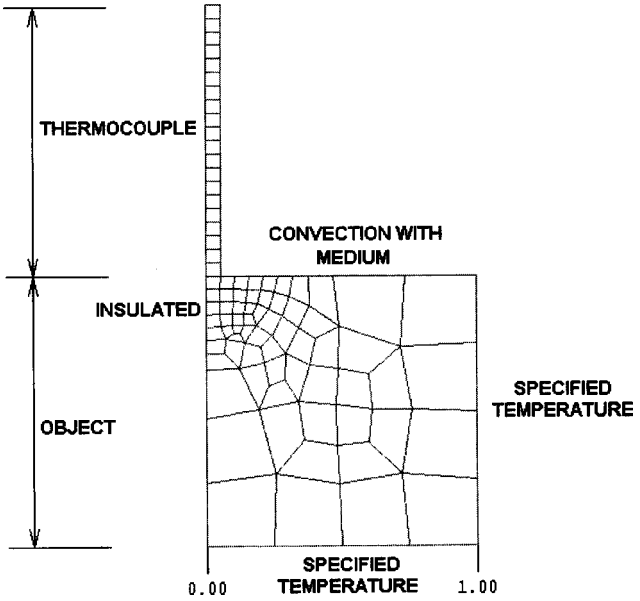

Fig. 9 Embedded computational model for calculating the temperature field in and around the thermocouple

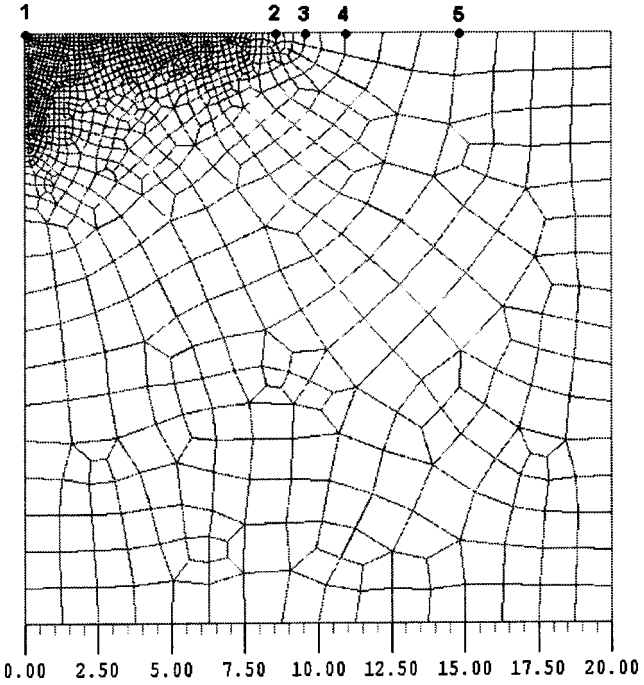

Fig. 10 Mesh system used in conjunction with the embedded computational model for calculating the temperature field in and around the thermocouple corresponding to the examples of Fig. 2. The mesh shown is the right half of the actual axisymmetric part. The thermocouple is located at the upper left corner of the domain.

determined by the diameter of the thermocouple wire. Only the top surface of the submodel is exposed to the environment; other surfaces of the domain are assigned with appropriate thermal boundary conditions as indicated in the Fig. 9. The submodel is superimposed at the actual location of surface-mounted thermocouples on the parent object that does not include thermocouple in the FEM mesh. The properties as well as the thermal boundary conditions for the submodel are changing according to the particular location of the surface-mounted thermocouple on the parent object. It is noted that the thermocouple submodel can be placed at any location of the surface-mounted thermocouples on the parent object, it does not necessarily have to be along the symmetric axis of the parent object. Hence, the proposed computational model has the great flexibility of considering the multiple surface-mounted thermocouple wires in a two-dimensional analysis.

The embedded computational model is used to calculate the temperature field in the same cases discussed in the previous section. The FEM mesh for the parent object is shown in Fig. 10, in which the model consists only the parent object. As have been used before, same thermophysical properties are assumed for the parent object and the thermocouple. Similar to that of Fig. 2, the top surface of the object is subjected to a constant heat transfer coefficient of 2 kW/m^2/K. For a thermocouple of wire diameter 0.4 mm (corresponding to that of Fig. 2(a)) and 1.88 mm in length, the calculated temperature at the center of the thermocouple center is shown in Fig. 11 together with that obtained earlier using the full model of Fig. 2(a). The difference between the calculated results from the two approaches is very small. We also observed that the results were about the same if the thermocouple wire of a greater length was used in the model.

The same submodel is applied to thermocouple of wire diameter 0.04 mm (corresponding to that of Fig. 2(b)) and 0.188 mm in length. The calculated temperature history at the center of the junction is shown in Fig. 11. Apparently, significant difference is found between the results from the submodel and that of the full model in Fig. 2(b). The difference is reduced when a longer thermocouple wire (0.376 mm) is used in the submodel, as shown in Fig. 11. Therefore, in the submodel, it is important to use the actual length of the exposed portion of the thermocouple wire.

For practical use of the submodel in an FEM calculation, there is uncertainty regarding the requirement of object meshing for satisfactory results. Ideally, the element size in the vicinity of the thermocouple junction should be no larger than the object portion of the submodel. In order to examine the sensitivity of calculated results to the mesh size in the parent object, five thermocouples are mounted on the top surface of the object in Fig. 10; each thermocouple location corresponds to different element size on the parent object in the vicinity of the thermocouple junction. The element size ranges from 0.14 mm×0.14 mm at TC no. 1 to 1.29 mm×1.29 mm at TC no. 5 in Fig. 10. The dimensions of the submodel are designed to be proportional to the wire size; thus, the object portion of the submodel is 0.76 mm×0.76 mm for a

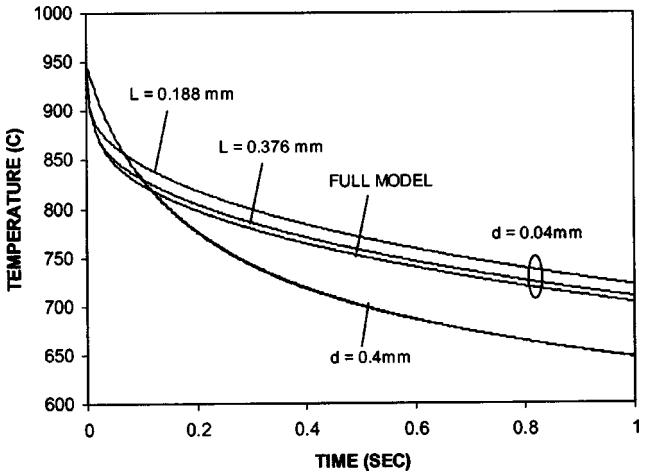

Fig. 11 Temperature histories at the center of the thermocouple junction when submodel is used. Wire diameter and length are indicated in each case. There are two coinciding curves for the case of wire diameter of 0.4 mm; one from the submodel and the other from the full model of Fig. 2.

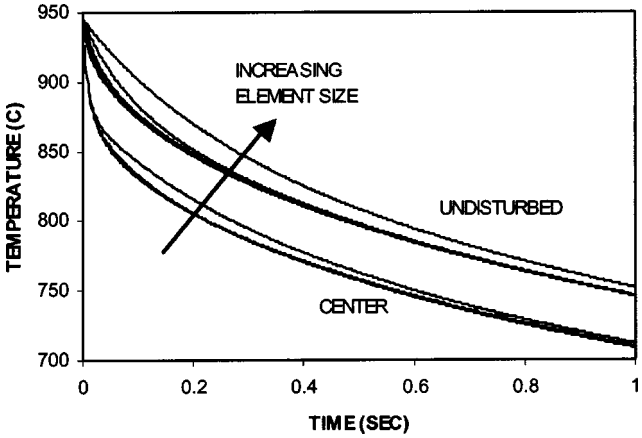

Fig. 12 Temperature history at the center of each thermocouple mounted at different locations on the top surface of the parent object (Fig. 10). Wire diameter=0.04 mm. The exact locations of thermocouple are shown in Fig. 10; different location corresponds to different element size in the parent object.

wire diameter of 0.04 mm. In this respect, the size of elements close to the location of thermocouple on the parent object in Fig. 10 is smaller than the object portion of the submodel at TC's no. 1–3. Figure 12 shows the calculated temperature histories at the center of the thermocouples. For reference, the undisturbed temperatures at the same surface locations of the parent object are also shown in the figure. Since the side of the parent object is thermally insulated except the top surface, the heat transfer is one-dimensional; therefore, the temperatures at all thermocouple locations should be the same. Except the TC no. 5 (element size is 1.29 mm), all the calculated temperature histories are very close to each other. It is noted that the undisturbed surface temperature corresponding to the location of TC no. 5 actually deviate appreciably from those at other locations. Since discretization error increases with the size of elements, the element size of the parent object in the region close to the surface has to be small enough in order to reasonably describe the high gradient of temperature field close to the surface. In this respect, the element size at TC no. 5 is too large to render sufficient accuracy. It can be concluded that, the submodel is less sensitive to the element size than that of the parent object.

For intrinsic junctions, there are actually two junctions with a spacing of about one or two wire diameters. The assumption that there is no interaction between the two junctions allows the use of single junction in the model. However, it is important to revisit the assumption for its soundness. The temperatures at locations of distance of one wire-diameter and two wire-diameters from the center of the junction are plotted in Fig. 13. The results shown Fig. 13 indicate that there is interaction between the two junctions even the spacing is as large as two wire-diameters. Further, the interactions seem to be more significant for the thermocouples with larger wire diameter. It can therefore be concluded that the fin effects as calculated in the model with single junction is underestimated; for cooling, the temperature appears at the junction would be even lower than the present results. In order to account for the interactions between the two junctions, a new approach employing three-dimensional submodel is being developed by one of the authors.

In all the above calculations, the same thermophysical properties are assumed for the parent object and the thermocouple (thermal conductivity $k=15\,\mathrm{W/m/K}$ and heat capacity $\rho c=5\times10^6\,\mathrm{J/m^3/K}$). At room temperature, the thermal conductivity k and heat capacity ρc for low carbon steels are $k=45\,\mathrm{W/m/K}$ and $\rho c=11\times10^6\,\mathrm{J/m^3/K}$, respectively. For the two materials of K-type thermocouple: $k=13.5\,\mathrm{W/m/K}$ and $\rho c=11\times10^6\,\mathrm{J/m^3/K}$ for Chromel and $k=29.4\,\mathrm{W/m/K}$ and $\rho c=13\times10^6\,\mathrm{J/m^3/K}$ for Alumel [20]. Thus, the heat capacity of K-type thermocouples is close to that of carbon steels, while the thermal conductivity of Chromel is about one third of the steels. In order to examine the effects of the different thermophysical properties on the temperature distribution in the vicinity of thermocouple junction, the thermal conductivity of thermocouple is assigned a value of 5 W/m/K while that of the parent object maintains a value of 15 W/m/K. The results are shown in Fig. 14, that also includes a case of very low thermal conductivity for reference. As one would expect, the lower thermal conductivity of thermocouple wire reduces the heat conduction from the substrate to the thermocouple; therefore, the temperature drop due to fin effect is reduced.

Applications of the Embedded Computational Model

This section presents the application of the developed computational method to a Jominy end quench test. Jominy test has been a popular test method for determining the hardenability of steels (ASTM A 255). The cooling curves at different distance from the quench end have been well studied in the past. Some data of the surface heat transfer coefficients at quenched end have also been

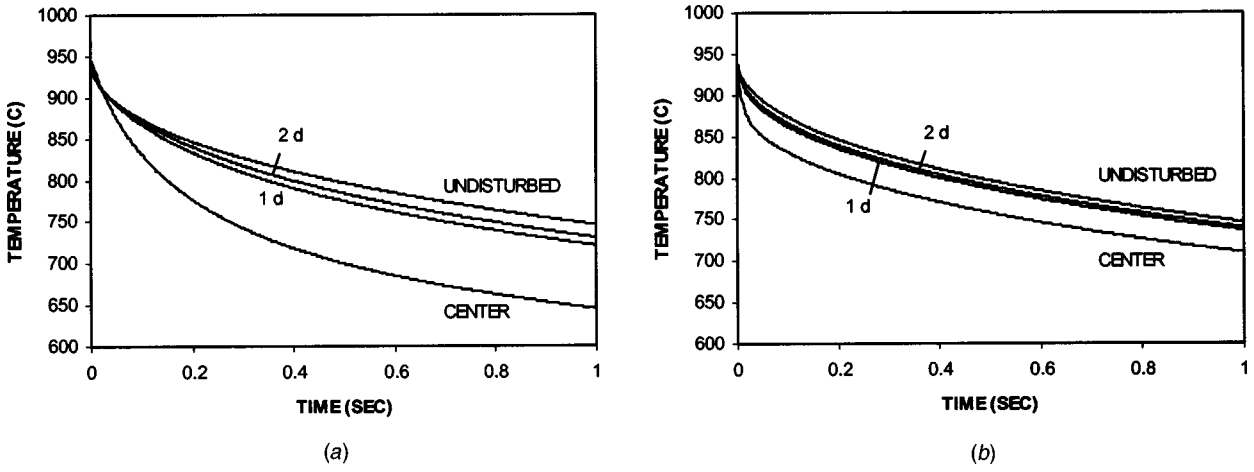

Fig. 13 Histories of surface temperature at locations of different distance from the center of the thermocouple junction; the distances are zero (center), one wire diameter, and two wire diameter. The parent object is in Fig. 10. (a) Wire diameter =0.4 mm, (b) wire diameter=0.04 mm.

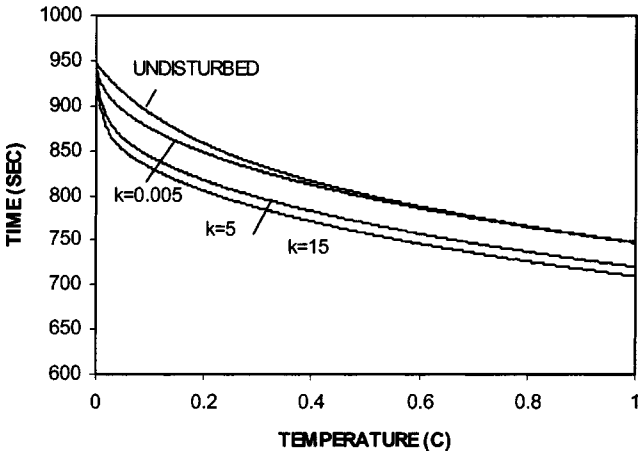

Fig. 14 Temperature history at the center of a thermocouple mounted at the center on the top surface of the parent object (Fig. 10). Wire diameter=0.04 mm. For the parent object, thermal conductivity $k=15$ W/m/K and heat capacity $\rho c=5\times10^6$ J/m^3/K. For the thermocouple material, thermal conductivity k has the values of 15, 5 or 0.005 W/m/K, and heat capacity $\rho c=5\times10^6$ J/m^3/K.

published. In this section, the theoretical calculation is compared with the measured temperatures on the Jominy test bar. In particular, the developed embedded thermocouple submodel will be used in conjunction with the inverse computation scheme also developed by one of the authors to determine the surface heat transfer coefficient. For more detailed discussion on the inverse calculation please consult Zhou and Tszeng [4], and Tszeng [8,19]. As a matter of fact, determining the surface heat transfer coefficients is one of the main uses of cooling curves in heat treating processes [6–11].

A Jominy bar of AISI 4142 steel with 25.4 mm (1 in.) in diameter and 101.6 mm (6 in.) in length was end-quenched after austenitizing at a temperature of 845°C for 30 minutes in furnace with oxidation control by placing cast iron blocks in a steel sleeve. Two K-type thermocouples having wire diameter of 0.25 mm were used to pick up the temperature at two locations. One thermocouple was mounted at the center on the quenched end of the Jominy bar and the other was mounted on the side at a distance of 3.8 mm from the quenched end. Note that the water does not wet the thermocouple mounted on the side. Intrinsic mounting technique was used to install the thermocouples. A schematic of the specimen is shown in Fig. 15. Labview 5.0 was used to register the data using National Instruments ATD board and signal conditioners equipped with PC computer. The sampling rate was kept at 150 Hz. The measured temperatures from the two thermocouples are shown in Fig. 16. Only the fast cooling stage is shown in the figure.

In calculating the temperature field, the geometry of the test bar and the boundary conditions allow the use of an axisymmetric model for the heat transfer analysis. Furthermore, due to predominant quenching power from the jet water on the bottom quench surface, the heat transfer phenomenon is very close to one-dimension in the axial direction. However, a complete FEM model that consisting of the test bas as well as the thermocouples is not axisymmetric. This difficulty is resolved by the use of embedded thermocouple submodel; the FEM model of the parent object (Jominy bar) is axisymmetric, as shown in Fig. 15. While the FEM allows different thermophysical properties for each material in the model, the same thermophysical properties are assumed for the object and the thermocouple, the same thermophysical properties of the AISI 4142 steel as shown in Table 1 were used for both the parent object and the thermocouple wire.

In this part of study, only the measured cooling curve at the

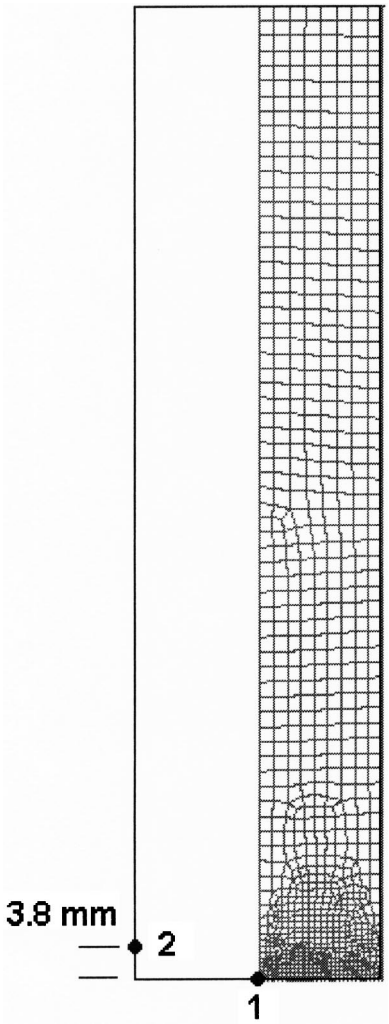

Fig. 15 Instrumented Jominy end quench specimen that is 100 mm-in-length×25.5 mm-in-diam. Two thermocouples of intrinsic junctions are installed at the indicated locations. TC 1 is located at the center of the end; TC 2 is located on the lateral surface (unwetted) at a distance of 3.8 mm from the quenched end. Wire diameter is 0.25 mm, and spacing between the two junctions is one wire diameter.

quenched end is used in the inverse calculation to determine the surface heat transfer coefficient. In that procedure, the temperature at the second thermocouple on the side will be calculated as well. The results of calculated temperature at both the thermocouple locations are shown in Fig. 16, with or without the fin effects by the thermocouple wires. First of all, the calculated temperature at the quenched end (0 mm) agrees very well with the measured temperature. The very small residual error in the temperatures at the quenched end indicates the good performance by the inverse calculation. Apparently, fin effects produce significant difference between the undisturbed surface temperature and the temperature at the thermocouple junctions. At 0.5 second in quenching, the fin effects lead to a temperature difference of about 150°. At the thermocouple on the side of a distance of 3.8 mm from the quenched end, the calculated and measured temperatures agree very well. Notice that the difference of temperature on the side of specimen increases at a later time. This is mainly due to the inaccurate thermophysical properties used in the model; more accurate data of thermophysical properties reduces the difference [4].

The calculated surface heat transfer coefficient as a function of temperature is shown in Fig. 17, in which the calculated heat transfer coefficient is plotted against the undisturbed (calculated)

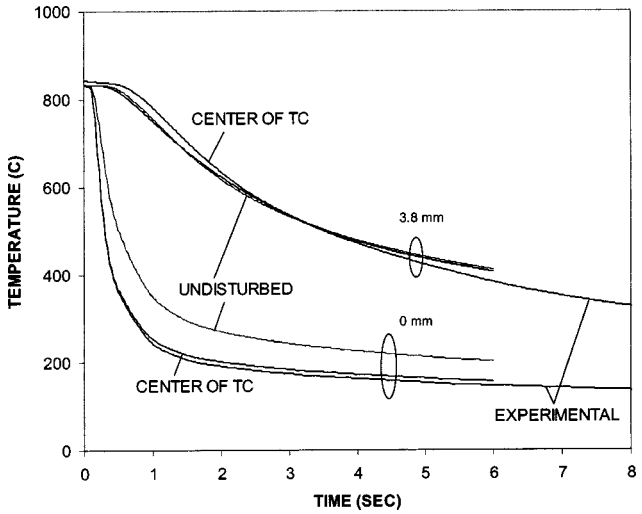

Fig. 16 Measured and calculated temperature at the thermocouple locations indicated in Fig. 14. The calculated temperatures are with or without the fin effects by the thermocouple wires. Wire diameter $d=0.25$ mm.

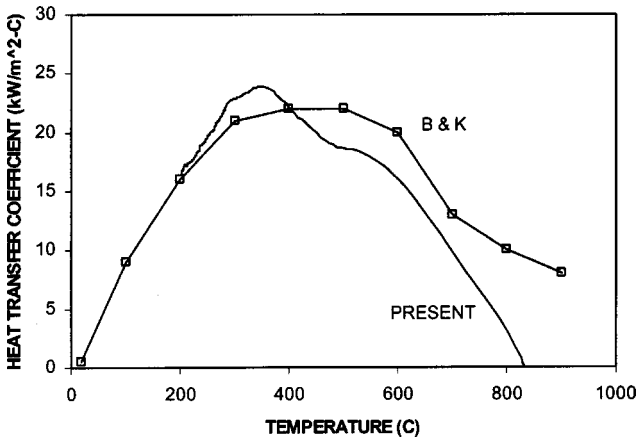

Fig. 17 A comparison between the calculated surface heat transfer coefficient and that obtained by Buchmayr and Kirkaldy [21]. The calculated HTC from the present study is plotted against the undisturbed surface temperature, not the temperature at the thermocouple junction. The calculated HTC only reached to about 200°C.

surface temperature. When the quenching started, the magnitude of heat transfer coefficient was very low, and reached the maximum a value at about 350°C. At even lower temperatures, the heat transfer coefficient decreases. The same figure also shows the heat transfer coefficient obtained by Buchmayr and Kirkaldy [21]. The two sets of data do not agree well at high temperatures, but the discrepancy decreases at a lower temperature. At temperatures below about 400°C, the agreement is very good.

The present development of the computational method that combines the inverse calculation on a regular FEM model with the submodel for the surface-mounted thermocouples provides the possibility of an efficient and low cost technique of measuring the surface temperatures as well as the determination of surface heat transfer coefficients. The surface heat transfer coefficients are one of the essential parameters for accurate modeling of the many thermal processing of metal components. Further, for a given quenching process of a heat-treated part, it is known that the surface heat transfer coefficient in most immersion quenching depends strongly on surface temperature, the location on the surface (Tensi et al. [22], Tensi and Totten [23], Segerberg and Bodin [24]). The developed method can be employed to fully explore this subject. More details are discussed in Zhou and Tszeng [4].

Table 1 Thermophysical properties of AISI 4142 steel

Temperature, °C	Thermal Conductivity, W/m/K
20.00	43.30
77.00	43.30
97.00	43.10
137.00	42.80
177.00	42.30
217.00	41.70
257.00	41.00
297.00	40.20
337.00	39.30
377.00	38.40
417.00	37.40
457.00	36.40
497.00	35.40
547.00	34.30
600.00	33.10
Temperature, °C	**Heat Capacity, 10^6 J/m^3/K**
20.00	3.94
204.00	4.02
427.00	4.75
648.00	5.72
773.00	4.64
830.00	4.26

Concluding Remarks

The present study investigated the fin effects of surface-mounted thermocouples on the measured temperature. It is found that the fin effects have great impact on the measured temperatures; the actual effects are dependent on the wire diameter. In order to overcome the difficulty of calculating the fin effects associated with a thermocouple attached at an arbitrary location on the object, we further developed an embedded computational submodel that can be used in conjunction with a regular FEM model for the multidimensional calculation of the heating or cooling of a part. The embedded computational model is shown to offer very accurate calculation of the temperature at the junction of thermocouple wire. It is also found that the solution behavior is less sensitive to the element size than the parent object.

In this study, we carried out a Jominy end quench test with thermocouples attached to the specimen. The measured cooling curve at the quenched end is used in the inverse calculation scheme to determine the surface heat transfer coefficient and the overall transient temperature field. It is found that the calculated temperature at the thermocouple junction agrees very well with the measured temperature. The developed computation method can be used in the efficient technique of determining the surface thermal boundary conditions for the calculation of changing temperature fields in heat-treated components.

Acknowledgments

This project is partially funded by the Thermal Processing Technology Center at Illinois Institute of Technology and by Center of Heat Treat Excellence, WPI. The authors are also thankful for the thorough reviews by the reviewers.

References

[1] Majorek, A., et al., 1992, "The Influence of Heat Transfer on the Development of Stresses, Residual Stresses and Distortions in Martensitically Hardened SAE 1045 and SAE 4140," *Quenching and Distortion Control*, G. E. Totten, ed., ASM International, pp. 171–179.

[2] Wallis, R. A., and Craighead, I. W., 1995, "Prediction of Residual Stresses in Gas Turbine Components," JOM, **47**(10), pp. 69–71.

[3] Schroder, R., 1984, ''Some Influences on the Development of Thermal and Residual Stresses in Quenched Steel Cylinders With Different Dimensions,'' 1984, *Proceedings of International Symposium on the Calculation of Internal Stresses in Heat Treatment of Metallic Materials*, **1**, E. Attebo and T. Ericsson, eds., Linkoping, Sweden, pp. 1–22.
[4] Zhou, G. F., and Tszeng, T. C., 2002, ''Determination of Heat Transfer Coefficients by Inverse Calculation in Conjunction With Embedded Model for Surface Mounted Thermocouples,'' paper in preparation.
[5] Park, J. E., Childs, K. W., Ludtka, G. M., and Chu, W., 1991, ''Correction of Errors in Intrinsic Thermocouple Signals Recorded During Quenching,'' *National Heat Treat Conference*, Minneapolis, MN, July 26–31.
[6] Cross, M. F., Bennett, J. C., Jr., and Bass, R. W., 1999, ''Developing Empirical Equations for Heat Transfer Coefficients on Metallic Disks,'' *19th ASM-HTS Conference Proceedings*, pp. 335–342.
[7] Saraf, V., 2001, ''Distortion Characterization and Quench Process Modeling in Heat Treated Components of IN 718 Superalloy and AISI 4142 Steel,'' M.S. thesis, Department of Mechanical, Materials and Aerospace Engineering, Illinois Institute of Technology, Chicago, IL, USA.
[8] Tszeng, T. C., 2000, ''Determination of Heat Transfer Boundary Conditions of Quenching Operations in Heat Treating Processes,'' SME Technical Paper CM00-123.
[9] Beck, J. V., and Osman, A. M., 1992, ''Analysis of Quenching and Heat Treating Processes Using Inverse Heat Transfer Method,'' Proceedings of the First International Conference, *Quenching and Control of Distortion*, G. E. Totten, ed., ASM International, pp. 147–153.
[10] Beck, J. V., Blackwell, B., and St. Clair, Jr., C. R., 1985, *Inverse Heat Conduction: Ill-Posed Problems*, Wiley-Interscience, New York.
[11] Gummadam, K. C., and Tszeng, T. C., 2001, ''An Integrated Approach to Estimate the Surface Heat Transfer Coefficients in Heat Treating Processes,'' *ASM International/IFHTSE Symposium on Quenching and Control of Distortion*, October 5–8, 2001, Indianapolis, IN.
[12] Doebelin, E. O., 1975, *Measurement Systems Applications and Design*, McGraw-Hill Book Company, New York, p. 522.
[13] Moffat, R. J., 1962, *The Gradient Approach to Thermocouple Circuitry, From Temperature—Its Measurement and Control in Science and Industry*, Reinhold, New York.
[14] Hennecke, D. K., and Sparrow, E. M., 1970, ''Local Heat Sink on a Convectively Cooled Surface—Application to Temperature Measurement Error,'' Int. J. Heat Mass Transfer, **13**, pp. 287–304.
[15] Sparrow, E. M., 1976, ''Error Estimates in Temperature Measurements,'' *Measurement in Heat Transfer*, 2nd ed., E. R. G. Eckert and R. J. Goldstein, eds., Hemisphere Publishing Corp., Chap. 1.
[16] Keltner, N. R., and Beck, J. V., 1983, ''Surface Temperature Measurement,'' ASME J. Heat Transfer, **105**, pp. 312–318.
[17] Litkouhi, B., and Beck, J. V., 1985, ''Intrinsic Thermocouple Analysis Using Multinode Unsteady Surface Element Method,'' AIAA J., **23**, pp. 1609–1614.
[18] Segall, A. E., 1994, ''Corrective Solutions for Intrinsic Thermocouples Under Polynomial Substrate Loading,'' ASME J. Heat Transfer, **116**, pp. 759–761.
[19] *HOTPOINT System Manual*, 2001, T. Calvin Tszeng, Illinois Institute of Technology, Chicago, IL, USA.
[20] Pollock, D. D., 1993, *Physical Properties of Materials for Engineers*, 2nd ed., CRC Press, Boca Raton, FL.
[21] Buchmayr, B., and Kirkaldy, J. S., 1990, ''Modeling of the Temperature Field, Transformation Behavior, Hardness and Mechanical Response of Low Alloy Steels During Cooling From the Austenite Region,'' ASME J. Heat Transfer, **8**, pp. 127–136.
[22] Tensi, H. M., Lanier, K., Totten, G. E., and Webster, G. M., 1996, ''Quenching Uniformity and Surface Cooling Mechanisms,'' *Proceedings of the 16th Heat Treating Society Conference & Exposition*, J. L. Dossett and R. E. Luetje, eds., Cincinnati, OH, pp. 3–8.
[23] Tensi, H. M., and Totten, G. E., 1996, ''Development of the Understanding of the Influence of Wetting Behavior on Quenching and the Merits in These Developments of Prof. Imao Tamura,'' *Proceedings of the Second International Conference on Quenching and the Control of Distortion*, pp. 17–27.
[24] Segerberg, S., and Bodin, J., 1992, ''Variation in the Heat Transfer Coefficient Around Components of Different Shapes During Quenching,'' *Quenching and Distortion Control*, G. E. Totten, ed., ASM International, pp. 165–170.

A Vascular Model for Heat Transfer in an Isolated Pig Kidney During Water Bath Heating

Cuiye Chen
School of Mechanical Engineering,
Purdue University, USA

Lisa X. Xu
e-mail: lisaxu@sjtu.edu.cn
School of Mechanical Engineering,
Department of Biomedical Engineering,
Purdue University, USA;
School of Life Science and Technology,
Shanghai Jiao Tong University,
People's Republic of China

Isolated pig kidney has been widely used as a perfused organ phantom in the studies of hyperthermia treatments, as blood perfusion plays an essential role in thermoregulation of living tissues. In this research, a vascular model was built to describe heat transfer in the kidney phantom during water bath heating. The model accounts for conjugate heat transfer between the paired artery and vein, and their surrounding tissue in the renal medulla. Tissue temperature distribution in the cortex was predicted using the Pennes bioheat transfer equation. An analytical solution was obtained and validated experimentally for predicting the steady state temperature distribution in the pig kidney when its surface kept at a uniform constant temperature. Results showed that local perfusion rate significantly affected tissue temperature distributions. Since blood flow is the driving force of tissue temperature oscillations during hyperthermia, the newly developed vascular model provides a useful tool for hyperthermia treatment optimization using the kidney phantom model. [DOI: 10.1115/1.1597625]

Keywords: Analytical, Bioengineering, Conjugate, Heat Transfer, Perfusion Rate

Introduction

The pig kidney has a well-organized vascular network. Its anatomic structure and size are very similar to that of the human [1]. It normally contains a single renal artery that allows good control of the inlet flow. The isolated pig kidney model developed by Holmes et al. [2] possesses a vasculature close to that of a living kidney. They have been widely used as perfused organ phantoms in the past to examine the inter-relation between blood flow and tissue temperature during hyperthermia. Zaerr et al. [3] used four preserved pig kidneys to simulate tissue temperature responses to the step and ramp changes of flow rates, and to the temperature controlled changes of flow rates. During their experiments, the kidneys were perfused with 80 percent ethanol solution via a pump and heated by an ultrasonic heating system with the constant acoustic power of 15 W. Xu [4] studied the steady state temperature field in an isolated pig kidney under various perfusion conditions through which the Pennes equation was validated in the cortex region. Brown et al. [5] measured tissue temperature distributions in an isolated canine kidney perfused with saline at 20–25°C that was situated in a water bath at 32°C. The flow largely affected the tissue temperature distribution. Kolios et al. studied transient temperature distributions in kidney during a 20s heat pulse delivered via an 18 gauge needle with hot water running at 60°C [6,7]. Their results showed that in the regions without large vessels, temperature predictions from the Pennes bioheat transfer equation [8] were in much better agreement with the experimental measurements than that predicted using the Weinbaum-Jiji countercurrent model [9]. However, in the vicinity of large vessels, the thermal effect of blood was found significant. Valvano et al. [10] observed similar results in the canine kidney cortex. Thus, modeling heat transfer between the vessels and their surrounding tissue is necessary for accurate temperature predictions in these regions.

In this study, an anatomic vascular model was developed to simulate blood-tissue heat transfer in the isolated pig kidney when its surface was kept at a uniform constant temperature. In the renal medulla, conjugate heat transfer between the paired artery and vein, and their surrounding tissue, was considered. In the cortex, tissue temperature distribution was predicted using the Pennes bioheat transfer equation. An analytical solution was obtained and validated experimentally for steady state temperature distribution in the kidney.

Vascular Model and Formulation

The shape of the pig kidney normally appears as a bean. The medial side of the kidney contains an indentation through which pass the renal artery and vein, nerves, and pelvis. If a kidney were cut in half, two regions became apparent: an outer region termed as the cortex and an inner region as the medulla. Shown in Fig. 1, the renal artery branches progressively and radially into the cortex region. There exist parallel arterial and venous systems. It is clear that in the medulla, arteries are closely paired with veins, and similar structures repeat periodically in each cross-section. Thus, an inverted conical cylinder was chosen as the tissue unit for modeling as shown in Figs. 1 and 2. The physical model shown in Fig. 2 consisted of two respective parts for the cortex and the medulla. The pelvis was not considered in the model since all the liquid (urine) in the pelvis was steady and at the same temperature as that of the kidney surface. The radius of the cylinder increased linearly along the z direction. A countercurrent artery-vein pair was embedded in the cylinder whose wall was assumed adiabatic. Fully developed laminar blood flow was assumed in the vessels since the entrance length was much shorter than the actual vessel length, and the Reynolds number was about ten under normal physiological conditions. Axial heat conduction in the vessel was neglected as compared to the advection by the flow at a large Peclet number (Pe$>$200). At steady state, the governing equations in the medulla region were given as follows.

Tissue:

$$\frac{1}{r}\frac{\partial}{\partial r}\left(r\frac{\partial T_{t2}}{\partial r}\right)+\frac{1}{r^2}\frac{\partial}{\partial \phi}\left(\frac{\partial T_{t2}}{\partial \phi}\right)+\frac{\partial^2 T_{t2}}{\partial z^2}=0 \qquad (1)$$

Contributed by the Heat Transfer Division for publication in the JOURNAL OF HEAT TRANSFER. Manuscript received by the Heat Transfer Division January 14, 2002; revision received May 12, 2003. Associate Editor: P. S. Ayyaswamy.

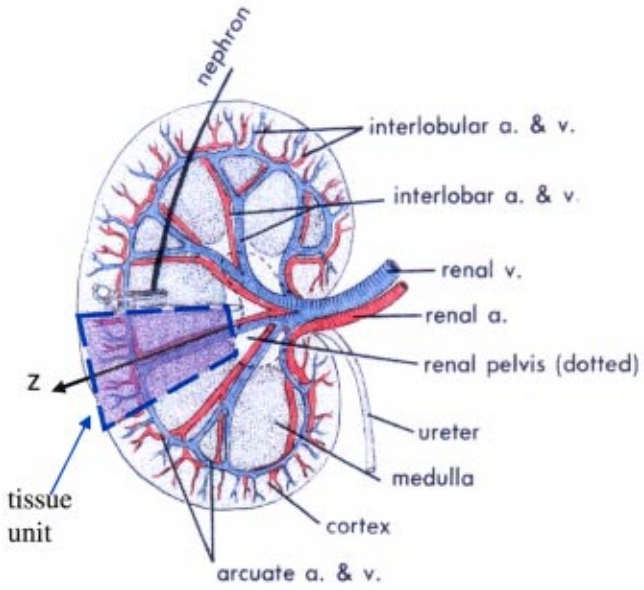

Fig. 1 Schematic of kidney vasculature. a. artery; v. vein (adopted from Frandson Anatomy and Physiology of Farm Animals, Philadelphia, PA, Lea and Febiger, 1986)

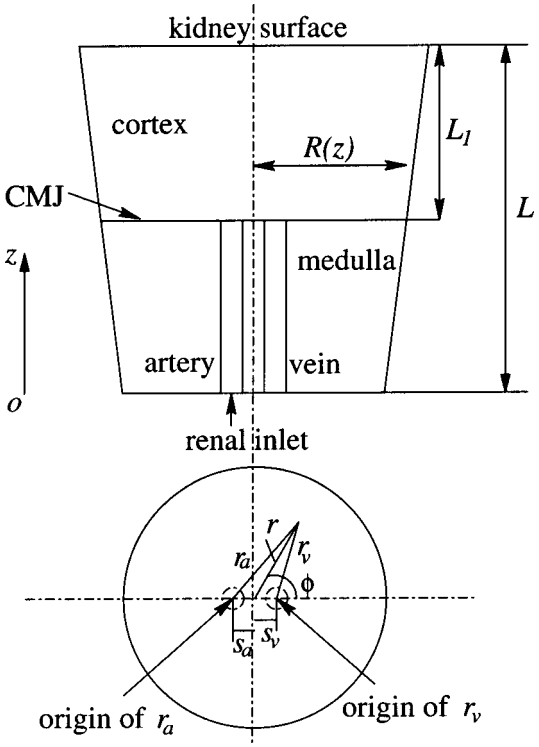

Fig. 2 Schematic of the inverted conical tissue unit and the vessel spacing

Artery:

$$\frac{1}{r_a}\frac{\partial}{\partial r_a}\left(r_a\frac{\partial T_a}{\partial r_a}\right)+\frac{1}{r_a^2}\frac{\partial}{\partial \phi_a}\left(\frac{\partial T_a}{\partial \phi_a}\right)=\frac{2u_{m,a}}{\alpha_b}\left[1-\left(\frac{r_a}{a_a}\right)^2\right]\frac{\partial T_a}{\partial z} \tag{2}$$

Vein:

$$\frac{1}{r_v}\frac{\partial}{\partial r_v}\left(r_v\frac{\partial T_v}{\partial r_v}\right)+\frac{1}{r_v^2}\frac{\partial}{\partial \phi_v}\left(\frac{\partial T_v}{\partial \phi_v}\right)=-\frac{2u_{m,v}}{\alpha_b}\left[1-\left(\frac{r_v}{a_v}\right)^2\right]\frac{\partial T_v}{\partial z} \tag{3}$$

where T is the temperature, α the thermal diffusivity, u_m the mean blood velocity (it was assumed that the mean arterial blood velocity, $u_{m,a}$, is the same as that of the venous blood, $u_{m,v}$), and a the radius of the blood vessel. The subscripts a, v, $t2$ denote the artery, vein, and medullar tissue, respectively. The basic geometry, symbols, and the coordinate system are shown in Fig. 2.

In the cortex, the vessel size is relatively small as compared to that in the medulla. It has been shown that the Pennes equation provides good predictions for the temperature distribution in this region [4,6]. Further, in this study, because the kidney surface temperature was kept uniform and constant by a water bath, tissue temperature distribution in the cortex primarily varied in the z direction (refer to Fig. 2). Thus, one-dimensional (1-D) Pennes equation was applied as

$$\alpha_t\frac{\partial^2 T_{t1}}{\partial z^2}-\frac{(\rho c_p)_b}{(\rho c_p)_t}\omega_b(T_{t1}-T_{a,\mathrm{CMJ}})=0 \tag{4}$$

where T_{t1} is the tissue temperature, $T_{a,\mathrm{CMJ}}$ the arterial flow temperature at the corticomedullary junction (CMJ), and ω_b the local perfusion rate in the cortex. Referring to Fig. 2, the boundary conditions were given as the constant kidney surface temperature (T_s) and the arterial inlet flow temperature (T_{a0}) in the following:

$$T_{t1}=T_s \quad z=L \tag{5}$$

$$T_{t2}=T_s, \quad T_a=T_{a0} \quad z=0 \tag{6}$$

At the CMJ, the local temperature and heat flux are continuous, and the local venous return temperature was nearly the same as that of the local tissue given the thermal equilibrium between the flow and tissue:

$$T_{t1}=T_{t2}=T_{t,\mathrm{CMJ}} \quad \frac{\partial T_{t1}}{\partial z}=\frac{\partial T_{t2}}{\partial z}, \quad T_v=T_{t1}, \quad z=L-L_1 \tag{7}$$

The side surface of the tissue cylinder was adiabatic because of the periodical arrangement:

$$\frac{\partial T_{t2}}{\partial \vec{n}}=0 \quad r=R(z) \tag{8}$$

where $\vec{n}$ the vector normal to the tissue cylinder side surface, $R(z)$ the tissue cylinder radius varying linearly with z. The local temperature and heat flux at the tissue-blood interfaces were continuous:

$$\frac{\partial T_a}{\partial r_a}=\frac{\partial T_{t2}}{\partial r_a} \quad r_a=a_a \tag{9}$$

$$T_{t2}=T_a \quad r_a=a_a \tag{10}$$

$$\frac{\partial T_v}{\partial r_v}=\frac{\partial T_{t2}}{\partial r_v} \quad r_v=a_v \tag{11}$$

$$T_{t2}=T_v \quad r_v=a_v \tag{12}$$

Analytical Solution

For simplicity, thermophysical properties of the blood and tissue were assumed the same. Temperature variations along the z direction were approximated by the bulk temperatures in the medulla as previously justified in [11,12]. To nondimensionalize the governing equations, the following parameters were defined

$$r^*=\frac{r}{a_{a0}},\quad r_a^*=\frac{r_a}{a_{a0}},\quad r_v^*=\frac{r_v}{a_{a0}},\quad R^*=\frac{R}{a_{a0}},$$
$$a_v^*=\frac{a_v}{a_{a0}},\quad a_a^*=\frac{a_a}{a_{a0}},\quad L_1^*=\frac{L_1}{a_{a0}},\quad L^*=\frac{L}{a_{a0}},$$
$$s_v^*=\frac{s_v}{a_{a0}},\quad s_a^*=\frac{s_a}{a_{a0}},\quad z^*=\frac{z}{a_{a0}},\quad \vec{n}^*=\frac{\vec{n}}{a_{a0}},\tag{13}$$
$$\theta_{t1,t2}=\frac{T_{t1,t2}-T_{a0}}{T_s-T_{a0}},\quad \theta_a=\frac{T_a-T_{a0}}{T_s-T_{a0}},\quad \theta_v=\frac{T_v-T_{a0}}{T_s-T_{a0}},$$
$$Pe=\frac{2(\rho c_p)_b a_{a0}u_{m,a}}{k_b}$$

where θ is the dimensionless temperature and s the vessel spacing, i.e., the center-to-center distance. Asterisks denote dimensionless variables. All length variables were scaled by the arterial inlet radius, a_{a0}. In this study, the venous and the arterial vessel radii were assumed constant. It led to $a_a^*=1$. All temperatures were scaled by the difference between the kidney surface temperature (T_s) and the arterial inlet temperature (T_{a0}). Thus, the governing equations became,

In the Medulla:

Tissue:

$$\frac{1}{r^*}\frac{\partial}{\partial r^*}\left(r^*\frac{\partial\theta_{t2}}{\partial r^*}\right)+\frac{1}{r^{*2}}\frac{\partial}{\partial\phi}\left(\frac{\partial\theta_{t2}}{\partial\phi}\right)=-\frac{d^2\theta_{t2b}}{dz^{*2}}\tag{14}$$

Artery:

$$\frac{1}{r_a^*}\frac{\partial}{\partial r_a^*}\left(r_a^*\frac{\partial\theta_a}{\partial r_a^*}\right)+\frac{1}{r_a^{*2}}\frac{\partial}{\partial\phi_a}\left(\frac{\partial\theta_a}{\partial\phi_a}\right)=\mathrm{Pe}(1-r_a^{*2})\frac{d\theta_{ab}}{dz^*}\tag{15}$$

Vein:

$$\frac{1}{r_v^*}\frac{\partial}{\partial r_v^*}\left(r_v^*\frac{\partial\theta_v}{\partial r_v^*}\right)+\frac{1}{r_v^{*2}}\frac{\partial}{\partial\phi_v}\left(\frac{\partial\theta_v}{\partial\phi_v}\right)=-\mathrm{Pe}\left(1-\frac{r_v^{*2}}{a_v^{*2}}\right)\frac{d\theta_{vb}}{dz^*}\tag{16}$$

where the bulk temperatures were defined as

$$\theta_{ab}=\frac{2}{\pi}\int_0^{2\pi}\int_0^1\theta_a(1-r_a^{*2})r_a^*dr_a^*d\phi_a\tag{17}$$

$$\theta_{vb}=\frac{2}{\pi a_v^{*2}}\int_0^{2\pi}\int_0^{a_v^*}\theta_v\left(1-\frac{r_v^{*2}}{a_v^{*2}}\right)r_v^*dr_v^*d\phi_v\tag{18}$$

$$\theta_{t2b}=\frac{1}{\pi R^{*2}}\int_0^{2\pi}\int_0^{R^*}\theta_{t2}r^*dr^*d\phi\tag{19}$$

In the Cortex:

$$\frac{\partial^2\theta_{t1}}{\partial z^{*2}}=\frac{a_{a0}^2\omega_b}{\alpha_t}(\theta_{t1}-\theta_{a,\mathrm{CMJ}})\tag{20}$$

where α_t is the thermal diffusivity of tissue. Boundary conditions, Eqs. (5–12), became,

$$\theta_{t1}=\theta_s\quad z^*=L^*\tag{21}$$

$$\theta_{t1}=\theta_{t2}=\theta_{t,\mathrm{CMJ}},\quad \theta_{vb}=\theta_{t1},\quad \frac{d\theta_{t1}}{dz^*}=\frac{d\theta_{t2b}}{\partial z^*},\quad z^*=L^*-L_1^*\tag{22}$$

$$\theta_{t2}=\theta_s,\quad \theta_a=\theta_{a0}\quad z^*=0\tag{23}$$

$$\frac{\partial\theta_{t2}}{\partial\vec{n}^*}=0\quad r^*=R^*(z^*)\tag{24}$$

$$\frac{\partial\theta_a}{\partial r_a^*}=\frac{\partial\theta_{t2}}{\partial r_a^*}\quad r_a^*=1\tag{25}$$

$$\theta_{t2}=\theta_a\quad r_a^*=1\tag{26}$$

$$\frac{\partial\theta_v}{\partial r_v^*}=\frac{\partial\theta_{t2}}{\partial r_v^*}\quad r_v^*=a_v^*\tag{27}$$

$$\theta_{t2}=\theta_v\quad r_v^*=a_v^*\tag{28}$$

It should be noted that, similar to the local temperature, the bulk venous temperature was assumed equal to the bulk tissue temperature at the CMJ, as shown in Eq. (22). The overall advection effect due to blood flow at CMJ was not accounted for in Eq. (22). This was because the Pennes equation was used in the modeling and its perfusion term accounted for the flow effect continuously in the cortex as if there were a volumetric heat source from the tissue infiltration of arterial blood at a constant $T_a=T_{\mathrm{CMJ}}$. The net energy advection due to the flow was equally distributed over the entire cortex region.

Following a derivation similar to that described in [13,14] (see Appendix for the detailed derivation), one could obtain the solutions for Eqs. (14–16). The solutions were comprised of the homogeneous and particular solutions,

$$\theta_a=\theta_h+\mathrm{Pe}\left(\frac{1}{4}r_a^{*2}-\frac{1}{16}r_a^{*4}-\frac{3}{16}\right)\frac{d\theta_{ab}}{dz^*}-\frac{1}{4}\mathrm{Pe}a_v^{*2}\ln\left(\frac{r_v^*}{a_v^*}\right)\frac{d\theta_{vb}}{dz^*}$$
$$-\frac{1}{4}\frac{d^2\theta_{t2b}}{dz^{*2}}\left[2\ln r_a^*+1+s_a^*-2r_a^*s_a^*\cos\phi_a-2R^{*2}\ln\left(\frac{r^*}{R^*}\right)\right]\tag{29}$$

$$\theta_v=\theta_h+\mathrm{Pe}a_v^{*2}\left(\frac{1}{4}r_v^{*2}-\frac{1}{16}\frac{r_v^{*4}}{a_v^{*2}}-\frac{3}{16}a_v^{*2}\right)\frac{d\theta_{vb}}{dz^*}$$
$$+\frac{1}{4}\mathrm{Pe}\ln r_a^*\frac{d\theta_{ab}}{dz^*}-\frac{1}{4}\frac{d^2\theta_{t2b}}{dz^{*2}}\left[2a_v^{*2}\ln\left(\frac{r_v^*}{a_v^*}\right)+a_v^{*2}+s_v^{*2}\right.$$
$$\left.-2r_v^*s_v^*\cos\phi_v-2R^{*2}\ln\left(\frac{r^*}{R^*}\right)\right]\tag{30}$$

$$\theta_{t2}=\theta_h+\frac{1}{4}\mathrm{Pe}\ln r_a^*\frac{d\theta_{ab}}{dz^*}-\frac{1}{4}\mathrm{Pe}a_v^{*2}\ln\left(\frac{r_v^*}{a_v^*}\right)\frac{d\theta_{vb}}{dz^*}$$
$$-\frac{1}{4}\frac{d^2\theta_{t2b}}{dz^{*2}}\left[r^{*2}-2R^{*2}\ln\left(\frac{r^*}{R^*}\right)\right]\tag{31}$$

where the homogeneous solution, θ_h, was

$$\theta_h=\left\{\sum_{n=0}^{\infty}a_nr^{*n}\cos[n(\phi-\pi)]\right\}\mathrm{Pe}\frac{d\theta_{ab}}{dz^*}$$
$$+\left(\sum_{n=0}^{\infty}b_nr^{*n}\cos n\phi\right)\mathrm{Pe}a_v^{*2}\frac{d\theta_{vb}}{dz^*}\tag{32}$$

and

$$a_n = -\frac{1}{4nR^{*n}}\left(\frac{s_a^*}{R^*}\right)^n, \qquad b_n = \frac{1}{4nR^{*n}}\left(\frac{s_v^*}{R^*}\right)^n \tag{33}$$

with $a_0=0$ and $b_0=0$. Substituting Eqs. (29–31) into Eqs. (17–19) led to

$$\theta_{ab} = a_{11}\frac{d\theta_{ab}}{dz^*} + a_{12}\frac{d\theta_{vb}}{dz^*} + a_{13}\frac{d^2\theta_{t2b}}{dz^{*2}} \tag{34}$$

$$\theta_{vb} = a_{21}\frac{d\theta_{ab}}{dz^*} + a_{22}\frac{d\theta_{vb}}{dz^*} + a_{23}\frac{d^2\theta_{t2b}}{dz^{*2}} \tag{35}$$

$$\theta_{t2b} = a_{31}\frac{d\theta_{ab}}{dz^*} + a_{32}\frac{d\theta_{vb}}{dz^*} + a_{33}\frac{d^2\theta_{t2b}}{dz^{*2}} \tag{36}$$

where the coefficients a_{ij} are

$$a_{11} = \left(\sum_{n=1}^{\infty} a_n s_a^{*n} - \frac{11}{96}\right) Pe \tag{37}$$

$$a_{12} = \left[\sum_{n=1}^{\infty} b_n s_a^{*n}\cos(n\phi) - \frac{1}{4}\ln\left(\frac{s_a^*+s_v^*}{a_v^*}\right)\right] \mathrm{Pe} a_v^{*2} \tag{38}$$

$$a_{13} = -\frac{1}{4}(s_a^{*2} - 0.5) \tag{39}$$

$$a_{21} = \left[\sum_{n=1}^{\infty} a_n s_v^{*n}\cos(n\phi) + \frac{1}{4}\ln(s_a^*+s_v^*)\right] \mathrm{Pe} \tag{40}$$

$$a_{22} = \left(\sum_{n=1}^{\infty} b_n s_v^{*n} + \frac{11}{96}\right) \mathrm{Pe} a_v^{*2} \tag{41}$$

$$a_{23} = -\frac{1}{4}(s_v^{*2} - 0.5a_v^{*2}) \tag{42}$$

$$a_{31} = \left(\frac{1}{4}\ln s_a^*\right) \mathrm{Pe} \tag{43}$$

$$a_{32} = -\frac{1}{4}\mathrm{Pe} a_v^{*2}\ln\left(\frac{s_v^*}{a_v^*}\right) \tag{44}$$

$$a_{33} = \frac{1}{4}R^{*2}(-1.5 + 2\ln R^*) \tag{45}$$

The solution for Eq. (20) was

$$\theta_{t1} = \theta_{a,\mathrm{CMJ}} + g_1 e^{A_c Z^*} + g_2 e^{-A_c Z^*} \tag{46}$$

where

$$A_c = a_{a0}\sqrt{\frac{\omega_b}{\alpha_t}} \tag{47}$$

Substituting Eq. (46) into the boundary conditions Eqs. (21) and (22) led to

$$g_1 = \frac{(\theta_s - \theta_{a,\mathrm{CMJ}})e^{-A_c(L^*-L_1^*)} - (\theta_{t,\mathrm{CMJ}} - \theta_{a,\mathrm{CMJ}})e^{-A_c L^*}}{e^{A_c L_1^*} - e^{-A_c L_1^*}} \tag{48}$$

$$g_2 = \frac{(\theta_s - \theta_{a,\mathrm{CMJ}})e^{A_c(L^*-L_1^*)} - (\theta_{t,\mathrm{CMJ}} - \theta_{a,\mathrm{CMJ}})e^{A_c L^*}}{e^{-A_c L_1^*} - e^{A_c L_1^*}} \tag{49}$$

To obtain the bulk temperatures, Eqs. (34–36) and Eq. (46) were solved simultaneously using numerical methods.

The thickness of the medulla and the cortex of the kidney used in this study were measured and approximately equal to 1 cm. At the CMJ, the most frequently encountered vessels were of 500 μm in diameter (d) [15]. It was thus assumed that the paired vessels in the medulla were the mother branches of the bifurcating vessels of $d=500$ μm at the CMJ. The paired artery and vein were assumed to be of the same size, and calculated according to [16,17] as

$$d_a^3 = d_v^3 = d^3 + d^3 \tag{50}$$

It was further assumed that the renal artery branched into the mother generation vessels immediately as it traveled into the medulla region. To calculate the mean velocity in the paired artery and vein, the total vessel number was determined as the following. Xu et al. [15] showed that the vessel number density was $f_n = 8.6\times10^4/\mathrm{m}^2$ for the vessels of 500 μm diameter at the CMJ. The dimension of the kidney was about 0.116 m$\times$0.0545 m$\times$0.0401 m. The kidney was approximated in the elliptic shape, and the estimated area at the CMJ was $A_{\mathrm{CMJ}} = 6.18\times10^{-3}\,\mathrm{m}^2$. The total vessel number was then calculated as $N = f_n \times A_{\mathrm{CMJ}} \approx 532$. Therefore, the number of the mother vessel pairs was $N_{\mathrm{unit}} = 0.25N \approx 133$ in the medulla. If the renal inlet volumetric flow rate was Q_{in}, the mean blood velocity could be calculated as

$$u_m = \frac{4Q_{\mathrm{in}}}{N_{\mathrm{unit}}\pi d_a^2} \tag{51}$$

When $Q_{\mathrm{in}} = 1.67\times10^{-6}\,\mathrm{m}^3/\mathrm{s}$, then $u_m = 4.02\times10^{-2}$ m/s. The tissue unit radius at the CMJ (R_{CMJ}) was calculated using the following formulation

$$R_{\mathrm{CMJ}} = \sqrt{\frac{A_{\mathrm{CMJ}}}{\pi N_{\mathrm{unit}}}} \tag{52}$$

When uniform blood perfusion was assumed in the cortex and all the inlet flow traveled to the cortex, the perfusion rate could be calculated based on Q_{in} and the mass fraction of the cortex with respect to the whole kidney (M_c/M_k). The return flow through the ureter was almost negligible in the isolated kidney. Using mass conservation,

$$Q_{\mathrm{in}} = \omega_b M_c \tag{53}$$

The blood density was approximately equal to $1.0\times10^3\,\mathrm{kg/m}^3$, and Eq. (53) became,

$$\omega_b = \frac{M_k}{M_c}\frac{Q_{\mathrm{in}}}{M_k} \tag{54}$$

For the kidney used in the present study, $M_k \approx 0.130$ kg and $M_k/M_c \approx 1.36$. All parameters used in the calculation are listed in Table 1.

Experimental Studies

Experiments were designed to measure the steady state tissue temperature distribution and the renal arterial inlet flow rate and temperature in the isolated pig kidney to validate the newly developed analytical model. During the experiments, the kidney was first heated to a uniform temperature 43°C. Then de-ionized water at 37°C was pumped into the renal artery until steady state was reached. The kidney surface temperature was kept at 43°C during each experiment. The experimental setup is shown in Fig. 3. To hold the kidney in position and keep a uniform surface temperature, the kidney was fitted in a thin-walled ($\approx$0.004 m of thickness) mold made of woodsmetal (METSPEC 158 manufactured by Metal Specialties, IL) and immersed in the water bath B1 (EX-221, NESLAB Instruments, Inc., Portsmouth, NH). The woodsmetal mold was made to keep uniform temperature at the kidney surface and to eliminate the convection effect of the water bath. Three T-type thermocouples were placed at different loca-

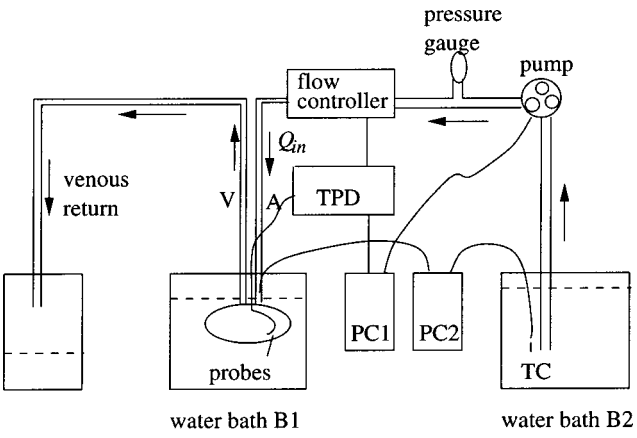

Fig. 3 Schematic of the experimental setup

tions on the kidney surface to assure the uniform temperature distribution during the experiment. Thermistor microprobes (0.0003 m diameter) of various lengths were inserted into the cortex and connected to the thermal pulse decay (TPD) system to measure the local perfusion rate and tissue temperature. To measure the tissue temperature distribution in the renal medulla, long microprobes (>0.01 m in length) were needed. However, these probes were very difficult to make given their small diameters, and were easily broken during insertion. Further, once inserted deeply in tissue, their exact locations could not be accurately determined. Due to these difficulties, tissue temperatures in the renal medulla were not measured in this study.

The de-ionized water pumped from the water bath B2 into the renal artery (A) was used to simulate blood flow. The venous return flow was collected in a container. The flow rates were controlled by the current-controlled roller pump and also measured using a voltage-controlled flow controller system (400-5L Flo-Controller, McMillan Company, Georgetown, TX). Considering heat loss to the environment through the transit conduit, the bath B2 temperature was kept >37°C to ensure the temperature of the renal artery inlet flow was about 37°C, while bath B1 was used to maintain the kidney surface temperature at 43°C. Temperatures of the two baths and the arterial inlet flow were continuously measured using T-type thermocouples. Prior to each experiment, blood perfusion rates were examined at various locations within the kidney using the TPD technique [18]. The well-perfused regions were chosen to perform temperature measurements. Two Pentium II 233 MHz Dell personal computers (PC) were used for data acquisition through LabView user interfaces. The temperature readings from the thermistor microprobes and flow rates were acquired by PC1, and the temperature readings from the thermocouples were recorded by PC2.

Results and Discussion

The temperature distribution at the $z=6$ mm cross-section in medulla (referring to Fig. 2) is shown in Fig. 4. The venous region is the hottest and the artery region is the coldest. Heat carried by the venous flow from the warmer cortex region is transferred into the arterial flow. Cooling effect of the flow is evident when tissue temperature is higher than that of the flow.

Shown in Fig. 5, the experimental data are compared with the predicted steady state bulk temperatures. Limited by the probe lengths, tissue temperatures were only measured at five different depths from the kidney surface in the cortex. At each depth, five to nine measurements were made to yield the average temperature and the standard deviation. In the middle region, the venous bulk temperature is higher than that of the tissue. This is due to the substantial cooling effect of the arterial flow. It is clear that the theoretical predictions are in good agreement with the experimental data in the cortex, which would be impossible without having good matching boundary conditions at the CMJ given by Eq. (22) since the temperature solution in the cortex (given by Eq. (20)) is unique. It, therefore, implies that the temperature predictions in the renal medulla are realistic although they could not be directly measured in this study.

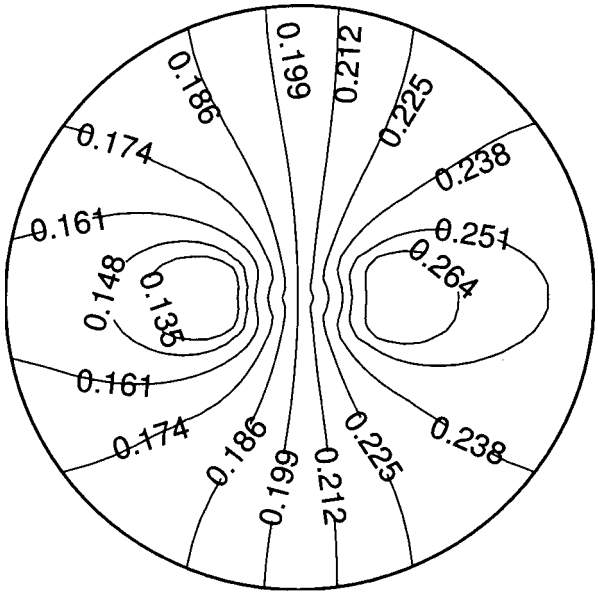

Fig. 4 Contour plot of the analytical solutions of the steady state temperature distribution at the cross-section at $z=6$ mm. The kidney surface temperature $T_s=43.0$°C, the arterial inlet flow temperature $T_{a0}=37.0$°C, and the blood perfusion rate $\omega_b=0.007$ m^3/s/m^3.

Figure 6 presents the analytical solutions of the steady state bulk temperature distributions under different flow rates. When the perfusion rate increases from 0.007 m^3/s/m^3 to 0.035 m^3/s/m^3, the magnitude of the arterial temperature elevation decreases, and the tissue temperature distribution appears to be more uniform in the middle region of the kidney. Large tissue temperature gradi-

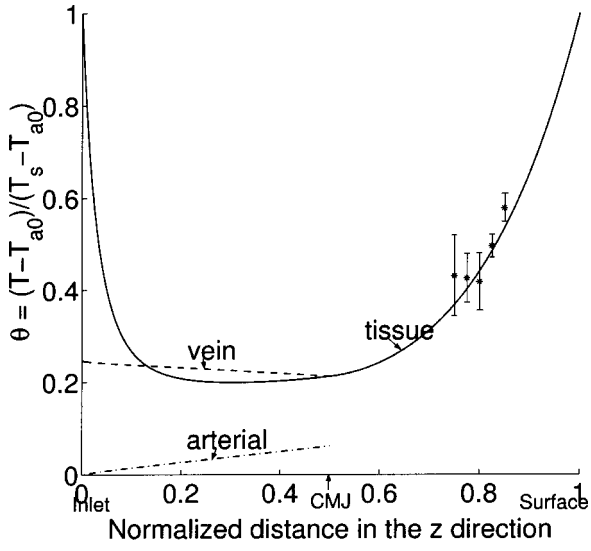

Fig. 5 Steady state temperature distributions in the pig kidney during water bath heating. The kidney surface temperature was $T_s=43$°C, the arterial inlet flow rate $Q_{in}=1.55\times10^{-6}$ m^3/s, and the initial kidney temperature and the arterial inlet flow temperature were the same, $T_i=T_{a0}=37$°C.

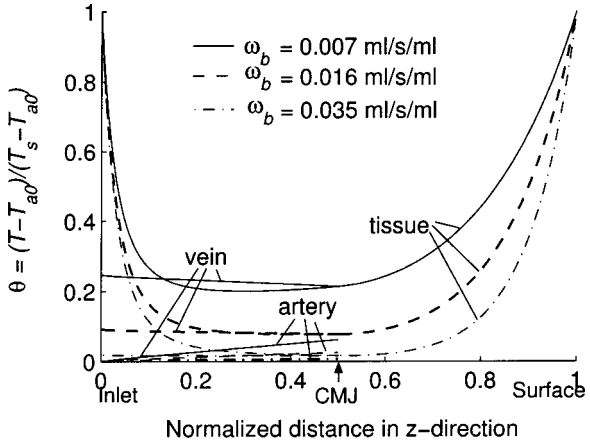

Fig. 6 The analytical predictions of the steady state bulk temperature distributions with respect to different blood perfusion rates. The kidney surface temperature T_s=43.0°C and the arterial inlet flow temperature T_{a0}=37.0°C.

ents occur near the kidney surface due to the cooling effect of the inlet arterial flow at a lower temperature. Artery flow temperature increases along the axial direction because of heat transfer from tissue and counter current heat exchange from the venous return flow. The temperature of the venous flow is higher than that of the arterial inlet flow since the venous blood collects heat from the surrounding tissue when subjected to heating. At the lowest flow rate ($\omega_b = 0.007\ m^3/s/m^3$), the predicted $T_{a,CMJ}$ is approximately 0.5°C higher than that at the highest ($\omega_b = 0.035\ m^3/s/m^3$) due to more counter current rewarming occurred in the arterial flow. Since $T_{a,CMJ}$ was used as the arterial supply temperature in the Pennes equation in the cortex, its value significantly affected the temperature distribution as shown in Fig. 6. The presently developed three-dimensional vascular model, that accounts for the counter current heat exchange between the paired artery and vein in the medulla region, can be used to accurately predict $T_{a,CMJ}$.

Conclusions

A vascular model was successfully developed to accurately predict the blood-tissue heat transfer in the perfused kidney model. Local perfusion rate significantly affected tissue temperature distributions, which is the driving force for tissue temperature oscillations. This model can be used to investigate the effect of blood flow change on tissue temperature oscillations during surface heating, for developing optimal treatment protocols of cancer hyperthermia.

Acknowledgments

This research was supported by National Cancer Institute #5 R29 CA67970 and Purdue Research Foundation 690-1288-2977.

Nomenclature

a = radius, m
a_{ij} = coefficients used in Eqs. (37–45)
a_n = coefficients used in Eq. (33)
A = tissue cross-sectional area, m^2
A_C = coefficient used in Eq. (46)
b_n = coefficients used in Eq. (33)
c_p = specific heat at constant pressure, J/kg/K
d = vessel diameter, m
k = thermal conductivity, W/m/K
L = length of the whole tissue unit, m
L_l = length of the cortex region, m
M_c = mass of the cortex region, kg
M_k = mass of the whole kidney, kg
n = vessel number density at the corticomedullary junction
N = total vessel number
N_{unit} = Number of tissue units used for a kidney
Pe = Peclet number
Q = volumetric blood flow rate, m^3/s
r = radial coordinate, origin at the centerline of tissue cylinder, m
r_a = radial coordinate, origin at the centerline of renal artery, m
r_v = radial coordinate, origin at the centerline of renal vein, m
R = radius of tissue cylinder, m
s_a = center-to-center distance of tissue and artery, m
s_v = center-to-center distance of tissue and vein, m
T = tissue temperature, °C
T_a = arterial blood temperature, °C
T_v = venous blood temperature, °C
u_m = mean velocity, m/s

Greek Symbols

α = thermal diffusivity, m^2/s
ϕ = angular coordinate, origin at the centerline of tissue cylinder
ϕ_a = angular coordinate, origin at the centerline of renal artery
ϕ_v = angular coordinate, origin at the centerline of renal vein
θ = dimensionless temperature
ρ = density, kg/m^3
ω_b = blood perfusion rate, $m^3/s/m^3$

Superscript

$*$ = dimensionless parameter

Subscripts

0 = inlet
1 = cortex region
2 = medullar region
a = artery
ab = bulk parameter of artery
b = blood
CMJ = corticomedullary junction
in = arterial inlet
p = particular solution
R = side surface of tissue cylinder
s = kidney surface
t = tissue
$t2b$ = bulk parameter of tissue
v = vein
vb = bulk parameter of vein

Vector

$\vec{n}$ = the vector normal to the tissue cylinder side surface

Appendix

Single Artery Case. First, consider that the tissue cylinder includes only one artery. Assuming that the particular solutions for artery and tissue are dependent on only radial coordinate, one can obtain the following:

Tissue.

$$\frac{1}{r^*}\frac{\partial}{\partial r^*}\left(r^*\frac{\partial \theta_{t2}}{\partial r^*}\right) = -\frac{d^2\theta_{t2b}}{dz^{*2}} \tag{55}$$

Artery.

$$\frac{1}{r_a^*}\frac{\partial}{\partial r_a^*}\left(r_a^*\frac{\partial \theta_a}{\partial r_a^*}\right) = \mathrm{Pe}(1-r_a^{*2})\frac{d\theta_{ab}}{dz^*} \tag{56}$$

The solutions for the above equations are

$$\theta_{t2} = -\frac{1}{4} r^{*2} \frac{d^2\theta_{t2b}}{dz^{*2}} + c_{t1} \ln r^* + c_{t2} \tag{57}$$

$$\theta_a = \mathrm{Pe}\left(\frac{1}{4} r_a^{*2} - \frac{1}{16} r_a^{*4}\right) \frac{d\theta_{ab}}{dz^*} + c_{a1} \ln r_a^* + c_{a2} \tag{58}$$

Substituting Eq. (57) into the boundary condition Eq. (24) and assuming $\vec{n}^* \approx r^*$ (this will be valid when the angle between the side surface of the tissue unit and the arterial inlet surface is small), one obtains

$$c_{t1} = \frac{R^{*2}}{2} \frac{d^2\theta_{t2b}}{dz^{*2}} \tag{59}$$

Therefore, the solution for Eq. (55) can be represented as

$$\theta_{t2} = -\frac{1}{4}\left(r^{*2} - 2R^{*2} \ln \frac{r^*}{R^*}\right) \frac{d^2\theta_{t2b}}{dz^{*2}} + c_{t2} \tag{60}$$

Consider the following homogeneous equation

$$\frac{1}{r_a^*} \frac{\partial}{\partial r_a^*}\left(r_a^* \frac{\partial \theta'}{\partial r_a^*}\right) = 0 \tag{61}$$

Its solution is

$$\theta' = c_1 \ln r_a^* + c_2 \tag{62}$$

Considering Eqs. (60) and (62), we choose the particular solution for tissue as,

$$\theta_{t2,p} = \theta' + \theta_{t2} = c'_{t1} \ln r_a^* - \frac{1}{4}\left(r^{*2} - 2R^{*2} \ln \frac{r^*}{R^*}\right) \frac{d^2\theta_{t2b}}{dz^{*2}} + c'_{t2} \tag{63}$$

Substituting Eqs. (58) and (63) into the boundary conditions Eqs. (25) and (26), define c_{a1}, c_{a2}, c'_{t1}, and c'_{t2} to be,

$$c'_{t1} = \frac{1}{4} \mathrm{Pe} \frac{d\theta_{ab}}{dz^*} \tag{64}$$

$$c'_{t2} = 0 \tag{65}$$

$$c_{a1} = -\frac{r_{*a}^{*2}}{2}\left(1 - \frac{R^{*2}}{r_{*a}^{*2}}\right)(1 - s_a \cos\phi_a) \frac{d^2\theta_{t2b}}{dz^{*2}} \tag{66}$$

$$c_{a2} = -\frac{3}{16} \mathrm{Pe} \frac{d\theta_{ab}}{dz^*} - \frac{1}{4} \frac{d^2\theta_{t2b}}{dz^{*2}}\left(r_{*a}^{*2} - 2R^{*2} \ln \frac{r_{*a}^*}{R^*}\right) \tag{67}$$

where

$$r_{*a}^{*2} = 1 + s_a^{*2} - 2s_a^* r_a^* \cos\phi_a \tag{68}$$

Then, the particular solutions for artery and tissue can be represented as

$$\theta_{a,p} = \mathrm{Pe}\left(\frac{1}{4} r_a^{*2} - \frac{1}{16} r_a^{*4} - \frac{3}{16}\right) \frac{d\theta_{ab}}{dz^*} + c'_{a1} \ln r_a^* + c'_{a2} \tag{69}$$

$$\theta_{t2,p} = \frac{1}{4} \mathrm{Pe} \ln r_a^* \frac{d\theta_{ab}}{dz^*} - \frac{1}{4} \frac{d^2\theta_{t2b}}{dz^{*2}}\left(r^{*2} - 2R^{*2} \ln \frac{r^*}{R^*}\right) \tag{70}$$

where

$$c'_{a2} = -\frac{1}{4} \frac{d^2\theta_{t2b}}{dz^{*2}}\left(r_{*a}^{*2} - 2R^{*2} \ln \frac{r_{*a}^*}{R^*}\right) \tag{71}$$

To ensure that the temperature and heat flux are continuous at the arterial wall, one has,

$$c'_{a2} = -\frac{1}{4} \frac{d^2\theta_{t2b}}{dz^{*2}}\left(1 + s_a^{*2} - 2r_a^* s_a^* \cos\phi_a - 2R^{*2} \ln \frac{r^*}{R^*}\right) \tag{72}$$

and

$$c'_{a1} = 2\left(-\frac{1}{4} \frac{d^2\theta_{t2b}}{dz^{*2}}\right) \tag{73}$$

Therefore, the final form of the particular solution for artery is

$$\theta_{a,p} = \mathrm{Pe}\left(\frac{1}{4} r_a^{*2} - \frac{1}{16} r_a^{*4} - \frac{3}{16}\right) \frac{d\theta_{ab}}{dz^*} - \frac{1}{4} \frac{d^2\theta_{t2b}}{dz^{*2}} \times \left(2 \ln r_a^* + 1 + s_a^{*2} - 2r_a^* s_a^* \cos\phi_a - 2R^{*2} \ln \frac{r^*}{R^*}\right) \tag{74}$$

The final form of the particular solution for tissue is Eq. (70). The homogeneous solution for both tissue and artery, $\theta_{h,a}$, takes the form [12]:

$$\theta_{h,a} = \left(a_0 + \sum_{n=1}^{\infty} a_n r^{*n} \cos n\phi\right) \frac{d\theta_{ab}}{dz^*} \tag{75}$$

Adding the particular solutions to the homogeneous solution for artery and tissue, respectively, one then obtains the solutions for the single artery case.

Single Vein. Similarly to the single artery case, one has the particular solutions for the vein and tissue:

$$\theta_{v,p} = \mathrm{Pe} a_v^* \left(\frac{1}{4} r_v^{*2} - \frac{1}{16} \frac{r_v^{*4}}{a_v^{*2}} - \frac{3}{16} a_v^{*2}\right) \frac{d\theta_{vb}}{dz^*} - \frac{1}{4} \frac{d^2\theta_{t2b}}{dz^{*2}}\left[2a_v^{*2} \ln\left(\frac{r_v^*}{a_v^*}\right) + a_v^{*2} + s_v^{*2} + 2a_v^* s_v^* \cos\phi_v - 2R^{*2} \ln \frac{r^*}{R^*}\right] \tag{76}$$

$$\theta_{t2,p} = -\frac{1}{4} \mathrm{Pe} a_v^{*2} \ln\left(\frac{r_v^*}{a_v^*}\right) \frac{d\theta_{vb}}{dz^*} - \frac{1}{4} \frac{d^2\theta_{t2b}}{dz^{*2}}\left(r^{*2} - 2R^{*2} \ln \frac{r^*}{R^*}\right) \tag{77}$$

and the homogeneous solution,

$$\theta_{h,v} = \left(b_0 + \sum_{n=1}^{\infty} b_n r^{*n} \cos n\phi\right) \mathrm{Pe} a_v^{*2} \frac{d\theta_{vb}}{dz^*} \tag{78}$$

Countercurrent Artery-Vein Case. Following a derivation similar to that presented in [11], one can obtain the solutions for Eqs. (14–16) by superposition of the solutions for single artery and single vein cases discussed above. Then, substituting the solution for tissue into the boundary condition Eq. (24) to determine the coefficients a_n and b_n for the homogeneous solution. The final forms of the solutions are Eqs. (29–31) in the main text.

References

[1] Dyce, K. M., Sack, W. O., and Wensing, C. J. G., 1996, *Textbook of Veterinary Anatomy*, W. B. Saunders Company, Philadelphia, PA.

[2] Holmes, K. R., Ryan, W., Weinstein, P., and Chen, M. M., 1984, "A Fixation Technique for Organs to be Used as Perfused Tissue Phantoms in Bioheat Transfer Studies," ASME Adv. in Bioeng., **11**, pp. 9–10.

[3] Zaerr, J., Roemer, R. B., and Hynynen, K., 1990, "Computer-Controlled Dynamic Phantom for Ultrasound Hyperthermia Studies," IEEE Trans. Biomed. Eng., **37**(11), pp. 1115–1120.

[4] Xu, L. X., 1999, "New Developments in Bioheat and Mass Transfer," *Ann. Rev. Heat Trans.*, C. L. Tien, ed., Begell House, Chap. 1.

[5] Brown, S. L., Li, X. L., Pai, H. H., Worthington, A. E., Hill, R. P., and Hunt, J. W., 1992, "Observations of Thermal Gradients in Perfused Tissues During

Water Bath Heating,'' Int. J. Hyperthermia, **8**(2), pp. 275–287.
[6] Kolios, M. C., Worthington, A. E., Sherar, M. D., and Hunt, J. W., 1998, ''Experimental Evaluation of Two Simple Thermal Models Using Transient Temperature Analysis,'' Phys. Med. Biol., **43**, pp. 3325–3340.
[7] Kolios, M. C., Worthington, A. E., Holdsworth, D. W., Sherar, M. D., and Hunt, J. W., 1999, ''An Investigation of the Flow Dependence of Temperature Gradients Near Large Vessels During Steady State and Transient Tissue Heating,'' Phys. Med. Biol., **44**(6), pp. 1479–149.
[8] Pennes, H. H., 1948, ''Analysis of Tissue and Arterial Blood Temperatures in the Resting Human Forearm,'' Appl. Physiol., **1**(2), pp. 93–122.
[9] Weibaum, S., Jiji, L. M., and Lemons, D. E., 1984, ''Theory and Experiment for the Effect of Vascular Microstructure on Surface Heat Transfer-Part I: Anatomical Foundation and Model Conceptualization,'' ASME J. Biomech. Eng., **106**, pp. 321–330.
[10] Valvano, J. W., Nho, S., and Anderson, G. T., 1994, ''Analysis of the Weinbaum-Jiji Model of Blood Flow in the Canine Kidney Cortex for Self-Heated Thermistors,'' ASME J. Biomech. Eng., **116**, pp. 201–207.
[11] Zhu, M., Weinbaum, S., and Jiji, L. M., 1990, ''Heat Exchange Between Unequal Countercurrent Vessels Asymmetrically Embedded in a Cylinder With Surface Convection,'' Int. J. Heat Mass Transfer, **33**(10), pp. 2275–2284.
[12] Chen, C., and Xu, L. X., 2000, ''Theoretical and Experimental Studies of Heat Transfer in the Vascularized Tissue Hyperthermic Conditions Using Preserved Pig Kidney,'' *Proc. 34th National Heat Transfer Conference*, Pittsburgh, PA, pp. 683–689.
[13] Wu, Y. L., Weinbaum, S., and Jiji, L. M., 1993, ''A New Analytic Technique for 3-d Heat Transfer From a Cylinder With Two or More Axially Interacting Eccentrically Embedded Vessels With Application to Countercurrent Blood Flow,'' Int. J. Heat Mass Transfer, **36**(4), pp. 1073–1083.
[14] Weinbaum, S., Xu, L. X., Zhu, L., and Ekpene, A., 1997, ''A New Fundamental Bioheat Equation for Muscle Tissue: Part I—Blood Perfusion Term,'' ASME J. Biomech. Eng., **119**, pp. 278–288.
[15] Xu, L. X., Holmes, K. R., Moore, B., Chen, M. M., and Arkin, H., 1994, ''Microvascular Architecture Within the Pig Kidney Cortex,'' Microvasc. Res., **47**, pp. 293–307.
[16] Murray, C. D., 1926, ''The Physiological Principle of Minimum Work Applied to the Angle of Branching of Arteries,'' J. Gen. Phys., **9**, pp. 835–841.
[17] Murray, C. D., 1926, ''The Physiological Principle of Minimum Work. I. The Vascular System and the Cost of Blood Volume,'' Proc. Natl. Acad. Sci. U.S.A., **12**, pp. 207–214.
[18] Arkins, H., Holmes, K. R., Chen, M. M., and Bottje, W. G., 1986, ''Thermal Pulse Decay Method for Simultaneous Measurement of Local Thermal Conductivity and Blood Perfusion: A Theoretical Analysis,'' ASME J. Biomech. Eng., **108**, pp. 208–214.

Journal of Heat Transfer

Technical Notes

This section contains shorter technical papers. These shorter papers will be subjected to the same review process as that for full papers.

Dissipation in Small Scale Gaseous Flows

Nicolas G. Hadjiconstantinou
Mechanical Engineering Department, Massachusetts Institute of Technology, Cambridge, MA 02139

We discuss the effect of shear work at solid boundaries in small scale gaseous flows where slip effects are present. The effect of shear work at the boundary on convective heat transfer is illustrated through solution of the constant-wall-heat-flux problem in the slip-flow regime. We also present predictions for the dissipation in terms of the mean flow velocity in pressure-driven and gravity-driven Poiseuille flows for arbitrary Knudsen numbers. All results are verified using direct Monte Carlo solutions of the Boltzmann equation. [DOI: 10.1115/1.1571088]

Keywords: Heat Transfer, Microscale, Molecular Dynamics, Monte Carlo, Nanoscale

In this paper we discuss two aspects of dissipation in small scale ideal-gas flows. We first discuss the effect of shear work at the boundary in slip flow and how this affects convective heat transfer in small scale channels. Shear work at the boundary has, incorrectly, been neglected in recent studies of viscous heat dissipation in slip-flow convective heat transfer. We show that this effect scales with the Brinkman number, and subsequently derive an expression for the fully developed slip-flow Nusselt number under constant-wall-heat-flux conditions in the presence of viscous dissipation and compare this expression to direct Monte Carlo solutions of the Boltzmann equation. The second aspect discussed is related to dissipation in transition-regime flows. Using the solution of the Boltzmann equation for gravity and pressure-driven flows in two-dimensional channels and energy conservation arguments, we provide expressions for the energy dissipation in these flows as a function of the flow speed for arbitrary Knudsen numbers. Our results are verified by direct Monte Carlo solutions of the Boltzmann equation.

For simplicity, we consider two-dimensional smooth channels of length L in the axial (x) direction, with perfectly accommodating walls that are a distance H apart in the transverse (y) direction. The flow in the axial direction is sustained either by an imposed pressure gradient or external field g. The gas velocity field is denoted $\vec{\mathbf{u}}=\vec{\mathbf{u}}(x,y)=(u_x(x,y),u_y(x,y),u_z(x,y))$, and $T=T(x,y)$, $P=P(x,y)$ and $\rho=\rho(x,y)$ denote the temperature, pressure and density fields respectively.

We first consider the case of pressure-driven flow that is heated or cooled by a constant wall-heat-flux. The channel dimensions are such that the flow and heat transfer characteristics are in the slip-flow regime where the usual slip-flow boundary conditions

$$u_{\text{gas}}|_{\text{wall}}=\alpha\frac{2-\sigma_v}{\sigma_v}\lambda\left.\frac{du}{d\tilde{\eta}}\right|_{\text{wall}} \tag{1}$$

$$T_{\text{gas}}|_{\text{wall}}-T_w=\beta\frac{2\gamma}{\gamma+1}\frac{2-\sigma_T}{\sigma_T}\frac{\lambda}{\text{Pr}}\left.\frac{dT}{d\tilde{\eta}}\right|_{\text{wall}} \tag{2}$$

are known to provide a good approximation to the velocity and temperature fields, respectively. Here λ is the molecular mean free path, σ_v is the momentum accommodation coefficient, $\tilde{\eta}$ is the coordinate normal to the wall, T_w is the local wall temperature, σ_T is the energy accommodation coefficient, Pr is the gas Prandtl number, and γ is the ratio of specific heats. The coefficients α and β introduce corrections to the original results of Maxwell ($\alpha=\beta=1$) that were obtained through an approximate method [1]. For air, α and β are usually taken to be equal to unity [2]. Linearized solutions of the Boltzmann equation [3,4] show that for hard spheres $\alpha\approx\beta\approx1.1$. In what follows we will assume, without loss of generality, that both accommodation coefficients are equal to unity, or equivalently that their contribution has been absorbed in α and β.

Under the assumption of a long channel ($L\gg H$) and low speed flow (small pressure gradient or external field) we approximate the flow as hydro-dynamically and thermally *locally* fully developed; we also assume that the temperature changes and compressibility cause the flow to deviate negligibly from this state. Under these assumptions we assume that *locally* the pressure gradient is constant, $u_x=u_x(y)$, $T=T(x,y)$ and $\tau_{xy}=\tau_{xy}(y)$, where τ_{xy} is the xy component of the shear stress tensor. The velocity profile is then given by the slip-flow ($\text{Kn}\lesssim0.1$) Poiseuille profile

$$u_x=\frac{u_b}{\alpha\text{Kn}+\frac{1}{6}}\left[\left(\alpha\text{Kn}+\frac{1}{4}\right)-\frac{y^2}{H^2}\right] \tag{3}$$

where u_b is the bulk (average) velocity over the channel cross-section and the Knudsen number is given by $\text{Kn}=\lambda/H$.

The temperature equation in the presence of viscous heat generation and flow work reduces to

$$\rho c_p u_x\frac{\partial T}{\partial x}-u_x\frac{dP}{dx}=-\frac{\partial q_y}{\partial y}+\tau_{xy}\frac{\partial u_x}{\partial y} \tag{4}$$

where c_p is the specific heat at constant pressure, and q_i is the component of the heat flux vector in the i^{th} direction. Our constitutive definitions follow those of [5]. Note that conservation laws will be given in their general form (without continuum constitutive models) applicable in all Knudsen regimes. Explicit use of the continuum constitutive models will be limited to the derivation of the Nusselt number in the slip-flow regime. The integral form of the above equation in the transverse direction under the assumption of negligible density variation in this direction is

Contributed by the Heat Transfer Division for publication in the JOURNAL OF HEAT TRANSFER. Manuscript received by the Heat Transfer Division July 12, 2002; revision received February 11, 2003. Associate Editor: P. S. Ayyaswamy.

$$\rho c_p u_b H \frac{dT_b}{dx} - u_b H \frac{dP}{dx} = 2q_o + \int_{-H/2}^{H/2} \tau_{xy} \frac{\partial u_x}{\partial y} dy \tag{5}$$

where q_o is the *thermal* energy transferred from the wall to the fluid, and T_b, the bulk temperature, is defined by

$$T_b = \frac{\int_{-H/2}^{H/2} u_x T dy}{u_b H} \tag{6}$$

In addition to the thermal energy transfer, there is also dissipation due to shear work between the wall and the slipping gas. It is the sum of these two contributions that is responsible for the axial temperature gradient (and perceived as a constant wall-heat-flux) as shown by the integral form of the total (mechanical plus thermal) energy equation

$$\rho c_p u_b \frac{dT_b}{dx} H = [u_x \tau_{xy} - q_y]_{-H/2}^{H/2} \tag{7}$$

Equations (5) and (7) are linked by the mechanical energy balance

$$0 = -u_x \frac{\partial P}{\partial x} + u_x \frac{\partial \tau_{xy}}{\partial y} = -u_x \frac{\partial P}{\partial x} + \frac{\partial (u_x \tau_{xy})}{\partial y} - \tau_{xy} \frac{\partial u_x}{\partial y} \tag{8}$$

which integrates to

$$[\tau_{xy} u_x]_{-H/2}^{H/2} = \int_{-H/2}^{H/2} \tau_{xy} \frac{\partial u_x}{\partial y} dy + u_b H \frac{dP}{dx} \tag{9}$$

and shows that the viscous heat and flow work terms in Eq. (5) are, in effect, representing the contribution of the shear work at the wall (Eq. (7)).

We proceed by nondimensionalizing Eq. (4) using $\theta = (T - T_w)/(q_o H/\kappa)$ and $\mathrm{Br}' = \mu u_b^2/(q_o H)$, where κ is the thermal conductivity of the gas, and $\eta = y/H$. When acceleration effects are negligible, for constant wall-heat-flux under fully developed conditions, $\partial T/\partial x = dT_b/dx = \text{const}$. We thus substitute for $\partial T/\partial x$ from Eq. (5) and for this slip-flow calculation use the Fourier conduction law to obtain

$$2 \frac{u_x}{u_b} \left(1 + 6\mathrm{Br}' \left(1 - \frac{u_s}{u_b} \right)^2 \right) - \mathrm{Br}' \left(\frac{\partial \left(\frac{u_x}{u_b} \right)}{\partial \eta} \right)^2 = \frac{\partial^2 \theta}{\partial \eta^2} \tag{10}$$

where u_s is the slip velocity, $u_x|_{\pm H/2}$, given by

$$\frac{u_s}{u_b} = \frac{6\alpha \mathrm{Kn}}{1 + 6\alpha \mathrm{Kn}} \tag{11}$$

We solve for θ using a symmetry condition at $\eta = 0$ and the slip-flow relation (2), and from this solution proceed to calculate $T_w - T_b$. The fully developed slip-flow Nusselt number based on the thermal energy exchange is then given by

$$\mathrm{Nu} = \frac{q_o 2H}{\kappa (T_w - T_b)} = \frac{\frac{140}{17} - 2\mathrm{Br} \left(1 - \frac{u_s}{u_b} \right)^2 \left(\frac{54}{17} - \frac{30}{17} \frac{u_s}{u_b} + \frac{12}{51} \left(\frac{u_s}{u_b} \right)^2 \right)}{1 - \frac{6}{17} \frac{u_s}{u_b} + \frac{2}{51} \left(\frac{u_s}{u_b} \right)^2 + \frac{140}{17} \beta \frac{\gamma}{\gamma + 1} \frac{\mathrm{Kn}}{\mathrm{Pr}}} \tag{12}$$

where $\mathrm{Br} = \mathrm{NuBr}'/2 = \mu u_b^2/(\kappa (T_w - T_b))$. The fully developed slip-flow Nusselt number based on the total energy exchange between wall and gas is then

$$\mathrm{Nu}_t = \mathrm{Nu} + \frac{(\tau_{xy} u_x)|_{H/2} 2H}{\kappa (T_w - T_b)} = \mathrm{Nu} - 12\mathrm{Br} \frac{u_s}{u_b} \left(1 - \frac{u_s}{u_b} \right) \tag{13}$$

Although the above expression is exact, it is only expected to hold for small Brinkman numbers since high velocities will violate the assumption of negligible compressibility and fluid acceleration. A more detailed discussion (albeit for the continuum case) of the competition between cooling and viscous heat dissipation, which ultimately leads to $\mathrm{Nu} \to \infty$ for fairly large negative Br, can be found in [6].

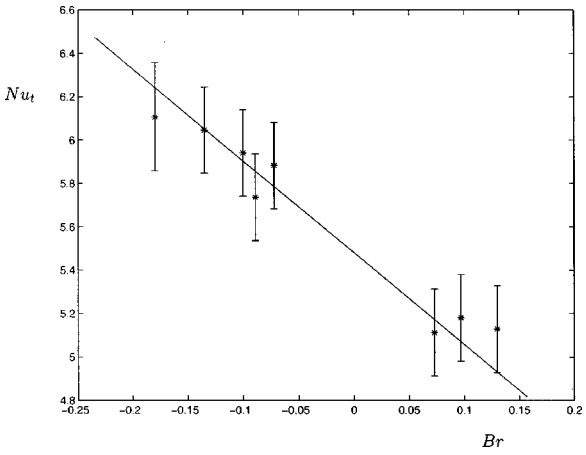

Fig. 1 Variation of the fully developed Nusselt number Nu_t with Brinkman number for Kn=0.07. The solid line is the prediction of Eq. (13), and the stars denote DSMC simulations.

We performed DSMC simulations [7] to verify Eq. (13). Our simulations were performed on a hard sphere system since for theory verification purposes it is preferable to perform simulations on a molecular system whose properties are well characterized. A constant wall-heat-flux was achieved by applying a linearly varying wall temperature. Our simulations represent the best compromise between high speeds for low relative statistical error and low speeds for negligible compressibility effects. Because the effect of the wall shear stress is of the order of 10 percent for $|\mathrm{Br}| \lesssim 0.1$, we tried to minimize all possible sources of error. As a result, we used the fourth order approximations for the transport coefficients (approximately 2 percent different from the typically-used first order approximations [8]) and also used the values $\alpha = 1.11$ and $\beta = 1.13$ recommended by [3,4]. We additionally corrected our results for the effects of finite cell sizes and timestep [9,10,11] in our numerical solution. Our resulting error estimate including statistical fluctuations is approximately 4 percent. The ratio of the expected average thermal creep velocity [12] to the bulk velocity, u_c/u_b, was less than 0.1.

The agreement between the DSMC simulations and the theoretical results is very good (see Fig. 1). This verifies the contribution of shear work at the boundary but also shows that the slip-flow prediction is accurate to within 4 percent at Kn=0.07. Also, despite the relatively large pressure gradients used ($P_{\mathrm{in}}/P_{\mathrm{out}} \sim O(1.5)$, $P_{\mathrm{out}} \approx 1\,\mathrm{bar}$, $L \approx 20\ \mu\mathrm{m}$) the assumption of negligible compressibility and fully developed flow and temperature fields seems to be reasonable. Given that slip-flow does not describe the correct state of the gas close to the wall (due to the presence of the Knudsen layer) but rather provides a recipe for obtaining the hydrodynamic fields far away from the wall [1], the importance of wall effects in this phenomenon makes the good agreement all the more remarkable.

In view of the interest in ever decreasing device sizes, it is interesting to explore dissipation in the transition regime ($0.1 \lesssim \mathrm{Kn} \lesssim 10$). It is well known [2] that Poiseuille profiles in this regime become flat (Eqs. (3) and (11) are not valid) and large amounts of slip are observed at the walls leading to significant dissipation there, which, as we saw above, does not affect the temperature field inside the channel. In the interest of simplicity, we will discuss steady, fully developed, Poiseuille-type flows with constant-temperature walls. These flows are the extension to arbitrary Knudsen numbers of the Poiseuille flow assumed in the con-

vective heat transfer problem solved above and are thus interesting to study in their own right as well as in connection with convective heat transfer in the transition regime [7]. Note that no linear constitutive closures for the shear stress tensor and heat flux vector are now assumed.

For these flows, the total energy equation simplifies to

$$\frac{\partial}{\partial y}(\tau_{xy}u_x - q_y) = \rho c_p u_x \frac{\partial T}{\partial x} = 0 \tag{14}$$

which shows that there is no net energy exchange with the boundary, and thus the thermal energy flux at the wall is balanced by the shear work at the boundary. Using Eq. (9) or the thermal energy equation we obtain

$$[q_y]_{-H/2}^{H/2} = u_b \frac{dP}{dx} H + \int_{-H/2}^{H/2} \tau_{xy} \frac{\partial u_x}{\partial y} dy \tag{15}$$

Note that the fully developed temperature profile will, in general, be non-uniform in the y direction with an average temperature that is different from the wall temperature. The temperature profile can be calculated if closures for the shear stress tensor and heat flux vector are provided.

The bulk velocity in Poiseuille flow for arbitrary Knudsen numbers is given by [12]

$$\mathrm{H}u_b = -\frac{1}{P}\frac{dP}{dx}\sqrt{\frac{RT}{2}} H^2 \overline{Q} \tag{16}$$

where $R = k_b/m$ is the gas constant, k_b is Boltzmann's constant, m is the molecular mass and $\overline{Q} = \overline{Q}(\mathrm{Kn})$ is a proportionality coefficient that has been determined semianalytically by solution of the Boltzmann Eq. [1] and found to be in good agreement with molecular simulations and experimental data [1,2]. In the transition regime, $\overline{Q}(\mathrm{Kn})$ varies slowly about its minimum value ($1.5 \lesssim \overline{Q}(0.1 < \mathrm{Kn} < 10) \lesssim 3$) occuring at $\mathrm{Kn} \approx 1$.

Since the flow is steady and fully developed $(dP/dx)H = [\tau_{xy}]_{-H/2}^{H/2}$. Thus,

$$[q_y]_{-H/2}^{H/2} = [\tau_{xy}u_x]_{-H/2}^{H/2} = -\frac{\rho u_b \sqrt{2RT}}{\overline{Q}} u_s \tag{17}$$

and

$$\int_{-H/2}^{H/2} \tau_{xy} \frac{\partial u_x}{\partial y} dy = \frac{\rho u_b \sqrt{2RT}}{\overline{Q}} (u_b - u_s) \tag{18}$$

The above equation suggests that as the Knudsen number increases and the velocity profile becomes flatter, most of the energy is dissipated at the walls, as expected.

For a steady and fully developed gravity-driven flow, we have

$$\frac{\partial}{\partial y}(\tau_{xy}u_x) + \rho g u_x = \frac{\partial q_y}{\partial y} \tag{19}$$

The total energy transfer to the wall, q_t, is equal to the work done by the gravity force

$$q_t = [q_y - \tau_{xy}u_x]_{-H/2}^{H/2} = \rho g u_b H \tag{20}$$

Here we use the fact that the bulk velocity in gravity-driven flow can be determined by utilizing the similarity between gravity and pressure-driven flows. Malek Mansour et al. [13] have shown that although from a Boltzmann equation perspective gravity and pressure-driven flows are different, the difference in the solutions scales with the *square* of the characteristic gravity parameter $\epsilon \equiv gmH/(2k_bT)$ which is expected to be small in practical applications. This parameter in our simulations was very small (significantly less than 0.1) so we expect that the solutions of the Boltzmann equation for pressure-driven flow to be valid for gravity-driven flow. Figure 2 shows that upon replacing $-dP/dx$ by ρg, $\overline{Q}$ as determined for pressure-driven flow accurately describes gravity-driven flow.

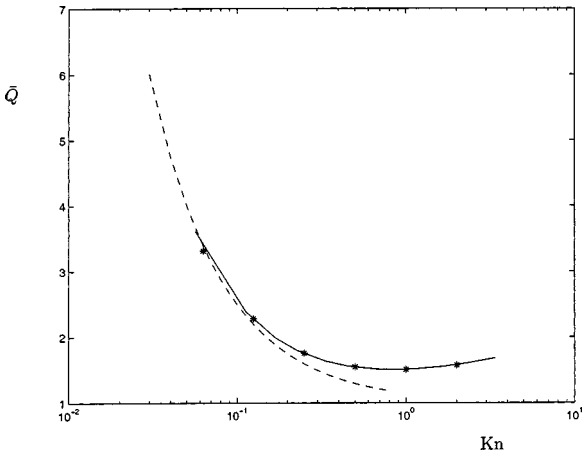

Fig. 2 Nondimensional flowrate $\bar{Q}$ as a function of the Knudsen number. The solid line denotes the numerical solution of the Boltzmann Eq. [12], the stars denote DSMC simulations of gravity-driven flow and the dashed line denotes the slip-flow prediction. Error estimates are given by the star size.

Substituting from above, we obtain

$$q_t = \frac{\rho u_b^2 \sqrt{2RT}}{\overline{Q}} \tag{21}$$

The energy dissipated inside the channel is

$$q_t + [\tau_{xy}u_x]_{-H/2}^{H/2} = \frac{\rho u_b \sqrt{2RT}}{\overline{Q}} (u_b - u_s) \tag{22}$$

We performed direct Monte Carlo simulations to verify these predictions. We show here results from the gravity-driven flow for

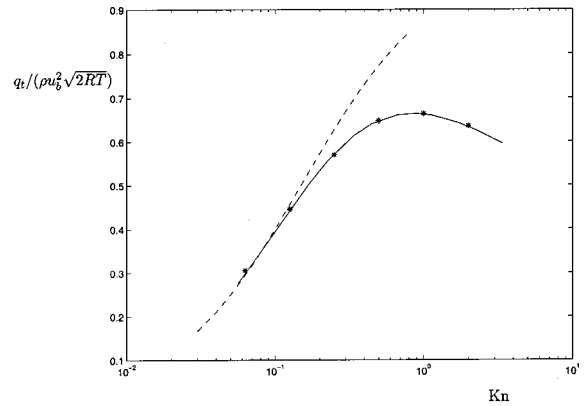

Fig. 3 Nondimensional total heat exchange $q_t/(\rho u_b^2\sqrt{2RT})$ as a function of the Knudsen number. The solid line denotes the theoretical prediction Eq. (21), the stars denote DSMC simulations of gravity-driven flow and the dashed line denotes the slip-flow prediction. Error estimates are given by the star size.

which a net energy exchange between wall and gas occurs and can thus be measured. Figure 3 shows that Eq. (21) is in good agreement with simulation results.

Acknowledgments

The author wishes to thank Pirouz Kavehpour, Lowell Baker and Professor John Lienhard V for helpful comments and discussions. This work was supported by the Singapore-MIT alliance.

References

[1] Cercignani, C., 1988, *The Boltzmann Equation and Its Applications*, Springer-Verlag, NY.
[2] Beskok, A., and Karniadakis, G. E., 1999, ''A Model for Flows in Channels and Ducts at Micro and Nano Scales,'' Microscale Thermophys. Eng., **3**, p. 43.
[3] Ohwada, T., Sone, Y., and Aoki, K., 1989, ''Numerical Analysis of the Shear and Thermal Creep Flows of a Rarefied Gas Over a Plane Wall on the Basis of the Linearized Boltzmann Equation for Hard-Sphere Molecules,'' Phys. Fluids A, **1**, p. 1588.
[4] Sone, Y., Ohwada, T., and Aoki, K., 1989, ''Temperature Jump and Knudsen Layer in a Rarefied Gas Over a Plane Wall: Numerical Analysis of the Linearized Boltzmann Equation for Hard-sphere Molecules,'' Phys. Fluids A, **1**, p. 363.
[5] Vincenti, W. G., and Kruger, C. H., 1965, *Introduction to Physical Gas Dynamics*, Krieger, FL.
[6] Ou, J. W., and Cheng, K. C., 1973, ''Viscous Dissipation Effects on Thermal Entrance Region Heat Transfer in Pipes With Uniform Wall Heat Flux,'' Appl. Sci. Res., **28**, p. 289.
[7] Hadjiconstantinou, N. G., and Simek, O., 2002, ''Constant-Wall-Temperature Nusselt Number in Micro and Nano Channels,'' J. Heat Transfer, **124**, p. 356.
[8] Chapman, S., and Cowling, T. G., 1970, *The Mathematical Theory of Non-Uniform Gases*, Cambridge University Press, Cambridge.
[9] Alexander, F., Garcia, A., and Alder, B., 1998, ''Cell Size Dependence of Transport Coefficients in Stochastic Particle Algorithms,'' Phys. Fluids, **10**, p. 1540, (Erratum: Phys. Fluids, **12**, p. 731(2000)).
[10] Hadjiconstantinou, N. G., 2000, ''Analysis of Discretization in the Direct Simulation Monte Carlo,'' Phys. Fluids, **12**, p. 2634.
[11] Garcia, A., and Wagner, W., 2000, ''Time Step Truncation Error in Direct Simulation Monte Carlo,'' Phys. Fluids, **12**, p. 2621.
[12] Ohwada, T., Sone, Y., and Aoki, K., 1989, ''Numerical Analysis of the Poiseuille and Thermal Transpiration Flows Between Parallel Plates on the Basis of the Boltzmann Equation for Hard-Sphere Molecules,'' Phys. Fluids A, **1**, p. 2042.
[13] Malek Mansour, M., Baras, F., and Garcia, A. L., 1997, ''On the Validity of Hydrodynamics in Plane Poiseuille Flows,'' Physica A, **240**, p. 255.

The Effect of a Cationic Surfactant on Turbulent Flow Patterns

G. Hetsroni
e-mail: hetsroni@tx.technion.ac.il
Fellow ASME

A. Mosyak

Department of Mechanical Engineering, Technion-Israel Institute of Technology, Haifa 32000, Israel

Y. Talmon
Department of Chemical Engineering, Technion-Israel Institute of Technology, Haifa 32000, Israel

A. Bernheim-Groswasser
Department of Chemical Engineering,
Ben Gurion University, Beer-Sheba 84105, Israel

J. L. Zakin
Ohio State University, Department of Chemical Engineering, Columbus, OH 43210, U.S.A.

The thermal pattern on a heated wall was studied for the flow of water and drag-reducing surfactant solutions in a channel. The wall of the channel was made of a thin foil, which was heated by direct current. The temperature of the foil, which reflects the local flow velocities, was measured by an infrared technique with high spatial and temperature resolution. The microstructure of the surfactant solution was studied by direct imaging cryogenic temperature transmission electron microscopy (Cryo-TEM). The most prevalent structures observed are thread-like micelles, which have been suggested to cause the modification of the thermal patterns. [DOI: 10.1115/1.1609482]

Keywords: Heat Transfer, Microstructures, Non-Newtonian, Polymers, Rheological, Thermal, Turbulence, Visualization, Vortex

1 Introduction

Reduction of friction losses in turbulent flows caused by the presence of polymer additives was first reported about fifty years ago. Virk [1] examined friction factor and velocity profile results for a large number of high polymer solutions, mostly but not all, in water. He noted that at relatively low concentrations many solutions reached lower limiting values in their friction factor/Reynolds number data. Virk [1] proposed an equation for the limiting maximum drag reduction asymptote (MDRA). Polymer effectiveness depends on the presence of high molecular weight species, which limits their applications because of the susceptibility of a high molecular weight components to degradation in high shear flows.

In the past decade considerable interest has developed in ''repairable'' drag reducing additives, such as surfactants for use in technological processes. Though surfactant drag reducing additives require higher concentrations than high polymers, their long life and greater percent of drag reduction make them very attractive for recirculation flows. Chara et al. [2] showed that the MDRA proposed by Virk [1] is not valid for the surfactant Habon G. (hexadecyldimethyl hydroxyethyl ammonium-2-hydroxy-3-naphtoate) solutions.

Investigation of the thermal development region for surfactant solutions was conducted by Gasljevic and Matthys [3]. Turbulent transport mechanism in a drag reducing flow with surfactant additive was investigated by Kawaguchi et al. [4]. They found that only large eddies are dominant near the wall. Warholic et al. [5] presented measurements of turbulence properties of a solution of tris-hydroxyethyl-ammonium acetate (Ethoquad T13-50) and sodium salicylate (NaSal) flowing in a 5.08 cm$\times$61 cm rectangular channel. The profiles of average velocity obtained by Warholic et al. [5] differ from those presented by Chara et al. [2] for surfactant solutions. If turbulence production depends on the properties of the surfactant solution, one should expect different systems to produce different velocity and temperature fields. Thus, it might be useful to connect the behavior of high drag-reducing surfactants with their microstructure.

One of the most outstanding characteristics of the near wall turbulence structure in a boundary layer of a channel flow is the presence of coherent structures. Coherent structures are responsible for most of the turbulence production, dissipation and transport phenomena. Donohue et al. [6], and Achia and Thompson [7] considering the near-wall coherent structures in so-called low

Contributed by the Heat Transfer Division for publication in the JOURNAL OF HEAT TRANSFER. Manuscript received by the Heat Transfer Division August 30, 2002; revision received June 18, 2003. Associate Editor: G. P. Peterson.

drag-reducing solutions, in which the drag reduction did not exceed 30%. Hetsroni et al. [8] studied this problem in high drag-reducing solution (drag reduction varied in the range of 46–85%). It was shown that the dimensionless streak spacing depends on the Reynolds number, based on wall-shear velocity of the solution.

On the other hand, the relation of steak spacing to the onset of turbulent drag reduction was not clarified. The first objective of the present study was to check whether or not the onset of turbulence drag reduction might be connected to spacing of near-wall turbulence structures. It was achieved by comparison of the experimental results obtained in the present study with data reported in [6,7].

Considerable research was also carried out to investigate microstructures of drag-reducing cationic surfactant systems [9]. The second aim of the present study was to gain more insight into the near-wall turbulence structure in high drag-reducing flow by analyzing solution micro-structure.

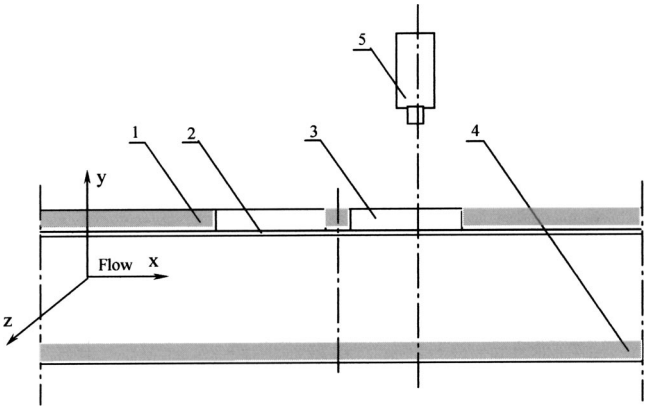

Fig. 2 Test section (1-top of the channel, 2-stainless steel strip, 3-window, 4-bottom of the channel, 5-IR camera)

2 Experiment

2.1 Experimental Facility. The experiments were conducted in a rectangular channel. The two-dimensional channel flow offers several advantages for studies of near-wall coherent structures, as flow visualization is then relatively easy.

The channel flow system is shown in Fig. 1. The 7.2 m long, 0.2 m wide, and 0.02 m deep rectangular channel comprised, twelve Plexiglas sections of length 0.6 m each. The sections were carefully joined to ensure a hydraulic smooth surface throughout. The temperature measurements were carried out in the test section. The heating strips 0.6×0.2 m each were installed inside the channel from the front end of the development section to a distance of 0.6 m beyond the test section. These strips were made of 0.05 mm thick stainless steel and arranged so that the boundary layer could be heated along different distances from the inlet to the test section. The latter was provided with two 0.2×0.16 m windows to which the strips were bonded with contact adhesive and coated on the air side with black mat paint about 0.02 mm thick. DC current up to 300A was applied to the heating strips, and measurements were taken at different lengths of the heated stretch. It was found that at the location of the test section, the temperature field was fully developed, i.e., the temperature distribution on the heated wall did not change in the streamwise direction. The test section is shown in Fig. 2.

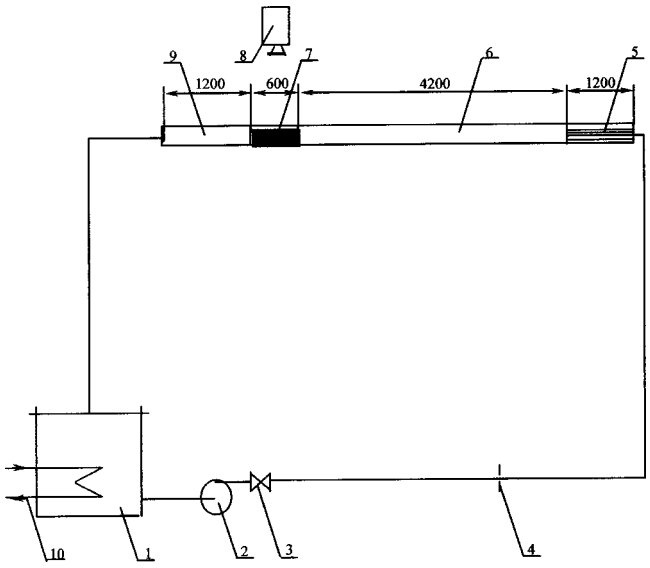

Fig. 1 Loop of rectangular channel (1-tank, 2-pump, 3-control valve, 4-flow meter, 5-strainghtener, 6-development section, 7-test section, 8-IR camera, 9-outlet section, 10-heat exchanger)

2.2 Measurement Techniques. To measure the temperature field on the heated wall a Thermal Imaging Radiometer was used with a typical horizontal and vertical resolution of 256 pixels per line, spatial resolution 0.05 mm, response time 0.04 s, sensitivity 0.1 K. Since the heating strip was very thin (0.05 mm), the temperature difference between its surfaces did not exceed 0.1 K, [8]. A computer program made it possible to store the information and to compute the statistics of the thermal field.

The water temperature was measured by a precision mercury thermometer with an accuracy 0.1 K. The mean flow velocity was measured with an accuracy $\pm1\%$, the electric power was determined with an accuracy $\pm0.5\%$. The pressure drop was measured by pressure transducers with an accuracy $\pm1.5\%$. The shear velocity was calculated with an accuracy $\pm4\%$.

2.3 Properties of the Surfactant Solution. The surfactant used was Habon G—a cationic surfactant of molecular weight 500. The content of delivered active material is 53.5% active surfactant, 10.2% isopropanol and 36.3% water. Concentrations reported are the concentrations of active surfactant. The head group of the surfactant is hexadecyldimethyl hydroxyethyl ammonium and the counter-ion is 3-hydroxy-2-naphthoate. The surfactant molecules form large thread-like micelles which are effective in causing drag reduction. In the present study we used an active surfactant concentration of 530 ppm (parts per million by weight in filtered, deionized water). Our data, based upon pressure drop and heat transfer measurements, did not show degradation of the solution during the experiments.

The kinematic viscosity was determined by a Cannon-Fenske capillary viscometer. The kinematic viscosity is $\nu=1.35\cdot10^{-6}$ m^2 s^{-1} at $t=20$°C and $1.15\cdot10^{-6}$ m^2 s^{-1} at $t=40$°C. In the experiments performed, the temperature of the surfactant solution was 22 ± 0.5°C, and the heated wall temperature ranged from 32 to 40°C. Thus, the Reynolds numbers for the 530 ppm Habon G solution were calculated based on a kinematic viscosity $\nu=1.25\cdot10^{-6}$ m^2 s^{-1}.

2.4 Microstructure Information. We examined the Habon G solution by direct imaging cryogenic temperature transmission electron microscopy (Cryo-TEM) [9]. Transmission electron microscopy is a direct imaging technique that affords microstructural information that does not require modeling for interpretation (contrary to indirect methods such as light and x-ray scattering). Cryo-TEM does not involve any staining or drying of the studied samples, thus it provides reliable images of the original microstructures in the studied systems.

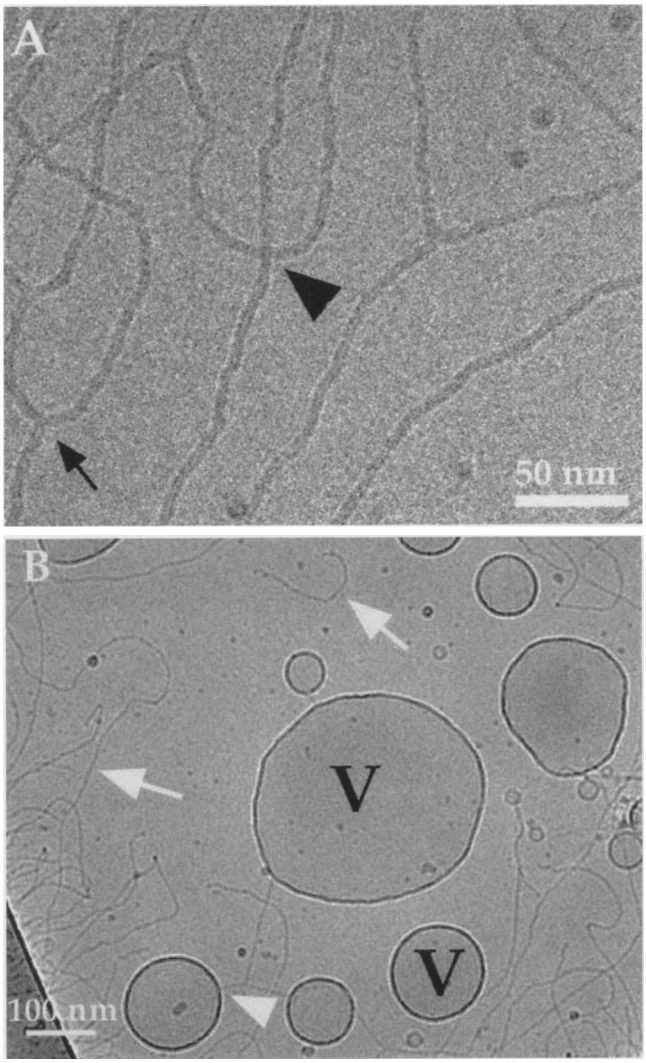

Fig. 3 Microstructure of the 530 ppm Habon G solution: (*a*) threadlike micelles; and (*b*) vesicles.

We prepared vitrified specimens for Cryo-TEM in a controlled environment vitrification chamber (CEVS) to ensure preservation of the original concentration, temperature, and thus the microstructure of the examined sample. As with all other types of material systems, TEM specimens of liquid systems have to be quite thin. The penetration power of even high energy electrons is rather limited. To avoid inelastic electron scattering that leads to image deterioration, and to take full advantage of phase-contrast in direct imaging, one needs to limit specimen thickness to about 0.2 μm.

The surfactant solution specimens were prepared for Cryo-TEM imaging by applying a small drop of the studied solution onto a perforated carbon film supported on an electron microscope grid, blotting it to form a thin (0.2 μm) film. By avoiding crystallization of water the microstructure is not disturbed and the images obtained reflect true microstructures in the original solutions. The solutions were quenched from 25°C, and 100% relative humidity. Specimens were examined in a Philips CM120 microscope, operated at 120 kV, using an Oxford CT-3500 cryo-holder maintained below −178°C. Micrographs were collected digitally [10] by a Gatan 791 MultiScan CCD camera with the DigitalMicrograph software package, using low-dose protocols to minimize electron-beam radiation-damage.

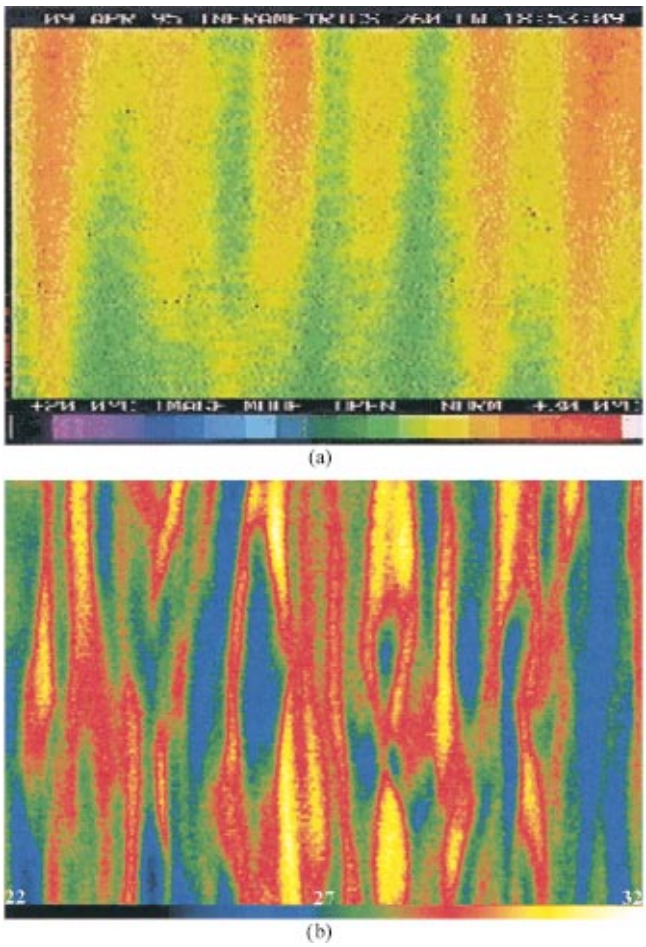

Fig. 4 Thermal pattern on the heated wall: (*a*) Flow of 530 ppm Habon G solution; and (*b*) Flow of water.

3 Results

3.1 Cryo-TEM Images. The most prevalent structures we observed are thread-like micelles, shown at high magnification in Fig. 3(*a*). Micrographs like this one show quite clearly inner structural details of the micelles such as branching domains (arrow) and overlap of micelles (arrowhead). It should be noted that threadlike micelles have been suggested as the one, possibly the most important, microstructural feature that modifies flow patterns in a flowing fluid and reduces drag [10].

Another feature seen in the examined solutions are vesicles, denoted by ''V'' in Fig. 3(*b*). These are balloon-like structures made of a double-layer membrane. Such structures are found in many biological and synthetic amphiphiles [11]. In this micrograph we see vesicles coexisting with threadlike micelles (arrows). Much to our surprise we have detected junctions between vesicles and threadlike micelles. In fact, three such junctions, one denoted by an arrowhead are seen in the lower left part of the field of view of Fig. 3(*b*). The three micelles connecting the three vesicles are connected by a three-fold junction seen just above the arrowhead. Zheng et al. [12] hypothesize that the straining actions of flow disrupt vesicles and thus induce structural instability of the fragments that leads to their reconstruction into networks of branching threadlike micelles.

3.2 Thermal Streaks at the Wall. One important aspect of turbulent flow is believed to be streamwise vortex structure with its accompanying low-speed streaks. The temperature distribution on the heated wall can be considered as a trace of the flow structure there, i.e., the turbulent structures in the boundary layer cause

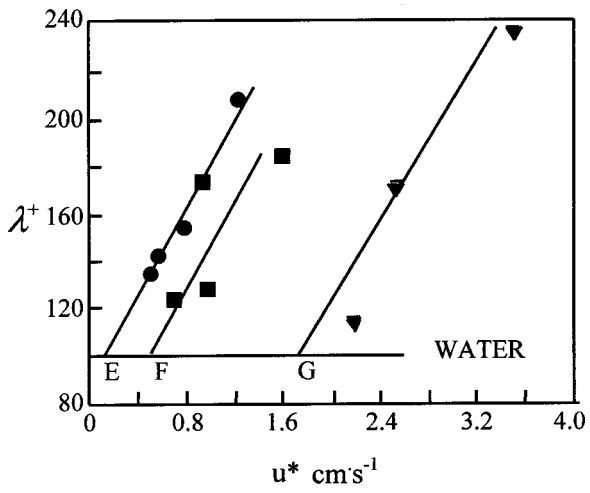

Fig. 5 Relationship between dimensionless streak spacing and wall shear velocity (●-present study; ■-Donohue et al. (1972); and ▼-Achia and Thompson (1977))

the temperature distribution on the wall, including the thermal streaks. The streak spacing results were obtained by IR visualization and from spatial correlation of the temperature. The images of thermal streak structures are shown in Figs. 4(*a*) and 4(*b*). Figure 4(*a*) shows a typical example of frames reproduced from a video motion picture of surfactant drag reducing flow. Figure 4(*b*) is a representative image of the thermal streak structure, at the same shear velocity, for water flow. These pictures are plan view, the flow moves from the bottom to the top of the figures. The thermal streak spacing was calculated by two-point correlation's [8]. The dimensionless thermal streak spacing $\lambda^+ = \lambda u^*/\nu$ (λ is the streak spacing, u^* shear velocity, calculated from the pressure drop, $u^* = \sqrt{\tau/\rho}$, τ shear stress, ρ density, ν kinematic viscosity) obtained from the temperature field on the heated wall in water flow was $\lambda^+ = 100 \pm 10$. The result agrees well with data reported by Iritani et al. [13]. In the drag reducing flows λ^+ increase when the shear velocity increases.

Figure 5 represents streak spacing measurements for different drag reducing solutions. The data of Donohue et al. [6] and Achia and Thompson [7] for polymer solutions are also shown for comparison. Points E, F, G, at which the lines $\lambda^+ = f(u^*)$ cross the line $\lambda^+ = 100$ indicate a threshold value of wall shear for the particular drag reducing solution. The increase in the value of λ^+ associated with drag reduction takes place at values of u^* higher than the onset wall shear. Thus, the drag reducing effect starts with wall shear stresses larger than a threshold value, which depends on the nature of the additive and its concentration. When surfactant flow is compared with flows of polymer solution, one can see that the 530 ppm Habon G solution has a significantly lower value of onset shear velocity. The correlation between λ^+ and the percentage of drag reduction was given by Oldaker and Tiederman [14]: $\lambda^+ = 1.9\mathrm{DR} + 99.7$. The fact that we refer here to parallel shift of the λ^+ profile, means that at the same value of friction velocity, the percentage of drag reduction increases with the decrease of the onset velocity. Correspondingly we consider the value of ν/u^*_{on} as the length scale and the value of $\nu/u^{*\,2}_{on}$ as the time scale. Different drag-reducing solutions produce velocity field with different length and time scale.

Conclusion

The shear velocity for onset of drag reduction for Habon G surfactant solutions is significantly lower than those for polymer solutions. Changes in the shape of thermal streaks and an increase in streak spacing are the main features in drag reduced flow. Dimensionless streak spacing, at given value of wall-shear, depends on onset of wall-shear, velocity of the solution. The results are consistent with the hypothesis that one of the prerequisites for the phenomenon of drag reduction is sufficiently enhanced length and time scale of the velocity field. Different drag-reducing solutions produce velocity field with different length and time scales.

The existence of an extremely low value of onset velocity is associated with microstructure of the solution. From the study of microstructure one can conclude that the surfactant used in the present study contains threadlike micelles with junctions between them. These data provide the first experimental demonstration that well developed network, including branched micelles, is connected with streak formation.

Acknowledgments

This research was supported by the Fund for the Promotion of Research at the Technion. A. Mosyak is supported by The Ministry of Absorption of Israel. This research was also supported by the Israeli Ministry of Science.

Nomenclature

D_h = channel hydraulic diameter
L = channel length
$u^* = (\tau/\rho)^{0.5}$, shear velocity
u^*_{on} = onset shear velocity
λ = thermal streaks spacing
$\lambda^+ = \lambda u^*/\nu$, dimensionless thermal streaks spacing
ρ = density
υ = kinematic viscosity
Δp = pressure drop
$\tau = \Delta p D_h/4L$, shear stress

References

[1] Virk, P. S., 1975, "Drag Reduction Fundamentals," AIChE J., **21**, pp. 625–656.
[2] Chara, Z., Zakin, J. L., Severa, M., and Myska, J., 1993, "Turbulence Measurements of Drag Reducing Surfactant Systems," Exp. Fluids, **16**, pp. 36–41.
[3] Gasljevic, K., and Matthys, E. F., 1997, "Experimental Investigation of Thermal and Hydrodynamic Development Regions for Drag Reducing Surfactant Solutions," J. Heat Transfer , **119**, pp. 80–88.
[4] Kawaguchi, Y., Tawaraya, Y., Yabe, A., Hishida, K., and Maeda, M., 1996, "Turbulent Transport Mechanism in Drag Reducing Flow With Surfactant Additive Investigated by Two Component LDV," in *Eighth International Symposium on Applications of Laser Techniques to Fluid Mechanics*, **2**, July 8–11, Lisbon, Portugal, pp. 29.4.1–29.4.7.
[5] Warholic, M. D., Schmidt, G. M., and Hanratty, T. J., 1999, "The Influence of a Drag-Reducing Surfactant on a Turbulent Velocity Field," J. Fluid Mech., **388**, pp. 1–20.
[6] Donohue, G. L., Tiederman, W. G., and Reischman, W. G., 1972, "Flow Visualization of the Near-Wall Region in Drag-Reducing Flow," J. Fluid Mech., **56**, pp. 559–575.
[7] Achia, B. U., and Thompson, D. W., 1977, "Structure of the Turbulent Boundary in Drag-Reducing Pipe Flow," J. Fluid Mech., **81**, pp. 439–464.
[8] Hetsroni, G., Zakin, J. L., and Mosyak, A., 1997, "Low-Speed Streaks in Drag-Reduced Turbulent Flow," Phys. Fluids, **9**, pp. 2397–2404.
[9] Talmon, Y., 1999, "Cryogenic Temperature Transmission Electron Microscopy in the Study of Surfactant Systems," *Modern Characterization Methods of Surfactants Systems*, B. P. Binks, Editor, Marcel Dekker, NY, pp 147–178, Chap. 6.
[10] Lu, B., Zheng, Y., Scriven, L. E., Davis, H. T., Talmon, Y., and Zakin, J. L., 1998, "Effect of Variations Counterion-to-Surfactant Ratio on Rheology and Microstructures of Drag Reducing Cationic Surfactant Systems," Rheol. Acta, **37**, pp. 528–548.
[11] Evans, F. E., and Wennerström, H., 1999, *The Colloidal Domain*, 2nd ed., VCH, New York.
[12] Zheng, Y., Lin, Z., Zakin, J. L., Talmon, Y., Davis, H. T., and Scriven, L. E., 2000, "Cryo-TEM Imaging the Flow-Induced Transition From Vesikles to Threadlike Micelles," J. Phys. Chem. B, **104**(22), pp. 5263–5271.
[13] Iritani, Y., Kasagi, N., and Hirata, N., 1983, "Heat Transfer Mechanism and Associated Turbulence Structure in the Near Wall Region of a Turbulent Boundary Layer," in *Fourth Symposium of Turbulent Shear Flows*, 12–14 September 1983, Karslruhe, F.R. Germany.
[14] Oldaker, O. K., and Tiederman, W. G., 1977, "Spatial Structure of the Viscous Sublayer in Drag-Reducing Channel Flow," Phys. Fluids, **20**(10), pp. 133–144.